SEVENTH FRAMEWORK PROGRAMME

THEME 6: Environment (including climate change)

Contract for: **Collaborative Project**

D.3.4. BRIDGE observation report

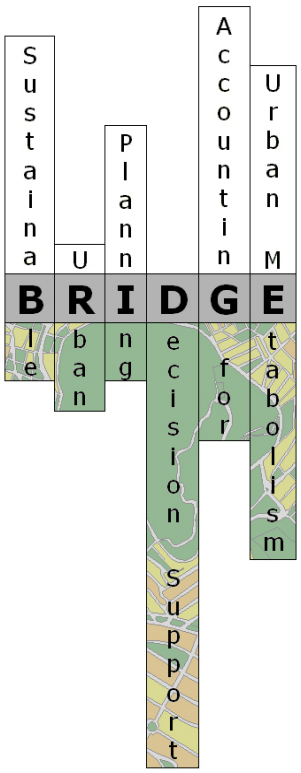

Project acronym: **BRIDGE**

Project full title: sustainaBle uRban planning Decision support accountinG for urban mEtabolism

Contract no.: 211345

Date: 08/07/2011

Document Reference: 211345_013_TR_CNR

Book Captain: Enzo Magliulo (CNR)

Authors: Afroditi Synnefa (NKUA), Anicenta Bubak (IETU), Annika Nordbo (UHEL), Anu Riikonen (UHEL), Barbara Jaros (IETU), Beniamino Gioli (CNR IBIMET), Chloe Franks (KCL), Cris Castillo (KCL), Donatella Spano (CMCC), Duick Young (KCL), Eero Nikinmaa (UHEL), Eero Nikinmaa (UHEL), Enzo Magliulo (CNR ISAFOM), Franco Miglietta (CNR IBIMET), Fredrik Lindberg (Goteborg University and KCL), Heikki Setälä (UHEL), Inês Cabrita Andrade Dos Santos (KCL), Jiangping He (KCL), Jinda Sae-Jung (KCL), Katy Francis (KCL), Leena Jarvi (UHEL), Lukas Pauscher (KCL), Marc Thomas (KCL) Helen Ward (KCL), Mariana Gouvea (KCL), Marina Stathopoulou (FORTH), Mark de Jong (KCL), Martin Wooster (KCL), Mattheos Santamouris (NKUA), Matthew Tallis (University of Southampton), Oscar Finnemore (KCL), Paul Smith (KCL), Piero Toscano (CNR IBIMET), Pierpaolo Duce (CNR IBIMET), Pru Robinson(KCL), Serena Marras (CMCC), Simone Kotthaus (KCL), Sue Grimmond (KCL), Timo Vesala (UHEL), Tom Smith (KCL), Tomasz Staszewski (IETU), Nektarios Chrysoulakis (FORTH), Mitraka Zina (FORTH)

Issue: 1.0

Deliverable no.: D.3.4

Dissemination Level: PU

Document Status Sheet

Issue	Date	Author	Comments
0.1	March 11/11	Enzo Magliulo	Draft preparation and dissemination for partners contribution collection
0.2	April 27/11	Enzo Magliulo	First draft circulated
0.3	May 15/11	Enzo magliulo	second draft circulated
0.4	June 10/11	Enzo magliulo	Final draft
0.5	June 27/11	Enzo magliulo	Final document
0.6	July 07/11	Nektarios Chrysoulakis	
1.0	July 08/11	Zina Mitraka	

Table of Contents

Part 1 – Measurements in situ

Part 2 - Remote Sensing and GIS data collection

Part 3 – Socio-economic data collection

Part 1 – Measurements in situ

1. Introduction

The term “urban metabolism” is used to indicate the exchange and transformation of energy and matter between a city and its environment. In the BRIDGE (sustainaBle uRban plannIng Decision support accountinG for urban mEtabolism) project, the WP4 is dedicated to collect data of urban fluxes measured in five European cities ((Helsinki, Athens, London, Firenze and Gliwice) as representative of the different city typologies and influenced by different policy and resource availability. Urban fluxes are strongly affected by the urban surface characteristics and changes in land use (e.g. new buildings construction, increasing of green areas etc.) mainly determine changes at regional scale.

Exchanges of energy, heat, moisture, carbon and pollutant are then measured using different techniques, during the project, for each case study. Also, local and regional urban fluxes are simulated by models in selected cities. In addition, GIS data and remote sensing methodologies are used to investigate on the role of land use in affecting the surface exchanges between the urban canopy and the atmosphere.

1.1 Purpose of the document

This document is the D.3.4 BRIDGE Observation Report, part 1 ‘in situ measurements’.

Task 3.1 has the role to systematically monitor the main fluxes using in situ techniques for each case study (Helsinki, Athens, London, Firenze and Gliwice).

The **aim of this document** is to describe in detail the main results obtained from each case study of the BRIDGE Project. In particular, it contains highlights of the main outcome of in situ measurements concerning, urban meteorology, turbulent fluxes, air quality, urban hydrology and plant and soil related measurements collected during the project - and it shows the different behavior of the five cities in release or sequester heat, water, carbon and pollutant. The master document describes the main characteristics of each case study and summarize the chief results attained. Comprehensive data analysis in graphical form is reported in annexes.

Methodologies used and protocols applied to collect data are described in details in D3.5.

1.2 Project Overview

Urban metabolism considers a city as a system and distinguishes between energy and material flows. “Metabolic” studies are usually top-down approaches that assess the inputs and outputs of food, water, energy, etc. from a city, or that compare the metabolic process of several cities. In contrast, bottom-up approaches are based on quantitative estimates of urban metabolism components at local scale, considering the urban metabolism as the 4D exchange and transformation of energy and matter between a city and its environment. Recent advances in bio-physical sciences have led to new methods to estimate energy, water, carbon and pollutants fluxes. However, there is poor communication of new knowledge to end-users, such as planners, architects and engineers.

BRIDGE aims at illustrating the advantages of considering environmental issues in urban planning. BRIDGE will not perform a complete life cycle analysis or whole system urban metabolism, but rather focuses on specific metabolism components (energy, water, carbon, pollutants). BRIDGE’s main goal is to develop a Decision Support System (DSS), which has the potential to propose modifications on the metabolism of urban systems towards sustainability.

BRIDGE is a joint effort of 14 Organizations from 11 EU countries. Helsinki, Athens, London, Firenze and Gliwice have been selected as case study cities. The project uses a “Community of Practice” approach, which means that local stakeholders and scientists of the BRIDGE meet on a regular basis to learn from each other. The end-users are therefore involved in the project from the beginning. The energy and water fluxes

are measured and modeled at local scale. The fluxes of carbon and pollutants are modeled and their spatio-temporal distributions are estimated. These fluxes are simulated in a 4D context and also dynamically by using state-of-the-art numerical models, which normally simulate the complexity of the urban dynamical process exploiting the power and capabilities of modern computer platforms. The output of the above models lead to indicators which define the state of the urban environment. The end-users decide on the objectives that correspond to their needs and determine objectives' relative importance. Once the objectives have been determined, a set of associated criteria are developed to link the objectives with the indicators. BRIDGE integrate key environmental and socio-economic considerations into urban planning through Strategic Environmental Assessment. The BRIDGE DSS evaluates how planning alternatives can modify the physical flows of the above urban metabolism components. A Multi-criteria Decision Making approach has been adopted in BRIDGE DSS. To cope with the complexity of urban metabolism issues, the objectives measure the intensity of the interactions among the different elements in the system and its environment. The objectives are related to the fluxes of energy, water, carbon and pollutants in the case studies. The evaluation of the performance of each alternative is done in accordance with the developed scales for each criterion to measure the performance of individual alternatives.

Several studies have addressed urban metabolism issues, but few have integrated the development of numerical tools and methodologies for the analysis of fluxes between a city and its environment with its validation and application in terms of future development alternatives, based on environmental and socio-economic indicators for baseline and extreme situations. The innovation of BRIDGE lies in the development of a DSS integrating the bio-physical observations with socio-economic issues. It allows end-users to evaluate several urban planning alternatives based on their initial identification of planning objectives. In this way, sustainable planning strategies will be proposed based on quantitative assessments of energy, water, carbon and pollutants fluxes.

1.3 Definitions and Acronyms

Acronyms

CAZ	Central Activity Zone
CoP	Community of Practice
DSS	Decision Support System
GIS	Geographical Information System
GLA	Greater London Authority
QA/QC	Quality assurance/quality Check
RS	Remote Sensing
DEM	Digital Elevation Model
ASTER	Advanced Thermal Emission and Reflection Radiometer

2. Summary

Urban communities consume material and energy and eliminate the wastes from the process. Energy and mass are exchanged by urban environments and fluxes are modulated by human activities, such as heating and air conditioning, vehicular traffic, changes in vegetative cover, waste production etc., in what has been termed "urban metabolism".

The workpackage three of BRIDGE project includes the Data Collection and Analysis activities in the various case studies, representing a unique attempt to collect and to analyze an integrated database suitable for the development and validation of models and methodologies for the analysis of fluxes between the city and its environment.

The work package is further subdivided into 3 tasks, aiming at investigating the urban environment and quantitatively assessing geographic, bio-physical and socio-economic variables by appropriate approaches.

Task 3.1 applies established and newly developed methodologies aimed at collecting comprehensive data sets by means of in situ observations.

The overall BRIDGE measurement plan in the 5 case studies is not orthogonal – in the sense that not all relevant parameters are measured or common methodologies applied in in every city – due to the limitation in available resources for the project.

A common core of measurements had been performed in all case studies. These concerns chiefly meteo data and the turbulent exchange of mass and energy as measured on an hourly basis by city adapted eddy covariance apparatus. All case studies but Athens feature a tower were such data are recorded on a continuous basis. Some of these sites have by now collected time series as long as five years (Firenze) or slightly less (Helsinki), thanks to installations that already existed and were operational when BRIDGE was started.

A new dedicated observation site was established in Gliwice, which was run regularly throughout the duration of BRIDGE producing high quality data. In the case of London and Helsinki, an eddy tower was operational when WP3 activity was initiated and was later followed by a companion installation at a later stage.

In some case studies, the main observation tower was complemented with other micrometeorological apparatus providing hourly measurements of the net flux of species different form CO_2 and H_2O, such as dust particles in Firenze and Helsinki. In the first instance fluxes were segregated by particle diameter and the net flux for several aerosol size classes could be assessed, in the other one only the overall net exchange across a range of sizes was available.

In the case of London – the most heavily instrumented BRIDGE site - an independent measurement of sensible heat flux could be carried out by means of scintillometer, which made for an useful independent data set to be used for comparison with the tower data. In this regard, London is a special case where a high level of redundancy in available data allows for better QA/QC operations, gap filling and comparative analysis aimed at assessing the most appropriate approach toward collecting meaningful environmental datasets.

While most of data collected are being used at the site level to evaluate various different models, only a common temporal window in these time series was extracted and could be used into the subsequent common project workflow for the final aim of developing and testing BRIDGE DSS. Both limitations in financial resources and computer time prevented running some of the models for the entire observation period. This was known *a priori* and did not in any way impair the achievements of project goals.

Full exploitation of the data collected during the course of the project is beyond the scope and the possibilities of BRIDGE, but available datasets represent a powerful tool for further development in this area and possible project follow-ups, allowing new insights into the many processes occurring in European city metabolism.

Beside the common batch of meteo and flux measurements, many were the site specific studies carried out by means of either environmental parameters collected routinely and by intensive campaigns.

In Firenze a 2 wavelength LIDAR was deployed on the observation tower, to provide dust profiles and planetary boundary layer height several times in a day. Also the biophysical essays of air quality are specific of this study site.

Helsinki was the only city where soil water, CO2 content and flux measurements where carried out as well as Stormwater quantity and quality. In the latter case, it could be shown that the contribution of urban trees to urban metabolism is a function of growing site conditions. As for stormwater, automated setups were deployed in sites differing for land use intensity, measuring runoff and water ion contents and turbidity.

Athens did not share the common core of environmental observations with the other case studies. The experimental plan was in fact specifically designed to address the peculiar environmental problems of the municipality of Egaleo, a suburb of Athens. Specific aims were the quantification and modeling of heat

island effects by means of ground based measurements; outdoor environmental assessment using a mobile meteorological station measuring wind and pollutant profiles as well as Radiative temperature at the street and building level; the assessment of the quality of the indoor environment of residential buildings and the impact of the heat island effect on cooling loads of buildings.

The outcome of few modeling exercises are reported here, rather then in WP4 deliverables. The reason for this relays in the fact that WP3 resources were used to carry bon the activities and that these appraoches were data-oriented and made use of specific subset of data which were not considered, in the first instance, in the batch of models adopted and developed in WP4. This is the case of the dust deposition simulations carried out for London and Firenze and for the ACASA model. In the latter case, the outcome of simulations was used as a development tool for measurements, I order to identify lack of representativeness or intrinsic problems of specific measurements

2.1 Partners involved

1. CNR
Consiglio Nazionale delle Ricerche, Italy
Enzo Magliulo (enzo.magliulo@cnr.it)
Franco Miglietta (f.miglietta@ibimet.cnr.it): Firenze case study leader

2. CMCC
Centro Euro- Mediterraneo per i Cambiamenti Climatici S.c.a.r.l, Italy
Donatella Spano (spano@uniss.it)

4. KCL
King's College London
Sue Grimmond (sue.grimmond@kcl.ac.uk): London case study leader

4. NKUA
National and Kapodistrian University of Athens, Greece
Mattheos Santamouris (msantam@phys.uoa.gr): Athens case study leader

5. FORTH
Foundation for Research and Technology – Hellas, Greece
Nektarios Crysoulakis (zedd2@iacm.forth.gr)

6. SOTON
School of Biological Sciences-United Kingdom
Prof. Gail Taylor (G.Taylor@soton.ac.uk)

7. UHEL
University of Helsinki, Finland
Timo Vesala (timo.vesala@helsinki.fi): Helsinki case study leader

8. IETU
Instytut Ekologii Terenów Uprzemysłowionych, Poland
Tomasz Staszewski (stasz@ietu.katowice.pl): Gliwice case study leader

3. London Case Study

3.1 Site description

The Greater London Authority (GLA), through The Greater London Authority Act 1999, has responsibility for strategic planning in London . The GLA consists of 32 Boroughs and the City of London. Of specific interest to BRIDGE is the Central Activity Zone (CAZ). This area is where the central government offices, headquarters and embassies, most of the financial and business services sector and the offices of trade, professional bodies, institutions, associations, communications, publishing, advertising and the media are located . The CAZ accounts for nearly 30% of all London's jobs and is projected to accommodate 36% of London's employment growth to 2026 .

The London Plan provides the background and expected changes in London for the next 20-25 years . The latest versions of the plan, GLA (2009) and GLA (2008) , provide descriptions of London now and in the future. In these documents the CAZ is identified as important terms of future planning of London. In addition to the London Plan, two other planning documents are relevant for providing the context for London :

1) The Draft Mayor's Transportation Strategy
2) The Mayor's Economic Development Strategy (GLA 2010)

3.2 Summary of results

London case study is characterized by a great complexity of investigations involving many different approaches and using up-to-date techniques for *in situ*, remote sensing and socio-economic measurements.

It has been decided to collate all this information in a comprehensive report attached as Annex 3

3.3 Conclusions

In this section a few of the lessons learnt from the BRIDGE project are identified. These are subdivided into the main components of the report.

From the site characterization

- The locations of street trees in London are a very political issue (GLA 2007[1], 2011) which has meant that obtaining data about the current location of trees was very time consuming.
- The Street Tree Inventory which was obtained was incomplete so could not very reliably used as a basis for identifying where new trees could be located.
- LiDAR data provided complete data coverage. Analysis of these data using methods developed here have allowed for consistent analysis across the CAZ.
- Green roofs have been built in locations beyond those identified as potential locations.
- The total roof area that could potentially be retrofitted with green roofs in the CAZ is 4,987,104 m^2 (~15 % of the total CAZ area) or ~ 92 % of the total roofed area. The target increase green roofs in of 100,000 m^2 by 2012 would require the development in 2011-12 to be over five times that of the past two years.
- Currently about 0.6% of the CAZ roofs are green.
- From comparison of field and LiDAR data, tree characteristics are well correlated with the LiDAR yielding greater diameters and very similar heights.
- Public trees are generally taller and have wider crown diameter than trees on private land.

From observations:

- Automated data archive and delivery system (KUMA) has been developed. This has facilitated the use of data and identification of potential data issues in a more rapid manner.
- Redundancy in instrumentation is extremely useful for evaluating and verifying data.
- There is the potential to use a wide range of different sources of climate data in London. However, care needs to be taken as the network have different siting, instrumentation and aims which mean that modifications to the data may be necessary to make one consistent data set.
- WXT510 rain gauges do not appear to be usable for precipitation measurements within the central city in somewhere as acoustically noisy as London.
- It may be possible to use ceilometer backscatter to identify rainfall occurrence. This will provide additional redundancy for rainfall observations.
- Data once ratified will provide new insight into a range of processes occurring in the central part of a European mega-city.
- The data collected will be used to evaluate models which are used within the Decision Support System.

Data analysis is continuing, when the data sets are finalized these will be released and published.

3.4 References

Akbari H, Pomerantz, M, Taha, H. (2001) Cool surfaces and shade trees to reduce energy use and improve air quality in urban areas. Solar Energy. 70(3), 295-310.

Allen L, F Lindberg, CSB Grimmond (2010) Global to city scale model for anthropogenic heat flux, International Journal of Climatology doi: 10.1002/joc.2210 http://onlinelibrary.wiley.com/doi/10.1002/joc.2210/pdf

Backsik, Z, Mink, J. & Keresztury, G. (2004) FTIR spectroscopy of the atmosphere. I. Principles and methods. Applied Spectroscopy Reviews. 39. 295 – 363.

Baldwin, V.C. Jr, Peterson, K.D, Burkhart. H.E, Amateis, R.L, and Dougherty, P.M. (1997) Equations for estimating loblolly pine branch and foliage weight and surface area distributions, Canadian Journal of Forest Research. 27, 918–927

Basara, J.B, Illston, B.G, Winning, T.E. and Fiebrich, C.A (2009) Evaluation of Rainfall Measurements from the WXT510 Sensor for Use in the Oklahoma City Micronet. The Open Atmospheric Science Journal, 3, 39–47.

Beckett, K.P. Freer-Smith, P.H. Taylor, G. 2000. The capture of particulate pollution by trees at five contrasting urban sites. Arboricultural Journal. 24: 209–230

Bhaskaran, S, Paramananda, S. and Ramnaryan, M. (2010) Per-pixel and object-oriented classification methods for mapping urban features using Ikonos satellite data. Applied Geography, 30, 650-665

Blasing, T. J. (2009) CDIAC - Recent greenhouse gas concentrations. [Online]. Available from: http://cdiac.ornl.gov/pns/current_ghg.html. [Accessed 17th January 2010].

Brandtberg T, Warner T, Landenberger RE, and McGraw JB (2003) Detection and analysis of individual leaf-off tree crowns in small footprint, high sampling density LiDAR data from the eastern deciduous forest in North America. Remote Sensing of Environment, 85, 290−303.

Campbell Scientific Ltd. (2010) ARG100 Tipping Bucket Raingauge: User Guide. [Online] Available from: ftp://ftp.campbellsci.com/pub/csl/outgoing/uk/manuals/arg100.pdf [Accessed 21 December 2010].

Chen Y, Su W, Li J, Sun Z. (2009) Hierarchical object oriented classification using very high resolution imagery and LIDAR data over urban areas. Advances in Space Research, 43, 1101-1110.

Christen A, Crawford B, Liss K, Siemens C. 2010 Soil properties at the Vancouver EPiCC experimental sites. Environmental Protection in Canadian Cities Technical Report No. 2

Christen, A, and R. Vogt, 2004: Energy and radiation balance of a central European city. International Journal of Climatology, 24, 1395-1421

Clark, M.L, Clark, D.B. and Roberts, D.A. (2004) Small-footprint LiDAR estimation of sub-canopy elevation and tree height in a tropical rain forest landscape, Remote Sensing of Environment, 9 (1), 68–89.

Coutts, A, J. Beringer, and N. Tapper, 2007a: Characteristics influencing the variability of urban CO2 fluxes in Melbourne, Australia. Atmos. Environ, 41, 51-62.

Coutts, A, J. Beringer, and N. Tapper, 2007b: Impact of increasing urban density on local climate: Spatial and temporal variations in the surface energy balance in Melbourne, Australia. J. Appl. Meteor. Clim, 46, 477-493.

CWOP (2010) Siting Guidelines [Online] Available at: http://www.davisnet.com/product_documents/weather/app_notes/apnote_30.pdf [Accessed 19th April]

Davis (2010) Vantage Pro instruction manual [Online] Available at: http://www.davisnet.com/support/weather/support_docs.asp?dtype=1 [Accessed 16th May 2010]

Del Campo L, R Pérez-Sáez, X Esquisabel, I Fernández, MTello, 2006: New experimental device for infrared spectral directional emissivity measurements in a controlled environment. Review of Scientific Instruments, 77,113 111.

Delta-T 1998 Theta probe soil moisture sensor: type ML2 user manual ML2-UM-1. Delta-T Devices Ltd.

Delta-T 1999 Theta probe soil moisture sensor: type ML2x user manual ML2x-UM-1.2.1. Delta-T Devices Ltd.

Delta-T 2010 User manual for SM300 soil moisture sensor – SM300-UM-1.1. Delta-T Devices Ltd, Cambridge, UK.

ERG – KCL: Environmental Research Group – King's College London

GATS Inc. (2009) Spectral calculator, atmospheric gas spectra, infrared molecular absorption spectrum [Online]. Available from: http://www.spectralcalc.com/spectral_browser/db_intensity.php. [Accessed 15th December 2009].

Getter K & Rowe D (2006) The role of green roofs in sustainable development. HortScience. 41, 1276–1286

GLA 2011 Branching out: The future for London's street trees. London Assembly, Environment Committee, 49pp. http://www.london.gov.uk/sites/default/files/FINAL%20street%20trees%20report.pdf

Goodwin, N.R, Coops, N.C, Tooke, T.R, Christen, A, and Voogt, J.A. (2009) Characterizing urban surface cover and structure with airborne LiDAR Technology. Canadian Journal of Remote Sensing. 35, 297-309.

Grant G (2006) Extensive Green Roofs in London. Urban Habitats, 4 (1), 51-65

Griffith, DWT & Jamie IM (2000) Fourier transform infrared spectrometry in atmospheric and trace gas analysis. Encyclopaedia of Analytical Chemistry. Meyers, R. A, Ed. Chichester: John Wiley & Sons Ltd

Griffith, DWT (2006) MALT 5 User's Guide, Version 5.2. [Electronic document] Available with MALT 5 software.

Grimmond CSB, HA Cleugh, and TR Oke, 1991: An objective urban heat storage model and its comparison with other schemes. Atmos. Environ, 25B, 311-326.

Grimmond CSB, Oke TR (1999) Aerodynamic properties of urban areas derived, from analysis of surface form. Journal of Applied Meteorology 38:1262-1292

Grutter M (2003b) Multi-gas analysis of ambient air using FTIR spectroscopy over Mexico City. Atmosfera. 16. 1-13.

Grutter, M, Flores, E, Basaldud, R. & Ruiz-Suarez, L. G. (2003a) Open-path FTIR spectroscopic studies of the trace gases over Mexico City. Atmospheric Ocean Optics. 16. 232-236.

Harrison, R.M. (2001) Pollution: causes, effects and control. Cambridge: RSOC.

Hinsley SA, Hill, RA, Gaveau DLA & Bellamy PE (2002) Quantifying woodland structure and habitat quality for birds using airborne laser scanning. Functional Ecology, 16, 851– 857.

Holmgren J, Persson Å (2004) Identifying species of individual trees using airborne laser scanner. Remote Sensing of Environment 90:415-423

Honjo T and Takakura T (1990-91) Simulation of thermal effects of urban green areas on their surrounding areas. Journal of Energy and Buildings, 15–16, 443–446.

http://aurn.defra.gov.uk/

http://badc.nerc.ac.uk/home/index.html

http://cf-pcmdi.llnl.gov/

http://geography.kcl.ac.uk/micromet/index.htm

http://geography.kcl.ac.uk/micromet/wordpress/?page_id=425,

http://livingroofs.org/2010022858/green-roof-types/greenrooftypes.html (17 April 2011)

http://livingroofs.org/2010030161/green-roof-types/intens.html

http://ukclimateprojections-ui.defra.gov.uk

http://weather.lgfl.org.uk/

http://weather.lgfl.org.uk/qgraphs.aspx

http://weather.lgfl.org.uk/qtables.aspx

http://www.bauder.co.uk/media-centre/

http://www.bauder.co.uk/media-centre/project-gallery

http://www.geog.ubc.ca/~epicc/reports/Vancouver-EPiCC-Tech-Report-2.pdf

http://www.greenbuildingpress.co.uk/article.php?article_id=700

http://www.greenbuildingpress.co.uk/article.php?article_id=700

http://www.greenroofs.com/projects/pview.php?id=1066

http://www.greenroofs.com/projects/pview.php?id=393

http://www.greenroofs.com/projects/pview.php?id=510

http://www.greenroofs.com/projects/pview.php?id=549

http://www.greenroofs.com/projects/pview.php?id=550

http://www.greenroofs.com/projects/pview.php?id=648

http://www.greenroofs.com/projects/pview.php?id=660

http://www.greenroofs.com/projects/pview.php?id=77

http://www.greenroofs.com/projects/pview.php?id=85

http://www.greenroofs.com/projects/pview.php?id=894

http://www.greenroofs.com/projects/pview.php?id=91

http://www.greenroofs.com/projects/pview.php?id=95

http://www.langley.co.uk/asx/six_acres_case_study_-_newsletter.pdf

http://www.langley.co.uk/asx/stonegrove_case_study.pdf

http://www.langley.co.uk/asx/william_gunn_case_study.pdf

http://www.lda.gov.uk/Documents/Economic_Development_Strategy_%282010%29_6543.pdf

http://www.lgfl.net/learningresources/curriculum/geography/weatherstations/pages/weatherstations.aspx

http://www.london.gov.uk/shaping-london/

http://www.london.gov.uk/shaping-london/london-plan/

http://www.london.gov.uk/shaping-london/london-plan/docs/london-plan.pdf

http://www.london.gov.uk/shaping-london/london-plan/docs/london-plan.pdf

http://www.london.gov.uk/thelondonplan/about.jsp [accessed 12 March 2011]

http://www.london.gov.uk/thelondonplan/caz/central_activities.jsp

http://www.london.gov.uk/thelondonplan/caz/central_activities.jsp

http://www.london.gov.uk/thelondonplan/docs/londonplan08.pdf

http://www.londonair.org.uk/london/asp/datadownload.asp

http://www.londonair.org.uk/london/asp/default.asp

http://www.londonair.org.uk/london/asp/default.asp

http://www.meto_ce.gov.uk/climate/uk/averages/19712000/sites/greenwich.html

http://www.metoffice.gov.uk/

http://www.tfl.gov.uk/corporate/13980.aspx

http://www.unidata.ucar.edu/software/netcdf/Unidata

http://www.urbanhabitats.org/v04n01/london_pdf.pdf

http://www.vaisala.com/Vaisala%20Documents/Technology%20Descriptions/RAINCAP_Technology.pdf

http://www.wunderground.com/

http://www.wunderground.com/history/

https://code.zmaw.de/projects/cdo/

Järvi, J, et al, 2009: The urban measurement station SMEAR III: Continuous monitoring of air pollution and surface-atmosphere interactions in Helsinki, Finland. Boreal Env. Res, 14 (suppli. A), 86-109.

Kaimal J. and J. Finnigan, 1994: Atmospheric Boundary Layer Flows: Their Structure and Measurement. Oxford University Press, New York, 289 pp.

Kim, S,. McGaughey, R.J, Andersen, H.E, Schreuder, G. (2009) Tree species differentiation using intensity data derivedfrom leaf-on and leaf-off airborne laser scanner data. Remote Sensing of Environment, 113, 1575-1586.

Knott W (2011) LiDAR: An Application for Measuring Urban Vegetation Parameters? A London Case Study. Independent Geographical Study, King's College London, 64 pp.

LAEI 2006. London Atmospheric Emissions Inventory 2006. Compiled by AEA, March 2009. (http://static.london.gov.uk/mayor/environment/air_quality/research/emissions-inventory.jsp)

Lanza, L.G. and Vuerich, E. (2009) The WMO Field Intercomparison of Rain Intensity Gauges. Atmospheric Research, 94, 534–543.

Lee X, J Finnigan, and K Paw U, 2004: Handbook of Micrometeorology : A guide for Surface Flux Measurement and Analysis, chap. Coordinate Systems and Flux Bias Error, Chapter 3. Kluwer Academic Publishers, Dordrecht.

Lee, A.C. and Lucas, R.M. (2007) A LiDAR derived canopy density model for tree stem and crown mapping in Australian forests Original Research Article. Remote Sensing of Environment, 111(4), 493-518.

Lefsky, MA (1997) Application of LiDAR remote sensing to the estimation of forest canopy and stand structure, Ph.D. thesis, Department of Environmental Science, University of Virginia, Charlottesville, VA

Lindberg F, CSB Grimmond (2011) The influence of vegetation and building morphology on shadow patterns and mean radiant temperatures in urban areas: London case study, Urban Ecosystems (accepted)

Lindberg F, Grimmond CSB (2011) The influence of vegetation and building morphology on shadow patterns and mean radiant temperatures in urban areas: Model development and evaluation. Theoretical and Applied Climatology DOI10.1007/s00704-010-0382-8

Living Roofs and Walls Report GLA 2008a

Livingroofs.org

London Councils (2004) [online]. Available from: www.londoncouncils.gov.uk.

London Natural History Society (2011) Londons Wildlife Habitats. [online]. Available from: http://www.lnhs.org.uk/habitats.htm last accessed 10/12/10.

Mauder, M, et al, 2007: The energy balance experiment EBEX-2000. part ii: Intercomparison of eddy-covariance sensors and post-field data processing methods. Bound. Lay. Met, 123, 29_54.

Mayor of London (2011) [online]. Available from: http://www.london.gov.uk/streettrees/ last accessed 7th February 2011.

McGaughey, R.J. (2009) FUSION/LDV: Software for LiDAR Data Analysis and Visualization. United States Departmentof Agriculture, Seattle.

Met Office, 2010

Moriwaki, R. and M. Kanda, 2004: Seasonal and diurnal fluxes of radiation, heat, water vapor, and carbon dioxide over a suburban area. J. Appl. Meteor, 43, 1700-1710.

Münkel et al. 2007

Næsset E (2004) Accuracy of forest inventory using airborne laser scanning: evaluating the first Nordic full scale operational project. Scandinavian journal of forest research.19, 554-557.

Nemitz E, K Hargreaves, A McDonald, J Dorsey, and D Fowler, 2002: Micrometeorological measurements of urban heat budget and CO2 emissions on a city scale. Environ. Sci. Technol, 36, 3139-3146.

Offerle B, CSB Grimmond, K Fortuniak, K Klysik, and TR Oke, 2006: Temporal variations in heat fluxes over a central European city centre. Theor. Appl. Climatol, 84, 103-115.

Office of National Statistics 2001

Oke TR (2004) Initial Guidance to Obtain Representative Meteorological Observations at Urban Sites. IOM Report 81, World Meteorological Organization, Geneva.

Oke, T. (1987) Boundary Layer Climates. London: Methuen and Co. Ltd.

Operant LLC (2009) Essential FTIR – FTIR Software. [Online]. Available from: http://www.essentialftir.com/ [Accessed 10th November 2009].

Ordinance Survey (2010) © Crown database right 2010. An Ordnance Survey/EDINA supplied service. Assessed 2009-10-13

Pohjola, H, Konkola, L, Hoikkanen, M. and Schultz, D.M. (2008) Adjusting radar-derived QPE with measured drop-size distributions at the surface. In: The fifth European conference on radar meteorology and hydrology. ERAD.

Popescu SC, Wynne RH, and Nelson RF (2003) Measuring individual tree crown diameter with lidar and assessing its influence on estimating forest volume and biomass. Canadian Journal of Remote Sensing, 29, 564–577.

Pu, R, P. Gong, R. Michishita, and T. Sasagawa, 2006: Assessment of multiresolution and multi-sensor data for urban surface temperature retrieval. Remote Sens. Environ, 104, 211-225.

R Development Core Team, 2005: R: A language and environment for statistical computing. Vienna, Austria, R Foundation for Statistical Computing, URL http://www.R-project.org,ISBN3-900051-07-0.

Reitberger, C, Schnörr, P, Krzystek and Stilla, U. (2009) 3D segmentation of single trees exploiting full waveform LIDAR data. ISPRS Journal of Photogrammetry and Remote Sensing, 64 (6), 561–574.

Roberts, S.D, Dean, T.J, Evans, D.L, McCombs, J.W. and Harrington R.L. (2005) Estimating individual tree leaf area in loblolly pine plantations using LiDAR-derived measurements of height and crown dimensions, Forest Ecology and Management, 213, 54–70.

Robinson P (2010) The London Meteorological Monitoring Network. MSc Environmental Monitoring, Modelling and Management Thesis, King's College London, London, UK

Rothman, L. S. et al. (2005) The HITRAN 2004 molecular spectroscopic database. Journal of Quantitative Spectroscopy and Radiative Transfer. 96. 139 – 204.

Rowell DL 1994 Soil science methods & applications. Longman, Harlow, UK. 350pp

Rowell DL 1994 Soil science methods & applications. Longman, Harlow, UK. 350pp

Schmid et al. (2003).

Schotanus P, F Nieuwstadt, and H. de Bruin, 1983: Temperature measurements with a sonic anemometer and its application to heat and moisture fluxes. Bound. Lay. Met, 26, 81-93.

Source overview map: http://www.bing.com/maps/print.aspx?mkt=en-gb&z=13&s=c&cp=51.518190,-0.060062&poi=Blackwall%20Tunnel%2C%20London%20SE10%200&pp=skhf41gzzvm1&b=1&pt=pb

Stewart ID, and TR Oke (2009). Conference notebook– A new classification system for urban climate sites. Bulletin of the American Meteorological Society, 90: 922–923.

Streutker, D.R. and Glenn, N.F. (2006) LiDAR measurement of sagebrush steppe vegetation heights. Remote Sensing of Environment, 10, 135-145.

Tallis, M, Freer-Smith, P, Sinnett, D. & Taylor, G, 2011. Estimating the removal of atmospheric particulate pollution by the urban tree canopy of London under current and future developments. Landscape and Urban Planning – Under review.

Tharpa, R. B. and Murayama, Y. (2009) Urban mapping, accuracy, & image classification: A comparison of multiple approaches in Tsukuba City, Japan. Applied Geography, 29, 135-144.

Upmanis H, Eliasson I, Lindqvist S (1998) The influence of green areas on nocturnal temperatures in a high latitude city (Goteborg, Sweden). International Journal of Climatology, 18, 681-700.

van Dijk, A, A. Moene, and H. de Bruin, 2004: The Proinciples of Surface Flux Physics: Theory, Practice and Description of the ECPACK library.

Velasco E, S Pressley, E Allwine, H Westberg, and B Lamb, 2005: Measurements of CO2 fluxes from the Mexico City urban landscape. Atmos. Environ, 39, 7433-7446.

Vesala T, et al, 2008: Surface-atmosphere interactions over complex urban terrain in Helsinki, Finland. Tellus, 60B, 188-199.

Webb E, G Pearman and R Leuning, 1980: Correction of the flux measurements for density effects due to heat and water vapour transfer. Quart. J. R. Met. Soc,106, 85-100.

Wilczak J, S Oncley, and S. Stage, 2001: Sonic anemometer tilt correction algorithms. Bound. Lay. Met, 99, 127-150.

Williams, M.L. 2007. UK air quality in 2050—synergies with climate change policies. Environ. Sci. Policy, 10: 169-175.

www.metoffice.gov.uk

4. Athens Case Study

4.1 Site description

The Athens Case Study is focused on the municipality of Egaleo, which is a densely built urban area that lies in Western part of Athens

Five main road axes divide the area in four quarters. One of the quarters is an industrial degraded area (brownfield) called Eleonas. The total area of Egaleo is 650 ha and it is flat in general. The population is 74.046, although it is estimated that at least 120000 people, mostly medium and low income, live and work in the area. The level of education of the inhabitants is low to medium and the rate of unemployment high. The average population density is estimated to be 225 inhabitants/ha. As it appears in the land use map of Egaleo, availability of free/ green spaces is limited.

Egaleo is considered an environmentally degraded area facing problems with:

- air pollution
- traffic and transport
- thermal discomfort
- lack of green/ free spaces
- poor quality of building stock
- energy

The observations for the Athens case study were performed at city scale, local (neighbourhood scale) and at building scale using different methodologies described in the following sections in the document D3.5. The main objectives were to collect the necessary information needed by the modellers in the framework of WP4 but also to estimate the urban heat island effect in the area, to assess the air quality and the thermal outdoor environmental conditions at the test site, to estimate the impact of outdoor environmental conditions on the cooling load of buildings in the area and the investigation of indoor environmental quality.

4.2 Summary of results

Athens case study observations include:

- tower based urban meteorology measurements,
- air quality measurements
- heat island measurements
- outdoor environmental assessment of the case study area with a mobile meteorological station also equipped with an infrared camera and thermometer and portable instrument for PM10 measurements.
- Building related observations including the assessment of the quality of the indoor environment of 10 residential buildings and an estimation of the impact of the heat island effect of cooling loads of buildings using numerical modeling.

The BRIDGE case study area has high solar radiation levels and sunlight availability throughout the year and air temperatures range from 3°C (February) to 40°C (July). The yearly average value of relative humidity is about 60%. Wind directions for the case study area are fairly consistent with the dominant wind direction being from the North-East reaching an average wind speed of 3m/s. Precipitation levels are quite low, especially during the summer.

Regarding air quality, it was found that exceeding of the limit occurred for certain pollutants, at the Egaleo area. More specifically,

- Particulate Matter, PM10: PM10 pollutants exceeded limits at a number of measurement stations.
- Nitrogen Dioxide, NO2: Nitrogen dioxide presented exceedings of the indicative yearly average value.
- Ozone, O3: Exceedings of the warning threshold as well as of the alert threshold occurred close to Egaleo suggesting an occurrence in Egaleo as well. These exceedings are due mostly to the high levels of sunshine and high temperatures, that favor the formation of ozone.

The BRIDGE case study area suffers from a strong heat island effect. Measurements between Egaleo and a suburban station indicate a mean heat island intensity for the monitoring period of 2 -3 oC, reaching however in many occations a difference of 6 - 8 °C.

The in situ monitoring campaign with the mobile meteorological station, throughout the case study area during summer, shows that increased surface and air temperatures and low wind speeds result in thermal discomfort for the people in the area.

Indoor environmental quality measurements and assesement at selected residential buildings in Egaleo indicate that thermal discomfort inside the houses is a serious problem. It was found that over 40% of the maximum indoor temperatures are up to 35 °C, while 70% of the mean indoor temperatures are up to 30°C for the specific monitoring period. Indoor temperatures up to 38ºC have been recorded as well as hot spells of almost 21 consecutive hours over 34ºC. Comparative analysis of the occupants' responses received from questionnaires and the measured indoor conditions indicate that the thermal comfort perception of the users is in agreement with the air temperature measurements. Also, particle number concentration measurements indoors is generally correlated with outdoor concentration characteristics in the absence of important indoor sources. In addition, although concentrations outside the residences were quite high, for well air tight buildings like R1 and R2, concentrations were significantly lower (given the fact that no internal PM sources were found inside). On the contrary, poor construction and high infiltration rates due to e.g. old wooden frames (as is the cse of R4) resulted in high indoor concentrations. The presence of internal sources e.g excessive smoking and cooking (e.g. frying) as expected resulted in high concentrations during the activity.. On the contrary, poor construction and high infiltration rates due to e.g. old wooden frames (as is the cse of R4) resulted in high indoor concentrations. The presence of internal sources e.g excessive smoking and cooking (e.g. frying) as expected resulted in high concentrations during the activity.

Finally, with the use of numerical modeling it was found that the impact of increased outdoor temperarures in Egaleo compared to temperatures recorded in a suburban area (i.e. the heat island effect) result in an increase in cooling load of 74%.

All the techniques used and the analysis of the results have been compiled in a report attached as Annex 2. The specific methodologies with their references are described in the Deliverable 3.5.

4.3 Conclusions

The BRIDGE Athens Case Study is focused on the municipality of Egaleo, a densely built urban area that lies in the Western part of the greater Athens area. The observations for the Athens case study were performed at city scale, local (neighbourhood scale) and at building scale using different methodologies including tower based measurements, a mobile meteorological station, indoor environmental quality assesement through questionnaires and on site measurements with portable and installed instrumentation. The main objectives were to collect the necessary information needed by the modellers in the framework of WP4 but also to estimate the urban heat island effect in the area, to assess the air quality and the the thermal outdoor environmental conditions at the test site, to estimate the impact of outdoor environmental conditions on the cooling load of buildings in the area and the investigation of indoor environmental quality.

All the above mentioned measurements have been verified through the results of CoPs meetings and have resulted to the proposed planning interventions aiming mainly to increase thermal comfort in the area during summer, reduce air pollution and decrease energy consumption for cooling.

4.4 References

EN ISO 7726 - 1998: Ergonomics of the thermal environment -- Instruments for measuring physical quantities

TRNSYS software

Ελληνική έκδοση του ΕΛ.ΙΝ.ΥΝ.Α.Ε. «1996 – Οριακές τιμές Χημικών Ουσιών και Φυσικών Παραγόντων και Δείκτες Βιολογικής Έκθεσης» της Αμερικανικής Εταιρίας Κυβερνητικών Υγειονολόγων Βιομηχανίας

J.A. Clarke, J.W. Hand, P. Strachan, J.L.M. Hensen, and C.E.E. Pernot 1991. ‘‘ESP

R A building and plant energy simulation research environment,’’ Energy Simulation Research Unit, ESRU Manual U91/2, University of Strathclyde, Glasgow

5. Firenze Case Study

5.1 Site description

Firenze (400.000 inhabitants) is located in the central part of Italy about 80 km east of the sea. The few big industries formerly present inside the town moved years ago from the centre; nevertheless the orographic configuration of the site (a closed basin) and its continental climate favor episodes with high atmospheric stability and heavy pollution. The city center of Firenze is characterized by small squares surrounded by a network of narrow streets linked to the ancient gates. According to the reconstruction plan of 1885, the city walls were demolished and were replaced by a ring of avenues surrounding the city center that are the busiest streets. There is almost no vegetation in the city-center area.

5.2 Summary of results

Meteorological measurements

Meteorological observation were collected in Osservatorio Ximeniano tower from 1700.

During BRIDGE project we improved the strumentation installing an automatic weather station.

The meteo data collected are:

· Air temperature

· Air humidity

· Wind speed

· Wind direction

· Global solar radiation

· Rainfall

· Atmospheric pressure

In 2010 we upgraded the weather station installing a new high precision set of sensors based on Campbell CR-1000 data logger and installed an Ozone Monitor for accurate and precise (±1.5 ppb) ozone measurements

The new weather station provide more detailed information on several parameters like:

- Solar radiation (short and long wave, incoming and outcoming)
- A-class rain gauge 0.1mm resolution,
- High precision barometer
- Infra-red thermometer for roof surface temperature
- High precision Vaisala temperature and air humidity sensors.

A secondary database is also available for a weather station located on the periphery of Firenze (43.8163° N 11.2028° E).

Modeling Dust Deposition

Considering the green space proposed for the Parco San Donato development the modelling approach described here suggests annual deposition of PM10 of between 232.8 kg yr-1 (sum of 54.5 and 178.3, Table 3) and 367.5 kg yr-1 (sum of 180.0 and 187.5, Table 3) depending on the value of deposition velocity used in the model. This gives an estimated removal rate of between 5.2 and 8.2 % of PM10 from the mixing layer over this site. Prior to this development the existing bare ground would contribute to the atmospheric [PM10] through surface emissions. The planned development can contribute to local air quality by both removing this emission source and providing surface characteristics that enhance atmospheric deposition.

The data modelled from the London Case Study site using the Tiwary *et al*. (2009) deposition velocity was comparable to measured data from the London Case Study site. Extrapolation of this London data allowed a prediction of 63.0 kg yr-1 of PM10 deposited to the broadleaf canopy at the Parco San Donato sITE. The comparable modelled data explicitly at this site estimates a deposition of 77.6 kg yr-1.

The deposition to grassland was modelled using a value for deposition velocity taken from two diverse measurement approaches (Fowler et al.,2004 and Vong et al., 2004) however, the estimate of modelled dry deposition to grassland were very similar 244.3 and 257.0 kg yr-1 respectively. Grass at this site appeared to contribute between 27% and 56% of the total annual deposition depending on modelling approach. However, management activities such as grass cutting could result in considerable re-suspension of PM10 back to the atmosphere.

LIDAR observations:

A back-scatter LIDAR device was installed and tested on the Ossrvatorio Ximeniano. The instrument emits upward a laser source and measures back scatter as a function of time, resolving the first 5 km of atmosphere. The purpose of this instrument is to detect boundary layer depth, and also to characterize the aerosol distribution.

This type of measurements can be used to assess aerosol distribution, and to obtain important information on PB development:since aerosols emitted from the surface are concentrated into the PBL, a clear PBL aerosol signature can be used to retrieve PBL depth information, to be used as model validation data.

Biomonitoring of air-quality

The moss *Hypnum cupressiforme* has been used as a bioindicator for the estimation of atmospheric traces metal deposition in the urban area of Firenze. Moss carpets were collected in a forested area of central Sardinia (municipality of Bolotana – Nuoro), which is characterised by absence of air pollution. In laboratory, the moss material was cleaned from particles of soil, dead material and attached litter and was washed seven consecutive times with distillate water. After cleaning, moss samples were air dried. Moss bags were prepared by weighing out 2 g air-dried weight, and packing it loosely in nylon nets of 25 cm in diameter with mesh of 4 mm2 (Figure 1). Moss bags were located in the urban area of Firenze close to three monitoring air quality stations of the Environmental Protection Agency of Tuscany (ARPAT) located in Via Ponte alle Mosse (FI1), Viale Gramsci (FI2), and Viale Ugo Bassi (FI3). The first two stations are located in high traffic roads whereas the third one is located in a road characterised by less traffic density.

Data analysis.

Summary statistics were used to obtain the means of trace element concentrations in moss and one-way ANOVAs and post-hoc comparison tests were conducted with element concentration (Cr, Cu, Fe, Ni, Pb, V, and Zn) as independent variable, and exposure site (FI1, FI2, and FI3) as the dependent factor. Differences between mean values were identified by LSD test.

Statistical analyses were performed using Statistica software v. 6.1 (StatSoft Inc., Tulsa, OK, USA).

In addition, the trace element concentrations in moss corresponding to each exposure site were used to calculate the Load Factor

Results

Tables 1, 2 and 3 show the differences between mean concentration of trace metals in moss bags after-exposure and the respective blanks in the three sample sites of Firenze (FI 1, FI 2, and FI 3) during the first three campaigns of measurement. The highest concentrations for almost all elements were recorded in site FI2 (Viale Gramsci), which is a high traffic road. Lower values were detected in site FI3 (Via Ugo Bassi) located in a road with less traffic density.

In particular, the elements Cu, Fe, and Zn show higher values than other analyzed elements. Decrease of V in moss bags after exposure in site FI2 indicates that moss as living material in the bag not only can absorb and contain element deposition from the air, but also has the ability of exchange with element in the air.

Significant higher mean values were detected for Cu and Fe elements in FI2 site compared to FI3 site. Concerning Zn element no significant difference has been observed between sample sites.

Moving to Load Factor data, the elements Cu, Ni, and Zn show higher values than other analyzed elements (Table 4).

The results obtained suggest that *Hypnum cupressiforme* has a high ability to accumulate trace metals and, therefore, can be good bioindicator to estimate the trend of air pollution in a urban area during a period time.

This study further confirm that the moss bag method is a simple, inexpensive and useful technique, which provides informative atmospheric metal deposition figures in terms of time and space.

Table 1 - Differences between mean concentrations of trace metals in moss bags after-exposure and the respective blanks in the three sample sites of Firenze (FI1, FI2, and FI3) during the first campaign of measurement. Period of exposure March-May 2010.

Elements		FI 1	FI 2	FI 3
Cr	(mg Kg-1)	179	289.5	311
As	(mg Kg-1)	< 0.1	< 0.1	< 0.1
Cu	(mg Kg-1)	66.6	64.6	4
Fe	(mg Kg-1)	618.5	270	93.5
Ni	(mg Kg-1)	58.5	56.5	160.5
Pb	(mg Kg-1)	224	219	138
V	(mg Kg-1)	36.7	20	20.4
Zn	(mg Kg-1)	347	357	350

Table 2 - Differences between mean concentrations of trace metals in moss bags after-exposure and the respective blanks in the three sample sites of Firenze (FI1, FI2, and FI3) during the second campaign of measurement. Period of exposure May-July 2010.

Elements		FI 1	FI 2	FI 3
Cr	(mg Kg-1)	2.2	7.0	0.8
As	(mg Kg-1)	< 0.1	< 0.1	< 0.1
Cu	(mg Kg-1)	14.6	30.9	1.8
Fe	(mg Kg-1)	501	686	151
Ni	(mg Kg-1)	4.7	4.6	3.8
Pb	(mg Kg-1)	5.9	5.8	3.6
V	(mg Kg-1)	2	-6.6	1.9
Zn	(mg Kg-1)	1160.9	1775.9	1748.9

Table 3 - Differences between mean concentrations of trace metals in moss bags after-exposure and the respective blanks in the three sample sites of Firenze (FI1, FI2, and FI3) during the third campaign of measurement. Period of exposure July-November 2010.

Elements		FI 1	FI 2	FI 3
Cr	(mg Kg-1)	2.3	9.7	1.4
As	(mg Kg-1)	< 0.1	< 0.1	< 0.1
Cu	(mg Kg-1)	21.4	46.7	1.9
Fe	(mg Kg-1)	460	625	190
Ni	(mg Kg-1)	10.6	9.9	7.1
Pb	(mg Kg-1)	4.4	5.5	3.5
V	(mg Kg-1)	1.5	1.8	1.3
Zn	(mg Kg-1)	1989	2252	2188

Table 4 - Trace element load factors in moss samples after the first three biomonitoring campaigns (March-May, May-July 2010, and July-November 2010) in the three sample sites of Firenze (FI 1, FI 2, and FI 3).

Elements	March-May 2010				May-July 2010				July-November 2010			
	FI1	FI2	FI3	FI1		FI2	FI3	FI1		FI2	FI3	
Cr	0,28	0,45	0,48	0,46		1,45	0,17	0,37		1,59	0,22	
As	-	-	-	-		-	-	-		-	-	
Cu	0,88	0,86	0,05	1,20		2,55	0,15	1,78		3,89	0,15	
Fe	0,23	0,10	0,03	0,43		0,59	0,13	0,33		0,45	0,14	
Ni	0,25	0,24	0,68	3,88		3,83	3,17	5,55		5,21	3,74	
Pb	0,38	0,37	0,23	0,40		0,40	0,24	0,25		0,31	0,20	
V	0,94	0,51	0,52	0,16		-0,54	0,16	0,11		0,13	0,09	
Zn	3,54	3,64	3,57	39,89		61,03	60,10	65,21		73,84	71,74	

Turbulent fluxes

Introduction

Measuring surface fluxes of energy, mass, and momentum form urban environments can provide important informations on the urban energy balance, and emisison dynamics to be used in a number of different tools, ranging from atmosphric models to emission models, and DSS systems. So far, the few observations that were made include Chicago, Illinois (Grimmond et al. 2002); the center of Edinburgh, United Kingdom (Nemitz et al. 2002); the metropolitan region of Copenhagen, Denmark (Soegaard and Møller-Jensen 2003); a Mexico City, Mexico, urban landscape (Velasco et al. 2005); Basel, Switzerland (Rotach et al. 2005; Vogt et al. 2006); and Marseille, France (Grimmond et al. 2004).

A flux measurement station was deployed in Firenze since 2005 for short term experiments (Matese et al 2009), while it was made fully operational on a continuous basis within the BRIDGE project. In this study we present dynamics of carbon and energy fluxes at various time scales, ranging from hourly to seasonal patterns, with the aim of quantifying the importance of different drivers of concentration of scalars in the atmosphere.

Methods

An eddy covariance (EC) flux station was installed in Firenze (438479N, 118159E) in at the Osservatorio Ximeniano, in the center of the city (Fig. 1), and was operated continuously for the project duration. A mast of 3m was mounted on a typical tile roof of an ancient building of the observatory at 33 m above the street level. Turbulent fluxes of CO2, momentum, and sensible heat were collected using a sonic anemometer and an open-path CO2/H2O infrared gas analyzer (Li7500). Ancillary measurements are provided by a Class A weather station. Flux data are computed at a 30 minutes time resolution, and quality checked with state of the art procedures (Foken et al 2006).

For the analysis presented in this study, data have been averaged across various time scales, in order to resolve daily courses, weekly, monthly and seasonal courses of energy balance and surface emissions. Seasonal analysis has been accomplished by grouping together periods with similar overall emissions: Nov-Dec-Jan-Feb ('winter' period), March-April-May-Sept-Oct ('spring-autumn' period), June-July-August ('summer' period). Averaging process has been accomplished only on quality-checked dataset.

Results

In this study we present temporal dynamics of surface fluxes at different time scales, with the aim of deriving robust estimates of temporal variability of fluxes, which ca be used to assess models or DSS systems.

Figure 2 reports CO2 emission data across the year, computed both as daily, weekly, and monthly averages across the study period. The most important result that coms from this analysis is the strong sesonaity of carbon emission: on average, CO2 average flux in the winterr spans across 35 umol m-2 s-1, while in the summer across 10 umol m-2 s-1. This difference is related to the presence of domestic heating, that is almost entirely based on methane combustion, which releases CO2 and water vapour. Such strong seasonlity is typically not observed in cities where a different energy mix exist for heating and transportation, and is driven by the dynamic of domestic heating and road traffic (Matese et al 2009). The absence of a significant seasonality in traffic amounts justifies the conclusion that traffic is repsonsible for ~100% of emisisons in summer time, and only ~ 30% in winter time. A similar pattern can be observed in CO2 concentration, reflecting the fact that a higher amount of carbon injected into the atmosphere on average drives a higher concentration. This is an average result, while dynamic at smaller time scales show different relations between flux and concentration as shown below.

A significant week-end reduction of emissions is present in all the periods, suggesting that in weekends both traffic and a part of domestic heating, related to public buildingd, offices, and business buildings, are reduced: percentage reduction with respect the average daily emisison of the week-days is ~20% (Saturday) and ~50% (Sunday) for winter time, ~15% and ~40% for spring-autumn, and ~5% and ~20% for summer time. These data support the hypothesis that week-end reduction is larger on domestic heating then on road traffic, due to the presence of a significant portion of business and public buildings.

The diurnal patterns were characterized by specific peculiarities: a low emission at night, driven by a lower flux and also possibly enhanced by storage processes occurring at the street level below the urban canopy top; a large flux peak in the early morning, which van be related to the burst of nocturnal CO2, as well as the switch on of heating systems and the increase in traffic.

For the different seasons: in all periods the same specific patterns are present: i) a nocturnal build up of concentration, where relatively small fluxes inject and concentrate carbon in a shallow stable layer; ii) a mixing in the first part of the morning, where despite very high surface fluxes, concentration tend to decrease; this can be related to the development of a well mixed layer, with associated entrainment of tropospheric air with a lower carbon amount; also advective procsses which transport horizontally air masses with lower carbon amounts could play a role; finally, a build up in the evening when a new nocturnal stable layer develops. These results suggest the hypothesis that vertical mixing and PBL development, together with emission strength at the surface, are playing a fundamental role in driving surface layer concentratons of scalars.

Such datasets can be direclty uised both to validate a modelling framewrok capable of simulating the couipliong between the PBL and the surface, and to drive modelling analysis based on scenario.

Dust turbulent fluxes

Materials and methods

Fluxes of particulate matter were measured at the Osservatorio Ximeniano (Firenze, Italy) by CMCC with the EOLO system, deploying the eddy covariance method (Fratini et al., 2007). EOLO is comprised of a sonic anemometer (WindMaster Pro by Gill Instruments Ltd.) and an Optical Particle Counter (OPC CI-3100 by Climet Instruments Co.). It measures high frequency wind components and particle number concentration, to provide particles number concentration (PM1, PM2.5 and PM10) and fluxes averaged over 30 minute spans. Observed particles fall in the optical range 0.26 to 7.00 m.

The observed period extends from June 6th to December, 10th 2010. Due to several periods of malfunctioning, available data cover some 60% of the whole period, corresponding to ca. 111 days. Data were processed as described in Fratini et al. (2007). In addition, two quality filters were applied, and the following analysis was performed using only high-quality data. The first filter is a despiking procedure, eliminating individual flux values that show too large differences with the respect to the preceding and the following values in the time series. The second quality criterion is based on particle counting uncertainty, estimated here as in Buzorius et al. (2003). Individual flux values were eliminated if relative uncertainty was larger than 40%. This led to elimination of most fluxes of small intensity, notably night-time fluxes. A more detailed description is reported in the Annex.

Results

The determination of the scaling factor was based on a comparison of daily concentration of PM2.5 from EOLO and the average from 2 slow stations (“Bassi” and “Gramsci”), and a scaling factor of 0.19 was estimated. A similar value of 0.21was confirmed for PM10. Eventually, an average value of 0.20 was used to rescale all fluxes discussed hereafter. Fluxes of PM aggregates (PM1, PM2.5 and PM10) showed very similar trends, thus the following discussion if performed only for PM2.5, with results being approximately valid also for PM1 and PM10.

The analyzed period is characterized by an abrupt change in the wind regimes occurring at the change of the season. Nighttime winds are dominated by the easterly Levante during the whole measurement period. However, summer’s daytimes are dominated by NW winds, while Southerly winds dominate during autumn daytimes. Such change in the wind regimes determines a dramatic modification of the footprint of the observed micrometeorological fluxes. For this reason, particulate fluxes have been analyzer separately for the two seasons.

During summertime fluxes are close to zero (0.1 ± 1.1 g m-2 s-1). At about 9 am in the morning fluxes start to build up, increasing to a maximum of about 3.3 g m-2 s-1 at 11 am. During the early afternoon fluxes tend to decrease slightly, to build up again from about 5 to 8 pm, when values of about 4.8 g cm-2 s-1 are eached. Afterwards, measured fluxes show a coherent peak extending from 8 to 11 pm, with average values rising up to 11.3 g cm-2 s-1. While the morning and late afternoon flux buildups can be confidently related to traffic intensifications, the highest evening peak is hardly explained in terms of urban dynamics, and should be probably related to the change in wind direction, and the consequent change in footprint structure, occurring in the same time.

Fluxes measured during the autumn period do not show any significant trend, with small daily fluxes, of the same magnitude of night time fluxes. This result is probably to be linked to an increased rainfall during autumn. Indeed, summer time was characterized by an average of 1.2 rainy days and 17 mm per week, increasing to 3.8 days and 37 mm per week during autumn, with a sharp increase occurring at the seasonal transition. Increased rainfall tends to trap particulate matter at the surface, preventing particles to be uplifted

and escape the urban canopy as an emissive turbulent flux. Furthermore, the modification of the wind regimes, with Southerly winds dominating the daytime hours during autumn, implies a modification of flux footprint as measured at instruments level with respect to the summer time, and possibly exposes the measurements to a less intense source are of particulate matter. This aspect requires further investigation.

ACASA modelling

The Advanced-Canopy-Atmosphere-Soil Algorithm (ACASA) model was applied by CMCC over Firenze case study and used to simulate energy and mass fluxes in the city centre. The simulation period covered one year from January to December 2008, and turbulent fluxes were simulated at 30 minute time steps.

Meteorological data used to drive the model came from the measured data collected at the Ximeniano Observatory. They consisted of air temperature, relative humidity, precipitation, and wind speed. In sunny days, solar radiation data collected at the Ximeniano were corrected due to a shadow effect using data from a nearby meteorological station, while downward long wave radiation was estimated starting from air temperature values. A constant CO2 concentration value (388 ppm) was chosen to drive the model.

Simulated fluxes were compared with Eddy Covariance flux measurements collected at the Ximeniano tower in the period January-April 2008. Sensible heat flux (H) was well simulated by the model during the entire period, confirming the model ability to reproduce the diurnal variation in H flux all over the months.

Latent heat flux values are generally low in a city, and in this case the low values also derive from the absence vegetation in Firenze city centre. The model was able to capture this typical feature of urban areas, showing only small differences between simulated and observed values during the three months.

In order to simulate the diurnal cycle of carbon flux, traffic data (number of vehicle per Km^2) were included in the ACASA model. Two peaks in CO^2 flux typically arise in the early morning and late afternoon in correspondence of the rush traffic hour. The model was able to capture this trend. The general model underestimation of CO^2 flux was mainly due to a lack of information about energy consumption for heating/cooling process to be accounted by the model.

Even if there were not measured data for model comparison, ACASA was run for the period May-December 2008 and net radiation, sensible heat, latent heat, and CO^2 flux were estimated.

Statistical analyses was made by calculating the root mean squared error (RMSE) and the relative error (%) of half-hourly data per sensible, latent, and CO^2 flux during the period January- April 2008. Errors are generally low and the differences in simulated and observed data are not statistically significant at 95 % confidence level. A more detailed analyses is necessary to better investigate on the small differences between modeled and measured data. Anyway, these results confirm the reliability of the ACASA model in simulating energy and mass fluxes over urban area.

5.3 Conclusions

In Firenze, special effort was put into collecting time series of turbulent data and by today over 5 years of continuous mass end energy fluxes are available along with continuous dust particle turbulent fluxes. These records were useful to compare with the outputs of the ACASA simulation models.

Ozone and dust hourly records are suitable reference air quality parameters, measured above roof level and thus representative of mean air quality of the historic city center. Air quality was also essayed by means of suitable bioindicators, providing a time averaged picture of air quality at street level.

High resolution radiative temperature and multispectral reflectance data from the airborne campaign will be the basis for developing a model of heat transfer and its spatial distribution.

5.4 References

Buzorius, G.-R., Ü. - Nilsson, E.D. - Vesala, T. - Kulmala, M.; 2003. Analysis of measurement techniques to determine dry deposition velocities of aerosol particles with diameters less than 100 nm. *J. Aerosol Sci.* 34, 747-764.

Fratini, G., Ciccioli, P., Febo, A., Forgione, A. and Valentini, R. 2007. Size-segregated fluxes of mineral dust from a desert area of northern China by eddy covariance. *Atmos. Chem. Phys.* 7, 2839-2854.

Fowler, D., Skiba, U., Nemitz, E., Choubedar, F., Branford, D., Donovan, R., Rowland, P. 2004. Measuring aerosol and heavy metal deposition on urban woodland and grass using inventories of 210Pb and metal concentrations in soil. *Water, Air and Soil Poll*. 4: 483-499.

Freer-Smith, P.H., El-Khatib, A.A., Taylor, G. 2004. Capture of particulate pollution by trees: A comparison of species typical of semi-arid areas (*Ficus nitida* and *Eucalyptus globulus*) with European and North American species. *Water, Air and Soil Poll*. 155: 173-187.

Nowak, D.J. 1994. Air pollution removal by Chicago's Urban Forest. In: McPherson E.G., Nowak D.J., Rowntree R.A. (Eds). Chicago's Urban Forest Ecosystem: Results of the Chicago Urban Forest Climate Project. US Department of Agriculture, Forest Service, Northeastern Forest Experiment Station, Radnor, PA, pp. 63-82.

Tallis, M., Freer-Smith, P., Sinnett, D. & Taylor, G. 2011. Estimating the removal of atmospheric particulate pollution by the urban tree canopy of London under current and future developments. *Landscape and Urban Planning* – Under review.

Tiwary A., Sinnett, D., Peachy, C., Chalabi, Z., Vurdoulakis, S., Fletcher, T., Leonardi, G., Grundy, C., and Hutchings, T.R. 2009. An integrated tool to assess the role of new planting in PM10 capture and the human health benefits: a case study in London. *Environ. Poll*. 157: pp. 2645-2653

Vong RJ, Vickers D and Covert DS 2004. Eddy correlation measurements of aerosol deposition to grass. *Tellus* 56B: 105-117.

6. Gliwice Case Study

6.1 Site description

Gliwice flux tower

The site is located on a building of the Silesian University of Technology on a balcony at the side of a gable roof (50°17'38.01"N, 18°40'53.21"E). The building up to the gable is approx. 25 m high. The mast was installed on the balcony and was 8 m high, i.e. the top of the mast is »3 m above the gable. The distance to the gable is »6 m. The line gable-to-mast points towards SW. In the direction WNW in approximately 70 m there is a higher roof which is a disturbing obstacle.

The top of the tower was equipped with an Eddy-Covariance (EC) measurement system (Young 81000V sonic anemometer, LiCor 7500 Infrared gas analyzer) and a four component net radiometer (pyranometer and pyrgeometer pairs facing upward and downward). Additionally air temperature and relative humidity were measured by a Vaisala HMP45. Date was acquainted with a Campbell Scientific data-logger CR1000. The measurement frequency of the EC-system was 10 Hz, for radiation, temperature and humidity it was 1 Hz.

The raw covariances (half hourly means) were rotated into a streamline coordinate system according to McMillen (1988). Sensible heat flux was calculated using the sonic temperature corrected for buoyancy effects of humidity fluctuation on the speed of sound (Schotanus et al., 1983). Latent heat flux and CO2 flux were adjusted after Webb et al. (1980) to compensate for the fluctuations of temperature and water vapor that affect the measured fluctuations in the density of CO2 and H2O.

EC data are available as half hourly averages, temperature and radiation data as 1 minute averages. All 10 Hz raw data of the EC-system were stored for further analysis.

Refer to annex 4 (Gliwice Case Study) for a more comprehensive site description, figures and details of the instrumental setup, data processing and data availability

6.2 Summary of results

Wind

Main wind directions were the SSW-NNW sector and the eastern sector. Wind regimes were very variable from month to month and depend strongly on the dominating synoptic situation, e.g. June was dominated by winds from the North-West, while August is dominated by south-westerly winds. Some months show frequent easterly winds during nighttime (e.g. APR, MAY, JUL, SEP, OCT, FEB). Generally the patterns during daytime and nighttime are very similar due to the flat terrain and the absence of large water bodies. Note that the sector from NW to NE may be influenced by the roof of the nearby building. Refer to annex 4 – Gliwice case study for further analysis of the prevailing flow conditions during the observation period.

Energy

Summer months show the highest energy input (343 and 324 MJ m-2 for JUN and JUL, respectively) and accordingly the largest fluxes of sensible (170 and 167 MJ m-2) and latent heat (78 and 87 MJ m‑ 2). Net radiation becomes negative during winter months. During May 2010 unusually wet conditions prevailed and resulted in below average net radiation. Low net radiation in NOV/DEC/JAN may also be associated with snow and/or ice covered radiation instruments. February 2011 was dominated by fine weather and many clear days. Typical for cities, sensible heat flux dominated evapotranspiration during the whole year because of large impervious areas and reduced vegetation. Sensible heat flux accounted for 53% and latent heat flux for 15% of net radiation during peak hours (11h to 13h), respectively, when averaged for the whole

measurement period. During summer months JUN and JUL, sensible heat flux accounted for about 41 % and 16 % of net radiation, respectively. This implies that a large amount of the incoming energy is absorbed by the urban canopy layer. Refer to annex 4 – Gliwice case study for further analysis of the radiation terms and sensible and latent heat fluxes.

carbon dioxide

CO2 fluxes and concentrations were analyzed with respect to season and daytime (monthly diurnal courses) and with respect to weekdays. . Lowest CO2 fluxes were measured during the vegetation period in JUN/JUL/AUG/SEP (partly). During these months the mean diurnal courses of CO2 flux and CO2 concentration show a minimum around midday, which is related to photosynthesis of the vegetation in the footprint of the flux tower. On the other hand, during fall/winter months OCT/NOV/DEC/JAN/FEB CO2 flux peaks around midday, while CO2 concentration is more or less uniform. If analyzed for weekdays, the mean diurnal courses of CO2 flux for weekends (SAT/SUN) show minimum values during the day, while for working days MON-FRI a prominent peak around midday and partly a secondary maximum in the evening can be observed. MON-FRI daytime values are related to increased traffic volume.

Monthly CO2 exchange was always positive which means that the source area of the flux tower is a source of CO2 throughout the year, i.e. the emission of CO2 prevails over the uptake. Based on mean monthly net fluxes the estimated total annual flux is 2.8 kg CO2 m-2 year-1. This is probably a too low value when compared with other studies. Local influences are dominating at the measurement site. The relation between mean monthly air temperature and total monthly CO2 exchange is surprisingly good. CO2 exchange and air temperature are negatively correlated, low temperatures relate to high CO2 exchange and vice versa. Though the shape and the direction of this ratio are typical for cities, absolute values are highly site specific and may not be regarded as representative for the city of Gliwice. Refer to annex 4 – Gliwice case study for the detailed analysis of the radiation terms and sensible and latent heat fluxes

6.3 Conclusions

Measurements of the Gliwice flux tower are presented for the period from APR 2010 to FEB 2011. Average and total values of the whole measurement period are shown as well as monthly averages/sums and mean monthly diurnal courses of radiation, energy and CO2 fluxes. Main features are: Positive CO2 flux dominates over the whole period which means that the source area of the flux tower is a net source of CO2 regardless of the season. However, the source is reduced during the vegetation period in summer. CO2 flux shows a strong linear dependence on air temperature, i.e. high CO2 fluxes are related to low air temperatures. Significant differences in mean diurnal courses calculated for weekdays suggest a specific weekly variability with lower emissions of CO2 during weekends due to reduced car traffic and industrial activities.

Although the Gliwice flux tower site is not an “ideal” urban site (if there is any) in terms of representativeness, the presented results show some typical urban features which may help to characterize the urban metabolism.

6.4 References

McMillen, R.T. 1988. 'An eddy correlation technique with extended applicability to non-simple terrain', Boundary Layer Meteorology, 43, 231-245

Schontanus, P., Nieuwstadt, F.T.M. and de Bruin, H.A.R. 1983. Temperature measurements with a sonic anemometer and its application to heat and moisture fluxes. Boundary-Layer Meteorology, 26, 81-93

Webb, E.K., G. Pearman and R. Leuning. 1980. Correction of flux measurements for density effects due to heat and water vapor transfer. Quarterly Journal of Royal Meteorological Society, 106, 85-10

References

McMillen, R.T. 1988. 'An eddy correlation technique with extended applicability to non-simple terrain', *Boundary Layer Meteorology*, 43, 231-245

Schontanus, P., Nieuwstadt, F.T.M. and de Bruin, H.A.R. 1983. Temperature measurements with a sonic anemometer and its application to heat and moisture fluxes. *Boundary Layer Meteorology*, 26, 81-93

Webb, E.K., G. Pearman and R. Leuning. 1980. Correction of flux measurements for density effects due to heat and water vapor transfer, *Quarterly Journal of Royal Meteorological Society*, 106, 85-100.

7. Helsinki Case Study

7.1 Site description

Most of the measurements made under Task 3.1 by UHEL are carried out at the SMEAR III station in Helsinki, Finland. The station covers two measurement locations, Kumpula and Viikki. Measurements cover basic meteorology, turbulent fluxes, air quality and physiology and ecology of street trees. These measurements have been continuous during the whole project. In addition, three water catchments were selected and the measurements there started in September/October 2010. Finally, we also present intercomparisons of measurements and Soil-Vegetation-Atmosphere-Model (ACASA).

Air quality, meteorological and turbulent flux measurements are made at the Kumpula site (60°12´N, 24°57'E, 26 meters above sea level), which is located at the University of Helsinki campus area around five kilometers from the Helsinki City centre. In Kumpula measurements are carried out in two locations: the basic meteorological measurements are made at the roof of University of Helsinki buildings at the height of 51 meters while turbulent fluxes and profile measurements are made in a 31 meters high triangular lattice tower. Instrumentation used for air quality measurements is located in a container next to the measurement tower. Surroundings of the tower are complex and three distinct areas (urban, road and vegetation) in different wind directions can be distinguished according to the typical surface cover in the area (Vesala *et al.* 2008). In direction 320-40°, lays the so called urban sector with high fraction of impervious surfaces. This area is the most urban type with high university of Helsinki buildings (mean height of 20 meters), roads and parking lots. The area north of the campus area is covered with single and detached houses with many of them equipped with wooden stoves. The area in direction 40-180° is called the road sector and it is dominated by one of the main roads leading to the Helsinki City centre with 45 000 vehicles per workday. The distance between the tower and the road is 150 meters and it is covered with deciduous forest. The vegetation sector in direction 180-320° has a high vegetation fraction as the University Botanical Garden and an allotment garden are located in the area.

The multidisciplinary urban ecosystem and tree research lies in Viikki, seven kilometers from the Helsinki city centre. Viikki area consists of the University campus area, new residential areas build since early 2000's and extensive green areas. The measurements are done on two streets with south –west north-east direction (Riikonen *et al.* 2010). The streets are paved with local pillar type black alder and lime trees growing there. The streets have been build in 2002 using normal construction techniques, one street in normal modern residential area and one in an office area. Three different urban load bearing soil mixtures currently used in Helsinki are tested at the sites.

In addition, the quantity and quality of stormwater in real time and with great accuracy has been measured at three catchment areas in Helsinki since September/October 2010. All three areas vary in population density and the amount of pervious and impervious surfaces.

7.2 Summary of results

Meteorology

Kumpula

The measurements on the roof of the University of Helsinki cover air pressure, relative humidity and precipitation. In addition, the vertical profiles of wind speed and direction and air temperature are measured at levels 4, 8, 16 and 31 meters at the measurement tower. On the top level the components of the net all-wave radiation (incoming and outgoing short- and long wave radiations) and PAR (photosynthetically active radiation) are measured.

In 2009-2010, air temperature showed a strong annual cycle with temperatures ranging from -23°C in winter to 30°C in summer. Year 2010 was untypical for Helsinki with colder winter and warmer summer than typically observed in Helsinki. The 30-year average monthly air temperatures vary from 4.9°C in February to in 17.2°C in July (Drebs *et al.* 2002) while an average temperature of -10.7°C in Jan 2010 and 22.1°C in August were observed. Wind speed and air pressure did not have a distinct annual behavior while relative humidity inversely followed the air temperature with lower values in summer than in winter. In both years the annual behavior of precipitation was typical for Helsinki with maximum precipitation in winter/late summer and minimum in spring. The most typical wind direction at the measurement site is south-west corresponding to flow downwind from the area of high vegetation.

The downward short-wave radiation has a strong annual behaviour with winter time values typically below 100 W m^{-2} and reaching 1000 W m^{-2} in summer. The periods of snow cover can clearly be distinguished from the reflected short-wave radiation with increased values in winter due to increases surface albedo. From a median summer value of 0.14 the surface albedo increases to 0.49 in 2009 and to 0.63 in 2010 in winter. Both downward and upward long-wave radiations have maxima in summer and minima in winter. The upward long-wave radiation is generally higher than the downward component reflecting the effect of higher surface temperatures of impervious surfaces.

Viikki

In addition to the meteorological measurements carried out in Kumpula, local PAR, air and soil temperatures are measured at both streets in Viikki. PAR is measured with QS2 sensors (Delta-T Devices Ltd) and air temperature with radiation shielded Pt100 at 7 meters height (see Figure 9). The time resolution of the measurements is 2 minutes in spring, summer and autumn, and 10 minutes in winter.

Air quality

As different sized of particles have different sources and physical properties, the measured aerosol particle size range has been divided to 3-30 nm, 30-100 nm and 100-950 nm sized particles corresponding to nucleation mode, Aitken mode and accumulation mode particles, respectively. All aerosol particle concentrations have their maxima in winter due to increased emissions from various combustion processes. These concentrations are strongly also affected by the mixing conditions of the boundary layer and in winter this is limited due to the lack of solar radiation. O_3 gets its maximum 35 ppb in spring/early summer and minimum 10 ppb in winter. This annual behavior is determined by the intensity of solar radiation and photo-oxidation of the precursor gases (Järvi *et al.* 2009a). NO_x and SO_2 get their maxima 20.7 and 1.6 ppb, respectively in winter when there is limited mixing and increased emissions from traffic and stationary emission sources.

Turbulent fluxes

The turbulent fluxes of momentum, sensible and latent heat, carbon dioxide (CO_2) and aerosol particle number are measured with the eddy covariance (EC) technique. These measurements are made on the top boom of the measurement tower at a height of 31 meters.

In general, friction velocity (momentum flux) did not have any distinct annual cycle and on average it remained below 1.8 m s^{-1}. Sensible and latent heat fluxes (Q_H and Q_E, respectively) followed measured solar radiation well with maxima in summer and minima in winter. Q_H was higher than Q_E and daytime averages of Q_H reached 300 W m^{-2} in summer while Q_E stayed below 225 W m^{-2}. In winter, both fluxes were close to zero. The source area around the tower acted as a source of CO2 (F_c) in winter with an average strength of 15.4 μmol m^{-2} s^{-1}. In summer, carbon uptake exceeded the emissions and a minimum average downward flux of 11 μmol m^{-2} s^{-1} was measured. The strong carbon sink visible from data in summer is caused by the prevailing wind direction downwind from the area of high vegetation cover (Figures 4 and 8). Highest particle emissions were measured in winter and the average daytime fluxes reached $1.2 \cdot 10^9$ m^{-2} s^{-1}.

F_c and particle flux (F_p) had strong dependence on wind direction as it is clear from the diurnal plots for each surface type area in summer. The highest emissions for both were measured from the road sector due to emissions from road traffic with F_c reaching 16 μmol m^{-2} s^{-1} and F_p 0.4·109 m^{-2} s^{-1}. Urban and vegetation sectors acted as a carbon sink in daytime reaching values of -8 and -11 μmol m^{-2} s^{-1}, respectively. For F_p, the fluxes in these directions stayed below $0.2 \cdot 10^9$ m^{-2} s^{-1}. Heat fluxes did not have such a strong dependence on wind direction but a slightly lower Q_H was observed in the area with high vegetation fraction in daytime than in other areas. Similarly highest Q_E was observed in the same direction as heat is consumed in evapotranspiration instead of direct heat flux. Nocturnal Q_H and Q_E were about the same for all directions.

Soil water, CO_2 content and soil CO_2 flux measurements

Urban construction has significant influence on the urban tree metabolism and growth. Soil volumetric water content (SWC) was continuously monitored in the tree growth media at two normal streets. Average SWC at site 1 was very high, around 25-30%. At site 2, SWC was around 15%, which can be considered more normal for an urban planting site. At site 2 soil water content varied clearly over the year decreasing during growing season as response to increasing tree leaf area, while at site 1, changes over the year were less obvious. Site 1 high water content reflected negatively on tree growth. Measured water use of black alder trees at site 2 was on average over the growing seasons 2007-2010, 0.5 l m-2 of leaf area d-1. For limes at site 1 similarly calculated water use was 0.4 l m-2 of leaf area d-1. Tree leaf area and tree water use changed during the examined period resulting in increase in total tree water use over the years. From 2007 to 2010, leaf area of both tree species increased by about 80%. Lime growth was inversely dependent on soil water status whereas Alder crown allometry showed occasional drought effects on a site with normal urban soil water conditions.

Soil gas samples were collected from soil air samplers installed in tree soils. Additionally, in late July 2009, continuous measurement of soil air CO2 content was started at 10 cm depth. At site 2, average soil CO2 concentration in continuous measurements in high summer was around 2 500 ppm, while at wetter site 1 it was 4-5 times higher. Samples analyzed with gas chromatograph showed a similar pattern but somewhat higher total concentrations probably due to spatial variability. Soil temperature differences between sites were small and differences in soil CO2 concentrations were mainly explained by different soil water conditions and street surfacing. CO2 flux from tree soils was measured only during growing season. In 2008, for example, flux from tree soils was on site 1 on average 0.03 ± 0.03 and at site 2 0.01 ± 0.01 mg m-2 s-1 of CO2, varying according to site conditions, surfacing permeability and the driving CO2, concentration under the surfacing.

Results show that the contribution of urban trees and their growing sites to urban metabolism is heavily influenced by the construction of adequate growing site conditions. Northern urban site can suffer from excess water while drought has impact on metabolism throughout the continent.

Stormwater quantity and quality

Data collection took place at three sub-catchment areas in Helsinki. The studied catchment areas differ in their population density and the amount of pervious and impervious surfaces, and are thus called low-density, medium-density and high-density catchment areas accordingly. The sites can also be referred to as low-, medium – and high-intensity areas as land use intensity determines the proportion of permeable and impermeable soil in the area.

Due to difficulties getting electricity at the stormwater-stations, the automatic measurements started in September/October 2010. Therefore only data from September onward has so far been analyzed and can be presented. In figure 13, urban runoff data for November 2010 is presented. During each rain event the amount of nutrients (N and P) and heavy metals (Cd, Cu, Al etc.) was analyzed. However, so far data on conductivity and turbidity of the run-off water according to Table 2 is available. The runoff flow was measured once per minute using an ultrasonic flow meter installed in a manhole of a sewer pipe at the catchment outlet. The amount of runoff differed clearly between the three catchment areas. Especially the high-density site showed extensive stormwater flows – even at times when the precipitation was low. The monthly total (cumulative) runoff was about seven times larger in the high-density area as compared to the low-density area. At the low-density site 7% of the precipitation in November escaped the system via runoff, while in the medium-density and high-density areas the numbers were 38% and 46 %, respectively.

At this stage of our project only a limited set of runoff quality data is available. However, the conductivity data described below can be applied as an indicator for the concentrations of soluble nutrients (e.g. nitrate and phosphate), metals, and chlorides in the water. Water samples were collected during each rain event using an automatic water sampler, but these data are under analysis at the time of writing this report. The conductivity of the runoff water is measured at 10 second intervals during the entire study period (September 2010 to September 2012) using a conductivity sensor. Conductivity, an indicator of e.g. dissolved salts and metals in stormwater, was lowest in the low-density Veräjänmäki catchment and clearly highest in the medium-density area. The stormwater was clearly most turbid in the high-intensity area, followed by medium-intensity area and clearly cleanest in the low-intensity catchment.

Table 2: Precipitation and the amount and quality (conductivity, mS cm-1 and turbidity, NTU) of stormwater in the Helsinki catchment sites in November 2010.

November 2010		**SITE**	
	Itä-Pasila (high-intensity)	Pihlajamäki (medium-intensity)	Veräjänmäki (low-intensity)
Precipitation (mm)	89*	89*	89*
Stormwater runoff (mm)	35,1	30,2	5,1
Median runoff conductivity	0,5	1,9	0,2
Median runoff turbidity	195,7	9,4	1,4

*) Precipitation value taken from the Kaisaniemi weather station (Finnish Meteorological Institute) ca. 5 km south of the Itä-Pasila catchment.

ACASA modelling

The Advanced-Canopy-Atmosphere-Soil Algorithm (ACASA) model is a SVAT (Soil-Vegetation-Atmosphere- Transport) model developed by the University of California, Davis (Pyles et al., 2000; 2003). It has been applied by the Euro-Mediterranean Centre for Climate Change (CMCC) over Helsinki case study and used to simulate energy and mass fluxes at the Kumpula measurement site. Turbulent fluxes have been simulated for the year 2008 from January to December, at 30 minute time steps, and compared with Eddy Covariance measured data collected by the University of Helsinki. Meteorological data and short wave and long wave downward radiation data were used to drive the model.

Simulated net radiation (Rn) flux perfectly matched the observed flux during the entire year. The model perfectly reproduced the trend and the magnitude of the observed Rn values (see Figures 14 and 15 of Annex).

Sensible heat flux (H) was well simulated by the model during the entire period with only small differences. In particular, a slightly overestimation of H was observed in March, June, and September (Figs. 16 and 17 of Annex), and more investigation are needed in order to better identify the reason for that.

Latent heat flux (LE) simulations matched well the observed flux during the year, both deriving for urban surface and vegetation. Even if we compare half-hourly values, we can see that ACASA was able to reproduce the measured LE values with only small differences (Figs. 19 and 19 of Annex).

In order to simulate the diurnal cycle of carbon flux, the emission curve of CO in Helsinki was used to parameterize the model. In general, the model was able to capture the diurnal trend of CO2 flux. Major differences between observations and model results were observed during the fall, when foliage in the trees fall down (Figures 20 and 21 of Annex), due to a constant LAI value set in the model.

In order to evaluate the model performance, the root mean squared error (RMSE) and the relative error (%) of half-hourly data were calculated both for net radiation, sensible, latent, and CO2 flux during the period January- December 2008 (see Table 3 of Annex). Errors are generally low and the differences in simulated and observed data are not statistically significant at 95 % confidence level. Further analyses is necessary to better investigate on the small differences between modeled and measured data, but results are promising for the use of ACASA to simulate urban fluxes.

7.3 Conclusions

The measurements sites in Helsinki consist of the two SMEAR III station sites in Kumpula and Viikki and the three catchment areas located in the Helsinki area. All measurement areas are located within an area of 6.5 km. All measurements, excluding the stormwater measurements at the different catchment areas, are continuous during the whole project. The continuous measurements of the quantity and quality of the stormwater in the three catchment sites did not start until September 2010. The measurements cover basic meteorology, turbulent fluxes of momentum, sensible and latent heat, CO_2 and aerosol particle number, concentration measurements of CO_2, H_2O, aerosol particles with size range 3-950 nm, O_3, NO_x and SO_2. The strong annual variation of solar radiation affected most of the measured variables. In calm winter days the pollutant levels can be very high since insolation is low and the boundary-layer may remain stable over the whole day. Also in winter, cold temperatures increase the need for heating via wood combustion and district heating.

Most of the measurements carried out in Kumpula (turbulent fluxes and air quality) are influenced by the complex measurement surroundings and clear differences between the different surface type areas can be distinguished. Particularly, the highly trafficked road passing the station has a great impact on the CO2 and

aerosol particle exchange. Similarly the effect of vegetation is evident with an average carbon uptake exceeding the emissions and increased fraction of radiation converted to latent heat.

The tree measurements show that trees respond to weather variables in urban conditions at least as strongly as those in natural sites. Further factors influencing urban tree behavior are the conditions and limitations set by the artificial growing site and the management history of trees making the prediction of urban tree contribution to urban metabolism more complex a task than in natural conditions.

Many of the features in observations were reproduced by ACASA SVAT model.

7.4 References

Drebs A., Nordlund A., Karlsson P., Helminen J. and Rissanen P. (2002). *Tilastoja Suomen ilmastosta 1971-2000 (in Finnish)*. Ilmatieteen laitos, Helsinki.

Järvi L. (2009). Turbulent vertical fluxes and air quality measured in urban air in Helsinki. *Report Series of Aerosol Science* no 103.

Järvi L., Hannuniemi H., Hussein T., Junninen H., Aalto P. P., Hillamo R., Mäkelä T., Keronen P., Siivola E., Vesala T. and Kulmala M. 2009a. The urban measurement station SMEAR III: Continuous monitoring of air pollution and surface-atmosphere interactions in Helsinki, Finland. *Boreal Env. Res.* 14 (Suppl. A), 86-109.

Järvi L., Rannik Ü. , Mammarella I. , Sogachev A. , Aalto P. P. , Keronen P. , Siivola E. , Kulmala M. and Vesala T. (2009b). Annual particle flux observations over a heterogeneous urban area. *Atmos. Chem. Phys.* 9, 7847-7856.

Pyles, R.D., Weare, B.C., and Paw U, K.T. (2000). The UCD Advanced Canopy-Atmosphere-Soil Algorithm: Comparison with observations from different climate and vegetation regimes. *Q.J.R. Meteorol. Soc.*,126: 2951-2980.

Pyles, R.D., Weare, B.C., Paw U, K.T., and Gustafson, W. (2003). Coupling between the University of California, Davis, Advanced Canopy-Atmosphere-Soil Algorithm (ACASA) and MM5: Preliminary Results for July 1998 for Western –North America. *J Appl. Meteorol*. 42: 557-569.

Riikonen, A., Lindén, L., Pulkkinen, M., and Nikinmaa, E. (2010). Post-transplant crown allometry and shoot growth of two species of street trees. *Urban Forestry & Urban Greening*, doi: 10.1016/j.ufug.2010.09.001.

Vesala T., Järvi L., Launiainen S., Sogachev A., Rannik Ü., Mammarella I., Siivola E., Keronen P., Rinne J., Riikonen A. and Nikinmaa E. 2008. Surface-atmosphere interactions over complex urban terrain in Helsinki, Finland. *Tellus* 60B, 188-199.

Part 2 - Remote Sensing and GIS data collection

1. Introduction

The term "*urban metabolism*" is used to indicate the exchange and transformation of energy and matter between a city and its environment. In the BRIDGE (sustainaBle uRban plannIng Decision support accountinG for urban mEtabolism) project, the WP3 is dedicated to collect data of urban fluxes measured in five European cities ((Helsinki, Athens, London, Firenze and Gliwice) as representative of the different city typologies and influenced by different policy and resource availability. Urban fluxes are strongly affected by the urban surface characteristics and changes in land use (e.g. new buildings construction, increasing of green areas etc.) mainly determine changes at regional scale.

Exchanges of energy, heat, moisture, carbon and pollutant are then measured using different techniques, during the project, for each case study, as well as local and regional urban fluxes are simulated by models in selected cities. In addition, GIS data and remote sensing methodologies are used to investigate on the role of land use in affecting the surface exchanges between the urban canopy and the atmosphere.

1.1 Purpose of the document

This document is the D.3.4_BRIDGE Observation Report. Task 3.2 has the role to systematically monitor the main fluxes using remote sensing techniques and models for the five case studies (Helsinki, Athens, London, Firenze and Gliwice).

The **aim of this document** is to provide the main results obtained by remote sensing techniques, GIS data and some model tools, for each case study of the BRIDGE Project. In particular, it contains a summary on the GIS and remote sensing data collected during the project. In addition, methodologies used to provide the data and maps of physical parameters are included into the document.

The final products of Task 3.2, are GIS data and maps of energy and water fluxes, pollution concentrations, land cover and vegetation per each case study. This document, then, contains the analysis of the main results obtained in each case study using different remote sensing methodologies and models and it shows the different behavior of the five cities in release or sequester heat, water, carbon and pollutant.

1.2 Definitions and Acronyms

Acronyms

CoP	Community of Practice
DSS	Decision Support System
GIS	Geographical Information System
RS	Remote Sensing
DEM	Digital Elevation Model
ASTER	Advanced Thermal Emission and Reflection Radiometer

1.3 Document References

Akbari, H., Pomerantz, M., Taha, H., (2001). Cool surfaces and shade trees to reduce energy use and improve air quality in urban areas. Solar Energy. 70(3), 295-310.

Backsik, Z., Mink, J. & Keresztury, G., (2004). FTIR spectroscopy of the atmosphere. I. Principles and methods. Applied Spectroscopy Reviews. 39. 295 – 363.

Baldwin, V.C. Jr, Peterson, K.D, Burkhart. H.E, Amateis, R.L, and Dougherty, P.M., (1997). Equations for estimating loblolly pine branch and foliage weight and surface area distributions, Canadian Journal of Forest Research. 27, 918–927.

Beckett, K.P., Freer-Smith, P.H., Taylor, G., (2000). The capture of particulate pollution by trees at five contrasting urban sites. Arboricultural Journal. 24: 209–230.

Bhaskaran, S., Paramananda, S. and Ramnaryan, M., (2010). Per-pixel and object-oriented classification methods for mapping urban features using Ikonos satellite data. Applied Geography, 30, 650-665.

Brandtberg, T., Warner, T., Landenberger, R.E., and McGraw, J.B., (2003). Detection and analysis of individual leaf-off tree crowns in small footprint, high sampling density LiDAR data from the eastern deciduous forest in North America. Remote Sensing of Environment, 85, 290−303.

Caselles, V., Lopez Garcia, M.J., Melia, J., and Perez Cueva, A.J., (1991). Analysis of the heat-island effect of the city of Valencia, Spain, through air temperature transects and NOAA satellite data. Theoretical and Applied Climatology, vol 43, pp.195-203.

Chander G., and Markham B.I., (2003). Revised Landsat-5 TM radiometric calibration procedures and post-calibration dynamic ranges. IEEE Transactions on Geoscience and Remote Sensing, vol. 41, pp. 2674-2677.

Chavez, P.S., (1996). Image-based atmospheric corrections- revisited and improved. Photogrammetric Engineering and Remote sensing, vol 62, pp. 1025-1036.

Chen, Y., Su, W., Li, J., Sun, Z., (2009). Hierarchical object oriented classification using very high resolution imagery and LIDAR data over urban areas. Advances in Space Research, 43, 1101-1110.

Chrysoulakis, N. and C. Cartalis, (2002). Improving the estimation of land surface temperature for the region of Greece: adjustment of a split window algorithm to account for the distribution of precipitable water. International Journal of Remote Sensing, 23, 871-880.

Clark, M.L, Clark, D.B. and Roberts, D.A., (2004). Small-footprint LiDAR estimation of sub-canopy elevation and tree height in a tropical rain forest landscape, Remote Sensing of Environment, 9 (1), 68–89.

Del Campo, L., R. Pérez-Sáez, X. Esquisabel, I. Fernández, M. Tello, (2006). New experimental device for infrared spectral directional emissivity measurements in a controlled environment. Review of Scientific Instruments, 77,113 111.

Getter, K. & Rowe, D., (2006). The role of green roofs in sustainable development. HortScience. 41, 1276–1286.

Goodwin, N.R., Coops, N.C., Tooke, T.R., Christen, A., and Voogt, J.A., (2009). Characterizing urban surface cover and structure with airborne LiDAR Technology. Canadian Journal of Remote Sensing. 35, 297-309.

Grant, G., (2006). Extensive Green Roofs in London. Urban Habitats, 4 (1), 51-65.

Griffith, D.W.T., (2006). MALT 5 User's Guide, Version 5.2. [Electronic document] Available with MALT 5 software.

Griffith, D.W.T., & Jamie, I.M., (2000). Fourier transform infrared spectrometry in atmospheric and trace gas analysis. Encyclopaedia of Analytical Chemistry. Meyers, R. A, Ed. Chichester: John Wiley & Sons Ltd.

Grimmond, C.S.B., Oke, T.R., (1999). Aerodynamic properties of urban areas derived, from analysis of surface form. Journal of Applied Meteorology 38:1262-1292.

Grutter, M., Flores, E., Basaldud, R. & Ruiz-Suarez, L.G., (2003a). Open-path FTIR spectroscopic studies of the trace gases over Mexico City. Atmospheric Ocean Optics. 16. 232-236.

Grutter, M., (2003b). Multi-gas analysis of ambient air using FTIR spectroscopy over Mexico City. Atmosfera. 16. 1-13.

Harrison, R.M., (2001). Pollution: causes, effects and control. Cambridge: RSOC.

Hinsley, S.A., Hill, R.A., Gaveau, D.L.A. & Bellamy, P.E., (2002). Quantifying woodland structure and habitat quality for birds using airborne laser scanning. Functional Ecology, 16, 851– 857.

Holmgren, J., Persson, Å., (2004). Identifying species of individual trees using airborne laser scanner. Remote Sensing of Environment 90:415-423.

Honjo, T. and Takakura, T., (1990-91). Simulation of thermal effects of urban green areas on their surrounding areas. Journal of Energy and Buildings, 15–16, 443–446.

Jiménez-Munõz, J.C. and Sobrino, J.A., (2003). A generalized single-channel method for retrieving land surface temperature. Journal of Geophysical Research, 108 (D22), 4688, doi:10.1029/2003JD003480.

Kim, S., McGaughey, R.J., Andersen, H.E., Schreuder, G., (2009). Tree species differentiation using intensity data derived from leaf-on and leaf-off airborne laser scanner data. Remote Sensing of Environment, 113, 1575-1586.

Knott, W., (2011). LiDAR: An Application for Measuring Urban Vegetation Parameters? A London Case Study. Independent Geographical Study, King's College London, 64 pp.

Lee, A.C. and Lucas, R.M., (2007). A LiDAR derived canopy density model for tree stem and crown mapping in Australian forests Original Research Article. Remote Sensing of Environment, 111(4), 493-518.

Lefsky, M.A., (1997). Application of LiDAR remote sensing to the estimation of forest canopy and stand structure, Ph.D. thesis, Department of Environmental Science, University of Virginia, Charlottesville, VA

Liang, S., (2001). Narrowband to Broadband Conversion of Land Surface Albedo. I. Algorithms, Remote Sensing of Environment, vol. 76, pp. 213-238.

Lindberg, F., Grimmond, C.S.B., (2011). The influence of vegetation and building morphology on shadow patterns and mean radiant temperatures in urban areas: Model development and evaluation. Theoretical and Applied Climatology DOI10.1007/s00704-010-0382-8.

McGaughey, R.J., (2009). FUSION/LDV: Software for LiDAR Data Analysis and Visualization. United States Department of Agriculture, Seattle.

Næsset E., (2004.) Accuracy of forest inventory using airborne laser scanning: evaluating the first Nordic full scale operational project. Scandinavian journal of forest research.19, 554-557.

Oke, T., (1987). Boundary Layer Climates. London: Methuen and Co. Ltd.

Popescu, S.C., Wynne, R.H., and Nelson, R.F., (2003). Measuring individual tree crown diameter with lidar and assessing its influence on estimating forest volume and biomass. Canadian Journal of Remote Sensing, 29, 564–577.

Pu, R., P. Gong, R. Michishita, and T. Sasagawa, (2006). Assessment of multiresolution and multi-sensor data for urban surface temperature retrieval. Remote Sens. Environ, 104, 211-225.

Reitberger, C, Schnörr, P, Krzystek and Stilla, U., (2009). 3D segmentation of single trees exploiting full waveform LIDAR data. ISPRS Journal of Photogrammetry and Remote Sensing, 64 (6), 561–574.

Roberts, S.D, Dean, T.J, Evans, D.L, McCombs, J.W. and Harrington, R.L., (2005). Estimating individual tree leaf area in loblolly pine plantations using LiDAR-derived measurements of height and crown dimensions, Forest Ecology and Management, 213, 54–70.

Rothman, L. S. et al., (2005). The HITRAN 2004 molecular spectroscopic database. Journal of Quantitative Spectroscopy and Radiative Transfer. 96. 139 – 204.

Stathopoulou, M., Cartalis, C. and Petrakis, M., (2007). Integrating Corine Land Cover data and Landsat TM for surface emissivity definition: application to the urban area of Athens, Greece. International Journal of Remote Sensing, vol. 28(15), pp. 3291 – 3304.

Streutker, D.R. and Glenn, N.F., (2006). LiDAR measurement of sagebrush steppe vegetation heights. Remote Sensing of Environment, 10, 135-145.

Tallis, M., Freer-Smith, P., Sinnett, D. & Taylor, G., (2011). Estimating the removal of atmospheric particulate pollution by the urban tree canopy of London under current and future developments. Landscape and Urban Planning – Under review.

Tharpa, R.B. and Murayama, Y. (2009). Urban mapping, accuracy, & image classification: A comparison of multiple approaches in Tsukuba City, Japan. Applied Geography, 29, 135-144.

Upmanis, H., Eliasson, I., Lindqvist, S., (1998). The influence of green areas on nocturnal temperatures in a high latitude city (Goteborg, Sweden). International Journal of Climatology, 18, 681-700.

Williams, M.L., (2007). UK air quality in 2050—synergies with climate change policies. Environ. Sci. Policy, 10: 169-175.

2. Summary

Task 3.4 aims to show a description of main data collected in each city using GIS data, remote sensing techniques, and different modeling approaches. Maps of energy, water, carbon and pollutant fluxes are shown per each case study and a description of the techniques used is reported.

For each case study, the following results will be showed:

- Maps of surface albedo in the visible part of the spectrum (NKUA) by satellite data
- Urban land cover/land use maps (NKUA)
- Surface characteristics by LiDAR measurements (KCL)
- Land surface temperature (NKUA) by satellite data and measurements using infrared thermometers and thermal cameras (KCL)
- Morphological characteristics and anthropogenic heat flux (CMCC)
- Maps of sensible heat flux (CMCC)
- Maps of surface emissivity (CMCC, NKUA) by modeling and satellite data
- Airborne images (KCL, CNR)
- Air quality measurements by modeling (SOTON) and infra red spectroscopy measurements (KCL)

Partners involved

1. CNR
Consiglio Nazionale delle Ricerche, Italy
Enzo Magliulo (enzo.magliulo@cnr.it)
Franco Miglietta (f.miglietta@ibimet.cnr.it): Firenze case study leader

2. CMCC
Centro Euro-Mediterraneo per i Cambiamenti Climatici S.c.a.r.l, Italy
Donatella Spano (spano@uniss.it)

3. KCL
King's College London
Sue Grimmond (sue.grimmond@kcl.ac.uk): London case study leader

4. NKUA
National and Kapodistrian University of Athens, Greece
Mattheos Santamouris (msantam@phys.uoa.gr): Athens case study leader

5. FORTH
Foundation for Research and Technology – Hellas, Greece
Nektarios Crysoulakis (zedd2@iacm.forth.gr)

6. SOTON
School of Biological Sciences-United Kingdom
Prof. Gail Taylor (G.Taylor@soton.ac.uk)

7. UHEL
University of Helsinki, Finland
Timo Vesala (timo.vesala@helsinki.fi): Helsinki case study leader

8. IETU
Instytut Ekologii Terenów Uprzemysłowionych, Poland
Tomasz Staszewski (stasz@ietu.katowice.pl): Gliwice case study leader

3. Satellite derived information used in meso-scale modeling for all Case Studies

3.1 Satellite derived DEMs that were used in BRIDGE meso-scale simulations

For the production of Digital Elevation Model (DEM) from optical satellite data, the respective satellite sensors should have stereo coverage capabilities (Toutin 2001). The methods for applying stereoscopy to push-broom scanners generally use the rigorous photogrammetric solution (collinearity and coplanarity conditions for the conic perspective of a single image line), but take into account the displacement of the satellite (cylindrical perspective) to link the equations between themselves (Toutin 2004). Since the parameters of neighbouring lines are highly correlated, and satellite positions and attitude can be computed from on-board recording systems, the mathematical equations can be reduced to a minimum of eight to ten unknowns, depending on the mathematical development and the algorithm implementation of the solution. A stereo matching process to extract elevation parallaxes is applied (Toutin 2008).

The basic characteristics of stereoscopy and its application to the ASTER (Advanced Spaceborne Thermal Emission and Reflection Radiometer) for DEM generation have been recently reviewed by Toutin (2008). ASTER consists of three separate instruments subsystems, each operating in a different spectral region, using separate optical system. These subsystems are the Visible - Near Infrared (VNIR), the Short-Wave Infrared (SWIR) and the Thermal Infrared (TIR). The spatial resolution varies with wavelength: 15 m in the VNIR, 30 m in the SWIR and 90 m in the TIR. The VNIR subsystem consists of two telescopes – one nadir looking with a three band detector (Channels 1, 2 and 3N) and the other backward looking (27.7° off-nadir) with a single band detector (Fujisada 1994, Abrams 2000). The data products provided by the ASTER have been summarized by Yamaguchi et al. (1998).

ASTER Level 1A data were used in BRIDGE to derive the DEM for the Cae Study of Athens. Level 1A data are projected to the map using the radiometric calibration and geometric correction coefficients for resampling Fujisada (1998). ASTER scenes acquired over the study area from 2004 to 2007 were used. Auxiliary and validation datasets for the study area provided by FORTH. These include contour lines and shoreline digitized from 1:50.000 topographic maps, GPS measurements and the road network. ASTER 3N and 3B channels, were used for DEM production. The methodology described by Chrysoulakis et al. (2004a, b) and Nikolakopoulos et al. (2006) was applied to extract a high resolution (15 m pixel) DEM, using ASTER channels 3N and 3B. The main difference in this study is that SILCAST software (SILC 2007) was used to analyze ASTER images and to extract DEM and orthorectified products from each ASTER scene.

A DEM from each of the ASTER scene was extracted and the respective VNIR and SWIR channels were orthorectified. Next, virtual images corresponding to the nine initial ASTER scenes were created using the respective VNIR and SWIR channels, as well as the extracted DEM. As a result, nine multispectral orthorectified images were created, each containing the respective DEM as a separate pseudochannel. These images were following used to provide a mosaic image covering the study area. In practice two mosaics were initially crated: One for the DEM pseudochannels and one for the VNIR and SWIR channels of each image. In the former case the radiometric values of each DEM were kept and a bilinear interpolation resampling method was used. In the latter case, the color balancing and histogram matching functions were used and the radiometric values of VNIR and SWIR channels were slightly modified ensuring the color homogeneity of all scenes. The two

mosaics were finally merged to one master mosaic covering the broader area of Athens Case Study. This mosaic was finally fine-tuned using the road network vectors of the area. In this way the plannimetric (xy) error was corrected to ± 0.5 pixel RMSE using a 2D transformation. This correction was automatically applied to the DEM since it was a pseudochannel of the multispectral mosaic. The planimetric accuracy of the corrected DEM was therefore better than 15 m. The shoreline derived from 1:50000 topographic maps was used to clip the corrected mosaic extracting in this way the area corresponding to land. The DEM pseudochannel was separated from the rest channels of the mosaic. The ASTER derived DEM is shown in Figure 1.

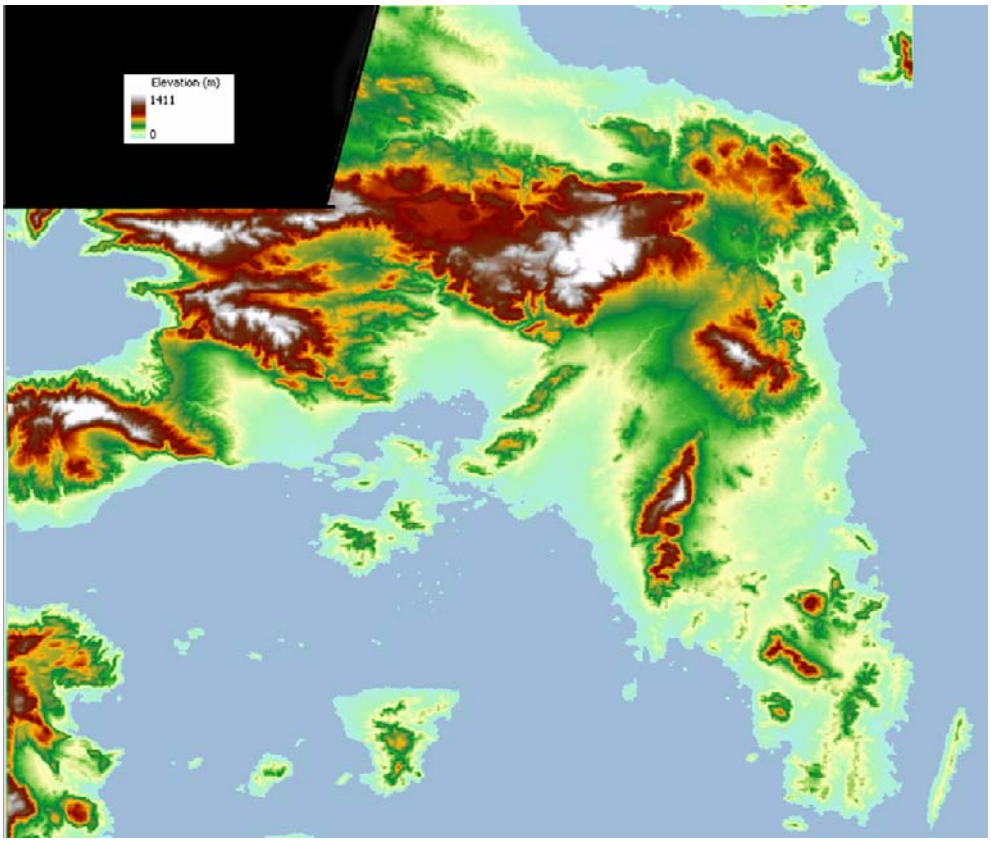

Figure 1. The ASTER derived DEM for the Vase Study of Athens.

The vertical accuracy of the final DEM product was assessed using GPS measurements. Elevation accuracy is generally of the order of the system instantaneous field of view (or approximately the pixel spacing), also taking into account the Base to Height ratio (B/H). However, in most cases, the accuracy obtained with real data was better than that predicted based on pre-launch information alone. The theoretical accuracy of ASTER DEMs is therefore governed by the accuracy of the control data, the B/H and the matching. Since an error of ± 0.5 - 1 pixel or better for the parallax measurements in the automated matching process has been achieved with different datasets from other sensors, the potential relative accuracy for the elevation with the ASTER stereo data (B/H = 0.6, pixel spacing of 15 m) could be of the order of 12 – 25 m or better depending of the type of terrain. In addition, the accuracy of the DEM will also be dependent on the geometric parameter calibration, as well as the accuracy of the ephemeris and attitude data for computing the direct georeferencing.

To have a more robust estimation of the quality of the produced DEM the RMSE were used. Assuming parallax difference correlation errors in the range of 0.5 to 1.0 pixels and taking into

account that the final mosaic was fine tuned using the road network vectors for the study areas as described in previous section, elevation errors (RMSEz) are expected to be in the ±12 to 25 m range (Chrysoulakis et al 2004a). In practice, 440 GPS observations were used to check DEM's vertical accuracy as described in Chrysoulakis et al. (2004a). A very good correlation (R^2 = 0.9983) was observed as shown in Figure 2, where a scatter-plot between ASTER derived elevation (Z_{ASTER}) vs GPS derived elevation (Z_{SM}) is presented. Moreover, the RMSE was used for a more quantitative evaluation of DEM's vertical accuracy. A RMSE of 14.39 m was calculated.

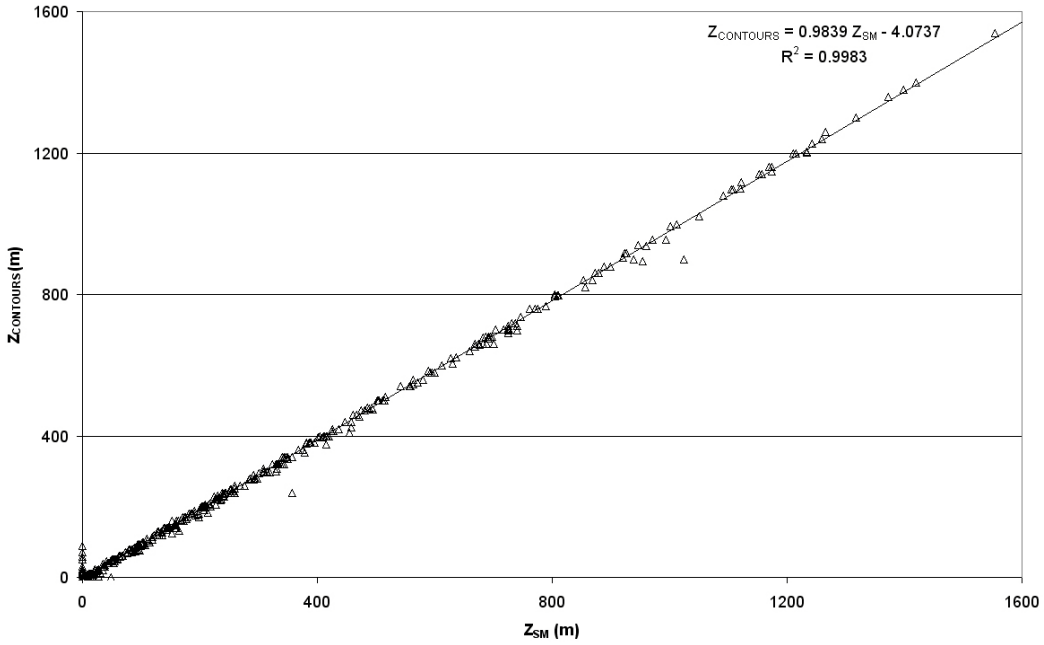

Figure 2. Scatter-plot between Z_{ASTER} and Z_{SM}. An excellent correlation is observed.

For the rest BRIDGE Case Studies (Helsinki, London, Firenze and Gliwice) a DEMs were extracted from the ASTER Global Digital Elevation Model (GDEM) which was released by Japan's Ministry of Economy, Trade and Industry (METI) and United States National Aeronautics and Space Administration (NASA) on June 29, 2009. GDEM is a global DEM generated using ASTER data, with 30 m posting. The ASTER GDEM was created by stereo-correlating the entire ASTER archive; stacking and averaging the individual DEMs; cloud screening; filling voids or holes using SRTM 3 arc-second data; and validating the GDEM against higher resolution DEMs worldwide (Abrams et al., 2010). It is noted that the ASTER DEM was evaluated in the framework of BRIDGE for the whole area of Greece (where in situ elevation information was available for validation) by Chrysoulakis et al (2011).

The resulted DEMs for broader areas of Helsinki, London, Firenze and Gliwice are shown in Figures 3, 4, 5, and 6 respectively. The derived DEMs for each Case Study, was delivered to the BRIDGE modelers (WP4) to be directly used in simulations of meso-scale models. The spatial resolution of this product is the spatial resolution of the ASTER GDEM (30 x 30 m), whereas especially for Athens where the DEM was produced by FORTH usinf ASTER raw data, it spatial resolution was 15 x 15 m. The Geographic WGS84 system has been used for the DEMs projection with the vertical datum EGM96.

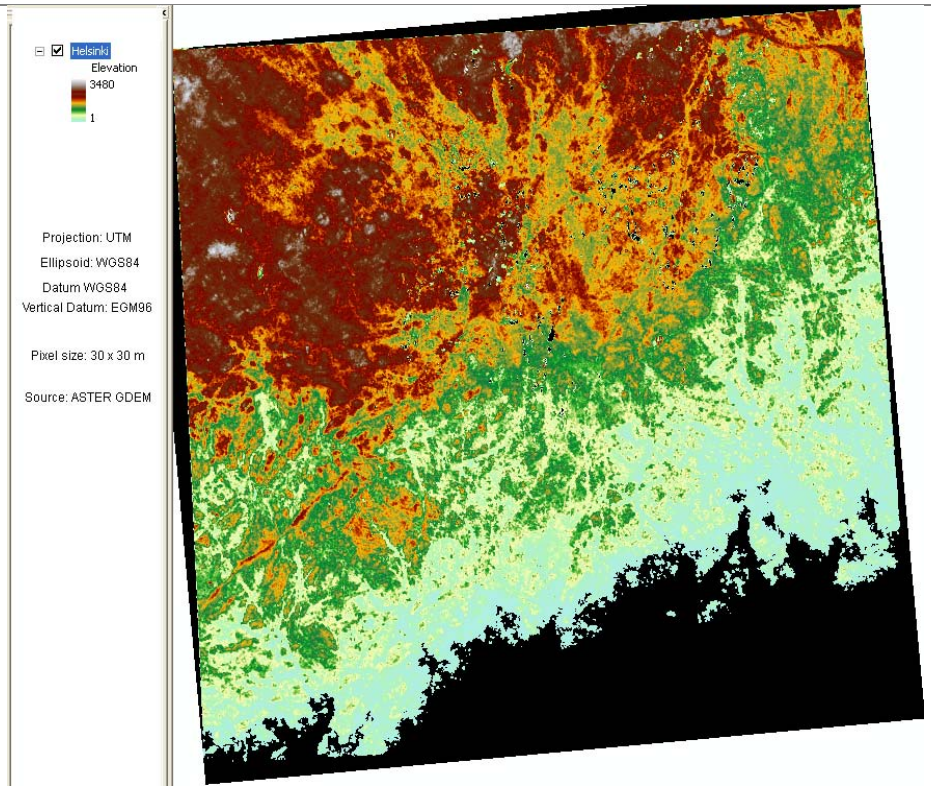

Figure 3. DEM for the broader area of Helasinki as extracted from ASTER GDEM.

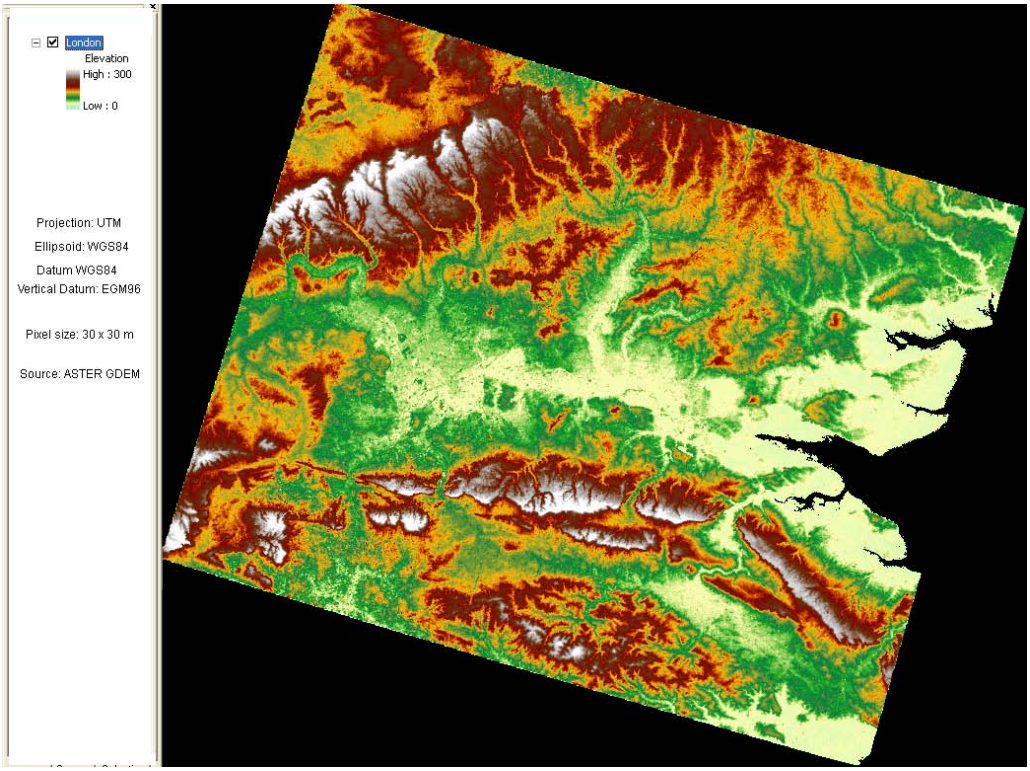

Figure 4. DEM for the broader area of London as extracted from ASTER GDEM.

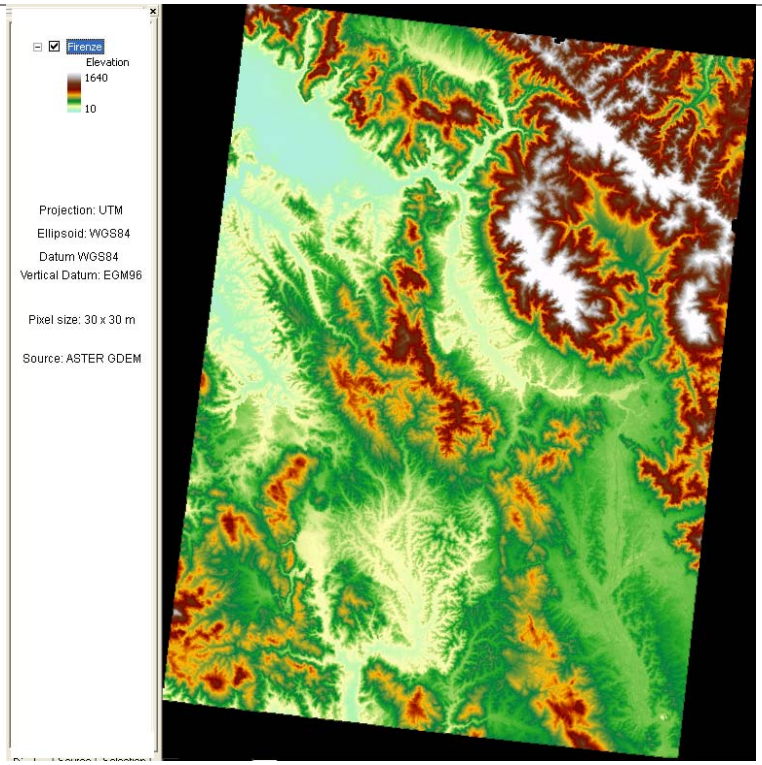

Figure 5. DEM for the broader area of Firenze as extracted from ASTER GDEM.

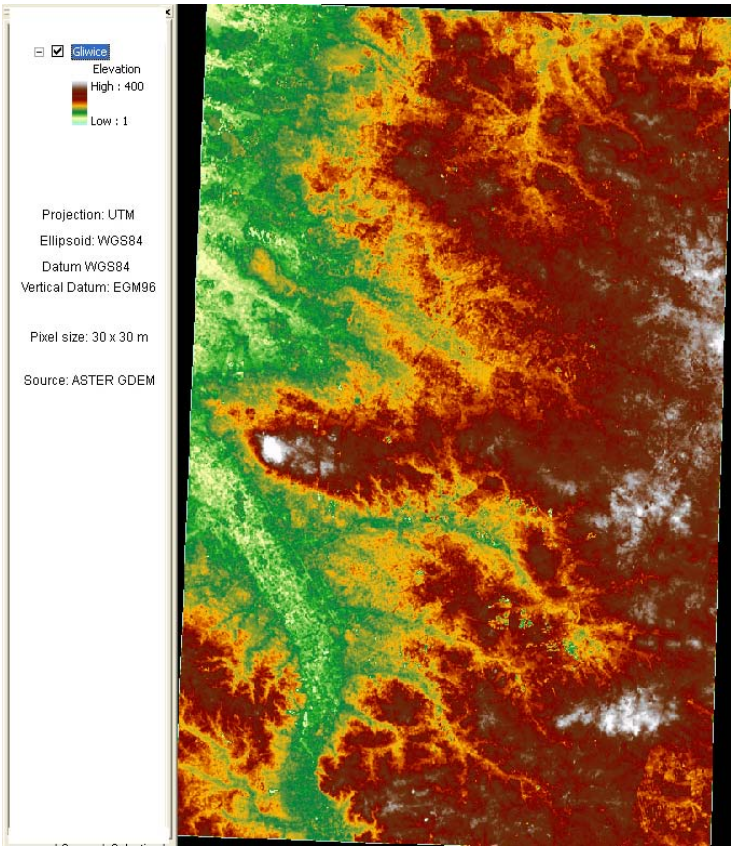

Figure 6. DEM for the broader area of Gliwice as extracted from ASTER GDEM.

References

Abrams, M., B. Bailey, H. Tsu, and Hato, M., 2010. The ASTER Global DEM. Photogrammetric Engineering and Remote Sensing, 76, 344 - 348.

Abrams, M., 2000. ASTER: data products for the high spatial resolution imager on NASA's EOS-AM1 platform. International Journal of Remote Sensing 21, 847-861.

Chrysoulakis, N., Abrams, M., Kamarianakis, Y. and Stanisławski, M., 2011. Validation of the ASTER GDEM for the area of Greece. Photogrammetric Engineering & Remote Sensing, 77, 157 - 165.

Chrysoulakis, N., Abrams, M., Feidas, H. and Velianitis, D., 2004a. Analysis of ASTER Multispectral Stereo Imagery to Produce DEM and Land Cover Databases for Greek Islands: The REALDEMS Project. In: Prastacos, P., Cortes, U. De Leon, J. L., Murillo, M. (Eds): Proceedings of e-Environment: Progress and Challege, 411 - 424

Chrysoulakis, N., Diamandakis, M. and Prastacos, P., 2004b. GIS based estimation and mapping of local level daily irradiation on inclined surfaces. In: Toppen, F. and P. Prastacos (Eds), Proceedings of the 7th AGILE Conference on Geographic Information Science, 587 – 597.

Fujisada, H., 1994. Overview of ASTER instrument on EOS-AM1 platform, In Proceedings of SPIE, 2268, 14–36.

Fujisada, H., 1998. ASTER Level-1 data processing algorithm, IEEE Transactions on Geoscience and Remote Sensing, 36, 1101 - 1112.

Nikolakopoulos, K., Kamaratakis, E. and Chrysoulakis, N., 2006. SRTM vs ASTER Elevation Products. Comparison for two regions in Crete, Greece. International Journal of Remote Sensing, 27, 4819-4838.

SILC, 2007. SILCAST Operational Manual, Version 1.5, Sensor Information Laboratory Corp., 107 Corp Tsukuba, Ibaraki, 305-0005 Japan (www.silc.co.jp).

Toutin, 2008. ASTER DEMs for geomatic and geoscientific applications: a review. Elevation Modelling from Satellite VIR Data: A Review, International Journal of Remote Sensing, 29, 1855 - 1875.

Toutin, Th., 2004. Geometric processing of remote sensing images: models, algorithms and method. International Journal of Remote Sensing, 25, 1893 - 1924.

Toutin, Th., 2001. Elevation Modelling from Satellite VIR Data: A Review, International Journal of Remote Sensing, 22, 1097 - 1125.

Yamaguchi, Y., Kahle, A., Tsu, H. Kawakami, T. and Pniel, M., 1998. Overview of advanceds spaceborne thermal emission and reflection radiometer (ASTER). IEEE Transactions on Geosciences and Remote Sensing, 36, 1062 - 1071.

3.2 Satellite derived surface albedo that was used in BRIDGE meso-scale simulations

Satellite derived surface albedo products have been used as inputs in BRIDGE meso-scale models simulations. FORTH has analyzed a time series of Moderate Resolution Imaging Spectroradiometer (MODIS) Level 2 albedo product.

The surface albedo was estimated from white-sky (completely diffuse) and black-sky (direct beam) albedo products that were retrieved by MODIS observations for each elementary (dependent on the sensors' spatial resolution) surface. MODIS do not directly measure the surface albedo. It receive signals representing radiances (radiation from a particular direction) in narrowbands at the top of the atmosphere. Albedo is related to land surface reflectance by directional integration and is therefore dependent on the Bidirectional Reflectance Distribution Function (BRDF), which describes how the reflectance depends on view and solar angles. Bi-directional reflectivity depends on the incident direction of the sun given by solar zenith and solar

azimuth and on the reflected direction of observation given by satellite zenith and satellite azimuth; therefore, bi-directional reflectivity is a function of 4 angles (2 directions).

A directional sampling of surface reflectances from sensors such as MODIS can only be obtained by the accumulation of sequential observations over a specified time period. Cloud obscuration routinely reduces the number of clear looks. A 16-day period (or more) should be chosen as a trade-off between the sufficiency of angular samples and the stability of surface reflectivity. These directional observations can be coupled with semi-empirical models to describe the BRDF and integrals necessary to provide spectral albedos. As discussed by Lucht et al. (2000), the BRDF can be expanded into a linear sum of terms (the so-called kernels), characterizing different scattering modes. The MODIS BRDF/Albedo algorithm makes use of a kernel-driven, linear BRDF model which relies on the weighted sum of an isotropic parameter and two functions (or kernels) of viewing and illumination geometry to determine reflectance (Schaaf et al., 2002).

The black-sky albedo $a^{dh}(\lambda;\theta_s,\phi_s)$, as well as the white-sky $a^{bh}(\lambda)$ albedo were computed using polynomial expressions of the kernel weights as described by Schaaf et al. (2002. The diffuse component then can be expressed as a function of wavelength, optical depth, aerosol type, and terrain contribution. Therefore, for partially diffuse illumination the actually occurring spectral albedo value may be approximated as a linear combination of the limiting cases:

$$a(\lambda) = \left[1 - f_{diffuse}(\lambda)\right] a^{dh}(\lambda;\theta_s,\phi_s) + f_{diffuse}(\lambda) a^{bh}(\lambda) \quad (1)$$

where $f_{diffuse}$ denotes the fraction of diffuse radiation and (θ_s,ϕ_s) the solar direction. Given the spectral albedos, the average broadband albedos can be predicted under general atmospheric conditions using spectral-to-broadband coefficients as per Liang (2000).

In BRIDGE, time series of MODIS black-sky and white sky albedo products were downloaded for the broader area of all BRIDGE Case Studies for 2008 and 2009. These products were 16-days composites as for example in Figure 1, where the MODIS derived black-sky and white-sky albeos, for the broader area of London, as produced by 16-days observations.

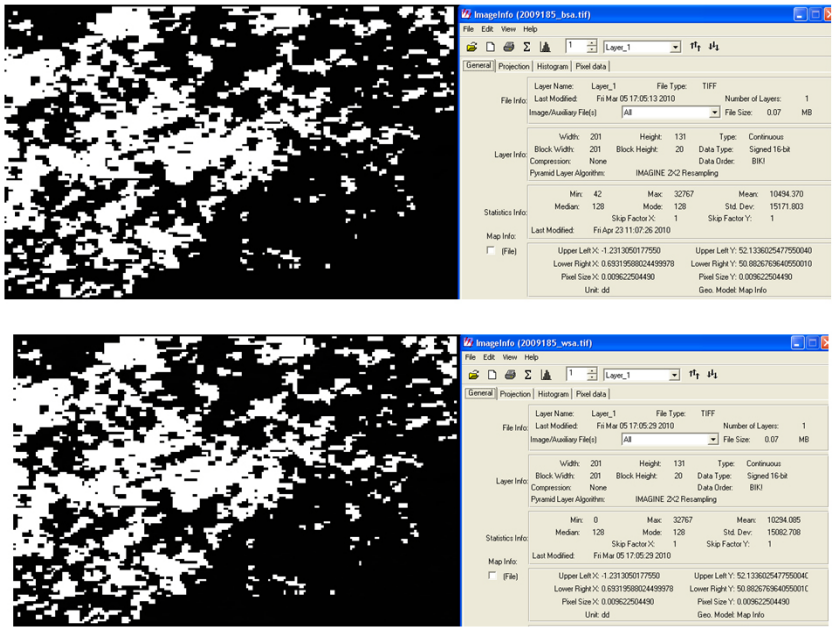

Figure 1. *Black-sky (upper part) and white-sky (lower part) albeo for the broader area of London, as produced by 16-days observations of MODIS (the 185th 16-day time interval of 2009 is presented).*

To calculate $f_{diffuse}$ in (1) a look-up table was used as shown in Figure 2. For each combination of solar zenith angle and AOT a value of $f_{diffuse}$ can be extracted from this look-up table. Therefore, by using the extracted $f_{diffuse}$ and the black and white sky albedo products, the surface albedo can be estimated using the Equation (1).

The above table and the black and white sky albedo products for each 16-days interval of 2008 and 2009, for each Case Study, was delivered to the BRIDGE modelers (WP4) to be used for direct calculations of surface albedos, using AOT simulations of meso-scale models. The spatial resolution of this product is the spatial resolution of the MODIS derived black and white sky albedo products (1 x1 km). Furthermore, a spatial model was develop in ERDAS Imagine environment using as inputs the blck-sky albedo, the white-sky albedo and the AOT, to calculate the surface albedo for solar zenith angles from 0° to 90° with step 10° as shown in Figure 3. Using the model shown in Figure 2 and the MODIS black-sky and white-sky products, time series of surface albedo was produce for each Case Study by FORTH: for each Case Study, for each 16-days interval of 2008 and 2009 that MODIS products were available, 3 multilayer images was produced one for AOT=0.1, one for AOT=0.5 and one for AOT=0.9. Each albedo image was a multilayer image and each layer corresponded to a specific solid angle as shown in Figure 2.

In Figure 3, an example of the surface albedo product for the 185th 16-days interval of 2009 for the area of London is given. The MODIS black and white sky albedo products that shown in Figure 1 have been used for solar zenith angle of 30° and several AOT. Finally in In Figure 4, an example of the surface albedo product for the 185th 16-days interval of 2009 for the area of London is given. The MODIS black and white sky albedo products that shown in Figure 1 have been used for AOT=0.5 and several solar zenith angles.

Table 1. *Look-up table for the calculation the fraction of diffuse radiation based on solar zenith angle and AOT.*

SOLAR ZENITH ANGLE (0 - 89°)	AEROSOL OPTICAL DEPTH (0 - 0.98)																
	0	0.02	0.04	0.06	0.08	0.1	0.12	0.14	0.16	0.18	0.2	0.22	0.24	0.26	0.28	0.3	0.32
0	0.068	0.08	0.09	0.101	0.112	0.122	0.132	0.142	0.152	0.161	0.171	0.18	0.189	0.198	0.207	0.215	0.224
1	0.068	0.08	0.09	0.101	0.112	0.122	0.132	0.142	0.152	0.161	0.171	0.18	0.189	0.198	0.207	0.215	0.224
2	0.068	0.08	0.09	0.101	0.112	0.122	0.132	0.142	0.152	0.161	0.171	0.18	0.189	0.198	0.207	0.215	0.224
3	0.068	0.08	0.091	0.101	0.112	0.122	0.132	0.142	0.152	0.161	0.171	0.18	0.189	0.198	0.207	0.216	0.224
4	0.068	0.08	0.091	0.101	0.112	0.122	0.132	0.142	0.152	0.162	0.171	0.18	0.189	0.198	0.207	0.216	0.224
5	0.069	0.08	0.091	0.101	0.112	0.122	0.132	0.142	0.152	0.162	0.171	0.18	0.19	0.198	0.207	0.216	0.224
6	0.069	0.08	0.091	0.102	0.112	0.122	0.133	0.143	0.152	0.162	0.171	0.181	0.19	0.199	0.208	0.216	0.225
7	0.069	0.08	0.091	0.102	0.112	0.123	0.133	0.143	0.152	0.162	0.172	0.181	0.19	0.199	0.208	0.216	0.225
8	0.069	0.08	0.091	0.102	0.112	0.123	0.133	0.143	0.153	0.162	0.172	0.181	0.19	0.199	0.208	0.217	0.225
9	0.069	0.08	0.091	0.102	0.113	0.123	0.133	0.143	0.153	0.163	0.172	0.181	0.191	0.2	0.208	0.217	0.226
10	0.069	0.08	0.091	0.102	0.113	0.123	0.133	0.143	0.153	0.163	0.172	0.182	0.191	0.2	0.209	0.218	0.226
11	0.069	0.081	0.092	0.102	0.113	0.123	0.134	0.144	0.154	0.163	0.173	0.182	0.191	0.2	0.209	0.218	0.227
12	0.069	0.081	0.092	0.103	0.113	0.124	0.134	0.144	0.154	0.164	0.173	0.183	0.192	0.201	0.21	0.219	0.227
13	0.07	0.081	0.092	0.103	0.114	0.124	0.134	0.145	0.154	0.164	0.174	0.183	0.192	0.201	0.21	0.219	0.228
14	0.07	0.081	0.092	0.103	0.114	0.124	0.135	0.145	0.155	0.165	0.174	0.184	0.193	0.202	0.211	0.22	0.228
15	0.07	0.081	0.093	0.104	0.114	0.125	0.135	0.145	0.155	0.165	0.175	0.184	0.193	0.203	0.212	0.22	0.229
16	0.07	0.082	0.093	0.104	0.115	0.125	0.136	0.146	0.156	0.166	0.175	0.185	0.194	0.203	0.212	0.221	0.23
17	0.07	0.082	0.093	0.104	0.115	0.126	0.136	0.146	0.156	0.166	0.176	0.185	0.195	0.204	0.213	0.222	0.23
18	0.071	0.082	0.094	0.105	0.116	0.126	0.137	0.147	0.157	0.167	0.177	0.186	0.195	0.205	0.214	0.223	0.231
19	0.071	0.083	0.094	0.105	0.116	0.127	0.137	0.147	0.158	0.168	0.177	0.187	0.196	0.205	0.214	0.223	0.232
20	0.071	0.083	0.094	0.106	0.117	0.127	0.138	0.148	0.158	0.168	0.178	0.188	0.197	0.206	0.215	0.224	0.233
21	0.072	0.083	0.095	0.106	0.117	0.128	0.138	0.149	0.159	0.169	0.179	0.188	0.198	0.207	0.216	0.225	0.234
22	0.072	0.084	0.095	0.107	0.118	0.128	0.139	0.149	0.16	0.17	0.18	0.189	0.199	0.208	0.217	0.226	0.235
23	0.072	0.084	0.096	0.107	0.118	0.129	0.14	0.15	0.16	0.171	0.18	0.19	0.2	0.209	0.218	0.227	0.236
24	0.073	0.085	0.096	0.108	0.119	0.13	0.14	0.151	0.161	0.171	0.181	0.191	0.201	0.21	0.219	0.228	0.237
25	0.073	0.085	0.097	0.108	0.119	0.13	0.141	0.152	0.162	0.172	0.182	0.192	0.202	0.211	0.22	0.23	0.239
26	0.074	0.086	0.097	0.109	0.12	0.131	0.142	0.153	0.163	0.173	0.183	0.193	0.203	0.212	0.222	0.231	0.24
27	0.074	0.086	0.098	0.109	0.121	0.132	0.143	0.154	0.164	0.174	0.184	0.194	0.204	0.214	0.223	0.232	0.241
28	0.074	0.087	0.099	0.11	0.122	0.133	0.144	0.154	0.165	0.175	0.186	0.195	0.205	0.215	0.224	0.234	0.243
29	0.075	0.087	0.099	0.111	0.122	0.134	0.145	0.155	0.166	0.177	0.187	0.197	0.207	0.216	0.226	0.235	0.244
30	0.075	0.088	0.1	0.112	0.123	0.135	0.146	0.157	0.167	0.178	0.188	0.198	0.208	0.218	0.227	0.236	0.246
31	0.076	0.088	0.101	0.112	0.124	0.136	0.147	0.158	0.168	0.179	0.189	0.199	0.209	0.219	0.229	0.238	0.247
32	0.077	0.089	0.101	0.113	0.125	0.136	0.148	0.159	0.17	0.18	0.191	0.201	0.211	0.221	0.23	0.24	0.249
33	0.077	0.09	0.102	0.114	0.126	0.138	0.149	0.16	0.171	0.182	0.192	0.202	0.212	0.222	0.232	0.241	0.251
34	0.078	0.09	0.103	0.115	0.127	0.139	0.15	0.161	0.172	0.183	0.193	0.204	0.214	0.224	0.234	0.243	0.253
35	0.078	0.091	0.104	0.116	0.128	0.14	0.151	0.163	0.174	0.184	0.195	0.205	0.216	0.226	0.235	0.245	0.255

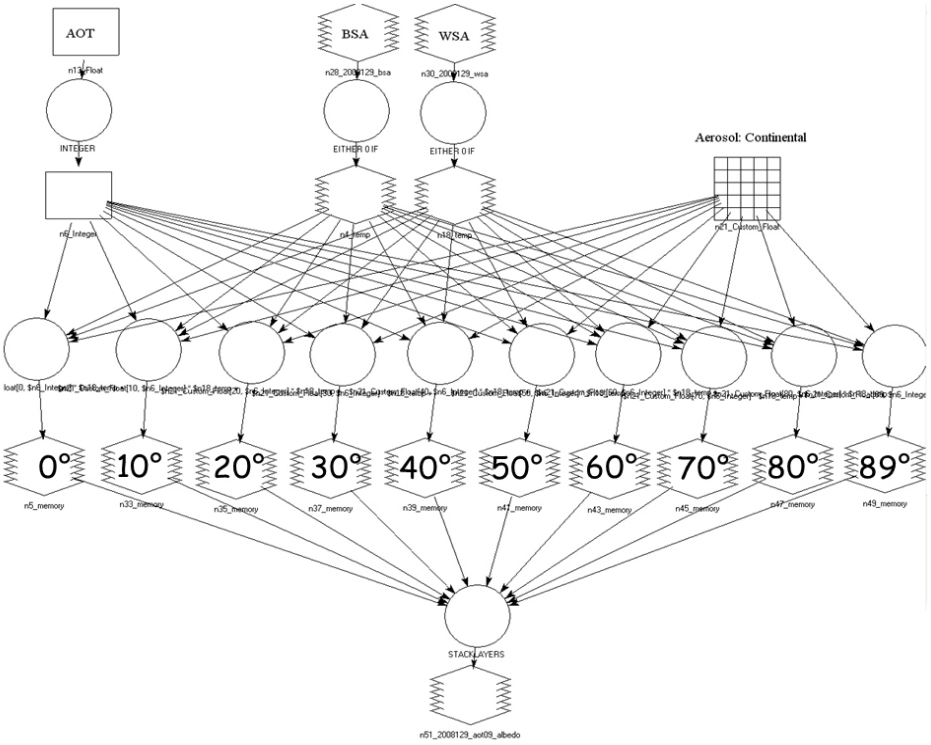

Figure 2. *Spatial model in ERDAS Imagine environment to calculate surface albedo for several solar zenith angles based on black-sky albedo, white-sky albedo and aerosol optical depth.*

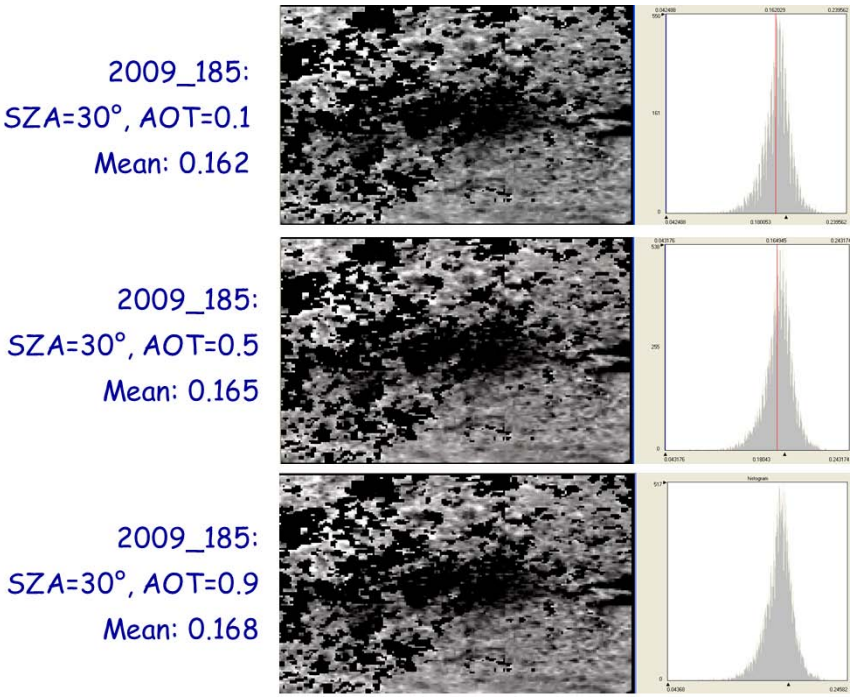

Figure 4. *Surface albedo for the 185th 16-days interval of 2009 for the area of London is given. The MODIS black and white sky albedo products that shown in Figure 1 have been used for solar zenith angle of 30° and AOT=0.1, 0.5 and 0.9.*

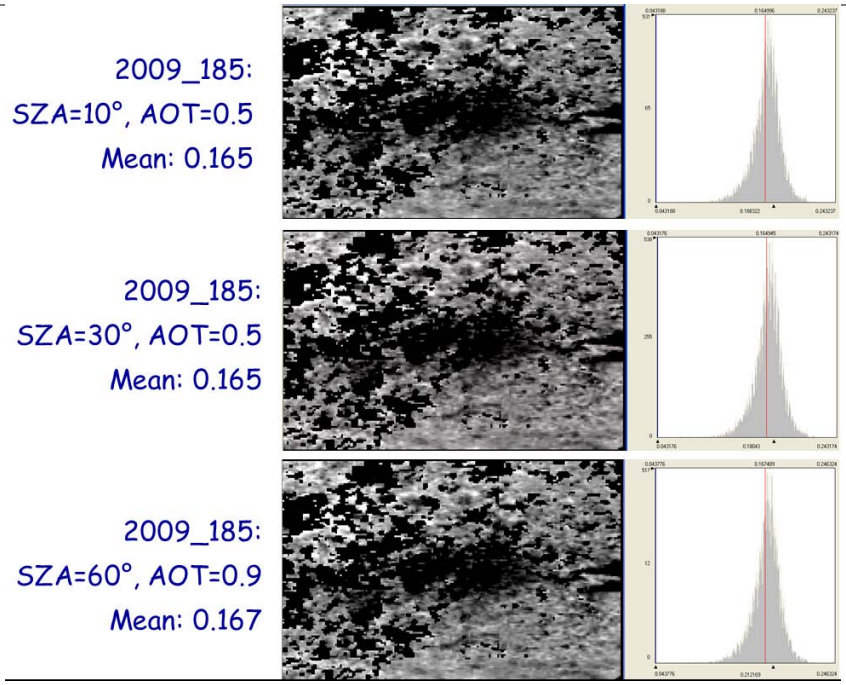

Figure 5. *Surface albedo for the 185th 16-days interval of 2009 for the area of London is given. The MODIS black and white sky albedo products that shown in Figure 1 have been used for AOT of 0.5 and solar zenith angle of 10°, 30° and 60°.*

References

Lucht, W., Schaaf, C. B. and Strahler, A., 2000. An algorithm for the retrieval of albedo from space using semiempirical BRDF models. IEEE Transactions on Geoscience and Remote Sensing, 38, 977 - 998.

Schaaf, C. B., et al. (2002), First operational BRDF, albedo and nadir reflectance products from MODIS, Remote Sens. Environ., 83, 135– 148.

3.3 Satellite derived surface emissivity that was used in BRIDGE meso-scale simulations

Satellite derived emissivity products have been used as inputs in BRIDGE meso-scale models simulations. FORTH has analyzed a time series of Moderate Resolution Imaging Spectroradiometer (MODIS) Level 2 emissivity product.

Daily emissivity maps were produced for 2008 for all BRIDGE Case Studies. The MODIS Level 2 emissivity product is available as daily global maps at 1 km spatial resolution. It has been produced using the classification based emissivity (Snyder et al., 1998). The classification-based emissivity method proposed by Snyder et al. (1998) to estimate emissivity from conventional static land cover classes and dynamic information and used it to develop an emissivity knowledge-base. The method was developed using linear Bidirectional Reflectance Distribution Function (BRDF) models, which have spectral coefficients derived from laboratory measurements (Salisbury and D'Aria 1992, 1994, Salisbury et al. 1994, Snyder et al. 1997), of material samples and structural parameters derived from approximate descriptions of the cover type (Snyder and Wan 1998).

Time series of MODIS channel 31 and channel 32 daily emissivty products were downloaded for the broader area of all BRIDGE Case Studies for 2008. Emissivity from MODIS channels 31 and 32 is estimated from the look up tables shown in Table 1.

Table 1. *Look up tables used to estimate surface emissivity from MODIS channels 31 and 32 observations, as per (Snyder et al., 1998).*

	Angle					
Emissivity class	10°		40°		65°	
Gr. Ndle. Forest	0·989	0·002	0·989	0·002	0·988	0·002
Sn. Ndle. Forest	0·986	0·003	0·986	0·003	0·985	0·004
Gr. Bdlf. Forest	0·987	0·003	0·987	0·003	0·986	0·003
*Sn. Bdlf. Forest	0·968	0·016	0·967	0·017	0·965	0·018
Gr. Woody Savanna	0·988	0·004	0·988	0·004	0·989	0·005
Sn. Woody Savanna	0·975	0·010	0·976	0·010	0·976	0·012
Gr. Grass Savanna	0·987	0·003	0·987	0·003	0·988	0·004
Sn. Grass Savanna	0·973	0·013	0·973	0·013	0·973	0·013
*Gr. Sparse Shrubs	0·972	0·006	0·973	0·007	0·976	0·007
*Sn. Sparse Shrubs	0·970	0·005	0·971	0·005	0·972	0·005
*Water	0·991	0·001	0·992	0·003	0·982	0·008
Org. Bare Soil	0·977	0·010	0·977	0·010	0·976	0·010
*Arid Bare Soil	0·966	0·017	0·965	0·017	0·964	0·017
Snow, Ice	0·988	0·006	0·988	0·006	0·987	0·006

	Angle					
Emissivity class	10°		40°		65°	
Gr. Ndle. Forest	0·991	0·003	0·991	0·003	0·990	0·003
Sn. Ndle. Forest	0·988	0·004	0·987	0·004	0·987	0·004
Gr. Bdlf. Forest	0·990	0·004	0·990	0·004	0·989	0·004
*Sn. Bdlf. Forest	0·971	0·009	0·970	0·010	0·968	0·010
Gr. Woody Savanna	0·991	0·003	0·991	0·004	0·992	0·004
Sn. Woody Savanna	0·978	0·009	0·978	0·009	0·979	0·011
Gr. Grass Savanna	0·991	0·003	0·991	0·003	0·991	0·004
Sn. Grass Savanna	0·975	0·011	0·975	0·011	0·975	0·013
*Gr. Sparse Shrubs	0·976	0·014	0·977	0·014	0·979	0·013
Sn. Sparse Shrubs	0·975	0·014	0·975	0·014	0·976	0·013
*Water	0·986	0·002	0·988	0·006	0·970	0·015
Org. Bare Soil	0·982	0·007	0·982	0·007	0·982	0·007
Arid Bare Soil	0·972	0·016	0·972	0·016	0·971	0·017
*Snow, Ice	0·977	0·013	0·979	0·012	0·976	0·021

The time series of these MODIS derived emissivity products were descaled, geometrically corrected and reprojected to Geographic WGS84, as shown in Figure 1, where an example of MODIS derived spectral emissivities for the broader area of Athens in shown. Finally, the surface emissivity was produced for each day, for each BRIDGE Case Study, as a spatial average of MODIS derived spectral emissivities, as shown in Figure 2.

The time series of surface emissivity for each day of 2008, for each Case Study, was delivered to the BRIDGE modelers (WP4) to be direct used in simulations of meso-scale models. The spatial resolution of this product is the spatial resolution of the MODIS derived spectral emissivities (1 x1 km).

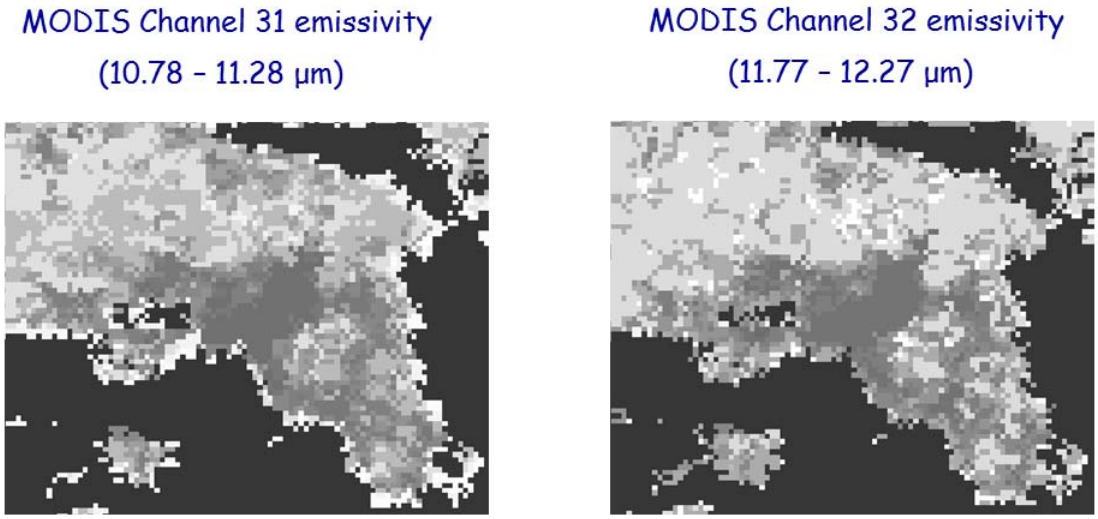

Figure 1. *MODIS derived spectral emissivities for channels 31 and 32 for the BRIDGE Case Study of Athens, for the Julian Day 240 of 2008.*

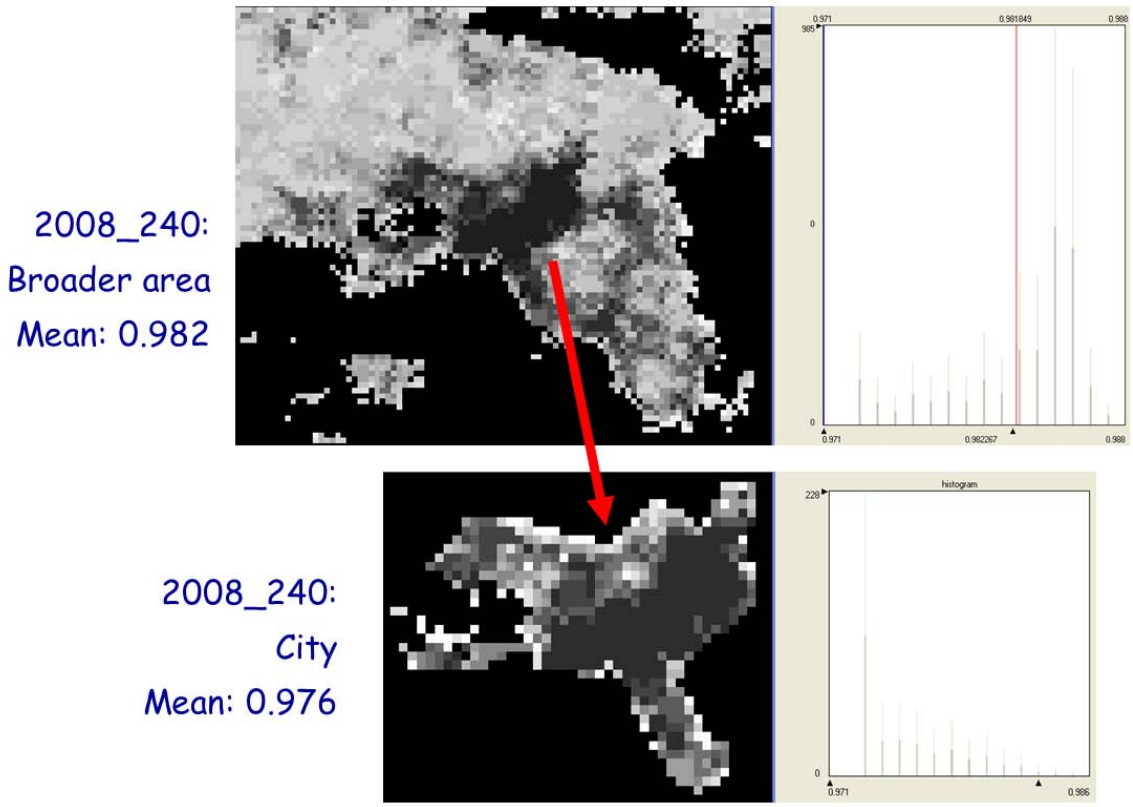

Figure 2. *Surface emissivity based on MODIS derived spectral emissivities for the BRIDGE Case Study of Athens, for the Julian Day 240 of 2008.* The result for the broader area of the city (upper), as well as a subset for the area corresponded to the continuous urban fabric (lower) are shown.

References

Salisbury, J. W., D'Aria, D. M., and Wald, A., 1994. Measurements of thermal infrared spectral reflectance of frost, snow, and ice. Journal of Geophysics Research, 99, 24,235 - 24,240.

Salisbury, J. W., and D'Aria, D. M., 1994. Emissivity of terrestrial materials in the 3 -5 μm atmospheric window. Remote Sens. Environ., 47, 345 - 361.

Salisbury, W., and D' Aria, D. M., 1992. Emissivity of terrestrial materials in the 8–14 mm atmospheric window. Remote Sens. Environ., 42, 83–106.

Snyder, W. C., Wan, Z., Zhang, Y. and Feng, Y. -Z., 1998. Classification-based emissivity for land surface temperature measurement from space. Int. J. Remote Sens., 19, 2753-2774. Valor, E. and Casseles, V., 1996. Mapping Land surface emissivity from NDVI: Application to European African and South American areas. Remote Sens. Environ., 57, 167 – 184.

Snyder, W. C., Wan, Z., Zhang, Y., and Feng, Y., 1997. Thermal infrared (3± 14 μm) bidirectional reflectance measurements of sands and soils. Remote Sens. Environ., 60, 101 - 109.

Snyder,W. C., and Wan, Z., 1998. BRDF models to predict spectral re¯ ectance and emissivity in the thermal infrared. IEEE T ransactions on Geoscience and Remote Sensing, 36, 214 - 225.

4. Helsinki

For Helsinki case studies, no measurements with remote sensing techniques were planned during the project. Results showed in this section are therefore coming from modelling tool, able to reproduce surface characteristics and fluxes using GIS data. The mesoscale model WRF (Weather and Forecast model), then, was run at 200 m horizontal grid spacing on a 5km by 5km gridded domain, which gives an effective horizontal resolution of about 600-800 meters. Initial and boundary conditions updated every 3 hours were provided for all of 2008 by UPM. In addition, a special set of surface characteristics were provided at 200m grid spacing to drive the simulations, as the standard WRF package contains these at 1x1 km only. The model was run for a single (non-nested) domain (using "*ndown"*).

For these simulations, WRF was run with ACASA (Advanced-Canopy-Atmosphere-Soil Algorithm) embedded as a column physics module that provides both the physical state and forcing between the surface-layer and the rest of the WRF atmosphere. This communication is fully dynamic in that WRF provides the meteorological and morphological forcing for ACASA, while ACASA responds back to WRF in a manner that alters the atmospheric state. ACASA was implemented in WRF using a similar subroutine calling architecture as that used by the existing NOAHLSM surface-layer module, since that particular platform provided needed morphological information while enabling the usage of fluxes directly as output. This architecture was chosen over the other three options in WRF due to the fact that it is easier for ACASA to "communicate" back to WRF with little modification to its output.

As is the case with Earth's actual surface-atmosphere system, WRF simulations of the same depend very heavily on the exchange of heat, mass, and momentum between the surface and atmosphere. For this to occur, ACASA specifically requires the following variables from WRF: temperature, humidity, wind speed, downwelling long- and short-wave radiation flux densities, precipitation rate and form, air pressure, and the surface morphology characteristics (LAI, soil type, minimum stomatal resistance, background albedo and background roughness length). Other quantities needed by ACASA, such as the canopy architecture index, mean leaf diameter, basal respiration rate, etc. are "hardwired" with the same values at each point.

ACASA updates sensible heat flux density, latent heat flux density, friction velocity (related to momentum flux density), turbulence kinetic energy, and the effective surface "skin" temperature, and bulk thermal emissivity every 30 minutes. As is done with NOAHLSM and other surface-layer packages, WRF uses this information to translate the ACASA forcing into the radiative transfer modules and the time-tendency components of wind velocity, temperature, and humidity in the lowest atmospheric layers.

In addition, the soil and/or snow and/or canopy thermal and hydrological states are stored at each point between time steps in order to estimate the ACASA suite of thermal storage fluxes and water retention, etc., all of which are needed for ACASA to estimate the main fluxes (and surface emissivity) properly. Included here are albedo modifications whenever snow or soil moisture is present. Other ACASA quantities are also used by WRF, but these are mainly diagnostic only, as surface (water) runoff, underground runoff, soil surface infiltration rate, carbon-dioxide flux density.

Data are provided hourly, and appear as daily files. Also monthly and annual composite averages for each hour of the day are also provided and presented in the following paragraphs. All maps showed below are for a 5km x 5km domain, centered on the urban core.

4.1 Surface characteristics

The land use change in Helsinki domain accounts for vegetated and urbanized surfaces, and the presence of water bodies (ocean). In the Figure 1 is shown the land use map used to run the coupled model WRF-ACASA.

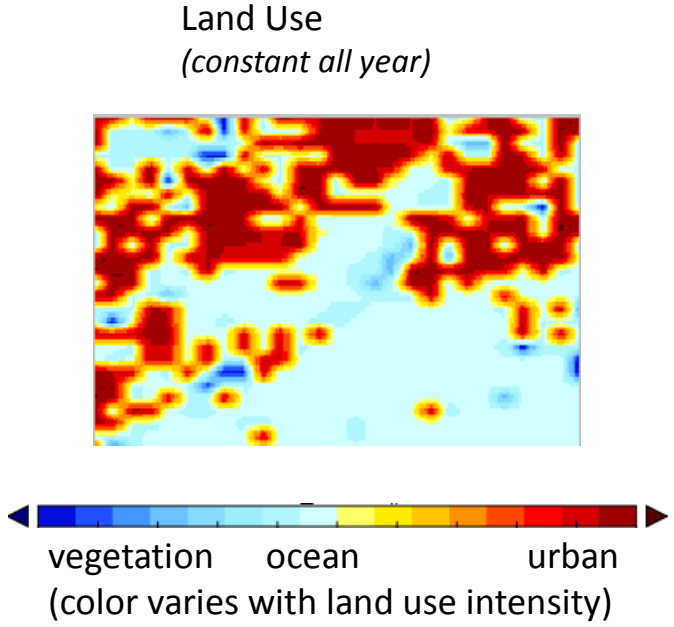

Figure 1. Helsinki land use map used to run the WRF-ACASA coupled model.

Urban heat island effects can be found during the day (sunlight > 0) during the year, with cross-city variations of several degrees Celsius between different land use types (Fig. 2). Temperatures are lower over open water than for land points during the day, with a reverse of this pattern evident at night, as expected. The contrast in 2m air temperatures between vegetated and urbanized surfaces is marked, with differences becoming most extreme during the daytime growing season (May through August).

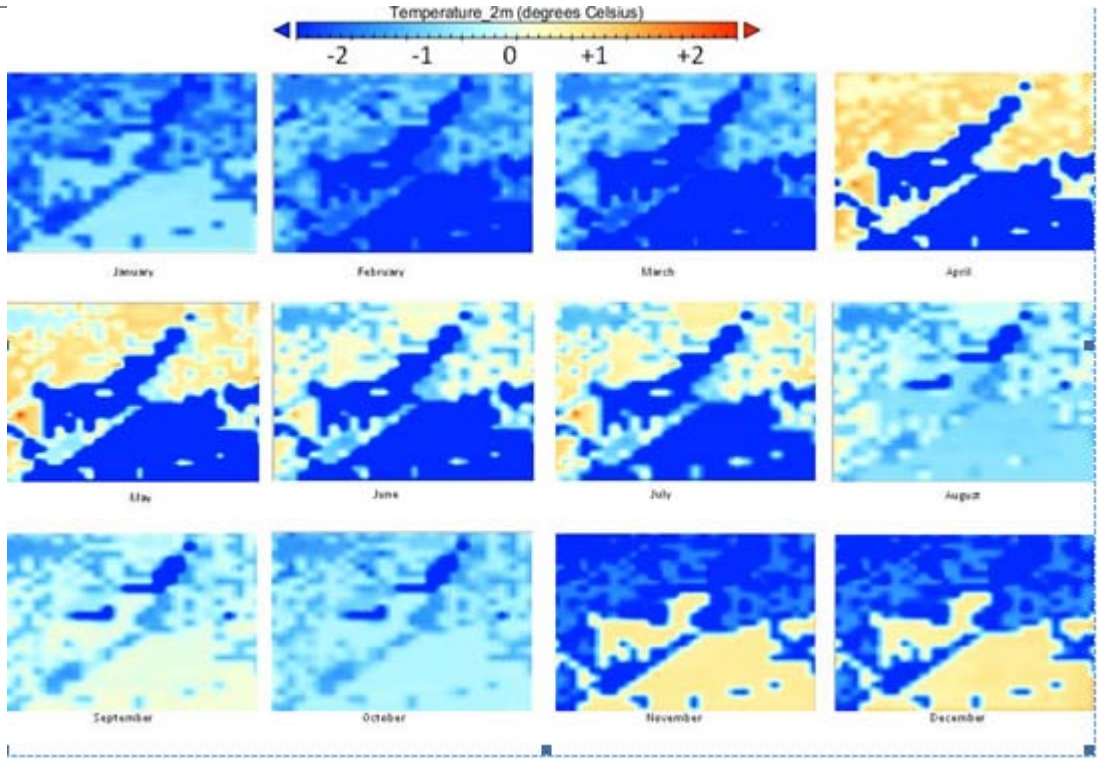

Figure 2. Monthly values (12:00 pm LT) of air temperatures at 2 meters (°C). A 5 degrees Celsius window normalized about the areal means was used to better visualize the urban heat island change throughout the year.

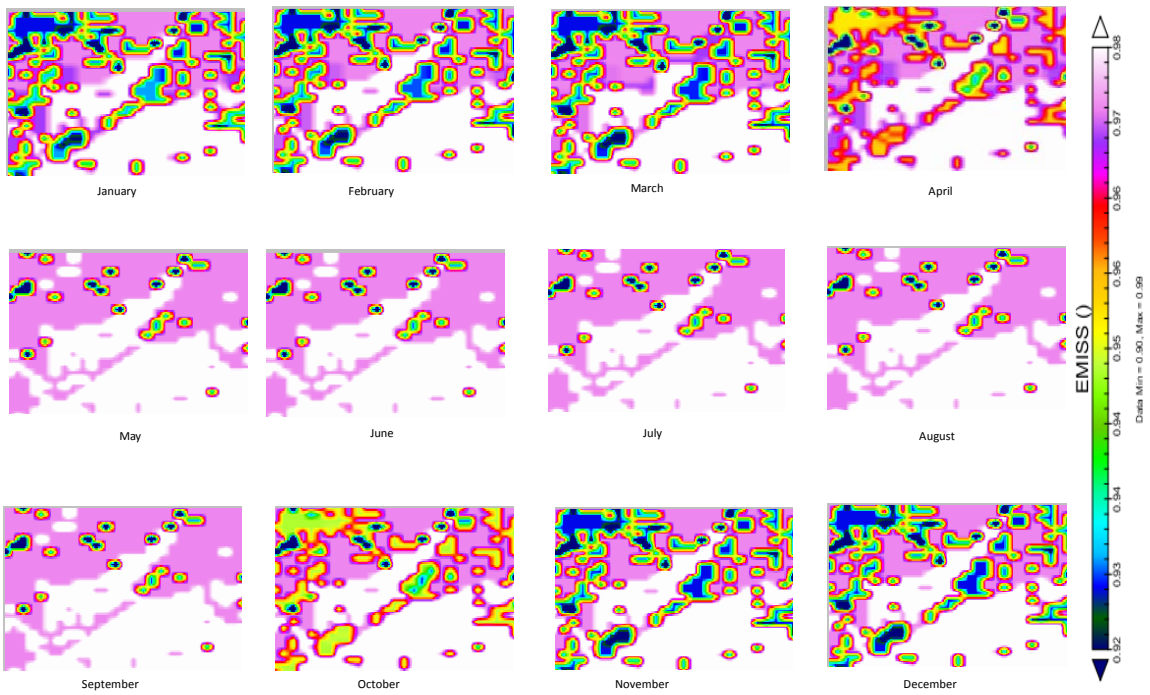

Figure 3. Emissivity monthly values (12:00 pm LT).

Thermal-IR emissivity exhibits subtle variations over time, mainly due to seasonal changes in vegetation density as well as stored water in the canopy. Notable differences can be found between vegetated and urbanized areas, due to differences in vegetation amount. Dense vegetation, present during the growing season, further depresses thermal emissivity values in relation to the urban core. Anyway, values don't change much during the year.

4.2 Energy fluxes

Sensible heat flux was simulated by WRF-ACASA at hourly time step and Figure 4 shows the monthly averages. The shorter summer of Helsinki is clearly apparent in this series, with maximum urban-core values exceeding 350 Wm^{-2} only during May through August, with more muted heating (or even cooling) prevailing throughout the rest of the year. The adjoining bay shows up as a moderating influence with more a muted annual cycle of fluxes.

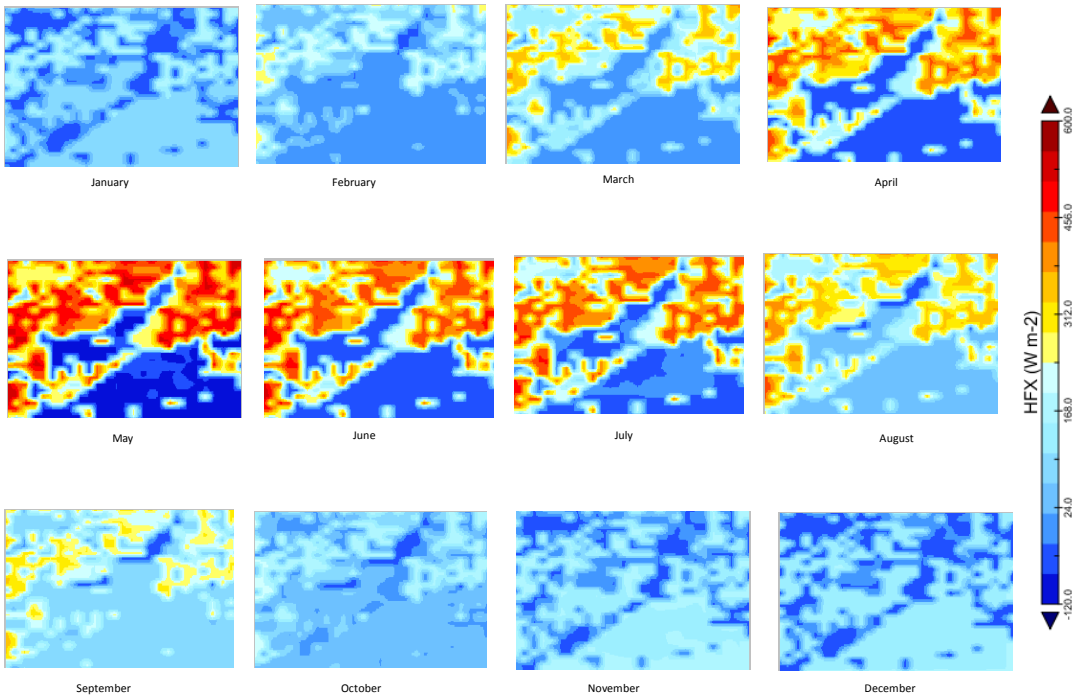

Figure 4. Sensible heat flux monthly values (12:00 pm LT) (W m^{-2}).

The time variations in anthropogenic storage flux density, monthly-averaged at midday, exhibits a long duration and high intensity (roughly 50% more losses in winter months) due to the freezing winter climate, despite the low population density. Internal temperatures were held constant at 19 °C throughout the year.

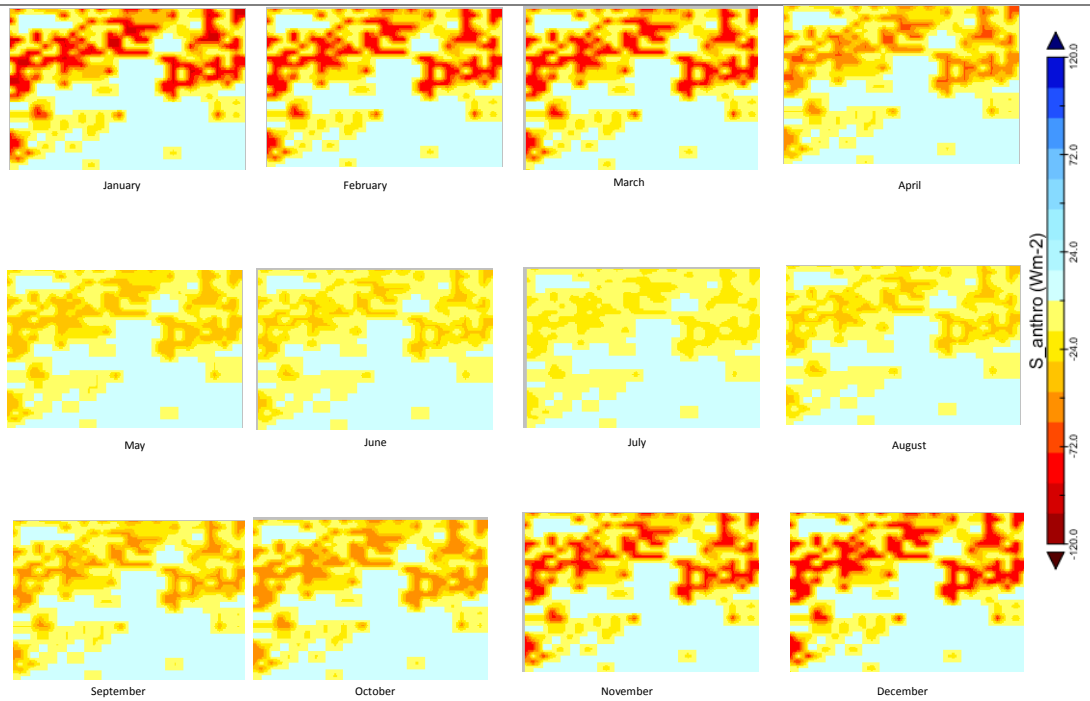

Figure 5. Monthly values (12:00 pm LT) of anthropogenic storage flux density (W m^{-2}).

4.3 Water exchanges

In general, weak values of evapotranspiration are noted throughout the year (Fig. 6). June-September period shows a lag of about 1 month as compared to maxima in sensible heating rates (Fig. 4).

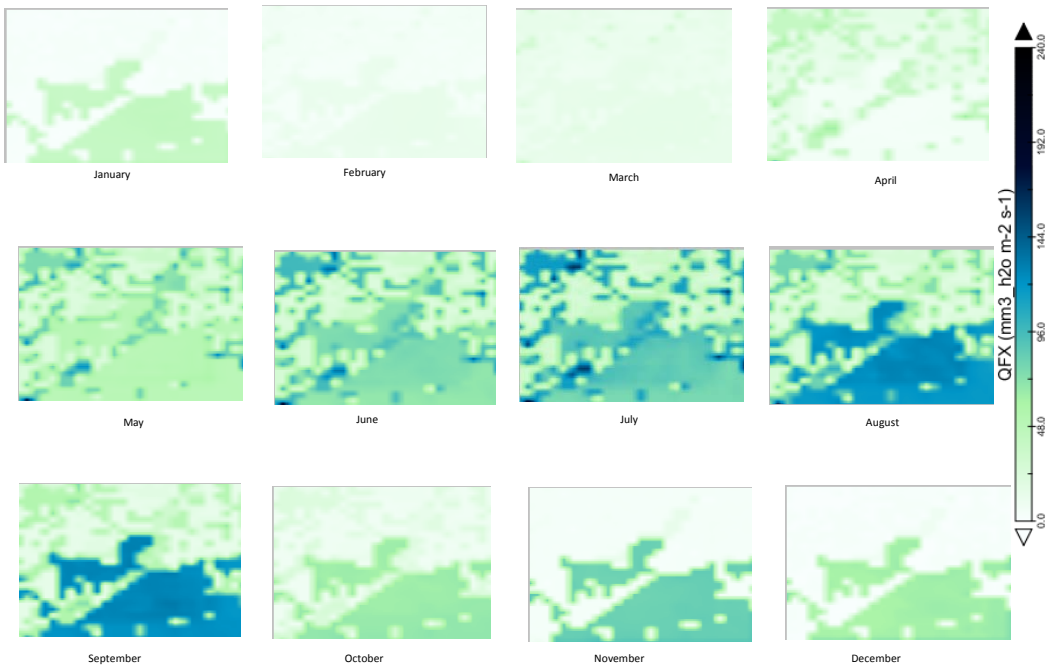

Figure 6. Monthly values (12:00 pm LT) of water vapor flux density (W m^{-2}).

4.4 Carbon fluxes

Strong contrasts between winter and summer are apparent, with mostly zero or positive values persisting everywhere in the domain November through February (Fig. 7). Strong negative values in the summer (indicating photosynthetic sequestration) occur alongside built-out areas in a pattern that suggests that simulations for this city show a near-neutral carbon footprint.

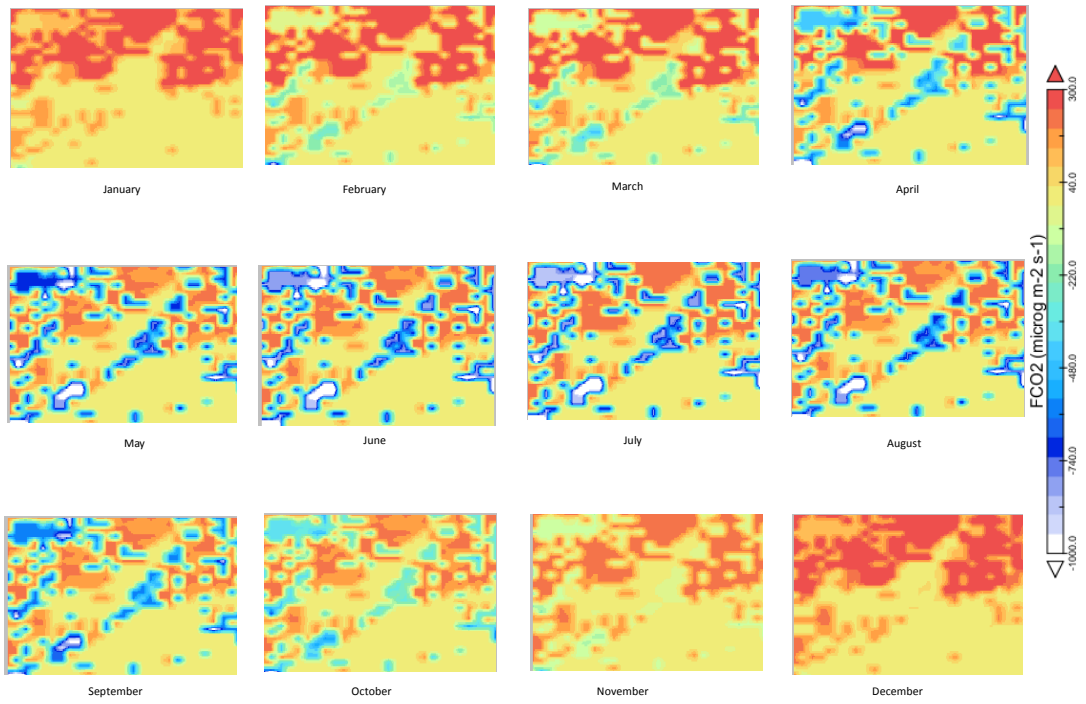

Figure 7. Monthly values (12:00 pm LT) of carbon dioxide flux density (microg m^{-2} s^{-1}).

4.5 Annual values of surface fluxes, emissivity, and air temperature at 2 meters

Daytime versus nighttime composite mean pattern differences in sensible heating rates, anthropogenic heat loss, evapotranspiration, and carbon dioxide exchange are correlated with both time of day and land use (Fig. 8). As is expected for this high-latitude city, the average intensity of sensible heating during the day is about half that for low-latitude cities. Daytime versus nighttime annual mean water vapor flux differences are more subtle than for the southern counterpart, also due mostly to cooler temperatures and sub-arctic insulation patterns. Carbon dioxide fluxes are more varied throughout the city due to the wider variety of land use patterns in the downtown core, where vegetation is heterogeneously interspersed with buildings. Annual values of thermal-IR emissivity and air temperature at 2 meters are shown in Figure 8 both at 5:00am and 12:00 pm LT. In Table 1 are reported the monthly and annual values of surface fluxes, emissivity, and 2m air temperature.

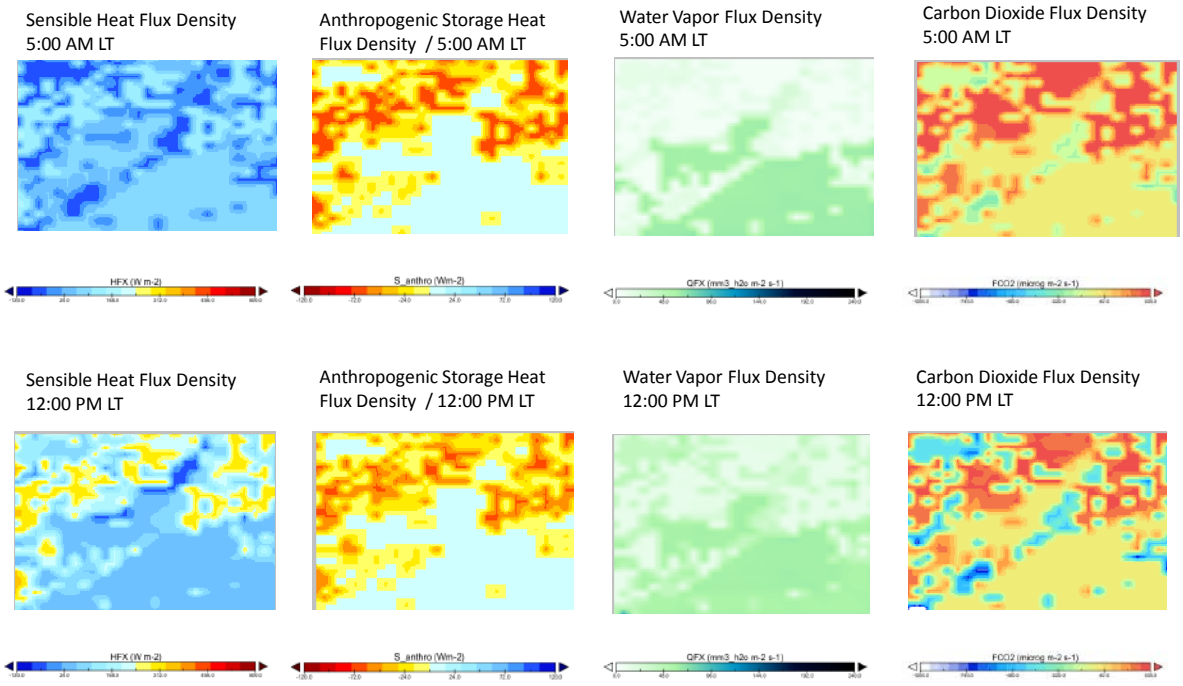

Figure 8. Annual values (5:00 am and 12:00 pm LT) of sensible heat, anthropogenic storage heat, water vapor (W m^{-2}), and carbon dioxide flux density (microg m^{-2} s^{-1}).

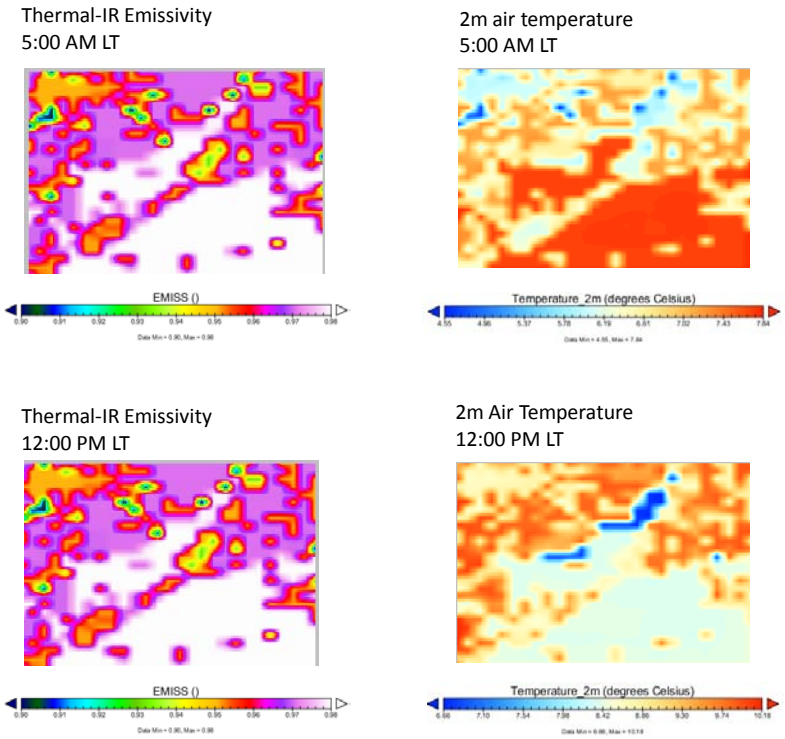

Figure 9. Annual values (5:00 am and 12:00 pm LT) of thermal-IR emissivity and air temperature at 2 meters (°C).

Table 1. Monthly and Annual Average Midday Values for Surface Fluxes, Air Temperature and Emissivity.

Helsinki	units	1	2	3	4	5	6	7	8	9	10	11	12	Annual
EMISS		0.98	0.98	0.98	0.98	0.98	0.98	0.98	0.98	0.98	0.98	0.98	0.98	0.98
FCO_2	microg m^{-2} s^{-1}	8.96	7.36	11.91	6.60	11.59	17.60	23.18	24.47	19.32	15.60	13.63	11.79	14.33
HFX	W m^{-2}	85.01	-15.18	-13.12	-65.10	-72.59	-48.67	-29.14	46.59	85.69	40.57	154.83	143.84	26.06
QFX	$mm^3\_h_2o$ m^{-2} s^{-1}	41.14	12.53	15.55	5.41	49.90	76.08	92.16	125.30	130.79	64.58	84.68	65.23	63.61
Temperature_2m	degrees Celsius	1.20	0.17	-0.33	3.76	9.57	14.35	17.75	17.66	14.00	11.03	7.14	4.17	8.37

Where EMISS is the Surface Emissivity; FCO2 is the CO_2 flux at the surface; HFX is the upward heat flux at the surface; QFX is the upward moisture flux at the surface, and Temperature_2m is the air temperature at 2 meters above the ground.

Contact info

CMCC:

Prof. Donatella Spano (spano@uniss.it)

Via de Nicola 9, 07100, Sassari, Italy

Tel. +39 079 229339

Dr. Serena Marras (serenam@uniss.it)

Via de Nicola 9, 07100, Sassari, Italy

Tel. +39 079 229372

5. Athens

5.1 Surface characteristics

High-spatial resolution satellite images together with GIS vector data were used to describe the surface characteristics of the metropolitan area of Athens: land cover and land use (LCLU), land surface albedo (LSA), land surface emissivity (LSE), land surface temperature (LST), vegetation and topography (DEM).

1. **Land cover and land use (LCLU):** Information on the spatial distribution of the various land cover and land use types found within the metropolitan Athens area was obtained from the Corine Land Cover 2000 (CLC00) database for Greece. CLC00 is a thematic vector map that describes land cover (and partly land use) according to a nomenclature of 44 classes organized into 5 main categories: 1) artificial surfaces, 2) agricultural areas, 3) forests and semi-natural areas, 4) wetlands and 5) water bodies (Fig. 10). The CLC00 vector map was provided by EEA (http://www.eea.europa.eu) on a mapping scale of 1:100 000 with a coordinate reference system GCS_ETRS_1989 (map units: degrees).

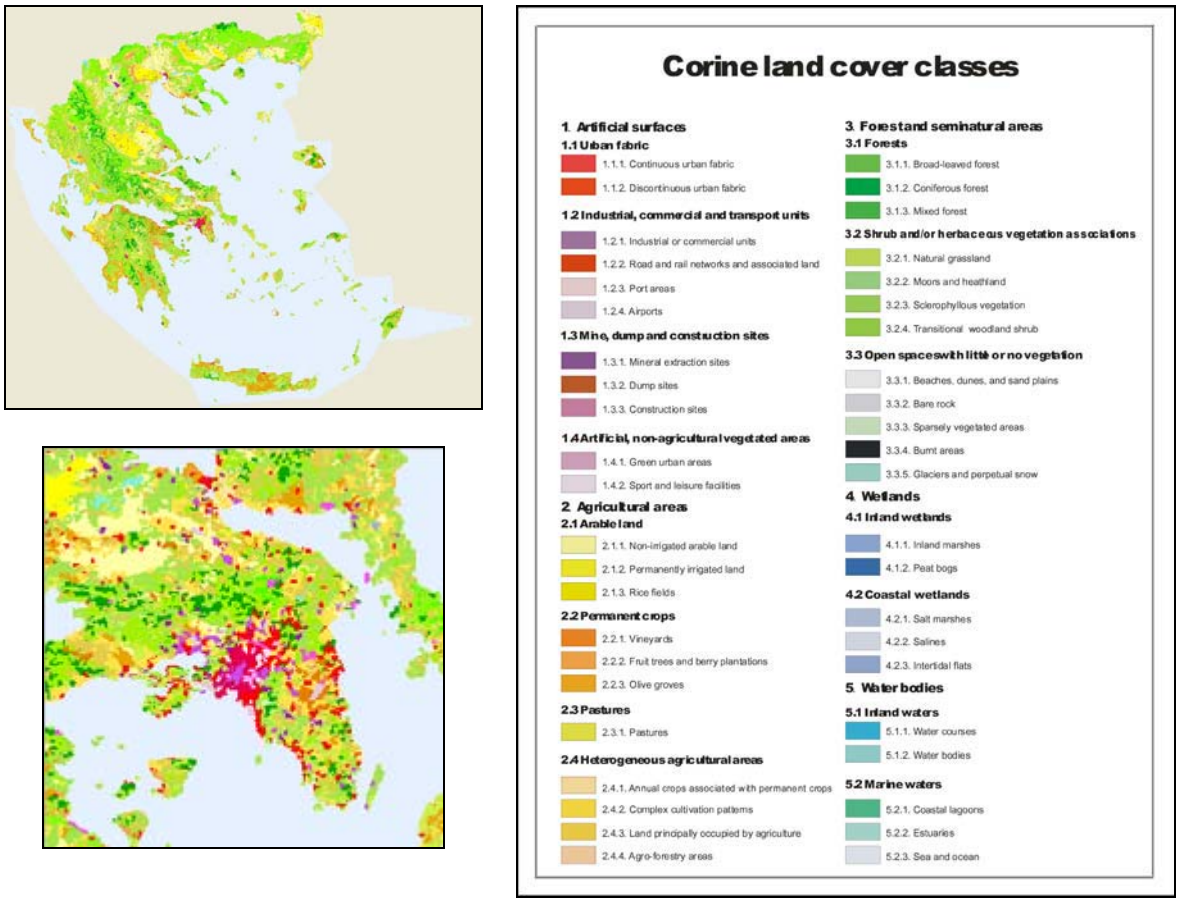

Figure 10. Corine Land Cover 2000 database for Greece.

2. **Land Surface albedo (LSA)**: This parameter was derived from a high-spatial resolution satellite image acquired over metropolitan Athens on 08/04/2005 from the TM sensor onboard the Landsat 5 satellite, under clear atmospheric conditions (no clouds over Athens). Using the band image data of TM recorded in the visible (TM1, TM2, TM3), near-infrared (TM4) and mid-infrared (MIR) part of the electromagnetic spectrum (TM1-5, TM7), the total shortwave albedo (0.25-5.1μm), the visible albedo (0.4-0.7 μm) and the near-infrared albedo (0.7-5.0 μm) for the metropolitan Athens area were calculated (Fig. 11, 12, 13) at the spatial resolution of 30m. The processing technique applied, included: a) atmospheric correction of the image data (TM 1-5, TM7) using the COST method developed by Chavez (1996), b) conversion of the digital number (DN) values of each image (TM1-5, TM7) to at-sensor spectral radiance and then to surface reflectance and c) narrowband to broadband surface albedo conversion applying the algorithms developed by Liang (2001). From zonal analysis, it can be concluded that the most densely built areas of Athens exhibit a mean total shortwave albedo value of 14.7%, whereas all types of urbanized surfaces of the city can be represented by a mean value of 15.85%. Especially for the case study of Egaleo, the total shortwave albedo ranges from 9% to 13%.

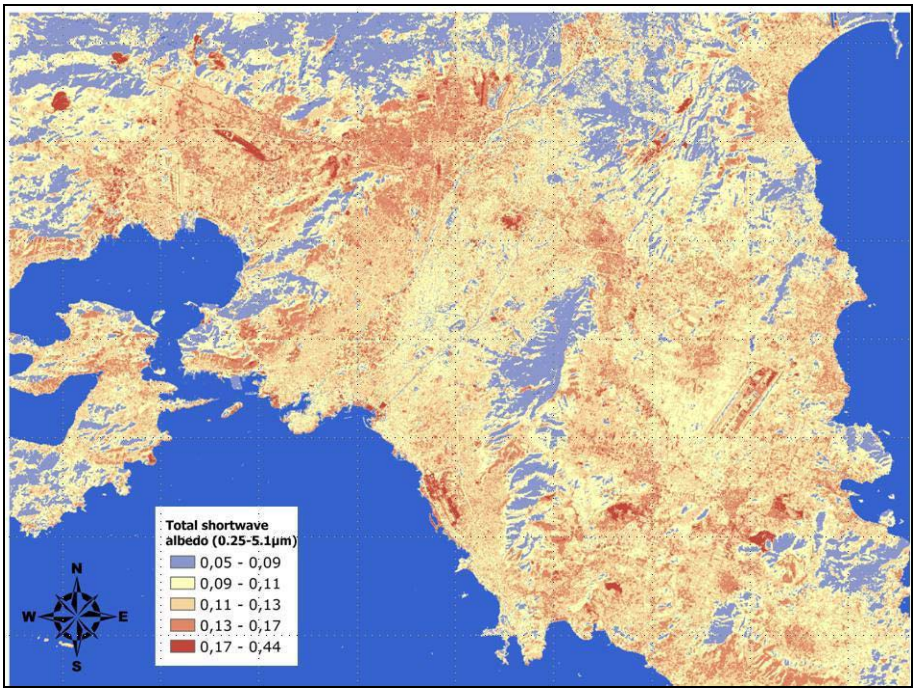

Figure 11. Total shortwave albedo for metropolitan Athens on 8/4/2005.

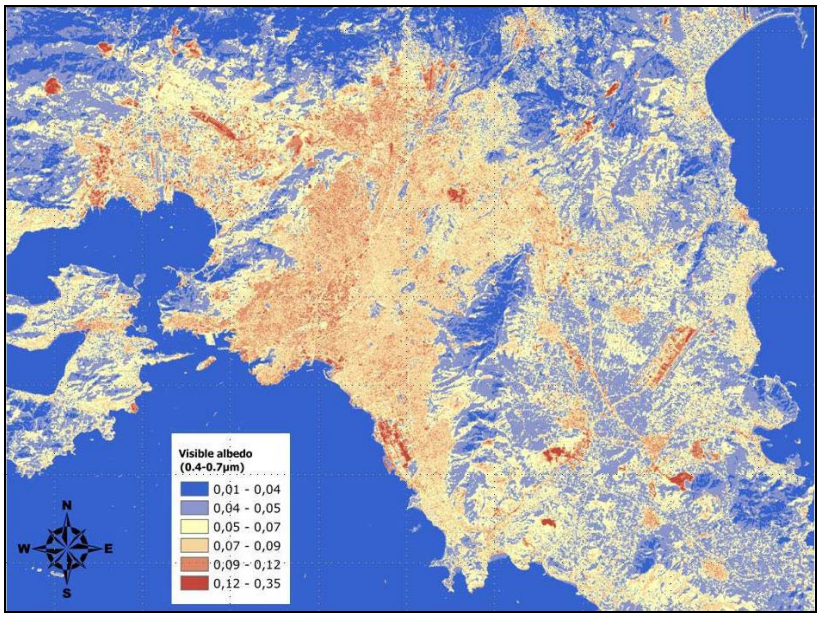

Figure 12. Visible albedo for metropolitan Athens on 8/4/2005.

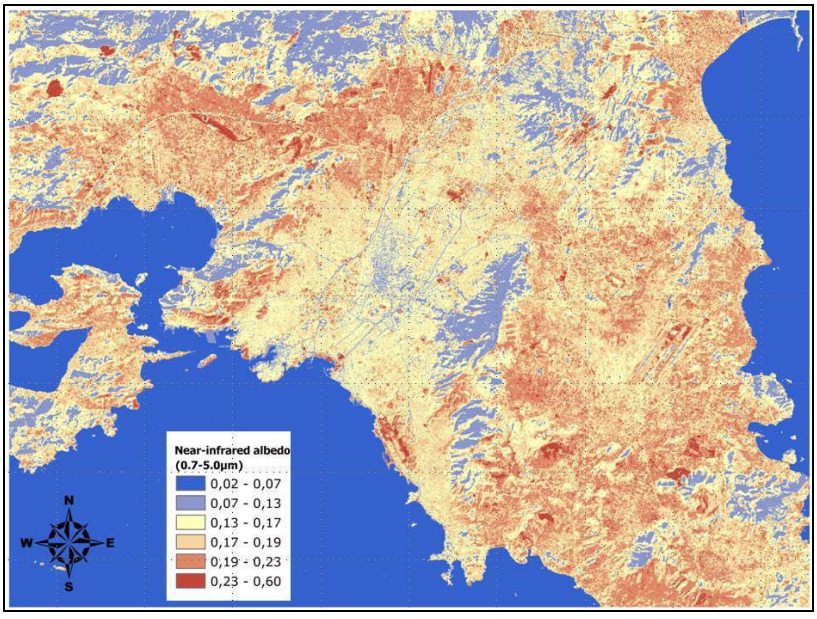

Figure 13. Near-infrared albedo for Athens on 8/4/2005.

3. **Land surface emissivity (LSE)**: This physical parameter of the surface was derived at a spatial resolution of 30m after processing three TM images collected over metropolitan Athens during the warm season of 2005 (8/4/2005, 27/6/2005, 14/8/2005). For each of these images, effective LSE in the 10-12μm waveband was derived applying the algorithm proposed by Caselles et al. (1991) and using a mean thermal emissivity value of 0.93 for the urbanized areas of Athens and a mean value of 0.98 for the vegetated surfaces (Stathopoulou et al. 2007). Then, a composite LSE image was produced as a result of LSE images overlay and considering a mean LSE value for each pixel. In this way, a seasonal LSE image of Athens was

produced (Fig. 14). As shown in Fig.5, the central and NW suburbs of Athens exhibit lower LSE values than the N and NE ones implying the presence of less vegetation and green open spaces in these areas. Especially for the Egaleo area, a mean LSE value of 0.931 is measured.

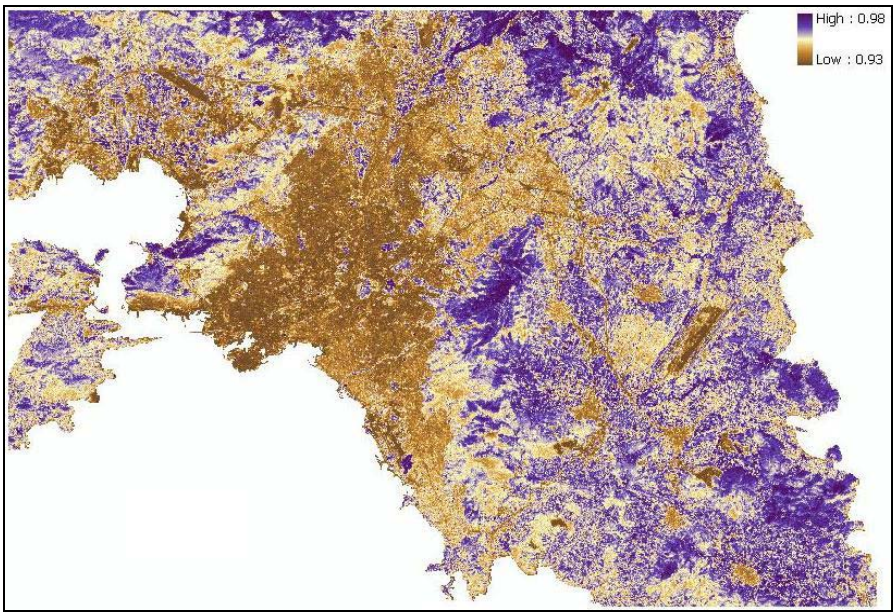

Figure 14. Seasonal surface emissivity image of Athens (April – August 2005).

4. **Land surface temperature (LST)**: Processing of a satellite image data in the near-infrared led to the measurement of the biophysical variable of LST for Athens. In particular, a summer TM image recorded on 10/7/2004 over metropolitan Athens was acquired and analyzed for LST estimation at the 120-m spatial resolution. After applying the calibration process of the thermal band image data (TM6) (Chander and Markham, 2003), the generalized single-channel algorithm for LST developed by Jiménez-Munõz and Sobrino (2003) was applied. The algorithm requires the knowledge of LSE for the application area as well as the atmospheric water vapor content for the observation day. Thus, the algorithm was applied using LSE values by land cover (Stathopoulou et al. 2007) and a mean value of water vapor content for July as measured from radiosonde data in Athens (Chrysoulakis and Cartalis, 2002). As shown in Fig. 15, the mid-morning summer LST spatial profile demonstrates the development of a negative SUHI, with the extended dry surfaces of bare soil or low vegetation in the surrounding rural areas presenting higher LST values than the urbanized surfaces of the Athens basin, as characterized by a higher thermal capacity they exhibit a lower warming rate due to incident solar radiation than the rural areas at the periphery of the city.

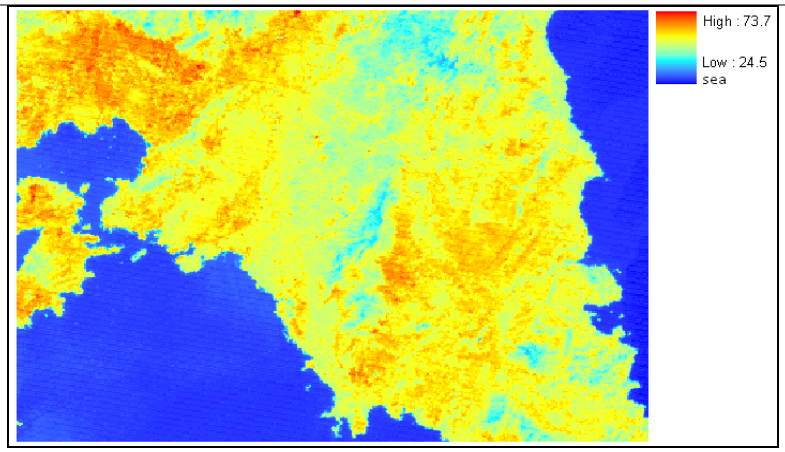

Figure 15. Image of LST (in degrees Celsius) for Athens on 10/7/2004 at 08:43 UTC.

5. **Vegetation**: In order to map the vegetation coverage for the metropolitan Athens area, the Normalized Difference Vegetation Index (NDVI) was measured from Landsat imagery. In particular, the images used were acquired during the warm season of 2005 on three different days: 8/4/2005, 27/6/2005 and 14/8/2005. The index was computed for each of the above images based on the LSA values derived from the DN image data of bands TM3 and TM4 of the TM sensor. Areas fully covered by vegetation are designated with an NDVI value of 1, whereas areas with no vegetation exhibit NDVI values close to 0. Water surfaces correspond to negative NDVI values. Figure 16 shows the spatial distribution of vegetation across the metropolitan Athens area at a 30-m spatial resolution. It was found that the urbanized surfaces of Athens present low NDVI values ranging from 0 to 0.5, with the densely built areas exhibiting NDVI values less than 0.25. The important role that vegetation plays on the LST levels is evidenced by comparing Fig. 15 with Fig. 16. Thus, surfaces with high NDVI values appear to be warmer than surfaces with low NDVI values and vice versa, a fact supporting the necessity for increasing vegetation in Athens.

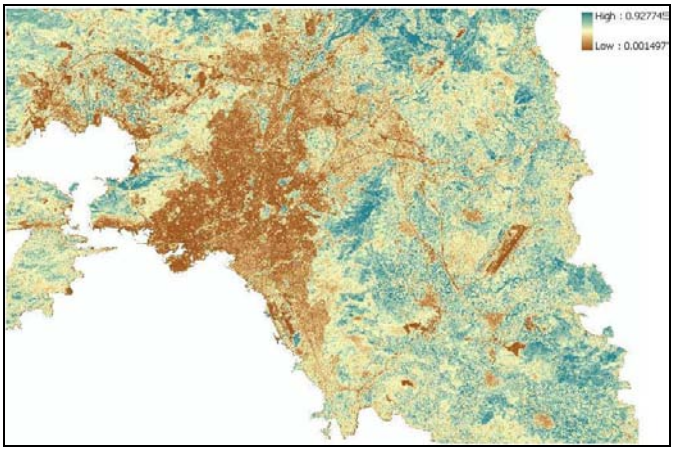

Figure 16. Composite NDVI image of Athens for the warm season (April – August 2005).

Contact info
Stathopoulou Marina (mstathop@phys.uoa.gr)
Research Assistant, Remote Sensing and Image Processing Laboratory,
Department of Physics, University of Athens. Tel.: +30 210 7276843

6. London

6.1 Surface characteristics

To characterize the Central Activity Zone and surrounding areas of London a range of data sets have been used (Table). Given there are multiple datasets which have similar characteristics (e.g. LiDAR[2] data sets) each has been given a code so that it is clear which data are used in which analysis.

A variety of methods are used to evaluate the current green infrastructure (

Table). These provide the context for observations and the starting conditions for any proposed changes. In addition they provide information that can be used for modelling. In the following sections the methods and the results of these analyses are presented.

Accurately mapping and modelling urban vegetation characteristics enables for a significant increase in our understanding to many of the functions of the urban system (Næsset, 2004), enabling for a higher success in the management and moderation of the urban environment (Honjo and Takakura, 1990-1991; Upmanis et al. 1998; Akbari et al., 2001). Accurate urban vegetation can provide a means to reduce the effect of the urban heat island whilst also affecting the energy requirements of many urban structures (Mayor of London 2011[3]). Vegetation mapping and modelling can also allow for the measurement of species distribution as well as urban habitat quantification (Hinsley et al., 2002; Brandtberg et al., 2003). These factors are becoming increasingly important in a rapidly growing and ever more dynamic urban environment (Chen et al., 2009). LiDAR as a measure of such data has been previously expressed as one of the more attractive ways to collect vegetation data (Goodwin et al., 2009).

In April 2011[4] the London Assembly Environment Committee published a report on the current and futures of street trees in London. The most detailed data presented are at the Borough level[5] which is coarser than what is needed for the modelling to be carried out as part of BRIDGE.

[2] Light Detecting And Ranging (LiDAR)

[3] Mayor of London (2011) [online]. Available from: http://www.london.gov.uk/streettrees/ last accessed 7th February 2011.

4 GLA 2011 Branching out: The future for London's street trees. London Assembly, Environment Committee, 49pp. http://www.london.gov.uk/sites/default/files/FINAL%20street%20trees%20report.pdf

http://www.london.gov.uk/publication/branching-out-future-london%E2%80%99s-street-trees

5 http://www.london.gov.uk/sites/default/files/11-04-19-street-trees-borough-data.pdf

Table 2: Data sets used to characterize London surface characteristics

Code	Source	Description
LN8	NERC Flight August 2008	Raw LiDAR data collected by Natural Environmental Research Council (NERC) Airborne Remote Sensing Facility flight: GB08/19 (0.71-m^{-2})
TL8	Derived from LN8 Lindberg & Grimmond (2011)	Trees taller than 2.5 m.
LI58	GLA	Infoterra LiDAR data summer 2008 and summer 2005 (1 m^2 resolution)
VL	GLA/ ERG[6] – KCL	Virtual London calculated from LiDAR data – has the building characteristics
OS	KCL	OS MasterMap® Topography Layer data
STI	Individual Boroughs, via the Forestry Commission	Street Tree Inventory data
GRP	Matthew Thomas, GLA	ArcGIS Layer with slopes and area of roofs that are potential locations for installing green roofs calculated from LiDAR data (probably LI58) by UCL
AP8	NERC Flight August 2008 (see LN8)	Rectified Aerial Photographs: three bands (RGB); approximate spatial resolution of 8 cm on the ground
LCC	Created here	Land cover data set created with surface characteristics

Table 3: Methods used to identify current surface characteristics and green infrastructure in London (see Table 2 for explanation of codes)

Surface Characteristic	Databases used	Methods
Green Roofs	Green roof contractors reports Aerial imagery	Visual inspection of aerial imagery to determine if green roofs present
Tree Height and crown diameter	Field observations TL8	Public property trees taller than 2.5 m were measured at 10 sites and compared to TL8 data
Trees	LN8, OS, VL, STI, AP8	LiDAR based methodology developed for 19 sites along a north/souch transect through London. Dataset created TL8
Vegetation	AP8	Maximum likelihood classification (MLC) of AP8 evaluated against LCC

[6] ERG – KCL: Environmental Research Group – King's College London

Current Green Roofs: Methods

Typically green roofs consist of a growing medium above a waterproof membrane with layers for drainage to prevent plant roots compromising a roof's structure. The substrate can consist of wide variety of materials from fertilised soil to recycled rubble. Generally green roofs are differentiated into three types, based on substrate depth and weight (Table): *Extensive, Semi intensive and Intensive.*

To identify current green roof locations several databases were used (Table). Particularly useful sources were the project reports of green roof contractors. The green roof location was verified using online image sources (in order of best resolution and most useful: Bing Maps, Yellow Pages Maps and Google Earth (GE)). Confirmation of a roof's location was important to ensure its continued existence and to build familiarity with their appearance in largely two-dimensional images. Sedum roofs, for example, tend to show up as a brownish-red colour which can be quite distinctive on a flat roof surface.

The green roof locations were geo-coded using GE. Although GE images have the poorest resolution they allow files to be created which can be uploaded into ArcMAP to 'identify' the green roofs inside the CAZ (Figure). These are then compared to the GLA provided dataset of where **G**reen **R**oofs could **P**otentially be located (GRP data set, Table). Note the areas calculated use the whole roof area from GRP so are larger than the actual roof area that is covered by vegetation.

Table 4. Characteristics of green roofs (Getter and Rowe 2006; Grant, 2006; Living roofs 2011[7])

	Extensive	**Semi-Intensive**	**Intensive**
Depth of substrate (mm)	60-200	120-250	150- 400
Weight (kg m^{-2})	60 -150	120-200	180-500
Type of vegetation	Mosses, herbs, grasses small, low growing species (e.g. sedum)	Grasses, herbs, shrubs	Lawn/perennial, shrubs, trees Large plants
Roof slope	Flat or sloped		Tend to be flat

Current green roofs: Results

There are approximately 24,000 ha of buildings in Greater London (GLA 2008a) which is 15-16% of the total land area (based on Grant 2006, GLA 2008a, respectively). The 35 green roofs (Table) cover 168,561 m^2 of the total roofed area of Greater London, which includes the CAZ (0.06 % of the area) (Table 6). In the CAZ, the five green roofs (GRP based areas) make up 0.6 % of the CAZ roof area. Although there is a higher percentage cover of green roofs in the CAZ, the total green area is greater outside the CAZ boundaries.

In the CAZ, the total roof area of all roofs, green and non-green, is dominated by sloping roofs, with increasingly smaller proportions of flat, intermediate and vertical roof cover. Not all the sites identified as currently having a green roof appeared in the GRP data set (viz, the Museum of London, the Tower of London Gift Shop, Inn The Park restaurant, 55 Broadway and 1 Wood Street), suggesting that there are more

[7] http://livingroofs.org/2010022858/green-roof-types/greenrooftypes.html (17 April 2011)

potential locations that identified in the GRP dataset. Currently the green roofs are disproportionately on flat and intermediate sloped roofs (Table ,

Figure). However, overall flat roof area with green cover is only 0.7 % of the total flat roof area of the CAZ (Table) and green sloping roofs account for only 0.51 % of all sloping roofs in the zone. Intermediate roofs have the largest percentage (0.88%) which is green but the smallest proportion of the total roof area of the CAZ.

The total roof area that could potentially be retrofitted with green roofs in the CAZ is 4,987,104 m^2 (~15 % of the total CAZ area) or ~ 92 % of the total roofed area. In 2008 the GLA report Living Roofs and Walls suggested 32 % of London's roofs could be greened (GLA 2008a). Since the start of 2009, six green roofs have been constructed (Table) with a total estimated area (five) of 15,161 m^2. Mayor Boris Johnson's target is to increase green roofs in London by 100,000 m^2 (based on 2008/9 baseline estimates) by the year 2012 (GLA 2009). This means that in the next two year years the amount of development of green roofs has to be over five times that of the past two years.

Table 5. Location of green roofs in London. T Type: E: extensive, I: intensive, B: both, SI: Semi-intensive, SE: Semi-extensive, U: Unknown; Reference: see footnotes; !In literature but not on maps,# in CAZ but not in GRP; *in CAZ but in GRP

Address	T	Area (m^2)	Year	Ref	Address	T	Area (m^2)	Year	Ref
1 Wood Street, EC2V 7WS*	E	5600	2009	[8]	Inn The Park rest., St. James's Park*	I	335	2004	[9]
11 Shaw's Cottages!	E	100	1993	[10]	Jacobs Island, Bermondsey	I	930	1997	[11]
1-5 Offord Street, Islington	E	65	2004	[12]	Jubilee School, Tulse Hill	E	3149	2002	14
1 Poultry (2/3 Queen Victoria St GNP)#	I	1966	1999	8	Kensington roof gardens, Derry Street	I	14956	1938	[13]
55 Broadway, Westminster*	E	-	2009	8	Laban Dance Centre, Deptford Creek	E	3748	2002	15
Adelaide Wharf, Haggerston	E	460	2007	[14]	Merrill Lynch HQ, King Edward St#	I	930	2000	11
Almeida Theatre, Islington	E	526	2002	[15]	Monument (under construction)!	SE	-	now	[16]
Beaufort Court, Lillie Road, Fulham	E	1936	2003	14	Museum of London*	I	1684	2010	[17]
Bishops Square, Spitalfields#	B	5400	2007	14	New Providence Wharf & Radisson	B	418	2006	14
Canary Wharf 1	E	11270	2000	10	North Harringay Jr School, Haringey	I	190	2005	14
Canary Wharf 2, 20 Cabot Square	E	12696	2000	10	Northern Line Control Cent, Highgate!	E	1950	2007	14
Canary Wharf 3, Barclays Building	E	6095	2000	10	Portland Grove, Lambeth	E	1000	2006	9
Canary Wharf 4, Jubilee Park	I	32974	2001	[18]	Royal Arsenal, Woolwich	I	22688	2005	[19]
Canary Wharf 5, Cabot Place	E	6046	2000	[20]	Six Acres Estate, Islington	E	3100	2009	[21]
Canary Wharf 6, Canary Wharf DLR	E	4206	2000	20	Springbok Works, Dalston	I	90	2000	14
Canon Street Station#	I	14723	-	[22]	St Martins in the Field HS Girls, Tulse	E	3700	2004	[23]

[8] Livingroofs.org

[9] http://www.bauder.co.uk/media-centre/project-gallery

[10] http://www.urbanhabitats.org/v04n01/london_pdf.pdf

[11] http://www.greenroofs.com/projects/pview.php?id=660

[12] http://www.greenroofs.com/projects/pview.php?id=85

[13] http://www.greenroofs.com/projects/pview.php?id=648

[14] Living Roofs and Walls Report GLA 2008a

[15] http://www.greenroofs.com/projects/pview.php?id=549

[16] http://www.greenroofs.com/projects/pview.php?id=894

[17] http://www.bauder.co.uk/media-centre/

[18] http://www.greenroofs.com/projects/pview.php?id=510

[19] http://www.greenroofs.com/projects/pview.php?id=393

[20] http://www.greenroofs.com/projects/pview.php?id=95

[21] http://www.langley.co.uk/asx/six_acres_case_study_-_newsletter.pdf

				Hill			
Center for Wildlife Gardening!	U-	-	10	Stonegrove Estate, Edgeware!	E	1200	2008 [24]
Creekside educational centre, Deptford Creek	E	100	2003 [25]	Michael Tippett School, Lambeth	E	2000	2008 9
Ethelred Estate, Kennington	E	4000	2005 [26]	The Muse, Islington!	B	-	2007 [27]
Gold Lane, Edgeware	E	400	2003 14	Tower of London gift shop*	I	5550	1992 9
Goldsmiths Place, Camden	E	1690	2006 [28]	Webheath Estate, Hampstead	SI	3867	2009 [29]
Horniman Museum, CUE	E	282	1995 10	William Gunn House, Hampstead	E	910	2009 [30]

Table 6. Total area (m^2) and percentage (%) of green roof cover in Greater London and the CAZ (including vertical and unmeasured roof class).

Total Area (m^2)	**Greater London**	**CAZ**	**GL-CAZ**
All	1,579,000,000	33,522,307	1,545,477,693
Roofed	240,000,000	5,404,602	234,595,398
Green Roofed	168,561,000	32,299	136,262
Utilisation of total roof area as green roofs (%)		0.60	0.06

Table 7. Areas of different roof classes for all roofs and for green roofs as a percentage (%) of the total CAZ area.

	All Roofs	Green Roofs
CAZ Roof Class	(% of Total Roofed Area)	
Flat	26	30
Intermediate	12	18
Sloping	55	47
Vertical	5	4
Unmeasured	2	1

[22] http://livingroofs.org/2010030161/green-roof-types/intens.html

[23] http://www.greenroofs.com/projects/pview.php?id=91

[24] http://www.langley.co.uk/asx/stonegrove_case_study.pdf

[25] http://www.greenroofs.com/projects/pview.php?id=550

[26] http://www.greenroofs.com/projects/pview.php?id=77

[27] http://www.greenroofs.com/projects/pview.php?id=1066

[28] http://www.greenbuildingpress.co.uk/article.php?article_id=700

[29] http://www.greenbuildingpress.co.uk/article.php?article_id=700

[30] http://www.langley.co.uk/asx/william_gunn_case_study.pdf

Table 8. Total potential green roof area in the CAZ based on roof slope classifications.

Area (m^2)	**Flat**	**Intermediate**	**Sloping**
Total Roof	1397273	659201	2961347
Green Roof	9830	5803	15084
Green Roof	0.70	0.88	0.51
Current green roof cover (%)			0.60
Potential green roof area (m^2)			4,987,104

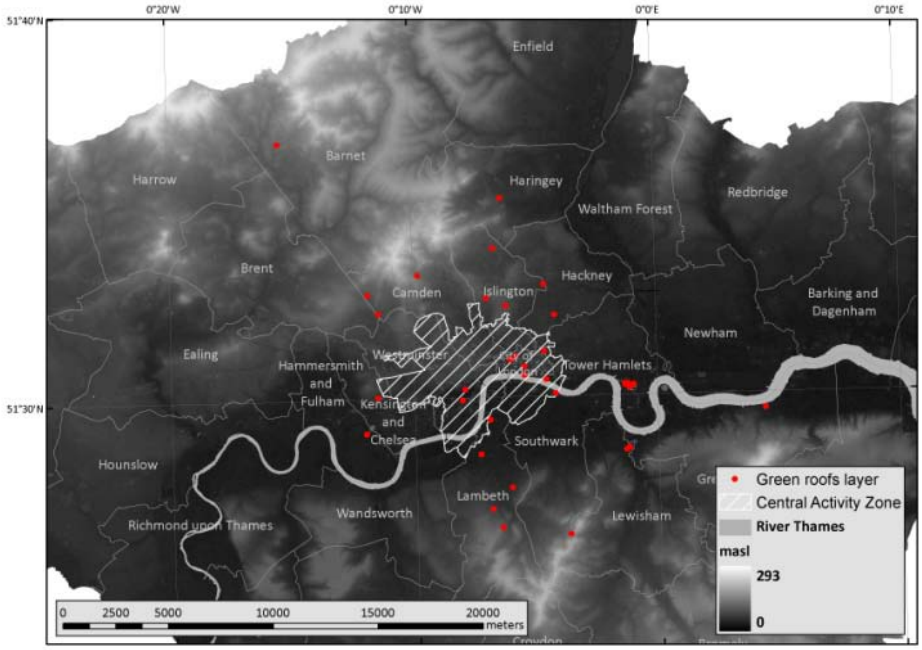

Figure 17. Existing green roof locations.

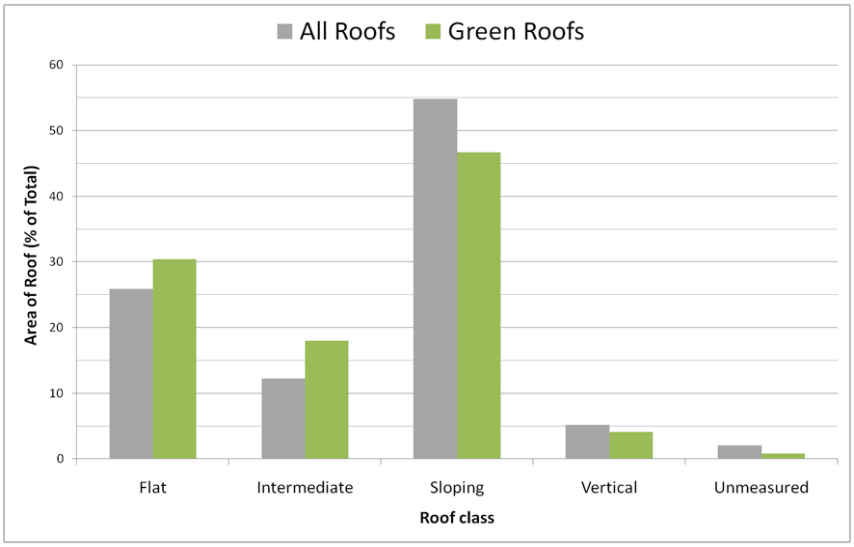

Figure 18. Percentage of total (grey) and green (green) roof area in the CAZ by slope class.

Current tree characteristics: methods

To analyse the current tree characteristics in London, data collected from a NERC ARSF north-south LiDAR flight (LN8,Table) transect through Greater London (Figure) are analysed. The spatial data were acquired on 14 August 2008 using an Optech ALTM 3033 LiDAR system, operating at a flight altitude of 900 m above ground level (agl). The sensor was configured to record first and last returns as well as intensity values with a pulse frequency of 33 kHz using a maximum off-nadir view angle of 20° and a wavelength of 1064 nm. The beam-divergence was set to 0.21 mrads. The area surveyed includes an approximately 0.65 km x 50 km north to south transect passing over the central parts of London; a single flight line was used. The average point density on the ground was 0.71 m^{-2}. Along the transect 19 study areas (400 m x 400 m analysed at 2 m resolution) were located centrally within the transect to exclude large off-nadir angles since the laser beam moves across the track resulting in a Z-shaped pattern with lower density distributed points at the edge of the field of view.

To derive the data, several steps and software systems were used. Most of the GIS pre-processing was done in ESRI's ArcInfo 9.3 and all filtering procedures presented used MathWorks MATLAB®. The input spatial datasets derived are: a ground and building Digital Elevation Model (DEM), a vegetation canopy DEM, and a trunk zone DEM. First the LiDAR points within each study area were extracted using FUSION/LDV (version 2.70- McGaughey 2009) from the main LiDAR cloud (46399632 points) (Figure a). The GroundFilter algorithm within FUSION/LDV was used to identify those last and single returns that correspond to probable bare-earth surface points. These points were gridded to create a bare earth DEM (Figure b). To separate points located on building roofs, building footprints extracted from the OS MasterMap® Topography Layer (Ordnance Survey 2010[31]) land use dataset were used. First and single returns outside the building footprints were stored separately to be used as 'potential' vegetation points. By combining the building points dataset and the bare earth DEM a ground and building DEM was created (Figure c) (hereafter referred to as building DEM).

Height attributes for each vegetation pixel were compared with the bare earth DEM and those lower than 2.5 m above ground were removed from the dataset. After points below 2.5 m agl were removed, urban features such as building walls, power lines, masts etc were still present and had to be removed in order to generate a vegetation canopy DEM (Figure d). To remove these non-vegetation features a similar filtering approach to Goodwin et al. (2009) was used. The first filter applied removed the linear features in the dataset. A 9 x 9 pixel moving window was used for a series of lines oriented 0° to 179°. When the number of pixels including vegetation points that intercepts a projected line was > 4 points of the possible 9, less than 3 of the surrounding pixels in the window were classified as vegetation, the vegetation pixels were removed. A second filter was applied to fill gaps caused by the sampling patterns of LiDAR and inconsistent detection of vegetation points. This was a 3 x 3 pixel moving kernel that classified a pixel as vegetation if 6 or more of the surrounding 8 pixels were classified as vegetation (Goodwin et al., 2009). A final 3 by 3 pixel kernel filter was applied to remove single pixels classified as vegetation when none of the surrounding 8 pixels were non-vegetation pixels (e.g. masts, lamp posts etc). Remaining vegetation pixels were used to generate the canopy DEM with a height value or non-tree pixels assigned 0 m (Figure e).

Vegetation has small gaps that allow laser light to penetrate and record additional returns at lower elevation. This was used to obtain a rough estimate of the crown base height needed to generate the trunk zone DEM. The approach used here was developed by Holmgren and Persson (2004) and has been applied by others (e.g. Kim et al. 2009). First, all the returns classified as vegetation were selected. Laser returns less than 2 m agl were omitted from the analysis to remove the effects of ground vegetation, cars and other obstacles found in the urban environment. The remaining laser points were classified as non-ground vegetation points. To estimate crown base height a 0.5 m interval was used. Each interval that contains ≤1% of the total number of

[31] Ordinance Survey (2010) © Crown database right 2010. An Ordnance Survey/EDINA supplied service. Assessed 2009-10-13

non-ground laser points within an individual tree was set to zero and others to one. The crown base height was defined as the distance from ground to the lowest height layer where > 1% of the data points were found. Holmgren and Persson (2004) used a segmentation process for separating different tree crowns and therefore could identify the returns that originated from a certain vegetation unit. As they had higher resolution laser data (0.44 m between laser hits on the ground) than this study, here vegetation laser returns were separated using a 10 m x 10 m grid for each study area. Within each grid cell a crown base height was estimated. Using this approach all vegetation pixels within a 10 m x 10 m grid have the same crown base height value. As an artefact of this if a grid cell was located at the edge of vegetation large overestimations may occur. After re-gridding the 10 m x 10 m grid to 2 m pixels this artefact was reduced by applying a 3 by 3 pixel median filter on single local maxima compared to the surrounding 8 pixels. If the crown base height and canopy height of a pixel were within 1 m the crown base height was altered using a median 3 by 3 pixel median filter. Finally, rare occasions with unlikely crown base heights (i.e., < 15 m) were classified as bush pixels. An example of a trunk zone DEM is shown in Figure f.

The building and canopy DEMs for the 19 sites are shown in Figure . In order to compare the sites, the building DEMs scale bars have a 45 m range except for 9S which is located on a relatively steep slope and therefore a higher range is used (60 m). Pixels with heights greater than the maximum height are shown as white pixels. All vegetation canopy DEMs have the same heights range (35 m) and pixels equal to 0 are transparent.

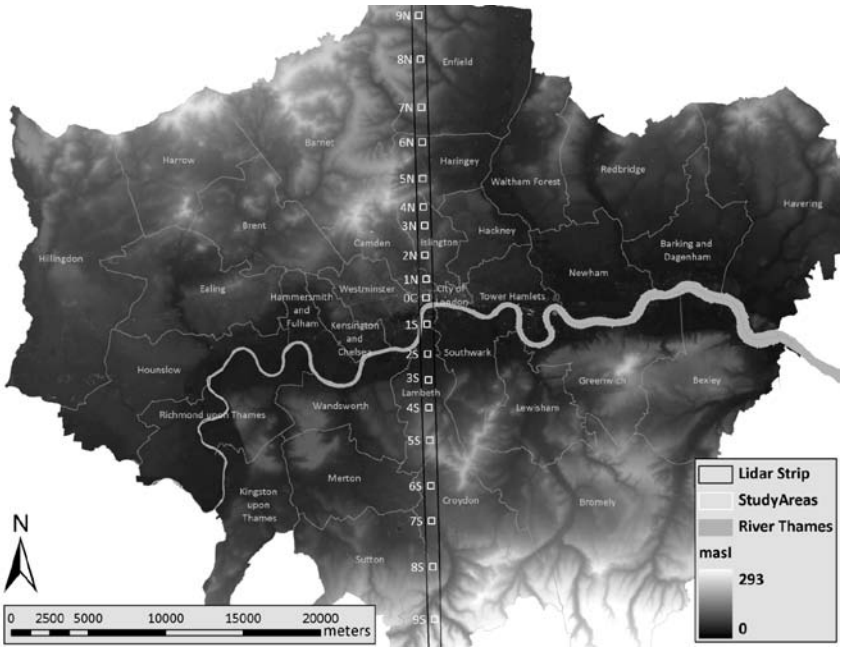

Figure 19. Greater London (with 32 Boroughs and the City of London) showing LiDAR transect and the 19 study areas.

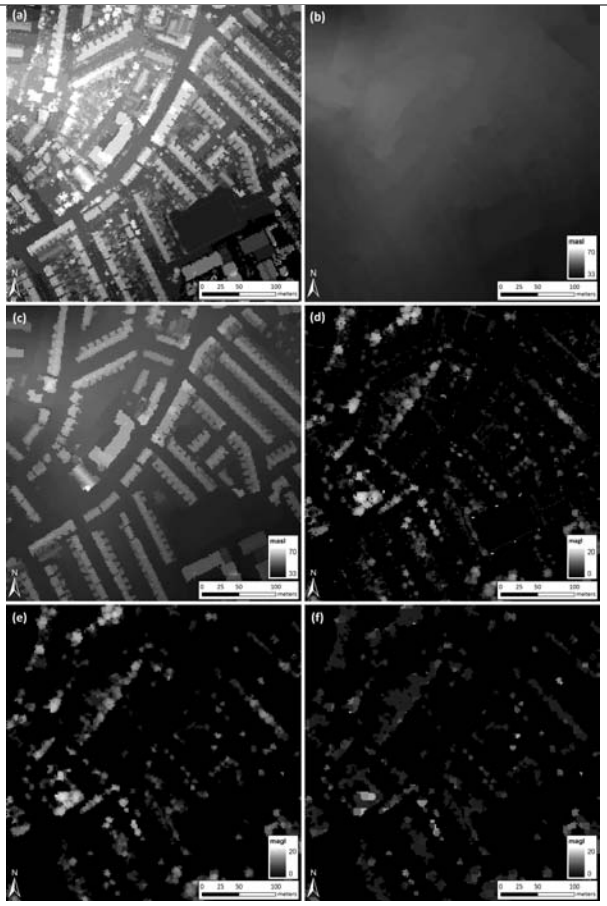

Figure 20. Results generated in creating the digital elevation models (DEM) from LiDAR data (site 5N, see Figure): a) unprocessed LiDAR data, b) ground DEM, c) ground and building DEM, d) canopy DEM before filtering, e) canopy DEM after filtering, and f) trunk zone DEM.

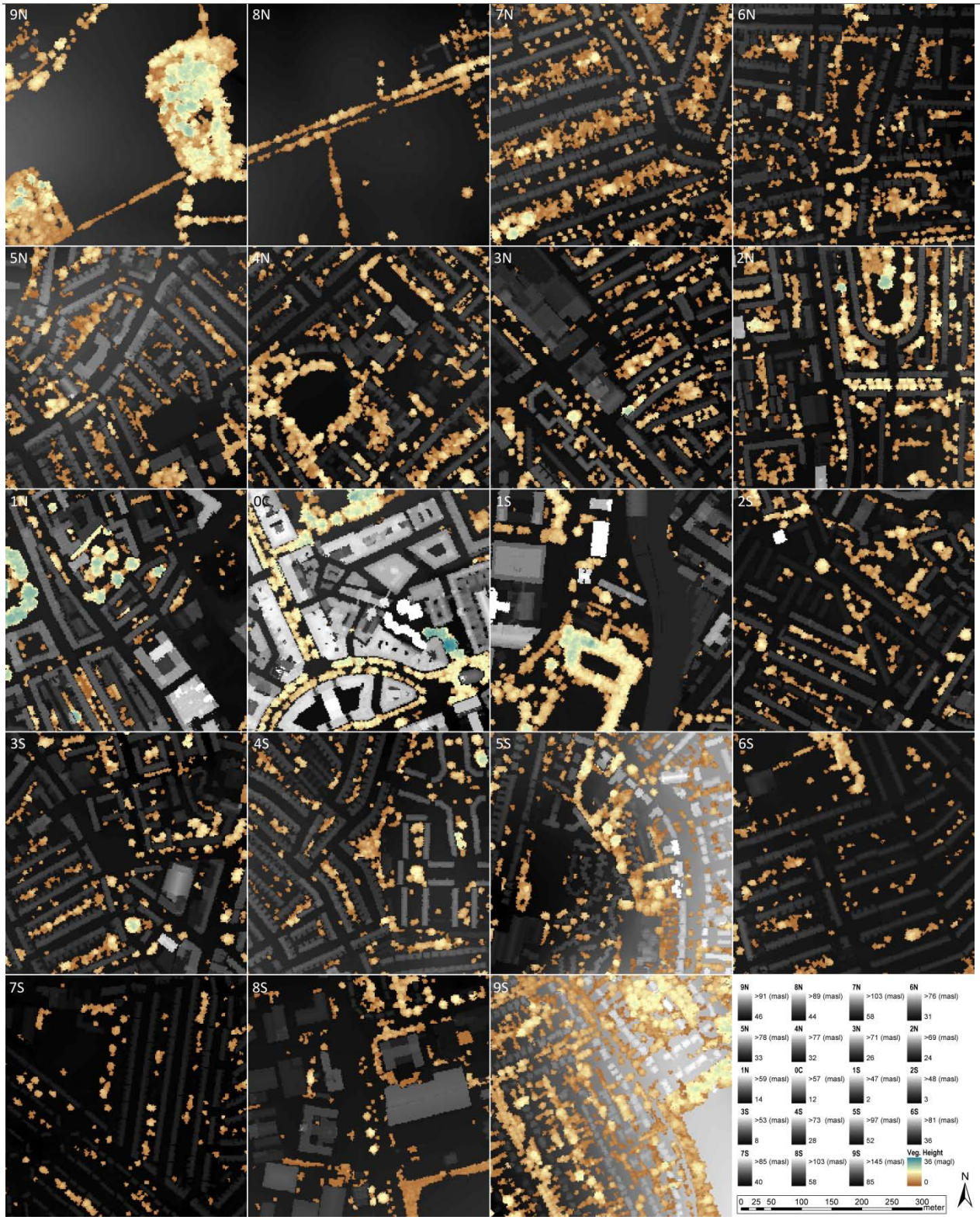

Figure 21. Building DEMs overlaid by canopy DEMs derived from LiDAR data for the 19 sites (see Figure).

Current Tree characteristics: Field observation methods

To evaluate the LiDAR derived data tree height and crown diameter were measured at 10 sites (Knott, 2011). The trees at these sites were identified from high resolution photographs (AP8 Table). The trees had to:

a) have a height and diameter > 2.5 m (so included TL8 – Table)

b) be publicly accessible

c) have foliage (LN8 data were obtained during leaf-on).

Given the variation in number of trees at the sites (Figure) there were different numbers of trees with the potential to fulfil these criteria. Field data were collected during two weeks in August 2010 the same time of year as the NERC ARSF (LN8) observations.

The maximum height and crown diameter measurements were recorded for each pre-selected tree. A clinometer was used at 10 m distance on the most level plane away from the base of the tree to determine the height. Crown diameter was obtained by using a measuring wheel between two perpendicular points of the trees longest axis (Goodwin et al., 2009). A subjective assessment is involved in determining where the top of the tree is and which axis is the longest when carrying out field estimations. It is assumed that the size of the tree has not changed significantly between 2008 and 2010. In an urban area both tree growth and tree management (pruning, removal) could cause differences (see discussion in Clark et al., 2004).

The maximum tree height for 164 trees and crown diameter for 160 trees were measured. However, 4 trees height could not be determined from the TL8 data and diameters for 8 trees could not be identified. These are excluded from the results. All trees excluded were < 10 m tall. Clustering is a well established source of error in LiDAR data (Goodwin et al., 2009) and refers to the overlap of tree crowns producing observational as well as technological difficulties when vegetation is a measured parameter (Lee et al., 2007). Goodwin et al. (2009) experienced much greater percentage of clustering of vegetation (34%) than this study (just less than 5%). There are means to extract individual tree characteristics from clustering (Reitberger et al., 2009) but are not used here. However, the tree selection process implemented in this study would have biased the sample to a small amount of clustering.

The majority of publicly accessible trees have been purposefully planted and are subject to regular maintenance (London Councils 2004[32]). Typically they occur equidistant in a uniform way in a vast majority of areas throughout London. Location (1) in Figure 22 shows the typical vegetation studied here with individual trees easily identified in aerial photographs. In the residential regions (location 2) the vegetation is dense and individual trees are increasingly indistinguishable.

[32] London Councils (2004) [online]. Available from: www.londoncouncils.gov.uk.

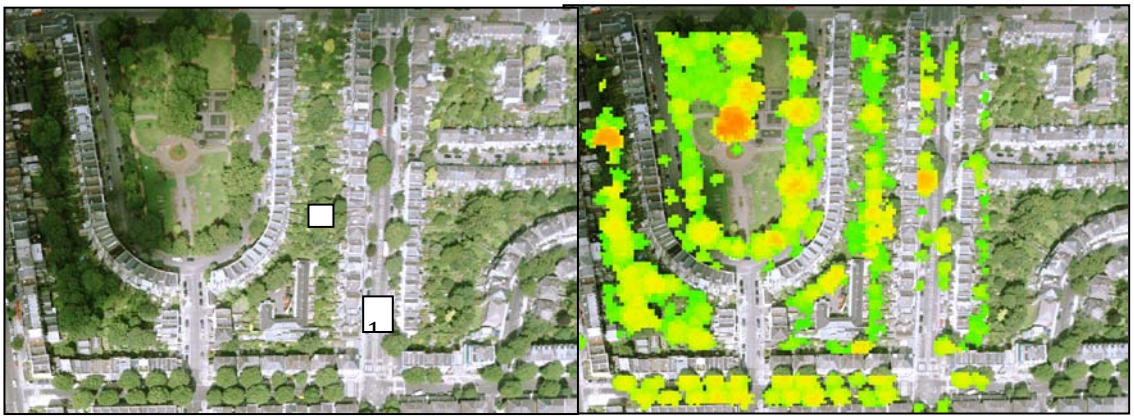

Figure 22. High resolution aerial photographs of study site 2N. (lower) overlaid LiDAR DEM (TL8) with green (shorter) to red (taller) vegetation.

Current Trees: Results

Site 9S (Figure 19; Figure 21) is the most vegetated of the sites measured. It has predominantly low rise residential housing consisting of small areas of light woodland and highly clustered areas of vegetation. At the other extreme is the densely populated area of South London (site 7S) with nearly four times more building fraction than vegetation. This demonstrates the high variability in vegetation cover throughout the metropolitan area.

The field heights have a mean difference of 0.27 m compared to the LiDAR derived (TL8) data (Table) with the largest difference of $\pm$ 0.42 m. These results are consistent with the literature (e.g. Clark et al., 2004, Streutker and Glenn 2006; Goodwin et al., 2009). The TL8 crown diameter values are consistently greater than the field values with a mean difference of 1.01 m and maximum diameter difference of 2.9 m. This is different to previous findings (Baldwin et al., 1997; Roberts et al., 2005). Both field and LiDAR methods indicate significant variability in the dimensions of the trees, the standard deviation of both crown diameter and height are relatively high compared to the mean.

As vegetation height increases diameter increases (Figure) with a slightly higher correlation (r^2= 0.676, N=160) from the field measurements than that the LiDAR (r^2= 0.616, N=160). As in previous studies (Lefsky 1997; Clark et al., 2004; Streutker and Glenn 2006; Goodwin et al. 2009), a high correlation for vegetation height between methods is obtained (Figure 23). The correlation is stronger for height (r^2= 0.902, N= 164) than diameter (r^2= 0.864, N= 160). As in Næsset and Økland (2002), there was a net overestimation in the LiDAR height.

The frequency distribution of the data (Figure) is similar for both field and LiDAR estimates with peaks and troughs in distribution at similar sizes. Based on Kolmogorov-Smirnov and Sharpo-wilk tests the data are determined to be not normally distributed so the non-parametric Mann-Whitney U test is used to assess if there are significant differences in the datasets.

The Mann-Whitney U test for diameter shows that the LiDAR data are statistically different from the field values, whereas the height results are not significant (p= 0.68) indicating no statistical difference between the two methods. The TL8 diameters are significantly larger from field by 13.18% or 1.02 m on average. This is consistent with previous work. Popescu et al. (2003) found diameter measurements obtained from LiDAR had greater inaccuracy than height derived measurements.

As Clark et al. (2004) found height of vegetation explained variations in accuracy and correlations the data were split into small ($\leq$ 10 m) and large (> 10 m) trees. Small trees are found to have significantly larger mean difference between the TL8 and field estimated data, for diameter most specifically but also for height

(Table). Of the trees measured 46.43% in this study were ≤ 10 m. This may be related to the size of pixels and the filters used to identify the vegetation during the development of the TL8 dataset.

To see if insights into differences could be related to tree types information on species were extracted from the Street Tree Inventory (STI) dataset (Table). The species that had the largest overestimation of diameter are, as expected, influenced by which species have the highest frequency of small trees (Table 11): Prunus, Sorbus, Acer, Crataegus and Betuaa. Plane trees, which make up over 50% of all trees > 10 m, are overestimated by an average of 8.36%. However, caution must be taken interpreting the results as many tree were not identified (29% of trees ≤ 10 m, 19% >10 m).

By comparing the characteristics of the field observed trees relative to all of the trees in the sample area one can assess the difference between public and private trees. When these are compared along the transect 90% of the sample sites have a lower mean than when just the trees are sampled (Table). When all vegetation is measured within a particular sample site an average difference of 2.24 m is observed in the height of trees between TL8 (sampled) and TL8 (all). This suggests that the street trees are taller on average. Whereas 90% of the sample sites have a smaller mean diameter with a mean difference of 0.96 m between TL8 (sampled) and TL8 (all) diameter. Again suggesting the street trees are larger.

Table 9. Mean TL8 and field heights and diameters and the differences *(Negative values TL8 underestimates)*

	Diameter (m)		Height (m)		Difference				Whole			Diameter (m)		Height (m)	
N	160		164		Diameter		Height		TL8	TL8	All	Field	TL8	Field	TL8
Site	Field	TL8	Field	TL8	(%)	(m)	(%)	(m)	D (m)	H (m)	Mean	3.37	3.49	4.70	4.80
9S	8.31	9.54	8.78	8.60	15.77	1.24	-1.60	-0.18	13.64	9.64	Std. Dev.	8.90	10.08	10.63	11.05
8S	8.96	9.75	10.95	10.11	8.94	0.79	-5.97	-0.84	11.48	6.73	Median	16.90	19.12	18.50	18.10
7S	9.73	10.65	10.10	8.25	9.40	0.92	-16.67	-1.85	11.34	6.15	Range	3.40	4.08	3.50	3.80
5S	8.34	9.83	10.42	11.08	20.08	1.48	3.60	0.37	11.96	8.18	Minimum	20.30	23.20	22.00	21.90
2S	8.62	9.76	10.58	10.32	13.97	0.94	-4.44	-0.56	10.48	8.73	Maximum	9.39	10.40	11.31	11.58
0C	13.39	14.49	16.55	18.35	8.06	1.09	11.26	1.80	14.81	15.00	Difference				
2N	11.60	12.57	15.81	16.38	9.65	0.96	4.47	0.57	12.79	9.80		(%)	(m)	(%)	(m)
4N	8.16	9.15	9.58	9.75	12.65	0.88	2.85	-0.04	10.57	8.74	All sites	**13.27**	**1.03**	**2.10**	**0.09**
5N	6.74	7.23	7.70	7.57	8.29	0.46	6.31	0.30	8.89	7.44	All trees	**13.18**	**1.02**	**3.87**	**0.27**
6N	7.91	9.47	8.81	10.17	25.94	1.56	21.16	1.36	10.03	7.15	Std. Dev.	**5.90**	**0.33**	**10.26**	**1.05**

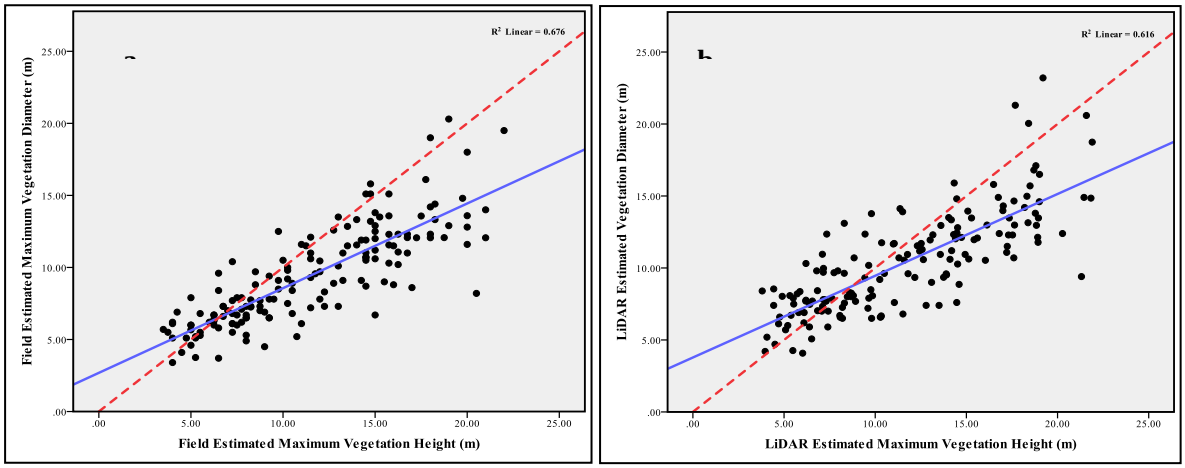

Figure 23. **Height versus diameter for individual trees from (a) field and (b) LiDAR measurements with the regression (blue solid) and 1:1 (red dotted) lines**

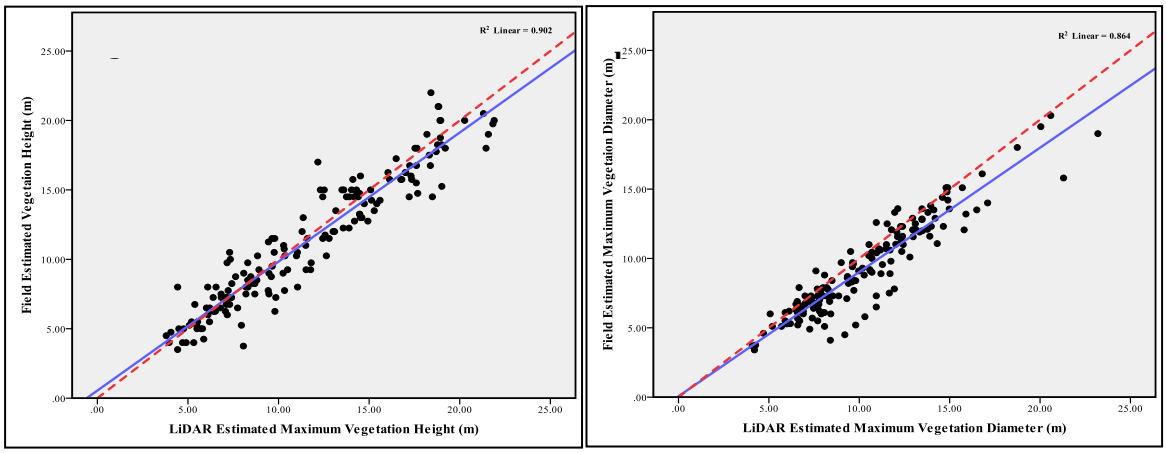

Figure 24. Comparison between LiDAR and field measurements of individual trees (a) height and (b)maximum diameter with the regression (blue solid) and 1:1 (red dotted) lines. ##

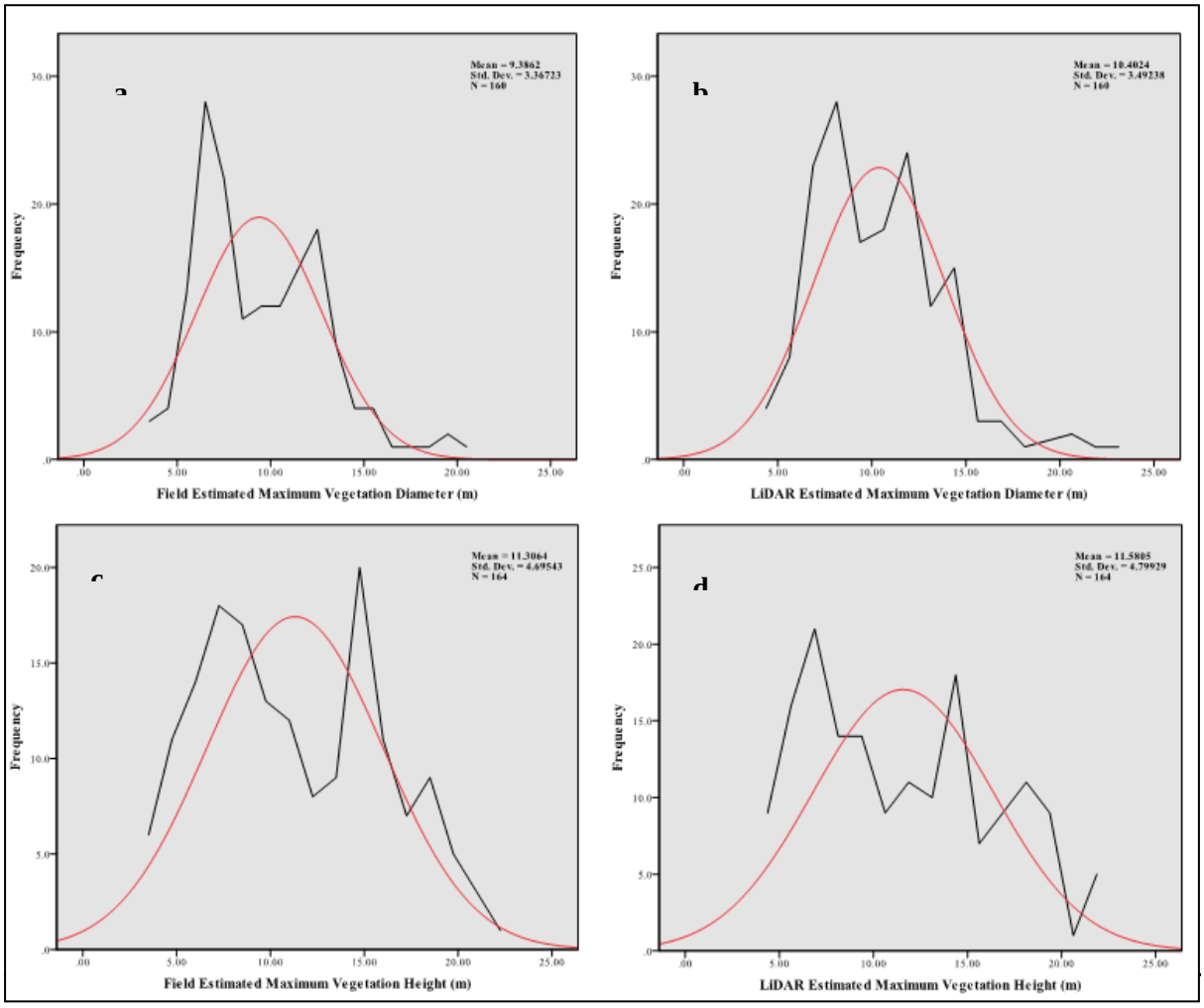

Figure 25. Frequency histograms (black) for diameter (a, b) and height (c,d) for field (a,c) and LiDAR (b,d) methods. A Normal curve (red) is shown for comparison purposes.

Table 10: Mean difference between LiDAR and field estimates by size of trees. What is N for the two?

	Diameter difference		Height difference	
	(%)	(m)	(%)	(m)
Small (≤ 10 m)	17.53	1.10	2.65	0.12
Large (> 10 m)	7.15	0.90	1.46	0.21

Table 11. Species of trees present by size

Spp.	Platanus	Not identified	Aesculus	Sorbus	Betula	Alnus	Acer	Tilia	Quercus	Fagus	Fraxinus	Malus	Prunus	Pyrus	Crataegus
Common	Plane		Horse chestnut	Rowan	Birch, Hazel, Ostrya	Alder	Maple	Elm	Oak	Beech	Ash	Apple	Cherry	Pear	Hawthorn
≤ 10 m		29		16	10		9					7	22	1	6
> 10 m	51	19	7	5	5	3	3	2	2	1	1	1	1		

Current characteristics: Results

The urban morphology characteristics for all 19 sites derived from the LiDAR (LN8) dataset and OS MasterMap data are shown in Figure 26. Clear local maxima of both mean building height (z_b) and building plan area density (λ_b) at the city centre are evident; the classical 'peak' where the strongest urban effect on the micro-climate usually is found (Oke, 1987). This is also evident by visual examination of Figure 21. A clear 'plateau' with local maxima and minima is also evident in λ_b. At the local scale, λ_b will influence the wind profile and roughness parameters (Grimmond and Oke 1999). Interesting patterns are evident in the characteristics of vegetation (taller than 2.5 m) at the 19 sites. As building heights increase vegetation height also increases (Figure 27). Although in the outskirts of London there is taller vegetation; see, for example, the forested area within 9N. Two vegetated sites (8N and 9N) are plotted but excluded from the calculation of the linear trend. These show the tendency of increasing vegetation heights that outside the central urban environment but still located within the London boroughs ("the Leafy Suburbs"). Note that the LiDAR transect does not go over the tallest buildings of London (Figure 19).

The plan area density of vegetation λv3 shows areas of denser vegetation i.e. parks and abundance of back gardens within certain areas of London. A trend of increased λv3 towards the outskirts of the urban area is also apparent. It should be noted that morphological parameters for vegetation (i.e. z_{v3} and λ_{v3}) only takes vegetation taller than 2.5-m into account. If shorter vegetation, such as grass and small shrubs is included, the values of z_{v3} and λ_{v3} would change considerably especially at the outer sites. Potential for a bias to be introduced by not accounting for vegetation when determining urban roughness parameters is evident.

The peaks in z_b and λ_b are also evident in sky view factors derived from the building DEMs (Ψ_b) (Lindberg and Grimmond 2010). Sky view factors are derived at different levels. Ψ_b on all horizontal surfaces (i.e. roofs and ground) ($\Psi_{b(all)}$) has similar values to Ψ_b on the ground $\Psi_{b(ground)}$ whereas $\Psi_{b(all)}$ have higher values as elevated roofs are included. The largest discrepancies between these two parameters occurs when extensive building structures (e.g. industrial plants) are present. Values of $\Psi_{b(ground)}$ also have a very similar pattern to λ_b with a strong negative correlation (R^2=0.83, not shown). The correlation between $\Psi_{b(all)}$ and λ_b is even higher (R^2=0.86, not shown). When including the vegetation DEMs to create Ψ from all essential 3D objects in the urban environment (Ψ_{all}) (Lindberg and Grimmond 2011), the patterns change to some extent compared to Ψ_b with a general reduction of Ψ. The peak is still located in the city centre but large reductions of Ψ are found at the outer sites where large amounts of vegetation are found. There is a positive correlation found between $\Psi_{b(ground)}$ and $\Psi_{all(ground)}$. However, the correlation is not very strong (R^2=0.48, not shown) highlighting the importance of including vegetation when deriving continuous images of Ψ in urban areas.

To gain a sense of the vertical distribution of roughness elements (buildings and trees) which are important for dispersion. Vertical cross sections of vegetation and buildings for the 19 sites are shown in Figure 18. The distribution of the raw LiDAR returns/0.5 m section (Figure 18a) is very similar to actual vertical distribution derived from the two vegetation DEMs (Figure 18b). The two major differences are the plan area

fraction at low levels. First, low level LiDAR returns are removed when generating the vegetation DEMs since these returns could include non-vegetation objects on the ground (e.g. vehicles, rubbish bins, humans etc.). Second, there seems to be a minor decrease of the plan area density from the vegetation DEMs compared to the raw LiDAR returns. This is probably due to the distribution of LiDAR returns that are higher within the centre of the canopy where the vegetation height also is high, whereas at the edges fewer and lower LiDAR returns are found. However, the pixel sizes of the DEMs are consistent (i.e. 2 m) and therefore appear to have lower mean heights that the actual LiDAR raw data (compare Figure 26, Figure 27, Figure 18). The vertical distribution of vegetation (Figure 18b) is in many ways similar to the vertical distribution of building structures (Figure 18c), where plan area densities are shifted upward when moving closer to the city centre. Exceptions are found at the limits of London. Interesting patterns are also found in the very city centre (0C in Figure 18a, b) where the plan area density of vegetation at low levels is very low indicative of the absence of near ground vegetation. This is probably because of the high level of maintenance required for vegetation in the dense central urban areas and the absence of residential gardens where low level vegetation is present typically. The big difference between the vertical distribution of buildings and vegetation is the increase found in vegetation at the outskirts of the city (also seen in Figure). The implication of this is that the urban limit (‘cliff’) is erased when combining the vertical distribution of all 3D objects (Figure 18d). Spots of low vegetation density are found at some more industrial sites (e.g. 6S and 7S).

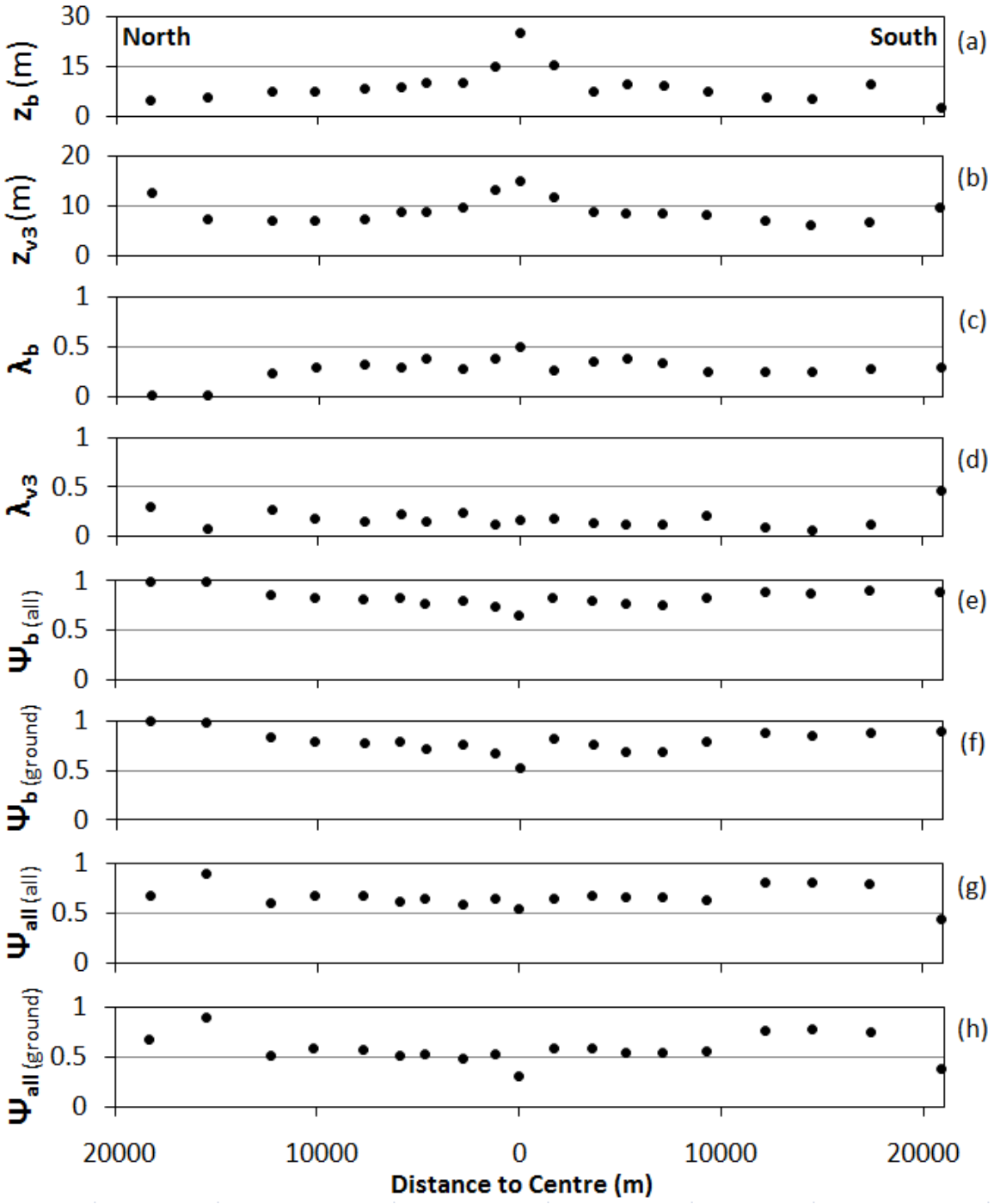

Figure 26. Variations of morphological characteristics for a North-South transect through London (see Figure): a) mean building height (z_b), b) mean vegetation height >2.5-m (z_{v3}), c) plan area fraction of buildings (λ_b), d) plan area fraction of vegetation > 2.5-m (λ_{v3}), e) sky view factor derived from building DEM (all pixels) ($\Psi_{b(all)}$), f) sky view factor derived from building DEM (ground level pixels) ($\Psi_{b(ground)}$), g) sky view factor from both building and vegetation DEMs (all pixels)($\Psi_{all(all)}$), and h) sky view factor derived from both building and vegetation DEMs (ground level pixels) ($\Psi_{all(ground)}$).

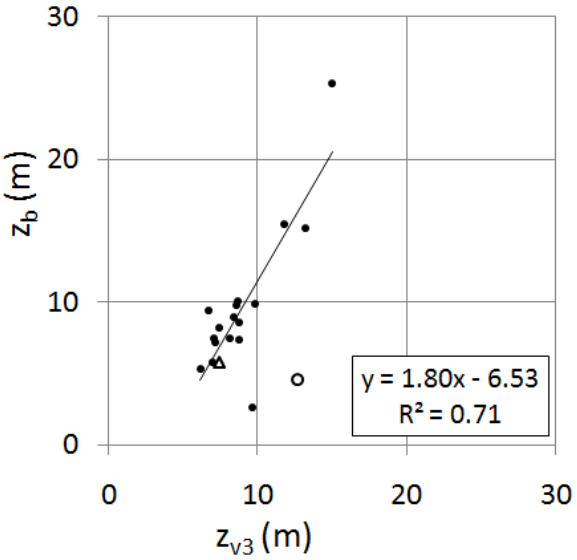

Figure 27. Mean building height (z_b) versus mean vegetation height (z_{v3}). The trend line is based on urbanised sites (black dots, n=17). The triangle (predominately agricultural land) and the circle (predominately forest) are the two 'rural' study areas within the Greater London Area (8N and 9N).

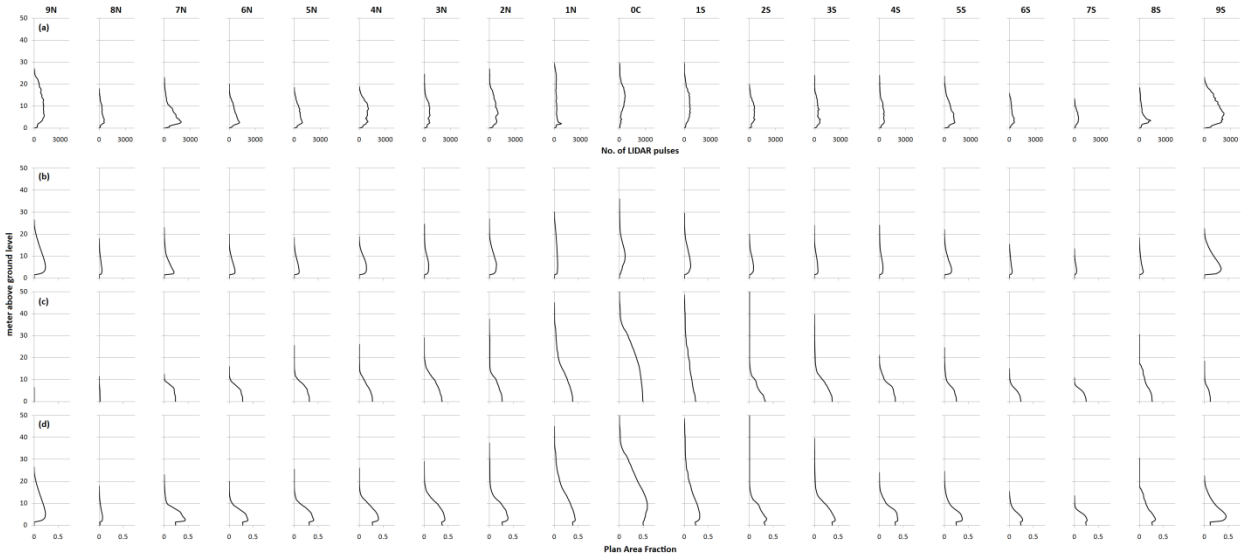

Figure 18. Vertical distribution (in 0.5-m intervals) of buildings and vegetation of the 19 sites: a) raw LiDAR returns classified as vegetation, b) vegetation, c) buildings, and d) buildings and vegetation.

Vegetation from Aerial Photography: Methods

An independent method to analyse the spatial vegetation cover and to provide information about the other types of vegetation (e.g. grass) based on aerial photography also was undertaken. This uses a supervised classification (Maximum Likelihood Classifier MLC) of the NERC 2008 flight high resolution aerial photography (AP8,Table) which were taken concurrently (Figure 29). MLC assigns pixels to a class by evaluating the variance and covariance of the spectral value of each pixel (Tharpa and Muryarna 2009). Each pixel is assigned to the class it is most statistically likely to belong to (Bhakaran et al., 2010).

Training sites were created for three land cover classes: grass, trees and non-vegetation. ArcGIS® 9.3 (2010) was used with the 'equal' *a priori* option so no weighting was applied to any class. Two smoothing filters (4 and 8 pixel 'majority filters') were applied to the MLC output raster with the objective of removing any speckling.

Figure 29. Example of the GIS layers for site 0C (Figure). See Table 2 for codes of the sources for all data. Location of site see.

Vegetation from Aerial Photography: Results

The supervised classification and two subsequent smoothing filters were carried out for each site (Figure 20). The minimum total vegetation occurs at the central site (site 0C, with 14% vegetation cover) while the maximum vegetation cover occurs at site 9N (82% vegetation cover) (Figure 31). The total vegetation cover has similar trends N and S of site 0C (seen more clearly in Figure) which reflect the historical growth of London. The decreased vegetation at site 4N and 5N (~ 7.5 km) is related to a shift towards urban

residential, characterised by small back gardens and no/very small front gardens. The drop in vegetation at site 8N is because the site is mainly industrial.

Comparison of MLC to TL8 can only be done for tree coverage (Figure 33). At site 0C MLC suggests 5% less trees and more trees at the suburban sites (max. 25% difference at site 6S). The smoothing filters had a very limited effect on the MLC tree estimation, with only one site recording a difference >±1%.

The underestimation of tree by MLC relative to TL8 in the central sites is explained by the misclassification of tree pixels as grass. The suburban overestimation of trees by MLC may be explained by the increasingly present shrubs in private gardens (typically hedges). Shrubs were included in the tree class due to their dark green colour. The other cause is the effect of shadow. The apparent overestimation is partly caused by an underestimation of trees by the LiDAR, where it has missed trees. Areas of well maintained coniferous trees (e.g. large hedges) may be removed in the filtering process used to remove building edges as the shape of these hedges is characteristic of building walls/ edges.

For statistical analysis sites 8N and 9N were excluded as visual inspection shows they are rural/ agricultural and their inclusion also had a negative impact on the normal distribution of the tree and grass areas. A number of statistically significant relations were found to exist between the non-vegetation and vegetation variables, the strongest is a moderately negative relations between average building height and MLC total vegetation fraction (r^2=0.65, p<0.001).

Figure 34 and Figure 35 show examples where grass in shadow has been misclassified as trees. This is due to the shadow causing the grass pixels to appear darker than their true value. Figure c shows where LiDAR data has misclassified an area where trees are not present. This has been caused by the building having a metal grid roof; this has probably resulted in the LiDAR sensing multiple returns characteristic of trees.

Figure 36 shows an example of errors induced by the aerial photos. Here the LiDAR tree outline and MLC do not match up, possibly caused by the area of the photo being off nadir whereas the LiDAR does not suffer from this error. The angle of the photo has also caused the buildings to hide areas of tree from view and therefore cannot be detected by the MLC.

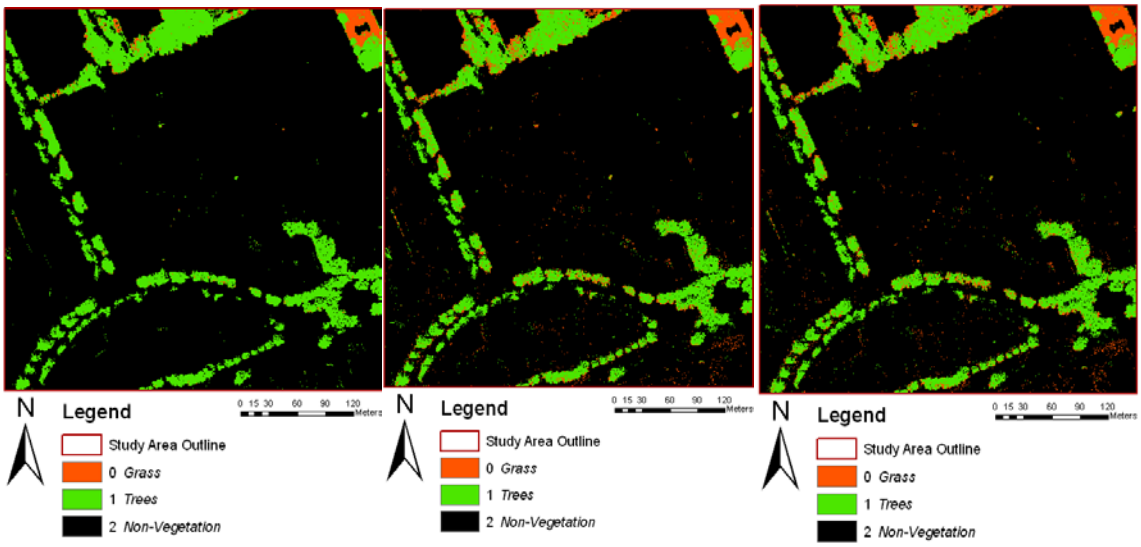

Figure 20. Example of results of supervised classification for site 0C (a) no smoothing (b) 8 pixel smoothing(c) 4 pixel smoothing

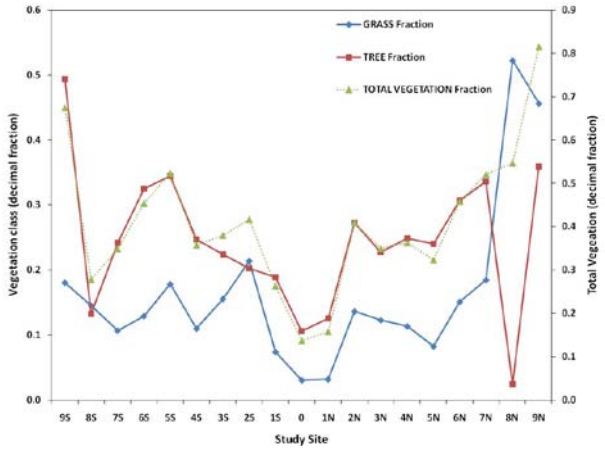

Figure 31. Fraction of each vegetation class (tree and grass) and total vegetation at each site.

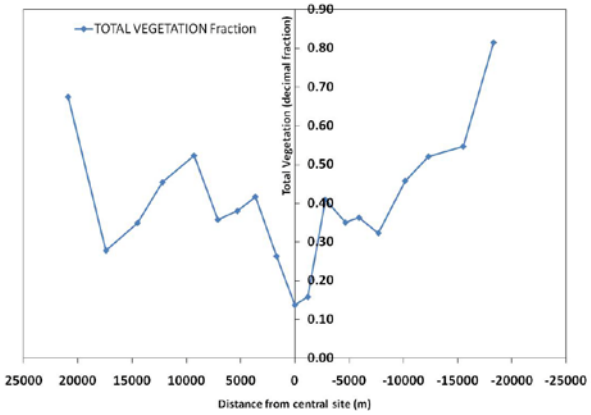

Figure 32. Total vegetation with distance from central site (positive South).

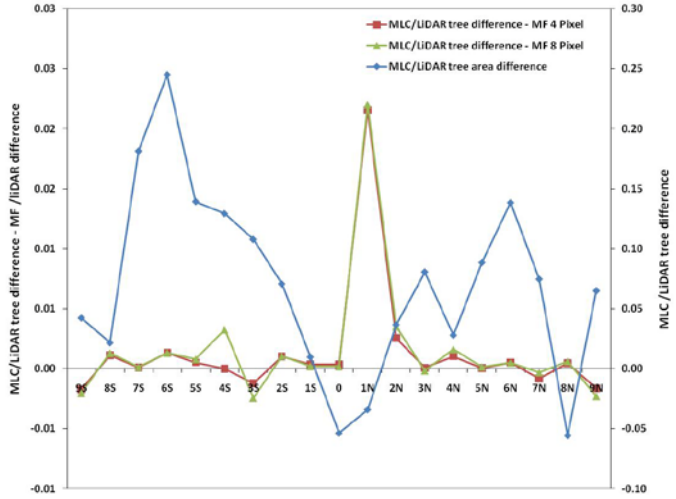

Figure 33. MLC tree fraction and MLC with smoothing filter (red, green) differs from the LiDAR tree fraction. (blue line) Difference between the TL8 tree fraction and the MLC tree fraction.

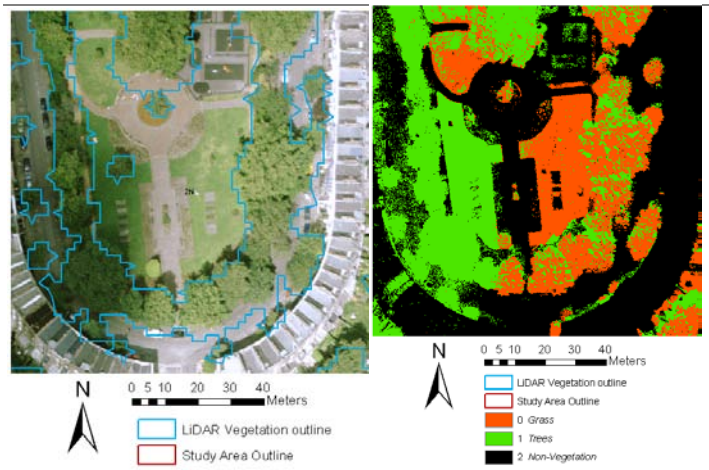

Figure 34. Example of misclassification of grass as trees cause by the effect of shadow.

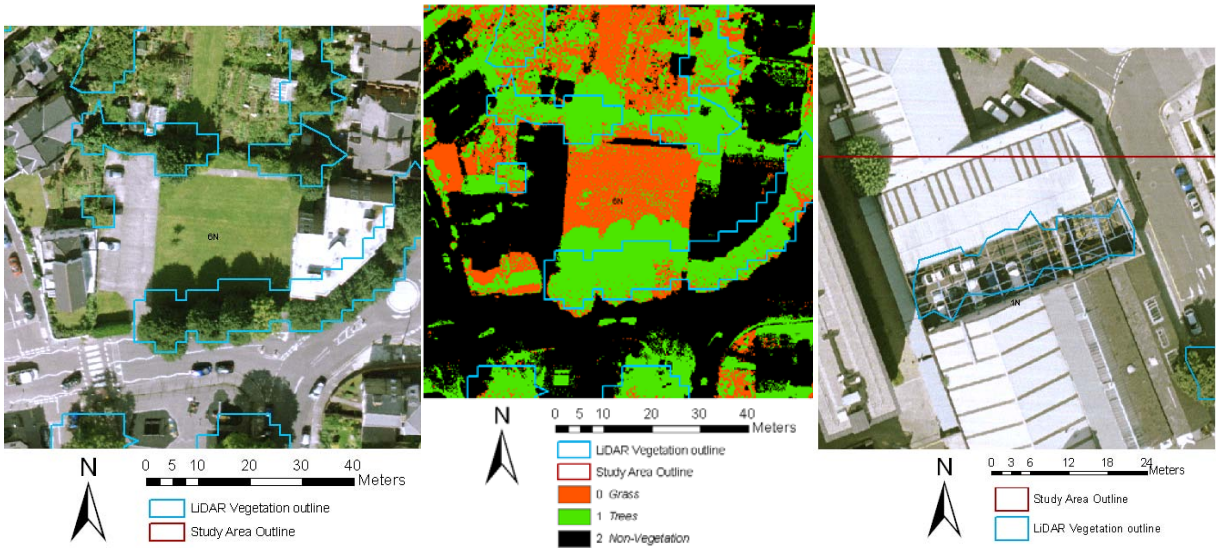

Figure 35. Example of misclassification of grass as trees cause by the effect of shadow and an area misclassified by the LiDAR

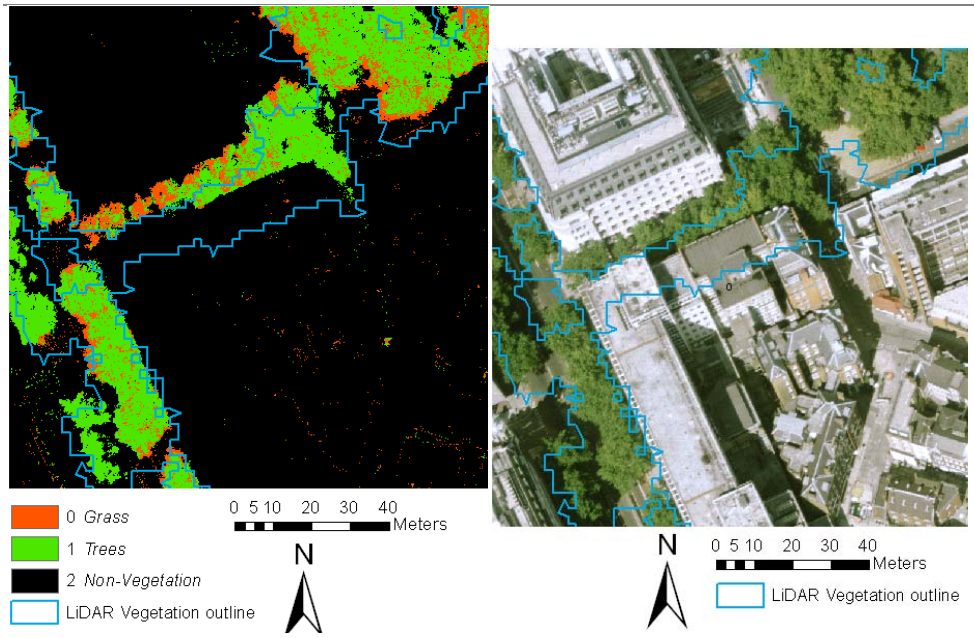

Figure 36. Aerial photo induced errors.

Spatial variability of urban morphology characteristics: Results

From the above analyses the surface characteristics for the Central Activity Zone that are used as the basis for describing observations and for doing modelling were completed. As the TL8 data set only covers a strip of the CAZ and the street tree inventory (STI, Table) is also not complete in the CAZ (with most notably the City of London data not being included) a new LiDAR data set at 1 m^2 resolution (LI58 provided by GLA, Table 2) was analysed. These data were analysed using the techniques developed and described in Lindberg and Grimmond (2011) are used to provide the data base.

Figure shows the spatial variability across the CAZ based on the database developed for the current vegetation status. The CAZ excluding those areas that are parks are clearly evident by the lack of trees.

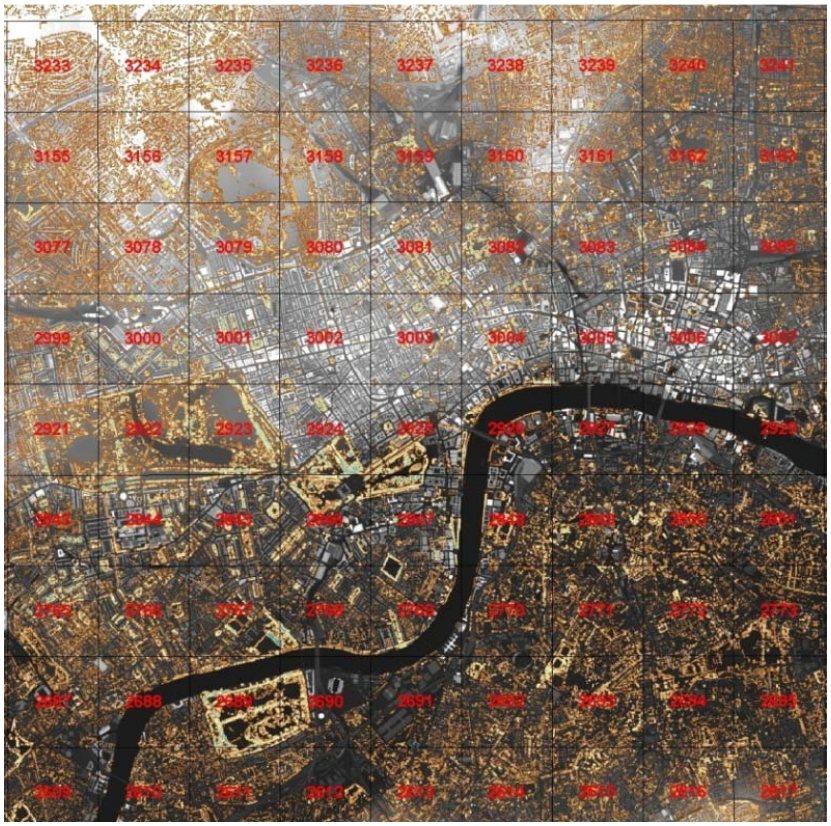

Figure 37. Central Activity Zone of London (with 1 km grid). Grid 3004 is where KCL is located. Topography and building height shown in black and white (white higher). Trees shown in brown to green scale with green being taller.

Potential Locations for New Green Infrastructure: Methods

The GLA planning interest for the DSS relates to the addition of vegetation within the Central Activity Zone of London. The rules outlined in Table 12 were developed in conjunction with GLA to determine where street trees and green roofs could be added. As the TL8 data set only covers a strip of the CAZ and the street tree inventory (STI, Table 2) is also incomplete in the CAZ (with most notably the City of London data not being included) a new LiDAR data set at 1 m^2 resolution (LI58 provided by GLA, Table) was analysed. These data were analysed using the techniques developed and described in Lindberg and Grimmond (2011) are used to provide the data base.

The roofs in the CAZ that potentially could have green roofs are shown in Figure 38a. These roofs are characterized by the class of slope and the area of that slope type. Figure 38b, for example, illustrates the fraction of the roof that is flat, with the actual area (m^2) shown in Figure 38c. Figure 39 shows two areas of the CAZ with the current location of street trees based on the STI and location identified where the trees could be located.

The impact of political boundaries and land ownership can be seen in Figure . The boundary between the Westminster and City of London can be detected based on where the STI data base is incomplete or the apparent lack of trees. When the map and the AP8 aerial photography are compared one can also see that the management of the trees changes (see for example lower right corner of photo in comparison to the map) from street trees to land that is managed by another institution. Comparing Figure 41. with Figure one can see the difference in tree coverage based on the source of the data. The LI58 data set is continuous so trees in the City of London are now evident. There also similar type of tree information beyond the STI data. Notably trees in parks and private land are now apparent.

Table 12. Rules developed for where new green infrastructure could be located in the CAZ based on discussions between Matthew Thomas (Greater London Authority), Dr Fredrik Lindberg (KCL, University of Göteborg) and Prof Sue Grimmond (KCL).

Location	Rule
Street Trees	(a) A tree has to be located on a pavement (b) The centre of the trunk should be ≥3 m from a building wall and exisiting vegetation. (c) The distance between **new** tree trunks should be ≥ 10 m (This is based on visual analysis of the current street tree database density) Buffer 10 m from STI when no TL8
Green Roofs	(a) Roof has to be flat (or below a certain slope e.g. less than 20%) (b) Roof area has to be larger than 25 m^2

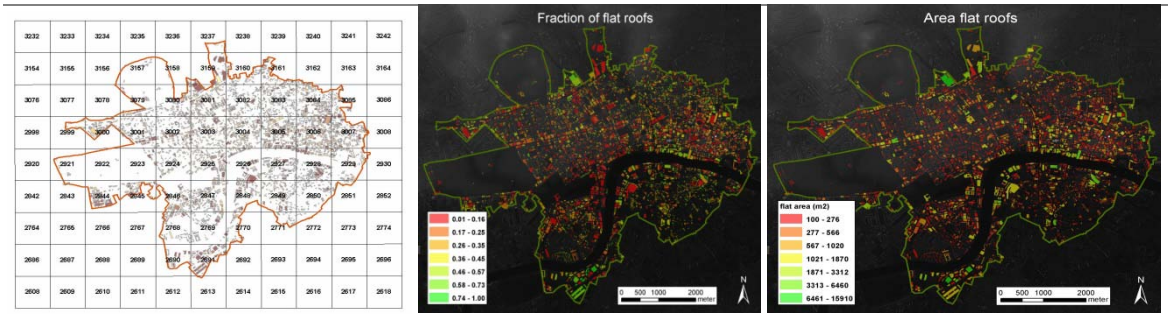

Figure 38. The CAZ (with 1 km grid) showing (a) the areas that potentially could have green roofs added (b) the fraction of the roof that is flat and (c) the area of the roof that is flat.

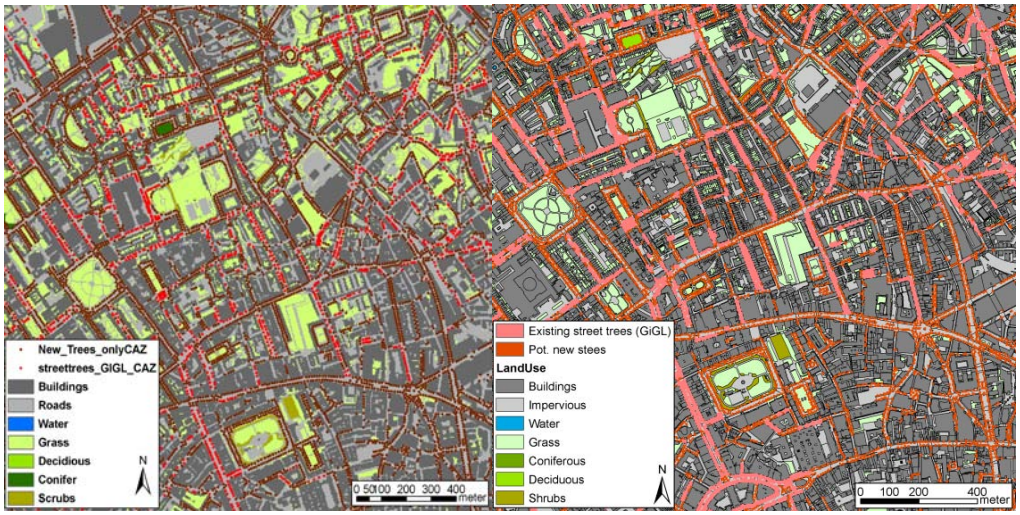

Figure 39. Street tree coverage within two areas of the CAZ. Current trees are shown (red or pink) and potential locations (brown or orange).

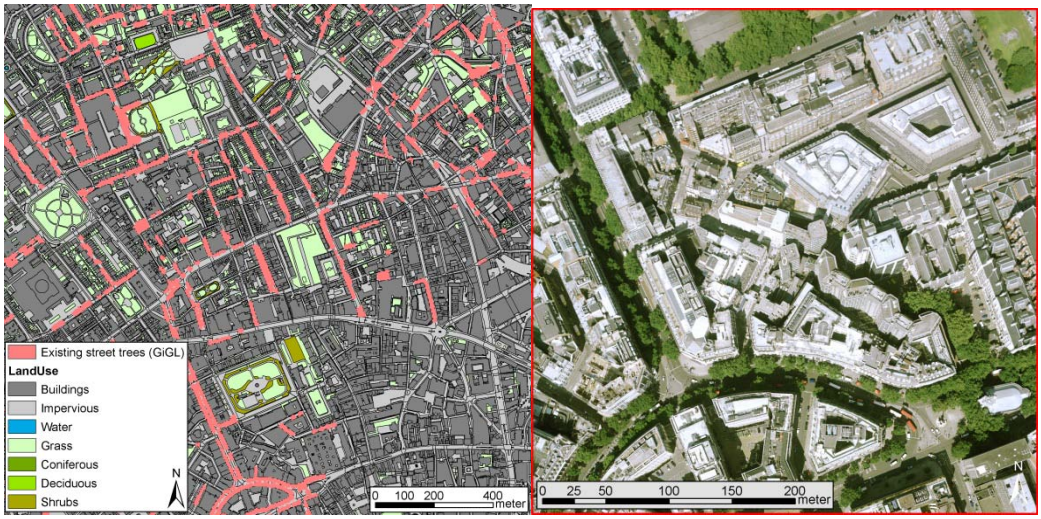

Figure 40. Location of street trees based on STI. The boundary between the Westminster and City of London can be detected based on where the STI data base is incomplete or the apparent lack of trees. Comparison with the AP8 aerial photography one can also see that the management of the trees changes (see for example lower right corner of photo in comparison to the map).

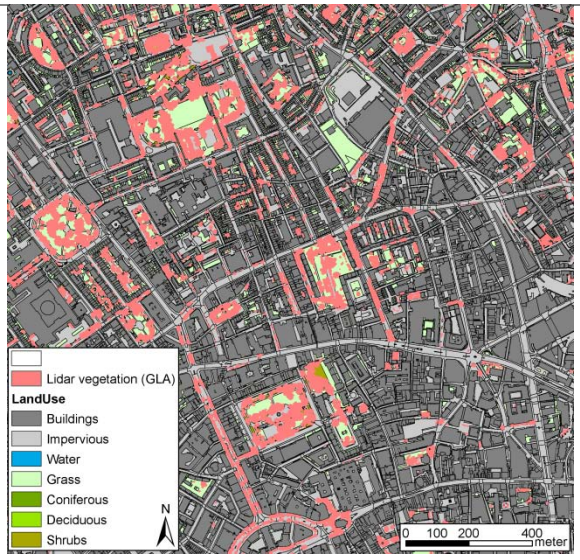

Figure 41. Location of trees based on analysis of LI58 dataset.

Surface Temperature

For the BRIDGE project, surface temperatures have been measured continuously using individual infrared thermometers pointing at different wall facets and roof types (Figure). These are complemented with an air temperature profile (Figure) which consists of fine wire unshielded thermocouples located on the KSS tower. The KSS_{roof} surface temperature is directly below the air temperature profile.

In addition, on occasion thermal cameras are used to collect wider spatial data (Figure 44). During the NERC flights over the city a number of thermal cameras were borrowed (EPSEC, NERC, other KCL researchers) to provide supplementary information. The NERC flights occurred in 14-15 August 2008 and 3-4 June 2010 during the day and night. The processing of that data is ongoing. The airborne observations are performed by ARSF (Airborne Research & Survey Facility) of NERC (Natural Environment Research Council, UK) were accompanied by extensive ground truth observations.

One TIR single channel and two hyperspectral instruments (VIS-SWIR) were operated on the plane 'Dornier 228: D-CALM' (Table 3), which had an average altitude of about 666 m during the day and 708 m at night. Data from TABI-320 (Thermal Airborne Broadband Imager) are deployed in the calculation of surface brightness temperature. It was set to Mode 3: Urban, with a temperature range of -20 to 110 °C and a thermal resolution of 0.1 °C. Observations from the AisaEAGLE sensor will be used for land cover classification. At maximum spectral binning this hyperspectral sensor still offers 60 spectral bands which contain sufficient information for the present study. Hence this setting is chosen in order to allow for maxiumum image rate (160 images s^{-1}). Currently, it is assumed that data gathered by AisaHAWK do not benefit the intended data processing since it's narrow FOV results in a rather small swath width. Additional information on heights of surface objects was collected with a ALS50-II LiDAR (Leica).

In 2010, four flight lines were acquired close to solar noon (12-13 UTC) and six close to maximum heat island intensity (23:50-01:00 UTC). All lines were flown in a north-south (or south-north) direction. An additional east-west orientated cross line completed the nighttime observations (around 01:20 UTC 04/06/2010). The acquired data cover a good fraction (at night >40%) of the CAZ area of interest (Figure). During day and night, the first line is centred over the flux towers and followed by three lines to the east, the prevailing surface wind direction on the study day.

Anticyclonic weather with clear sky conditions observed during the whole measurement period (Figure). The airborne measurements were accompanied by extensive ground truth observations. Fixed Infrared thermometers (IRT) from Raytek and Apogee are part of the permanent observations at the KCL sites (Figure). These sensors measure the brightness temperature of brick walls of four orientations (S, W, N and E) as well as roofs of different materials (concrete, gravel, roofing paper and black tiles). In addition, hand held IRTs (Omega and Maplin) were used to monitor surface temperature of large homogeneous areas including green spaces (Jubilee Gardens, Park at Imperial War Museum), roof materials (Macadam Roof), impervious surface materials (Southbank, Temple Tube Station, Paternoster Square, Waterloo Bridge) and water (River Thames). Water temperature is also monitored in River Thames using a TG-4100 data logger from Tinytag, which is installed at about 20 cm below water level. Temporal evolution of roof and wall temperatures was monitored with a FLIR SC640 thermal imager which was installed on the Strand building (9UTC on 03/07/2010 to 2UTC on 04/07/2010). Additional mobile thermal cameras were used to observe wall and road temperatures during the flight time (Thermoteknix MIRICLE 307K and TESTO TESTO 875-2). All IRTs and thermal imagers - including the TABI -are calibrated against a black body system, allowing for a detailed comparison between the sensors.

Remote sensing in the VNIR range requires detailed information on the state of the atmosphere in order to allow for reliable atmospheric correction. Atmospheric transmissivity, water vapour content and aerosol optical depth is retrieved from sunphotometer observations which were collected by UCL (University College London). In addition, solar irradiance at the surface was measured with two field spectrometers (GER 1500, Spectra Vista Corporation and ASD Fieldspec3, Analytical Spectral Devices), collecting samples of spectralon reflectance panels in a frequency of 10 s. Also, downwelling longwave radiation is derived from FTIR spectrometer (Fourier Transform InfraRed) measurements during day- and nighttime observations. Atmospheric correction further requires knowledge on atmospheric temperature and humidity profiles. Radiosonde data from the nearest operational station at Herstmonceaux (WMO 03882) can provide this information.

The interpretation of spectral reflectance observations in the process of land cover identification can be improved if spectra of some locations of differing brightness are known. This information was collected before and after the daytime flight. Reflectance of three large ground targets (3 m x3 m, black, white and grey) that were located close to the centre of the first flight line, was measured using the ASD Fieldspec3. On the day after the flight observations (2010/155), weather conditions were very similar to the preceding day. No clouds were observed (Figure 46).

On the second day, further ground truth spectra were collected from impervious surfaces (Temple Tube Station and Waterloo Bridge) and grass (Jubilee Gardens). All field spectroscopy equipment is calibrated and quality controlled before and after the measurements by NERC FSF (Field Spectroscopy Facility).

All data collected during the SOP are incorporated into the retrieval of LST Ts (Figure). The radiometric calibration of TABI-320 Raw digital numbers (DN) is performed by the Laboratory of Remote Sensing, National Technical University of Athens, which is the owner of the airborne sensor. Hence, the TABI-320 output is provided in brightness temperature T_b [°C]. For the Eagle readings, the first processing step is undertaken by ARSF-DAN (Data Analysis Node). At-sensor radiance is compared to irradiance, allowing the calculation of at-sensor spectral reflectance (α).

Incorporating a DEM (digital elevation model) for the study area, the AZGCORR software is used to perform geometric correction of both remotely sensed datasets, resulting in maps of T_b and α. A combination of observations from radiosondes, field spectrometers (GER1500 and ASD Fieldspec3) and the sun photometer are used as input for the atmospheric transfer model MODTRAN5 (MODerate resolution atmospheric TRANsmission) in order to calculate atmospheric transmissivity t_a and downwelling longwave radiation $L\downarrow$. The latter is also measured by the FTIR spectrometer. Finally, effective mean atmospheric temperature T_a is required as a third input variable for atmospheric corrections.

The Eagle spectral information, supported by ground truth spectra and urban spectral libraries (e.g. Herold et al., 2004), is used to identify land cover types. Based on the derived land cover map, spatial variation of

surface emissivity is incorporated. In order to gather a database which allows the assignment of spectral emissivity to land cover classes, samples of various urban surfaces are taken with a FTIR spectrometer. This instrument allows for the direct measurement of spectral emissivity ε_λ (Del Campo et al., 2006).

The relation between at-sensor radiation, which is a function of T_b, and the desired LST, is not trivial. It can be solved using for example the mono window algorithm (MWA) developed by Pu et al. (2006). Based on the land cover map, spectral emissivity is incorporated in the process in order to convert brightness temperature in actual Ts. Finally, ground truth observations of surface, wall and roof temperatures are combined to assess the reliability of the performed LST retrieval.

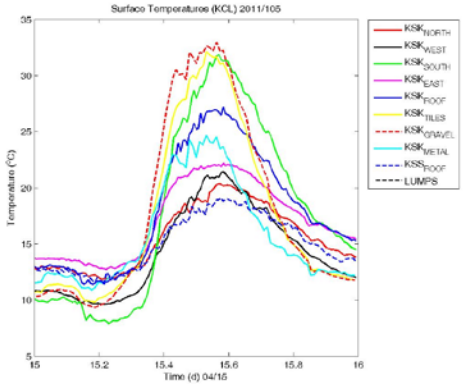

Figure 42. Infrared temperatures for one day from different facets.

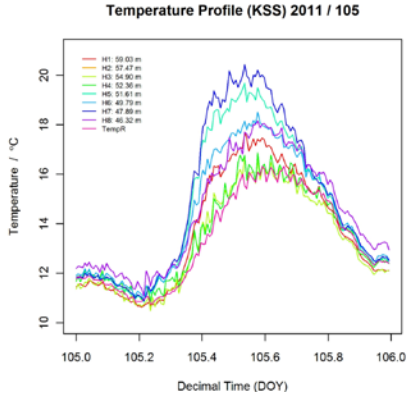

Figure 43. Air temperature profile on KSS.

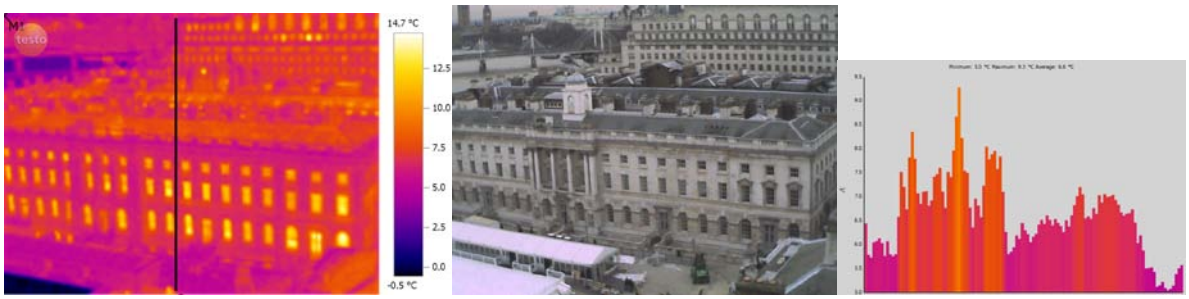

Figure 44. Example of imagery taken near KSS (a) Thermal (b) Visible (c) temperature profile along the line indicated in (a). These do not have emissivity corrections. Image taken 16:07 24 January 2011. Ice rink can be seen in the lower left hand corner.

Table 31. Remote sensing instrumentation and settings as operated by NERC Flight during 2010. The FOV (field of view) of Eagle applies for the chosen lens ($OLE_{18.5}$). Eagle is set to maximum spectral binning. All three instruments work on a push broom technique, pixels/swaths denotes the number of across track pixels. Swath width and pixel size are calculated for an altitude of 700m. AisaHAWK channels are mainly located in the short wave infrared (SWIR) region.

Sensor	TABI-320	AisaEAGLE	AisaHAWK
Manufacturer	*ITRES*	*Specim*	*Specim*
Spectral range	TIR, $8-12\,\mu$m	VNIR, $0.4-0.97\,\mu$m	SWIR, $0.97-2.45\,\mu$m
Spectral bands	single band	60	254
FOV	48°	37.7°	24°
Pixels/swath	320	1024	320
swath width [m]	623	482	298
pixel size [m]	1.9	0.5	0.9

Figure 45. Day and night time flight lines (03/06/2010). Centre of the lines (white), Outer boundary of area covered by TABI (Eagle) (red (green)). Pink scale indicates a) 5 km, b) 1 km, c) 500 m and d) 100 m. GoogleEarth 2010.

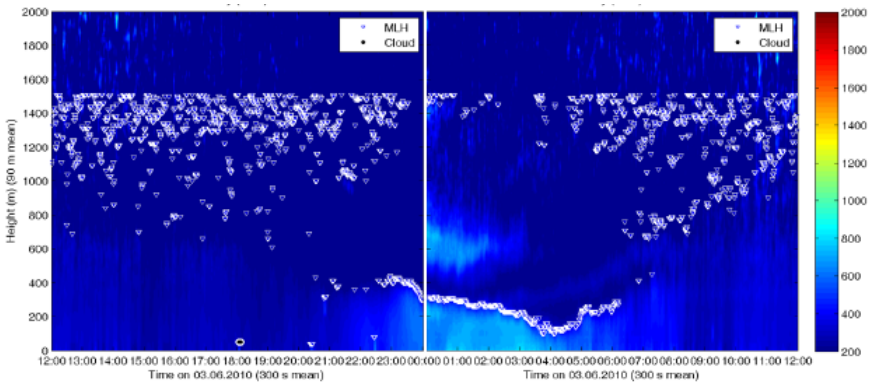

Figure 46. Ceilometer (KSK45W) observations of backscatter for 2010/154.

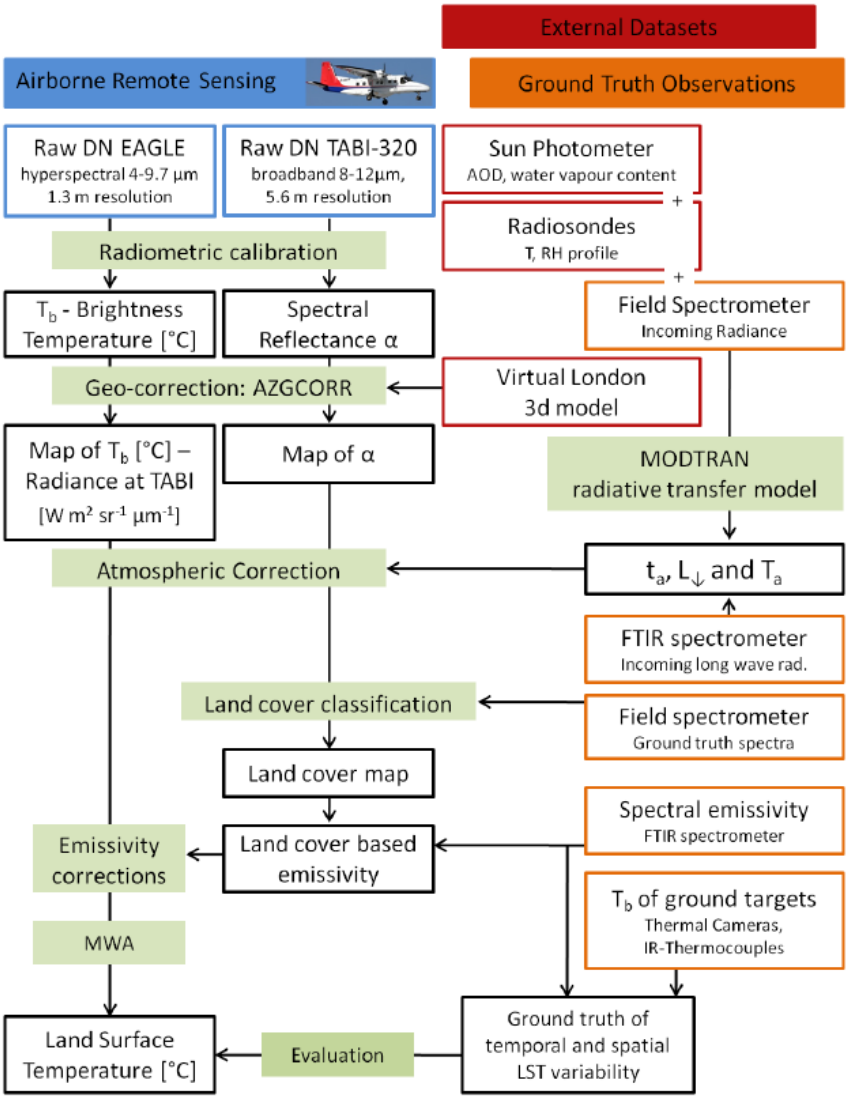

Figure 47. Overview of processing procedure for TABI and Eagle data to retrieve LST distribution. Airborne data (blue), ground truth measurements (orange), other input data (red), intermediate results (framed black), methods/ processing steps (light green).

6.2 Air quality

As part of this study, two types of analyses have been conducted that are concerned with air quality:

a) The LAQN data were used to model the impact of vegetation cover on air quality using the UFORE model
b) Measurements were taken at one LAQN site to evaluate the fourier transform infra red spectroscopy (FTIR) for conducting air quality measurements.

Air Quality Methods: UFORE

Using the adapted UFORE approach described in Tallis et al. (2011) the potential of current street tree cover and a future maximum density of street tree cover is investigated to remove dust pollution (particulate matter of a diameter less than 10 x 10^{-6}m (PM_{10}) within the London case study site (the CAZ). The aim of this work is to provide estimates of total annual removal of PM_{10} resulting from dry deposition, from the mixing layer above the CAZ. Furthermore the removal of PM_{10} (g m^{-2} of canopy) was estimated for the whole range of PM_{10} concentrations [PM_{10}] experienced by street trees within the CAZ. This allowed for a comparison of modelled estimates with measured PM_{10} deposition to trees within the CAZ and also provides estimates of removal potential dependent on local [PM_{10}]. This approach was expanded to the whole Greater London Authority (GLA) area to examine the annual PM_{10} removal of the urban canopy for the whole of London and to allow comparisons with data from other cities and assess the applicability for a city wide approach (Tallis et al. 2011).
The input data required for the adapted UFORE model described in Tallis et al. (2011) to estimate dry deposition of PM_{10} to tree canopies are (i) [PM_{10}] (µg m^{-3}), (ii) tree canopy cover, deciduous or coniferous (m^2) and (iii) meteorology required to calculate Pasquill-Turner stability class (season, wind speed (m s^{-1}), cloud cover (Oktas). The model was applied to three different scenarios within the CAZ; these were (i) current street tree cover with current [PM_{10}] and meteorology (ii) a maximum possible street tree planting density with current [PM_{10}] and meteorology and (iii) a maximum possible street tree planting density with [PM_{10}] and meteorology estimated for 2050. Current and future [PM_{10}] were obtained from the LAEI pollution dispersal maps for London (LAEI 2009[33]) and Williams (2007) respectively, the [PM_{10}] data used for model inputs are given in Table 14. Current and future street tree canopy covers within the CAZ were obtained from Lindberg and Grimmond (2011) and the data used for model inputs are given in

Table 15. Mapped meteorological data for the GLA were extracted from the UKCP09 gridded data sets of monthly values[34] (Perry and Hollis 2005) for 2006 (cloud cover was for 2004 due to absent data) at a 5 km resolution for the whole GLA area. Input data to describe the future climate in the GLA were extracted from UKCP09[35] . The absolute values (for a 50% probability) were extracted from the 'UK probabilistic projections of climate change over land' based on the medium emissions scenario (SRES A1B) for London in the 2050s. Wind speed for the London area was estimated from the UKCP02 maps for the mean of the medium emissions scenarios for 2080 (the only data available at the time of analysis).

.

[33] LAEI 2006. London Atmospheric Emissions Inventory 2006. Compiled by AEA, March 2009. (http://static.london.gov.uk/mayor/environment/air_quality/research/emissions-inventory.jsp)

[34] www.metoffice.gov.uk

[35] http://ukclimateprojections-ui.defra.gov.uk

Table 14. The values of [PM_{10}] used as input data for the modified UFORE model. * extracted from a 20 m area either side of the street using ArcMap®, ** taken from the upper values of the range predicted by Williams (2007).

	Whole CAZ area (15.68 ha) [PM_{10}]			CAZ Street buffer* [PM_{10}]		
	Mean	Min	Max	Mean	Min	Max
Current (2006)	23.8	21.5	79.8	30	21.8	79.8
Future (2050)	19**	-	-	22**	-	-

Table 15. The values of street tree canopy cover used as input data for the modified UFORE model. *Estimated using the placement rules of Lindberg and Grimmond (2011).

Scenario	Canopy cover (m^2)	
	Deciduous	Coniferous
Current	21437 (14%)	9 (0.01%)
Maximum planting density*	36699 (23%)	9 (0.01%)

Air Quality Modelling Results

Two adaptations to the UFORE model (described in detail in Tallis et al., 2011) allow deposition to be estimated assuming 50% re-suspension of particles (referred to as UFORE) and zero re-suspension (referred to as adapted UFORE). The results of both model outputs are given in Table 16. The inputs from future climates had little influence in parameterising the values for resistance terms in the model and little change was estimated for the mixing layer height which reduced from an annual mean of 435 m (2006) to 430 m (2050) according to model calculations. The [PM_{10}] experienced by street trees within the CAZ ranged from 21 – 79 µg m^{-3}.

The estimated annual uptake of PM_{10} deposited to street trees (g m^{-2}) through dry deposition were compared with measured data from a site within the CAZ (Portman Square 51° 30`55.32``N and 00° 09`21.90``W species *Platanus* x *hybrida*, (London plane) a common London street tree). Mean deposition to trees at the Portman square site was 1735 g $tree^{-1}$ (Beckett et al. 2000) taking the diameter range (measured from Google Earth) of 15 – 25 m for trees at this site this allows a measured approximation of between 4 – 10 g m^{-2} of PM_{10} deposited to these canopies. This measured value is within the modelled estimates which range from 2 – 16 g m^{-2} for broadleaved trees depending on local [PM_{10}] and model type with outputs from the adapted UFORE model (no re-suspension) being closer to this range (Figure).

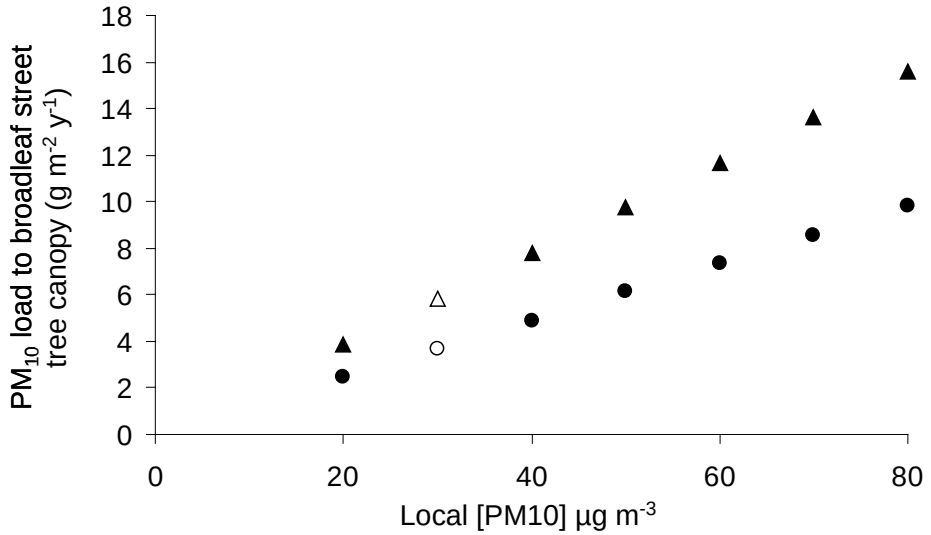

Figure 48. Estimates of the annual dry deposition to street trees across the 20 m street buffer exposure range of [PM_{10}]. Estimates are given for UFORE (●) and adapted UFORE (▲) and clear symbols give the estimated PM_{10} load deposited to the street tree canopy for the mean street buffer exposure.

Table 16 Estimates of PM_{10} removal by the street tree canopy from within the CAZ using the mean exposure concentrations reported in Table 14.

	Scenario					
	Current canopy [PM_{10}] and climate		Maximum canopy, current [PM_{10}] and climate		Maximum canopy, current [PM_{10}] and climate	
	UFORE	Adapted	UFORE	Adapted	UFORE	Adapted
Total Uptake (kg y^{-1})	79	126	135	215	99	158
Reduction in CAZ boundary layer (%)	0.6	0.9	1.1	1.8	0.9	1.4
Uptake to Broadleaf (g m^{-2})	3.7	5.8	3.7	5.8	2.7	4.3
Uptake to Coniferous (g m^{-2})	6.1	62.0	6.1	62.0	4.4	45.5

FTIR test: Remote sensing of Air Quality

The open path (OP) fourier transform infra-red spectroscopy (FTIR) OP-FTIR technique was evaluated at the Blackwall Tunnel Northern Approach (BTNA), London (51° 30' 53.51" N, 0° 00' 29.79" W). BTNA is a 6-lane road that experiences a high volume of traffic, and high concentrations of pollutants, ideal for testing the technique. The London Air Quality Network (LAQN) has a monitoring site located here (TH4), allowing for a comparison between LAQN and spectrometer measurements. The majority of the spectrometer path was located in an area with low pedestrian use, reducing path obstructions.

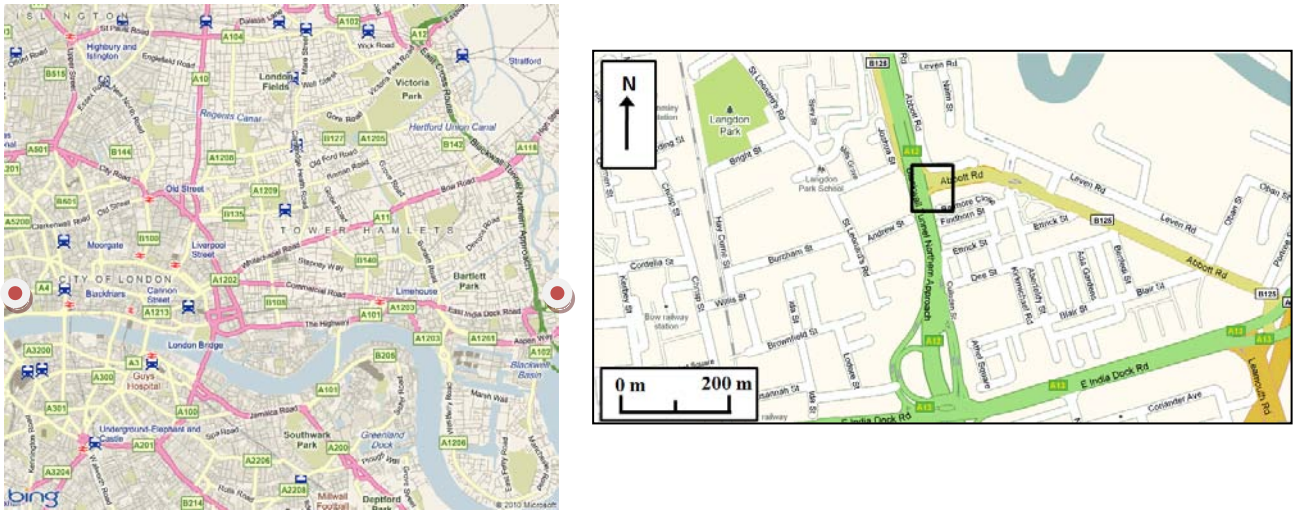

Figure 49. (left) [36] Location of BTNA site (right hand side dot) relative to KCL site (LHS dot) (right) FTIR sample site location (black square) (Google 2009).

[36] Source overview map: http://www.bing.com/maps/print.aspx?mkt=en-gb&z=13&s=c&cp=51.518190,-0.060062&poi=Blackwall%20Tunnel%2C%20London%20SE10%200&pp=skhf41gzzvm1&b=1&pt=pb

FTIR Test: Methods

Sampling was carried out on 04/11/09 between 15:15 and 20:30 in order to sample the afternoon traffic peak. A MIDAC M2000 spectrometer was aligned with a MIDAC 20 cm IR field source (bistatic configuration – Figure) adjacent to BTNA, providing a path length of 49.3 m. The path bisected Abbott Rd at the junction with BTNA, so the spectrometer and the IR source were raised on tripods (~ 1.5 m above street level), avoiding vehicle obstructions. 12 volt batteries were used as power sources for both the spectrometer and IR source.

A Vaisala WXT510 weather station was setup (aligned north) near the spectrometer, measuring relative humidity (RH), temperature, pressure, rainfall, wind speed and wind direction. Meteorological factors affect pollutant dispersal (and therefore concentration), so measurements are used to help interpret pollutant data. Temperature and pressure data was required to calculate pollutant concentration, and RH was used to validate spectroscopic water concentration data.

Spectrometer data were collected and transformed using MIDAC AutoQuant software (8 scans were averaged, producing a recorded spectrum every 7 - 9 s). WXT510 data was recorded every 5 s. A video camera setup on top of the spectrometer recorded traffic flow on BTNA. Figure shows the sample site and instrument set up. A flow diagram showing the data collection process is provided in Figure 52.

To identify specific chemical species, 21 spectra were averaged using Essential FTIR (Operant LLC 2009[37]) from around 17:30 (i.e. high traffic flow period) to increase the signal-to-noise (SN) ratio. Absorption spectra were then obtained (GATS Inc 2009[38]) for species expected to be present during sampling, and from these, strong species absorbance regions were identified. Absorbance features related to specific species could then be identified in the urban air spectrum. Despite the sample site being selected for having high levels of combustion related species, ambient concentrations were lower than concentrations of many species OP-FTIR is usually used to measure. Overlaying the urban spectrum with a biomass fire spectrum where much greater concentrations of combustion species are present, enabled easier identification of spectral features.

The forward modelling software MALT 5 was used to calculate species concentrations from the spectra. Using environmental data from the sampling site (mean temperature and pressure, path length), and species specific molecular data (for factors affecting molar absorptivity) from the HITRAN database (Rothman et al., 2005) and approximate atmospheric concentrations for the species, MALT simulates absorption spectra at a specified wavenumber range. The synthetic spectrum is fit to the observed spectrum iteratively, with MALT adjusting species concentrations each iteration until the mean-squared residual between the spectra is minimised (Griffith, 2006). Background spectra are not required using this modelling method; MALT simulates the background by fitting polynomials to the sample spectra.

[37] Operant LLC (2009) Essential FTIR – FTIR Software. [Online]. Available from: http://www.essentialftir.com/ [Accessed 10th November 2009].

[38] GATS Inc. (2009) Spectral calculator, atmospheric gas spectra, infrared molecular absorption spectrum [Online]. Available from: http://www.spectralcalc.com/spectral_browser/db_intensity.php. [Accessed 15 Dec. 2009]

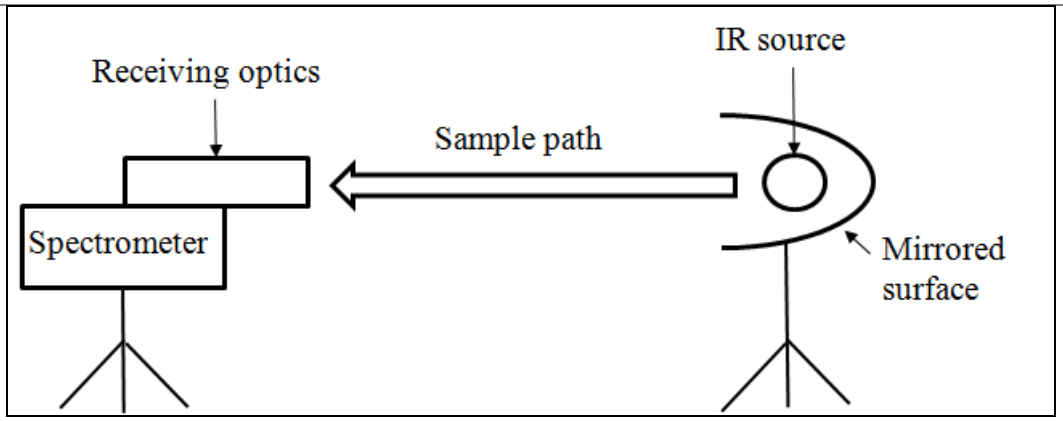

Figure 50. Bistatic spectrometer configuration (After Backsik et al., 2004).

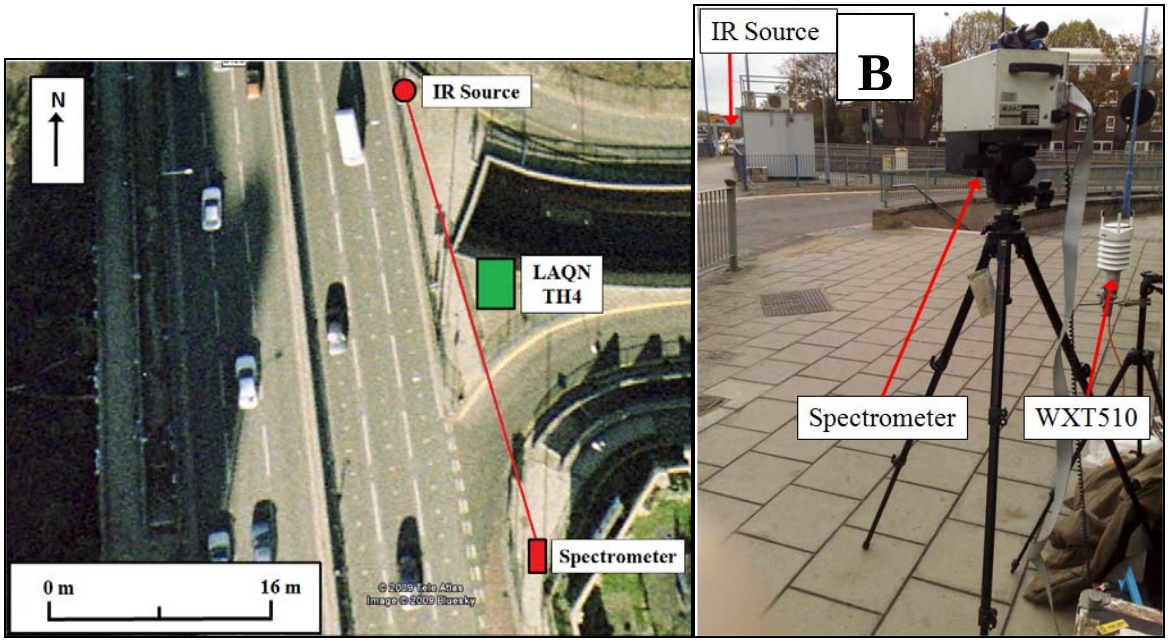

Figure 51. (A) Site setup and approximate spectrometer path (Google 2009) and (B) Looking north along the spectrometer path. LAQN TH4 station visible in top left.

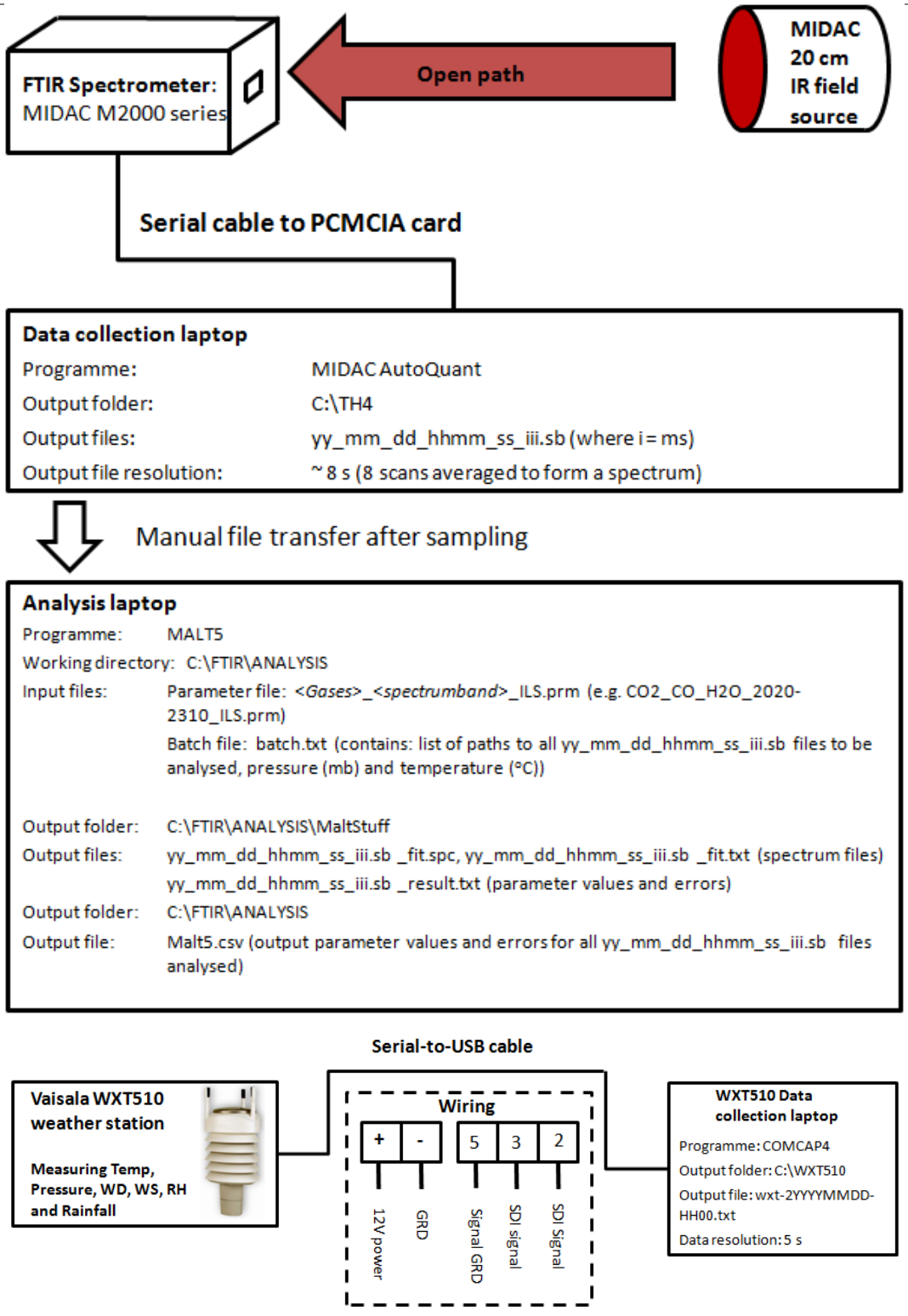

Figure 52. Flow diagram of FTIR data collection.

Table 17. Species identified or quantified using FTIR spectroscopy.

Species	*Successful MALT quantification? (Yes/No)*	*Visual identification in spectra if not quantified? (Yes/No)*
Carbon dioxide (CO_2)	Yes	N/A
Carbon monoxide (CO)	Yes	N/A
Water (H_2O)	Yes	N/A
Methane (CH_4)	Yes	N/A
Nitrous oxide (N_2O)	Yes	N/A
Ozone (O_3)	No	Yes
Sulphur dioxide (SO_2)	No	Yes
Nitrogen monoxide (NO)	No	No
Nitrogen dioxide (NO_2)	No	No

Table 18. Mean species experimental and background concentrations. [a] Blasing (2009), [b] WHO (2000).

Species	***Mean FTIR Concentration***	***Average global background concentration***
	Concentrations in ppm	
CO_2	477.7	384.8 [a]
	Concentrations in ppb	
CH_4	1985.5	1865/1741 [a]
CO	785.6	50 – 120 [b]
N_2O	328.5	322/321 [a]

FTIR test: Results

Table 17 provides a summary of the species could and could not be quantified in this study. Unfortunately no gaseous pollutant species monitored at the LAQN site (Nitrogen monoxide (NO), nitrogen dioxide (NO_2) and ozone (O_3)) were able to be quantified using spectroscopy, so no direct comparison of measurements could be made. Plotting carbon dioxide (CO_2) and carbon monoxide (CO) against LAQN TH4 NO data (from Dr B. Barrett, personal communication, KCL, 12/11/09) however allows for a comparison of trends over the sampling period (Figure) as they are primary pollutants mainly sourced from vehicular combustion. No clear increase in pollutant concentrations is observed to indicate the start of the traffic peak, but a clear decrease in NO is mirrored in CO and very clearly in CO_2 between 18:45 and 19:45, when traffic flow at the site was observed from video data to have significantly decreased (Figure 54). Short term variation in NO concentration also agrees well with variation in CO and CO_2 data.

The evolution of methane (CH_4), water (H_2O) and nitrous oxide (N_2O) concentration is shown in Figure and Figure 56. Methane is not a combustion product so does not correlate with traffic patterns, and is likely to be influenced by regional concentrations (Grutter, 2003b). Temperature inversion development at the end of the day may partially account for the general increase in CH_4 concentration over time (Oke, 1987).

WXT510 RH data and FTIR water concentration show good agreement in the overall trend and in short term variation. The general concentration increase is likely to be a result of increased combustion from an increase in traffic and possibly the formation of a temperature inversion. Contrasting with other pollutant trends, N_2O concentration generally decreases over time, suggesting that concentrations are dominated by regional sources (Grutter, 2003b).

From a comparison with global background values (Table), FTIR concentration values appear reasonably accurate. Mean values for CO_2 and CO greatly exceed global background values, as expected in urban areas with large combustion sources. CH_4 and N_2O levels show relatively good agreement, evidence for concentrations being regionally dominated.

O_3 and sulphur dioxide (SO_2) concentrations were not successfully modelled with MALT (either unrealistic concentrations or very high % error values were calculated) but small spectral features associated with the species were observed in the urban air spectrum (Figure , Figure 58). The biomass fire spectrum is also shown to aid feature recognition.

A more objective identification analysis based on fit residuals was carried out. The mean of the squared residuals is smaller for a MALT run with O_3 defined as a component (1.33×10^{-5}) than a run without O_3 defined (1.40×10^{-5}). It was also smaller for a MALT run with SO_2 (1.47×10^{-5}) than without (1.57×10^{-5}), implying that both O_3 and SO_2 must be present as they can account for some absorption. Residuals for the model runs are shown graphically in Figure 59. Neither identification nor quantification was possible for NO_2 and NO, as they have large spectral features in regions where high absorbance occurs from interfering species.

Wind speed and direction can have a significant impact on pollutant dispersal and therefore concentrations (Harrison, 2001). Over the course of the sampling period, relatively little variation in wind speed or wind direction was observed (Figure 60). Average wind speed was 1-2 m s^{-1}, and the dominant direction was SSE, parallel to the road. As a result, variations in pollutant concentrations are more likely to have been caused by other factors.

Concentrations of pollutant species typically measured at urban monitoring sites (e.g. SO_2, NO_x, O_3) were below the detection limits (DL) of this FTIR setup. For this to prove a viable method for meso-scale monitoring of these species, method alterations are needed. Spectral features are very small in the urban spectra, resulting in poor MALT fits. According to the Beer-Lambert law (2) absorption increases (and therefore DL decreases) linearly as sample path length increases. Long path lengths are commonly used/recommended in literature to obtain low ppb concentration measurements (Griffith & Jamie, 2000; Grutter et al., 2003a), though unobstructed paths of >100 m are difficult to find in urban areas. Raising equipment above street level may make this possible. Reducing DL by increasing SN would require much longer measurement averaging times, resulting in lower time resolution data than most continuous analysers. Using a modulated radiation beam like Grutter et al. (2003a) would also improve DL by reducing the detection of stray radiation.

Despite not having a direct comparison between FTIR and LAQN data, comparing primary pollutant levels and water vapour with RH showed that general trends and small scale variation is measured accurately using the FTIR. This suggests that if the DL are reduced, reliable FTIR measurements are likely to be obtained.

The OP-FTIR method used successfully measured species with concentrations in the high ppb – ppm range (H_2O, CO_2, CO, N_2O, CH_4) and data trends reflected those found in species monitored by other methods. Concentration values for these compounds are considered relatively accurate. The inability of the method to measure lower concentration pollutants (NO, NO_2, SO_2, O_3) that are widely monitored in urban areas mean that the technique, without alteration, is unsuitable for urban air quality monitoring. Reducing detection limits by increasing the sample path length and using a modulated IR beam should make this a more viable option.

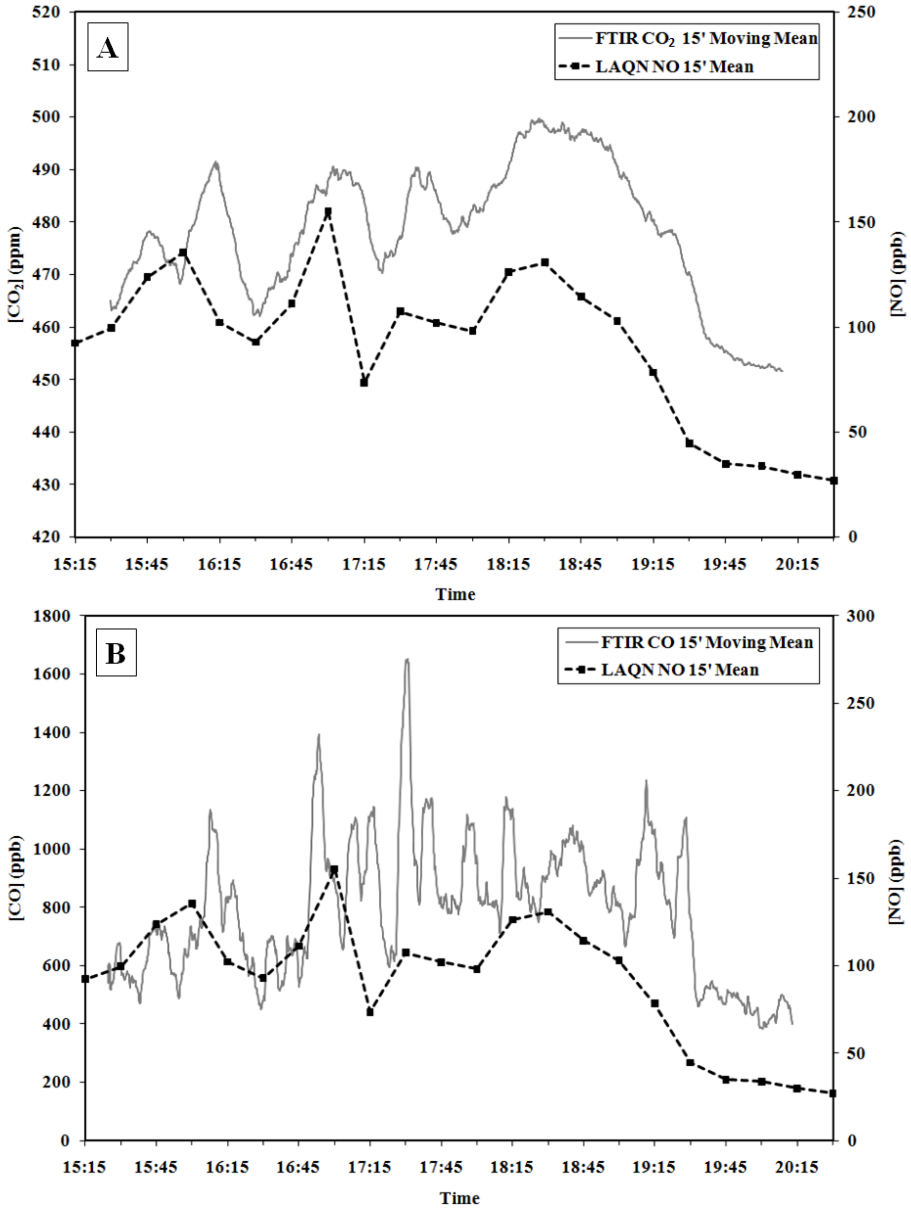

Figure 53. Time series of (A) CO_2 and (B) CO concentrations plotted against LAQN NO data, BTNA, London.

Figure 54. Video stills from (A) before (~18:30) and (B) after (~19:30) the decrease in afternoon peak traffic, Blackwall Tunnel Northern Approach. London

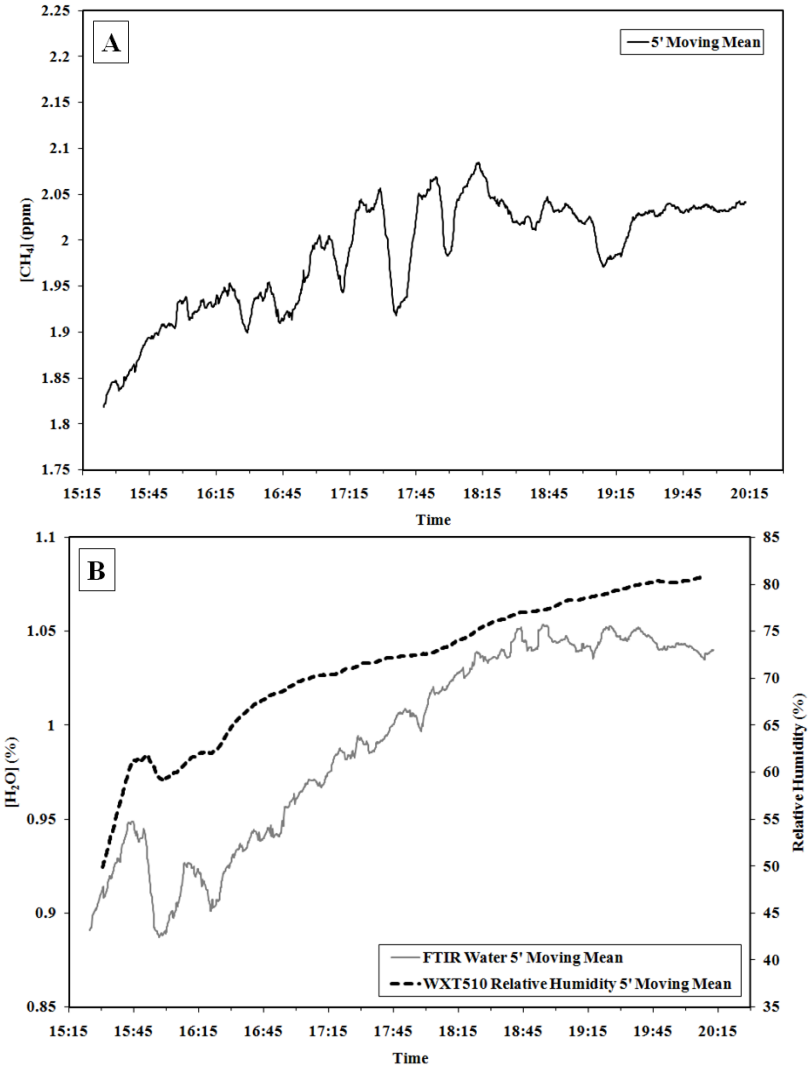

Figure 55. Time series of (A) CH_4 concentration and (B) H_2O concentration alongside WXT510 relative humidity data, BTNA, London.

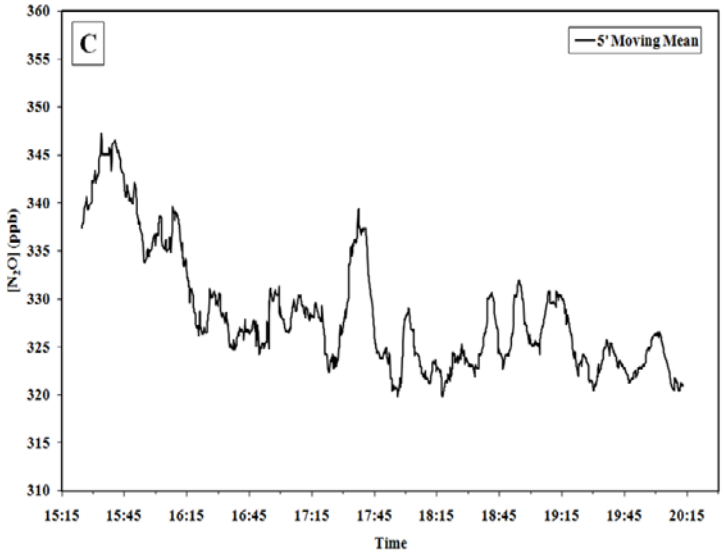

Figure 56. Time series of N_2O concentration, BTNA, London.

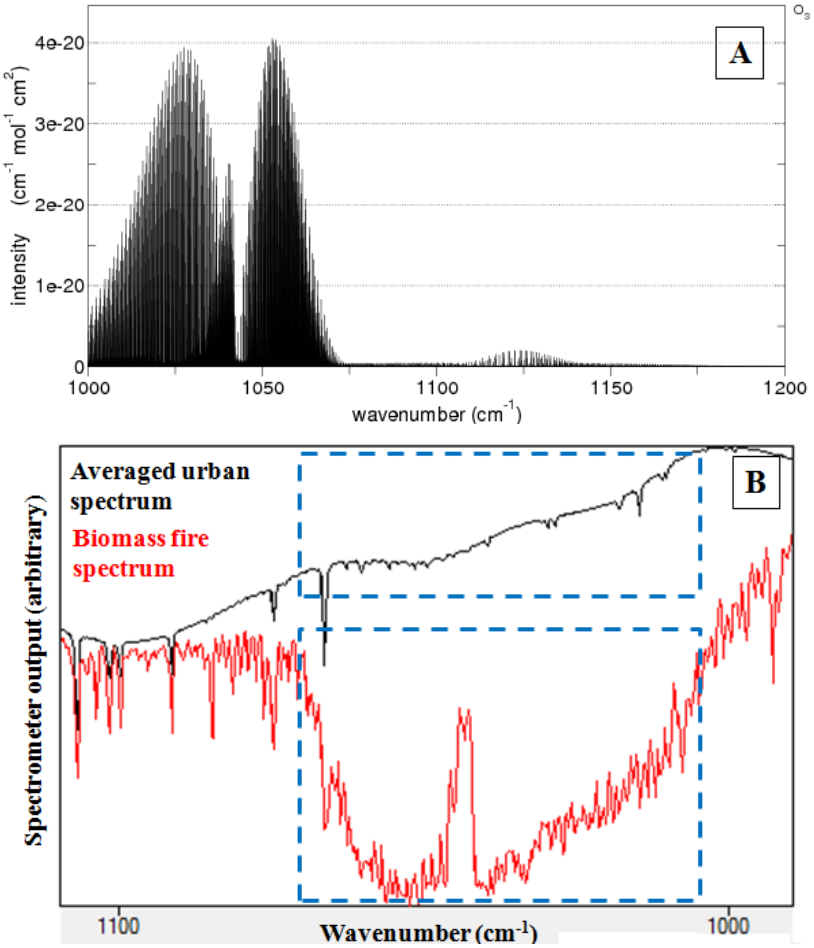

Figure 57. (A) ozone double peaked absorbance feature (1000 – 1070 cm^{-1}) (GATS Inc 2009) (B) identified in the biomass fire and urban air spectra (dashed boxes). Note that the absorbance double peak feature in (A) becomes a double trough in (B), as the y-axis is detector output of the spectrometer, not absorbance.

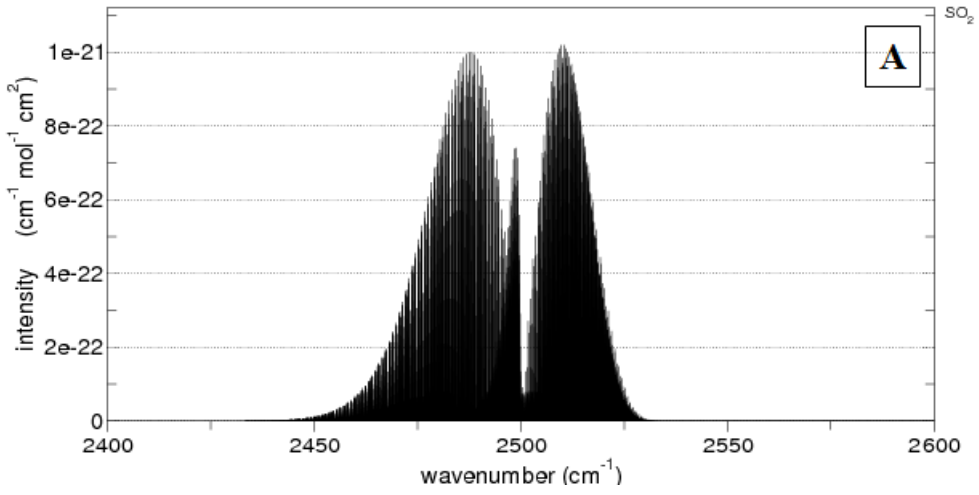

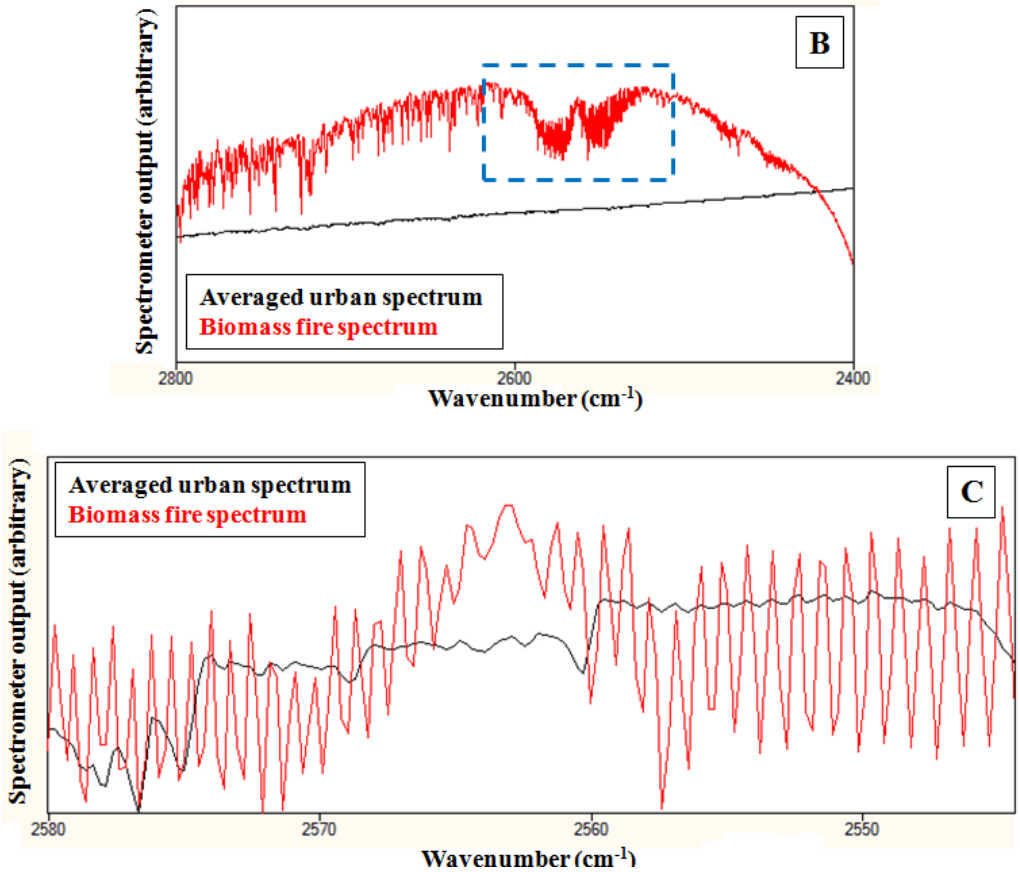

Figure 58. (A) SO_2 double peaked absorbance feature (2400 – 2600 cm^{-1}) (GATS Inc 2009) (B) SO2 large scale absorbance feature (only clear in biomass fire spectrum, (dashed box)) (C) Small scale SO2 absorbance features in both spectra.

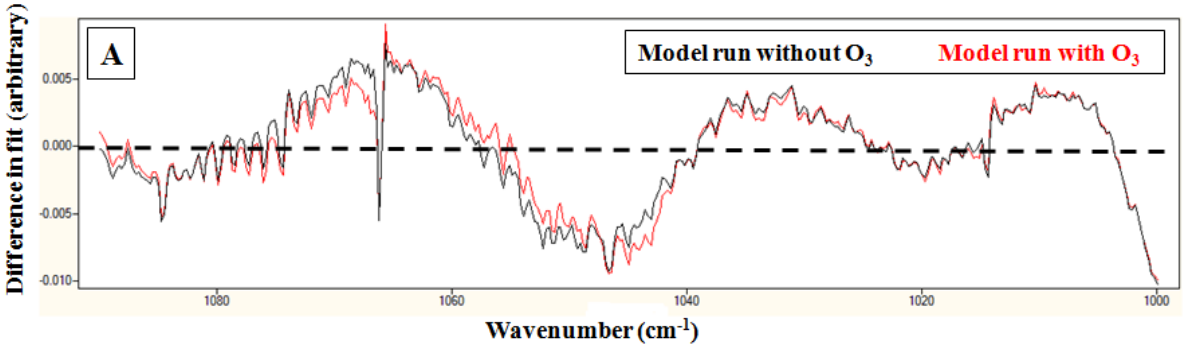

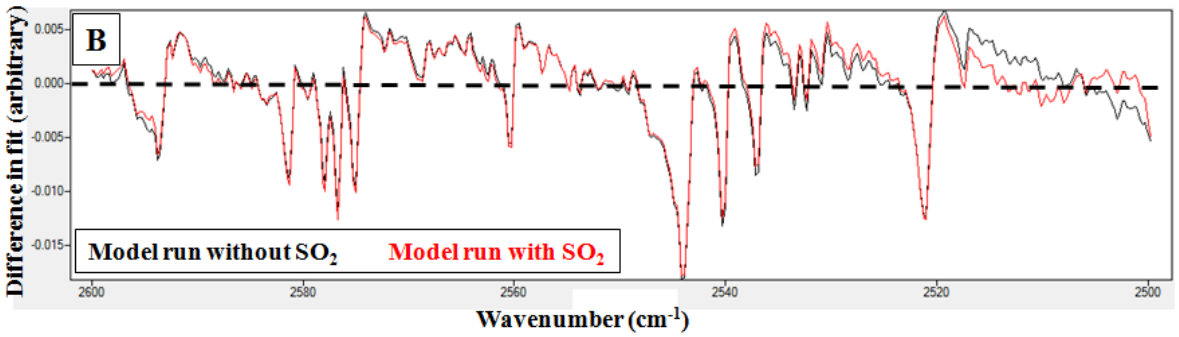

Figure 59. Comparison of fit residuals for (A) O_3 and (B) SO_2.

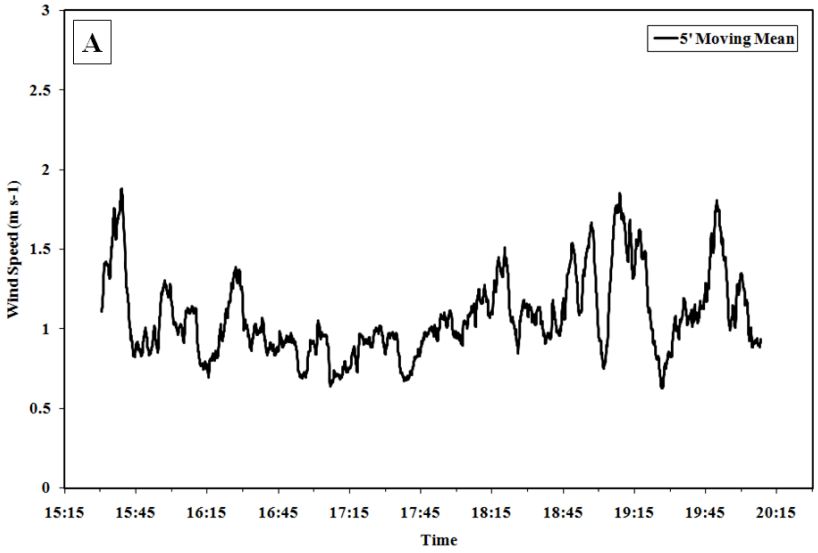

Figure 60. Plots of (A) mean wind speed and (B) wind direction, BTNA, London.

Contact info

KCL:

Prof. Sue Grimmond (sue.grimmond@kcl.ac.uk)

Dr Sean Beevers (sean.beevers@kcl.ac.uk)

SOTON:
Prof. Gail Taylor (G.Taylor@soton.ac.uk)
Dr. M J. Tallis (M.J.TALLIS@soton.ac.uk)

7. Firenze

The WRF-ACASA coupled model was run at 200 m horizontal grid spacing on a 5km by 5km gridded domain for the Firenze case study. Initial and boundary conditions updated every 3 hours for the year 2008, and a special set of surface characteristics at 200m grid spacing were provided by UCM to drive the simulations. The model was run for a non-nested domain.

ACASA (Advanced-Canopy-Atmosphere-Soil Algorithm) model provides both the physical state and forcing between the surface-layer and the rest of the WRF (Weather and Forecast model) atmosphere, while WRF provides the meteorological and morphological forcing for ACASA. For the coupling, ACASA was implemented in WRF using a similar subroutine calling architecture as that used by the existing NOAHLSM surface-layer module, in order to obtain fluxes directly as output.

Some meteorological and morphological characteristics are needed from WRF to run ACASA. The meteorological variables are the temperature, humidity, wind speed, downwelling long- and short-wave radiation flux densities, precipitation rate and form, and the air pressure; while the surface morphology characteristics are LAI, soil type, minimum stomatal resistance, background albedo and background roughness length. Quantities as the canopy architecture index, mean leaf diameter, basal respiration rate, etc. are “hardwired” with the same values at each point.

ACASA substitutes the NOAHLSM surface-layer package and provides the sensible heat flux density, latent heat flux density, friction velocity (related to momentum flux density), turbulence kinetic energy, the effective surface “skin” temperature, and bulk thermal emissivity every 30 minutes. With this information, WRF translates the ACASA forcing into the radiative transfer modules and the time-tendency components of wind velocity, temperature, and humidity in the lowest atmospheric layers. Thermal and hydrological states for soil, snow, and canopy are stored at each point between time steps. This allows ACASA to estimate the thermal storage fluxes, water retention, etc., needed by ACASA to estimate the main fluxes and emissivity. Albedo is modified whenever snow or soil moisture is present. Other ACASA diagnostic variables are used by WRF as surface (water) runoff, underground runoff, soil surface infiltration rate, and carbon-dioxide flux density.

Output data are provided hourly, and appear as daily files. In the following paragraphs, monthly (at 12:00 pm LT) and annual (at 5:00 am and 12:00 pm LT) composite averages are shown. . All maps showed below are for a 5km x 5km domain, centered on the EC flux tower located at the Ximeniano Observatory in the city centre.

7.1 Surface characteristics

The Firenze land use change used by the WRF-ACASA coupled model is shown in Figure 61. Most of the domain is represented by urban surface and only in a small area is present vegetation. The water body is represented by the Arno river as the “dot line” crossing the centre of the domain.

During the day, with positive values of solar radiation, the urban heat island effects is evident even with variations of several degrees Celsius in the air temperature at 2 meters between different land use types (Fig. 62). As expected, temperatures are lower over the river and higher for land surfaces during the day, and the opposite trend is seen during the night. Vegetated and urbanized surfaces show temperatures markedly differences becoming most extreme during the daytime growing season (May through August).

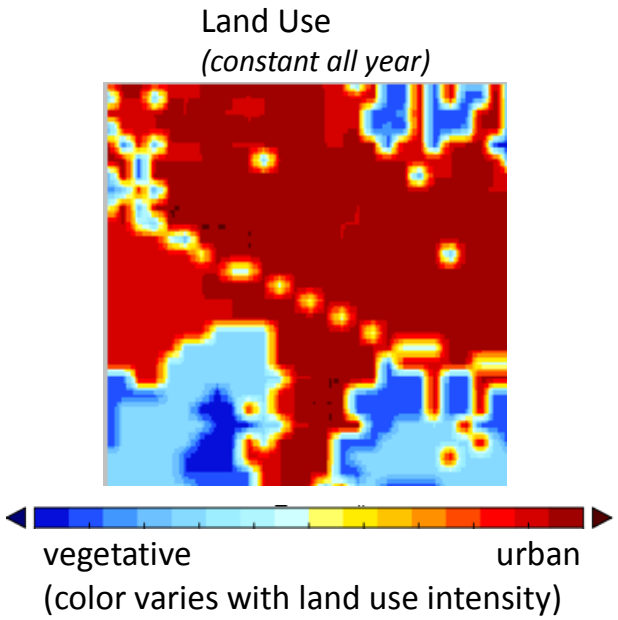

Figure 61. Land use maps used to run the WRF-ACASA coupled model.

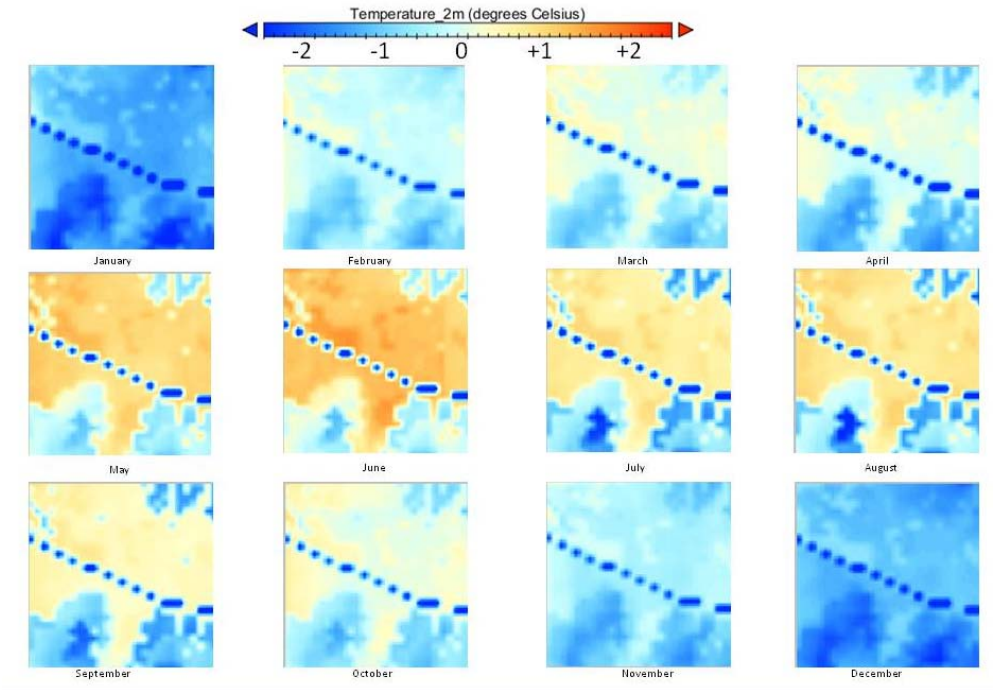

Figure 62. Monthly values (12:00 pm LT) of air temperatures at 2 meters (°C). A 5 °C window normalized about the areal means was used to better visualize the urban heat island change throughout the year.

The thermal-IR emissivity in Figure 63 shows small variations over time, depending on seasonal changes in vegetation density and water stored in the canopy. More evident variations can be noted between vegetated and urbanized areas, due to differences in vegetation amount. During the growing season, in fact, emissivity is depressed. Annual values of thermal-IR emissivity are however constant.

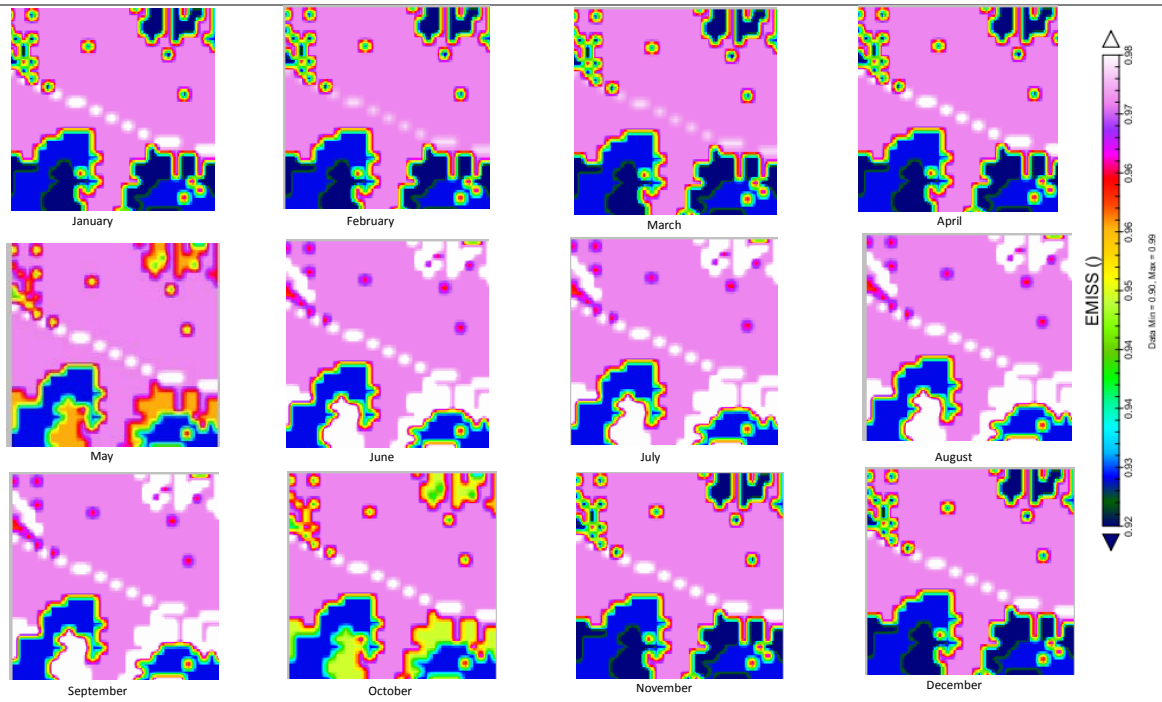

Figure 63. Monthly values (12:00 pm LT) of thermal-IR emissivity.

7.2 Energy fluxes

Seasonality is markedly apparent in simulated sensible heat flux density, with maximum values in the downtown core in June-July (Fig. 64). Contrasts between the urban core and surrounding vegetated zones is most extreme in the summer, as expected, since there is very little vegetation in the city center.

Anthropogenic storage flux density (S) values note similarity in pattern and magnitude in wintertime with values of sensible heat flux density (H), indicating increased energy use resulting from colder environmental conditions. The magnitude of S is negligible during the summer months (Fig. 65).

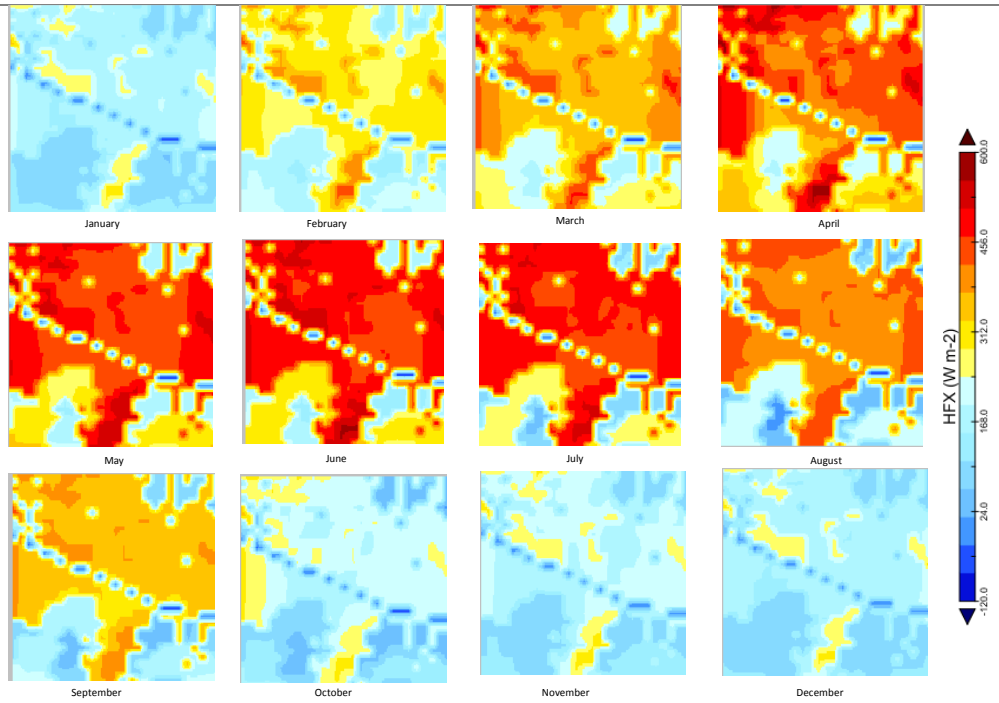

Figure 64. Monthly values (12:00 pm LT) of sensible heat flux density (W m^{-2}).

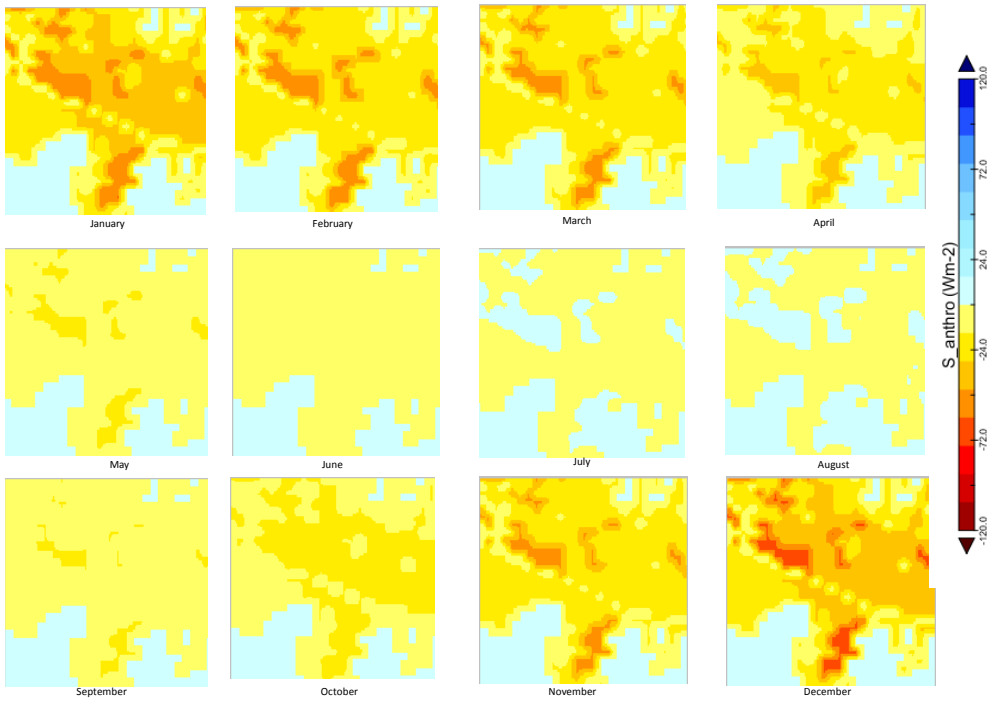

Figure 65. Monthly values (12:00 pm LT) of anthropogenic storage flux density (W m^{-2}).

7.3 Water exchanges

Water vapor flux density is most active during the summer, with higher values over the vegetated areas that exceeds even those near the Arno River during this season (Fig. 66). This is due to lower heat capacity values in vegetation than in open water bodies, fuelling a tendency for the absorbed energy to go to increased sensible heating and/or evapotranspiration.

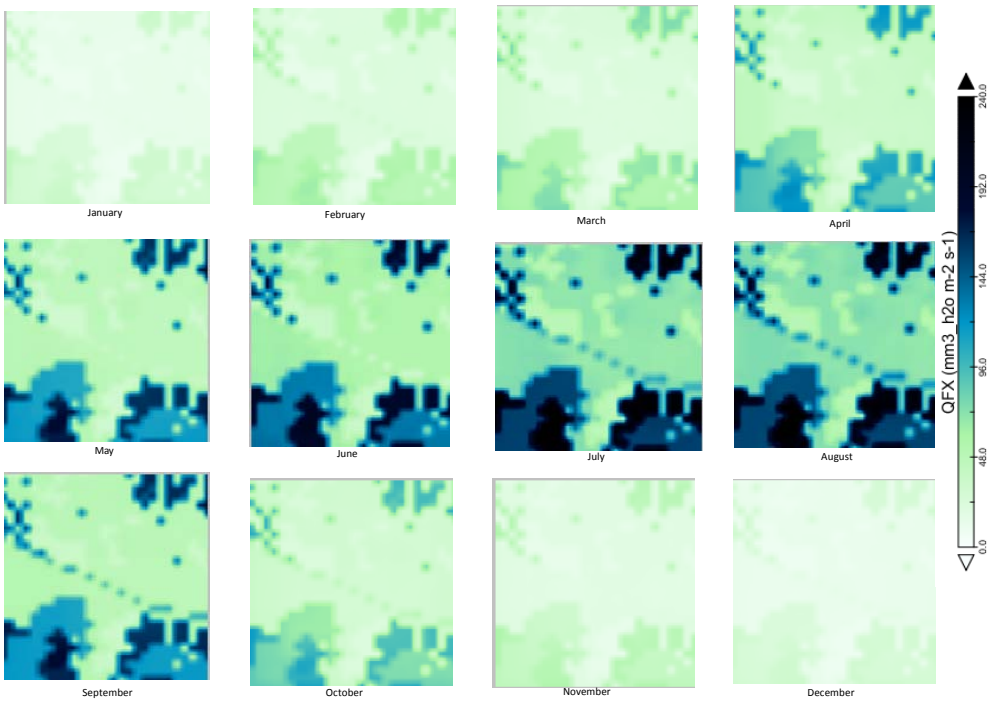

Figure 66. Monthly values (12:00 pm LT) of water vapor flux density (W m^{-2}).

7.4 Carbon fluxes

Carbon dioxide flux density values indicated over urban terrain are relatively “smooth” throughout the year as compared to the vegetated areas outside the downtown core (Fig. 67). This is due mainly to how the anthropogenic component of the flux was calculated in WRF. The urban core CO_2 flux density values might be lower than reality and some modifications should be performed to improve the estimation of this variable in WRF-ACASA.

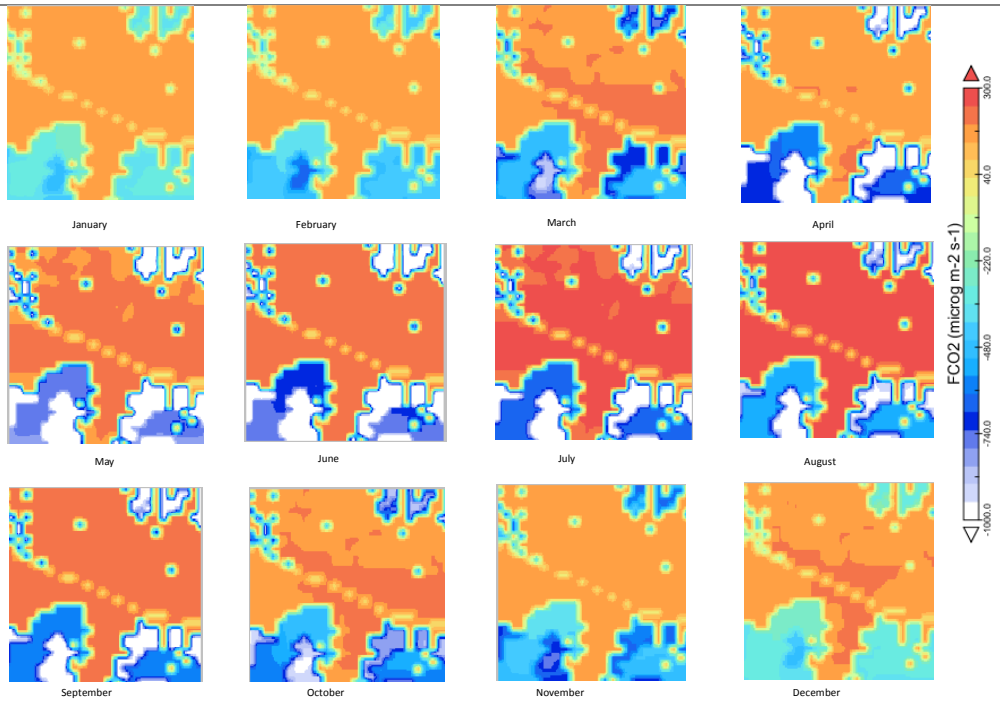

Figure 67. Monthly values (12:00 pm LT) of carbon dioxide flux density (microg m^{-2} s^{-1}).

7.5 Annual values of surface fluxes, emissivity, and air temperature at 2 meters

Annualized averages of surface fluxes (nocturnal and daytime values) are presented in Figure 68 at 5:00 am and 12:00 pm LT, showing the contrasts in surface forcing between the two averaging time periods. Daytime values show more activity, as expected, especially for sensible heat, water vapor, and carbon dioxide fluxes. There is a diurnal variation in the intensity of anthropogenic storage flux density maybe due to conduction processes through the building walls. Positive values indicate a loss of energy to the atmosphere, which is most prevalent at night when conditions are cooler on average. Note the similarity in magnitudes of the “urban heat island” pattern between sensible heat and anthropogenic storage flux density. In all simulations presented here, building interiors were assumed to be held at constant temperature (19 °C) throughout the year.

Annual values of thermal-IR emissivity and air temperature at 2 meters are also shown in Figure 69 both at 5:00am and 12:00 pm LT. In Table 19 are reported the monthly and annual values of surface fluxes, emissivity, and 2m air temperature.

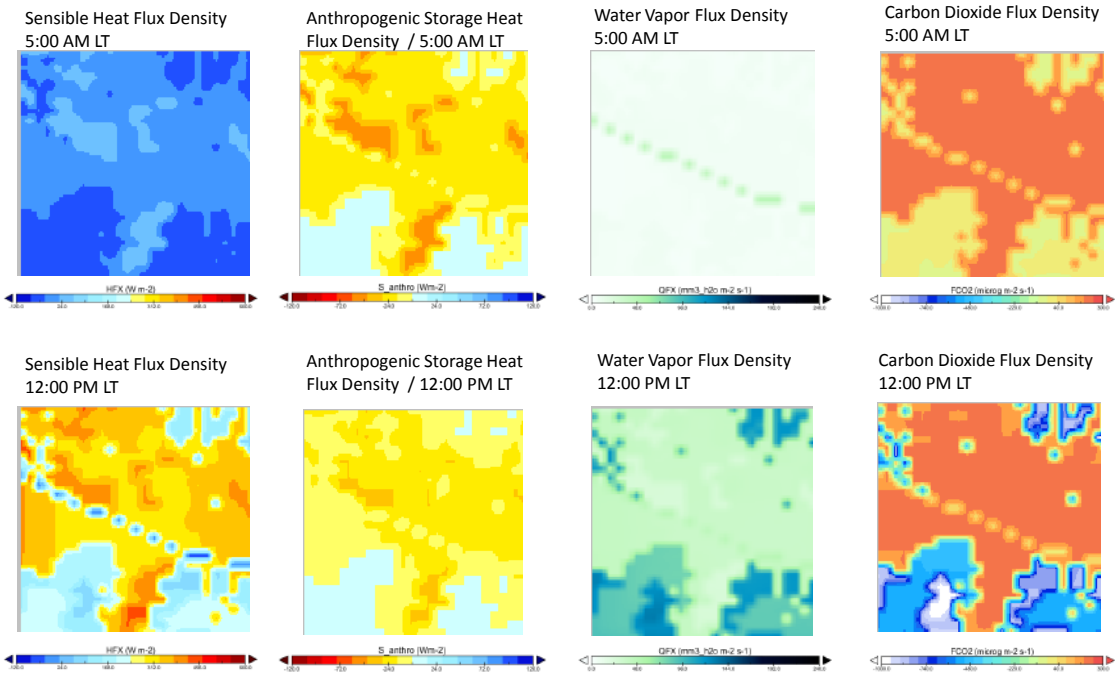

Figure 68. Annual values (5:00 am and 12:00 pm LT) of sensible heat, anthropogenic storage heat, water vapor (W m^{-2}), and carbon dioxide flux density (microg m^{-2} s^{-1}).

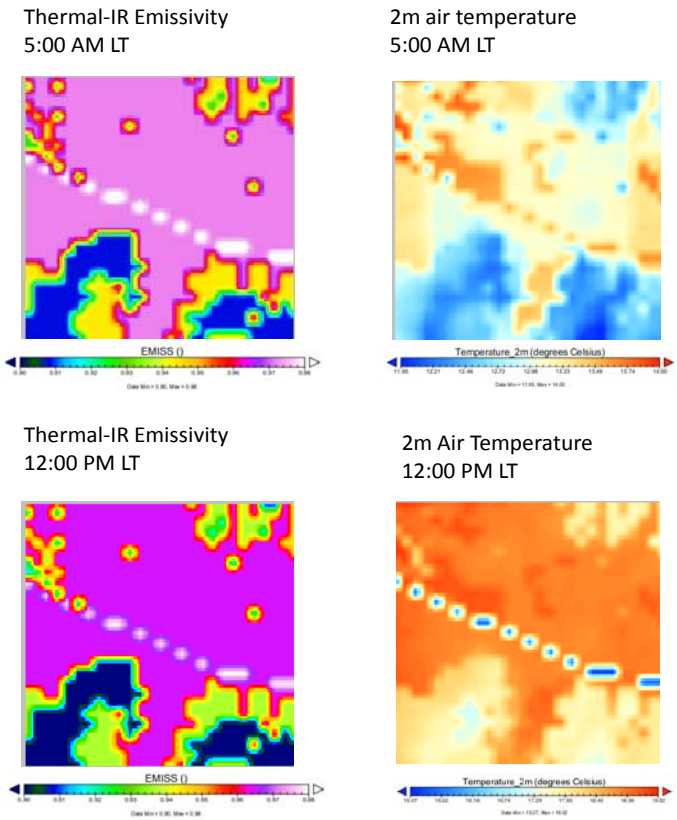

Figure 69. Annual values (5:00 am and 12:00 pm LT) of thermal-IR emissivity and 2 meters air temperature (°C).

Table 19. Monthly and Annual Average Midday Values for Surface Fluxes, Air Temperature and Emissivity.

	units	1	2	3	4	5	6	7	8	9	10	11	12	Annual
EMISS		0.97	0.97	0.97	0.97	0.97	0.97	0.97	0.97	0.97	0.97	0.97	0.97	0.97
FCO2	microg m^{-2} s^{-1}	179.03	177.53	195.28	185.89	205.78	235.87	258.47	266.87	220.41	195.12	182.97	190.95	207.85
HFX	W m^{-2}	194.03	285.89	361.72	421.48	435.50	463.44	460.40	399.72	339.82	211.35	196.24	181.85	329.29
QFX	mm^3_h_2o m^{-2} s^{-1}	13.26	21.77	21.32	35.06	44.01	55.61	67.62	70.37	46.30	29.70	18.22	12.35	36.30
Temperature_2m	degrees Celsius	10.23	10.96	12.99	17.36	22.25	25.83	28.81	29.63	23.79	20.54	13.88	9.27	18.80

Where EMISS is the Surface Emissivity; FCO2 is the CO_2 flux at the surface; HFX is the upward heat flux at the surface; QFX is the upward moisture flux at the surface, and Temperature_2m is the air temperature at 2 meters above the ground.

Contact info

CMCC:
Prof. Donatella Spano (spano@uniss.it)
Via de Nicola 9, 07100, Sassari, Italy
Tel. +39 079 229339

Dr. Serena Marras (serenam@uniss.it)
Via de Nicola 9, 07100, Sassari, Italy
Tel. +39 079 229372

4. Conclusions

The document reports a summary of the GIS data and maps collected and produced during the project by remote sensing techniques. LiDAR measurements and models.
Data for Helsinki and Firenze case studies were obtained by the coupled model WRF-ACASA and maps of surface emissivity, sensible (H) and latent (LE) heat fluxes, air temperature, and carbon fluxes (FCO2) were produced. The simulated period covered one year, from January to December 2008. Seasonality in fluxes is showed per each city by maps of monthly values. Emissivity showed no variations during the year, while higher values of H, LE, and FCO2 are reported during the summer in both cities.
Data for Athens case study were obtained by high-spatial resolution satellite images together with GIS vector data. Surface characteristics of the metropolitan area of Athens were, therefore described. In particular, maps of land cover and land use (LCLU), land surface albedo (LSA), land surface emissivity (LSE), land surface temperature (LST), vegetation and topography (DEM) are showed.

London surface characteristics were obtained by LiDAR measurements which provided a complete description of green roof, trees and vegetation characteristics. Green roofs have been built in locations beyond those identified as potential locations. The total roof area that could potentially be retrofitted with green roofs in the CAZ is 4,987,104 m2 (~15 % of the total CAZ area) or ~ 92 % of the total roofed area. The target increase green roofs in of 100,000 m^2 by 2012 would require the development in 2011-12 to be over five times that of the past two years. Currently about 0.6% of the CAZ roofs are green. From comparison of field and LiDAR data, tree characteristics are well correlated with the LiDAR yielding greater diameters and very similar heights. Also, infrared thermometers and thermal cameras were used to measure the surface temperature in London. In this city, the air quality analysis was made by using both the UFORE model and infra red spectroscopy (FTIR).

No GIS and remote sensing data were due for Gliwice case study, therefore no results are showed for this city.

Part 3: Socio-economic data collection

1. Introduction

Task 3.3 estimates the main dimensions of social and economic impact generated by urban metabolism in five different case studies (Helsinki, Athens, London, Firenze and Gliwice).

The aim of this document is to provide the main results on socioeconomic issues for each case study of the BRIDGE Project. In particular, it contains a summary on chosen sustainability objectives and socio-economic indicators during the CoP meetings in case studies.
The final products of Task 3.3 are GIS data and maps on spatial, socio-economic development and impact indicators per each case study. These GIS products will be produced using the appropriate spatio-temporal analysis techniques on the collected socio-economic data.

This document, then, contains the analysis of the main results obtained in each case study using different socioeconomic indicators and it shows the different behavior of the five cities in defining the most important issues of the city.

1.2 Definitions and Acronyms

Acronyms

CoP	Community of Practice
DSS	Decision Support System
GIS	Geographical Information System

1.3 Partners involved

1. CNR
Consiglio Nazionale delle Ricerche, Italy
Enzo Magliulo (enzo.magliulo@cnr.it)
Franco Miglietta (f.miglietta@ibimet.cnr.it): Firenze case study leader

2. CMCC
Centro Euro-Mediterraneo per i Cambiamenti Climatici S.c.a.r.l, Italy
Donatella Spano (spano@uniss.it)

3. KCL
King's College London
Sue Grimmond (sue.grimmond@kcl.ac.uk): London case study leader

4. NKUA
National and Kapodistrian University of Athens, Greece
Mattheos Santamouris (msantam@phys.uoa.gr): Athens case study leader

5. FORTH
Foundation for Research and Technology – Hellas, Greece
Nektarios Crysoulakis (zedd2@iacm.forth.gr)

6. SOTON
School of Biological Sciences-United Kingdom
Prof. Gail Taylor (G.Taylor@soton.ac.uk)

7. UHEL
University of Helsinki, Finland
Timo Vesala (timo.vesala@helsinki.fi): Helsinki case study leader

8. IETU
Institute for Ecology ofIndustr , Poland
Tomasz Staszewski (stasz@ietu.katowice.pl): Gliwice case study leader

2. Summary

Task 3.4 aims to show a description of main socio-economic indicators chosen in each case study city selected during CoP meetings. On the basis of the indicators there was prepared the final set of indicators described in D.5.1 Socio-Economic and Environmental Workshops Report. This set of indicators will be integrated into the DSS, where the end-user will be prompted to provide relevant data. The agreement was reached at the Umbrella CoP meeting on the core (i.e. common) and discretionary (i.e. case specific) sustainability objectives and indicators. These indicators are shown in Table 1. For each case study, the following results will be showed .

Table 7The final list of socio-economic indicators

Objectives	Indicators	Indicator unit
Common Aspects (Core)		
Urban land use	• New urbanized areas (land use changes including greenfield and brownfield) • Brownfields re-used • Density of development	m^2 (or % change) m^2 (or % of total) built m2/total m2
Ensure Economic Viability	• Cost of proposed development • Effects on local economy (employment) • Effects on local economy (revenue)	€ (or €/m^2) No. of new jobs created € (or €/m^2)
Improve Mobility & accessibility	• Quality of pedestrian sideways • Length of cycleways provided • Length of new roads provided • Use of public transport • Number of inhabitants with access to public transport	N/A (qualitative) m m % of total population No. of inhabitants (within 500m of public transport node)
Enhance Human Well-being	• Number of inhabitants exposed to NO_2 concentrations above the threshold • Number of inhabitants exposed to PM_{10} concentrations above the threshold • Number of inhabitants exposed to 0_3 concentrations above the threshold	No. of inhabitants exposed No. of inhabitants exposed No. of inhabitants exposed
City-Specific Aspects (Discretionary)		
Promote Social Inclusion	• Number of inhabitants with access to social housing • Number of inhabitants with access to services	No. of inhabitants (% of total) Number of services/m^2 (or number of inhabitants/service
Enhance Human Well-being	• Number of inhabitants affected by flash flooding • Number of inhabitants affected by heat waves	No. of inhabitants No. of inhabitants

3. Helsinki

3.1 City characteristics

Helsinki is a northern city with a whole year average temperature of 6.1°C (warmest month June, mean temperature 17.2°C and coldest month February, mean temperature –3.6°C). Helsinki is the capital of Finland but also the centre of the Helsinki Region, a functional urban region of about 1.3 million inhabitants spread over 3,841 km^2 and 738,000 jobs. City of Helsinki has 583,350 inhabitants and land area of 214 km^2. The population is 10.9 % of the population of Finland. The number of inhabitants per km^2 of land is 2730. The average age of the population is 38 years with 14.5% under 15 years and 14.5% above 65 years. 36% of the population older than 15 years have received tertiary education. The life expectancy is 78.7 years and the population growth rate is about 1%. The total of dwellings in Helsinki is 324,110, out of which 13.3 % are detached houses, 44.7% are owned by occupier and 44.5 are rented dwellings. The housing density is 34.2 m^2/person. There are 408,395 jobs in Helsinki out of which only 11.8% are in processing and primary production. The self-sufficiency of jobs is 131.6%. The economic activity rate is 74.8% with an unemployment rate of 6.4%. there are 386 cars per 1000 inhabitants and there was a total of 196.1 million journeys in public transportation within the city in 2009.

3.2 Short description of CoP meetings

The Bridge project has organised 4 CoP meetings out of which two have been with the representatives of Bridge CoP activity and two have been internal meetings with City of Helsinki stakeholder groups and Bridge researchers. The City of Helsinki City Planning Department, Environment Centre, Economic and Planning Centre and Public works department along with the representatives of the City energy company Helsingin Energia have been participating in the meeting so that the representatives of the City Planning Department have been present in all meetings. The City Planning Department has also been the representative of City of Helsinki in the CoP meetings at Bridge level.

The CoP meetings have addressed the case study selection, case study objectives and planning alternatives to be used in the Bridge exercises. The new development at Meri-Rastila area was selected as the Helsinki case study. The Meri-Rastila development plan relies on the existing Rastila Metro station. The neighbourhood is suburban, characterized by buildings built in the 1960s and 1980s (the population has increased from 16,000 inhabitants in the 60s to 30,000 today). The area lacks urban structure and urban services; the area borders forested areas. The area is predominantly inhabited by immigrants. There are no social problems reported yet, but one fears that these type of problems might occur in the future. Due to a well established greenway network,the area has an important recreational function for the inhabitants of the city of Helsinki and its surroundings. The planning objectives for the area are:

- At the city level: to provide new housing for the growing metropolitan areas (100.000 people is expected), built to address climate change (i.e. densification of urban structure, focus on railway and metro stations), and places of work mixed with housing.
- At the neighbourhood level/ Meri-Rastila level: to deal with demographic polarization (i.e. immigration issue), to move towards more owned dwellings and bigger apartments, to improve services and to provide a more positive image to the area (to attract new residents).
- With regards to green space –nature: to maintain sufficient and continuous recreation and habitats, and to improve accessibility to nature areas.

During the meetings also the chosen sustainability objectives that are most important to Helsinki were brought forward and socio-economic indicators related to them discussed. The CoP meetings gave also a lot of constructive feedback to planned Bridge DSS.

3.3 Chosen sustainability objectives

The discussions in CoP meetings established the planning priorities in Helsinki, which included: housing, public transport and energy sources. Based on these priorities, and taking into account the previously defined challenges, the core sustainability objectives were established for the city by the CoP- participants: These objectives can be summarized as follows:

- ***Optimize energy consumption***: save energy and increase use of renewable energy sources.
- ***Protect the water balance***: manage storm water to minimize flooding and to avoid water pollution through untreated surface runoff.
- ***Improve air quality***: minimize emissions and, particularly, reduce CO_2 emissions to mitigate climate change.
- ***Enhance human well-being in the city***: improve attractiveness of housing, promote a spatial balance, and improve the public transport system.

3.4 Socio-economic indicators

Planning objective	Indicator
Optimize Energy Consumption	• Energy demand (i.e. electricity consumption per dwelling) • Energy balance in buildings (i.e. heating energy) • Percentage of energy from renewable sources
Protect Water Resources	• Water balance: surface run-off, evapotranspiration, and filtration. • Concentration of pollutants • Conveyance, storage, and quality mitigation structures present • Percentage (surface area) of imperviousness
Improve Air Quality	• Concentration of pollutants (ozone and particulate matter) • Greenhouse gases and CO_2 emissions per capita • Emissions from transport, split per type: private and public
Enhance Human Well-being	• Density of development (persons/m^2) • Population exposure to air pollutants (vs. clean air) • Population exposure to polluted waters (vs. e.g. swimmable waters) • Population exposure to contaminated soils • Presence of citizen health promoting/mitigating urban and natural structures
Anticipating climate change	• Carbon intake (i.e. carbon sinks) • Material reuse (e.g. soils) • Number of zero-carbon buildings

Key Issue or Consideration	Indicator
Housing Demand	• Number and type of dwellings • Population growth • Demand for housing types • Percentage of owned/rented dwellings
Social Inclusion	• Access to housing • Social class/ethnical group • Age group of residents • Number of family households
Accessibility (Transport and connectivity)	• Travel time to work • Access to public transport

Services and Infrastructure	
Amenity and Recreation (physical and psychological health)	
Cost/Benefits of Planning Intervention (Building costs and job creation)	

3.5 Conclusions

The selected Helsinki case study is rather small but typical example of new construction in Helsinki in which the attempt is to increase housing density in areas well connected with the public transport network. In that sense it is offering good testing opportunity of DSS as it represents a typical panning situation.

CoP meetings established that there exists already currently a wide range of different planning tools in use in Helsinki. At the moment, the benefits of the BRIDGE projects in terms of the DSS remain to be seen. It depends to great extend how well the DSS provides enough detailed information and precision to be of help in the decision making process of the end users. The collaboration between experts/practitioners in the field of urban planning and scientist has started which is a benefit.

Contact info

Eero Nikinmaa (eero.nikinmaa@helsinki.fi)

Annika Nordbo (annika.nordbo@helsinki.fi)

4. Athens

4.1 City characteristics

The Athens Case Study is focused on the municipality of Egaleo, which is a densely built urban that lies in Western part of Athens.

Egaleo in the greater Athens area (A). [Source: Google Earth]

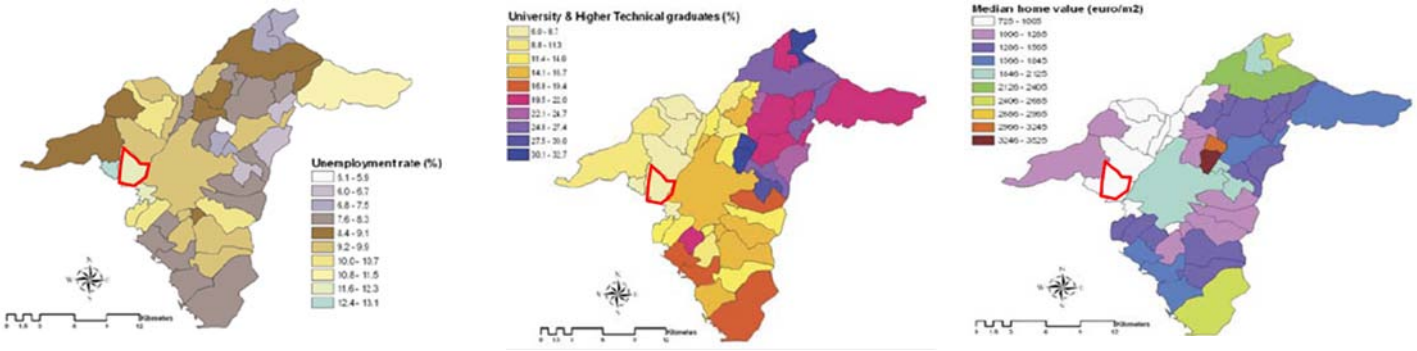

Egaleo is suffering from high unemployment rates, low levels of education and very low house values

Five main road axes divide the area in four quarters. One of the quarters is an industrial degraded area (brownfield) called Eleonas. The total area of Egaleo is 650 ha and it is flat in general. The population is 74.046, although it is estimated that at least 120000 people, mostly medium and low income, live and work in the area. The level of education of the inhabitants is low to medium and the rate of unemployment high.

The average density is estimated to be 225 inhabitants/ha. According to onsite observations and research it was found that most of the buildings in the area were built between 1950's – 1980's, with several of them built around 1950s. These buildings are made of reinforced concrete, and have one to three floors height. A small amount of houses were built in the 1920's and onwards. These residences are made of stone and are in poor condition. Finally, there are buildings built in the last decades made of reinforced

concrete reaching a height of up to 6 floors. As it appears in the land use map of Egaleo, there very little free/ green spaces.

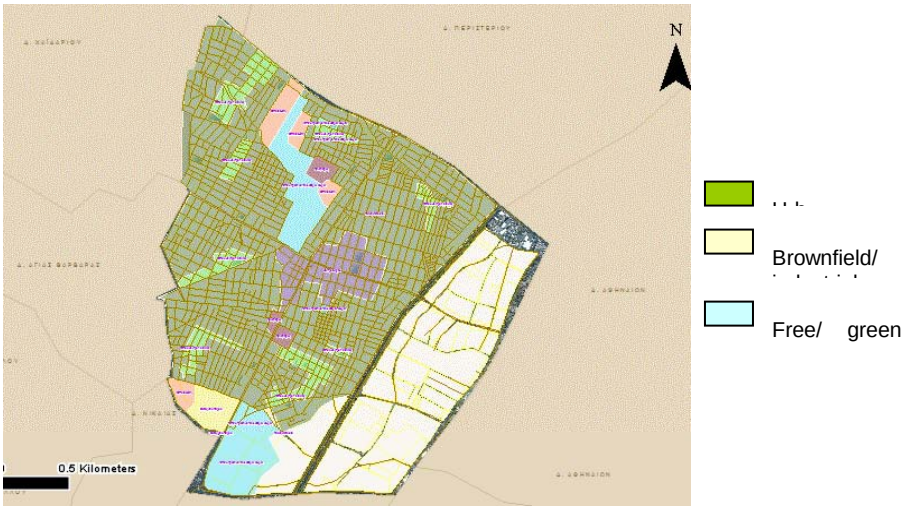

Land use map of Egaleo [Source: www.aigaleo.gr]

Egaleo is considered an environmentally degraded area facing problems with:

- air pollution
- traffic and transport
- thermal discomfort
- lack of green/ free spaces
- poor quality of building stock
- energy.

4.2 Short description of CoP meetings

In the framework of the Bridge project 2 CoP local meetings (in total 4 meetings, counting the 2 CoP meetings with participants from all the case studies) have been organized for the case study of Athens. These two local meetings were convened at the Municipality of Egaleo, which is the specific case study area for Athens. The participants included, apart from the BRIDGE researchers, academics, urban planners, architects, engineers and researchers all interested in sustainable urban planning. Most of them are working in the technical and planning dept. of the Municipality of Egaleo. The main outcomes of the CoP meetings were the following:

- enabling the Bridge partners and Athens planners to interact with each other and share experience on sustainable urban planning issues in Athens
- discussion of key issues of sustainable development in Athens and especially in Egaleo
- identification of planning priorities; Sustainability objectives and corresponding indicators with which to assess progress towards sustainable development (described below)
- selection, accordingly, of a planned intervention for the Athens case study and definition of underlying challenges, planning alternatives and collected indicators

During the CoPs several planning interventions for the area of Egaleo have been proposed and discussed. More specifically, and in order to meet the Bridge and the sustainability objectives defined, the final alternatives proposed for the Athens case study were the following:

1. Apply cool materials on all buildings at Egaleo municipality and on roads.
2. Change the land use of Eleonas (an industrial area of Egaleo) from brownfield area to built environment.
3. Change the land use of Eleonas from brownfield area to green space.

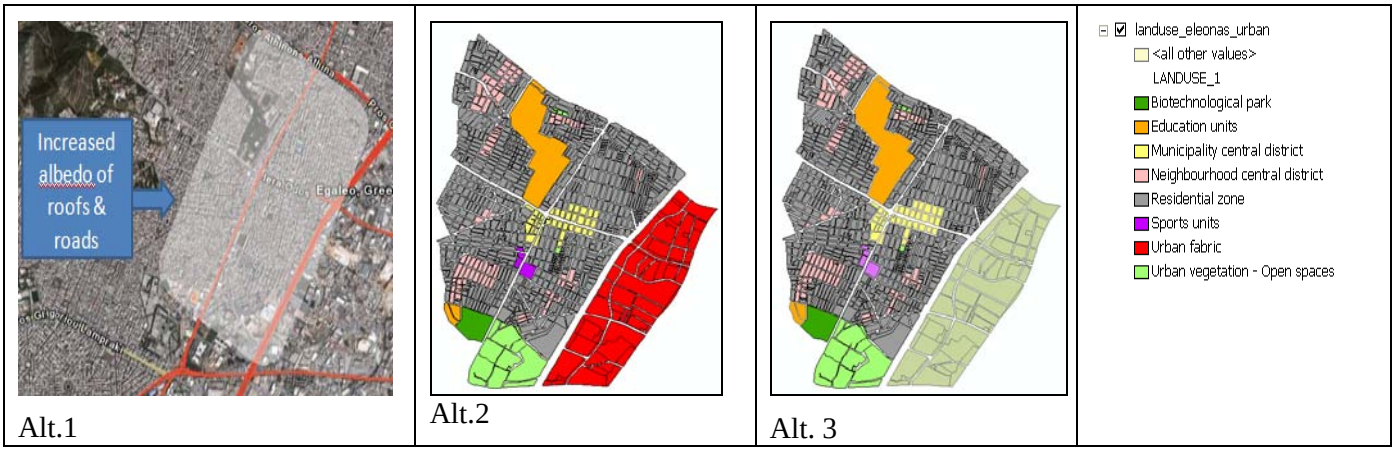

Alt.1 Alt.2 Alt. 3

Representation of the three planning alternatives for Egaleo

4.3 Chosen sustainability objectives

The discussions in CoP meetings identified the following priorities for sustainable city planning in Athens: Thermal discomfort, Energy, Quality of building stock, Transport, Green spaces and the Land use of Eleonas. Based on these sustainability priorities, and taking into account the previously defined challenges, the core sustainability objectives were established for the city by the CoP- participants: These objectives were divided to environmental and socioeconomic ones and can be summarized below:

Environmental

1. Reduce Thermal Discomfort
2. Improve Air Quality and Reduce Emissions
3. Increase Green Space Areas
4. Optimize Water Use
5. Improve Energy Efficiency
6. Optimize Quality of Materials Used

Socio - Economic

7. Improve mobility: including both public and private transportation, pedestrian areas and parking slots.
8. Improve public health and safety: including both car and pedestrian accidents, and the inhalation of the air pollutants. Lack of green areas make the situation worse.
9. Mind for social inclusion: social inclusion has been mentioned in relation to marginalized groups (families with children, elderly people) being most exposed and vulnerable to further deterioration of living conditions in the area
10. Include economic criteria: include financial costs of the planning alternatives, but also side-effect to local community, as a result of improved situation/living conditions. Furthermore, saving in water and energy use

have been highlighted should the situation improve (e.g. less energy use for air conditioning should the in- and outdoor thermal comfort improve, less water needed for basic sanitation).

11. Maintain/ improve place identity: aesthetic value of the area and changes due to planning intervention

4.4 Socio-economic Indicators

Sustainability Objective (in order of priority)	Socio-economic complement of the Environmental indicators
1. Mobility	• road traffic intensity, • quality of pedestrian sideways, • number of parking slots.
2. Public health and safety	• number and severity of road accidents and pedestrian injuries, • number of people suffering from short term effect of air pollution (upper respiratory infections such as bronchitis and pneumonia, allergic reactions) • number of people suffering from long term effects of air pollution (e.g. chronic respiratory disease, lung cancer, heart disease)
3. Social inclusion	• extent to which roads and sideways can be used by disabled or differently able people and groups (e.g. number of safe-street-crossing points, number of repose places along the street), • local community composition – compared to other areas: % of elderly people, foreigners, low-income families etc.
4. Economic criteria	• financial costs of the interventions, • estimated side-effects on local economy
5. Place identity	• aesthetic value of the area and changes due to planning intervention

4.5 Conclusions

The case study area chosen for Athens, is a typical example of an urban, degraded municipality in Athens (mostly western Athens), facing environmental and socioeconomic challenges. The planned interventions are large scale interventions aiming to achieve some of the most important sustainability objectives defined. An initial analysis of the planning alternatives demonstrated that benefits exist in all cases and their assessment with the DSS would be quite challenging and very useful, as there are not many tools and data available for such kind of analysis for urban planners to use. This will be verified by the testing of the DSS. A very positive outcome is the collaboration between experts in the field of urban planning and scientists.

Contact info

Stathopoulou Marina (mstathop@phys.uoa.gr), Afroditi Synnefa (asynnefa@phys.uoa.gr)

Research Assistant, Remote Sensing and Image Processing Laboratory,

Department of Physics, University of Athens.

Tel.: +30 210 7276843

5. London

5.1 City characteristics

(for example number of inhabitants, area, population density, unemployment rate)

5.2 Short description of CoP meetings

In the framework of the BRIDGE project 2 CoP local meetings have been organized for the case study of London.

The vegetation in London is highly variable with grassed parks or gardens (public and privately owned) and trees (deciduous and coniferous species). The planning activities that are of specific interest to the GLA for the BRIDGE project relate to the use of green infrastructure within the CAZ to reduce flooding and thermal stress. The alternatives being considered are to:

(a) add vegetation to roofs with consideration given to the slopes of the roofs
(b) add street trees
(c) add street trees and green roofs

make roads pervious with the addition of street trees and green roofs.

The Central Activity Zone (CAZ) (Figure 1) was chosen as a case study for the application of the Bridge DSS in London. The CAZ covers the London central area, including the CBA (Central Business Area), and the commercial centre, with an overall area of approx. 3300 ha, covering 10 boroughs either entirely or partially with ca. 280,000 residential inhabitants. It includes three major parks (Hyde Park, Regent's Park and Green Park) and some minor urban green areas. It is targeted and delimited by the London planning strategies for ca 10 years, and is the subject of specific planning objectives and goals which are also related to urban metabolism issues.

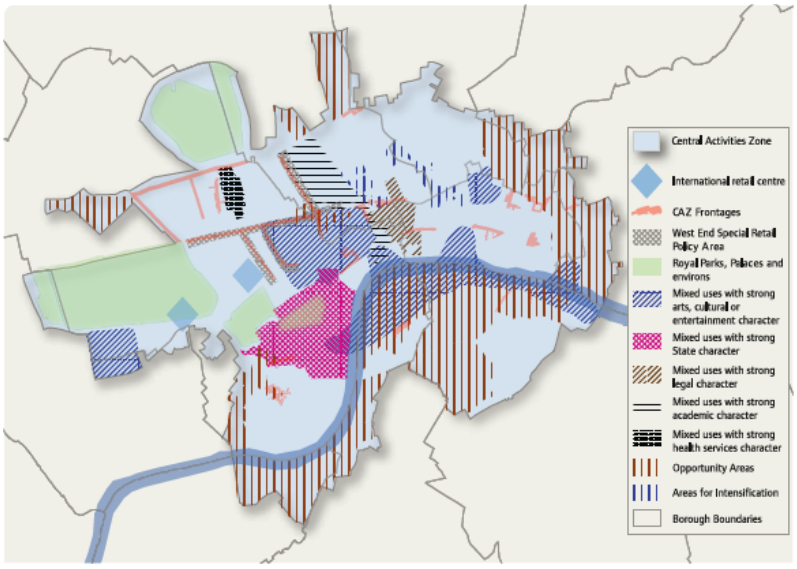

Source: Source: GLA 2009 © Crown copyright. All rights reserved. Greater London Authority 100032379 (2009)

Figure 1: Delimitations of the CAZ (The Major of London, 2008, London Plan, Spatial Development Strategy for Greater London; Consolidated with Alterations since 2004).

5.3 Chosen sustainability objectives

The sustainability objectives identified were as follows:

- **To reduce overheating**
- **To increase urban greenspace**
- **To mitigate flash flooding**
- **To reduce water consumption**
- **To decentralize energy production: heating/cooling and power generation, and**
- **To improve air quality.**

5.4 Socio-economic indicators

Planning goal	Socio-economic indicators
Increase urban greening	– Access to green areas – Costs of maintenance – Benefits in terms of reduced flood risk
Reduce water consumption	– to be developed
Decentralize energy generation	–
Mitigate urban heat island effect	– No of deaths / day – Health impacts
Improve air quality	– Health impacts – Health damage costs
Mitigate flash flooding	– No of people affected – Values at risk – Cost of drainage

5.5 Conclusions

There was no time, during the meeting, to discuss social and economic issues of urban metabolism, but these issues should be included.

Contact info
KCL:
Prof. Sue Grimmond (sue.grimmond@kcl.ac.uk)
Dr Sean Beevers (sean.beevers@kcl.ac.uk)

SOTON:
Prof. Gail Taylor (G.Taylor@soton.ac.uk)
Dr. M J. Tallis (M.J.TALLIS@soton.ac.uk)

6. Firenze

6.1 City characteristics

Firenze, or Firenze, is a city situated in the central region of Tuscany in Italy, where it serves as the capital of the region and of the province of Firenze.

Firenze is typically considered to have a Mediterranean climate, although under the Köppen climate classification it may be borderline humid subtropical. It has hot, humid summers with little rainfall and cool, damp winters. Surrounded by hills in a river valley, Firenze can be hot and humid from June to August. As Firenze lacks a prevailing wind, summer temperatures are higher than along the coast. Rainfall in summer is convectional, while relief rainfall dominates in the winter, with some snow.

The year average temperature is 14.6 °C (warmest month July, mean temperature 24.1 °C and coldest month January, mean temperature 5.7 °C).

Firenze is Tuscany's most important city, serving as its commercial, manufacturing, and transportation center. It's an important market for Tuscan wines, olive oil, flowers, and fresh produce. Its industries include the manufacture of agricultural machinery, fertilizers, automotive parts, motorcycles, precision instruments, chemicals, and plastics. Traditional Florentine handicrafts, such as jewelry, silverwork, glass, pottery, leather goods, furniture, wood carvings, and embroidery, are prominent items for the thousand of tourists that visit Firenze each year. The textile and fashion industry have also made its mark in the Florentine market.

The population of the city proper is 371.944 (1 February 2010), while Eurostat estimates that 696,767 people live in the urban area of Firenze. The Metropolitan Area of Firenze, Prato and Pistoia, constituted in 2000 over an area of roughly 4.800 km^2, is home to 1.5 million people. Within Firenze proper, 46.7% (173.711) of the population was male and 53.3% (198283) were female. The average age of Firenze resident is 49 years compared to the Italian average of 42 years, with 11.8% under 14 years, and 25.5% above 65 years. In the five years between 2002 and 2007, the population of Firenze grew by 3.22 percent, while Italy as a whole grew by 3.56 percent. The birth rate of Firenze is 7.66 births per 1000 inhabitants compared to the Italian average of 9.45 births.

90.45% of the resident population is Italian. An estimated 60,000 Chinese live in the city. The largest immigrant group came from other European countries (mostly from Albania and Romania, for a total of 3.52%), East Asia (2.17%), Americas (1.41%), and North Africa (0.9%).

Households in Firenze are 184043, 84 518 of which consist of a single component. Tourism is, by far, the most important of all industries and most of the Florentine economy relies on the money generated by international arrivals and students studying in the city. Manufacturing and commerce, however, still remain highly important. Firenze is also Italy's 17th richest city in terms of average workers' earnings, with the figure being €23,265 (the overall city's income is that of €6,531,204,473),

6.2 Short description of CoP meetings

During the Bridge project several internal meetings were organised with City of Firenze stakeholder groups, Bridge researchers. The CoP meetings have addressed the case study selection, case study objectives and planning alternatives to be used in the Bridge exercises. All this was done while considering the restrictions to which is subject the city of Firenze, in terms of architectural and landscape constraints.

The three alternatives presented are:
- complete reforestation of a green area and a sport arena in the Cascine Park. The alternative is an increase of trees (deciduous) by about 27% of the total,
- redevelopment of a former industrial area (FIAT) in the north of the Cascine Park, San Donato Park,
- implementation of both planning alternatives.

Municipality of Firenze also provided during the meetings a list of additional projects and initiatives, future or ongoing, which could certainly be of interest and in order to choose the sustainability objectives for Firenze case study.

6.4 Socio-economic indicators

Planning objective	Indicator
Optimize Energy Consumption	• Heating/cooling buildings efficiency • ..Energy use • Renewable energy • Better and cleaner technologies for private mobility (hybrid, Euro 5, electric and gas vehicles) • Impacts and the costs of town planning or of single building or infrastructure • Public transport use (%) and net improvement (tramway)
Protect Water Resources	• Concentration of pollutants • Conveyance, storage, and quality mitigation structures present • Constructed wet-land (to re-use rain water)
Improve Air Quality	• Concentration of pollutants (ozone and particulate matter) • Greenhouse gases and CO_2 emissions • Emissions from transport, split per type: private and public
Enhance Human Well-being	• Population exposure to air pollutants • Presence of citizen health promoting/mitigating urban and natural structures: heat wave mitigation
Anticipating climate change	• Carbon intake (i.e. carbon sinks) • Urban/street green furniture and reforestation • Number of new zero-carbon buildings

6.5 Conclusions

Firenze is a representative European old city with strong historic character and substantial cultural heritage. Considering the restrictions to which is subject the city of Firenze, in terms of architectural and landscape constraints, the three options for Firenze and the list of new actions proposed by Municipality seem the best way to improve urban mobility as well as to limit emissions of air pollutants, to improve energy efficiency of public and private buildings, to decrease waste production and to raise awareness on environmental responsibility.

Contact info
CNR-IBIMET:
Piero Toscano (p.toscano@ibimet.cnr.it)
Via Caproni 8, 50145 Firenze, Italy
Tel.:+390553033741

Beniamino Gioli (b.gioli@ibimet.cnr.it)
Via Caproni 8, 50145 Firenze, Italy
Tel.:+390553033741

CMCC:
Prof. Donatella Spano (spano@uniss.it)
Via de Nicola 9, 07100, Sassari, Italy
Tel. +39 079 229339

Dr. Serena Marras (serenam@uniss.it)
Via de Nicola 9, 07100, Sassari, Italy
Tel. +39 079 229372

7. Gliwice

7.1 City characteristics

In 2008 the total number of inhabitants amounted 191 232 and with decreasing tendency (100.149 woman and 91.083 man) In 2010 the total number of inhabitants fell and amounted 188 268. There is a decreasing tendency as in other big cities in Silesia Voivodeship. The tendency is mainly connected with migration. Area of Gliwice is 133,9 km^2, what means that population density was 1.428 per km^2. Between 2006 and 2008 moderate increase of birth indicator were observed at low rate.

The number of people in working age in comparison to total number of inhabitants exceeded 25% in 2008. Mean salary amounted 3.146,53 PLZ in national economy in Gliwice (2933,32 PLZ in Silesian Voivodeship and 2735,28 PLZ in Poland). In 2008 the number of unemployed amounted 4249, including 467 people with university education. In 2010 the number of unemployed amounted 6480. The unemployment rate amounts to 6,7%. In the end of 2008 there were in Gliwice: 53 existing land use plans, 8 land use plans within Strategic Impact Assessment procedure, 3 land use plans before Strategic Impact Assessment procedure. 64,7% of Gliwice city area was covered by land use plans in late 2009.

7.2 Short description of CoP meetings

In two BRIDGE CoP meetings urban planners, city development experts, spatial information system specialists, environmentalists, air pollution and modeling experts, toxicologist, EIA and SEA practitioners and researchers participated.

During the BRIDGE CoP kick-off meeting in Gliwice researchers described purposes and scheme of DSS taking into account multi criteria analysis of negative and positive socio-economic and environmental impacts on Gliwice case study. Results of "BRIDGE Questionnaire Community of Practice" were used for assessment the strengths, weaknesses, pressures and challenges, as well as the definition of objectives and the development of indicators during the BRIDGE CoP kick-off meeting in Gliwice.
Two groups of the objectives were dedicated socio-economic issues as follows:

- ***Improve mobility:*** improve road infrastructure; minimize through-traffic in the city centre; reduce private-car dependency; improve public transport (i.e. railway); and provide alternative means (e.g. cycle-ways).
- ***Control expansion of urban areas:*** through local land use plans; through provision better access to the city centre; improvement of local services; diversification of the city centre functions and enhancement of the public open space.

During the second CoP meeting four alternatives for transformation of existing or new land uses were presented:

A) Alternative 1 – "Minimum" – refers to the actual municipal development plan, which foresees a new highway to improve access to the Polytechnic area from the region of Silesia,

B) Alternative 2 - "Sport Hall" – the "sport-hall" alternative foresees, further to the highway, the construction of a new, bigger stadium in place of the existing one, creating a multifunctional building for big sports- and music-events and the relative parking places, as already under discussion in the municipality. As the plans for the highway, also the project for a building for sports and music events apparently is already in an advanced planning phase (plans are exposed in the City-hall); it will have a surface of approx. 70.000 square meters or 510.000 cube meters and will be able to host between 14.000 and 15.000 spectators for the events. 800 parking places will be required,

C) Alternative 3 - Centre of New Technologies – consists of a project for a centre for new technologies as part of an extension of existing university institutes. The building is supposed to be projected according to the most advanced concepts for intelligent building with low emissions, with a surface of 65.000 m^3 and 14.000 m^2 usable space,

D) Alternative 4 - the realisation of all mentioned above projects; the last of the alternatives to be considered foresees the realisation of all projects considered singularly under the precedent alternatives, leading to a full load of the district, and will add the creation of a pedestrian road in the area of the university.

Available information for socio-economic issues like demographic data, number of building applications and permits in Gliwice case study was briefly illustrated.

7.3 Chosen sustainability objectives

In BRIDGE the proposed list of indicators was confronted with the real needs of local communities during the process of Community of Practice meetings (there were some questions in the BRIDGE CoP Questionnaire such as "What are the most useful indicators to monitor the achievement of the objective(s) in the Development Plan for Gliwice?"). Finally there were chosen two most important sustainablility socio-economic objectives. These are: Improve Mobility (Objective 1) and Control Expansion of Urban Areas (Objective 2).

7.4 Socio-economic indicators

Sustainable objectives with their sets of socio-economic indicators defined during the BRIDGE kick-off CoP in Gliwice were discussed in detail and verified with priorities. They are presented below.

SOCIO-ECONOMIC		
Sustainable Objectives	**Indicators**	**Priority**
Improve Mobility	• Number of pedestrian streets (Km) • Public transport use (%) • Length of new roads built (Km) • Length of cycle-ways provided (Km) • Number of parking places built up	1 1 1 1 1
Control Expansion of Urban Areas	• Number of administrative decisions • Accessibility of district from Silesia metropolitan area (hours to/from) • Number of specific services in the district • % of new public space • Increase on incomes	2 1 4 4 3

The Municipal Planning Department of Gliwice City Hall underlined that they use also the relative to the number of newly elaborated land use plans as indicator for monitoring the need of updating their planning documents.

7.5 Conclusions

During the further debates the first Alternative refered to the actual municipal development plan was rejected. Currently there are three options for Gliwice case study (Polytechnic District) : Alternative 1 - "Sport Hall" (previously it was Alternative 2), Alternative 2 – "Centre of New Technologies" (previously it was Alternative 3),Alternative 3 – the realization of Alternative 1 and Alternative 2 (previously it was Alternative 4).

In Gliwice case the construction of new road is the main development factor which could generate better access to Polytechnic District from the region of Silesia. Analysis of three planning alternatives shows potential increase of district's attractiveness. The third alternative - construction of New Sport Hall and Technology Center presents high investment dynamic and offers new social opportunities.

All participants of CoP meetings agreed that for mentioned options the improved accessibility of the area by car, using the motorway, is seen as crucial for assuring development.

Contact info

IETU
Barbara Jaros (bjaros@ietu.katowice.pl)
ul. Kossutha 6, 40-844 Katowice
Tel. +48 32 254 60 31 ext. 140

IETU
dr Anicenta Bubak (bubak@ietu.katowice.pl)
ul. Kossutha 6, 40-844 Katowice
Tel. +48 32 254 60 31 ext. 277

Gliwice City Hall, Bureau of City Development:
Katarzyna Kobierska (brm@um.gliwice.pl)
ul. Zwycięstwa 21
Tel.+48 32 2391100

8. Conclusions

The case study areas chosen for the five cities are typical examples of an urban areas, facing environmental and socioeconomic challenges.
In all case-studies the most important task connected with enhacement of human well-being in the city is the improvement of mobility and accessibility (public and private transportation, parking slots, pedestrian areas, cycle-ways, new roads, etc.). The second important factor which aim is to enhace human wellbeing is the improvement of the quality of air. The third one is the promotion of social inclusion.

In selected case-studies the priorities were as follows:

- Helsinki – improve attractiveness of housing, promote social inclusion and improve accessibility to the Meri-Rastila area by public transport systems,
- Athens – improve mobility in the Municipality of Egaleo including public and private transportation, public health and safety, promote social inclusion,
- Firenze – enhance human well-being in the Cascine Park expressed as a number of inhabitants affected by heat waves and air pollutants,
- Gliwice – improve mobility in Polytechnic District both by private and public transport system, control expansion of urban areas.

As one can see (see Summary section) the above mentioned indicators and sustainability objectives were used to develop the final list of socio-economic indicators for the BRIDGE project.

Annex 1 - Firenze case study in situ measurements

1. Meteorological measurements

Meteorological observation were collected in Osservatorio Ximeniano tower from 1700.
During BRIDGE project we improved the strumentation installing an automatic weather station.

The meteo data collected are:

- Air temperature
- Air humidity
- Wind speed
- Wind direction
- Global solar radiation
- Rainfall
- Atmospheric pressure

In 2010 we upgraded the weather station installing a new high precision set of sensors based on Campbell CR-1000 data logger and installed an Ozone Monitor for accurate and precise (±1.5 ppb) ozone measurements
The new weather station provide more detailed information on several parameters like:

- Solar radiation (short and long wave, incoming and outcoming)
- A-class rain gauge 0.1mm resolution,
- High precision barometer
- Infra-red thermometer for roof surface temperature
- High precision Vaisala temperature and air humidity sensors.

A secondary database is also available for a weather station located on the periphery of Florence (43.8163° N 11.2028° E).

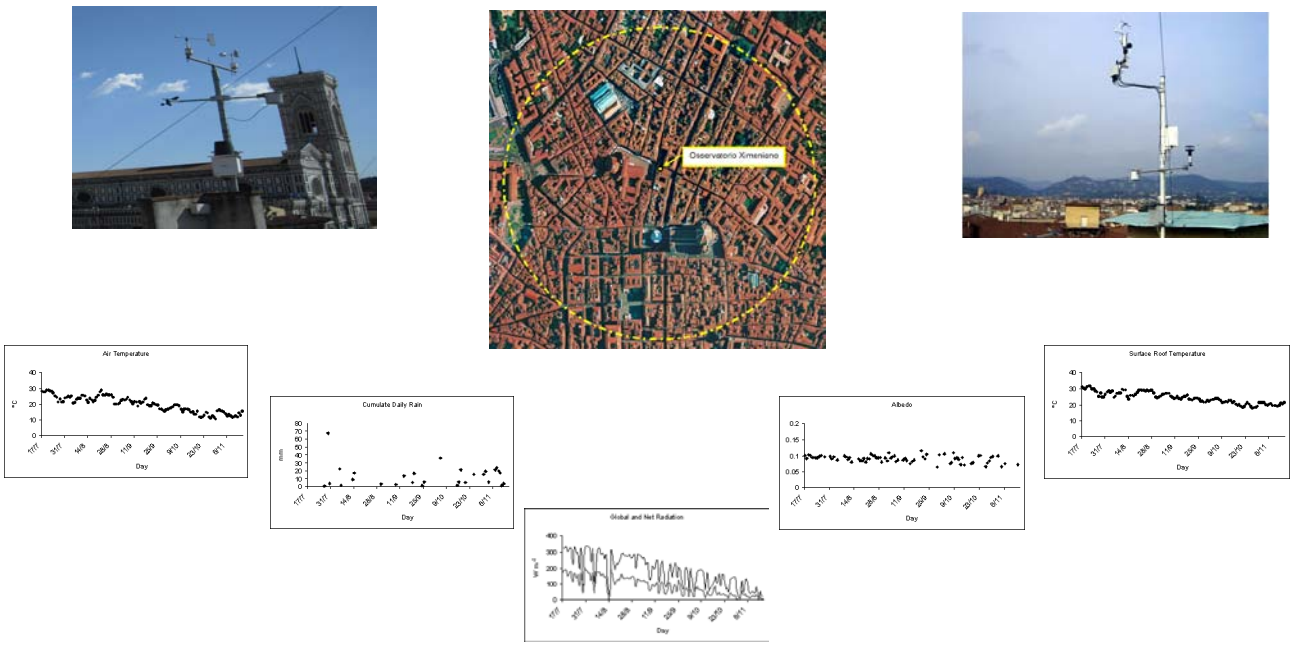

2. Air quality measurements

Tuscany Regional Agency for Environmental Protection (ARPAT) under BRIDGE project provided the whole database of a Network of 5 air quality monitoring stations installed in order to measure concentration of pollutants (PM_{10}, CO_2, NO_2, SO_2, CO). Data are available for the period 01/01/2003 – 31/12/2010. The location of the air quality monitoring stations is shown in Figure 1.

Fig 1 Air quality monitoring Network - Florence

Ponte alle Mosse and Viale Gramsci stations are typical traffic monitoring stations, while Boboli, Via Bassi and Via di Scandicci stations, although are located next to roads, are indicative of green/residential area (table 1)

Station_name	Distance Road	Traffic Station
Boboli	*>100 m*	NO
Via di Scandicci	*10 m*	NO
Ponte alle Mosse	*6 m*	YES
Viale Gramsci	*6 m*	YES
Via Bassi	*20 m*	NO

Results

For the **PM_{10}** is a clear decreasing trend started in 2004, and in particular the 2008-2010 period was characterized by a definite decreasing trend of all stations. In particular, in 2010, for the first time, there were no cases of discrepancies regarding the annual average for any of the stations of the network. Remain, however, on some stations, the excess of the limits on the frequency of daily surplus. The highest levels of PM10 are found near roads with heavy traffic and the in residential areas where a greater atmospheric stability at night results in accumulation of pollutants (figure 2-3)

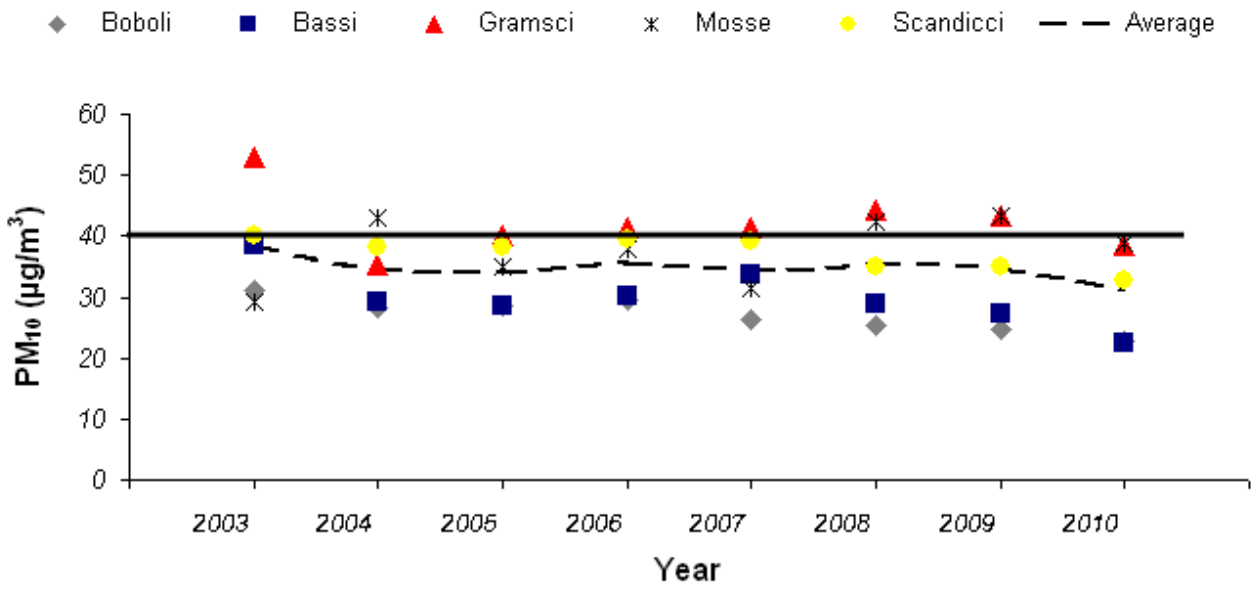

Fig 2 PM_{10} yearly average. 40 µg/m^3 is the threshold value for the safety of health

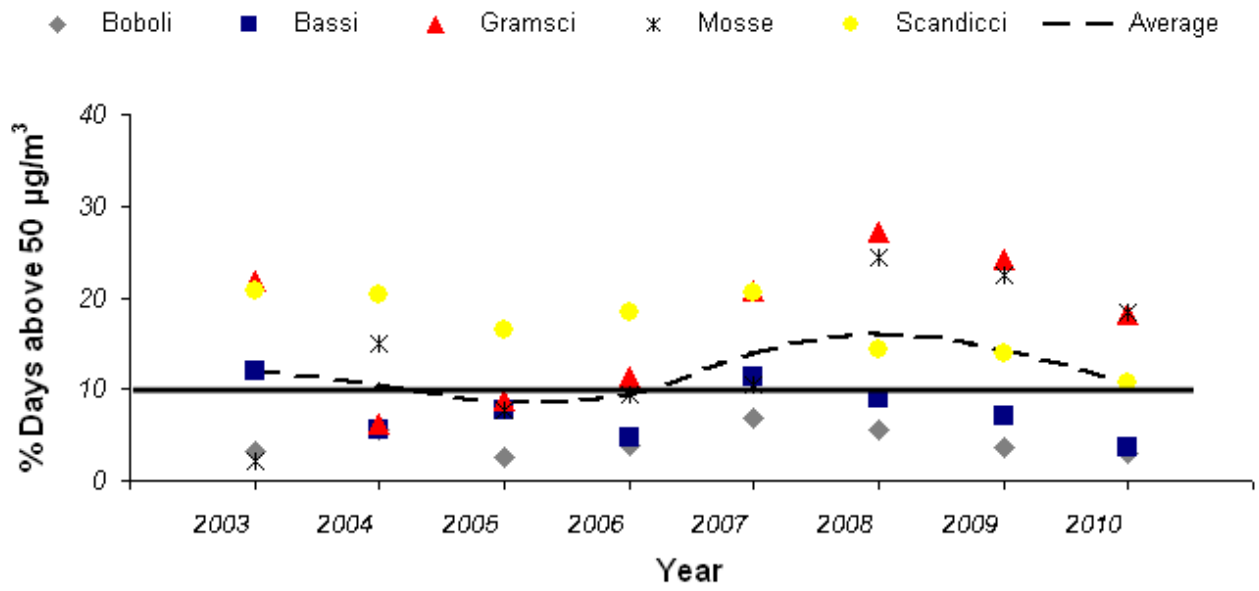

Fig 3 PM_{10}. % days above threshold of 50 µg/m^3. 10% is the threshold value for the safety of health

For the **NO_2** is clear a critical situation in the monitoring sites close to roads with heavy traffic. Since 2006 the gap between the green/residential stations and traffic stations tends to increase, and in particular a clear tendency to worsening of the latter. As for the green/residential stations, however, is confirmed a decreasing trend (Figure 4).

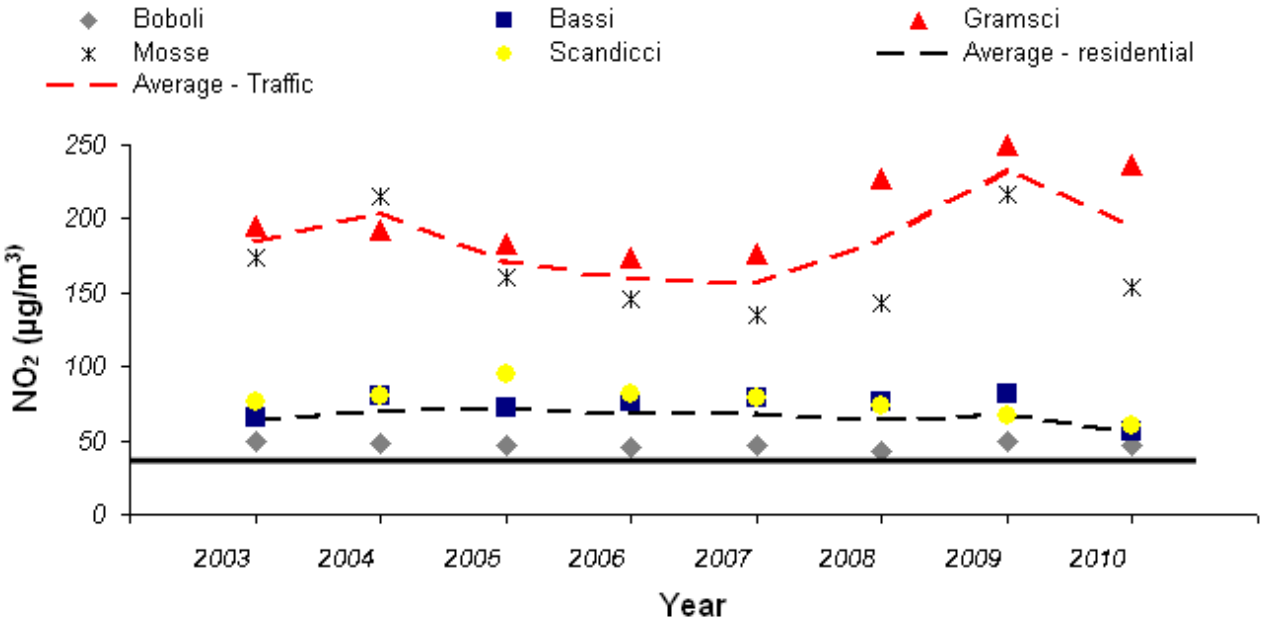

Fig 4 NO_2 yearly average. 40 µg/m^3 is the threshold value for the safety of health

For the **SO2** concentrations are below the threshold values for some years. After the slight inversion for the period 2005-2006, which could be due to the conversion of certain system from natural gas to heavy fuel oil, is confirmed a decreasing trend.

Concentrations of carbon monoxide was well within limits even for the traffic monitoring stations and continues the decreasing trend thanks to vehicle fleet renewal, banning non-catalysed petrol cars.

Dust deposition modeling

Introduction.

The aim of this work was to estimate the influence the proposed green space within the Parco San Donato would have on the local PM_{10} environment. Additionally findings from the London Case Study analysis were extrapolated to this site to assess how this modelling approach can be applied to different cities.

Results

1. Green space characteristics planned for Parco San Donato.

The architectural plans (542009 / A1 (19.00) POO – 350016 / 00 1 1) and the proposed grassland area and planned tree inventory (both provided by Piero Toscano, CNR-IBIMET) were used to obtain required green space characteristics. The architectural plans were analysed in ImageJ V1.44 (http://imagej.nih.gov/ij/) and the green space area was calibrated to the known 60, 240 m^2 of proposed grassland, the green space characteristics are given in Table 1.

Table 1. Estimates of the tree canopy areas for the proposed Parco San Donato development.

	Grass		Deciduous canopy		*Evergreen canopy	
	(m2)	(%)	(m2)	(%)	(m2)	(%)
Area	60, 240	100	16, 275	27	1820	3

*This also consists of *Taxodium disticum* (Swamp Cypress) due to coniferous habit.

2. Using the PM_{10} deposition predictions from the London study to estimate PM_{10} deposition to the proposed broadleaf canopy of Parco San Donato.

The modelling approach described in Tallis *et al.* (2011) suggests that broadleaf trees remove between 3 and 5% of PM_{10} via annual dry deposition from the turbulent mixing layer above the broadleaf canopy. The deposition load from the upper value of a 5 % reduction compared well with limited measurement of annual deposition to street trees in the London case study site (### in this document).

The mean annual [PM_{10}] above the site (39.0 µg m^{-3}) was estimated from the daily [PM_{10}] for 2010 measured from a local street monitoring site (Mosse station, situated 6 m from the roadside and approx 1.3 Km SE of this site). The mean annual mixing layer height (217 m) was estimated from Pasquill-Turner stability classes using input data for 2010 (Piero Toscano, CNR-IBIMET). The estimated annual PM_{10} deposited to the proposed broadleaved canopy using the predictions from the London study are given in Table 2.

Table 2: Predicting the annual deposition of PM_{10} to the estimated broadleaf canopy area of Parco San Donato using deposition rates estimated for the London Case study site.

	PM_{10} removal estimate taken from the London Study	
	3.3%	5.2%
Predicted annual PM_{10} load (kg yr^{-1})	40	63

3. Modelling the deposition of PM_{10} to the whole green space proposed for the Parco San Donato development.

The modelling approach developed in Tallis *et al*. (2011) was applied to estimate PM_{10} deposition to the proposed broadleaf canopy area. Further to the deposition velocity terms derived from UFORE (0.0064 m s^{-1}) and Tiwary *et al.* (2009) a UFORE term assuming zero re-suspension (0.0128 m s^{-1}) and a value from Fowler et al. (2004) derived from ^{210}Pb soil inventories (0.009 m s^{-1}) were used. Annual deposition to the grass land area was also estimated using a value from Fowler *et al*. (2004) derived from ^{210}Pb soil inventories over short grass (< 10 cm) (0.0033 m s^{-1}) and using measured relationships between deposition velocities and Pasquill's stability classes (Vong *et al*., 2004) to long grass (75 – 100 cm). The results from these modelling approaches are given in Table 3. We did not model deposition to the evergreens because of the small area of development planned with evergreen planting (3%) and the very wide range of canopy types.

Table 3: Estimating the annual PM_{10} deposited to the proposed green space of the Parco San Donato development considering meteorology and local [PM_{10}] for 2010.

Deposition velocity value		Annual estimated PM_{10} deposition to green space: Grass land no trees (60, 240 m^2)		Grass land surface remaining after tree planting (43, 965 m^2)		Broad leaved deciduous trees (16, 275 m^2)	
Source	m s^{-1}	Kg yr^{-1}	Kg ha^{-1} yr^{-1}	Kg yr^{-1}	Kg ha^{-1} yr^{-1}	Kg yr^{-1}	Kg ha^{-1} yr^{-1}
Nowak *et al*., 1994	0.0064	-	-	-	-	54.5	33.5
Nowak *et al*., 1994	0.0128	-	-	-	-	109.0	67.0
Tiwary *et al*., 2009	*	-	-	-	-	77.6	47.7
Fowler *et al*., 2004	0.009	-	-	-	-	180.0	110.6
Fowler *et al*., 2004	0.0033	244.3	40.6	178.3	40.6	-	-
Vong *et al*., 2004	*	257.0	42.6	187.5	42.6	-	-

* Deposition velocity is derived from a modelled value against either (i) wind speed Tiwary et al. (2009) or (ii) Pasquill's stability classes Vong et al. (2004).

Summary

Considering the green space proposed for the Parco San Donato development the modelling approach described here suggests annual deposition of PM_{10} of between 232.8 kg yr^{-1} (sum of 54.5 and 178.3, Table 3) and 367.5 kg yr^{-1} (sum of 180.0 and 187.5, Table 3) depending on the value of deposition velocity used in the model. This gives an estimated removal rate of between 5.2 and 8.2 % of PM_{10} from the mixing layer over this site. Prior to this development the existing bare ground would contribute to the atmospheric [PM_{10}] through surface emissions. The planned development can contribute to local air quality by both removing this emission source and providing surface characteristics that enhance atmospheric deposition.

The data modelled from the London Case Study site using the Tiwary *et al*. (2009) deposition velocity was comparable to measured data from the London Case Study site. Extrapolation of this London data allowed a prediction of 63.0 kg yr^{-1} of PM_{10} deposited to the broadleaf canopy at the Parco San Donato site (Table 1). The comparable modelled data explicitly at this site estimates a deposition of 77.6 kg yr^{-1} (Table 3).

The deposition to grassland was modelled using a value for deposition velocity taken from two diverse measurement approaches (Fowler et al.,2004 and Vong et al., 2004) however, the estimate of modelled dry deposition to grassland were very similar 244.3 and 257.0 kg yr^{-1} respectively. Grass at this site appeared to contribute between 27% and 56% of the total annual deposition depending on modelling approach (Table 3). However, management activities such as grass cutting could result in considerable re-suspension of PM_{10} back to the atmosphere.

LIDAR observations :

A back-scatter LIDAR device was installed and tested on the Ossrvatorio Ximeniano. The instrument emits upward a laser source and measures back scatter as a function of time, resolving the first 5 km of atmosphere. The purpose of this instrument is to detect boundary layer depth, and also to characterize the aerosol distribution.

Figure 2 reports a daily course os measured backscatter, highligthing the presence and the diurnal development of a well mixed layer up to approx. 1 km; the presence of clouds at the PBL top inhibits obtaining a signal from above in the second part of the day. Overall, this type of measurements can be used to assess aerosol distribution, and to obtain important information on PB development:since aerosols emitted from the surface are concentrated into the PBL, a clear PBL aerosol signature can be used to retrieve PBL depth information, to be used as model validation data.

Figure 1
The CNR LIDAR system installed on the Osservatorio Ximeniano, without protection metal cover for continuous operation.

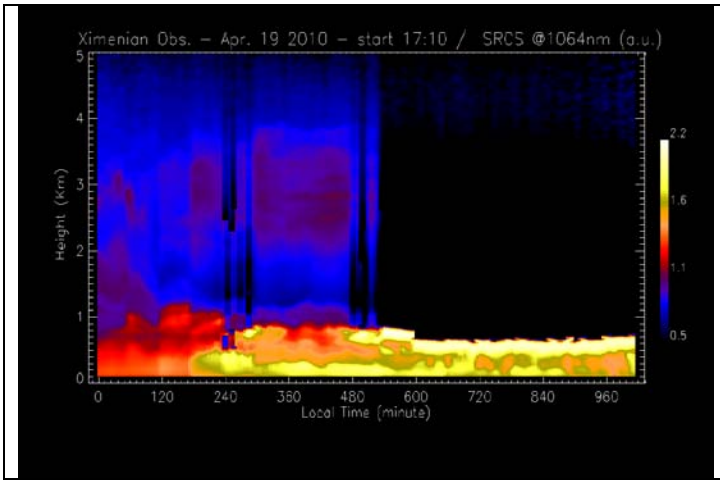

Figure 2.
Daily profile of LIDAR backscatter at 1064nm measured from Osservatorio Ximeniano, as a function of distance from the ground.

BIOMONITORING OF AIR-QUALITY
authors: Pierpaolo Duce, Grazia Pellizzaro, Annalisa Canu

The moss *Hypnum cupressiforme* has been used as a bioindicator for the estimation of atmospheric traces metal deposition in the urban area of Florence. Moss carpets were collected in a forested area of central Sardinia (municipality of Bolotana – Nuoro), which is characterised by absence of air pollution. In laboratory, the moss material was cleaned from particles of soil, dead material and attached litter and was washed seven consecutive times with distillate water. After cleaning, moss samples were air dried. Moss bags were prepared by weighing out 2 g air-dried weight, and packing it loosely in nylon nets of 25 cm in diameter with mesh of 4 mm^2 (Figure 1). Moss bags were located in the urban area of Florence (Figure 2) close to three monitoring air quality stations of the Environmental Protection Agency of Tuscany (ARPAT) located in Via Ponte alle Mosse (FI1), Viale Gramsci (FI2), and Viale Ugo Bassi (FI3). The first two stations are located in high traffic roads whereas the third one is located in a road characterised by less traffic density.

Figure 1 - Moss-bag exposed near monitoring air quality station.

Figure 2 - Location of the three sample sites in Florence (FI 1, FI 2, and FI 3).

The results of the first three campaigns of measurement conducted during the periods March-May, May-July, and July-November are reported.
Samples of the fourth campaign conducted in fall will be analyzed as soon as possible for As, Cr, Cu, Fe, Ni, Pb, V, and Zn by Inductively Coupled Plasma Atomic Emission Spectrometry.
The fifth bioaccumulation campaign is running since the moss bags were located in the three monitoring air quality stations of ARPAT at the beginning of March.

Data analysis.
Summary statistics were used to obtain the means of trace element concentrations in moss and one-way ANOVAs and post-hoc comparison tests were conducted with element concentration (Cr, Cu, Fe, Ni, Pb, V, and Zn) as independent variable, and exposure site (FI1, FI2, and FI3) as the dependent factor. Differences between mean values were identified by LSD test.
Statistical analyses were performed using Statistica software v. 6.1 (StatSoft Inc., Tulsa, OK, USA).
In addition, the trace element concentrations in moss corresponding to each exposure site were used to calculate the Load Factor defined as:

$$LF = \frac{C_{after} - C_{before}}{C_{before}}$$

where:
C_{after} is the content of an element in the moss samples after exposure;
C_{before} is the content of the same element determined in the moss samples before exposure.

Results
Tables 1, 2 and 3 show the differences between mean concentration of trace metals in moss bags after-exposure and the respective blanks in the three sample sites of Florence (FI 1, FI 2, and FI 3) during the first three campaigns of measurement. The highest concentrations for almost all elements were recorded in site FI2 (Viale Gramsci), which is a high traffic road. Lower values were detected in site FI3 (Via Ugo Bassi) located in a road with less traffic density.
In particular, the elements Cu, Fe, and Zn show higher values than other analyzed elements.
Decrease of V in moss bags after exposure in site FI2 indicates that moss as living material in the bag not only can absorb and contain element deposition from the air, but also has the ability of exchange with element in the air.

Significant higher mean values were detected for Cu and Fe elements in FI2 site compared to FI3 site (Figure 3, 4). Concerning Zn element no significant difference has been observed between sample sites (Figure 5).
Moving to Load Factor data, the elements Cu, Ni, and Zn show higher values than other analyzed elements (Table 4).
The results obtained suggest that *Hypnum cupressiforme* has a high ability to accumulate trace metals and, therefore, can be good bioindicator to estimate the trend of air pollution in a urban area during a period time.
This study further confirm that the moss bag method is a simple, inexpensive and useful technique, which provides informative atmospheric metal deposition figures in terms of time and space.

Table 1 - Differences between mean concentrations of trace metals in moss bags after-exposure and the respective blanks in the three sample sites of Florence (FI1, FI2, and FI3) during the first campaign of measurement. Period of exposure March-May 2010.

Elements		**FI 1**	**FI 2**	**FI 3**
Cr	(mg Kg^{-1})	179	289.5	311
As	(mg Kg^{-1})	< 0.1	< 0.1	< 0.1
Cu	(mg Kg^{-1})	66.6	64.6	4
Fe	(mg Kg^{-1})	618.5	270	93.5
Ni	(mg Kg^{-1})	58.5	56.5	160.5
Pb	(mg Kg^{-1})	224	219	138
V	(mg Kg^{-1})	36.7	20	20.4
Zn	(mg Kg^{-1})	347	357	350

Table 2 - Differences between mean concentrations of trace metals in moss bags after-exposure and the respective blanks in the three sample sites of Florence (FI1, FI2, and FI3) during the second campaign of measurement. Period of exposure May-July 2010.

Elements		**FI 1**	**FI 2**	**FI 3**
Cr	(mg Kg^{-1})	2.2	7.0	0.8
As	(mg Kg^{-1})	< 0.1	< 0.1	< 0.1
Cu	(mg Kg^{-1})	14.6	30.9	1.8
Fe	(mg Kg^{-1})	501	686	151
Ni	(mg Kg^{-1})	4.7	4.6	3.8
Pb	(mg Kg^{-1})	5.9	5.8	3.6
V	(mg Kg^{-1})	2	-6.6	1.9
Zn	(mg Kg^{-1})	1160.9	1775.9	1748.9

Table 3 - Differences between mean concentrations of trace metals in moss bags after-exposure and the respective blanks in the three sample sites of Florence (FI1, FI2, and FI3) during the third campaign of measurement. Period of exposure July-November 2010.

Elements		FI 1	FI 2	FI 3
Cr	(mg Kg^{-1})	2.3	9.7	1.4
As	(mg Kg^{-1})	< 0.1	< 0.1	< 0.1
Cu	(mg Kg^{-1})	21.4	46.7	1.9
Fe	(mg Kg^{-1})	460	625	190
Ni	(mg Kg^{-1})	10.6	9.9	7.1
Pb	(mg Kg^{-1})	4.4	5.5	3.5
V	(mg Kg^{-1})	1.5	1.8	1.3
Zn	(mg Kg^{-1})	1989	2252	2188

Table 4 - Trace element load factors in moss samples after the first three biomonitoring campaigns (March-May, May-July 2010, and July-November 2010) in the three sample sites of Florence (FI 1, FI 2, and FI 3).

Elements	March-May 2010			May-July 2010			July-November 2010		
	FI1	FI2	FI3	FI1	FI2	FI3	FI1	FI2	FI3
Cr	0,28	0,45	0,48	0,46	1,45	0,17	0,37	1,59	0,22
As	-	-	-	-	-	-	-	-	-
Cu	0,88	0,86	0,05	1,20	2,55	0,15	1,78	3,89	0,15
Fe	0,23	0,10	0,03	0,43	0,59	0,13	0,33	0,45	0,14
Ni	0,25	0,24	0,68	3,88	3,83	3,17	5,55	5,21	3,74
Pb	0,38	0,37	0,23	0,40	0,40	0,24	0,25	0,31	0,20
V	0,94	0,51	0,52	0,16	-0,54	0,16	0,11	0,13	0,09
Zn	3,54	3,64	3,57	39,89	61,03	60,10	65,21	73,84	71,74

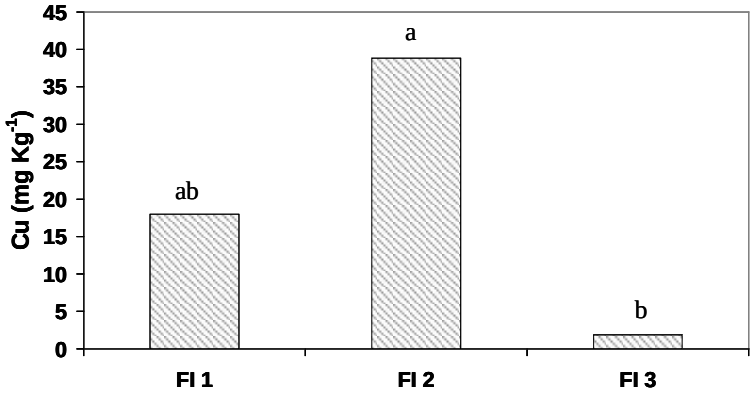

Figure 3 - Comparison of mean values of Cu concentration recorded during exposure in the three sample sites of Florence (FI1, FI 2, and FI 3). (Values with the same letter are not significantly different for p≤ 0.05 by LSD Test).

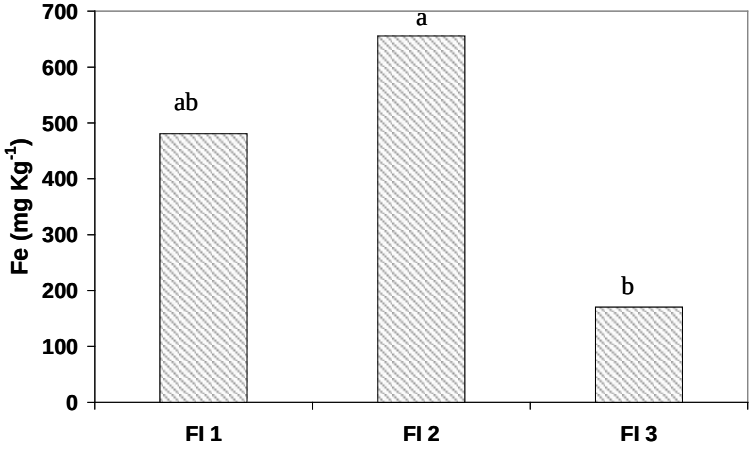

Figure 4 - Comparison of mean values of Fe concentration recorded during exposure in the three sample sites of Florence (FI1, FI 2, and FI3). (Values with the same letter are not significantly different for p≤ 0.05 by LSD Test).

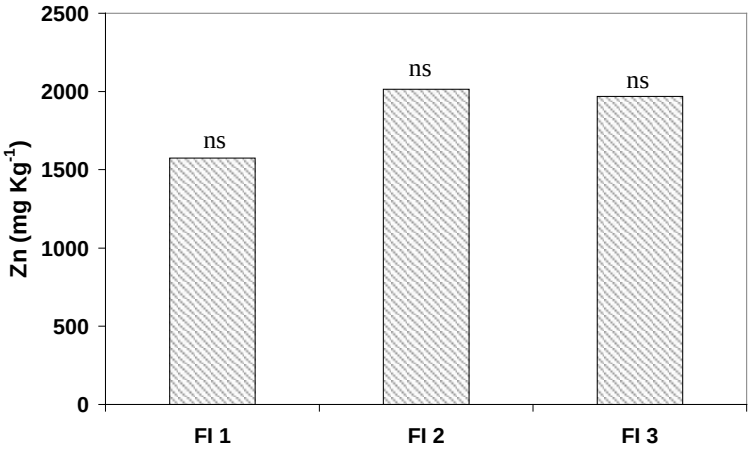

Figure 5 - Comparison of mean values of Zn concentration recorded during exposure in the three sample sites of Florence (FI1, FI2, and FI3).

3. Turbulent fluxes

Introduction
Measuring surface fluxes of energy, mass, and momentum form urban environments can provide important informations on the urban energy balance, and emisison dynamics to be used in a number of different tools, ranging from atmosphric models to emission models, and DSS systems. So far, the few observations that were made include Chicago, Illinois (Grimmond et al. 2002); the center of Edinburgh, United Kingdom (Nemitz et al. 2002); the metropolitan region of Copenhagen, Denmark (Soegaard and Møller-Jensen 2003); a Mexico City, Mexico, urban landscape (Velasco et al. 2005); Basel, Switzerland (Rotach et al. 2005; Vogt et al. 2006); and Marseille, France (Grimmond et al. 2004).
A flux measurement station was deployed in Firenze since 2005 for short term experiments (Matese et al 2009), while it was made fully operational on a continuous basis within the BRIDGE project. In this study we present dynamics of carbon and energy fluxes at various time scales, ranging from hourly to seasonal patterns, with the aim of quantifying the importance of different drivers of concentration of scalars in the atmosphere.

Methods
An eddy covariance (EC) flux station was installed in Firenze (438479N, 118159E) in at the Osservatorio Ximeniano, in the center of the city (Fig. 1), and was operated continuously for the project duration. A mast of 3m was mounted on a typical tile roof of an ancient building of the observatory at 33 m above the street level. Turbulent fluxes of CO2, momentum, and sensible heat were collected using a sonic anemometer and an open-path CO2/H2O infrared gas analyzer (Li7500). Ancillary measurements are provided by a Class A weather station. Flux data are computed at a 30 minutes time resolution, and quality checked with state of the art procedures (Foken et al 2006).
For the analysis presented in this study, data have been averaged across various time scales, in order to resolve daily courses, weekly, monthly and seasonal courses of energy balance and surface emissions. Seasonal analysis has been accomplished by grouping together periods with similar overall emissions: Nov-Dec-Jan-Feb (‘winter’ period), March-April-May-Sept-Oct (‘spring-autumn’ period), June-July-August (‘summer’ period). Averaging process has been accomplished only on quality-checked dataset.

Results
In this study we present temporal dynamics of surface fluxes at different time scales, with the aim of deriving robust estimates of temporal variability of fluxes, which ca be used to assess models or DSS systems.
Figure 2 reports CO2 emission data across the year, computed both as daily, weekly, and monthly averages across the study period. The most important result that coms from this analysis is the strong sesonaity of carbon emission: on average, CO2 average flux in the winterr spans across 35 umol m-2 s-1, while in the summer across 10 umol m-2 s-1. This difference is related to the presence of domestic heating, that is almost entirely based on methane combustion, which releases CO2 and water vapour. Such strong seasonlity is typically not observed in cities where a different energy mix exist for heating and transportation, and is driven by the dynamic of domestic heating and road traffic (Matese et al 2009). The absence of a significant seasonality in traffic amounts (data not shown) justifies the conclusion that traffic is repsonsible for ~100% of emisisons in summer time, and only ~ 30% in winter time. A similar pattern can be observed in CO2

concentration, reflecting the fact that a higher amount of carbon injected into the atmosphere on average drives a higher concentration. This is an average result, while dynamic at smaller time scales show different relations between flux and concentration as shown below.

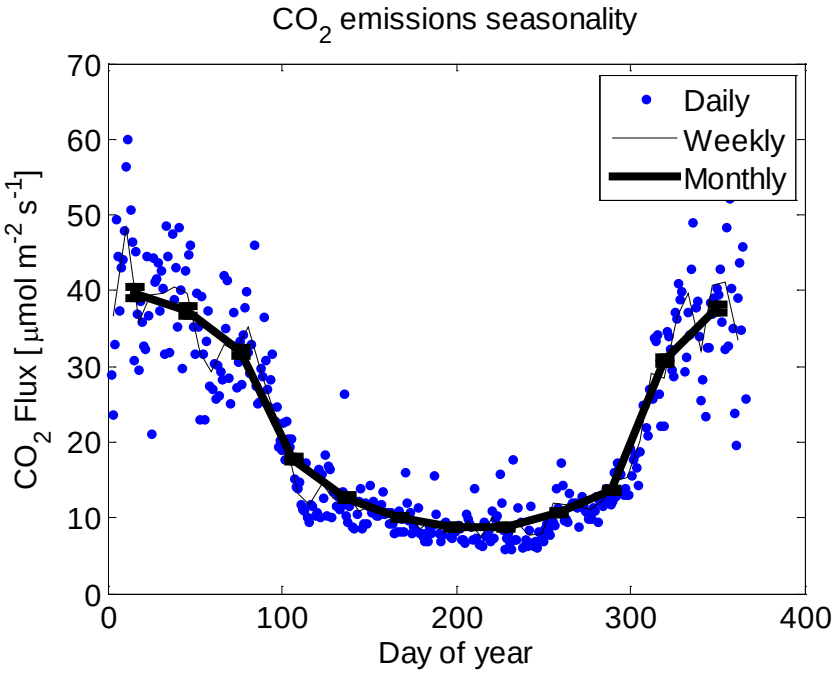

Figure 2
Seasonal trend of CO2 emissions expressed as daily averages (blu points), weekly averages (thin line), monthly averages (large line), across the entire study period.

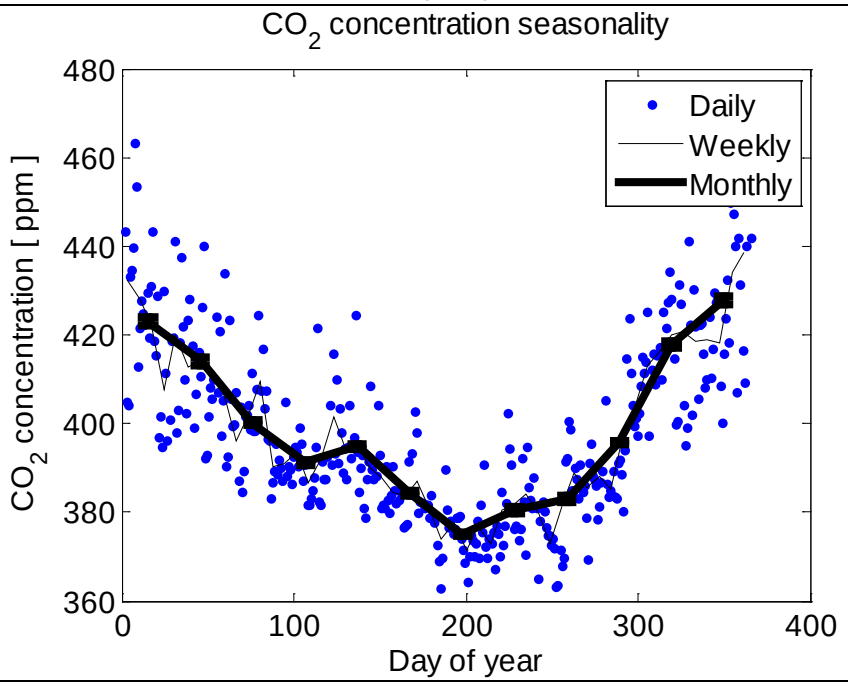

Figure 3
Seasonal trend of CO2 concentration expressed as daily averages (blu points), weekly averages (thin line), monthly averages (large line), across the entire study period.

Figure 4 reports average daily CO2 emission for the different week days, and for the three seasons. A significant week-end reduction of emissions is present in all the periods, suggesting that in weekends both traffic and a part of domestic heating, related to public buildingd, offices, and business buildings, are reduced: percentage reduction with respect the average daily emisison of the week-days is ~20% (Saturday) and ~50% (Sunday) for winter time, ~15% and ~40% for spring-autumn, and ~5% and ~20% for summer time. These data support the hypothesis that week-end reduction is larger on domestic heating then on road traffic, due to the presence of a significant portion of business and public buildings.

Figure 5 reports hourly distribution of fluxes across the daily course for the 3 seasons. This result highlights the diurnal pattern characterized by specific peculiarities: a low emission at night, driven by a lower flux and also possibly enhanced by storage processes occurring at the street level below the urban canopy top; a large flux peak in the early morning, which van be related to the burst of nocturnal CO2, as well as the switch on of heating systems and the increase in traffic.
Figure 6 highlights the trend of concentration in the different seasons: in all periods the same specific patterns are present: i) a nocturnal build up of concentration, where relatively small fluxes (Fig 5) inject and concentrate carbon in a shallow stable layer; ii) a mixing in the first part of the morning, where despite very high surface fluxes, concentration tend to decrease; this can be related to the development of a well mixed layer, with associated entrainment of tropospheric air with a lower carbon amount; also advective procsses which transport horizontally air masses with lower carbon amounts could play a role; finally, a build up in the evening when a new nocturnal stable layer develops. These results suggest the hypothesis that vertical mixing and PBL development, together with emission strength at the surface, are playing a fundamental role in driving surface layer concentratons of scalars.
Such datasets can be direclty uised both to validate a modelling framewrok capable of simulating the couipliong between the PBL and the surface, and to drive modelling analysis based on scenario.

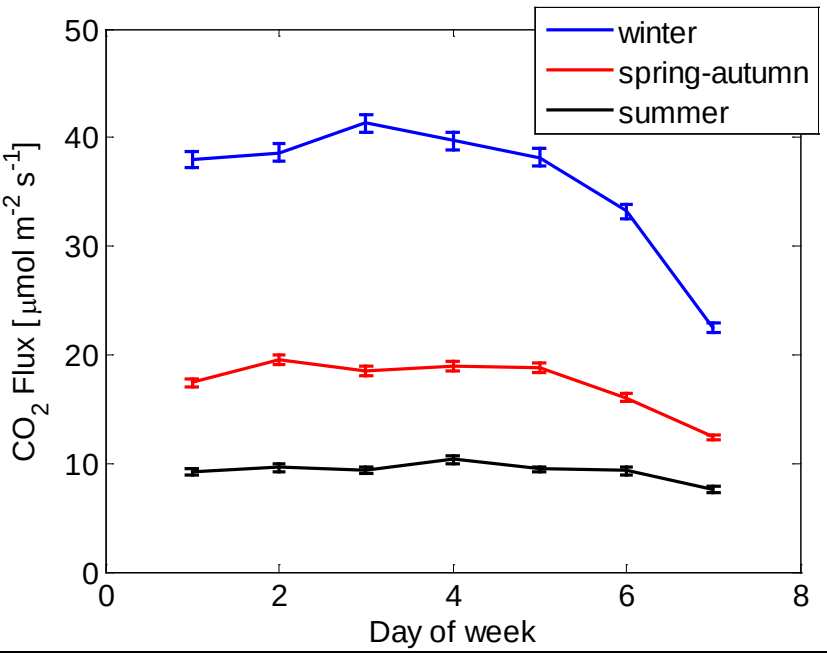

Figure 4
Weeky trend of CO2 emissions expressed as daily averages and respective standard errors, over three seasons, across entire study period.

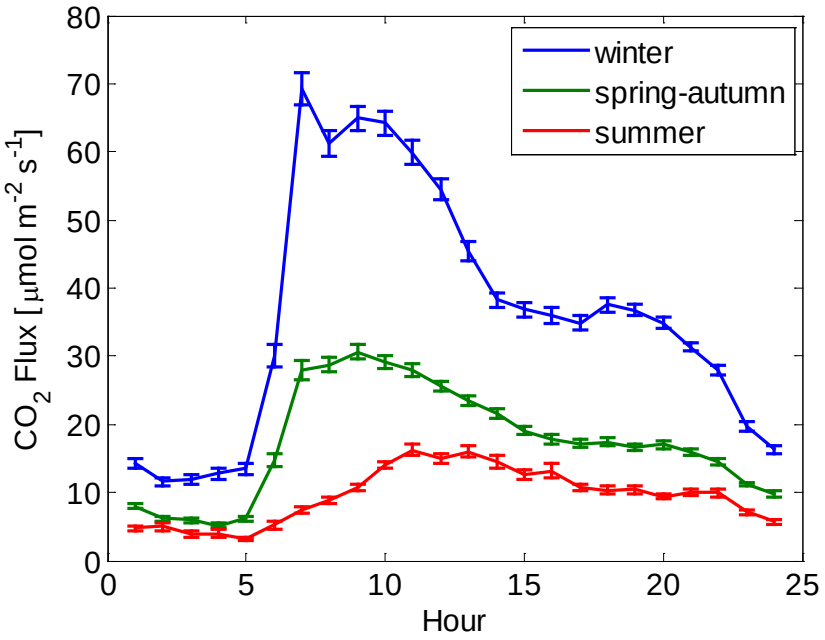

Figure 5
Dailyy trend of CO2 emissions expressed as hourly averages and respective standard errors, over three seasons, across entire study period.

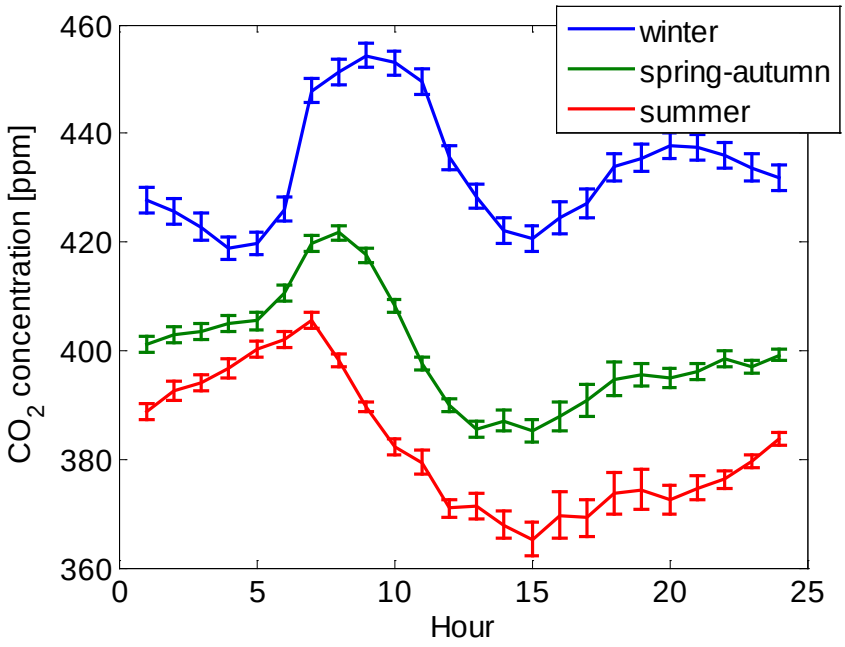

Figure 6
Dailyy trend of CO2 concentration expressed as hourly averages and respective standard errors, over three seasons, across entire study period.

Dust turbulent fluxes

Materials and methods

Fluxes of particulate matter were measured at the Osservatorio Ximeniano (Florence, Italy) by CMCC with the EOLO system, deploying the eddy covariance method (Fratini et al., 2007). EOLO is comprised of a sonic anemometer (WindMaster Pro by Gill Instruments Ltd.) and an Optical Particle Counter (OPC CI-3100 by Climet Instruments Co.). It measures high frequency wind components and particle number concentration, to provide particles number concentration and fluxes averaged over 30 minute spans. Observed particles fall in the optical range 0.26 to 7.00 µm. The corresponding aerodynamic range is somewhat shifted toward larger values, the actual conversion depending on the refraction index of sampled particles. For desert dust, the corresponding range is ca. 0.35 – 9.5 µm. Thus, in terms of mass, the full range provides a close estimation of PM_{10}. In the present case, however, the refraction index of particles is unknown, thus an empirical approach was adopted to estimate PM_1, $PM_{2.5}$ and PM_{10} from available measurements. The processing software provides a first estimate of surface, volume and mass concentrations and fluxes, assuming a spherical shape and a constant particle density. Mass information was then refined, based on an *in situ* rescaling of concentration measurements. Aggregated $PM_{2.5}$ and PM_{10} averaged on a daily basis were compared to similar concentration measurements available for the observed urban area, performed with the gravitational method. From such comparison, a (multiplicative) scaling factor was derived, applicable to both concentration and fluxes. As a consequence, absolute concentration and flux values shall be considered with due care, and shall be used primarily for analyzing trends rather than for quantitative analysis, such as mass budgets closure.

The observed period extends from June 6th to December, 10th 2010. Due to several periods of malfunctioning, available data cover some 60% of the whole period, corresponding to ca. 111 days. Data were processed as described in Fratini et al. (2007). In addition, two quality filters were applied, and the following analysis was performed using only high-quality data. The first filter is a despiking procedure, eliminating individual flux values that show too large differences with the respect to the preceding and the following values in the time series. The threshold difference was determined empirically, by visual inspection, for the PM_1 number flux; when a spike was detected for PM_1, also all other fluxes related to the same interval were eliminated. The second quality criterion is based on particle counting uncertainty, estimated here as in Buzorius et al. (2003). Individual flux values were eliminated if relative uncertainty was larger than 40%. This led to elimination of most fluxes of small intensity, notably night-time fluxes.

Results

Figure 1 shows the determination of the scaling factor, based on a comparison of daily concentration from EOLO and the average from 2 slow stations (“Bassi” and “Gramsci”). The calculation was performed on $PM_{2.5}$ concentrations, because it showed a better agreement than PM_{10} (while PM_1 is not available from the slow stations) providing a more reliable estimate. From such comparison, a scaling factor of 0.19 was estimated. A similar value of 0.21was confirmed for PM_{10}. Eventually, an average value of 0.20 was used to rescale all fluxes discussed hereafter. Fluxes of PM aggregates (PM_1, $PM_{2.5}$ and PM_{10}) showed very similar trends, thus the following discussion if performed only for PM2.5, with results being approximately valid also for PM_1 and PM_{10}.

The analyzed period is characterized by an abrupt change in the wind regimes occurring at the change of the season. Figure 2 shows frequency distributions of wind directions observed at the site. Nighttime winds are dominated by the easterly Levante during the whole measurement period. However, summer’s daytimes are dominated by NW winds, while Southerly winds dominate during

autumn daytimes. Such change in the wind regimes determines a dramatic modification of the footprint of the observed micrometeorological fluxes. For this reason, particulate fluxes have been analyzer separately for the two seasons.
Figure 3 shows daily course of $PM_{2.5}$ mass fluxes as observed during summer and autumn. During summertime fluxes are close to zero (0.1 ± 1.1 µg m^{-2} s^{-1}). At about 9 am in the morning fluxes start to build up, increasing to a maximum of about 3.3 µg m^{-2} s^{-1} at 11 am. During the early afternoon fluxes tend to decrease slightly, to build up again from about 5 to 8 pm, when values of about 4.8 µg cm^{-2} s^{-1} are reached. Afterwards, measured fluxes show a coherent peak extending from 8 to 11 pm, with average values rising up to 11.3 µg cm^{-2} s^{-1}. While the morning and late afternoon flux buildups can be confidently related to traffic intensifications, the highest evening peak is hardly explained in terms of urban dynamics, and should be probably related to the change in wind direction, and the consequent change in footprint structure, occurring in the same time.
Fluxes measured during the autumn period do not show any significant trend, with small daily fluxes, of the same magnitude of night time fluxes. This result is probably to be linked to an increased rainfall during autumn. Indeed, summer time was characterized by an average of 1.2 rainy days and 17 mm per week, increasing to 3.8 days and 37 mm per week during autumn, with a sharp increase occurring at the seasonal transition. Increased rainfall tends to trap particulate matter at the surface, preventing particles to be uplifted and escape the urban canopy as an emissive turbulent flux. Furthermore, the modification of the wind regimes, with Southerly winds dominating the daytime hours during autumn, implies a modification of flux footprint as measured at instruments level with respect to the summer time, and possibly exposes the measurements to a less intense source are of particulate matter. This aspect requires further investigation.

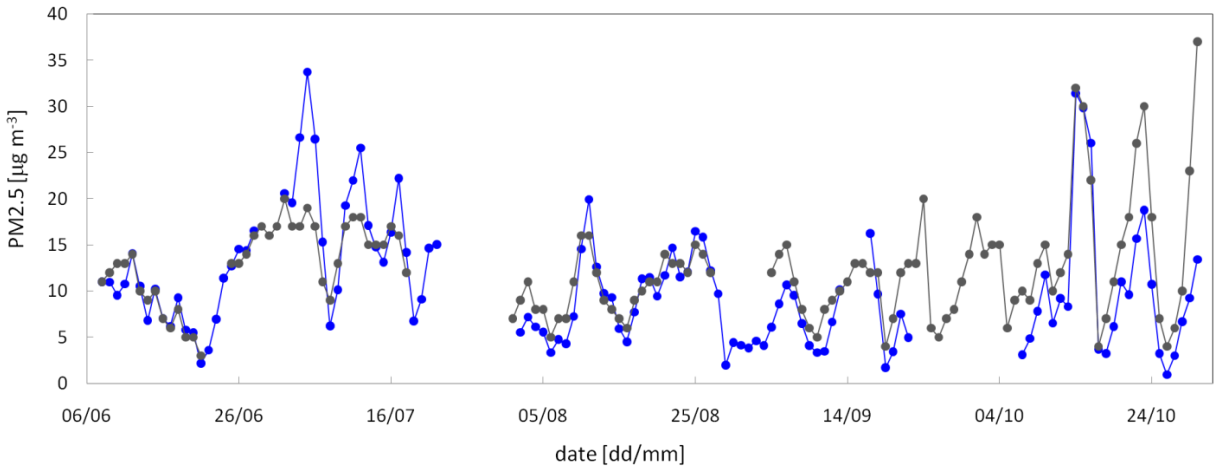

Figure 1. Daily average PM2.5 concentrations (mg m-3). Blue: EOLO after rescaling (factor 0.19); dark gray: average of “Gramsci” and “Bassi” concentrations.

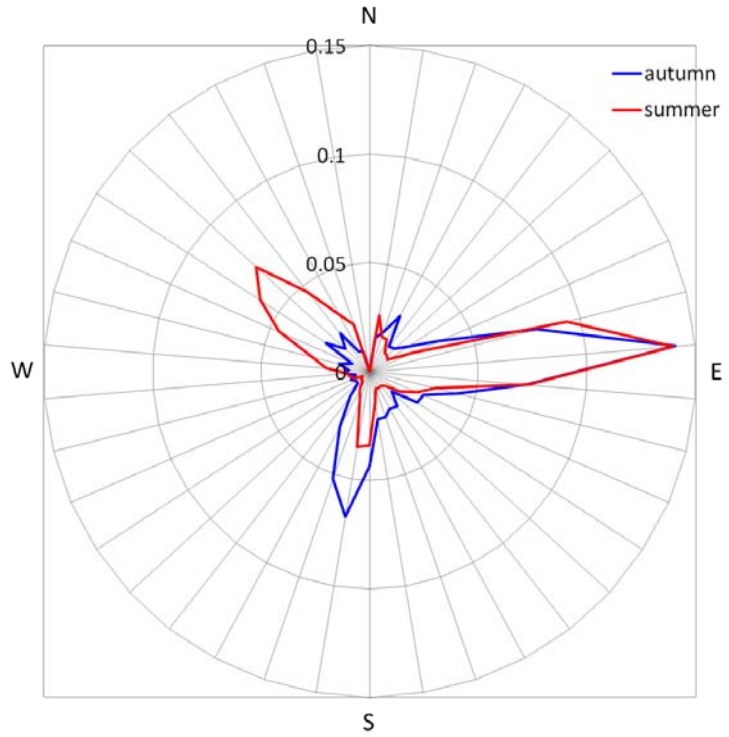

Figure 2. Summer (red) and autumn (blue) distribution of wind directions. The eastern peaks are mainly associated to night time winds, while the other two (NW and S peaks) with daytime winds.

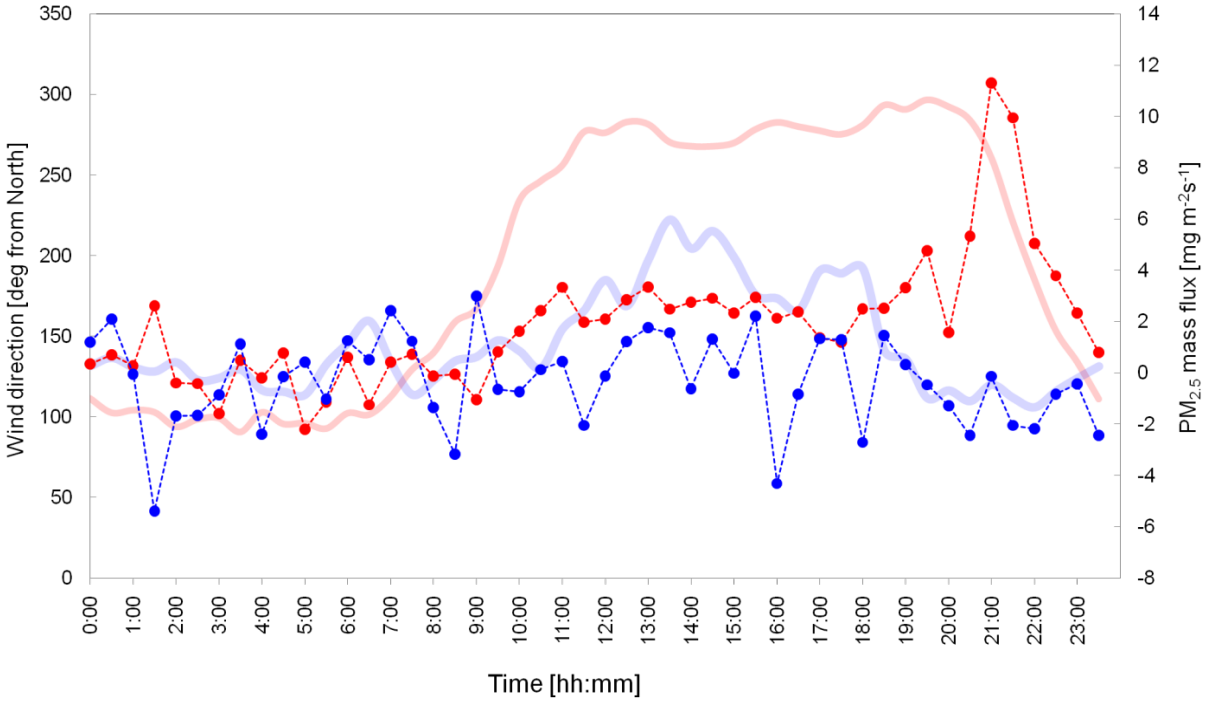

Figure 3. Summer (red) and autumn (blue) daily courses of $PM_{2.5}$ fluxes (full circles and dashed lines) and wind direction (think solid lines).

Author: Gerardo Fratini (gerardo.fratini@licor.com)

4. ACASA modelling

The Advanced-Canopy-Atmosphere-Soil Algorithm (ACASA) model was applied by CMCC over Florence case study and used to simulate energy and mass fluxes in the city centre. The simulation period covered one year from January to December 2008, and turbulent fluxes were simulated at 30 minute time steps.
Meteorological data used to drive the model came from the measured data collected at the Ximeniano Observatory. They consisted of air temperature, relative humidity, precipitation, and wind speed. In sunny days, solar radiation data collected at the Ximeniano were corrected due to a shadow effect using data from a nearby meteorological station, while downward long wave radiation was estimated starting from air temperature values. A constant CO_2 concentration value (388 ppm) was chosen to drive the model.
Simulated fluxes were compared, for the model validation, with Eddy Covariance flux measurements collected at the Ximeniano tower in the period January-April 2008. The main results of the analyses are presented here.
Sensible heat flux (H) was well simulated by the model during the entire period. In Fig. 1 are showed simulated (solid line) and observed (dots) data for January, February, and April 2008. Similar trend between simulated and observed fluxes was observed confirming the model ability to reproduce the diurnal variation in H flux all over the months.

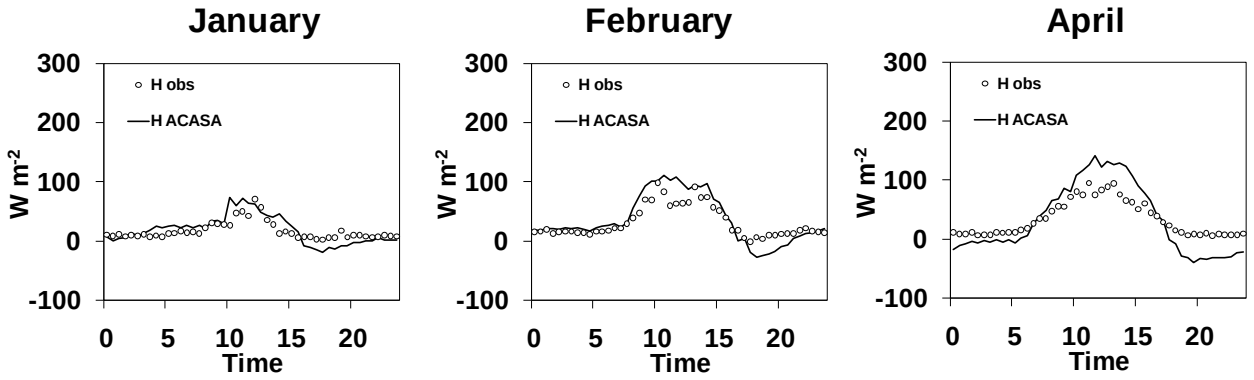

Figure 1. Comparison between simulated (solid line) and observed (dots) sensible heat flux (H). Data are sorted by time and averaged.

Looking in more detail, half-hourly data were compared in Fig. 2 for short time period: a week in February (a), and 10 days in April (b), showing also in this case the model ability to reproduce H flux at half-hourly time step.

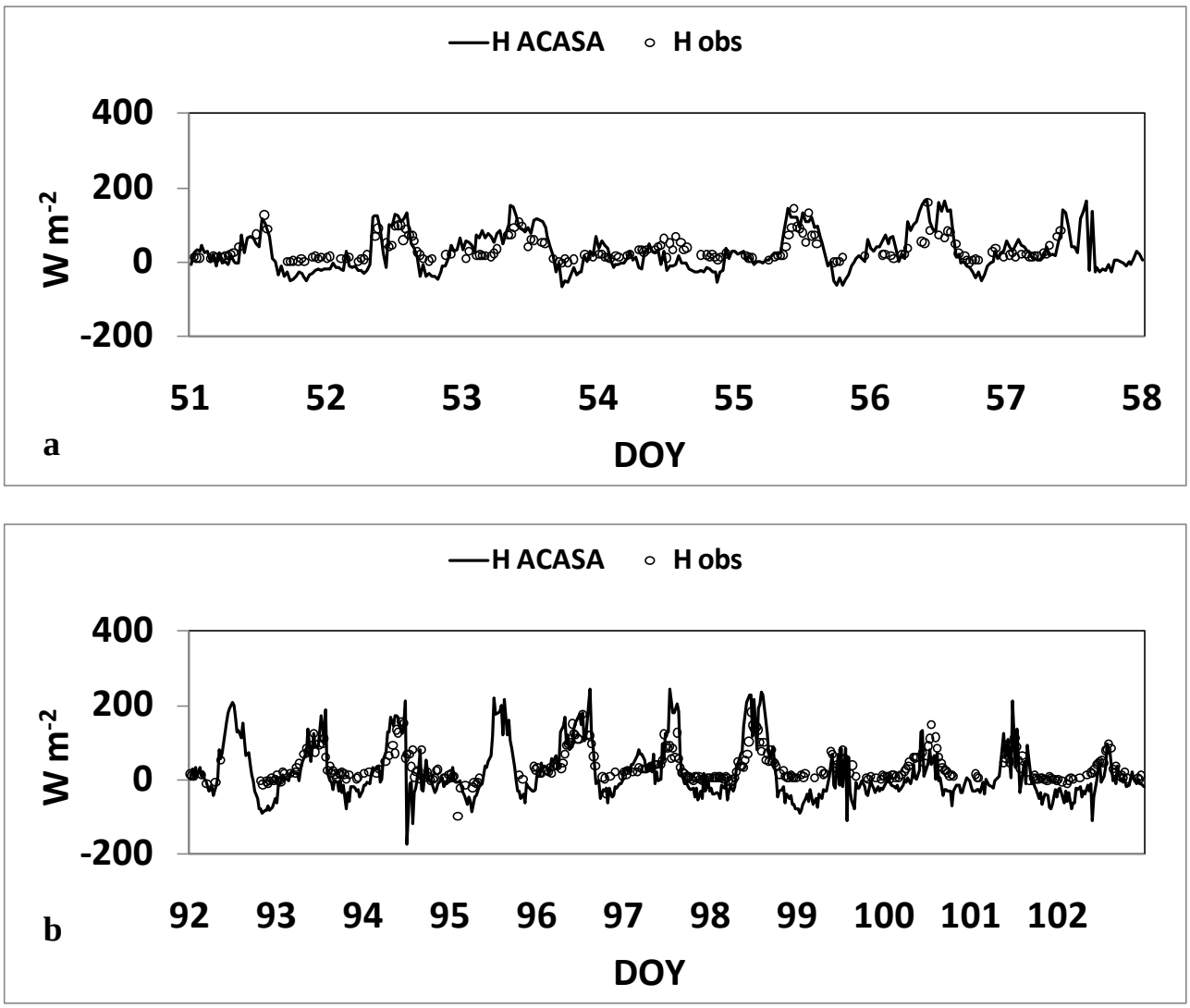

Figure 2. Comparison between half-hourly simulated (solid line) and observed (dots) sensible heat flux (H) during a week in February (a) and 10 days in April (b).

Latent heat flux values are generally low in a city, and in this case the low values also derive from the absence vegetation in Florence city centre. The model was able to capture this typical feature of urban areas, showing only small differences between simulated and observed values during the three months (Fig. 3). Just for example, the fluxes comparison for a 10 days period in April is showed in Fig. 4 at half hourly time step.

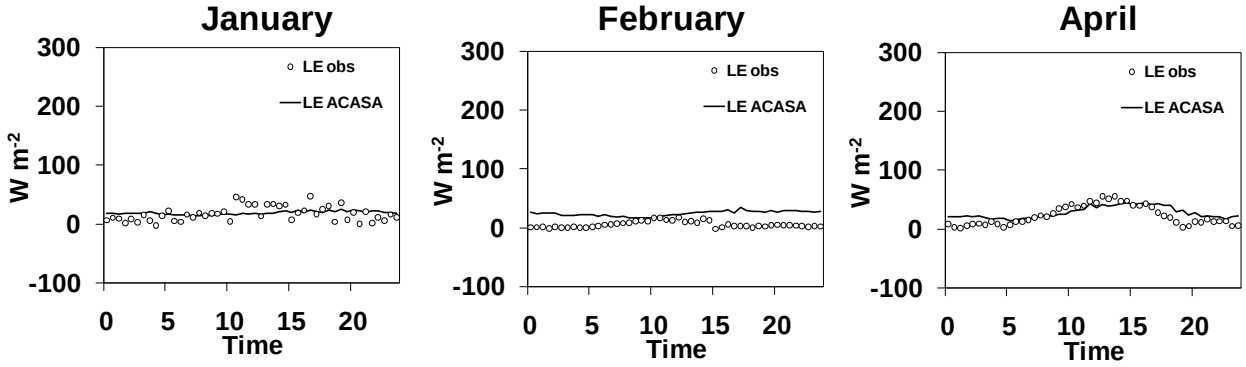

Figure 3. Comparison between simulated (solid line) and observed (dots) latent heat flux (LE). Data are sorted by time and averaged.

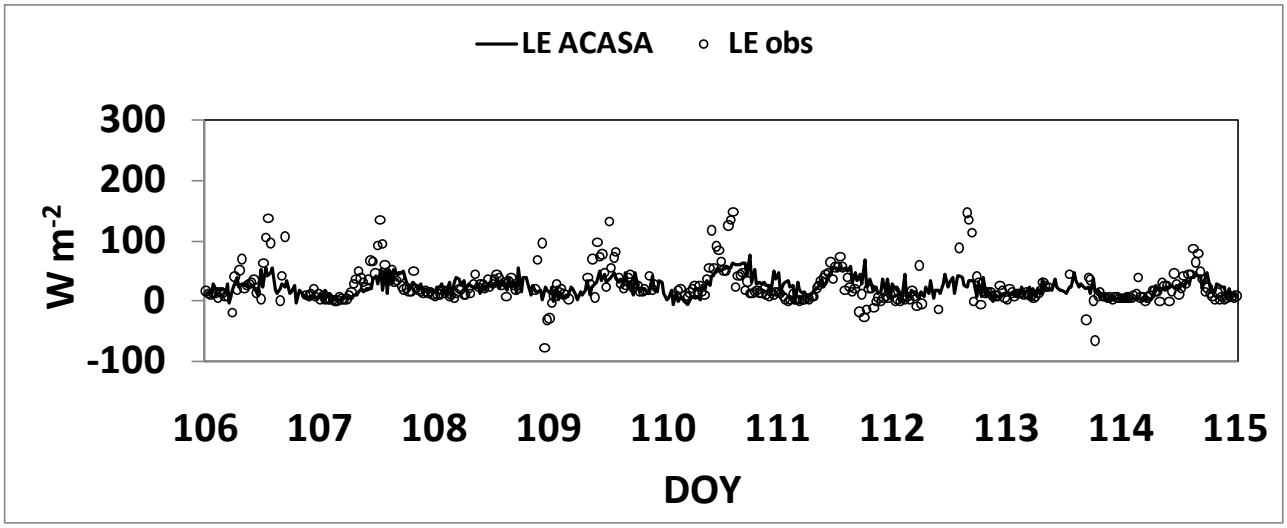

Figure 4. Comparison between half-hourly simulated (solid line) and observed (dots) latent heat flux (LE) during 10 days in April.

In order to simulate the diurnal cycle of carbon flux, traffic data (number of vehicle per Km^2) were included in the ACASA model. Two peaks in CO_2 flux typically arise in the early morning and late afternoon in correspondence of the rush traffic hour. The model was able to capture this trend. The general model underestimation of CO_2 flux was mainly due to a lack of information about energy consumption for heating/cooling process to be accounted by the model. Also for CO_2 flux, a short period of half hourly data is shown in Fig. 6.

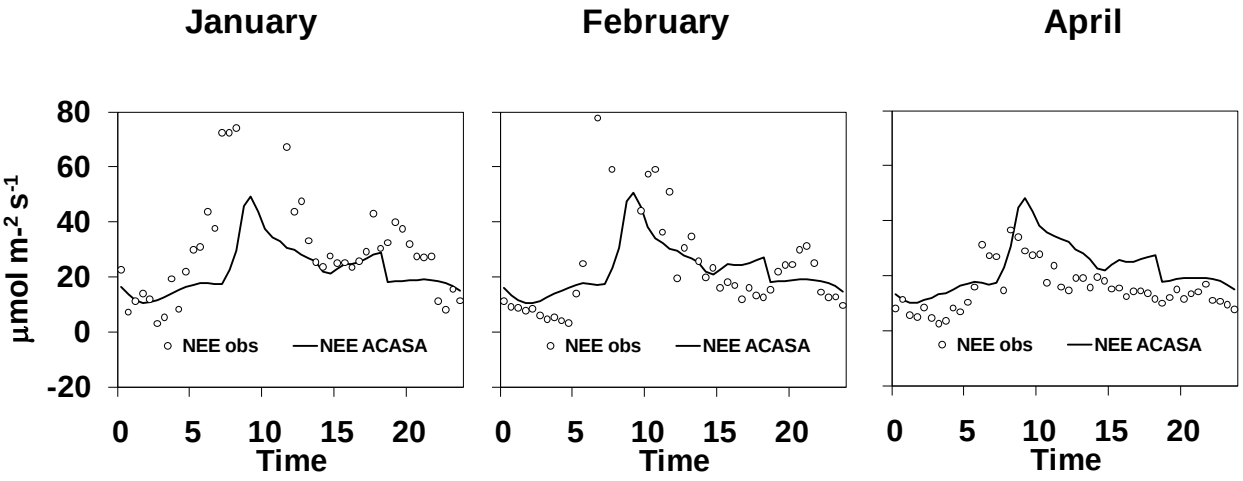

Figure 5. Comparison between simulated (solid line) and observed (dots) net ecosystem exchange (NEE). Data are sorted by time and averaged.

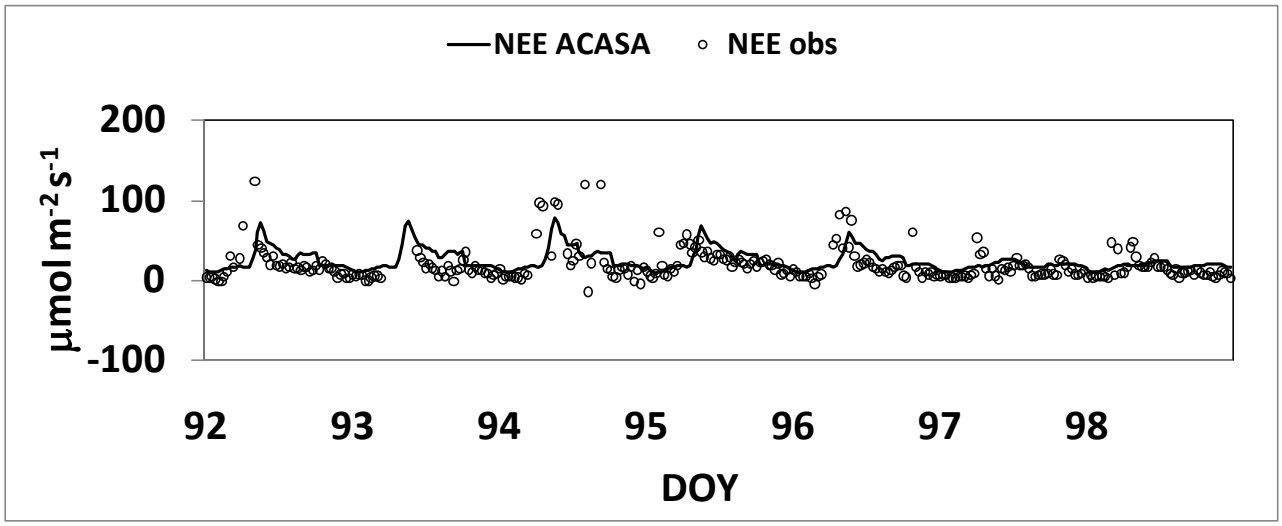

Figure 6. Comparison between half-hourly simulated (solid line) and observed (dots) net ecosystem exchange (NEE) during a week in April.

Even if there were not measured data for model comparison, ACASA was run for the period May-December 2008 and net radiation, sensible heat, latent heat, and CO_2 flux were estimated. In Fig. 7 are reported fluxes for the month of August, typically showing the increase in sensible heat flux values and the decrease of CO_2 flux during the summer (see the smoothed line with not evident peaks due to traffic).

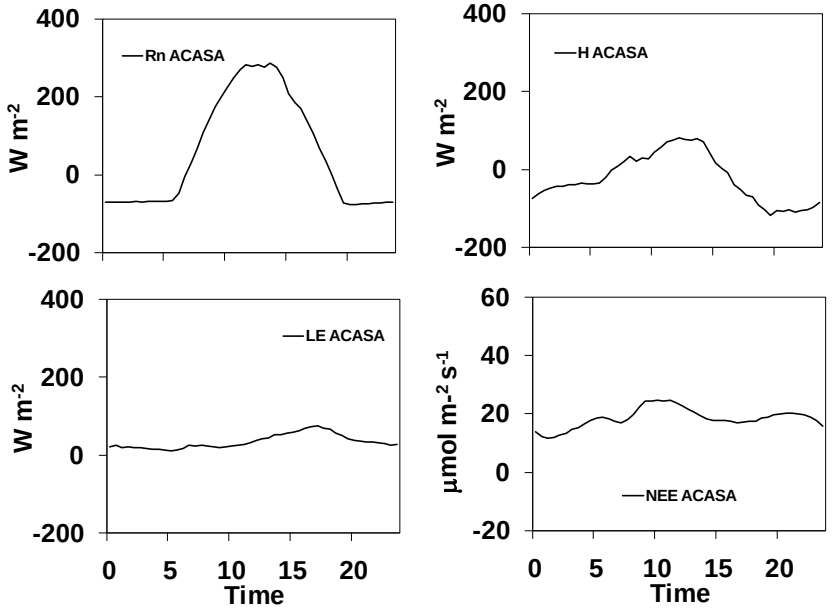

Figure 7. Simulated fluxes of net radiation (Rn), sensible heat (H), latent heat (LE), and net ecosystem exchange (NEE) during August 2008. Data are sorted by time and averaged.

Statistical analyses was made by calculating the root mean squared error (RMSE) and the relative error (%) of half-hourly data per sensible, latent, and CO_2 flux during the period January- April 2008. Values are reported in Table 1. Errors are generally low and the differences in simulated and observed data are not statistically significant at 95 % confidence level. A more detailed analyses is necessary to better investigate on the small differences between modeled and measured data.

Anyway, these results confirm the reliability of the ACASA model in simulating energy and mass fluxes over urban area.

Table 1. Root mean squared error (RMSE) and relative error (%) per sensible, latent and CO_2 flux during the period January-April 2008.

Flux	**Range**	**RMSE**	**Relative Error (%)**	**N**
H (Wm^{-2})	294	52	17	1302
LE (Wm^{-2})	459	30	6	1915
NEE ($mmolm^{-2}s^{-1}$)	312	26	8	1846

Annex 2 - Athens case study in situ measurements

1. Urban meteorology

authors: M. Laskari, A. Synnefa, M. Santamouris

1.1 Tower based measurements

The meteorological data used in this analysis were retrieved from the Thission meteorological station of the National Observatory of Athens. The station is located on a hill in the center of Athens (Latitude = 37°58.3/N, Longitude = 23°43/E and altitude = 107 m.) very close to Egaleo, the case study area. The meteorological station site is characterized by some vegetation and it is surrounded by a dense urban area presenting a high anthropogenic heat, and some relatively open spaces.

Hourly data for the following meteorological parameters were taken from the Thission meteorological station:

- Air temperature (^{o}C)
- Relative humidity (%)
- Wind speed (m/s)
- Wind direction (deg)
- Precipitation (mm)
- Diffuse solar radiation (W/m2)
- Total solar radiation (W/m2)
- Sunshine duration (hours)
- Air pressure (hPa)

The data cover the entire year of 2009.

Information on instruments and monitoring procedures

Dry bulb temperature is monitored with electronic Pt-100 thermometers housed in a Stevenson screen at 1.5m above ground level.

Relative humidity is calculated from the readings of dry and wet bulb thermometers (August psychrometer).

Wind velocities between 0 and 0.3 m/s are considered as calms, while the (-) symbol indicates missing data. Wind measurements are taken at 10 m above ground level.

Total precipitation is measured with standard raingauges. The total amount and the highest recorded value are obtained for a nominal day (24 hours) that begins and ends at 0800 LST.

Diffuse illuminance is measured with an Eppley pyranometer on a horizontal surface but is not corrected for shadow-ring effect.

Total illuminance is measured with an Eppely pyranometer on a horizontal surface.

Atmospheric pressure is recorded through mercury barometers and barographs and refers to sea level.

Figure 1 Monitoring instruments of Thissio meteorological station a) instruments for the measurement of global, UV and IR radiation on a horizontal surface, b) Kipp and Zonen Pyranometer for the measurement of Total solar radiation on an inclined surface, facing South, c) instrument for the measurement of Total and Diffuse solar radiation on a horizontal surface, d) A'Class Meteorological and Actinometric Station of NOA/IERSD, e) Eppley pyranometer and Eppley shadow rings for the measurement of Diffuse solar radiation (Source: NOA/IERSD)

2 Solar radiation

Due to its climate and geographical location, Athens has high solar radiation levels and sunlight availability throughout the year (

Figure 2). As shown in Table 1, in 2009 sunshine was available for a total of 2834 hours. The shorter days occurred in January with a total of 102.5 hours and the longer days occurred in July with a total of 386 hours of sunshine.

As shown in Figure 3, during summer, total solar radiation levels are at their highest and diffuse solar radiation levels are significantly low due to limited cloud cover. During spring and in September, total solar radiation levels are lower than in summer, but still considerably high. However, diffuse solar radiation levels are higher due to more cloud cover. The lowest solar radiation levels occur in December when the sun is at its lowest angle and the highest in June when the sun is at its highest angle (Figure 3).

3 Temperature

For Athens the coldest month of the year is February and the hottest month July. For these months the average temperature in 2009 was 9.7 ^{o}C and 29.3 ^{o}C, respectively. The lowest temperature of the year was 2.3 ^{o}C and the highest 39.8 ^{o}C (Table 2). The yearly average temperature was 18.9 ^{o}C. As shown in Figure 4, almost 90% of the hourly temperatures were below 20 ^{o}C from October through April while almost 80% were over 20 ^{o}C from May through September. Diurnal variation is greater in summer than it is in winter (Figure 5). For the colder months it is around 4 ^{o}C and for the warmer months around 8 ^{o}C. Figure 6 shows the monthly daily temperature profile.

4 Relative Humidity

For Athens the most humid season is winter while the driest is summer. The lowest relative humidity value recorded for year 2009 was 18/% and occurred in July. The highest recorded value was 97% and was recorded both in February and in March (Table 3). The yearly average relative humidity was 63%. Figure 8 shows the monthly daily relative humidity profile.

5 Wind

Wind directions for Athens are fairly consistent with the dominant wind direction being from the North-East (Figure 9). As shown in Figure 10 higher wind speeds occur for the warmer months (May through September) and come mainly from the North-East (Figure 11). The average wind velocity for 2009 was 3 m/s.

6 Precipitation

As shown in Figure 12 Athens has limited to no precipitation in summer. The wettest period of the year is September through March. For year 2009 the total precipitation was 566 mm. The wettest month was December with 112 mm and the driest was August with 0 mm of rainfall (Table 4).

7 Atmospheric pressure

The yearly average atmospheric pressure for 2009 was 1001.7 hPa. Although no clear seasonal variation is observed in the atmospheric pressure values, Figure 13 suggests that atmospheric pressure is more stable during warmer months.

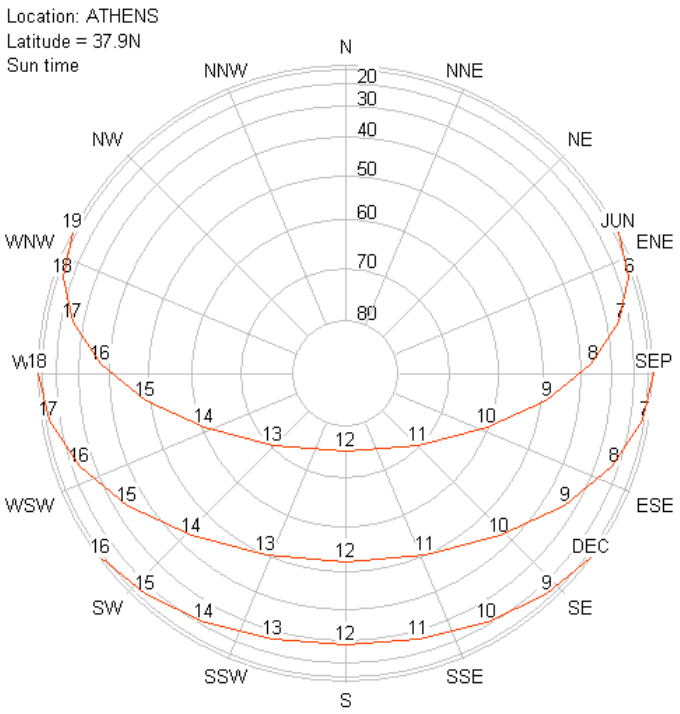

Figure 2 Athens sunpath diagram

Table 1 Monthly sunshine duration and maximum total solar radiation for year 2009

Month	Sunshine Duration (hours)	Maximum total solar radiation (W/m2)
Jan	102.5	701
Feb	146.4	744
Mar	197.9	908
Apr	214.0	1008
May	312.1	1008
Jun	365.6	1050
Jul	386.0	1024
Aug	366.8	1022
Sep	239.1	916
Oct	191.6	766
Nov	206.4	597
Dec	105.4	506
TOTAL	**2833.6**	

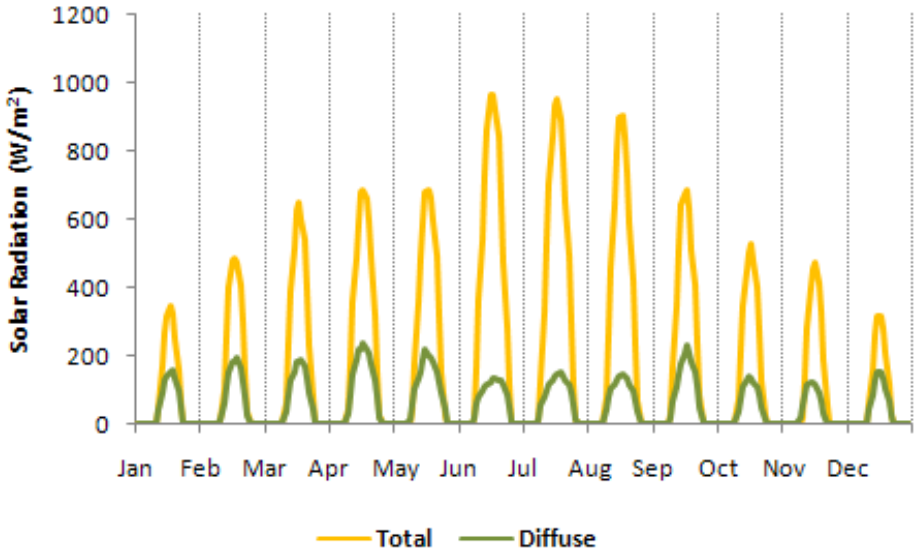

Figure 3 Monthly 24-hour profile for direct and diffuse solar radiation for year 2009

Table 2 Monthly absolute maximum and minimum and average temperatures for year 2009

Month	Jan	Feb	Mar	Apr	May	Jun	Jul	Aug	Sep	Oct	Nov	Dec
max T (oC)	18.8	18.6	24.8	25.1	34.5	39.2	39.8	36.9	33.8	30.7	23.4	20.4
average T (oC)	11.3	9.7	12.2	16.2	21.9	26.4	29.3	28.1	22.8	19.5	15.5	13.6
min T (oC)	3.8	2.3	4.2	9.4	11.7	18.8	20.8	21.4	14.8	9.7	9.1	6.3

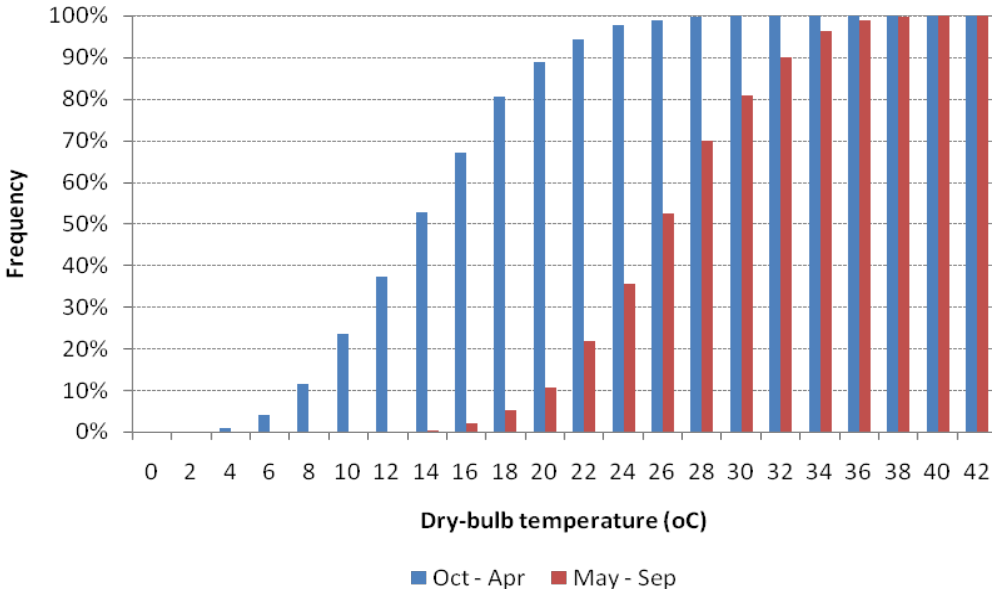

Figure 4 Cumulative frequency distribution of temperature for the warmer months (May to September) and for the colder months (October to April) for year 2009

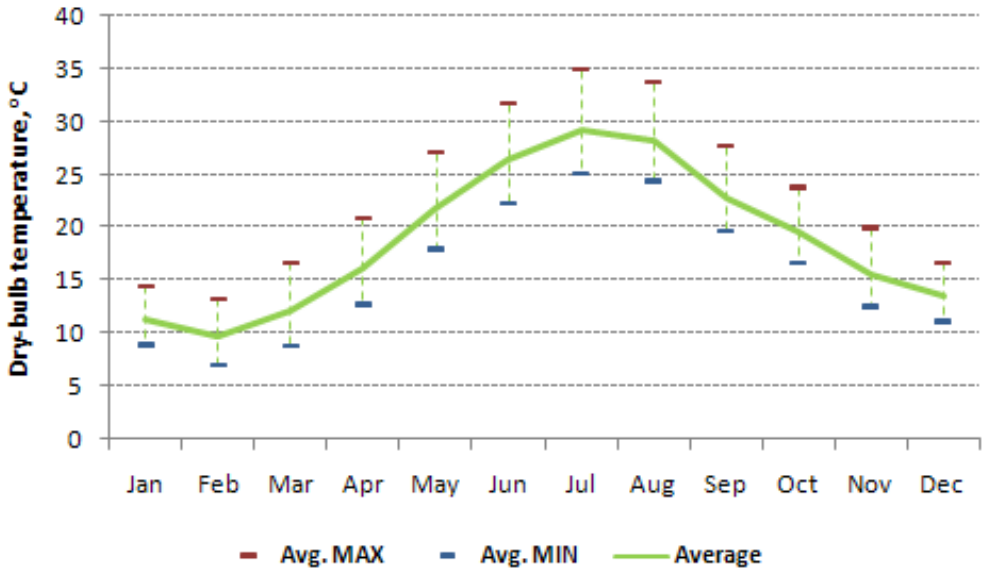

Figure 5 Monthly maximum, minimum and average temperatures for year 2009

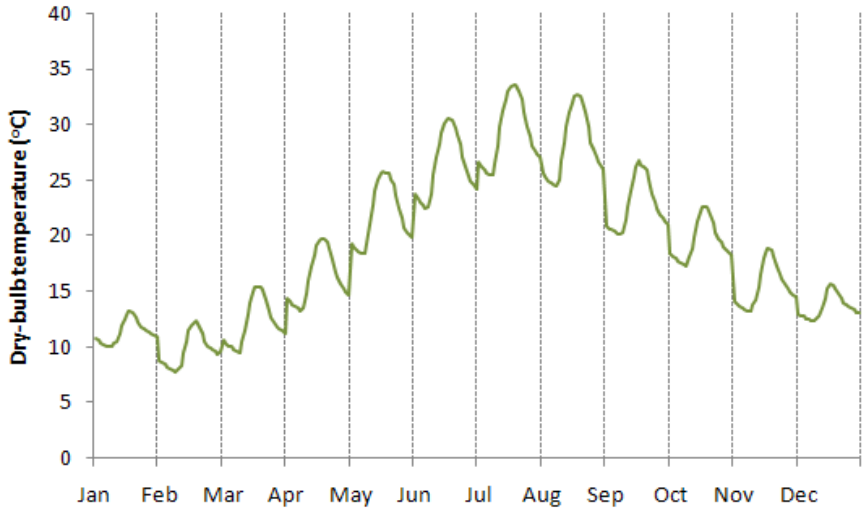

Figure 6 Monthly 24-hour profile for average temperature for year 2009

Table 3 Monthly absolute maximum and minimum and average relative humidity for year 2009

Month	Jan	Feb	Mar	Apr	May	Jun	Jul	Aug	Sep	Oct	Nov	Dec
max RH (%)	96	97	97	93	90	86	81	73	95	95	95	96
average RH (%)	76	69	67	62	56	51	45	45	63	70	73	78
min RH (%)	53	39	31	34	28	20	18	24	34	30	42	46

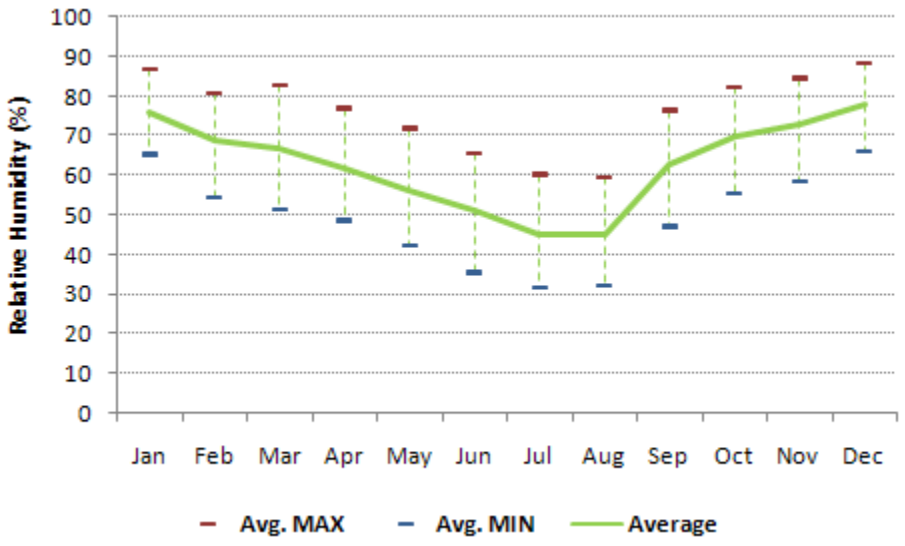

Figure 7 Monthly maximum, minimum and average relative humidity for year 2009

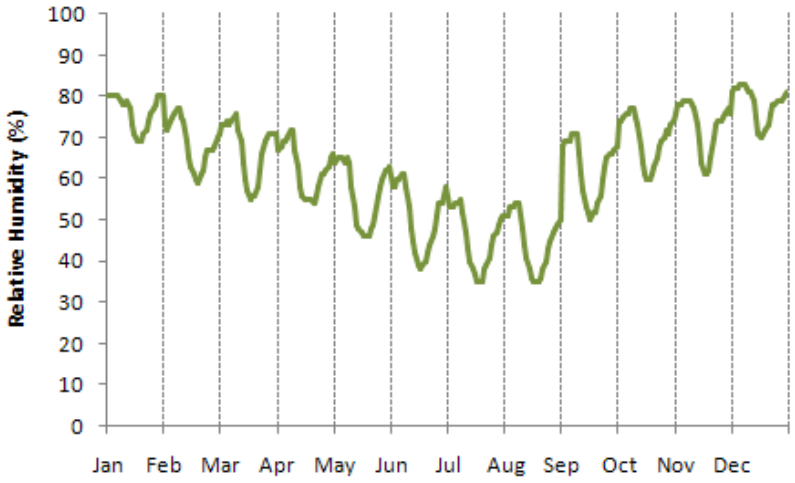

Figure 8 Monthly 24-hour profile for average relative humidity for year 2009

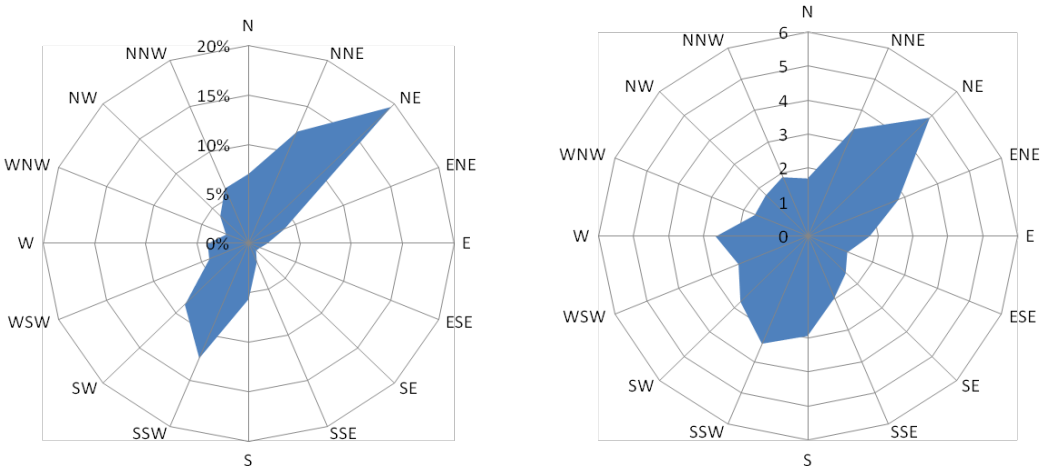

Figure 9 Wind rose of a) frequency and b) wind velocity for year 2009

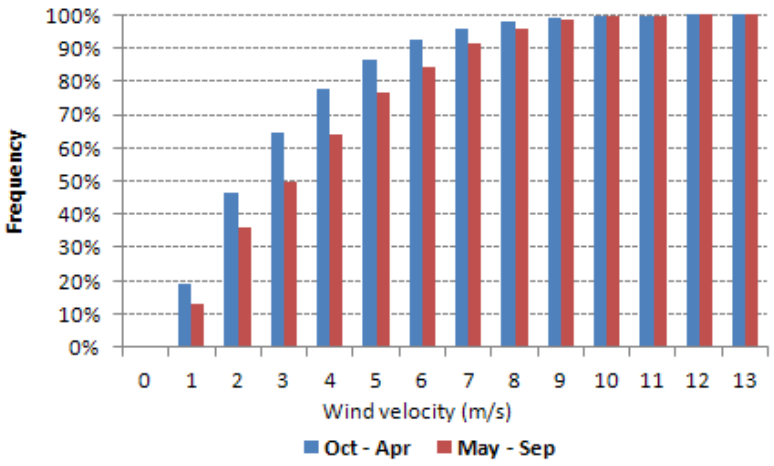

Figure 10 Cumulative frequency distribution of wind velocity for the warmer months (May through September) and for the colder months (October through April) for year 2009

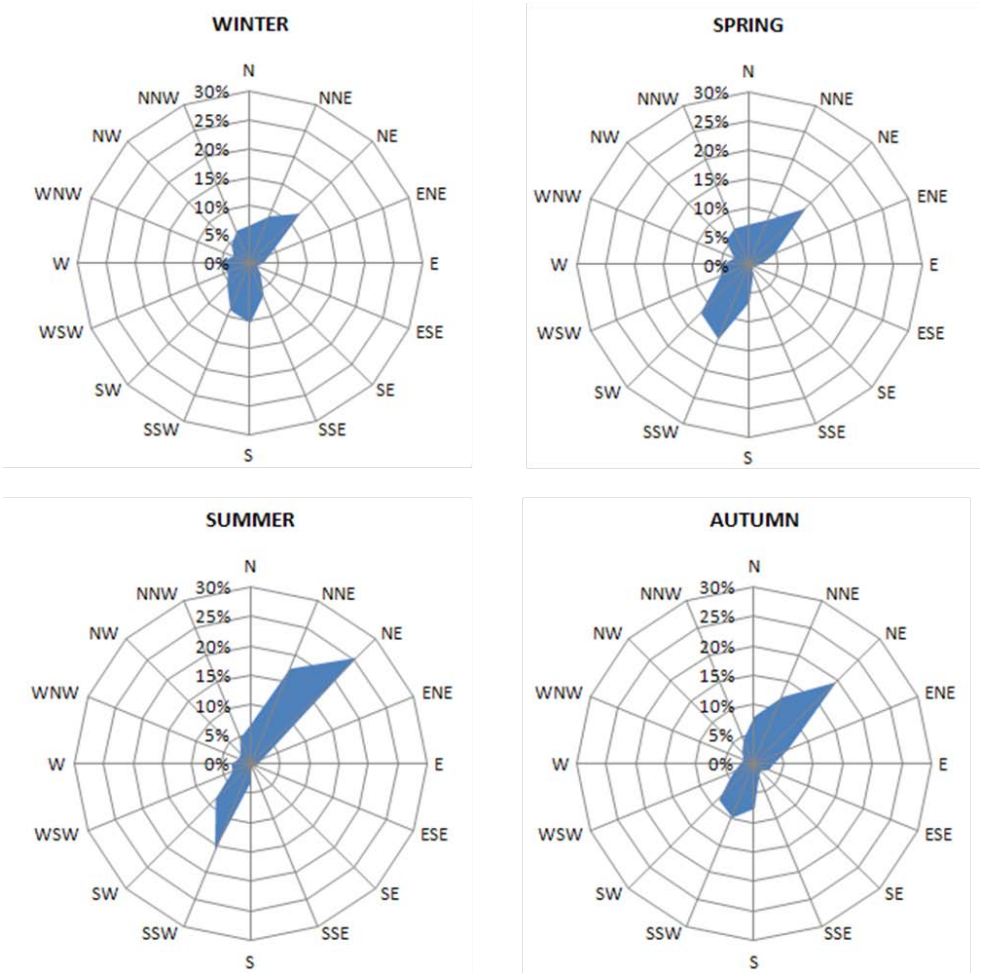

Figure 11 Wind rose of frequency for the four seasons for year 2009

Table 4 Monthly precipitation for year 2009

Month	Jan	Feb	Mar	Apr	May	Jun	Jul	Aug	Sep	Oct	Nov	Dec	Total
Precipitation (mm)	80	45	90	32	4	1	2	0	80	74	46	112	566

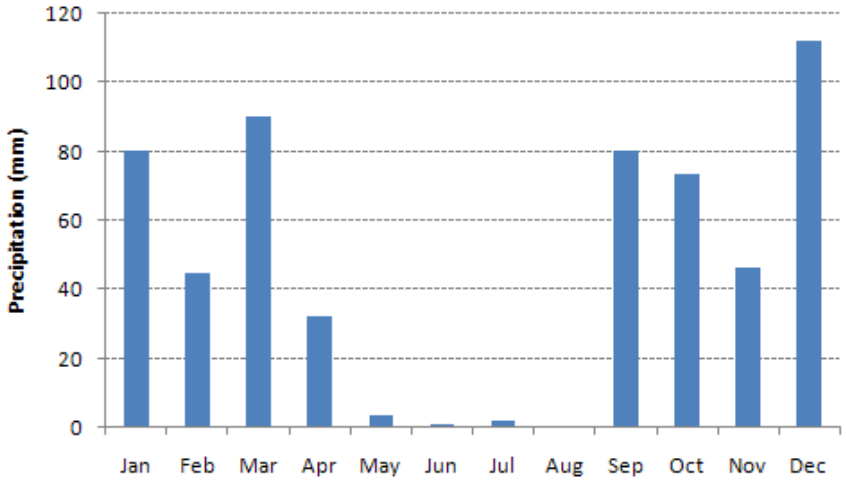

Figure 12 Monthly precipitation for year 2009

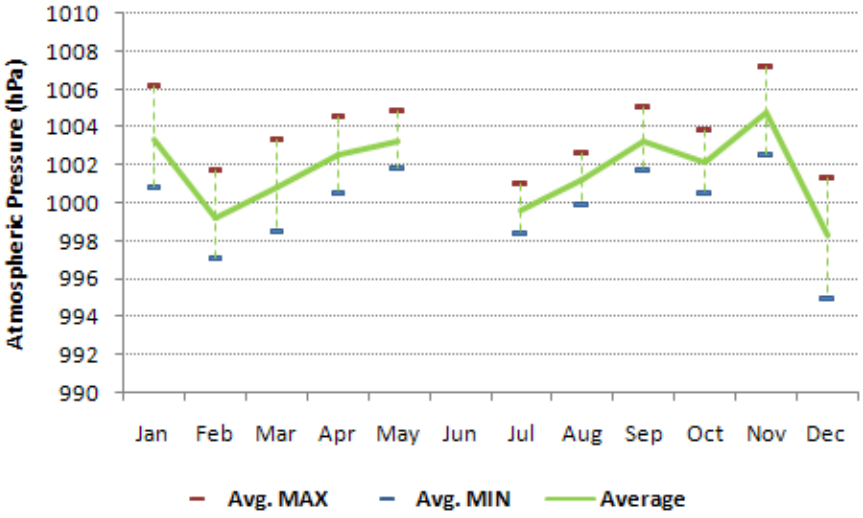

Figure 13 Monthly maximum, minimum and average atmospheric pressure for year 2009

Table 5 Monthly absolute maximum and minimum and average atmospheric pressure for year 2009

Month	Jan	Feb	Mar	Apr	May	Jun	Jul	Aug	Sep	Oct	Nov	Dec
max P (hPa)	1021.4	1008.5	1011.2	1011.3	1009.4		1005.7	1005.7	1012.7	1009.3	1016.8	1011.3
avg. P (hPa)	1003.4	999.2	1000.8	1002.5	1003.3		999.6	1001.2	1003.3	1002.1	1004.8	998.3

min P (hPa)	982.1	987.6	981.4	991	994.9		992.8	993.9	992.3	990.2	983.2	984.6

2. Air Quality

authors: A.Synnefa, M. Laskari, M. Santamouris

2.1 Urban air quality

The air quality data used in this analysis were retrieved from the Directorate of Air Pollution & Noise of the Greek Ministry of Energy, Environment and Climate Change. This Directorate is responsible for the operation of a network of stations installed in the greater Athens area that measure air pollution (Figure 14).

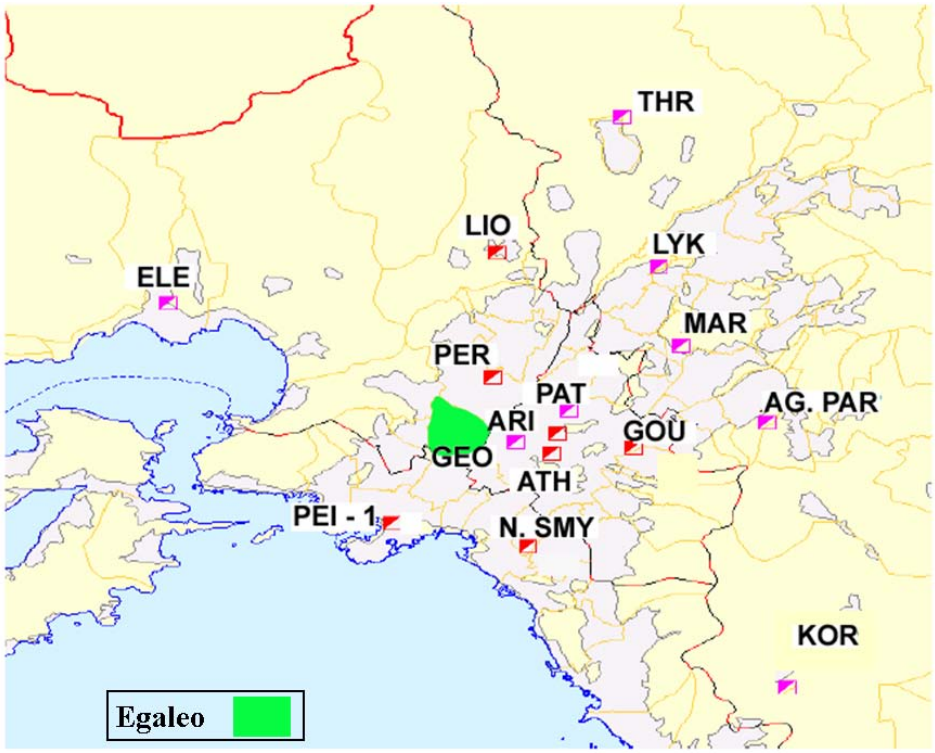

Figure 14 Air pollution measurement stations for the greater Athens area.

For the purposes of this report only data from the 6 stations considered the closest to the Egaleo area were analysed (Table 6). The data cover the entire year of 2009.

Table 6 Air pollution monitoring stations closest to the Egaleo area

Station	Measured Pollutants

Location				Characterization	SO_2	NOx	CO	O_3	PM10	PM2.5	C_6H_6
Name	Long.	Lat.	Alt.								
Athinas (ATH)	23° 43' 30"	37° 58' 42"	100	Urban-Traffic	√	√	√	√			
Aristotelous (ARI)	23° 43' 39"	37° 59' 16"	95	Urban-Traffic		√			√		
Geoponiki (GEO)	23° 42' 25"	37° 59' 01"	50	Suburban-Industrial	√	√	√	√			
Patision (PAT)	23° 43' 59"	37° 59' 57"	105	Urban-Traffic	√	√	√	√			√
Peiraias (PEI-1)	23° 38' 51"	37° 56' 36"	20	Urban-Traffic	√	√	√	√	√	√	
Peristeri (PER)	23° 41' 46"	38° 00' 55"	80	Urban-Background	√	√	√	√			

Measured pollutants

The measured pollutants and corresponding measurement methods are listed in Table 7. The measurements are conducted on a constant basis throughout the day. The response time of the automatic analyzers is one minute, meaning that approximately one value is given every minute by each analyzer. A microprocessor is located in every automatic station and is connected to the automatic analyzers. Through this microprocessor the hourly average values for pollution are calculated every hour. These values are transferred to the central computer of the Authority via phone line. In this way, the constant monitoring of the atmospheric pollution levels of the area is achieved.

Table 7 Measured pollutants and measurement methods

Pollutant	Measurement method
Carbon monoxide (CO)	Infrared absorption (NDIR)
Nitrogen oxides (NO, NO_2)	Chemiluminescence
Ozone (O_3)	UV absorption
Sulphur dioxide (SO2)	Fluorometry
Particulate matter (PM10 - PM2.5)	Beta radiation absorption[1]
Benzene (C_6H_6)	Gas chromatography (GC)

Calibration of automatic analyzers (particulate matter not included)

Calibration includes the checking of good instrument operation and regulation. It is based on the transfer of a gas with a pollutant of known concentration, through the instrument. The preparation of this standard gas, involves the use of a dynamic dilution apparatus that is connected to a "clean" air source and the use of a bottle containing a mixture of nitrogen gas at a known standard concentration. This "clean" air is free of main pollutants and is produced by sending air through special filters that remove pollutants. By changing the provision of "clean" air and bottled gas, it is possible to achieve gas mixtures that contain the corresponding pollutant at known concentrations. This process of calibration is performed in regular intervals and after maintenance or repair of an analyzer.

Monthly variation of the pollutants' concentration for year 2009

In Figure 16 the monthly variation of pollutants is illustrated for stations close to the Egaleo area. From this figure it is observed that for CO, NO, SO2, C6H6 and PM10 the concentration values are higher during winter months. For SO2 this is due to the operation of central heating, while for CO it is due to the increased traffic occuring during the winter months and to the bad condition of the car engines (start with cold engine). Even though benzene is a volatile hydrocarbon, it presents higher values during winter for the same reasons as CO, while during summer the lower values occur due to reduced traffic and because part of the benzene is destroyed from participating in photochemical reactions. The secondary pollutant, ozone (O_3), presents higher values during the summer period, while nitrogen dioxide (NO_2) does not present any significant variation during the year. PM2.5 concentrations are higher in the summer months while PM10 values are higher during winter months (natural and anthropogenic). The increased concentrations of secondary pollutants and mainly O3 during the summer months are a result of the increased sunshine duration and intensity, since solar radiation plays a defining role in its formation (photochemical procedure).

Daily variation of the pollutants' concentration for year 2009

As shown in Figure 17 all pollutants, apart from O3, present in a smaller or greater extent, a reduction during the weekend, clearly stating the impact of human activities on air quality.

Hourly variation of the pollutants' concentration for year 2009

As shown in Figure 18, the highest values for the primary pollutants CO, SO2, NO, NO2 and C6H6 occur between 8-10am (peak morning hours) and between 9-11pm (evening hours). This is attributed to the fact that during these hours the meteorological conditions are favorable for the buildup of atmospheric pollutants but also to the fact that they coincide with the central heating operation hours and with peak traffic. The daily peak value for ozone, O3, occurs during the mid-day hours, when the solar radiation and ambient temperature are at their highest.

Comparison of atmospheric pollution values with limit values for year 2009

Particulate matter (PM10)

Exceedings for particulate matter involve the daily average and yearly average values (Table 11).

The average values recorded for year 2009 close to Egaleo are summarized below. Colored in red are the values that exceeded the limit value, while in brackets appears the estimated contribution from dust transport (in μg/m3) from remote arid areas (i.e. the Sahara) to the average value of the measured PM10 concentration.

Table 8 Yearly PM10 values (in μg/m3) and days of daily average value exceedance for year 2009

	PEI-1	ARI
Yearly average value (μg/m3)	35 (3)	49 (4)
Days of daily average exceedance	30	122

Sulphur dioxide (SO2)

The exceedings for sulphur dioxide involve the hourly average and the daily average values (Table 12).

No exceedance of the hourly average value occurred at any station for year 2009.
No exceedance of the daily average value occurred at any station for year 2009.

Nitrogen dioxide (NO2)

The exceedings for nitrogen dioxide involve the yearly average and the hourly average values (Table 13).

The incidences of exceedance of the indicative yearly limit values close to Egaleo for year 2009 are highlighted in red the following table.

Table 9 Comparison between yearly NO2 values (μg/m3) and the corresponding indicative limiting value

Station	2009 (indicative limiting value 42 μg/m3)
Athinas (ATH)	66
Aristotelous (ARI)	41
Geoponiki (GEO)	46
Nea Smyrni (N. SMY)	33
Patision (PAT)	91
Peiraias (PEI-1)	71
Peristeri (PER)	43

In year 2009 the indicative average value (210 μg/m3) was exceeded more than 18 times at the Patision station. Specifically, the indicative value was exceeded 20 times at this station.

Ozone (O3)

The limit values for Ozone are summarized in Table 14.

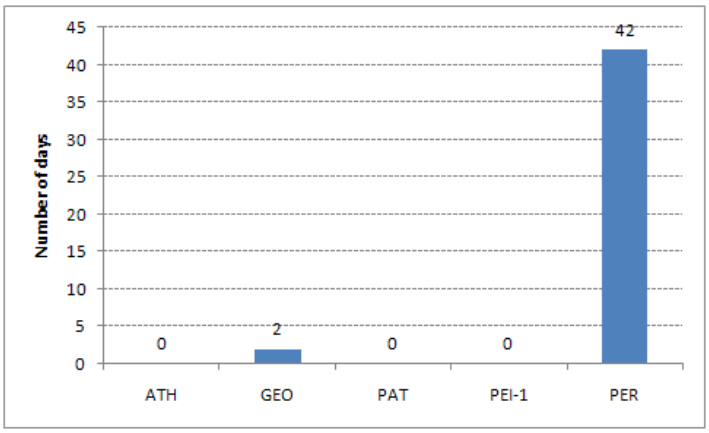

Figure 15 Number of days for year 2009 with O3 hourly value greater than 180 μg/m3

Figure 15 summarizes the number of hours for which the warning threshold for O3 was exceeded at the stations closest to Egaleo.
In the following Table the dates and duration (in hours) of the alert threshold (240 μg/m3) exceedance close to Egaleo are summarized. It is noted that for emergency measures to be taken the alert threshold should be exceeded for three consecutive hours.

Table 10 Dates and duration of the alert threshold exceedance (in hours) per station for year 2009

Station	2009	
	date of exceedance	duration of exceedance (hours)
Peristeri (PER)	4\8	2

Carbon monoxide (CO)

The limit value for Carbon Monoxide is given in Table 15.

No exceedance of carbon monoxide occurred for year 2009.

Benzene (C6H6)

The limit values for Benzene are summarized in Table 16.

The limit value for benzene came into effect on 1/1/2010. Until then the indicative limit values were reduced gradually every year to meet the 2010 value.
No exceedance of the indicative limit value occurred for year 2009.

Evaluation of the atmospheric pollution in the Egaleo area

By comparing the concentrations of measured pollutants with the atmospheric pollution limits in force in year 2009 and with the indicative limit values determined for by the European Commission Directives, it has been found that exceeding of the limit occurred for certain pollutants, in locations close to the Egaleo area. For year 2009, the condition of atmospheric pollution per pollutant around the Egaleo area formed as follows:

- **Particulate Matter, PM10:** PM10 pollutants exceeded limits at a number of measurement stations. These pollutants are a problem for the majority of Member States.
- **Sulphur Dioxide, SO_2:** This pollutant had been a problem in previous years, but has now been combated and does not exceed limits at any measuring location.
- **Nitrogen Dioxide, NO_2:** Nitrogen dioxide presented exceedings of the indicative yearly average value. If these values are not reduced there will be further exceedings of the limit values that apply as from January 1st 2010.
- **Ozone, O_3:** Exceedings of the warning threshold as well as of the alert threshold occurred close to Egaleo suggesting an occurrence in Egaleo as well. These exceeding are due mostly to the geographical location of the country (high levels of sunshine and high temperatures are conditions that favor the formation of ozone) and are common for all Southern European countries.
- **Carbon Monoxide, CO:** No exceedance of the limit value was recorded for this pollutant.
- **Benzene, C_6H_6:** No exceedance of the indicative limit value was recorded. If these values are not reduced, there will be exceedance of the limit values that will apply from January 1st 2010.

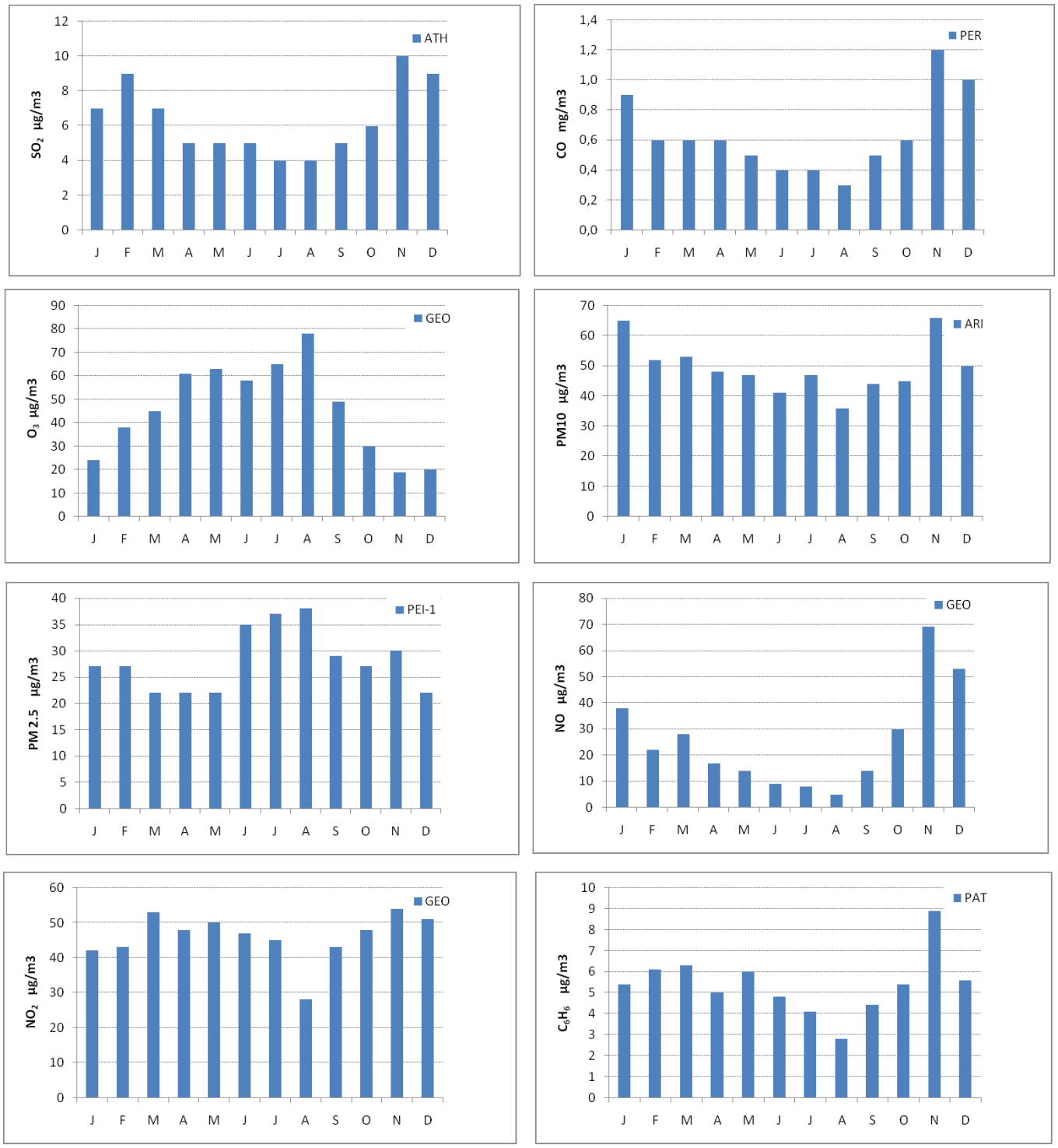

Figure 16 Monthly average air pollutant values close to Egaleo

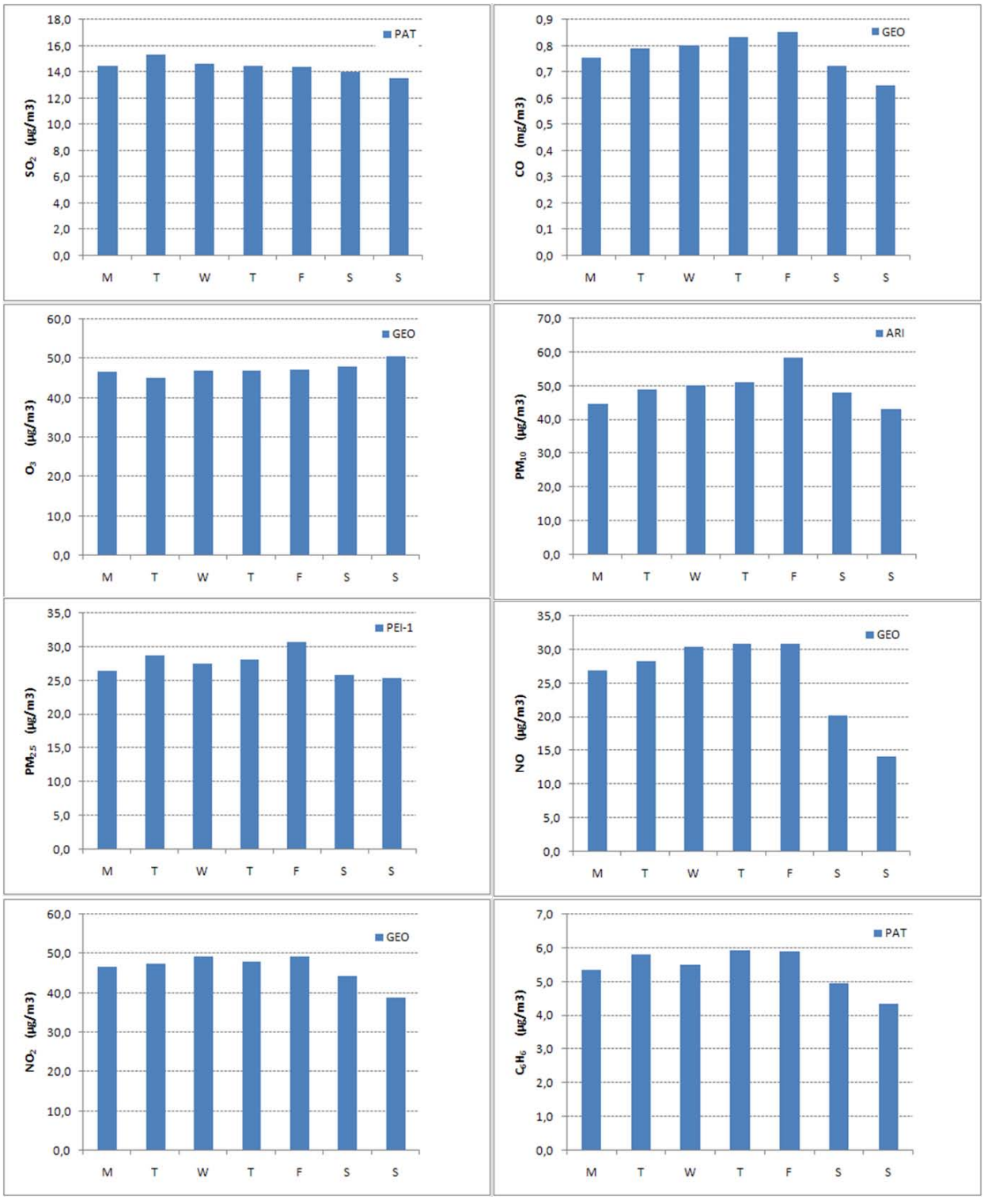

Figure 17 Daily average air pollutant values close to Egaleo

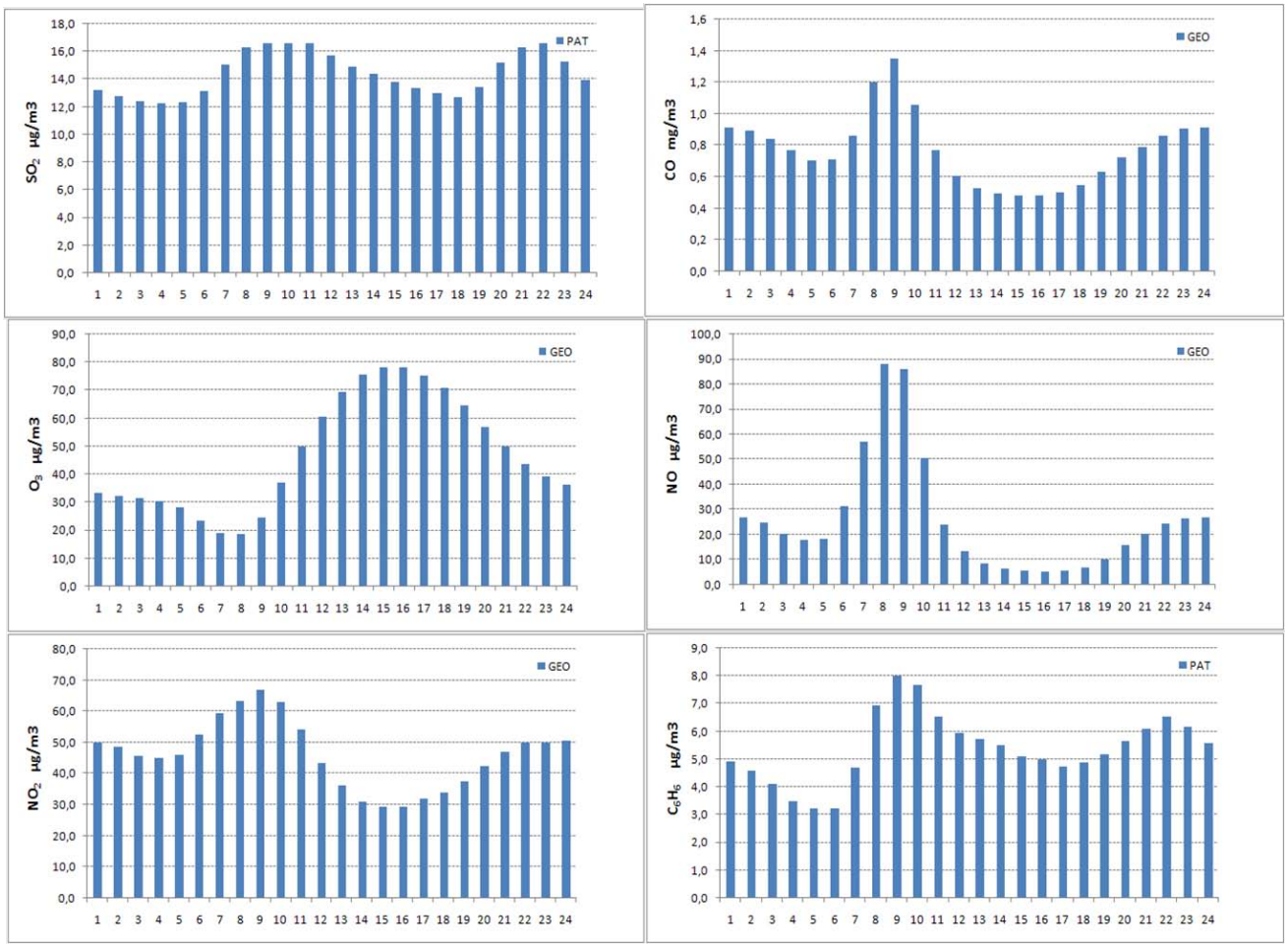

Figure 18 Hourly average air pollutant values close to Egaleo

Table 11 Limit values for Particulate Matter (PM10)

	Limit value
Daily average value, not to be exceeded for more than 35 times in one year	**50 µg/m^3**
Yearly average value	**40 µg/m^3**

Table 12 Limit values for Sulphur Dioxide (SO2)

	Limit value

Hourly average value, not to be exceeded for more than 24 times in one year	**350 µg/m^3**
Daily average value, not to be exceeded for more than 3 times in one year	**125 µg/m^3**

Alert threshold	Hourly value greater than **500 µg/m^3** for 3 consecutive hours

Table 13 Limit values for Nitrogen Dioxide (NO2)

	Indicative Limit values (2009)
Hourly average value, not to be exceeded for more than 24 times in one year	**210 µg/m^3**
Daily average value, not to be exceeded for more than 3 times in one year	**42 µg/m^3**

Alert threshold	Hourly value greater than 40**0 µg/m^3** for 3 consecutive hours

Table 14 Limit values for Ozone (O3)

		Limit value
Warning threshold	**Hourly average value**	**180 µg/m^3**
Alert threshold	**Hourly average value**	**240 µg/m^3**
Target value for the protecion of human health. Valid from year 2010	**Maximum daily 8-hour value**, not to be exceeded for more than 25 times per year for a time interval of 3 years	**120 µg/m^3**

Table 15 Limit values for Carbon Monoxide (CO)

	Limit value
Maximum daily 8-hour value	**10 mg/m^3**

Table 16 Limit values for Benzene (C6H6)

	Indicative Limit values		Limit value
	2008	2009	2010
Yearly average value	7 µg/m^3	6 µg/m^3	5 µg/m^3

3 Heat island measurements

authors: M.Laskari, K. Giannopoulou, A. Synnefa, M. Santamouris

3.1 Heat island measurements

In order to study the heat island phenomenon in the greater Athens city area, data were retrieved from 17 fixed temperature stations. These stations were located in four different zones grouped into Western, Eastern, Southern and Northern zone stations according to their geographical location and thermal balances (Table 17). The Nea Erythrea station, was selected as reference station because of the area's suburban characteristics (i.e. lower development density).

Figure 19 The Athens greater area with the Egaleo (case study area) and Nea Erythrea area (reference area)

In all stations the data were measured with fully calibrated high precision automatic miniature sensors, which were placed in white wooden boxes with lateral slots approximating the Stevenson screen to be protected for solar radiation and rain (Figure 20). Temperatures were measured at 15 minute intervals.

Figure 20 a) Miniature sensor (Source: Tinytag) and b)wooden box containing the sensors, used for air temperature measurements

Given that the heat island intensity is greater in the summer than it is in the winter the analysis for the greater Athens area focuses on July and August, the warmest months of year 2009. However, the analysis for the case study area, Egaleo, covers a larger time period, that of June through October, 2009.

3.1.1 Urban heat island for Egaleo area only

For the monitored period of June to October 2009, as shown in Figure 21, the daily average temperatures for Egaleo were constantly higher than those for Nea Erythrea, suggesting a heat island between the two areas. The mean heat island intensity for this period was 2 ^{o}C. For this period of time the temperature in Egaleo exceeded the temperature in Nea Erythrea for 91% of monitored hours. In fact the temperatures in Egaleo exceeded the temperatures in Nea Erythrea by more than 6 ^{o}C in 14 occasions and by more than 8 ^{o}C in 2 occasions. For the remaining 9% of monitored hours the temperatures in Nea Erythrea exceeded the temperatures in Egaleo by no more than 6 ^{o}C (Figure 22).

Figure 22 suggests that the heat island effect has a trend in reducing and in some occasions reversing as the temperature at the reference area increases. Also, as shown in Figure 23, the heat island intensity for the two areas is greater at late morning hours and after that reduces significantly until it reaches its minimum at late afternoon. Figure 28 suggests that for July and August the heat island was approximately 2.3 ^{o}C and 2.0 ^{o}C, respectively. As shown in Figure 23 the time of day most likely for the temperature in Nea Erythrea to exceed the temperature in Egaleo is at late afternoon. Nontheless, this phenomenon only lasts a few hours, as after sunset the heat island starts increasing to reach intensities slightly over 2 ^{o}C and stay at these levels until the next morning. In fact, while in Nea Erythrea only 1 hour with temperatures over 30 ^{o}C was recorded for July evenings (22:00 to 06:00), the corresponding number of hours recorded in Egaleo was 26 (Table 20).

July was the hottest month of 2009 for which on average the Egaleo area presented higher temperatures than Nea Erythrea (Figure 25). For this month the mean temperature for Egaleo was 29.3 ± 1.8 ^{o}C, while for Nea Erythrea it was 27,0 ± 2.0 ^{o}C. Also, the mean maximum temperature for July was 33,8 ± 2.4 ^{o}C and 32.4 ± 3.2 ^{o}C for Egaleo and Nea Erythrea, respectively. For

August, the second hottest month for 2009, Egaleo remained hotter than Nea Erythrea (Figure 26). The mean maximum temperature was 28.3 ± 1.3 °C for Egaleo and 26.3 ± 1.3 °C for Nea Erythrea, while the mean maximum temperatures were 32.5 ± 1.5 °C and 31.4 ± 2.6 °C, respectively.

3.1.2 Urban heat island fot the greater Athens area

As shown in Figure 25 and Figure 26 Nea Erythrea, the reference area, is the coolest of all Athens areas. In general, as shown in Figure 27, the Northern zone in which Nea Erythrea is located is the coolest geographical zone of the greater Athens area while the Southern is the hottest. The Western zone in which Egaleo is located is the second hottest geographical zone. Figure 24 gives the heat island intensity distribution in Athens for the 7th of July 2009, the day with the greatest daily average heat island intensity.

For July 2009 the mean temperature for the Southern zone was 29.8 ± 1.6 °C, while for the Western zone it was 29.6 ± 1.9 °C. Also, the mean maximum temperature for July was 35.0 ± 2.3 °C and 34.1 ± 2.4 °C for the Southern and Western zone, respectively. For August, the mean temperature for the Southern zone was 29.0 ± 1.2 °C, while for the Western zone it was 28.3 ± 1.3 °C, while the mean maximum temperatures were 34.6 ± 1.5 °C and 32,7 ± 1.7 °C, respectively.

Mean heat island intensity is also greater for the Southern zone than it is for the Western zone (Figure 29). For July 2009 mean heat island intensity was 2.7 °C for the Southern zone and 2.6 °C for the Western zone, while for August it was 2.7 °C and 2.2 °C, respectively. However, as shown in Table 20, the temperature of 30 °C was exceeded more times in the Western zone than in the Southern zone in July, suggesting that the temperatures over 30 °C for the Southern zone were much higher than those in the Western zone.

The coolest geographical zone is the Northern zone in which Nea Erythrea is located. For July 2009 the mean temperature was 28.3 ± 2.0 °C, while for August it was 27.2 ± 1.4 °C (Table 18). The mean maximum temperature was 33.4 ± 2.9 °C and 31.5 ± 2.1 °C for July and August, respectively (Table 19). As shown in Table 20 the temperature in the Northern zone rarely exceeds 30 °C in the summer evenings.

As shown in Figure 28 the heat island intensity is greater in July than it is in August for all stations except for three stations of the Southern zone: Elliniko, Glyfada and Renti. Also, even though the mean temperature is higher in July than it is in August as observed for all other stations, the mean maximum temperature is higher in August than it is in July, except for Glyfada station for which it is 0.2 °C lower (Table 18, Table 19). This behaviour could be related to the proximity of the Southern zone to the sea.

Table 17 Fixed temperature stations for the study of the Athens heat island per geographical zone

No.	Station	Latitude	Longtitude	Altitude (m)
Western zone				
1	Egaleo	37°59'50.40"N	23°40'4.29"E	58
2	Agia Varvara	37°59'22.58"N	23°39'36.70"E	62
3	Korydallos	37°58'44.84"N	23°38'32.82"E	85
4	Haidari	38° 0'44.42"N	23°39'34.40"E	108

5	Zefyri	38° 3'3.33"N	23°42'40.90"E	132
Eastern zone				
6	Agia Paraskevi	38° 0'50.34"N	23°49'27.79"E	220
7	Vyronas	37°57'24.21"N	23°45'44.23"E	172
8	Ilioupoli	37°55'57.37"N	23°45'30.88"E	162
9	Kessariani	37°58'8.95"N	23°45'42.44"E	147
Southern zone				
10	Elliniko	37°54'27.35"N	23°44'32.43"E	55
11	Glyfada	37°51'52.72"N	23°44'39.97"E	4
12	Kallithea	37°57'25.18"N	23°42'9.91"E	21
13	Moschato	37°57'12.44"N	23°40'55.58"E	4
14	Renti	37°57'45.94"N	23°40'27.88"E	8
Northern zone				
15	Kamatero	38° 3'34.80"N	23°42'50.66"E	130
16	Nea Filadelfia	38° 2'6.78"N	23°44'17.99"E	103
17	Nea Erythrea	38° 5'23.69"N	23°49'9.11"E	312

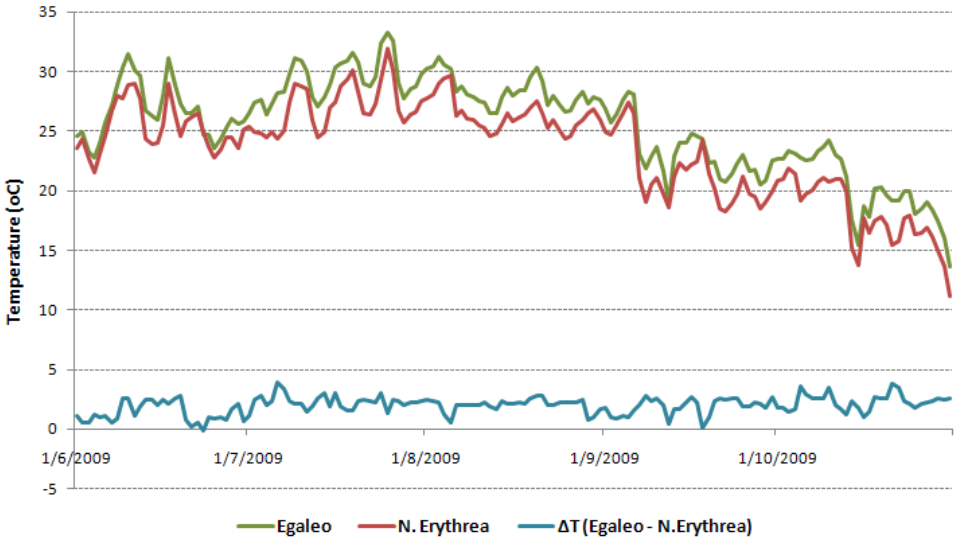

Figure 21 Daily average temperature distribution for the Egaleo and Nea Erythrea area and temperature difference, ΔT ($T_{Egaleo} - T_{N.Erythrea}$) for months June to October, 2009

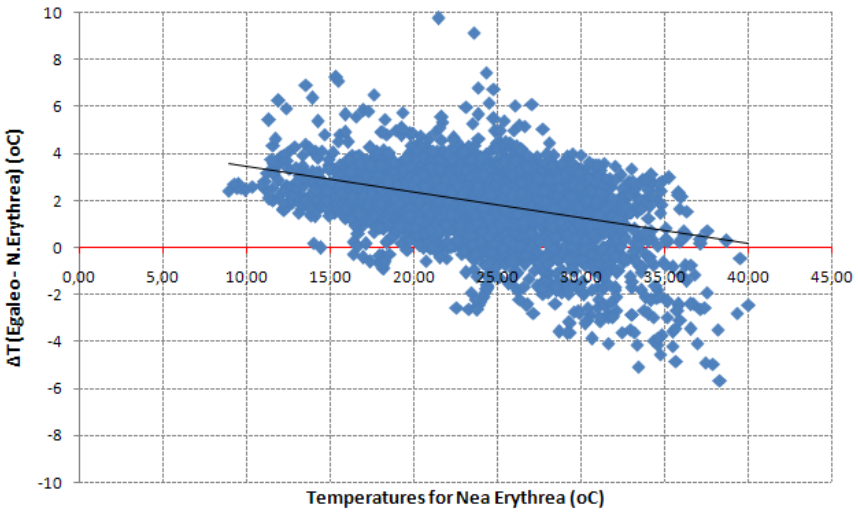

Figure 22 Hourly temperature difference between the Egaleo area (case study) and the Nea Erythrea area (reference) for months June to October, 2009

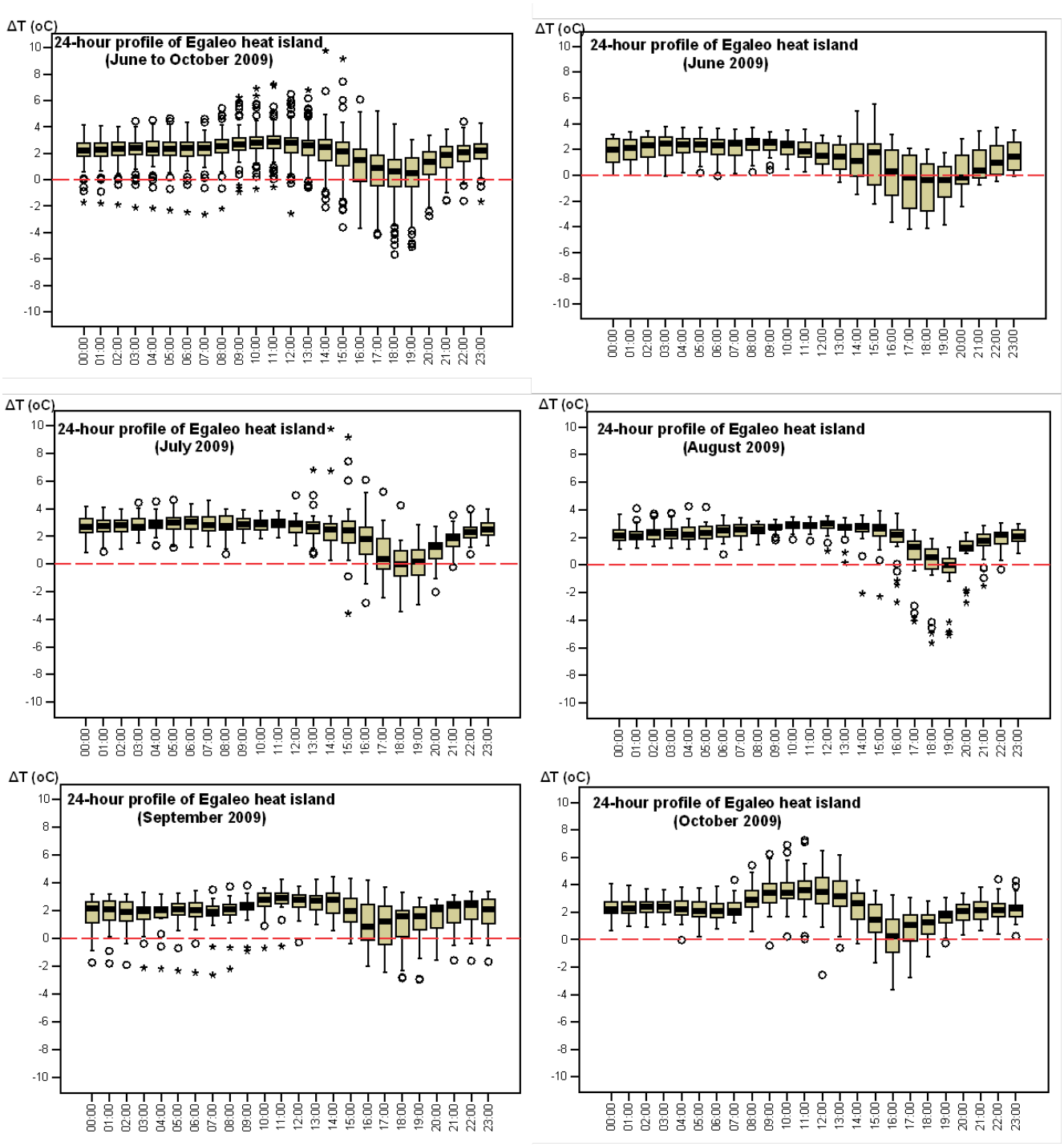

Figure 23 Hourly profile of Egaleo heat island (for June to October 2009)

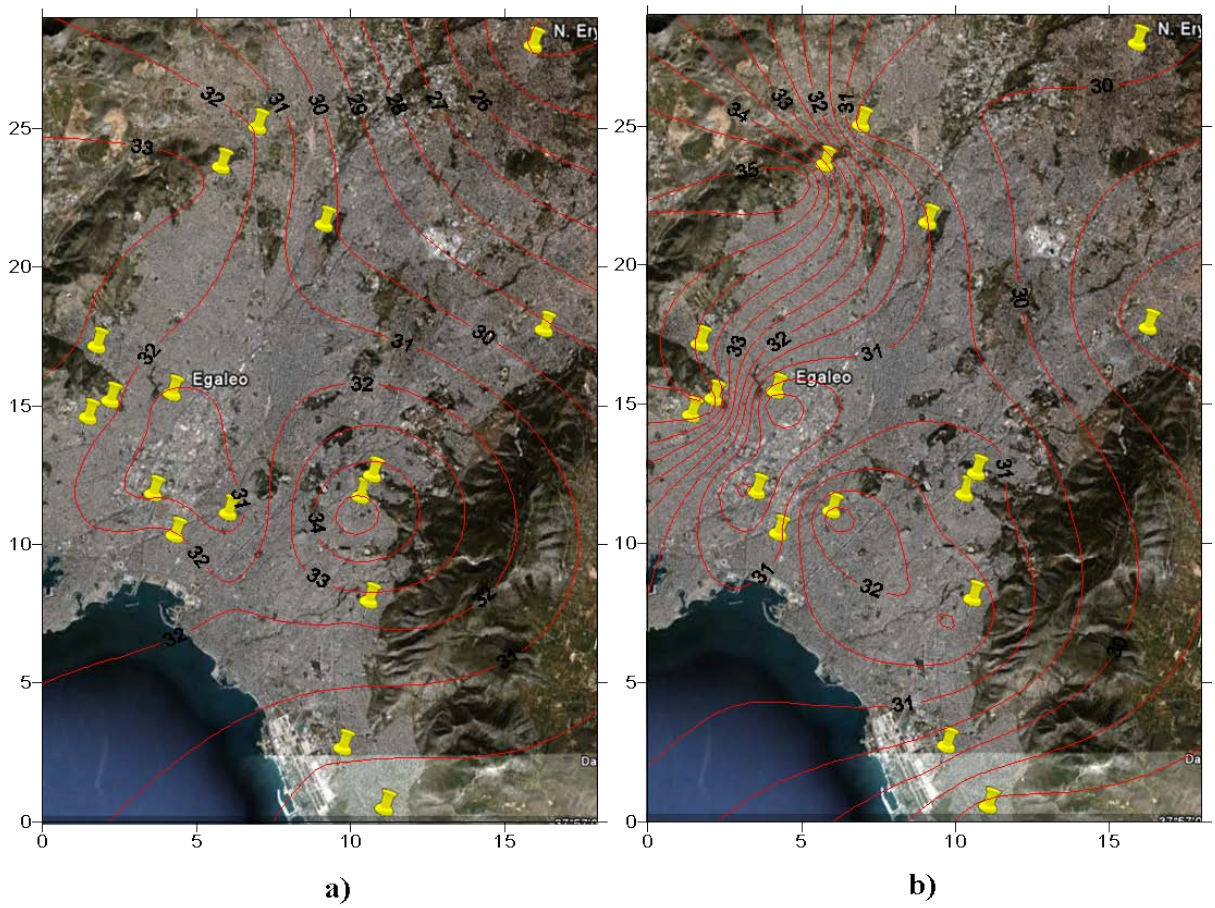

Figure 24 Heat island distribution in the greater Athens area on 7/7/2009 at a) 13:00 and b) 19:00

Table 18 Monthly mean and s.d. air temperature values for all stations for July and August, 2009

No.	Station	July	August
Western			
1	Egaleo	29,3 ± 1,8	28,3 ± 1,3
2	Agia Varvara	30,1 ± 1,8	28,3 ± 1,4
3	Korydallos	29,7 ± 1,8	28,1 ± 1,4
4	Haidari	29,5 ± 1,8	28,2 ± 1,3
5	Zefyri	29,2 ± 2,1	28,5 ± 1,2
	Mean	29,6 ± 1,9	28,3 ± 1,3
Eastern			
6	Agia Paraskevi	28,5 ± 1,8	27,7 ± 1,2
7	Vyronas	30,4 ± 1,9	29,4 ± 1,3

8	Ilioupoli	28,9 ± 1,8	27,4 ± 1,2
9	Kessariani	28,9 ± 2,0	27,5 ± 1,4
	Mean	29,2 ± 1,9	28,0 ± 1,3
Southern			
10	Elliniko	29,3 ± 1,6	28,7 ± 1,4
11	Glyfada	29,0 ± 1,6	28,4 ± 1,2
12	Kallithea	29,9 ± 1,7	28,8 ± 1,2
13	Moschato	30,8 ± 1,3	29,9 ± 1,0
14	Renti	29,9 ± 1,8	29,4 ± 1,3
	Mean	29,8 ± 1,6	29,0 ± 1,2
Northern			
15	Kamatero	29,4 ± 2,1	27,7 ± 1,6
16	Nea Filadelfia	28,6 ± 1,9	27,5 ± 1,3
17	Nea Erythrea	27,0 ± 2,0	26,3 ± 1,3
	Mean	28,3 ± 2,0	27,2 ± 1,4

Table 19 Monthly mean maximum and s.d. air temperature values for all stations for July and August, 2009

No.	Station	July	August
Western			
1	Egaleo	33,8 ± 2,4	32,5 ± 1,5
2	Agia Varvara	34,2 ± 2,3	31,8 ± 1,8
3	Korydallos	33,1 ± 2,1	31,2 ± 1,6
4	Haidari	34,1 ± 2,5	33,1 ± 2,5
5	Zefyri	35,3 ± 2,8	35,0 ± 1,4
	Mean	34,1 ± 2,4	32,7 ± 1,7
Eastern			
6	Agia Paraskevi	31,0 ± 2,0	30,7 ± 1,5
7	Vyronas	35,1 ± 2,7	33,5 ± 2,1
8	Ilioupoli	33,7 ± 2,2	31,5 ± 1,7
9	Kessariani	33,8 ± 2,9	31,5± 2,3
	Mean	33,4 ± 2,5	31,8 ± 1,9
Southern			

10	Elliniko	35,0 ± 2,4	35,9 ± 1,6
11	Glyfada	32,8 ± 2,1	32,6 ± 1,3
12	Kallithea	35,0 ± 2,1	33,6 ± 1,6
13	Moschato	35,9 ± 1,8	34,5 ± 1,3
14	Renti	35,9 ± 2,9	36,2 ± 1,8
	Mean	35,0 ± 2,3	34,6 ± 1,5
Northern			
15	Kamatero	35,3 ± 3,1	32,1 ± 2,2
16	Nea Filadelfia	32,6 ± 2,4	31,0 ± 1,5
17	Nea Erythrea	32,4 ± 3,2	31,4 ± 2,6
	Mean	33,4 ± 2,9	31,5 ± 2,1

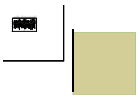

Figure 25 Monthly temperature values for each of the monitored stations for July 2009

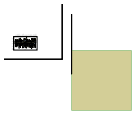

Figure 26 Monthly temperature values for each of the monitored stations for August 2009

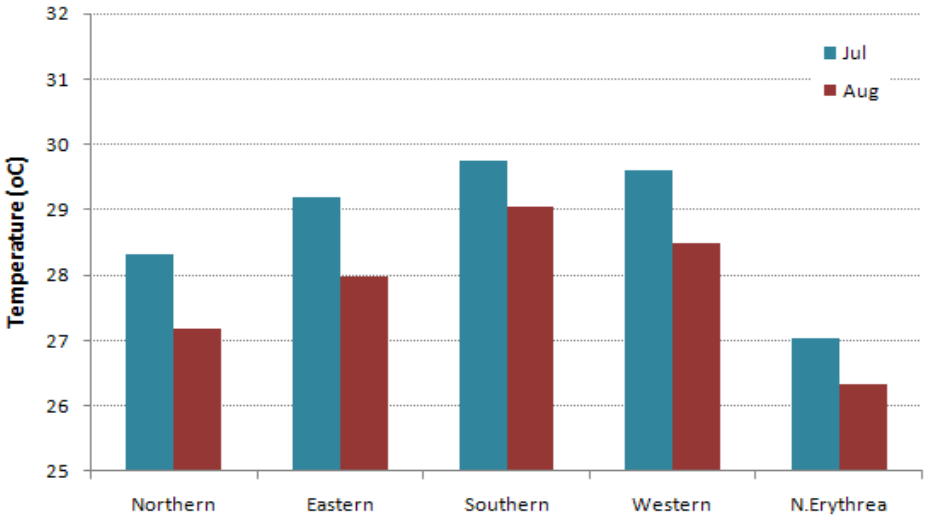

Figure 27 Monthly average temperatures for the four geographical zones and the reference station (Nea Erythrea) for months July and August, 2009

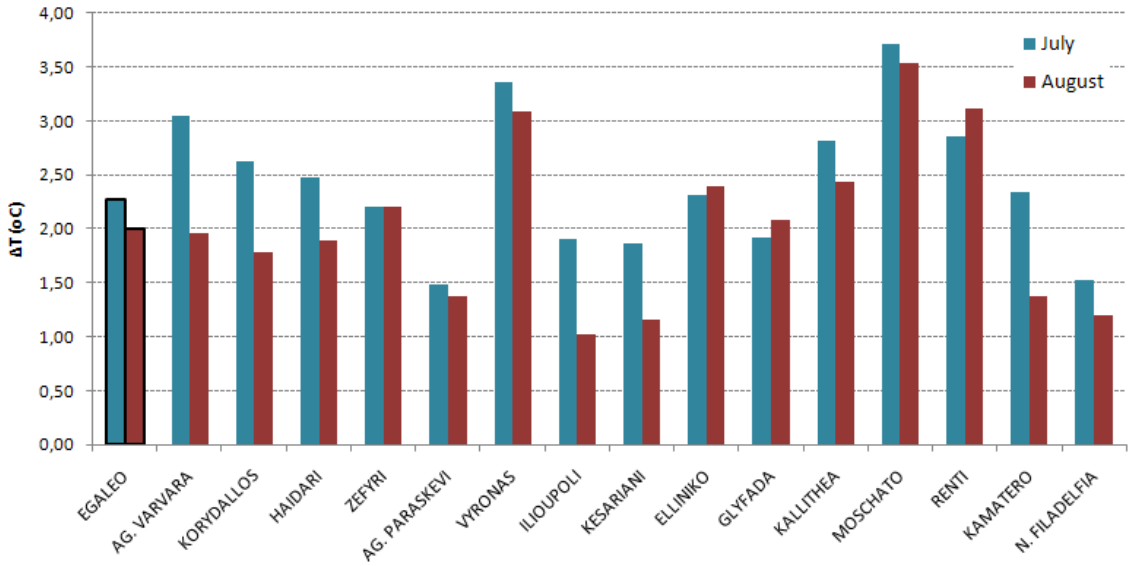

Figure 28 Average temperature differences between non-reference stations and reference station for months July and August, 2009

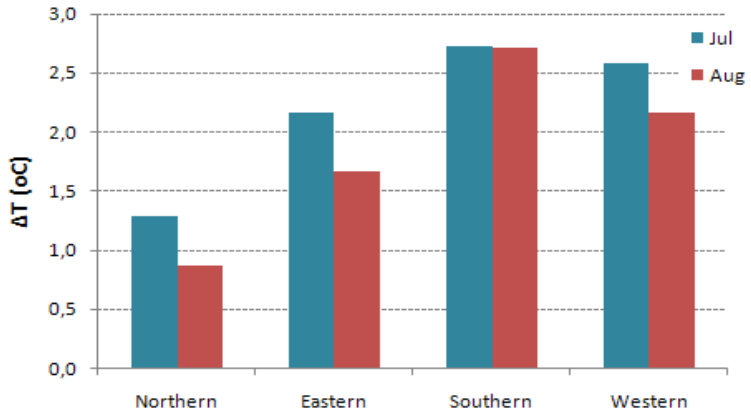

Figure 29 Average temperature differences between the four geographical zones and the reference station for months July and August, 2009

Table 20 Diurnal (07:00 – 21:00) and nocturnal (22:00 – 06:00) number of hours with temperatures above 30 ^{o}C for July and August, 2009

No.	Station	July (day)	July (night)	August day)	August (night)

Western					
1	Egaleo	265	26	223	4
2	Agia Varvara	327	38	197	6
3	Korydallos	305	28	177	4
4	Haidari	295	19	198	3
5	Zefyri	285	8	278	0
	Mean	295,4	23,8	214,6	3,4
Eastern					
6	Agia Paraskevi	173	15	130	1
7	Vyronas	323	50	282	13
8	Ilioupoli	260	10	155	0
9	Kessariani	265	9	142	0
	Mean	255,3	21,0	177,3	3,5
Southern					
10	Elliniko	275	3	287	0
11	Glyfada	239	13	213	3
12	Kallithea	290	23	248	4
13	Moschato	339	44	297	13
14	Renti	299	18	298	4
	Mean	288,4	20,2	268,6	4,8
Northern					
15	Kamatero	294	13	195	1
16	Nea Filadelfia	227	13	154	0
17	Nea Erythrea	161	1	99	0
	Mean	227,3	9,0	149,3	0,3

4 Outdoor environmental assessment

authors: M. Saliari ,A. Sakka, A. Synnefa, M. Santamouris

The main scope of this study was to assess the quality of the outdoor environment of the BRIDGE case study area (heat island assesement has been reported in a previous section), and also to provide the necessary input to the WP4 models. The following measurements have been carried out:

- Wind speed (m/s) and direction out of a selected canyon (cup anemometer).
- Three components of the wind's speed-x,y,z (3xis anemometers)
- PM1, PM2.5, PM10 (Units: mg/m³)
- wind speed and direction by anemometers that have been placed in three different heights-3.5, 7.5, 15.5m – in the antenna of NKUA's mobile station.
- Air temperature (^{o}C), Humidity (%), Air velocity (m/s) and Radiant temperature (C) at the height of 1.5m.
- Measurements of the surface temperature of the urban fabric (building facades, roads and pavements) using an infrared thermometer (Cole Palmer) and infrared camera (Thermovision 570)

Part of the instrumentation used is shown in the images below.

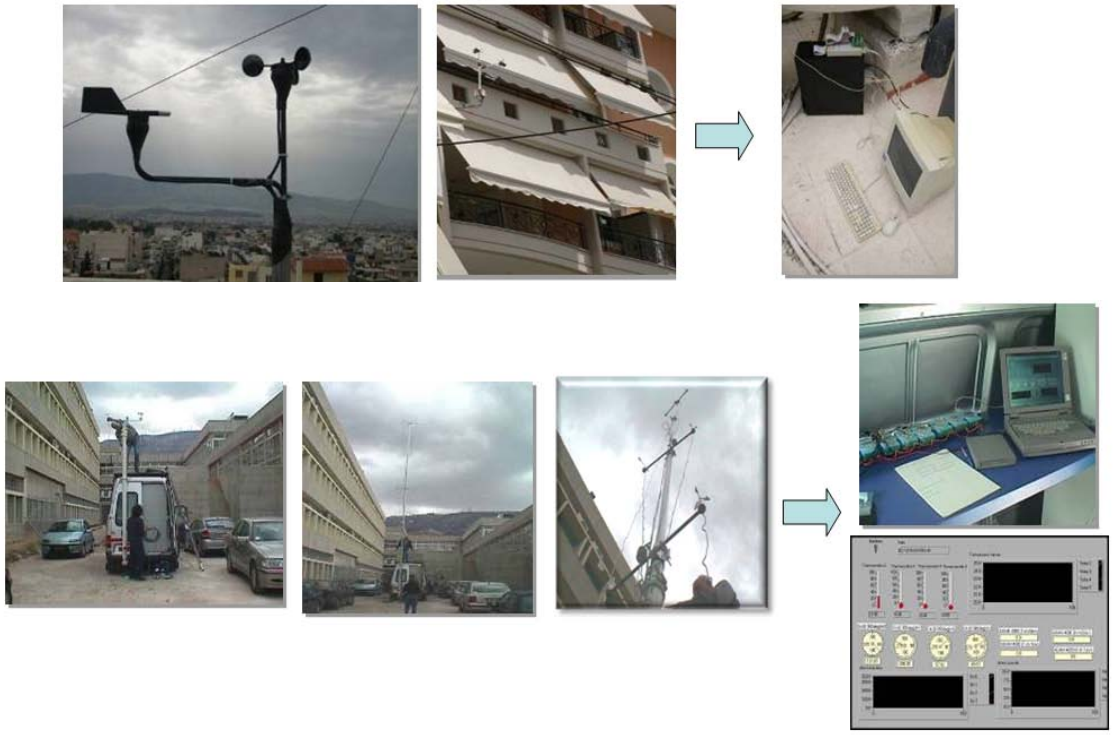

Figure 30 Wind speed and direction measurements and mobile meteorological station-telescopic mast

The monitoring campaign with the mobile meteorological station and the infrared camera was conducted in several several days during the summer of 2009 between 10:00 and 17:30.

Measurements of surface and air temperature were conducted in the area of Egaleo, including the Thivon Avenue, one of the busiest streets of the municipality.

Figure 31 Some of the measurement points in the area of Egaleo.

Using infrared thermography we recorded surface temperatures of different building materials and surfaces around the area of Egaleo. Infrared images where corrected for emissivity using the software IRwin Report 5.22. Emissivity values were either measured using a portable emissometer (Devices and Services), where samples were available, or taken from bibliographic references (Clarke J. et al, 1991, ESP USA).

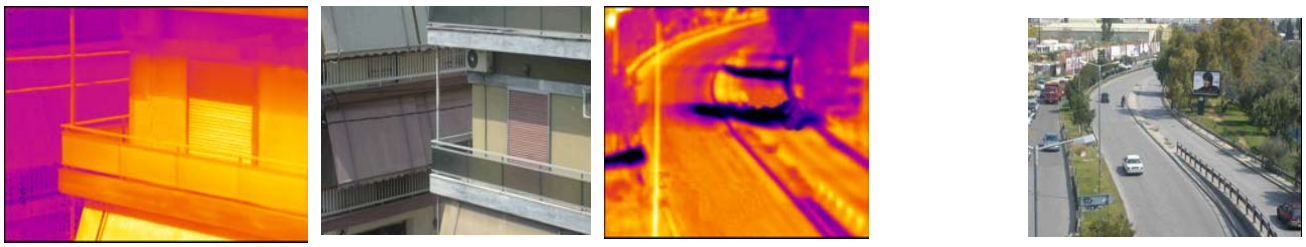

Figure 32 Examples of infared and visible images taken in the case study area to assess the thermal environment

On a representative hot summer day the following surface temperatures have been recorded during midday:

Table 21 Representative surface temperatures of different materials in the area of Egaleo during summer at around 14.00LST

Surface	Temperature
Unshaded asphalt paving	70°C
Concrete pavement slabs	46°C
Building walls	49°C
Building roofs (dark colored concrete or asphalt membrane)	65°C
Building roofs (concrete with white coating)	35°C
Green space	30°C

Figure 33 Representative surface temperatures of different materials in the area of Egaleo during summer at about (14.00LST)

These measurements have demonstrated the high impact of the use of appropriate building materials. The use of high albedo urban surfaces is an inexpensive measure that can reduce summertime temperatures. Increasing the reflectance of surfaces can be achieved by using ‘‘cool’’ materials that are characterized by a high solar reflectance and high infrared emittance values. The use of cool materials on the building envelope would result in the reduction of the heat penetrating into the building and for a surface in the urban environment it would contribute to the reduction of the ambient air temperature because the heat convection intensity from a cooler surface is lower. For this reason one of the proposed alternatives was the use of Cool materials in the Egaleio area.

Air temperature was measured several times during the day and in several points in the BRIDGE case study area and at different heights through the antenna of the mobile meteorological station.

The following figure depicts the spatiotemporal air temperature distribution at 1.5 m height on the 16th of April 2009. It can be noted, that air temperatures were quite high. The air temperature in

Thivon avenue was found to be quite uniform, achiving its maximum value at around 15.00 - 16.00 LST.

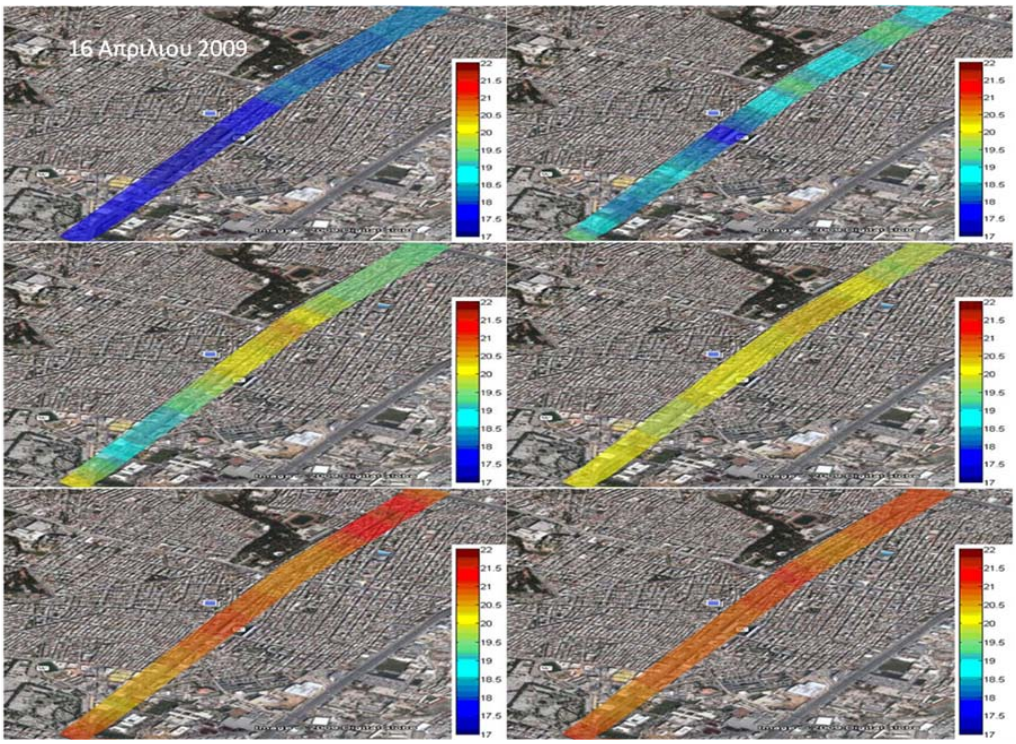

Figure 34 Spatiotemporal air temperature distribution at Thivon Avenue in the BRIDGE case study area (April 2009).

The following figure shows the spatiotemporal distribution of air temperature in the quarter of Egaleo that is near Eleonas, one of the intervention areas and between two important road axes (Kifisos Avenue and Iera Odos avenue). The air temperature throughout the area is quite high reaching 30°C even at 12.00pm. The areas where increased air temperature is recorded (they appear deep red on the graph) suffer from increased anthropogenic heat (e.g more car traffic), increased surface temperatures due to the materials and complete lack of green spaces. Eleonas is characterised by very high air temperatures.

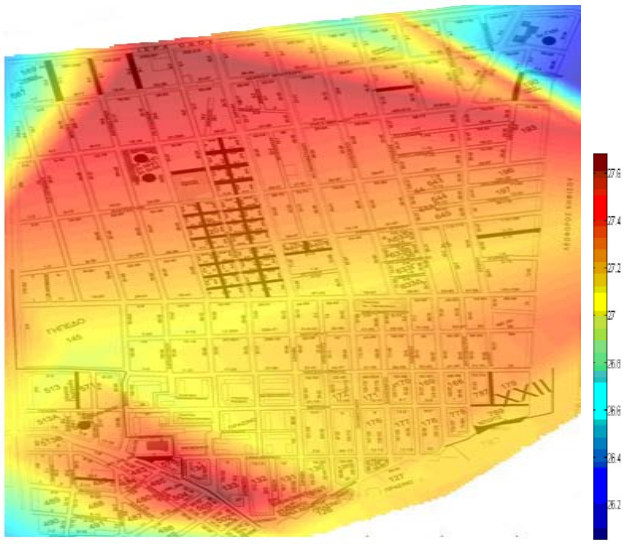

Figure 35 Spatial air temperature distribution in the BRIDGE case study area (June 2009).

Relative humidity values measured at 1.5m at the 8 spots indicated in Figure 31 (Σ1-Σ9) and for several times during the day are shown in the figure below:

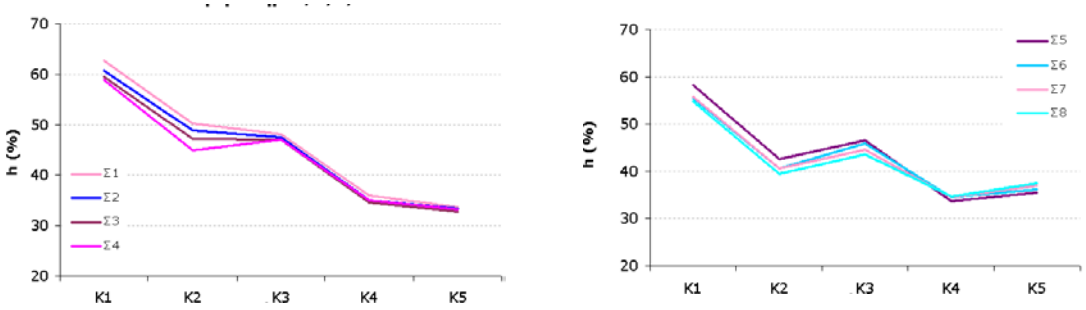

Figure 36 Temporal variation of relative humidity in the monitored BRIDGE area (16th April 2009). RH ranges between 35-60% [K1:10.30, K5:17.00LST]

Wind speed measurements at 3.5m were also recorded at the same measurement points (Σ1-Σ8) and for the same time intervals. The figures below show the wind speed measurements at points Σ1-Σ8 and for one day[K1:10.30, K5:17.00LST] (16th April 2009). The frequency distribution is also demonstrated in the charts at each point.

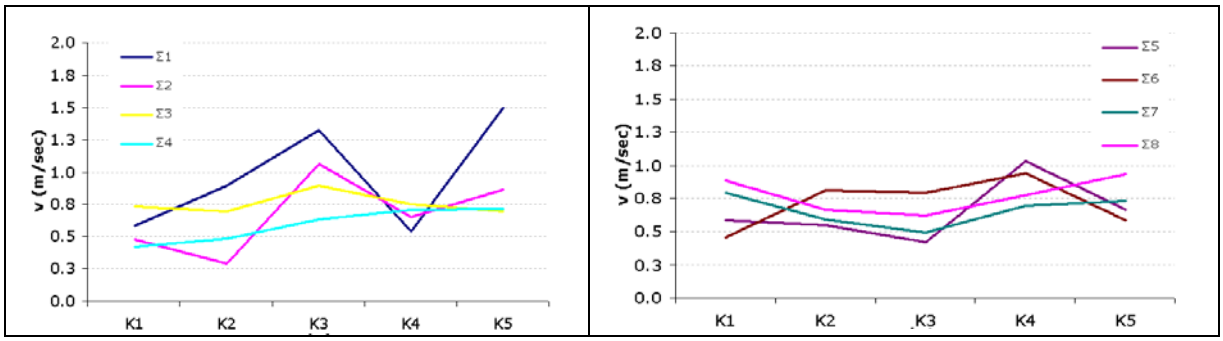

Figure 37 Temporal variation of wind speed at 3.5m in the monitored BRIDGE area (16th April 2009). Wind speed ranges between 0.26m/s-1.41m/s [K1:10.30, K5:17.00LST]

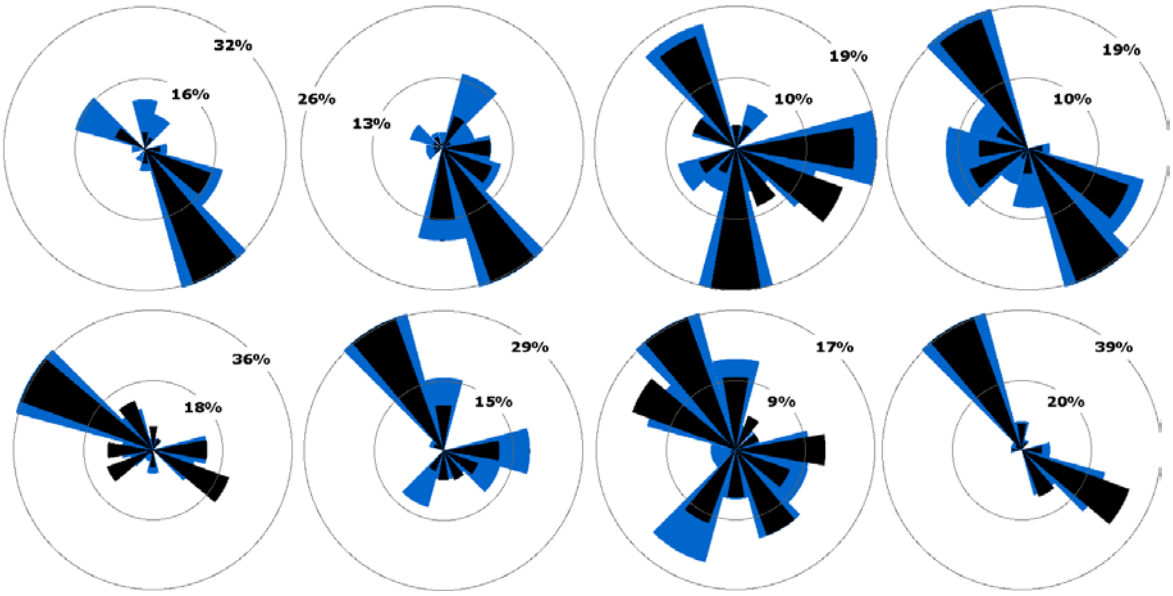

Figure 38 Wind speed distribution (30° wind sectors) at the 8 measurement points through out one day (16th April 2009)

Based on the above described measurements we were able to calculate two thermal comfort indicators:

- The wet bulb globe temperature (WBGT) and
- Cooling power (CP)

The **Wet Bulb Globe Temperature** (**WBGT**) is a composite temperature used to estimate the effect of temperature, humidity, wind speed and solar radiation on humans.

It is derived from the following formula:

WBGT = 0.7Tw + 0.2Tg + 0.1Td

Where:

Tw = Natural wet-bulb temperature (humidity indicator)

Tg = Globe thermometer temperature (measured with a globe thermometer, also known as a black globe thermometer, to measure solar radiation)

Td = Dry-bulb temperature (normal air temperature)

Temperatures may be in either Celsius or Fahrenheit

The process for determining the WBGT is also described in ISO 7243, Hot Environments - Estimation of the Heat Stress on Working Man, Based on the WBGT Index.

According to the Greek Standard 130427/26-6-90 of the Greek Ministry of Labour and Social Affairs, based on the level of the physical activity, the following categories-limits are defined:

Limit values of thermal exposure (WBGT) (^{o}C)			
Working -intermission	**Level of physical activity**		
	Light	**Medium**	**Heavy**
Continuous labour	30.0^{0}C	26.7^{0}C	25.0^{0}C
75% labour – 25% intermission per hour	30.6^{0}C	28.0^{0}C	25.9^{0}C
50% labour – 50% intermission per hour	31.4^{0}C	29.4^{0}C	27.9^{0}C
25% labour – 75% intermission per hour	32.2^{0}C	31.1^{0}C	30.0^{0}C

The second bioclimatic indicator, called **Cooling Power (CP)**, expresses the rate of heat loss from the surface of a body kept at a temperature of 36.5^{o}C, when this surface is exposed at the atmospheric air. This method calculates the heat dissipated to the air per time unit and per surface unit. i.e. Cooling power index is a measure of the air's ability to increase heat loss from a body. The index is calculated by the formula:

V<=1m/sec $CP=(0.2 + 0.4 \cdot V^{1/2}) (36.5 – T) \cdot 41.868$

V>1m/sec $CP=(0.13 + 0.47 \cdot V^{1/2}) (36.5 – T) \cdot 41.868$

where:

V: wind velocity (m/sec)

T: air temperature (^{o}C)

Based on the range of CP values, Petrovic- Kacvinski have classified the thermal environmnent in the following categories:

CP index values	Thermal environmnt
CP >2100	Exceptionaly cold
1680<CP=<2100	Very cold
1260<CP=<1680	Cold

840<CP=<1260	Cool
630<CP=<840	Slighlty cool
420<CP=<630	Neutral
210<CP=<420	Warm
CP=<210	Very warm

The outdoor thermal environment of Egaleo municipality was characterized as warm or very warm for most of the days where measurements were conducted.

The following two graphs give the values of WBGT and CP for the 16th April 2009. The values of the two indices indicate that thermal comfort conditions were not achieved in the area even since April.

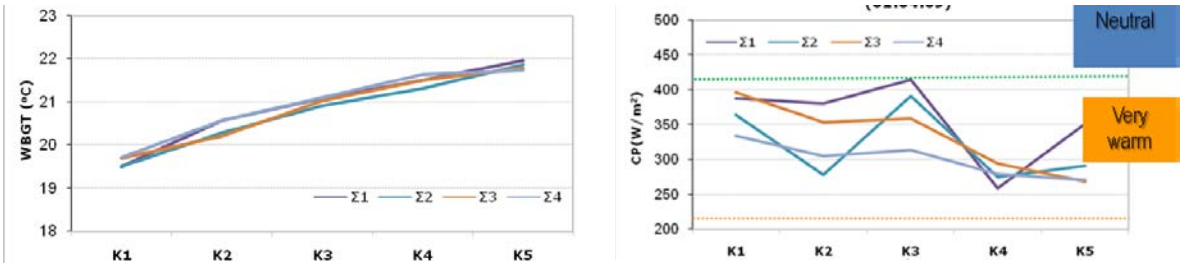

Figure 39 WBGT and CP index values for Egaleo 's outdoor environment area (16th April 2009), [K1:10.30, K5:17.00LST]

Concentration of Particulate matter with diameter smaller than 10μm (PM10) was also measured at several points throughout Egaleo area and during several days from 10.00 to 17.30. During several occassions, it was found that measured concentrations exceed the limit of 50 μg/m^3 set by the European Union for PM10 concentration. PM10 concentration was found to be higher during morning hours, which is probably due to the increased traffic load.

The following graph presents PM10 concentrations in several municipalities in the greater Athens area. The concentration corresponding to Egaleo is marked with a red arrow. The values shown in this graph indicate high values of PM10, exceeding the the EU limit.

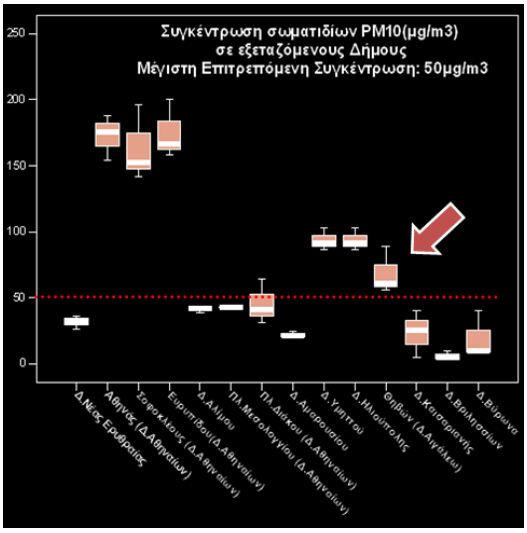

Figure 40 PM10 concentration at several municipalities in Athens. In Egaleo (marked with red arrow) PM10 values exceed the EU limit.

Table 22 Mean PM10 concentration at the measurement points (Σ1-Σ8) of Thivon Ave on 16th April 2009.

PM10 (μg/m^3) μέση τιμή					
Θηβών	K1	K2	K3	K4	K5
Σ1	88.7	109.8	45.6	16.5	17.0
Σ2	55.7	61.8	36.3	19.3	14.5
Σ3	60.6	63.8	64.8	24.3	18.5
Σ4	67.1	50.1	41.1	21.3	13.9
Σ5	63.2	32.0	35.6	13.9	12.7
Σ6	57.6	30.8	37.7	14.8	10.0
Σ7	65.1	45.4	46.1	15.5	12.2
Σ8	57.2	53.1	39.9	15.3	14.0

5. Building related observations

authors: A. Sakka, M. Saliari, M. Santamouris

The main aim of this part of the research was to assess the impact of the outdoor environmental conditions (mainly thermal comfort and air pollution) on the indoor environment of residential buildings in the case study area. The process that has been followed is outlined below:

a) Data collection on the residential building stock of Egaleo municipality and selection of ten representative buildings

b) Data collection of the selected residential buildings (plans, construction details etc.).

c) Distribution and collection of questionnaires based on ASHRAE std 55 (long and short) from the residents

d) Indoor thermal comfort measurements: Air temperature (^{o}C), relative humidity (%), Air velocity (m/s) and mean radiant temperature (^{o}C)

e) Measurements of PM1, PM2.5, PM10 concentrations (units: mg/m^{3}),

5.1 Building selection

Several data have been collected regarding the building stock of Egaleo (Figure 41). The building stock is generally of poor quality due to the fact that a significant percentage of them was constructed between the 50s and 80s, before the adoption of the insulation law. This means that most of the buildings are poorly or not at all insulated. In addition, a lot these buildings have single glazing windows, are naturally ventilated and in most of the cases have no cooling equipment or cooling is provided by AC split units. These buildings are made of reinforced concrete, and have one to three floors height. A small amount the building stock was built in the 1920's and onwards. These residences are made of stone and are in poor condition. Finally, buildings built in the last decades made of reinforced concrete reaching a height of up to 6 floors.

In addition, and upon the WP4 participants requests we have also collected gas consumption data for Egaleo (Table 23).

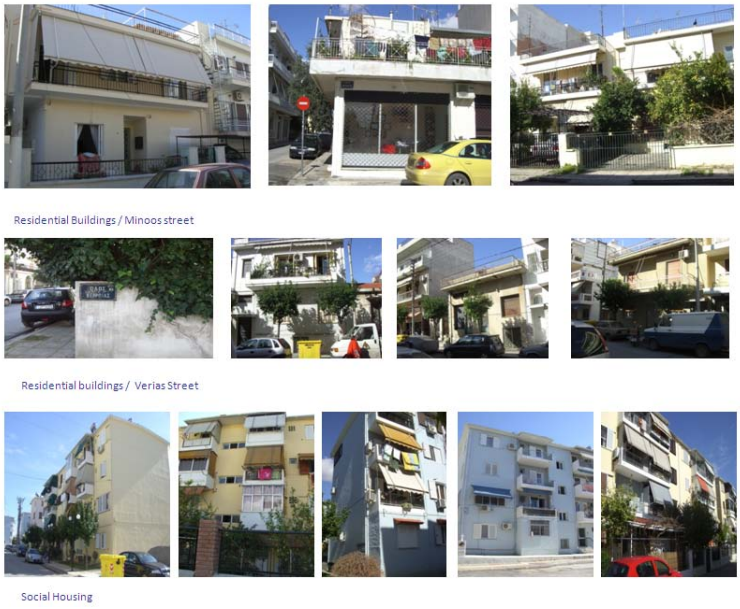

Figure 41 Representative pictures of Egaleo's residential building stock.

Ten residential buildings have been selected at the case study area and were monitored during the summer of 2009. Information on the selected buildings has also been collected (plans, construction details etc.). The location of these buildings is given in Figure 42 and in Table 24.

Figure 42 Location of the monitored residential buildings in Egaleo.

Table 23 Monthly natural gas consumption for Egaleo.

Table 24 Characteristics of the 10 selected residential buildings in Egaleo.

i/i	location	Stories* (monitored appt)	Apt. area (m^2)	Year of construction	Ventilation system	cooling	Building characteristics (values reported are only an estimate)	photo
R1	Lat. 37°59'13.39"N Long. 23°40'50.63"E	5 (3^{rd} floor)	110	2000	Yes	AC unit 12000 BTU Set point T: 22C	U_{wall} = 0.446 W/m^2K U_{floor} = 2.415W/m^2K U_{roof}= 0.395 W/m^2K Double glazing Aluminum frame	
R2	Lat. 37°59'13.72"N Long. 23°40'50.59"E	5 (3^{rd} floor)	122	2000	yes	AC unit 12000 BTU Set point T: 22C	U_{wall} = 0.446 W/m^2K U_{floor} = 2.415W/m^2K U_{roof} = 0.395 W/m^2K Double glazing Aluminum frame	

i/i	location	Stories* (monitored appt)	Apt. area (m^2)	Year of construction	Ventilation system	cooling	Building characteristics (values reported are only an estimate)	photo
R3	Lat. 37°59'19.39"N Long. 23°40'52.64"E	3 (2^{nd} floor)	85	1963-1965	Naturally ventilated	No cooling	U_{wall} = 0.708 W/m^2K U_{floor} = 2.366W/m^2K U_{roof} = 0.422 W/m^2K Single glazing Wooden frame	
R4	Lat. 37°59'19.39"N Long. 23°40'52.64"E	2 (2^{nd} floor)	65	1950-1952	Naturally ventilated	AC unit 12000 BTU Set point T: 22C	U_{wall} = 0.446 W/m^2K U_{floor} = 2.415W/m^2K U_{roof} = 0.395 W/m^2K Single glazing Wooden frame	
R5	Lat. 37°59'6.51"N Long. 23°40'45.24"E	3 (2^{nd}floor)	70	1945-1946	Naturally ventilated	No cooling	U_{wall} = 0.708 W/m^2K U_{floor} = 2.366W/m^2K U_{roof} = 0.422 W/m^2K Double glazing Aluminum frame	

i/i	location	Stories * (monitored appt)	Apt. area (m^2)	Year of construction	Ventilation system	Cooling	Building characteristics (values reported are only an estimate)	photo

R6	Lat. 37°59'22.70"N Long. 23°40'45.45"E	4 (1st floor)	72	1962-1965	Naturally ventilated	No cooling	U_{wall} = 0.708 W/m^{2}K U_{floor} = 2.366W/m^{2}K U_{roof}= 0.422 W/m^{2}K Double glazing Aluminum frame	
R7	Lat. 37°59'22.69"N Long. 23°41'6.42"E	3 (2nd floor)	80	1940-1943	Naturally ventilated	AC unit Set point T: 22C	U_{wall} = 0.446 W/m^{2}K U_{floor} = 2.415W/m^{2}K U_{roof}= 0.395 W/m^{2}K Single glazing Aluminum frame	
R8	Lat. 37°59'14.10"N Long. 23°40'39.93"E	5 (3rd floor)	112	1960-1965	Naturally ventilated	No cooling	U_{wall} = 0.446 W/m^{2}K U_{floor} = 2.415W/m^{2}K U_{roof}= 0.395 W/m^{2}K Double glazing Aluminum frame	

i/i	**location**	**Floors* (monitored appt)**	**Apt. area (m^2)**	**Year of construction**	**Ventilation system**	**cooling**	**Building characteristics** (values reported are only an estimate)	**photo**

R9	Lat. 37°59'20.96"N Long. 23°40'40.67"E	5 (3rd)	120	1968-1970	Naturally ventilated	No cooling	U_{wall} = 0.446 W/m^{2}K U_{floor} = 2.415W/m^{2}K U_{roof}= 0.395 W/m^{2}K Double glazings Aluminum frame	
R10	Lat. 37°59'9.73"N Long. 23°40'52.08"E	2 (1st)	90	1940-1945	Naturally ventilated	No cooling	U_{wall} = 0.708 W/m^{2}K U_{floor} = 2.366W/m^{2}K U_{roof} = 0.422 W/m^{2}K Single glazing Aluminum frame	

*average floor height 2.7m (new construction)-3m (old construction)

5.2 Assessment of the indoor environmental quality

In order to assess the indoor environmental quality of the 10 selected buildings the following parameters have been measured:

- Air temperature
- Relative humidity

The sensors were placed in the center of the living room, at a height of about 1m above the floor. Measurements were taken every 10min during the monitoring period. An additional sensor was placed just outside of the apartment at a height of 1.5m from the floor (ref. Tout). Air temperature was also monitored by a meteorological station located at the municipality of Egaleo central building at about 2.5m height (ref. Turban). Measurements were taken between the May and September 2009 for the following parameters:

- Concentrations of PM1, PM2.5, PM10 -values for each residential building. (units: mg/m³). Measurements were taken on specific days during the monitoring period.
- Air temperature (°C), radiant temperature (°C), relative humidity (%) and air velocity (m/s) in order to assess the thermal comfort. Measurements were taken on specific days during the monitoring period.
- Surface temperature of the structural elements. Measurements were taken on specific days during the monitoring period.

Figure 43 The set of equipment used for the assesement of the indoor environmental quality

In addition to the measurements, 2 questionnaires based on the ASHRAE std 55(long and short) methodology were prepared and distributed to the residents of the monitored buildings. Occupants had to fill in the questionnaires once per day, resulting in 7 surveys per dwelling occupant per week. In the questionnaire, all aspects relevant to comfort, such as room temperature, air velocity, humidity were addressed. All questions had to be answered within a 7-point-scale rating by the occupants. Sections for free comments were also provided. In this case, the mean participation rate was 89%, and 1002 questionnaires in total were available for the statistical evaluation.

The most important results are summarised below:

Figure 44 depicts the mean indoor temperatures of the 10 monitored residential buildings in Egaleo. The residential buildings R1, R2 are mechanically ventilated buildings while all the others are naturally ventilated buildings.

	R1	R2	R3	R4	R5	R6	R7	R8	R9	R10
T_in	28.15	27.80	29.80	28.32	29.89	29.20	28.92	29.91	30.05	29.20
T_out	28.88	28.88	28.88	28.88	28.88	28.88	28.88	28.88	28.88	28.88
Turban	24.98	24.98	24.98	24.98	24.98	24.98	24.98	24.98	24.98	24.98

Figure 44 Mean indoor temperatures of the 10 monitored residential buildings

The mean indoor temperature in all the houses varied between 27.2°C and 30°C. The mean outdoor Temperature was 27.9°C for this period of time. For the specific period of time the mean outdoor temperature recorded from a logger at an open air station was 24.3°C.

Figure 45 presents the cumulative percentage of mean indoor and maximum indoor temperatures. The graph shows that over 40% of the maximum indoor temperatures were up to 35 °C, while 70% of the mean indoor temperatures were up to 30°C for the specific monitoring period. Indoor temperatures up to 38ºC were recorded as well as hot spells of over for almost 21 consecutive hours.

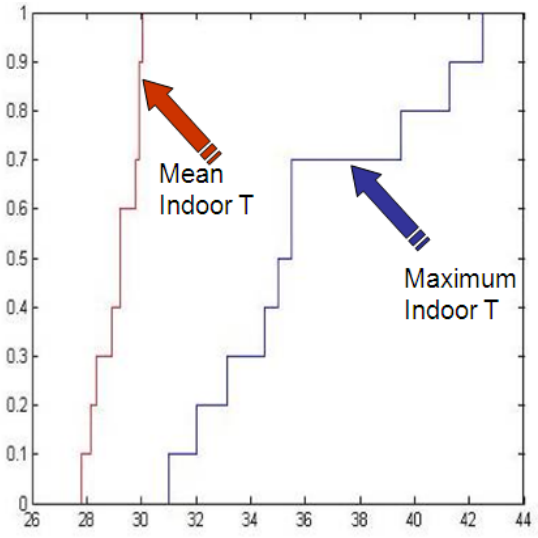

Figure 45 Cumulative percentage of mean and maximum recorded indoor temperatures of the 10 monitored residential buildings

In addition to the above assesement, specific analysis to estimate the thermal comfort sensation of the occupants was performed through the statistical analysis of the questionnaires and the thermal comfort measurements (Air temperature, Mean radiant temperature, Relative humidity and Air velocity) that allowed us to calculate two indicators: the Predicted Mean Vote (PMV - on the thermal sensation scale) of a population of people exposed to a certain environment and the Predicted Percent of Dissatisfied People (PPD).

Thermal comfort is maintained when the heat generated by human metabolism is allowed to dissipate, thus maintaining thermal equilibrium with the surroundings (heat conduction, convection, radiation, and evaporative heat loss).

PMV correlates the physics of heat transfer combined with an empirical fit to sensation (-3 up to 3). Even when PMV equals zero there will be at least 10% of people that are dissatisfied with their thermal environement (warm or cold). According to ISO 7730 in order to achieve thermal comfort there must be at the same time PPD<10% and -0.5<PMV<0.5. In the following graphs the results of the PMV – PPD calculation are shown indicatively, for 2 summer days (10th June 2009 and 15th July 2009). The hatched part of the diagram indicates values within the acceptable range of the thermal comfort according to ISO 7755. As it can be seen, on the first day only R1 which is mechanically ventilated achieves thermal comformort conditions. On the second day, none of the residential buildings achieved thermal comfort conditions. Overheating problems are evident.

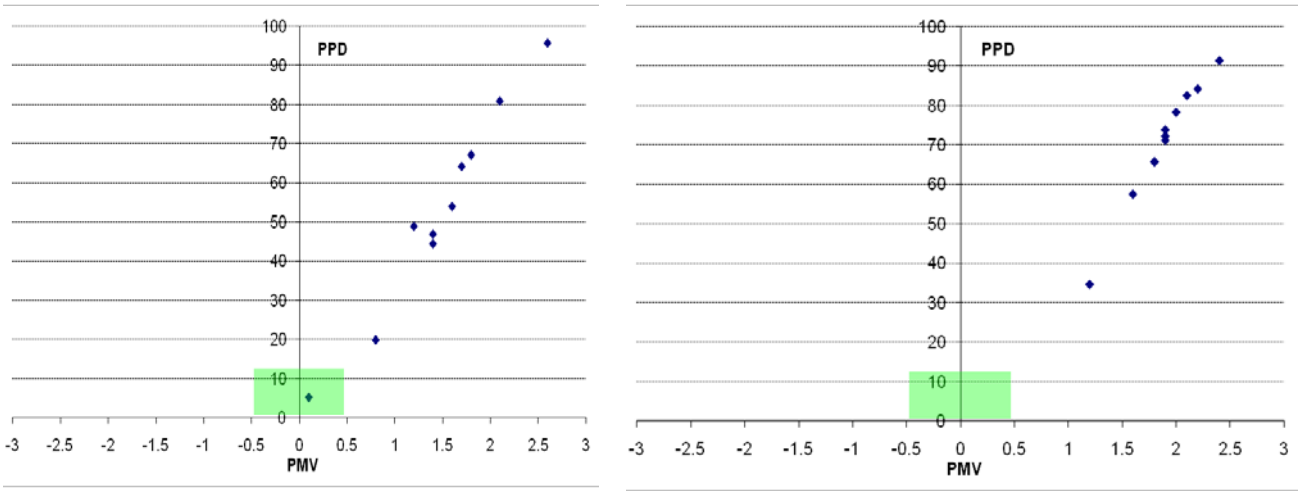

A B

Figure 46 Calculation of PMV and PPD indicators for the 10 residential buildings on two representative summer days (A: June 2009 and B: 15th July 2009)

Comparative analysis of the occupants' responses received from the questionnaires and the measured indoor conditions indicate that the thermal comfort perception of the users is in agreement with the air temperature measurements.

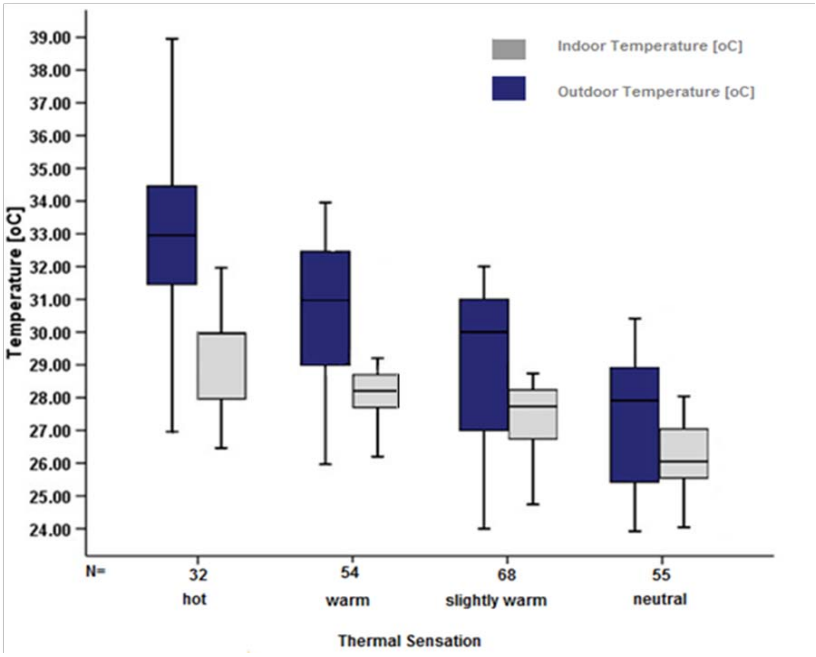

Figure 47 The thermal comfort perception of the users from the analysis of the questionnaires is in agreement with the Tair measurements

In order to evaluate the impact of outdoor pollution on the indoor environment, measurements of the Particulate Matter with diameter less than 1 mm, 2.5 mm and 10pm (in the literature denoted as PM1, PM2.5 and PM10, respectively) have been conducted during several days of the monitoring period in the interior and the exterior of the residential buildings.

The instrument used is the DUSTTRAK™ Aerosol Monitor, a laser photometer which gives a real-time digital readout and is also a data logger. The response time of the analyzer is one minute, meaning that one value is given approximately every minute by the analyzer. Through this process the hourly average values for concentrations are calculated each hour.

In the following tables the measured concentrations of PM1, 2.5 and 10 for a repsresentative summer day are reported.

Table 25 PM1, 2.5,10 concentrations (μg/m3) of the indoor environment in the ten residential buildings on 10/06/2009

Residential building	PM1			PM2.5			PM1		
	mean	max	min	mean	max	min	mean	max	min
R1	4.40	4.64	4.28	6.46	6.87	6.21	5.55	6.87	6.21
R2	4.39	4.76	4.28	6.23	7.20	5.88	4.56	7.20	5.88
R3	4.43	4.64	4.28	6.50	6.87	6.21	5.55	6.87	6.21
R4	12.18	12.44	11.96	27.36	27.99	26.67	25.35	27.99	26.67
R5	4.13	4.16	4.04	5.58	5.88	5.22	4.56	5.88	5.22
R6	4.22	4.28	4.16	6.00	6.21	5.55	4.89	6.21	5.55
R7	4.45	4.88	4.28	6.45	6.87	5.88	4.89	6.87	5.88
R8	4.39	5.12	4.04	6.02	6.54	5.55	6.02	6.54	5.55
R9	4.76	5	4.64	7.73	8.85	6.87	7.73	8.85	6.87
R10	4.97	3.20	3.62	8.50	7.42	6.45	7.89	8.24	6.23

Table 26 PM1, 2.5,10 concentrations (μg/m3) of the outdoor environment of the ten residential buildings on 10/06/2009

Residential building	PM1			PM2.5			PM1		
	mean	min	max	mean	min	max	mean	min	max
R1	9.32	9.08	9.68	21.39	20.07	26.01	28.97	24.99	36.94
R2	8.24	7.88	8.96	17.43	16.11	20.07	42.92	19.51	49.44
R3	8.36	7.76	9.20	17.10	16.11	19.08	21.00	19.01	24.49
R4	7.64	7.28	10.88	20.40	15.45	43.50	22.00	16.02	46.90
R5	5.48	5.24	6.68	9.51	8.19	12.15	11.04	8.06	14.03
R6	6.56	6.20	7.88	13.14	12.48	14.46	18.02	15.03	29.47
R7	7.04	6.80	7.88	13.47	12.48	15.45	18.51	14.53	73.29
R8	3.45	7.04	9.32	13.14	12.48	14.13	19.01	13.53	52.38

R9	7.16	6.92	8.00	12.81	12.15	15.12	17.02	14.53	20.51
R10	8.12	6.23	9.32	12.97	10.91	14.56	18.06	17.8	20.23

The analysis of the measurements in parallel with recording of internal sources and estimations of the ventilation rates for each building had the following outcomes:

In general the variability of concentration in a room without major sources of PM is small compared to the outdoor concentration. Also, indoor particle number concentration characteristics are generally correlated with outdoor concentration characteristics in the absence of important indoor sources. In addition, although concentrations outside the residences were quite high, indoor concentrations for well air tight buildings like R1 and R2, concentrations were significantly lower (given the fact that no internal PM sources were found inside). On the contrary, poor construction and high infiltration rates due to e.g. old wooden frames (as is the cse of R4) resulted in high indoor concentrations. The presence of internal sources e.g excessive smoking and cooking (e.g. frying) as expected resulted in high concentrations during the activity.

5.3 Estimation of the impact of UHI on building cooling loads

In an effort to estimate the impact of outdoor environmental conditions, namely of the documented urban heat island effect, on Egaleo's buildings cooling load, the following process was implemented. Based on the collected data previously analysed, we have selected a building typology that is representative of Egaleo's residential building stock. Numerical analysis using TRNSYS software was then performed in order to estimate the cooling load of this same building in three different sites a)Egaleo (urban area), b) Center of Athens (urban area), c) Nea Erithrea (suburban area). In order to run the model and estimate the impact of outdoor thermal conditions on the building load, we have used the meteorological measurements performed at those sites.

The following sections describe the meterological parameters used in the model and the buildings boundary conditions and characteristics (location, geometry, structure, thermo physical properties as well as its operational conditions. etc.). The final section presents the simulation results that aim to assess the impact of the heat island characteristics on cooling loads and on thermal comfort of the residents.

The following measured and collected data have been used for the period of June 2009 to May 2010:

- Air temperature
- Relative humidity
- Total horizontal radiation
- Wind speed and direction
- Diffuse horizontal radiation

Total and diffuse radiation is presented per month in the following figures:

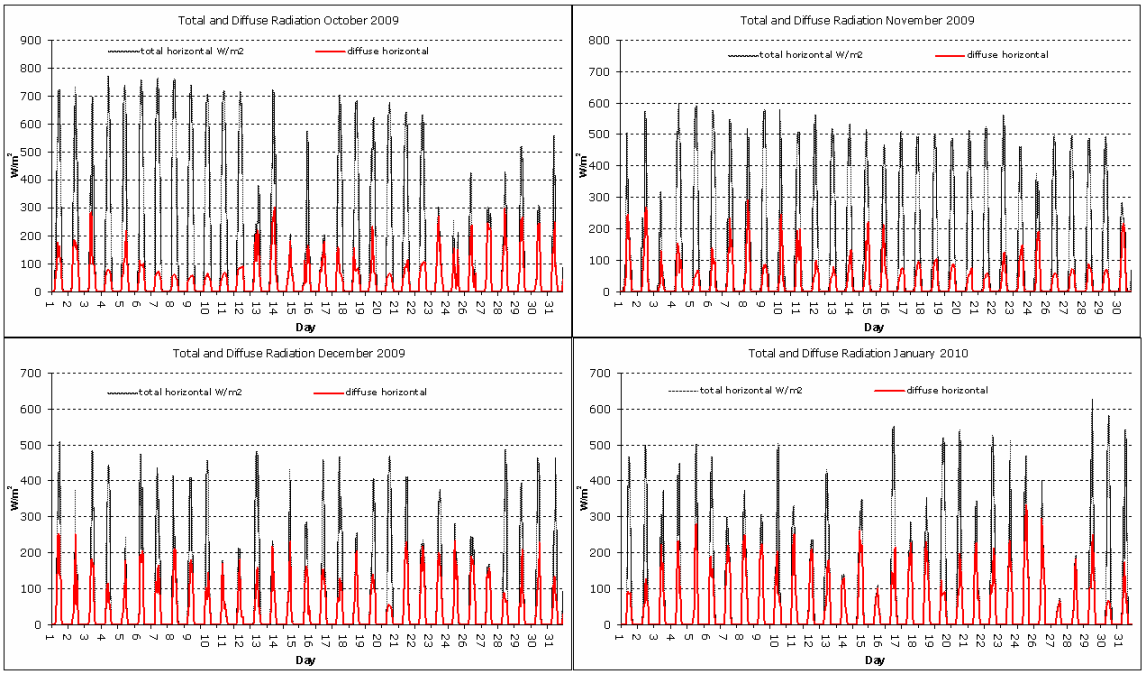

Figure 48 Total and diffuse radiation June 2009 to January 2010.

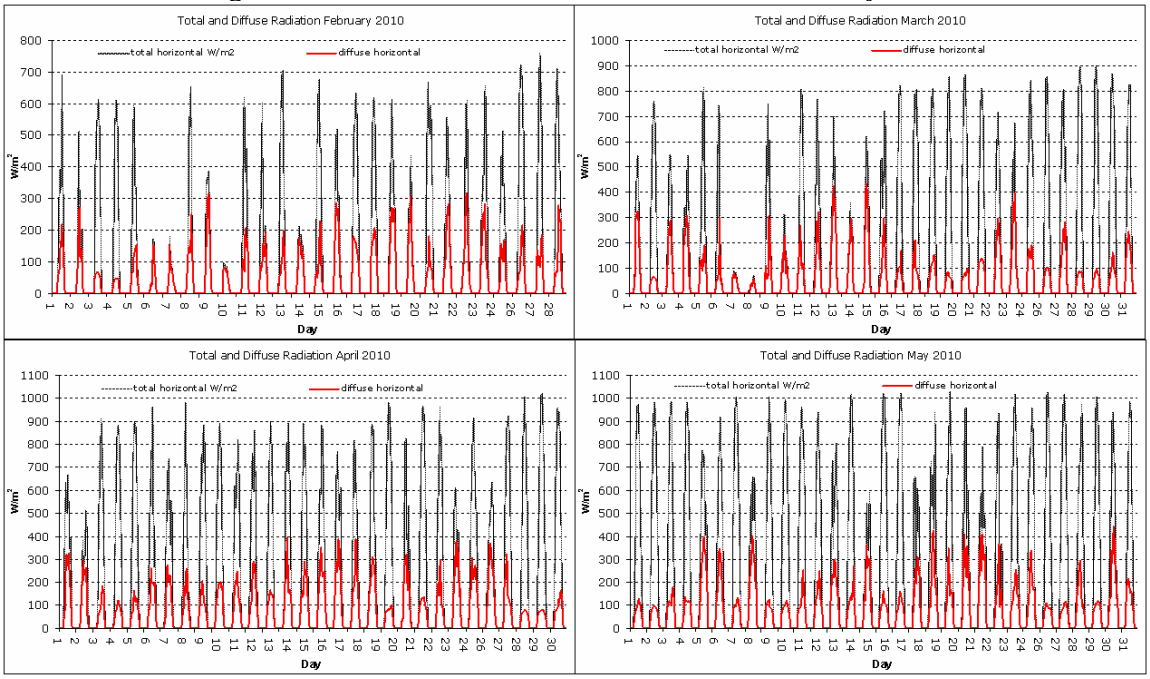

Figure 49 Total and diffuse radiation February 2010 to May 2010.

Air temperature per month for all the examined areas is presented in the following graphs:

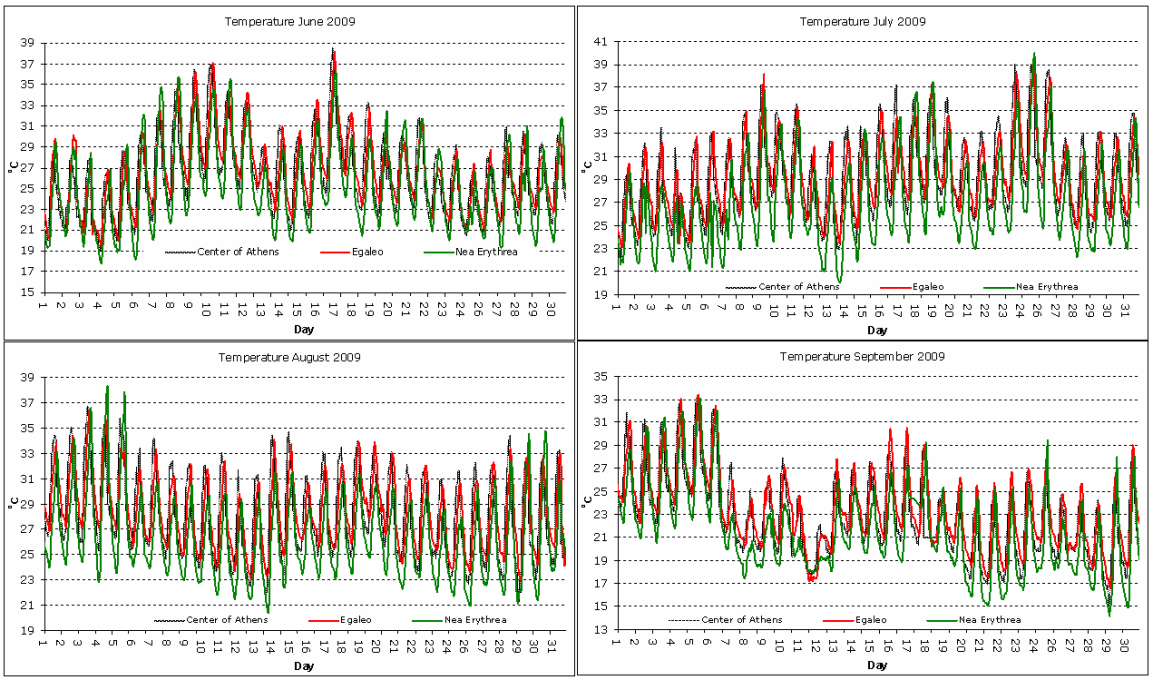

Figure 50 Air temperature measurements at the three sites for the period June 2009 to September 2009

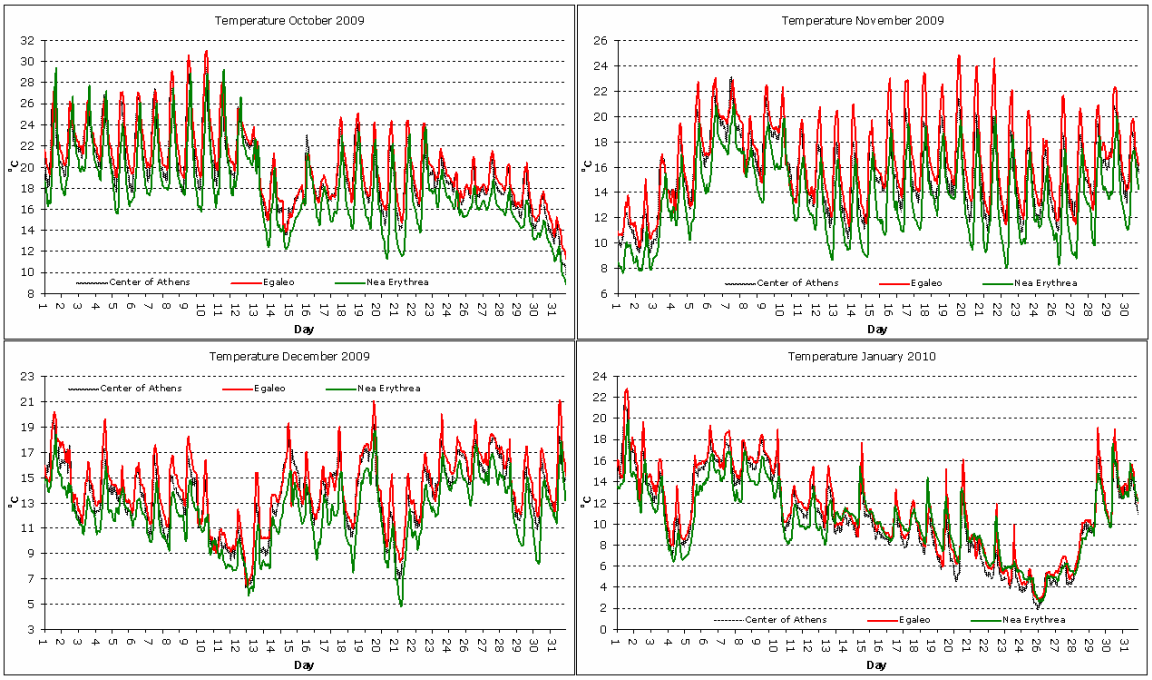

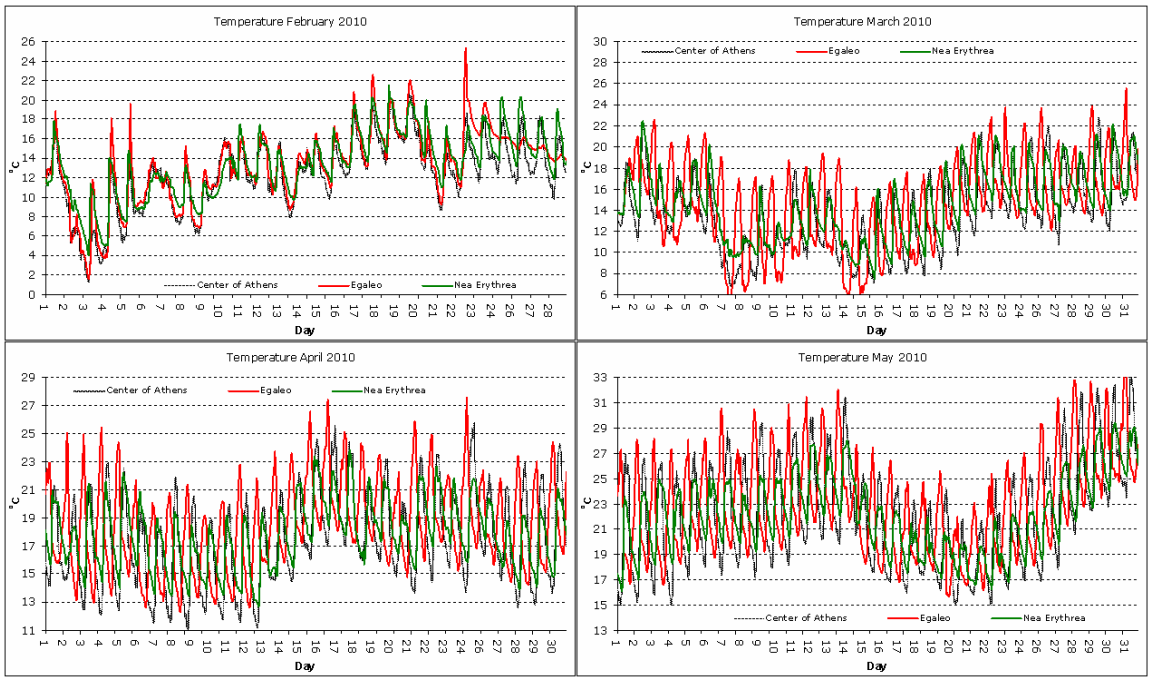

Figure 51 Air temperature measurements at the three sites for the period October 2009 to May 2010

5.3.1 Building description

The building considered is a two story residential building representative of the Egaleo area. On the ground floor are located a kitchen, a living room, one WC and one bedroom. In the first floor are two bedrooms, one WC and a storage space. The ground floor and the first floor are connected with an internal staircase. Figure 52 and Figure 53 display the ground plan of the building for both floors.

The area and the volume of each floor of the building as well as the area of the roof are presented in Table 27. The use as well as the area of each thermal zone is described in

Table 28.

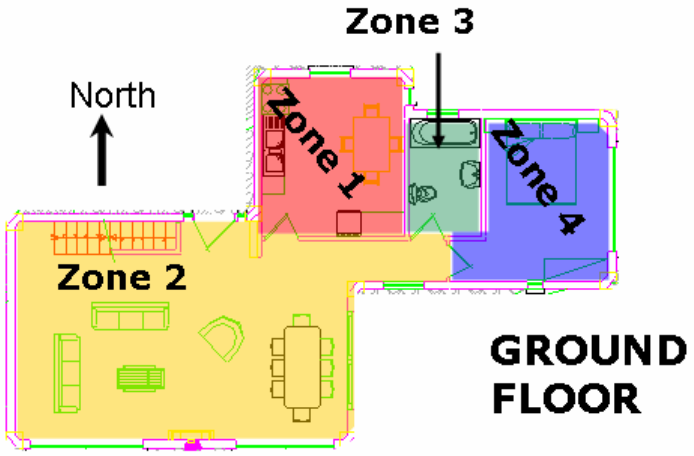

Figure 52 Ground plan and orientation of the residential building's ground floor.

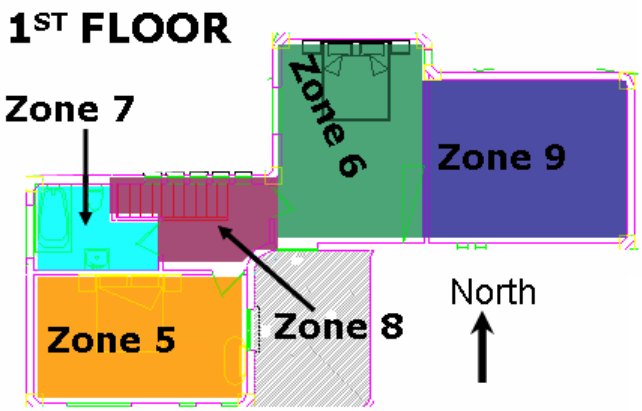

Figure 53 Ground plan and orientation of the residential building's 1st floor.

Table 27 Area and volume of each floor of the building as well as the area of the roofs

	Area	Volume
	m^2	m^3
Ground floor	76.5	206.4
Roof	14.7	
1st floor	61.8	161.2
Roof	61.8	

Table 28 Use of each thermal zone

Thermal Zone	Area	Volume	Comments
1	13.6	Kitchen	
2	44.8	Living room	
3	5.2	WC	
4	12.9	Bedroom	
5	16.5	Bedroom	
6	17.5	Bedroom	
7	5.4	WC	
8	3.0	Staircase	
9	19.4	Storage Room	No airconditioning

The load bearing structure of the residential building is of reinforced concrete and an overall concrete masonry construction that is uninsulated. The windows are assumed to be single glazed wood frame windows.

The building's characteristics are summarized in the following table:

Table 29 Thermophysical characteristics of the building envelope

Building envelope:	U value (W/m^2K)	SR

Reinforced Concrete	2.57	0.7 (white coating)
External Walls	1.80	0.7 (white coating)
Internal Walls	2.75	
Roof	3.01	0.35 (light color)
Windows	5.68	
Floor	3.05	

Shading factor of 0.2 was considered for the winter period and 0.8 for the summer period.

The operational conditions are described below. Lighting is provided from building doors and windows as well by the use of fluorescent lamps. The residence is occupied by four persons. The operation schedule of the building is:

Table 30 Operation schedule of the building

Day:		Timeschedule	%	T (^{o}C)	RH %
% Occupancy	Monday to Sunday	00:00 - 23:00	100		
% Lighting	Monday to Sunday	00:00 - 18:00	5		
		18:00 - 23:00	100		
Heating	Monday to Sunday	06:00 – 00:00		26	40
Cooling	Monday to Sunday	06:00 – 00:00		21	50

Natural ventilation of 15m^3/h/person was considered and infiltration 0.4ACH.

5.3.2 Building model

The building model was set up with the assistance of the TRNBuild tool. Main components were the weather data reader and processor with its accompanying Psychometrics and Sky Temp components as well as the building component. The central part of the simulation model was the Type 56 - Multi-Zone Building. This component simulates the thermal behaviour of a building and generates its own set of monthly and hourly summary output files. The thermal zones that were used for the simulation of this building are presented in Figure 52 and Figure 53.

The simulation was run in 1 h time steps for the period of June 2009 to May 2010.

5.3.3 Analysis of the results

All the results refer to the three examined sites:

1. **Suburban Area**. Nea Erithrea
2. **BRIDGE Area**. Egaleo
3. **Urban Area** Central Athens

All the results are presented for the cooling period as we are aiming to examine the impact of UHI on Cooling loads.

A) Impact of UHI on indoor temperatures

Hourly air temperature were calculated for the summer period for a flee floating (non AC) building (no energy is being offered in order to heat or cool the building although it is fully functional).

For each month the average 24h profile was calculated. The results are presented in the following figures.

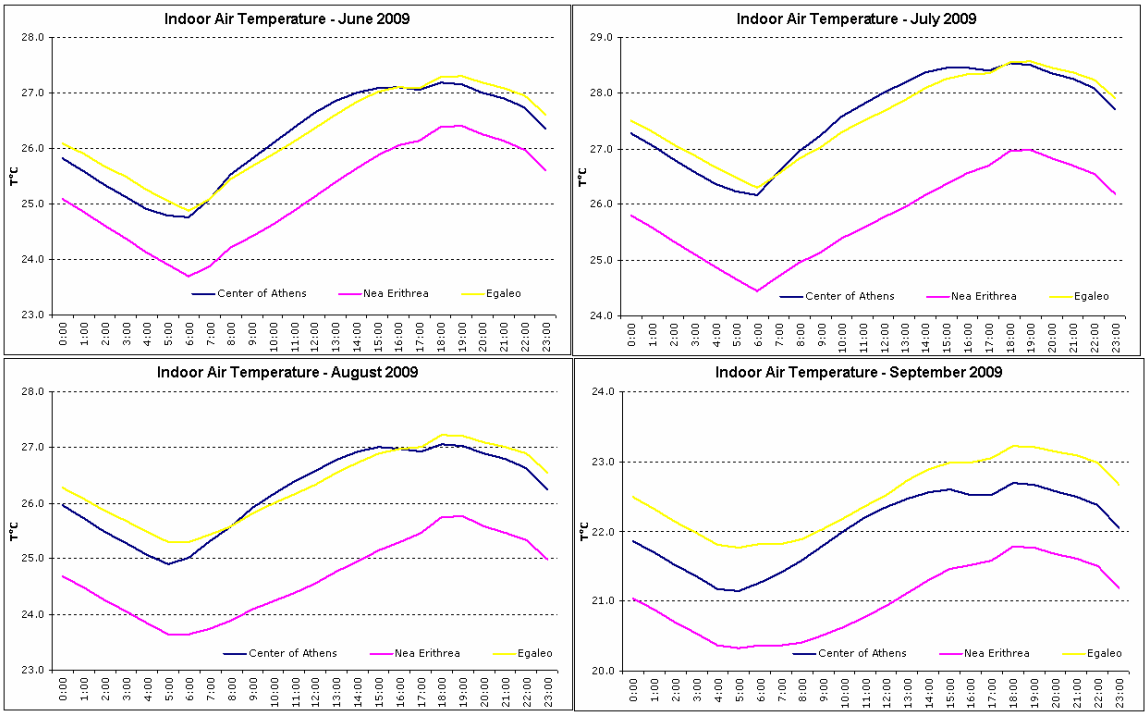

Figure 54 Indoor Air Temperature for June. July, August and September 2009

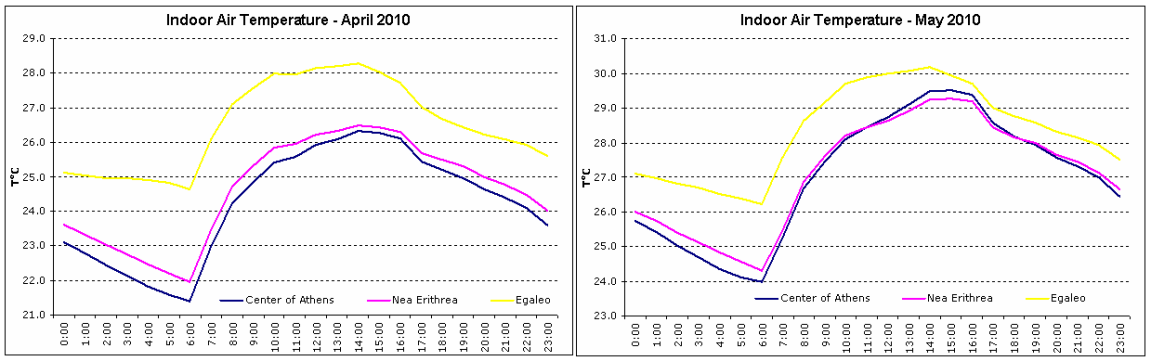

Figure 55 Indoor Air Temperature for April and May 2010

In all cases the indoor air temperature of the building in Nea Erithrea is the lowest, whereas the indoor air temperature of Egaleo is the highest with temperature differences of up to 3.6^{o}C.

B) Impact of heat island characteristics on energy loads

In order to estimate the impact of heat island on energy loads it has been assumed that the building is cooled during the summer and heated during the winter.

The figure below displays the absolute and percentage variation of the annual cooling loads for all the simulation scenarios that have been carried out.

As expected, the assumed building in Egaleo area has a greater energy demand for cooling than the suburban area of Nea Erithrea.

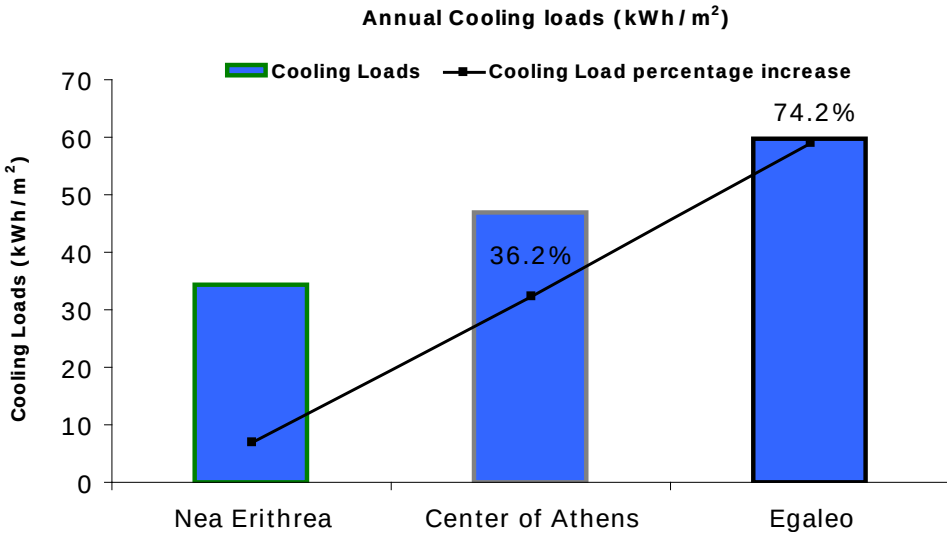

Figure 56 Annual cooling loads.

In the following Table the monthly values of cooling loads are given for the building of the suburban area (Nea Erithrea) and for the BRIDGE case study area. Additionally, the annual cooling loads are given for each case as well as the % variation between the suburban and urban area.

Table 31 Annual values of cooling loads.

	Cooling loads (kWh/m^2)		
	Nea Erithrea Suburban area	**Egaleo BRIDGE Area**	**Central Athens**
ANNUAL	**34.4**	**59.9**	**46.8**
% variation		**+74.2%**	**+36.2**

Annex 3 - London case study in situ measurements

3 London Case Study[1]

[1] Authors are indicated by subsection. All contributing authors listed here in alphabetical order
Inês Cabrita Andrade Dos Santos (KCL), Cris Castillo (KCL), Mark de Jong (KCL), Mariana Gouvea (KCL), Katy Francis (KCL), Chloe Franks (KCL),Oscar Finnemore (KCL), Sue Grimmond (KCL), Jiangping He(KCL), Simone Kotthaus (KCL), Fredrik Lindberg (Goteborg University and KCL) Pru Robinson(KCL), Lukas Pauscher (KCL), Jinda Sae-Jung (KCL), Paul Smith (KCL), Tom Smith (KCL),Matthew Tallis (University of Southampton), Marc Thomas (KCL) Helen Ward (KCL), Martin Wooster (KCL), Duick Young (KCL)

3.1 Introduction [Author: Grimmond]

The Greater London Authority (GLA), through The Greater London Authority Act 1999, has responsibility for strategic planning in London[2]. The GLA consists of 32 Boroughs and the City of London (Figure 1). Of specific interest to BRIDGE is the Central Activity Zone (CAZ) (Figure 1). This area is where the central government offices, headquarters and embassies, most of the financial and business services sector and the offices of trade, professional bodies, institutions, associations, communications, publishing, advertising and the media are located[3]. The CAZ accounts for nearly 30% of all London's jobs and is projected to accommodate 36% of London's employment growth to 2026[4].

The London Plan provides the background and expected changes in London for the next 20-25 years[5]. The latest versions of the plan, GLA (2009)[6] and GLA (2008)[7], provide descriptions of London now and in the future. In these documents the CAZ is identified as important terms of future planning of London. In addition to the London Plan, two other planning documents are relevant for providing the context for London[8]:

1) The Draft Mayor's Transportation Strategy[9]
2) The Mayor's Economic Development Strategy[10] (GLA 2010)

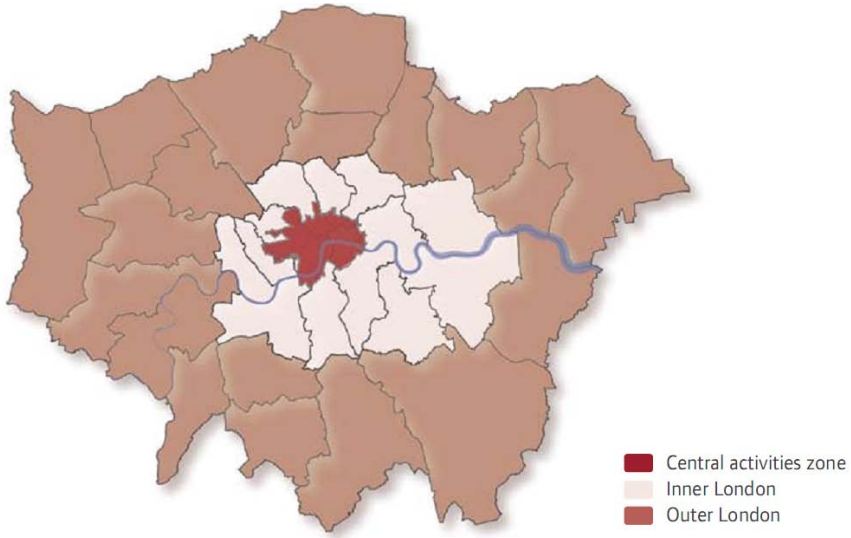

Figure 1 Central Activity Zone within London[11] with the 32 Boroughs plus the City of London and the River Thames shown.

3.2 The BRIDGE Planning Alternatives [Author: Grimmond]

[2] http://www.london.gov.uk/thelondonplan/about.jsp [accessed 12 March 2011]
[3] http://www.london.gov.uk/thelondonplan/caz/central_activities.jsp
[4] http://www.london.gov.uk/thelondonplan/caz/central_activities.jsp
[5] http://www.london.gov.uk/shaping-london/london-plan/
[6] http://www.london.gov.uk/shaping-london/london-plan/docs/london-plan.pdf
[7] http://www.london.gov.uk/thelondonplan/docs/londonplan08.pdf
[8] http://www.london.gov.uk/shaping-london/
[9] http://www.tfl.gov.uk/corporate/13980.aspx
[10] http://www.lda.gov.uk/Documents/Economic_Development_Strategy_%282010%29_6543.pdf
[11] http://www.london.gov.uk/shaping-london/london-plan/docs/london-plan.pdf

The vegetation in London is highly variable with grassed parks or gardens (public and privately owned) and trees (deciduous and coniferous species) (LNHS 2011[12]). The planning activities that are of specific interest to the GLA for the BRIDGE project relate to the use of green infrastructure within the CAZ to reduce flooding and thermal stress. The alternatives being considered are to:

(a) add vegetation to roofs with consideration given to the slopes of the roofs
(b) add street trees
(c) add street trees and green roofs
(d) make roads pervious with the addition of street trees and green roofs

Here we summarise and synthesise studies we have undertaken in London to document the:
(1) nature of the surface currently, and the potential for additional green infrastructure
(2) observations of hydro-meteorological data collected
These analyses involve the use of data collected by remote sensing and direct measurement. These data provide context for the observations and the modelling which are part of the development of the decision-support system (DSS) for its application in London.

3.3 City characterization [Author: Grimmond & Knott]

To characterize the Central Activity Zone and surrounding areas of London a range of data sets have been used (Table 1). Given there are multiple datasets which have similar characteristics (e.g. LiDAR[13] data sets) each has been given a code so that it is clear which data are used in which analysis.

A variety of methods are used to evaluate the current green infrastructure (Table 2). These provide the context for observations and the starting conditions for any proposed changes. In addition they provide information that can be used for modelling. In the following sections the methods and the results of these analyses are presented.

Accurately mapping and modelling urban vegetation characteristics enables for a significant increase in our understanding to many of the functions of the urban system (Næsset 2004[14]), enabling for a higher success in the management and moderation of the urban environment (Honjo and Takakura 1990-1991[15]; Upmanis *et al*. 1998[16]; Akbari *et al*. 2001[17]). Accurate urban vegetation can provide a means to reduce the effect of the urban heat island whilst also affecting the energy requirements of many urban structures (Mayor of London 2011[18]). Vegetation mapping and modelling can also allow for the

[12] London Natural History Society (2011) Londons Wildlife Habitats. [online]. Available from: http://www.lnhs.org.uk/habitats.htm last accessed 10/12/10.
[13] Light Detecting And Ranging (LiDAR)
[14] Næsset E (2004) Accuracy of forest inventory using airborne laser scanning: evaluating the first Nordic full scale operational project. Scandinavian journal of forest research.19, 554-557.
[15] Honjo T and Takakura T (1990-91) Simulation of thermal effects of urban green areas on their surrounding areas. Journal of Energy and Buildings, 15–16, 443–446.
[16] Upmanis H, Eliasson I, Lindqvist S (1998) The influence of green areas on nocturnal temperatures in a high latitude city (Goteborg, Sweden). International Journal of Climatology, 18, 681-700.
[17] Akbari H, Pomerantz, M, Taha, H. (2001) Cool surfaces and shade trees to reduce energy use and improve air quality in urban areas. Solar Energy. 70(3), 295-310.
[18] Mayor of London (2011) [online]. Available from: http://www.london.gov.uk/streettrees/ last accessed 7th February 2011.

measurement of species distribution as well as urban habitat quantification (Hinsley *et al*. 2002[19], Brandtberg *et al.* 2003[20]). These factors are becoming increasingly important in a rapidly growing and ever more dynamic urban environment (Chen *et al.* 2009[21]). LiDAR as a measure of such data has been previously expressed as one of the more attractive ways to collect vegetation data (Goodwin *et al*. 2009).

In April 2011[22] the London Assembly Environment Committee published a report on the current and futures of street trees in London. The most detailed data presented are at the Borough level[23] which is coarser than what is needed for the modelling to be carried out as part of BRIDGE.

[19] Hinsley SA, Hill, RA, Gaveau DLA & Bellamy PE (2002) Quantifying woodland structure and habitat quality for birds using airborne laser scanning. *Functional Ecology*, 16, 851– 857.

[20] Brandtberg T, Warner T, Landenberger RE, and McGraw JB (2003) Detection and analysis of individual leaf-off tree crowns in small footprint, high sampling density LiDAR data from the eastern deciduous forest in North America. *Remote Sensing of Environment*, 85, 290–303.

[21] Chen Y, Su W, Li J, Sun Z. (2009) Hierarchical object oriented classification using very high resolution imagery and LIDAR data over urban areas. Advances in Space Research, 43, 1101-1110.

[22] GLA 2011 Branching out: The future for London's street trees. London Assembly, Environment Committee, 49pp. http://www.london.gov.uk/sites/default/files/FINAL%20street%20trees%20report.pdf
http://www.london.gov.uk/publication/branching-out-future-london%E2%80%99s-street-trees

[23] http://www.london.gov.uk/sites/default/files/11-04-19-street-trees-borough-data.pdf

Table 1 : Data sets used to characterize London surface characteristics

Code	Source	Description
LN8	NERC Flight August 2008	Raw LiDAR data collected by Natural Environmental Research Council (NERC) Airborne Remote Sensing Facility flight: GB08/19 (0.71-m^{-2})
TL8	Derived from LN8 Lindberg & Grimmond (2011)	Trees taller than 2.5 m.
LI58	GLA	Infoterra LiDAR data summer 2008 and summer 2005 (1 m^2 resolution)
VL	GLA/ ERG[24] – KCL	Virtual London calculated from LiDAR data – has the building characteristics
OS	KCL	OS MasterMap® Topography Layer data
STI	Individual Boroughs, via the Forestry Commission	Street Tree Inventory data
GRP	Matthew Thomas, GLA	ArcGIS Layer with slopes and area of roofs that are potential locations for installing green roofs calculated from LiDAR data(probably LI58) by UCL
AP8	NERC Flight August 2008 (see LN8)	Rectified Aerial Photographs: three bands (RGB); approximate spatial resolution of 8 cm on the ground
LCC	Created here	Land cover data set created with surface characteristics

Table 2: Methods used to identify current surface characteristics and green infrastructure in London (see Table 1 for explanation of codes)

Surface Characteristic	Databases used	Methods
Green Roofs	Green roof contractors reports Aerial imagery	Visual inspection of aerial imagery to determine if green roofs present
Tree Height and crown diameter	Field observations TL8	Public property trees taller than 2.5 m were measured at 10 sites and compared to TL8 data
Trees	LN8, OS, VL, STI, AP8	LiDAR based methodology developed for 19 sites along a north/souch transect through London. Dataset created TL8
Vegetation	AP8	Maximum likelihood classification (MLC) of AP8 evaluated against LCC

[24] ERG – KCL: Environmental Research Group – King's College London

3.3.1 Current Green Roofs: Methods [Author: Lister & Grimmond]

Typically green roofs consist of a growing medium above a waterproof membrane with layers for drainage to prevent plant roots compromising a roof's structure. The substrate can consist of wide variety of materials from fertilised soil to recycled rubble. Generally green roofs are differentiated into three types, based on substrate depth and weight (Table 3): *Extensive*, *Semi intensive and Intensive.*

To identify current green roof locations several databases were used (Table 4). Particularly useful sources were the project reports of green roof contractors. The green roof location was verified using online image sources (in order of best resolution and most useful: Bing Maps, Yellow Pages Maps and Google Earth (GE)). Confirmation of a roof's location was important to ensure its continued existence and to build familiarity with their appearance in largely two-dimensional images. Sedum roofs, for example, tend to show up as a brownish-red colour which can be quite distinctive on a flat roof surface.

The green roof locations were geo-coded using GE. Although GE images have the poorest resolution they allow files to be created which can be uploaded into ArcMAP to 'identify' the green roofs inside the CAZ (**Figure** 2). These are then compared to the GLA provided dataset of where **G**reen **R**oofs could **p**otentially be located (GRP data set, Table 1). Note the areas calculated use the whole roof area from GRP so are larger than the actual roof area that is covered by vegetation.

Table 3 Characteristics of green roofs (Getter and Rowe 2006[25], Grant 2006[26], Living roofs 2011[27])

	Extensive	**Semi-Intensive**	**Intensive**
Depth of substrate (mm)	60-200	120-250	150- 400
Weight (kg m^{-2})	60 -150	120-200	180-500
Type of vegetation	Mosses, herbs, grasses small, low growing species (e.g. sedum)	Grasses, herbs, shrubs	Lawn/perennial, shrubs, trees Large plants
Roof slope	Flat or sloped		Tend to be flat

3.3.2 Current green roofs: Results [Author: Lister, Lindberg & Grimmond]

There are approximately 24,000 ha of buildings in Greater London (GLA 2008a) which is 15-16% of the total land area (based on Grant 2006, GLA 2008a, respectively). The 35 green roofs (Table 4) cover 168,561 m2 of the total roofed area of Greater London, which includes the CAZ (0.06 % of the area) (Table 5). In the CAZ, the five green roofs (GRP based areas) make up 0.6 % of the CAZ roof area. Although there is a higher percentage cover of green roofs in the CAZ, the total green area is greater outside the CAZ boundaries.

In the CAZ, the total roof area of all roofs, green and non-green, is dominated by sloping roofs, with increasingly smaller proportions of flat, intermediate and vertical roof cover. Not all the sites identified as currently having a green roof appeared in the GRP data set (viz, the Museum of London, the Tower of London Gift Shop, Inn The Park restaurant, 55 Broadway and 1 Wood Street), suggesting that there are more potential locations that identified in the GRP dataset. Currently the green roofs are disproportionately on flat and intermediate sloped roofs (Table 6, Figure 3). However, overall flat roof area with green cover is only 0.7 % of the total flat roof area of the

[25] Getter K & Rowe D (2006) The role of green roofs in sustainable development. HortScience. 41, 1276–1286
[26] Grant G (2006) Extensive Green Roofs in London. Urban Habitats, 4 (1), 51-65
[27] http://livingroofs.org/2010022858/green-roof-types/greenrooftypes.html (17 April 2011)

CAZ (Table 7) and green sloping roofs account for only 0.51 % of all sloping roofs in the zone. Intermediate roofs have the largest percentage (0.88%) which is green but the smallest proportion of the total roof area of the CAZ.

The total roof area that could potentially be retrofitted with green roofs in the CAZ is 4,987,104 m^2 (~15 % of the total CAZ area) or ~ 92 % of the total roofed area. In 2008 the GLA report Living Roofs and Walls suggested 32 % of London's roofs could be greened (GLA 2008a). Since the start of 2009, six green roofs have been constructed (Table 4) with a total estimated area (five) of 15,161 m^2. Mayor Boris Johnson's target is to increase green roofs in London by 100,000 m^2 (based on 2008/9 baseline estimates) by the year 2012 (GLA 2009). This means that in the next two year years the amount of development of green roofs has to be over five times that of the past two years.

Table 4: Location of green roofs in London. T Type: E: extensive, I: intensive, B: both, SI: Semi-intensive, SE: Semi-extensive, U: Unknown; Reference: see footnotes; !In literature but not on maps,# in CAZ but not in GRP; *in CAZ but in GRP

Address	T	Area (m^2)	Year	Ref	Address	T	Area (m^2)	Year	Ref
1 Wood Street, EC2V 7WS*	E	5600	2009	[28]	Inn The Park rest., St. James's Park*	I	335	2004	[29]
11 Shaw's Cottages!	E	100	1993	[30]	Jacobs Island, Bermondsey	I	930	1997	[31]
1-5 Offord Street, Islington	E	65	2004	[32]	Jubilee School, Tulse Hill	E	3149	2002	34
1 Poultry (2/3 Queen Victoria St GNP)#	I	1966	1999	28	Kensington roof gardens, Derry Street	I	14956	1938	[33]
55 Broadway, Westminster*	E	-	2009	28	Laban Dance Centre, Deptford Creek	E	3748	2002	35
Adelaide Wharf, Haggerston	E	460	2007	[34]	Merrill Lynch HQ, King Edward St#	I	930	2000	31
Almeida Theatre, Islington	E	526	2002	[35]	Monument (under construction)!	SE	-	now	[36]
Beaufort Court, Lillie Road, Fulham	E	1936	2003	34	Museum of London*	I	1684	2010	[37]
Bishops Square, Spitalfields#	B	5400	2007	34	New Providence Wharf & Radisson	B	418	2006	34
Canary Wharf 1	E	11270	2000	30	North Harringay Jr School, Haringey	I	190	2005	34
Canary Wharf 2, 20 Cabot Square	E	12696	2000	30	Northern Line Control Cent, Highgate!	E	1950	2007	34
Canary Wharf 3, Barclays Building	E	6095	2000	30	Portland Grove, Lambeth	E	1000	2006	29
Canary Wharf 4, Jubilee Park	I	32974	2001	[38]	Royal Arsenal, Woolwich	I	22688	2005	[39]
Canary Wharf 5, Cabot Place	E	6046	2000	[40]	Six Acres Estate, Islington	E	3100	2009	[41]
Canary Wharf 6, Canary Wharf DLR	E	4206	2000	40	Springbok Works, Dalston	I	90	2000	34
Canon Street Station#	I	14723	-	[42]	St Martins in the Field HS Girls, Tulse Hill	E	3700	2004	[43]
Center for Wildlife Gardening!	U	-	-	30	Stonegrove Estate, Edgeware!	E	1200	2008	[44]
Creekside educational centre, Deptford Creek	E	100	2003	[45]	Michael Tippett School, Lambeth	E	2000	2008	29
Ethelred Estate, Kennington	E	4000	2005	[46]	The Muse, Islington!	B	-	2007	[47]
Gold Lane, Edgeware	E	400	2003	34	Tower of London gift shop*	I	5550	1992	29
Goldsmiths Place, Camden	E	1690	2006	[48]	Webheath Estate, Hampstead	SI	3867	2009	[49]
Horniman Museum, CUE	E	282	1995	30	William Gunn House, Hampstead	E	910	2009	[50]

Table 5 Total area (m^2) and percentage (%) of green roof cover in Greater London and the CAZ (including vertical and unmeasured roof class).

Total Area (m^2)	**Greater London**	**CAZ**	**GL-CAZ**
All	1,579,000,000	33,522,307	1,545,477,693

[28] Livingroofs.org
[29] http://www.bauder.co.uk/media-centre/project-gallery
[30] http://www.urbanhabitats.org/v04n01/london_pdf.pdf
[31] http://www.greenroofs.com/projects/pview.php?id=660
[32] http://www.greenroofs.com/projects/pview.php?id=85
[33] http://www.greenroofs.com/projects/pview.php?id=648
[34] Living Roofs and Walls Report GLA 2008a
[35] http://www.greenroofs.com/projects/pview.php?id=549
[36] http://www.greenroofs.com/projects/pview.php?id=894
[37] http://www.bauder.co.uk/media-centre/
[38] http://www.greenroofs.com/projects/pview.php?id=510
[39] http://www.greenroofs.com/projects/pview.php?id=393
[40] http://www.greenroofs.com/projects/pview.php?id=95
[41] http://www.langley.co.uk/asx/six_acres_case_study_-_newsletter.pdf
[42] http://livingroofs.org/2010030161/green-roof-types/intens.html
[43] http://www.greenroofs.com/projects/pview.php?id=91
[44] http://www.langley.co.uk/asx/stonegrove_case_study.pdf
[45] http://www.greenroofs.com/projects/pview.php?id=550
[46] http://www.greenroofs.com/projects/pview.php?id=77
[47] http://www.greenroofs.com/projects/pview.php?id=1066
[48] http://www.greenbuildingpress.co.uk/article.php?article_id=700
[49] http://www.greenbuildingpress.co.uk/article.php?article_id=700
[50] http://www.langley.co.uk/asx/william_gunn_case_study.pdf

Roofed	240,000,000	5,404,602	234,595,398
Green Roofed	168,561,000	32,299	136,262
Utilisation of total roof area as green roofs (%)		0.60	0.06

Table 6 Areas of different roof classes for all roofs and for green roofs as a percentage (%) of the total CAZ area.

CAZ Roof Class	All Roofs (% of Total Roofed Area)	Green Roofs (% of Total Roofed Area)
Flat	26	30
Intermediate	12	18
Sloping	55	47
Vertical	5	4
Unmeasured	2	1

Table 7 Total potential green roof area in the CAZ based on roof slope classifications.

Area (m^2)	**Flat**	**Intermediate**	**Sloping**
Total Roof	1397273	659201	2961347
Green Roof	9830	5803	15084
Green Roof	0.70	0.88	0.51
Current green roof cover (%)			0.60
Potential green roof area (m^2)			4,987,104

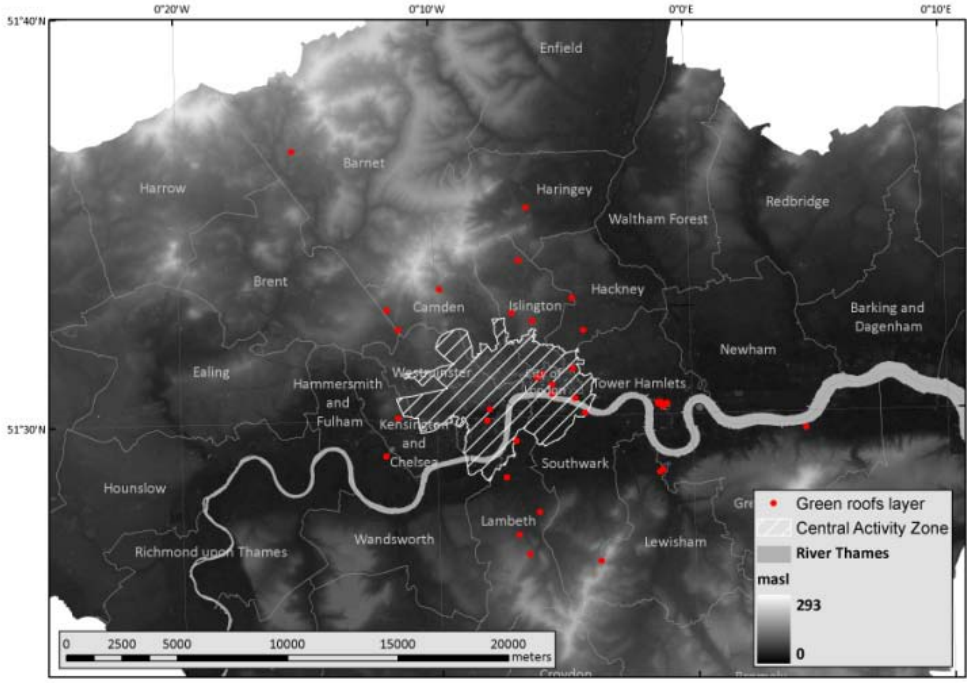

Figure 2: Existing green roof locations.

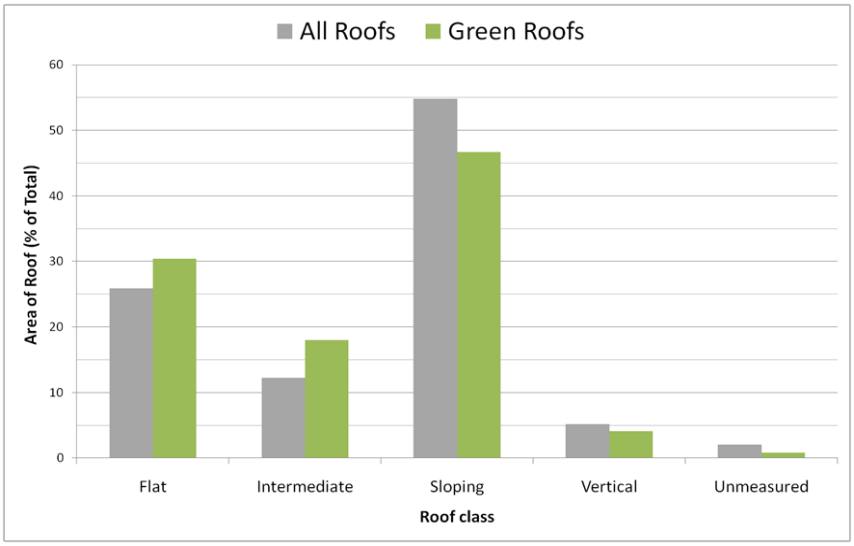

Figure 3 Percentage of total (grey) and green (green) roof area in the CAZ by slope class

3.3.3 Current tree characteristics[51]: methods [Author: Lindberg & Grimmond]

To analyse the current tree characteristics in London, data collected from a NERC ARSF north-south LiDAR flight (LN8, Table 1) transect through Greater London (Figure 4) are analysed. The spatial data were acquired on 14 August 2008 using an Optech ALTM 3033 LiDAR system, operating at a flight altitude of 900 m above ground level (agl). The sensor was configured to record first and last returns as well as intensity values with a pulse frequency of 33 kHz using a maximum off-nadir view angle of 20° and a wavelength of 1064 nm. The beam-divergence was set to 0.21 mrads. The area surveyed includes an approximately 0.65 km x 50 km north to south transect passing over the central parts of London; a single flight line was used. The average point density on the ground was 0.71 m^{-2}. Along the transect 19 study areas (400 m x 400 m analysed at 2 m resolution) were located centrally within the transect to exclude large off-nadir angles since the laser beam moves across the track resulting in a Z-shaped pattern with lower density distributed points at the edge of the field of view.

To derive the data, several steps and software systems were used. Most of the GIS pre-processing was done in ESRI's ArcInfo 9.3 and all filtering procedures presented used MathWorks MATLAB®. The input spatial datasets derived are: a ground and building Digital Elevation Model (DEM), a vegetation canopy DEM, and a trunk zone DEM. First the LiDAR points within each study area were extracted using FUSION/LDV (version 2.70- McGaughey 2009[52]) from the main LiDAR cloud (46399632 points) (Figure 5a). The GroundFilter algorithm within FUSION/LDV was used to identify those last and single returns that correspond to probable bare-earth surface points. These points were gridded to create a bare earth DEM (Figure 5b). To separate points located on building roofs, building footprints extracted from the OS MasterMap® Topography Layer (Ordnance Survey 2010[53]) land use dataset were used. First and single returns outside the building footprints were stored separately to be used as 'potential' vegetation

[51] This section and the results from this section are from:
Lindberg F, CSB Grimmond (2011) The influence of vegetation and building morphology on shadow patterns and mean radiant temperatures in urban areas: London case study, *Urban Ecosystems* (in review)
[52] McGaughey, R.J. (2009) FUSION/LDV: Software for LiDAR Data Analysis and Visualization. United States Departmentof Agriculture, Seattle.
[53] Ordinance Survey (2010) © Crown database right 2010. An Ordnance Survey/EDINA supplied service. Assessed 2009-10-13

points. By combining the building points dataset and the bare earth DEM a ground and building DEM was created (Figure 5c) (hereafter referred to as building DEM).

Height attributes for each vegetation pixel were compared with the bare earth DEM and those lower than 2.5 m above ground were removed from the dataset. After points below 2.5 m agl were removed, urban features such as building walls, power lines, masts etc were still present and had to be removed in order to generate a vegetation canopy DEM (Figure 5d). To remove these non-vegetation features a similar filtering approach to Goodwin et al. (2009[54]) was used. The first filter applied removed the linear features in the dataset. A 9 x 9 pixel moving window was used for a series of lines oriented 0° to 179°. When the number of pixels including vegetation points that intercepts a projected line was > 4 points of the possible 9, less than 3 of the surrounding pixels in the window were classified as vegetation, the vegetation pixels were removed. A second filter was applied to fill gaps caused by the sampling patterns of LiDAR and inconsistent detection of vegetation points. This was a 3 x 3 pixel moving kernel that classified a pixel as vegetation if 6 or more of the surrounding 8 pixels were classified as vegetation (Goodwin et al. 2009). A final 3 by 3 pixel kernel filter was applied to remove single pixels classified as vegetation when none of the surrounding 8 pixels were non-vegetation pixels (e.g. masts, lamp posts etc). Remaining vegetation pixels were used to generate the canopy DEM with a height value or non-tree pixels assigned 0 m (Figure 5e).

Vegetation has small gaps that allow laser light to penetrate and record additional returns at lower elevation. This was used to obtain a rough estimate of the crown base height needed to generate the trunk zone DEM. The approach used here was developed by Holmgren and Persson (2004[55]) and has been applied by others (e.g. Kim et al. 2009[56]). First, all the returns classified as vegetation were selected. Laser returns less than 2 m agl were omitted from the analysis to remove the effects of ground vegetation, cars and other obstacles found in the urban environment. The remaining laser points were classified as non-ground vegetation points. To estimate crown base height a 0.5 m interval was used. Each interval that contains ≤1% of the total number of non-ground laser points within an individual tree was set to zero and others to one. The crown base height was defined as the distance from ground to the lowest height layer where > 1% of the data points were found. Holmgren and Persson (2004) used a segmentation process for separating different tree crowns and therefore could identify the returns that originated from a certain vegetation unit. As they had higher resolution laser data (0.44 m between laser hits on the ground) than this study, here vegetation laser returns were separated using a 10 m x 10 m grid for each study area. Within each grid cell a crown base height was estimated. Using this approach all vegetation pixels within a 10 m x 10 m grid have the same crown base height value. As an artefact of this if a grid cell was located at the edge of vegetation large overestimations may occur. After re-gridding the 10 m x 10 m grid to 2 m pixels this artefact was reduced by applying a 3 by 3 pixel median filter on single local maxima compared to the surrounding 8 pixels. If the crown base height and canopy height of a pixel were within 1 m the crown base height was altered using a median 3 by 3 pixel median filter. Finally, rare occasions with unlikely crown base heights (i.e., < 15 m) were classified as bush pixels. An example of a trunk zone DEM is shown in Figure 5f.

---

[54] Goodwin NR, Coops NC, Tooke TR, Christen A, and Voogt JA (2009) Characterizing urban surface cover and structure with airborne LiDAR Technology. *Canadian Journal of Remote Sensing*. 35, 297-309.

[55] Holmgren J, Persson Å (2004) Identifying species of individual trees using airborne laser scanner. Remote Sensing of Environment 90:415-423

[56] Kim S, McGaughey RJ, Andersen HE, Schreuder G (2009) Tree species differentiation using intensity data derivedfrom leaf-on and leaf-off airborne laser scanner data. *Remote Sensing of Environment,* 113, 1575-1586.

The building and canopy DEMs for the 19 sites are shown in Figure 6. In order to compare the sites, the building DEMs scale bars have a 45 m range except for 9S which is located on a relatively steep slope and therefore a higher range is used (60 m). Pixels with heights greater than the maximum height are shown as white pixels. All vegetation canopy DEMs have the same heights range (35 m) and pixels equal to 0 are transparent.

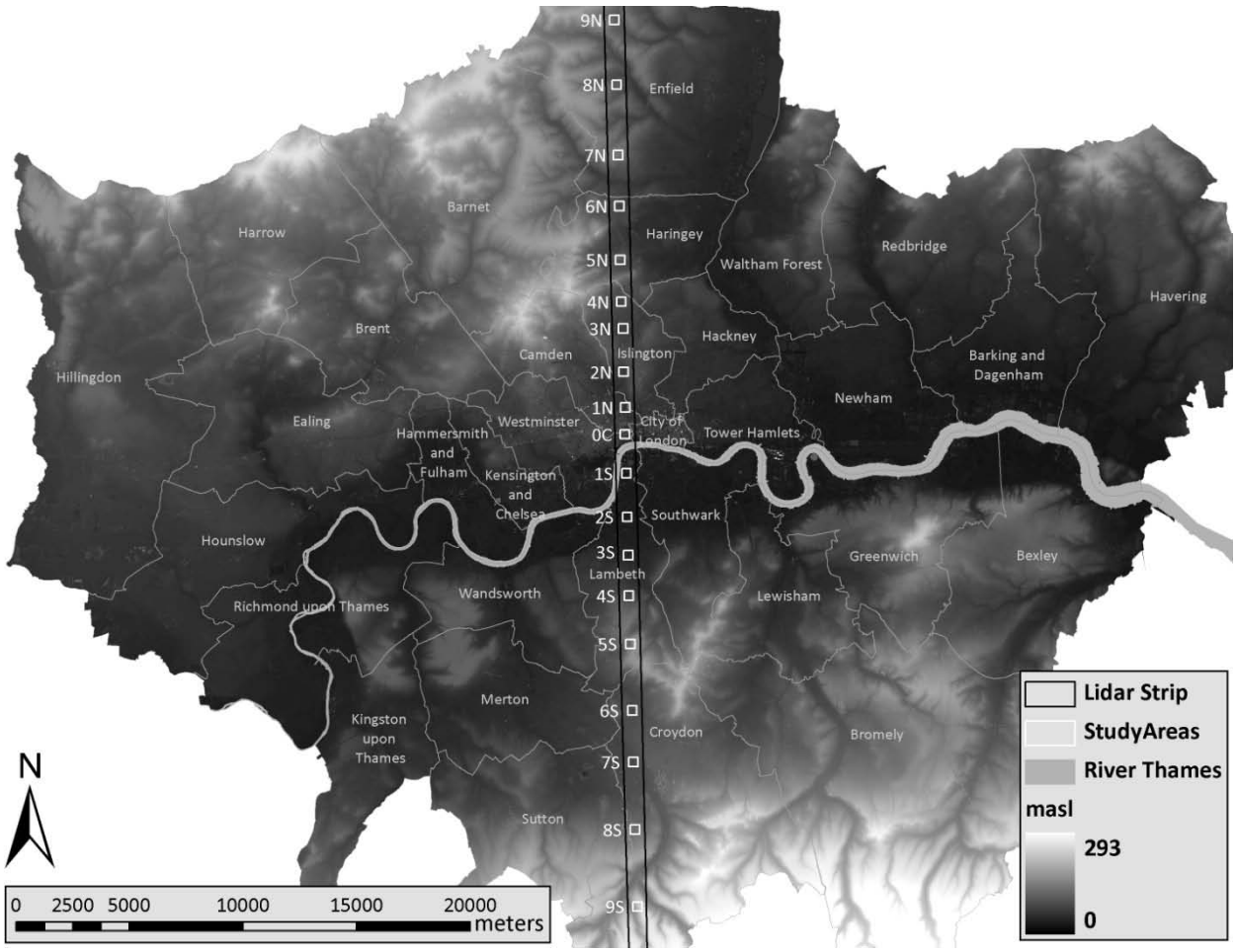

Figure 4: Greater London (with 32 Boroughs and the City of London) showing LiDAR transect and the 19 study areas.

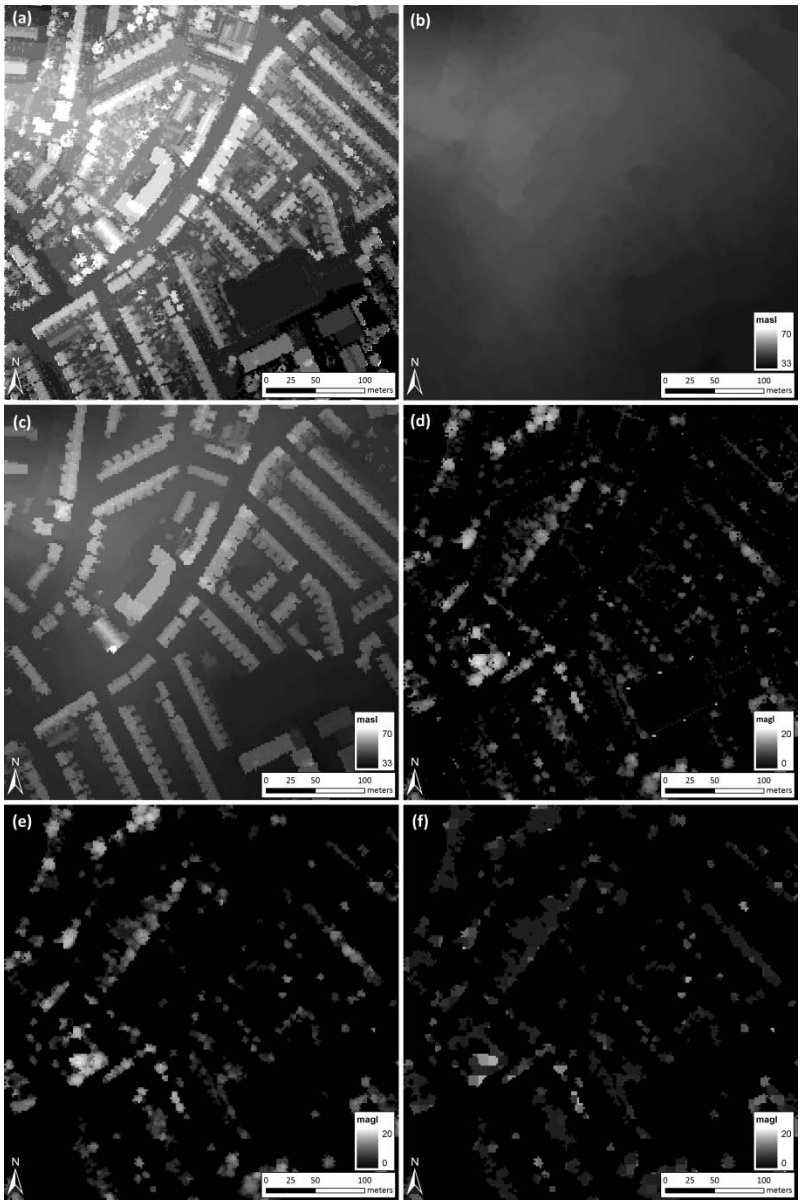

Figure 5 : Results generated in creating the digital elevation models (DEM) from LiDAR data (site 5N, see Figure 4): a) unprocessed LiDAR data, b) ground DEM, c) ground and building DEM, d) canopy DEM before filtering, e) canopy DEM after filtering, and f) trunk zone DEM.

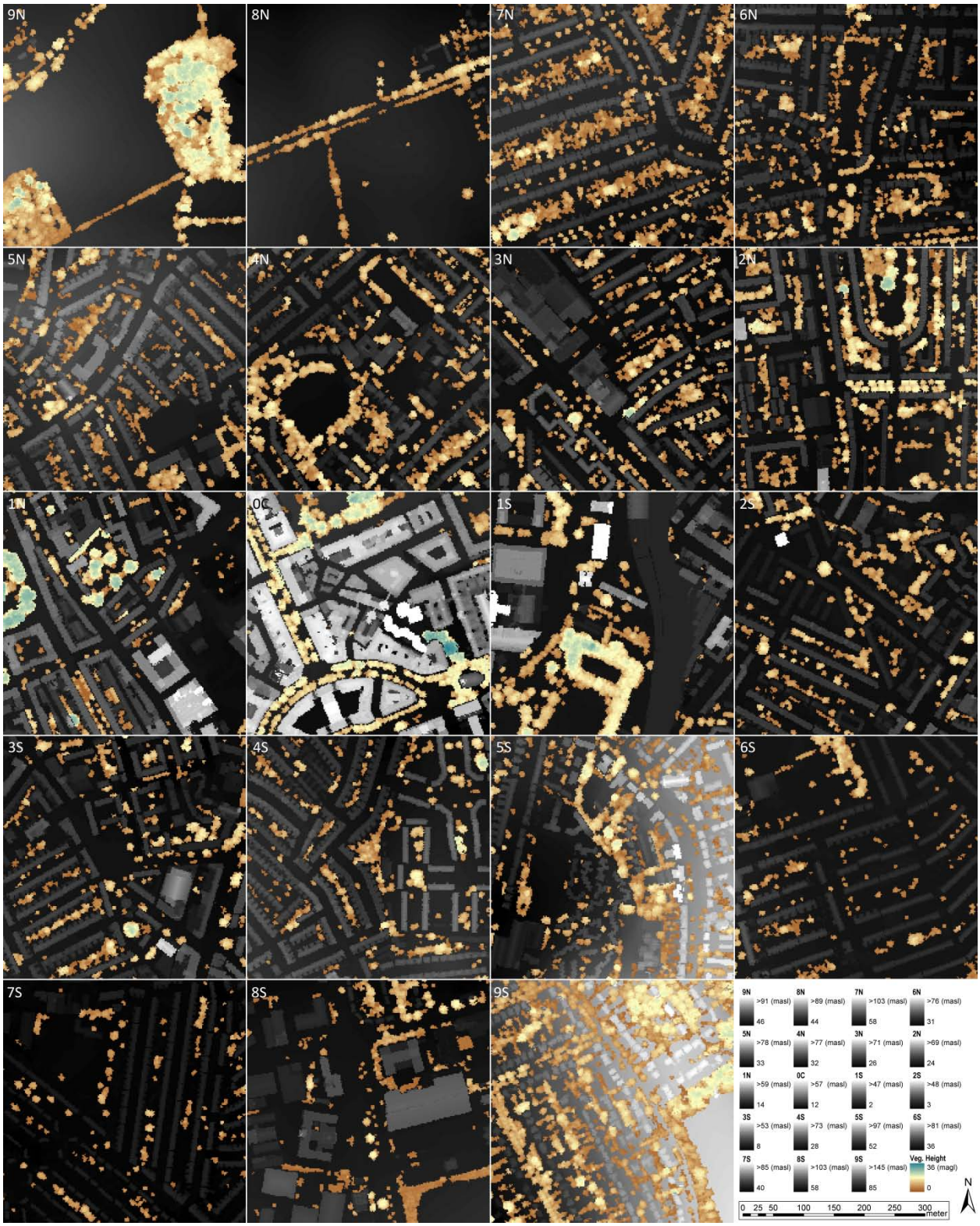

Figure 6: Building DEMs overlaid by canopy DEMs derived from LiDAR data for the 19 sites (see Figure 4).

3.3.4 **Current Tree characteristics: Field observation methods**[57] [Author: Knott & Grimmond]

To evaluate the LiDAR derived data tree height and crown diameter were measured at 10 sites. The trees at these sites were identified from high resolution photographs (AP8, Table 1). The trees had to:

a) have a height and diameter > 2.5 m (so included TL8 - Table 1)

b) be publicly accessible

c) have foliage (LN8 data were obtained during leaf-on).

Given the variation in number of trees at the sites (Figure 6) there were different numbers of trees with the potential to fulfil these criteria. Field data were collected during two weeks in August 2010 the same time of year as the NERC ARSF (LN8) observations.

The maximum height and crown diameter measurements were recorded for each pre-selected tree. A clinometer was used at 10 m distance on the most level plane away from the base of the tree to determine the height. Crown diameter was obtained by using a measuring wheel between two perpendicular points of the trees longest axis (Goodwin *et al.* 2009). A subjective assessment is involved in determining where the top of the tree is and which axis is the longest when carrying out field estimations. It is assumed that the size of the tree has not changed significantly between 2008 and 2010. In an urban area both tree growth and tree management (pruning, removal) could cause differences (see discussion in Clark *et al*. 2004[58]).

The maximum tree height for 164 trees and crown diameter for 160 trees were measured. However, 4 trees height could not be determined from the TL8 data and diameters for 8 trees could not be identified. These are excluded from the results. All trees excluded were < 10 m tall. Clustering is a well established source of error in LiDAR data (Goodwin *et al.* 2009) and refers to the overlap of tree crowns producing observational as well as technological difficulties when vegetation is a measured parameter (Lee *et al.* 2007[59]). Goodwin *et al*. (2009) experienced much greater percentage of clustering of vegetation (34%) than this study (just less than 5%). There are means to extract individual tree characteristics from clustering (Reitberger *et al.* 2009[60]) but are not used here. However, the tree selection process implemented in this study would have biased the sample to a small amount of clustering.

The majority of publicly accessible trees have been purposefully planted and are subject to regular maintenance (London Councils 2004[61]). Typically they occur equidistant in a uniform way in a vast majority of areas throughout London. Location (1) in

[57] This section and the results from it are drawn from:
Knott W (2011) LiDAR: An Application for Measuring Urban Vegetation Parameters? A London Case Study. Independent Geographical Study, King's College London, 64 pp.

[58] Clark, M.L, Clark, D.B. and Roberts, D.A. (2004) Small-footprint LiDAR estimation of sub-canopy elevation and tree height in a tropical rain forest landscape, Remote Sensing of Environment, 9 (1), 68–89.

[59] Lee, A.C. and Lucas, R.M. (2007) A LiDAR derived canopy density model for tree stem and crown mapping in Australian forests Original Research Article. Remote Sensing of Environment, 111(4), 493-518.

60 Reitberger, C, Schnörr, P, Krzystek and Stilla, U. (2009) 3D segmentation of single trees exploiting full waveform LIDAR data. ISPRS Journal of Photogrammetry and Remote Sensing, 64 (6), 561–574.

[61] London Councils (2004) [online]. Available from: www.londoncouncils.gov.uk.

Figure 7 shows the typical vegetation studied here with individual trees easily identified in aerial photographs. In the residential regions (location 2) the vegetation is dense and individual trees are increasingly indistinguishable.

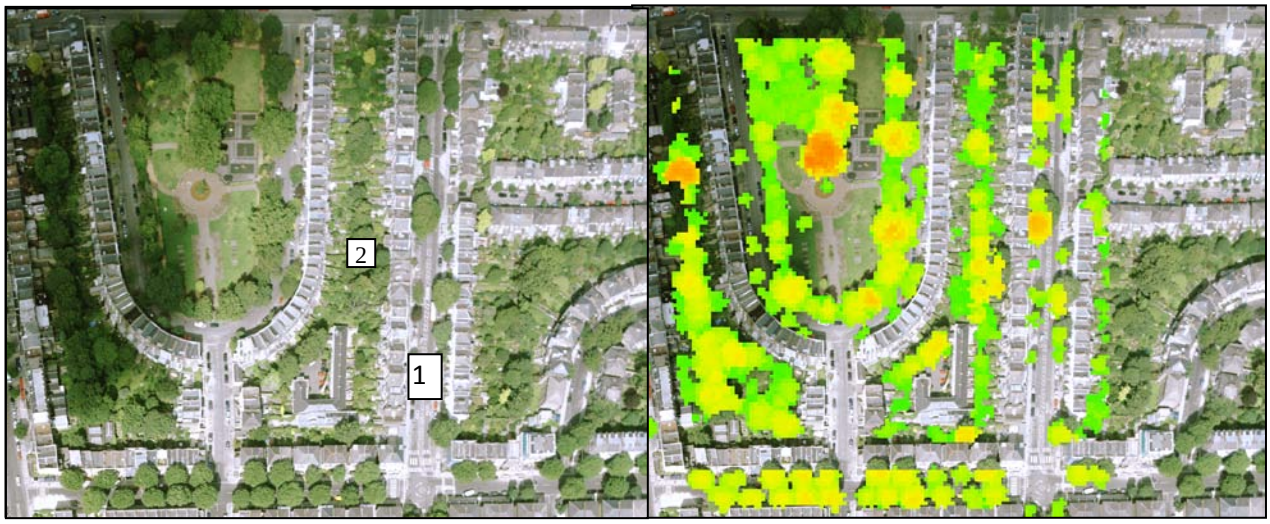

Figure 7: High resolution aerial photographs of study site 2N. (lower) overlaid LiDAR DEM (TL8) with green (shorter) to red (taller) vegetation.

3.3.5 **Current Trees: Results** [Author: Knott & Grimmond]

Site 9S (Figure 4, Figure 6) is the most vegetated of the sites measured. It has predominantly low rise residential housing consisting of small areas of light woodland and highly clustered areas of vegetation. At the other extreme is the densely populated area of South London (site 7S) with nearly four times more building fraction than vegetation. This demonstrates the high variability in vegetation cover throughout the metropolitan area.

The field heights have a mean difference of 0.27 m compared to the LiDAR derived (TL8) data (Table 8) with the largest difference of $\pm$ 0.42 m. These results are consistent with the literature (e.g. Clark *et al*. 2004, Streutker and Glenn 2006[62], Goodwin *et al*. 2009). The TL8 crown diameter values are consistently greater than the field values with a mean difference of 1.01 m and maximum diameter difference of 2.9 m. This is different to previous findings (Baldwin *et al*. 1997[63], Roberts *et al*. 2005[64]). Both field and LiDAR methods indicate significant variability in the dimensions of the trees, the standard deviation of both crown diameter and height are relatively high compared to the mean.

As vegetation height increases diameter increases (Figure 8) with a slightly higher correlation (r^2= 0.676, N=160) from the field measurements than that the LiDAR (r^2= 0.616, N=160). As in previous

[62] Streutker, D.R. and Glenn, N.F. (2006) LiDAR measurement of sagebrush steppe vegetation heights. *Remote Sensing of Environment*, 10, 135-145.
[63] Baldwin, V.C. Jr, Peterson, K.D, Burkhart. H.E, Amateis, R.L, and Dougherty, P.M. (1997) Equations for estimating loblolly pine branch and foliage weight and surface area distributions, Canadian Journal of Forest Research. 27, 918–927
[64] Roberts, S.D, Dean, T.J, Evans, D.L, McCombs, J.W. and Harrington R.L. (2005) Estimating individual tree leaf area in loblolly pine plantations using LiDAR-derived measurements of height and crown dimensions, Forest Ecology and Management, 213, 54–70.

studies (Lefsky 1997[65], Clark et al. 2004, Streutker and Glenn 2006, Goodwin et al. 2009), a high correlation for vegetation height between methods is obtained (
Figure 9). The correlation is stronger for height (r^2= 0.902, *N*= 164) than diameter (r^2= 0.864, *N*= 160). As in Næsset and Økland (2002), there was a net overestimation in the LiDAR height.

The frequency distribution of the data (Figure 10) is similar for both field and LiDAR estimates with peaks and troughs in distribution at similar sizes. Based on Kolmogorov-Smirnov and Sharpo-wilk tests the data are determined to be not normally distributed so the non-parametric Mann-Whitney U test is used to assess if there are significant differences in the datasets.

The Mann-Whitney U test for diameter shows that the LiDAR data are statistically different from the field values, whereas the height results are not significant (*p*= 0.68) indicating no statistical difference between the two methods. The TL8 diameters are significantly larger from field by 13.18% or 1.02 m on average. This is consistent with previous work. Popescu *et al*. (2003[66]) found diameter measurements obtained from LiDAR had greater inaccuracy than height derived measurements.

As Clark *et al*. (2004) found height of vegetation explained variations in accuracy and correlations the data were split into small (≤ 10 m) and large (> 10 m) trees. Small trees are found to have significantly larger mean difference between the TL8 and field estimated data, for diameter most specifically but also for height (Table 9). Of the trees measured 46.43% in this study were ≤ 10 m. This may be related to the size of pixels and the filters used to identify the vegetation during the development of the TL8 dataset.

To see if insights into differences could be related to tree types information on species were extracted from the Street Tree Inventory (STI) dataset (Table 1). The species that had the largest overestimation of diameter are, as expected, influenced by which species have the highest frequency of small trees (Table 10): Prunus, Sorbus, Acer, Crataegus and Betuaa. Plane trees, which make up over 50% of all trees > 10 m, are overestimated by an average of 8.36%. However, caution must be taken interpreting the results as many tree were not identified (29% of trees ≤ 10 m, 19% >10 m).

By comparing the characteristics of the field observed trees relative to all of the trees in the sample area one can assess the difference between public and private trees. When these are compared along the transect 90% of the sample sites have a lower mean than when just the trees are sampled (Table 8). When all vegetation is measured within a particular sample site an average difference of 2.24 m is observed in the height of trees between TL8 (sampled) and TL8 (all). This suggests that the street trees are taller on average. Whereas 90% of the sample sites have a smaller mean diameter with a mean difference of 0.96 m between TL8 (sampled) and TL8 (all) diameter. Again suggesting the street trees are larger.

Table 8: Mean TL8 and field heights and diameters and the differences *(Negative values TL8 underestimates)*

	Diameter (m)		Height (m)		Difference				Whole			Diameter (m)		Height (m)	
N	160		164		Diameter		Height		TL8	TL8	All	Field	TL8	Field	TL8
Site	Field	TL8	Field	TL8	(%)	(m)	(%)	(m)	D (m)	H (m)	Mean	3.37	3.49	4.70	4.80

[65] Lefsky, MA (1997) Application of LiDAR remote sensing to the estimation of forest canopy and stand structure, Ph.D. thesis, Department of Environmental Science, University of Virginia, Charlottesville, VA

[66] Popescu SC, Wynne RH, and Nelson RF (2003) Measuring individual tree crown diameter with lidar and assessing its influence on estimating forest volume and biomass. *Canadian Journal of Remote Sensing*, 29, 564–577.

9S	8.31	9.54	8.78	8.60	15.77	1.24	-1.60	-0.18	13.64	9.64	Std. Dev.	8.90	10.08	10.63	11.05
8S	8.96	9.75	10.95	10.11	8.94	0.79	-5.97	-0.84	11.48	6.73	Median	16.90	19.12	18.50	18.10
7S	9.73	10.65	10.10	8.25	9.40	0.92	-16.67	-1.85	11.34	6.15	Range	3.40	4.08	3.50	3.80
5S	8.34	9.83	10.42	11.08	20.08	1.48	3.60	0.37	11.96	8.18	Minimum	20.30	23.20	22.00	21.90
2S	8.62	9.76	10.58	10.32	13.97	0.94	-4.44	-0.56	10.48	8.73	Maximum	9.39	10.40	11.31	11.58
0C	13.39	14.49	16.55	18.35	8.06	1.09	11.26	1.80	14.81	15.00	Difference				
2N	11.60	12.57	15.81	16.38	9.65	0.96	4.47	0.57	12.79	9.80		(%)	(m)	(%)	(m)
4N	8.16	9.15	9.58	9.75	12.65	0.88	2.85	-0.04	10.57	8.74	All sites	**13.27**	**1.03**	**2.10**	**0.09**
5N	6.74	7.23	7.70	7.57	8.29	0.46	6.31	0.30	8.89	7.44	All trees	**13.18**	**1.02**	**3.87**	**0.27**
6N	7.91	9.47	8.81	10.17	25.94	1.56	21.16	1.36	10.03	7.15	Std. Dev.	**5.90**	**0.33**	**10.26**	**1.05**

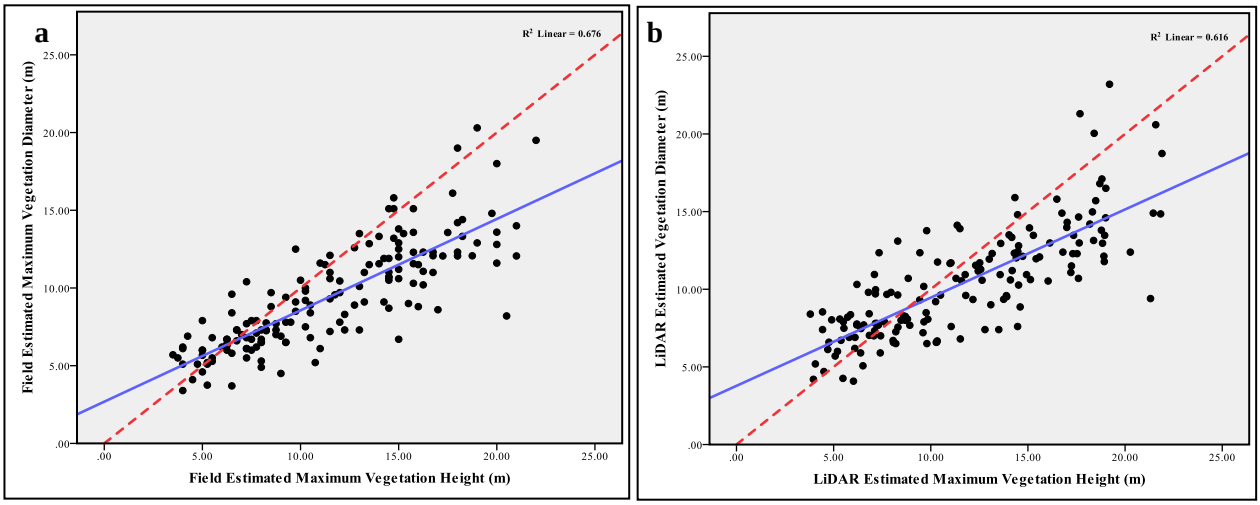

Figure 8: Height versus diameter for individual trees from (a) field and (b) LiDAR measurements with the regression (blue solid) and 1:1 (red dotted) lines

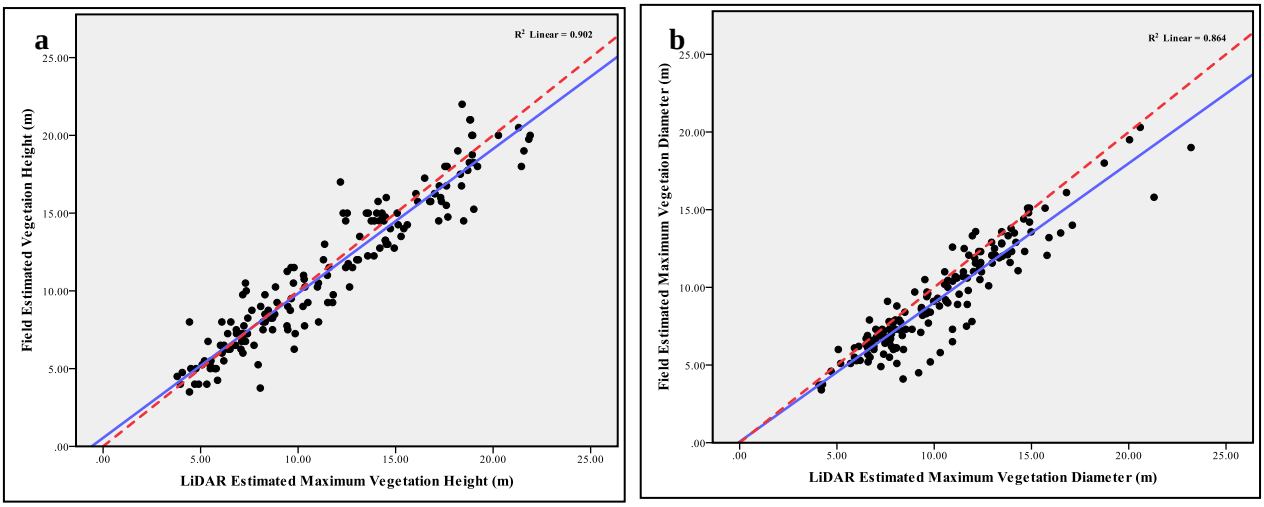

Figure 9: Comparison between LiDAR and field measurements of individual trees (a) height and (b)maximum diameter with the regression (blue solid) and 1:1 (red dotted) lines. ##

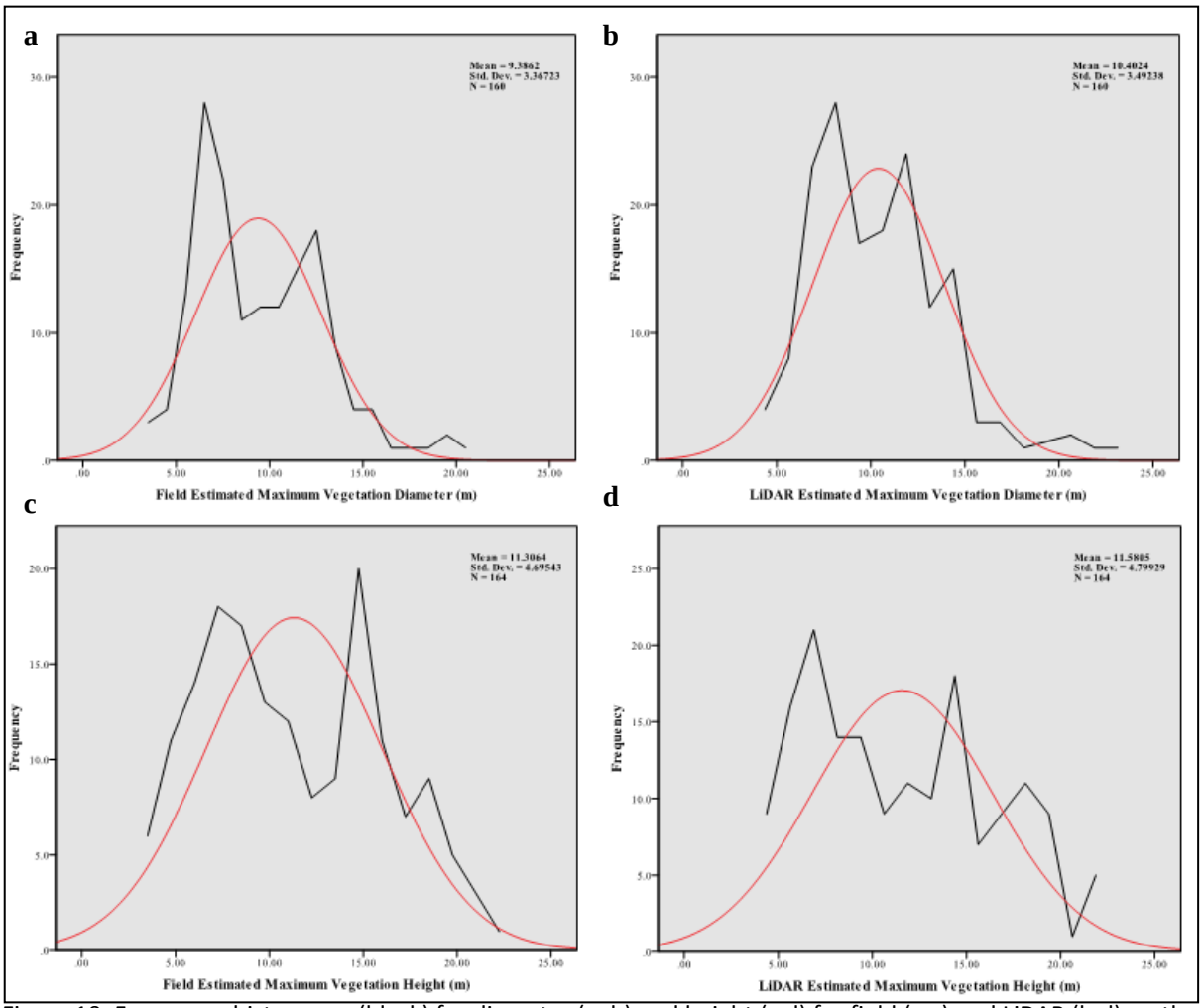

Figure 10: Frequency histograms (black) for diameter (a, b) and height (c,d) for field (a,c) and LiDAR (b,d) methods. A Normal curve (red) is shown for comparison purposes.

Table 9: Mean difference between LiDAR and field estimates by size of trees. What is N for the two?

	Diameter difference		Height difference	
	(%)	(m)	(%)	(m)
Small (≤ 10 m)	17.53	1.10	2.65	0.12

Large (> 10 m)	7.15	0.90	1.46	0.21

Table 10: Species of trees present by size

Spp.	Platanus	Not identified	Aesculus	Sorbus	Betula	Alnus	Acer	Tilia	Quercus	Fagus	Fraxinus	Malus	Prunus	Pyrus	Crataegus
Common	Plane		Horse chestnut	Rowan	Birch, Hazel, Ostrya	Alder	Maple	Elm	Oak	Beech	Ash	Apple	Cherry	Pear	Hawthorn
≤ 10 m		29		16	10		9					7	22	1	6
> 10 m	51	19	7	5	5	3	3	2	2	1	1	1	1		

3.3.6 Current characteristics: Results [Author: Lindberg & Grimmond]

The urban morphology characteristics for all 19 sites derived from the LiDAR (LN8) dataset and OS MasterMap data are shown in Figure 11. Clear local maxima of both mean building height (z_b) and building plan area density (λ_b) at the city centre are evident; the classical 'peak' where the strongest urban effect on the micro-climate usually is found (Oke 1987). This is also evident by visual examination of Figure 6. A clear 'plateau' with local maxima and minima is also evident in λ_b. At the local scale, λ_b will influence the wind profile and roughness parameters (Grimmond and Oke 1999[67]). Interesting patterns are evident in the characteristics of vegetation (taller than 2.5 m) at the 19 sites. As building heights increase vegetation height also increases (Figure 12). Although in the outskirts of London there is taller vegetation; see, for example, the forested area within 9N. Two vegetated sites (8N and 9N) are plotted but excluded from the calculation of the linear trend. These show the tendency of increasing vegetation heights that outside the central urban environment but still located within the London boroughs ("the Leafy Suburbs"). Note that the LiDAR transect does not go over the tallest buildings of London (Figure 4).

The plan area density of vegetation λv3 shows areas of denser vegetation i.e. parks and abundance of back gardens within certain areas of London. A trend of increased λv3 towards the outskirts of the urban area is also apparent. It should be noted that morphological parameters for vegetation (i.e. z_{v3} and λ_{v3}) only takes vegetation taller than 2.5-m into account. If shorter vegetation, such as grass and small shrubs is included, the values of z_{v3} and λ_{v3} would change considerably especially at the outer sites. Potential for a bias to be introduced by not accounting for vegetation when determining urban roughness parameters is evident.

The peaks in z_b and λ_b are also evident in sky view factors derived from the building DEMs (Ψ_b) (Lindberg and Grimmond 2010). Sky view factors are derived at different levels. Ψ_b on all horizontal surfaces (i.e. roofs and ground) ($\Psi_{b(all)}$) has similar values to Ψ_b on the ground $\Psi_{b(ground)}$ whereas $\Psi_{b(all)}$ have higher values as elevated roofs are included. The largest discrepancies between these two parameters occurs when extensive building structures (e.g. industrial plants) are present. Values of $\Psi_{b(ground)}$ also have a very similar pattern to λ_b with a strong negative correlation (R^2=0.83, not shown). The correlation between $\Psi_{b(all)}$ and λ_b is even higher (R^2=0.86, not shown). When including the vegetation DEMs to create Ψ from all essential 3D objects in the urban environment (Ψ_{all}) (Lindberg and

[67] Grimmond CSB, Oke TR (1999) Aerodynamic properties of urban areas derived, from analysis of surface form. Journal of Applied Meteorology 38:1262-1292

Grimmond 2011[68]), the patterns change to some extent compared to Ψ_b with a general reduction of Ψ. The peak is still located in the city centre but large reductions of Ψ are found at the outer sites where large amounts of vegetation are found. There is a positive correlation found between $\Psi_{b(ground)}$ and $\Psi_{all(ground)}$. However, the correlation is not very strong (R^2=0.48, not shown) highlighting the importance of including vegetation when deriving continuous images of Ψ in urban areas.

To gain a sense of the vertical distribution of roughness elements (buildings and trees) which are important for dispersion. Vertical cross sections of vegetation and buildings for the 19 sites are shown in Figure 13. The distribution of the raw LiDAR returns/0.5 m section (Figure 13a) is very similar to actual vertical distribution derived from the two vegetation DEMs (Figure 13b). The two major differences are the plan area fraction at low levels. First, low level LiDAR returns are removed when generating the vegetation DEMs since these returns could include non-vegetation objects on the ground (e.g. vehicles, rubbish bins, humans etc.). Second, there seems to be a minor decrease of the plan area density from the vegetation DEMs compared to the raw LiDAR returns. This is probably due to the distribution of LiDAR returns that are higher within the centre of the canopy where the vegetation height also is high, whereas at the edges fewer and lower LiDAR returns are found. However, the pixel sizes of the DEMs are consistent (i.e. 2 m) and therefore appear to have lower mean heights that the actual LiDAR raw data (compare Figure 11, Figure 12, Figure 13). The vertical distribution of vegetation (Figure 13b) is in many ways similar to the vertical distribution of building structures (Figure 13c), where plan area densities are shifted upward when moving closer to the city centre. Exceptions are found at the limits of London. Interesting patterns are also found in the very city centre (0C in Figure 13a, b) where the plan area density of vegetation at low levels is very low indicative of the absence of near ground vegetation. This is probably because of the high level of maintenance required for vegetation in the dense central urban areas and the absence of residential gardens where low level vegetation is present typically. The big difference between the vertical distribution of buildings and vegetation is the increase found in vegetation at the outskirts of the city (also seen in Figure 12). The implication of this is that the urban limit ('cliff') is erased when combining the vertical distribution of all 3D objects (Figure 13d). Spots of low vegetation density are found at some more industrial sites (e.g. 6S and 7S).

[68] Lindberg F, Grimmond CSB (2011) The influence of vegetation and building morphology on shadow patterns and mean radiant temperatures in urban areas: Model development and evaluation. Theoretical and Applied Climatology DOI10.1007/s00704-010-0382-8

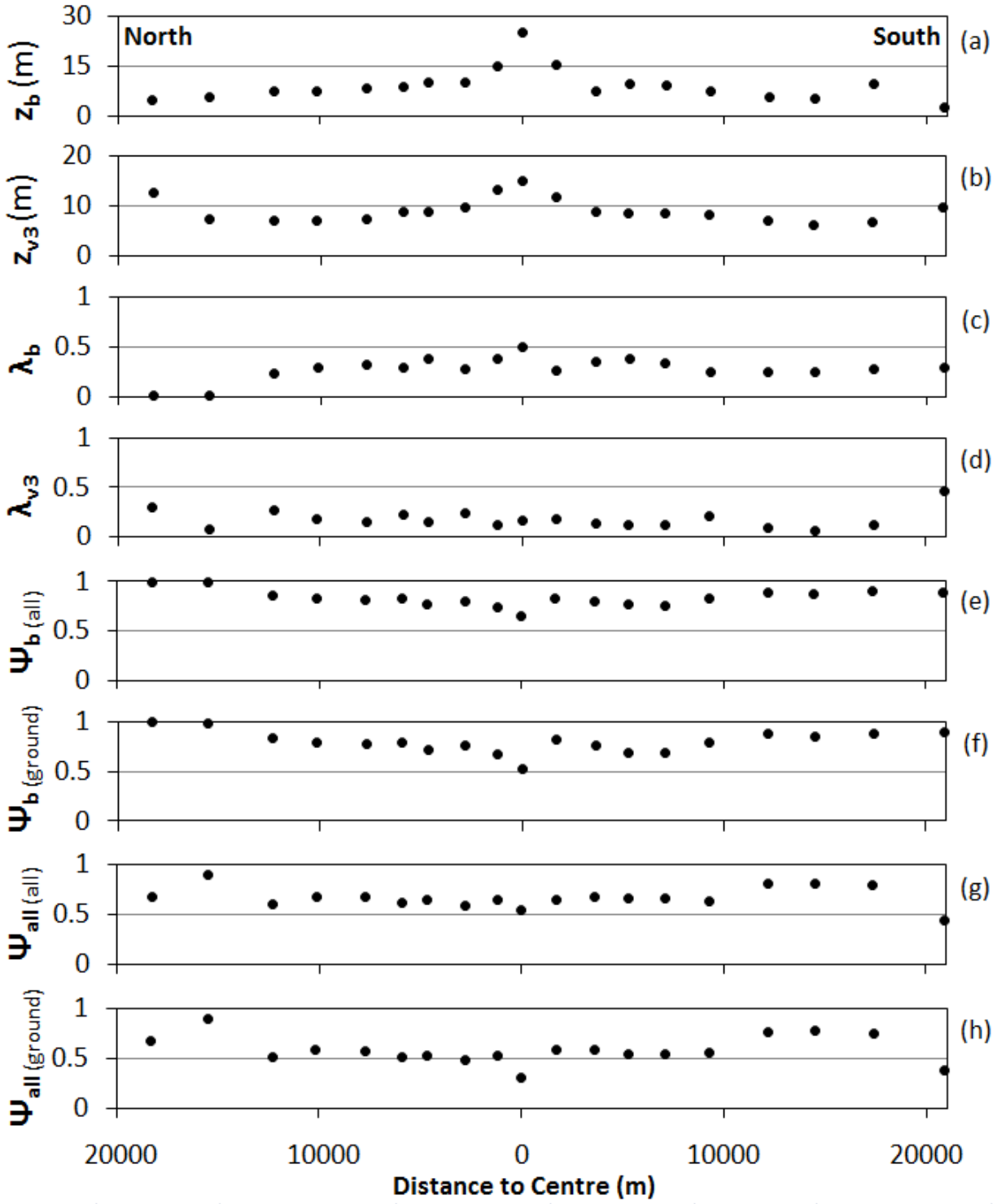

Figure 11: Variations of morphological characteristics for a North-South transect through London (see Figure 4): a) mean building height (z_b), b) mean vegetation height >2.5-m (z_{v3}), c) plan area fraction of buildings (λ_b), d) plan area fraction of vegetation > 2.5-m (λ_{v3}), e) sky view factor derived from building DEM (all pixels) ($\Psi_{b(all)}$), f) sky view factor derived from building DEM (ground level pixels) ($\Psi_{b(ground)}$), g) sky view factor from both building and vegetation DEMs (all pixels)($\Psi_{all(all)}$), and h) sky view factor derived from both building and vegetation DEMs (ground level pixels) ($\Psi_{all(ground)}$).

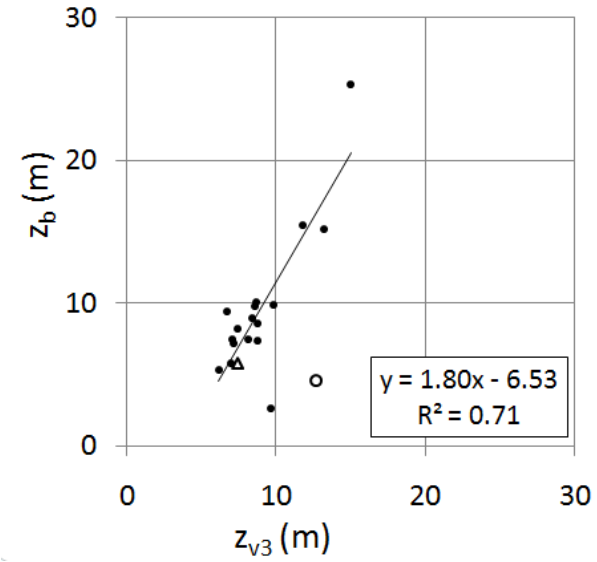

Figure 12: Mean building height (z_b) versus mean vegetation height (z_{v3}). The trend line is based on urbanised sites (black dots, n=17). The triangle (predominately agricultural land) and the circle (predominately forest) are the two 'rural' study areas within the Greater London Area (8N and 9N).

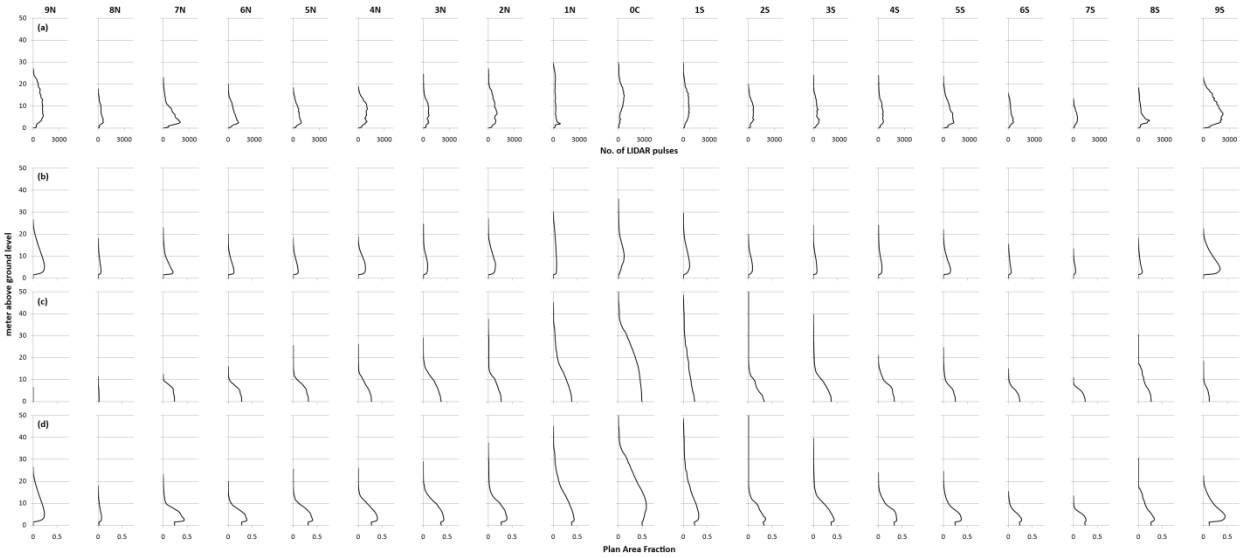

Figure 13: Vertical distribution (in 0.5-m intervals) of buildings and vegetation of the 19 sites: a) raw LiDAR returns classified as vegetation, b) vegetation, c) buildings, and d) buildings and vegetation.

3.3.7 **Vegetation from Aerial Photography: Methods** [Author: Francis & Grimmond]

An independent method to analyse the spatial vegetation cover and to provide information about the other types of vegetation (e.g. grass) based on aerial photography also was undertaken. This uses a supervised classification (Maximum Likelihood Classifier MLC) of the NERC 2008 flight high

resolution aerial photography (AP8, Table 1) which were taken concurrently (Figure 14). MLC assigns pixels to a class by evaluating the variance and covariance of the spectral value of each pixel (Tharpa and Muryarna 2009[69]). Each pixel is assigned to the class it is most statistically likely to belong to (Bhakaran *et al*. 2010[70]).

Training sites were created for three land cover classes: grass, trees and non-vegetation. ArcGIS® 9.3 (2010) was used with the 'equal' *a priori* option so no weighting was applied to any class. Two smoothing filters (4 and 8 pixel 'majority filters') were applied to the MLC output raster with the objective of removing any speckling.

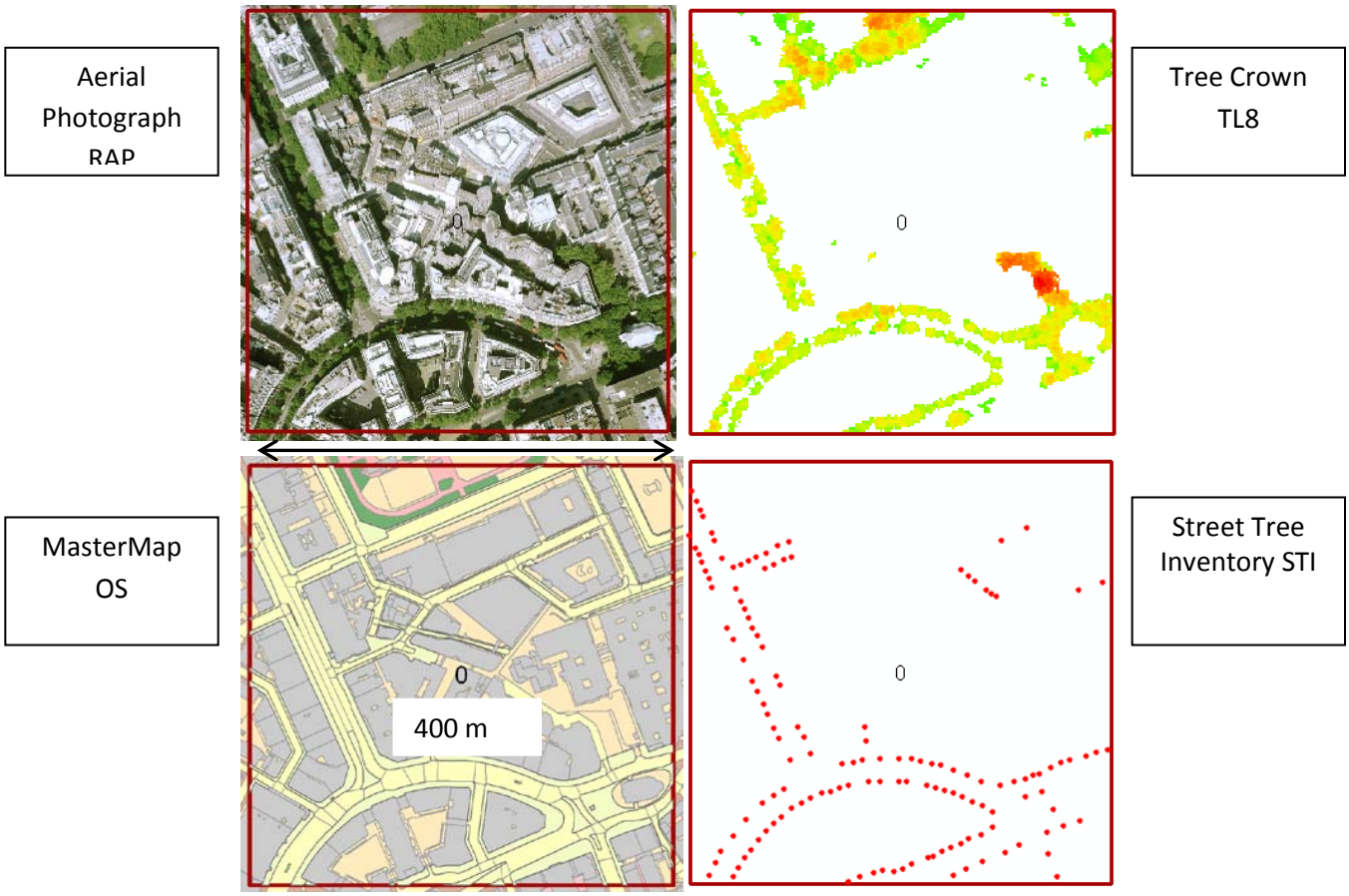

Figure 14: Example of the GIS layers for site 0C (Figure 4). SeeTable 1 for codes of the sources for all data. Location of site see.

3.3.8 **Vegetation from Aerial Photography: Results** [Author: Francis & Grimmond]

The supervised classification and two subsequent smoothing filters were carried out for each site (Figure 15). The minimum total vegetation occurs at the central site (site 0C, with 14% vegetation cover) while the maximum vegetation cover occurs at site 9N (82% vegetation cover) (Figure 16). The total vegetation cover has similar trends N and S of site 0C (seen more clearly in Figure 17) which reflect the historical growth of London. The decreased vegetation at site 4N and 5N (~ 7.5 km) is related to a shift towards urban residential, characterised by small back gardens and no/very small front gardens. The drop in vegetation at site 8N is because the site is mainly industrial.

[69] Tharpa RB and Murayama Y (2009) Urban mapping, accuracy, & image classification: A comparison of multiple approaches in Tsukuba City, Japan. Applied Geography, 29, 135-144.
[70] Bhaskaran S, Paramananda S and Ramnaryan M (2010) Per-pixel and object-oriented classification methods for mapping urban features using Ikonos satellite data. Applied Geography, 30, 650-665

Comparison of MLC to TL8 can only be done for tree coverage (Figure 18). At site 0C MLC suggests 5% less trees and more trees at the suburban sites (max. 25% difference at site 6S). The smoothing filters had a very limited effect on the MLC tree estimation, with only one site recording a difference >±1%. The underestimation of tree by MLC relative to TL8 in the central sites is explained by the misclassification of tree pixels as grass. The suburban overestimation of trees by MLC may be explained by the increasingly present shrubs in private gardens (typically hedges). Shrubs were included in the tree class due to their dark green colour. The other cause is the effect of shadow. The apparent overestimation is partly caused by an underestimation of trees by the LiDAR, where it has missed trees. Areas of well maintained coniferous trees (e.g. large hedges) may be removed in the filtering process used to remove building edges as the shape of these hedges is characteristic of building walls/ edges.

For statistical analysis sites 8N and 9N were excluded as visual inspection shows they are rural/ agricultural and their inclusion also had a negative impact on the normal distribution of the tree and grass areas. A number of statistically significant relations were found to exist between the non-vegetation and vegetation variables, the strongest is a moderately negative relations between average building height and MLC total vegetation fraction (r^2=0.65, p<0.001).

Figure 19 and Figure 20 show examples where grass in shadow has been misclassified as trees. This is due to the shadow causing the grass pixels to appear darker than their true value. Figure 20c shows where LiDAR data has misclassified an area where trees are not present. This has been caused by the building having a metal grid roof; this has probably resulted in the LiDAR sensing multiple returns characteristic of trees.

Figure 21 shows an example of errors induced by the aerial photos. Here the LiDAR tree outline and MLC do not match up, possibly caused by the area of the photo being off nadir whereas the LiDAR does not suffer from this error. The angle of the photo has also caused the buildings to hide areas of tree from view and therefore cannot be detected by the MLC.

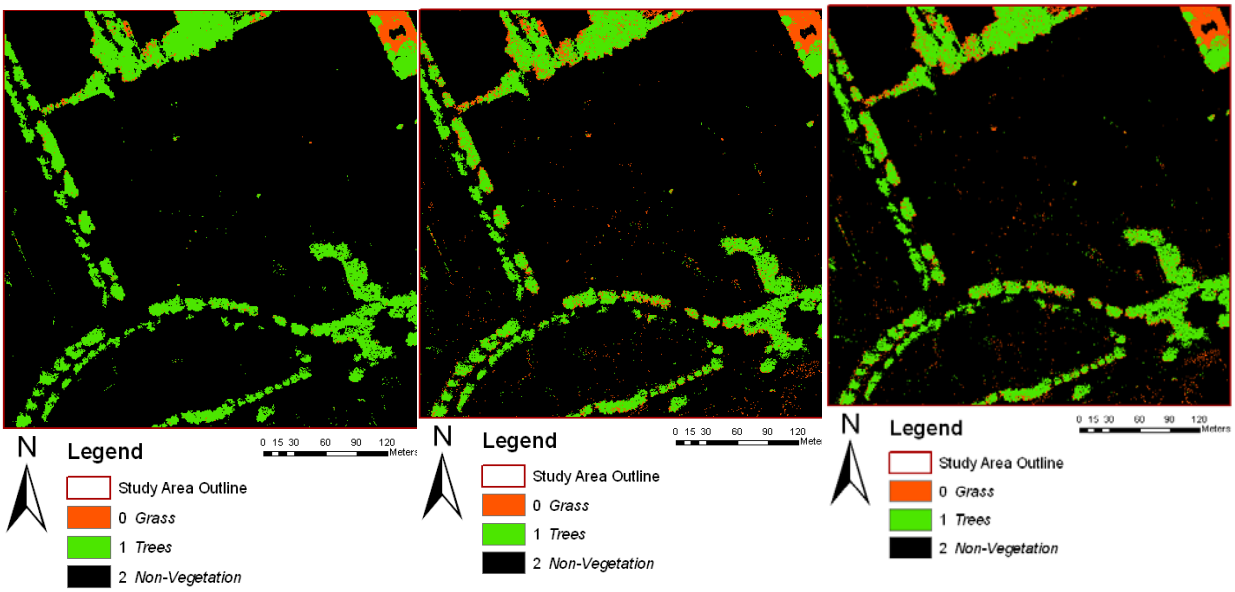

Figure 15 Example of results of supervised classification for site 0C (a) no smoothing (b) 8 pixel smoothing(c) 4 pixel smoothing

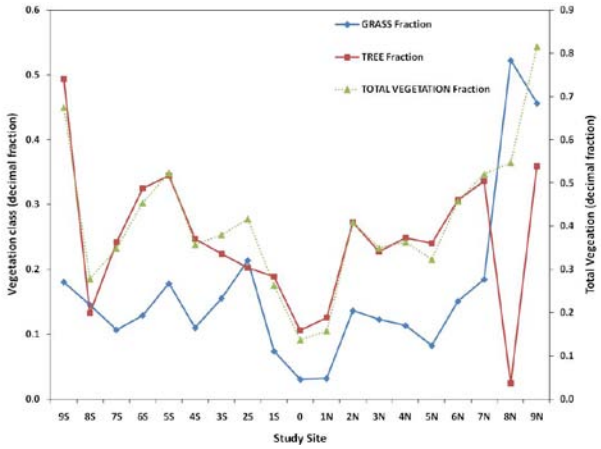

Figure 16 Fraction of each vegetation class (tree and grass) and total vegetation at each site.

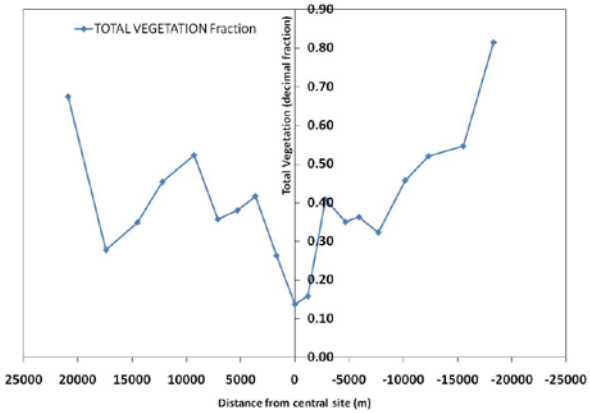

Figure 17 Total vegetation with distance from central site (positive South).

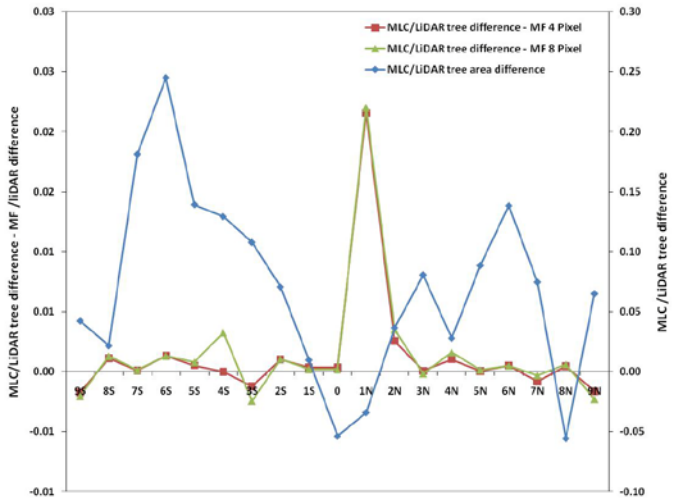

Figure 18: MLC tree fraction and MLC with smoothing filter (red, green) differs from the LiDAR tree fraction. (blue line) Difference between the TL8 tree fraction and the MLC tree fraction.

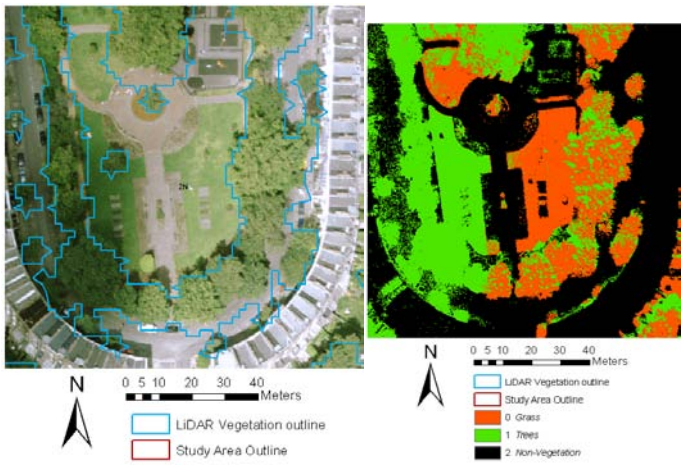

Figure 19: Example of misclassification of grass as trees cause by the effect of shadow.

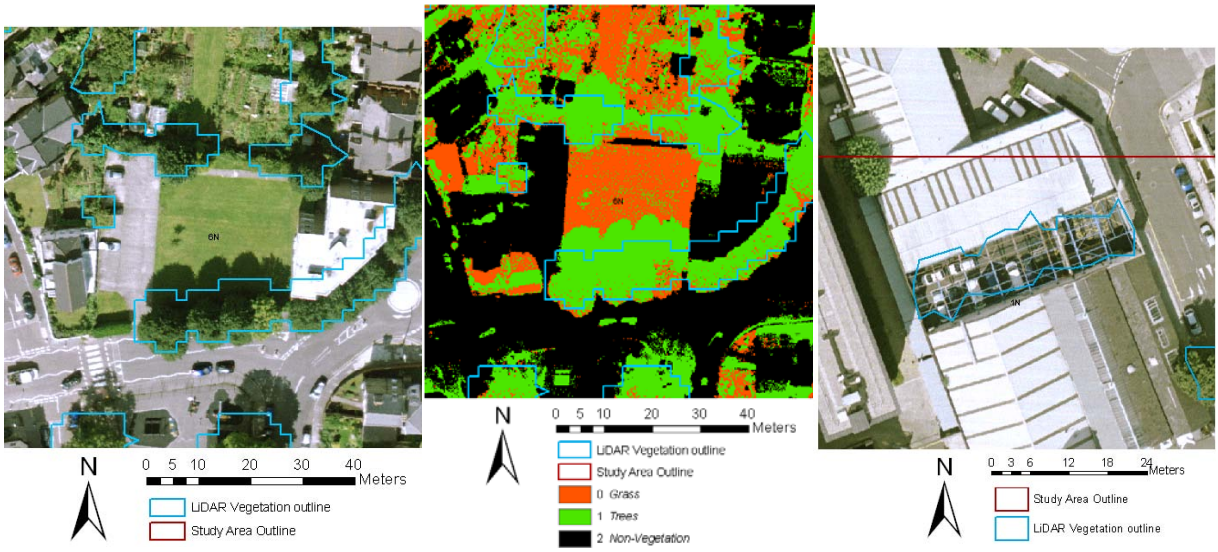

Figure 20 Example of misclassification of grass as trees cause by the effect of shadow and an area misclassified by the LiDAR

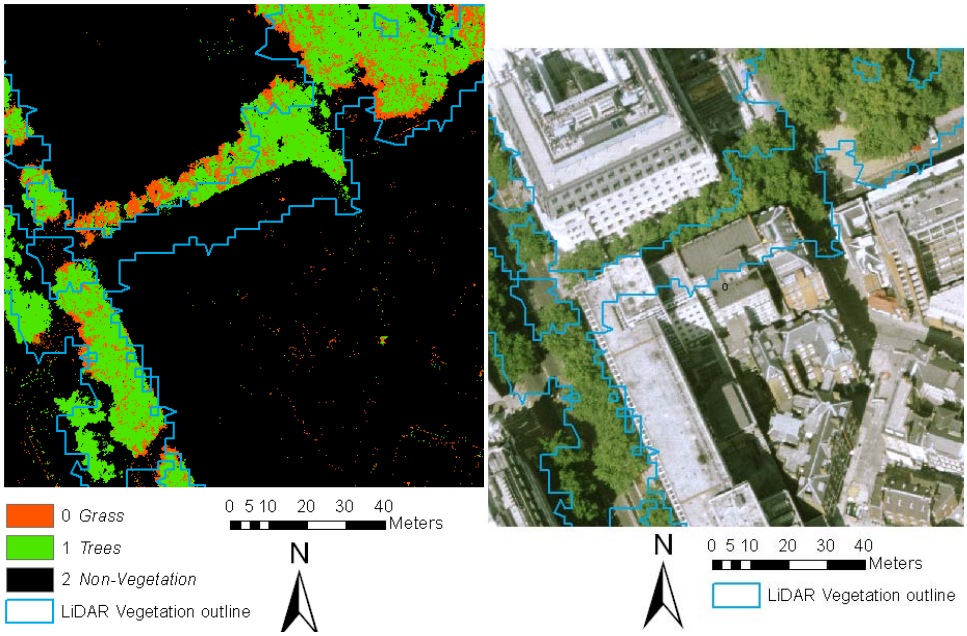

Figure 21 Aerial photo induced errors.

3.3.9 **Spatial variability of urban morphology characteristics: Results** [Author:Lindberg & Grimmond]

From the above analyses the surface characteristics for the Central Activity Zone that are used as the basis for describing observations and for doing modelling were completed. As the TL8 data set only covers a strip of the CAZ and the street tree inventory (STI, Table 1) is also not complete in the CAZ (with most notably the City of London data not being included) a new LiDAR data set at 1 m^2 resolution (LI58 provided by GLA, Table 1) was analysed. These data were analysed using the techniques developed and described in Lindberg and Grimmond (2011 repeated here in sections: 3.3.3 and 3.3.6) are used to provide the data base.

Figure 22 shows the spatial variability across the CAZ based on the database developed for the current vegetation status. The CAZ excluding those areas that are parks are clearly evident by the lack of trees.

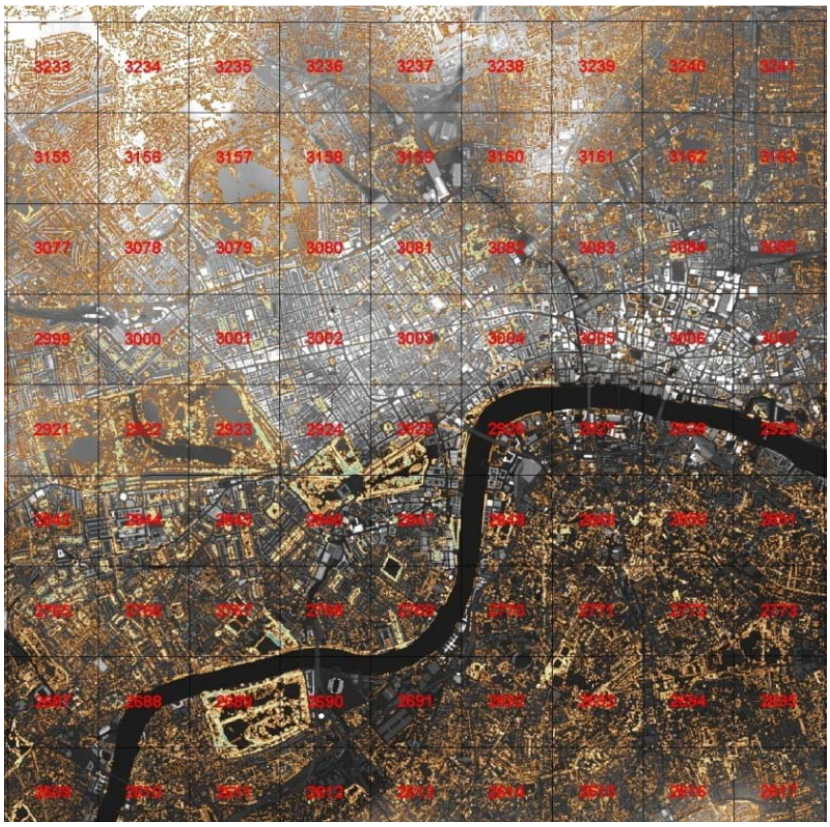

Figure 22: Central Activity Zone of London (with 1 km grid). Grid 3004 is where KCL is located. Topography and building height shown in black and white (white higher). Trees shown in brown to green scale with green being taller.

3.3.10 **Potential Locations for New Green Infrastructure: Methods** [Author: Lindberg and Grimmond]

The GLA planning interest for the DSS (section 3.2) relates to the addition of vegetation within the Central Activity Zone of London. The rules outlined in Table 11 were developed in conjunction with GLA to determine where street trees and green roofs could be added. As the TL8 data set only covers a strip of the CAZ and the street tree inventory (STI, Table 1) is also incomplete in the CAZ (with most notably the City of London data not being included) a new LiDAR data set at 1 m^2 resolution (LI58 provided by GLA, Table 1) was analysed. These data were analysed using the techniques developed and described in Lindberg and Grimmond (2011 repeated here in sections: 3.3.3 and 3.3.6) are used to provide the data base.

The roofs in the CAZ that potentially could have green roofs are shown in Figure 23a. These roofs are characterized by the class of slope and the area of that slope type. Figure 23b, for example, illustrates the fraction of the roof that is flat, with the actual area (m^2) shown in Figure 23c. Figure 24 shows two areas of the CAZ with the current location of street trees based on the STI and location identified where the trees could be located.

The impact of political boundaries and land ownership can be seen in Figure 25. The boundary between the Westminster and City of London can be detected based on where the STI data base is incomplete or the apparent lack of trees. When the map and the AP8 aerial photography are compared one can also see that the management of the trees changes (see for example lower right corner of photo in comparison to the map) from street trees to land that is managed by another institution. Comparing Figure 26 with Figure 25 one can see the difference in tree coverage based on the source of the data. The LI58 data set is continuous so trees in the City of London are now evident. There also similar type of tree information beyond the STI data. Notably trees in parks and private land are now apparent.

Table 11: Rules developed for where new green infrastructure could be located in the CAZ based on discussions between Matthew Thomas (Greater London Authority), Dr Fredrik Lindberg (KCL, University of Göteborg) and Prof Sue Grimmond (KCL).

Location	Rule
Street Trees	(a) A tree has to be located on a pavement (b) The centre of the trunk should be ≥3 m from a building wall and exisiting vegetation. (c) The distance between **new** tree trunks should be ≥ 10 m (This is based on visual analysis of the current street tree database density) Buffer 10 m from STI when no TL8
Green Roofs	(a) Roof has to be flat (or below a certain slope e.g. less than 20%) (b) Roof area has to be larger than 25 m^2

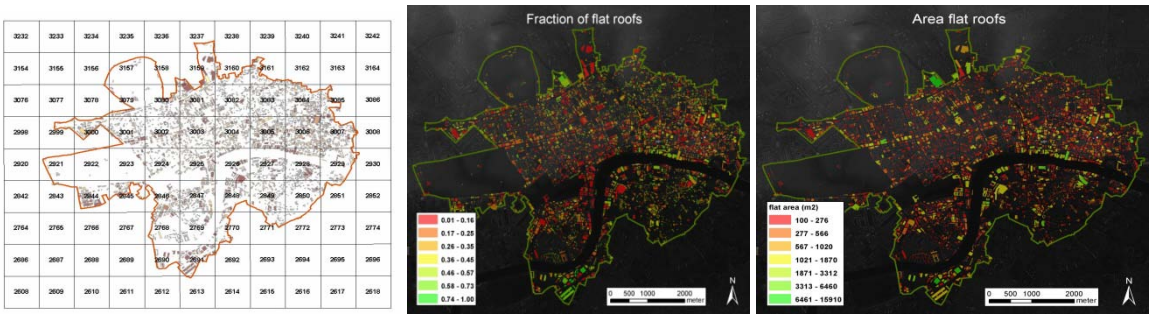

Figure 23: The CAZ (with 1 km grid) showing (a) the areas that potentially could have green roofs added (b) the fraction of the roof that is flat and (c) the area of the roof that is flat.

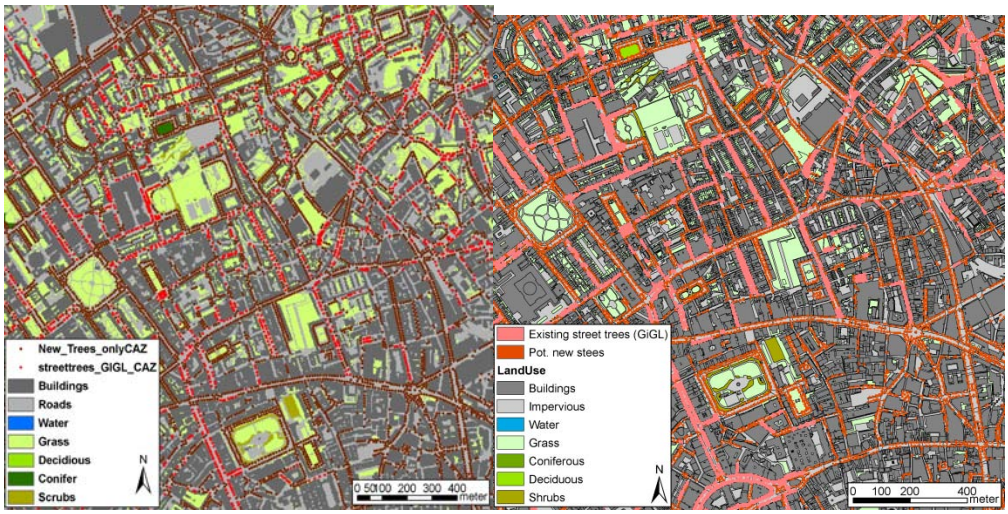

Figure 24: Street tree coverage within two areas of the CAZ. Current trees are shown (red or pink) and potential locations (brown or orange).

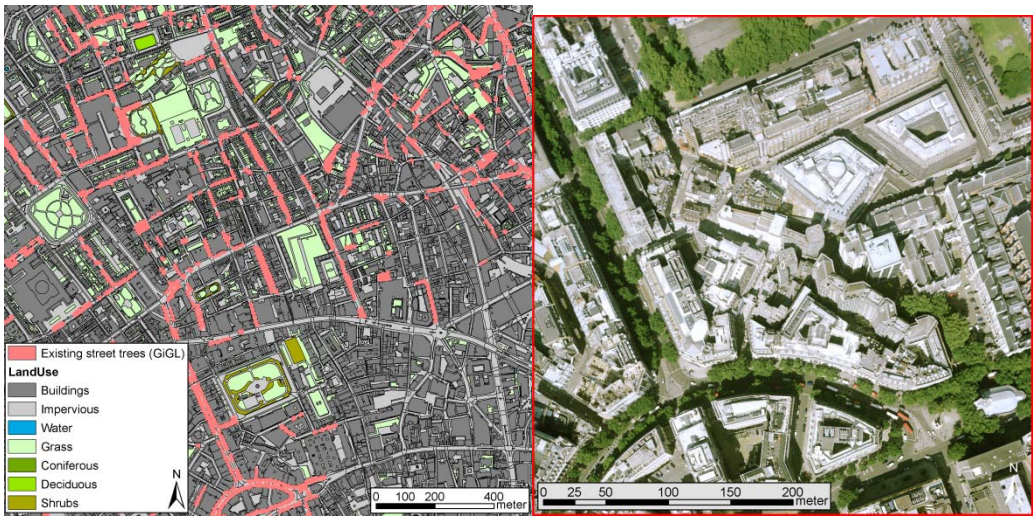

Figure 25: Location of street trees based on STI. The boundary between the Westminster and City of London can be detected based on where the STI data base is incomplete or the apparent lack of trees. Comparison with the AP8 aerial photography one can also see that the management of the trees changes (see for example lower right corner of photo in comparison to the map).

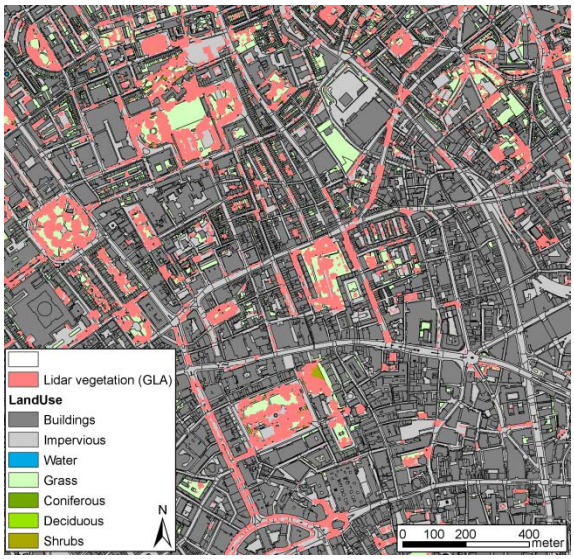

Figure 26: Location of trees based on analysis of LI58 dataset.

3.4 **Atmospheric and Hydrologic Observations** [Author: Grimmond]

Observational data used in the BRIDGE project have been collected at three types of sites:

a) Standard meteorological and air quality data collected at a wide range of sites across London by a number of agencies.
b) Auxiliary spatial sites: established or maintained as part of this project, specifically to measure soil moisture, river temperature, and phenology
c) Intensive Research sites: established or maintained as part of this project, specifically the flux measurement site in the centre of London and the locations for Large Aperture Scintillometry (LAS)

In the following sections the sites and the methods used to collect and analyse data are described, along with initial results. A data archive has been established, hereafter referred to as KUMA (KCL Urban Meteorology Data Archive) to provide access to the data. This is described first as this is used for all data collected and is an important output of this project.

3.5 **KUMA: KCL Urban Meteorology Data Archive** [Author: Kotthaus & Grimmond; Contributors: Castillo, De Jong, He]

Data output produced by the group for Urban Micrometeorology is aggregated in a database called KUMA (King's College London Urban Micromet Data Archive). Micrometeorological observations, processed measurements as well as model data files are stored as netCDF (network Common Data Format[71]). In order to ensure compatibility with netCDF software applications, we aim to fulfil CF metadata conventions version 1.4 ([72]) where possible. All files are written using R (R Foundation for Statistical Computing 2010) or Matlab (2010a, The MathWorks) or result from operations using cdo (Climate Data Operators[73]).

The advantage of netCDF is that additional information can be attached directly either to the whole file (*global attributes*) or to the variable (*variable attributes*). This way, specifications describing measurement (e.g. serial number of the instrument), data processing (e.g. details on quality control) or model settings (e.g. temporal resolution of input dataset) are automatically incorporated in the dataset itself. This allows for efficient organisation of the database and forms the basis for the automatic data extraction procedure and meta information are inherently available to the data user. Since meteorological variables, no matter if measured or modelled, depend on their context (defined for example by instrumentation and model input setting) as much information as possible should be offered to the user in order to allow for a well-founded application and interpretation of the data provided.

In order to organise the different data sets in the archive twelve attributes are defined (Table 12) which can be categorized:

1) Location of the data collection: Institution, Area, Site, and Spatial information
2) Content of the data: Source, Title, Temporal resolution, Base resolution, Name, Long name, Unit and Category
3) Level of processing: Data level. Additional information is provided to the user to allow decoding of these levels.

[71] *http://www.unidata.ucar.edu/software/netcdf/Unidata*
[72] *http://cf-pcmdi.llnl.gov/*
[73] *https://code.zmaw.de/projects/cdo/*

These attributes are essential for the internal organisation of the database and are included into a master list ('contents.csv') each time a new variable is entered into the database. Additional global and variable attributes are stored in the netCDF files but these vary extensively with context.

The archive is filled in stages that depend on data source and quality level. Most observational raw data gathered at sites of the KCL urban micrometeorology network are entered to the archive almost in real time. All observations are monitored on a daily basis[74] in order to detect malfunctioning of instruments, data loggers or PCs as soon as possible. All data are downloaded, plotted and formatted every night and daily files are written to the archive. These are then appended to annual files using cdo. These files depict the source for the automatic extraction procedure and plots of their content are also updated on a daily basis. Other data types (e.g. those that require quality control, data processing or the ones provided by other measurement networks) enter the archive on a less frequent basis. Hence the availability in the archive varies between the datasets.

To retrieve data an automatic download procedure has been developed. The procedures are indicated by white arrows in Figure 25. As described in the online instructions[75] a registered user can select required variables from the list of available datasets. The latter are comprised in a simple file (csv format) which can be processed with ordinary spreadsheet tools (e.g. Microsoft Excel, Open Office Calc). After reducing the list to the variables of interest, the user submits the request file via email. An automatic extraction procedure (python and cdo) selects the desired data from the archive, the data are then made available for download to the user.

Table 12: KUMA database structure with attributes and description

Attribute	Description
Area	Commonly the name of the city represented in the dataset. If several cities are included a larger area is specifies the country or continent, e.g. *UK*, *Europe*, *global*
Site	Most datasets represent a specific measurement site. Its name in form of an acronym is specified here. If several sites of one city or country are included, this has the value *ALL*.
Source	The source specifies if data represent a measurement, a processed product, model input or model output.
Title	The title specifies the actual content. It can be the name of the instrument used for the measurements, the software used for the calculation, the name of the model that produced the data or the content of the model input information.
Data level	Data level increases with processing steps and quality control. Raw measurements are always of level L0. All further steps of processing are stored in increasing level.
Temporal resolution	Temporal resolution of the dataset.
Base Resolution	Base resolution gives the temporal resolution of the dataset that was used to produce the current dataset. It can either be the input resolution before processing or the temporal resolution of model input.
Spatial information	Spatial information details the spatial resolution and extent of a grid dataset or the information on measurement network.
Name	Short name of variable.
Long name	More detailed name of variable.
Unit	Unit in which variable is stored.
Category	Variables are grouped to thematic categories which facilitates the search for specific data set.
Linked variables	Variables that connected to the specified variable. These will automatically be

[74] *http://geography.kcl.ac.uk/micromet/index.htm*
[75] *http://geography.kcl.ac.uk/micromet/wordpress/?page_id=425*,

	provided to the user requesting variable *Name*, e.g. standard deviation or quality flag can be linked to the respective variable.

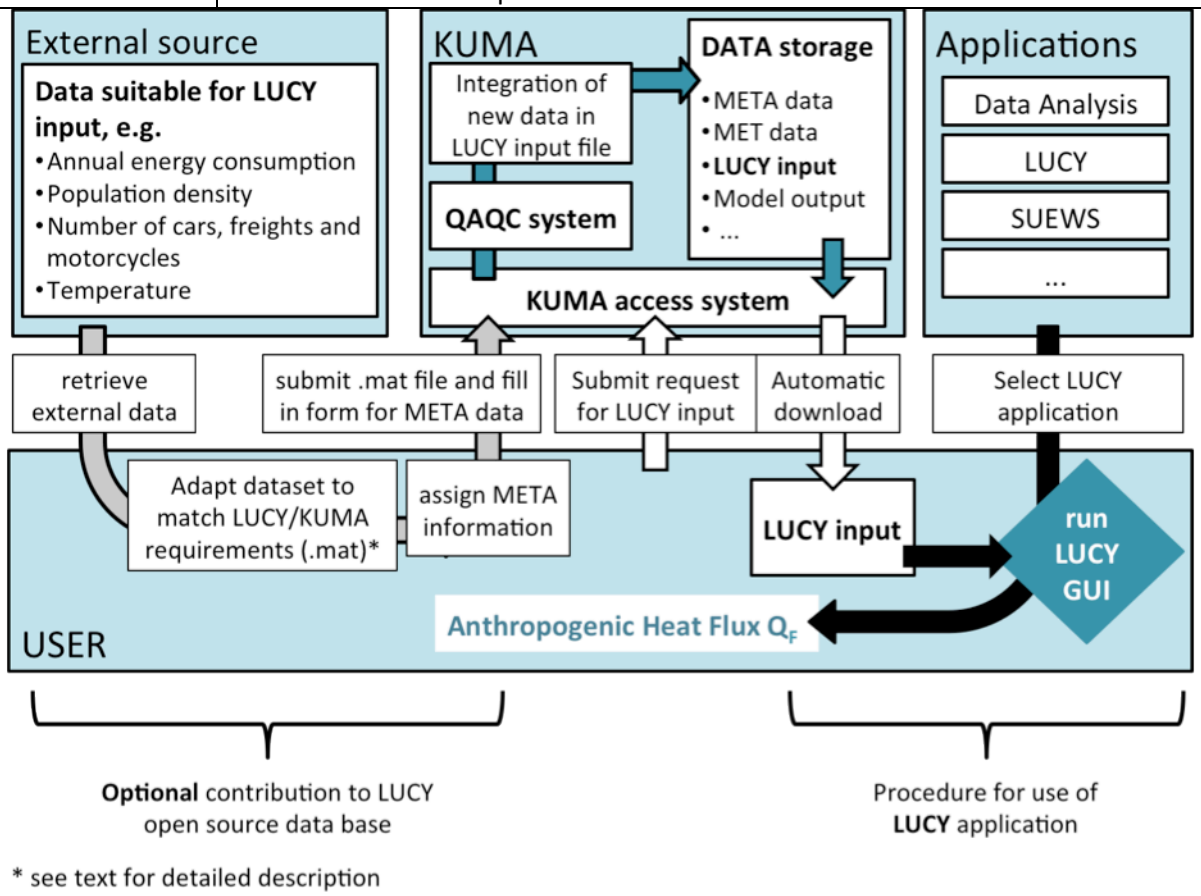

Figure 27: Flow chart of KUMA downloading procedure for various applications. The example is for of using KUMA for data exchange for LUCY (Allen et al. 2010) anthropogenic heat flux (Lindberg et al. In preparation)

3.6 **Extensive observations sites** [Author: Robinson & Grimmond, Contributors: Lindberg, Pauscher, Thomas, Kotthaus]

Here we describe the standard meteorological and air quality data collected across London. Following Robinson (2010)[76] , the various networks are collectively referred to as the London Meteorological Monitoring Network (LMMN). The LMMN consists of data collected by four different groups:

a) London Air Quality Network (LAQN)[77]
b) London Grid for Learning (LGfL)[78],[79]
c) UK Met Office (UKMO) [80]
d) Weather Underground (WU)[81]

Given the data are collected for very different purposes (Table 13), each network has different siting criteria. As part of this study a number of sites have been evaluated within each network in terms of siting and data compared across the networks. Overall there are 149 sites in the LMMN (Figure 26). This includes sites both within London and outside of the Greater London area. However, only four sites (3 LAQN and 1 LGfL) are within the CAZ (Figure 29). At each of these sites an Automated Meteorological Station (AMS) is installed.

To characterize the sites, the WMO Urban Climate Zones (UCZ) (Oke 2004[82]) (Figure 30) and the Stewart and Oke (2009[83]) Local Climate Zones (LCZ) (Figure 31) are used.

[76] Robinson P (2010) The London Meteorological Monitoring Network. MSc Environmental Monitoring, Modelling and Management Thesis, King's College London, London, UK
[77] http://www.londonair.org.uk/london/asp/default.asp
[78] http://www.lgfl.net/learningresources/curriculum/geography/weatherstations/pages/weatherstations.aspx
[79] http://weather.lgfl.org.uk/
[80] http://www.metoffice.gov.uk/
[81] http://www.wunderground.com/
[82] Oke TR (2004) Initial Guidance to Obtain Representative Meteorological Observations at Urban Sites. IOM Report 81, World Meteorological Organization, Geneva.
[83] Stewart ID, and TR Oke (2009). Conference notebook– A new classification system for urban climate sites. Bulletin of the American Meteorological Society, 90: 922–923.

Table 13: Characteristics of the London Meteorological Monitoring Network (LMMN) sites

	LAQN	LGfL	UKMO	WU
Name	London Air Quality Network	London Grid for Learning	UK Met Office	Weather Underground
Type of network	Environmental Research Group (ERG) of KCL operates network of stations that are owned by the individual boroughs. In addition UK Department of Environment, Food and Rural Affairs (Defra) funds some sites which are part of the Automatic Urban and Rural Network (AURN)[84].	Learning Grid for London in collaboration with Imperial College London and Open Air Laboratories (OPAL) network.	Met Office	Individuals owned and operated
Primary objective of network	Air quality for regulatory purposes	Weather /Climate	Synoptic forecasting	Weather hobbyists
Siting criteria	Urban background industrial locations, roadside/ kerbside suburban	Schools in each Borough	WMO specifications	Wide range of approaches taken. At private residences
No. of stations	37	41	7	64
Availability of data	Can download for each station from their website[85]	Historic plots[86] Tables[87] or by membership to LGfL	Available from the BADC[88]	Can download averaged values[89]
Instrument model	Varied	Davis Vantage Pro2 Plus™	n/a	Varied
Instrument height	~2.6 m (Wind either 2.6 m or 4.6 - 5.6 m agl)	Roof top- actual height variable	n/a	No common height
UCZ	All except 7 (semi rural)	All except 1 and 7	6	5 and 6
LCZ	City: Modern core/ Old core/ Blocks/ Extensive lowrise/ House and garden Mixed: Open grounds	City: House and garden Mixed: Open grounds	City: Extensive lowrise	City: House and garden
Contact	Boroughs and private owners- ERG KCL	Schools- Atomwide and Imperial College London		WU internal mail and weather websites
Access	Variable depending on location of site	Restricted as based in schools		Restricted as private residences
KCL code	D0-D36	C0-C40	A0-A6	B0-B63
Network QC	Yes	No	Yes	No

[84] http://aurn.defra.gov.uk/
[85] http://www.londonair.org.uk/london/asp/datadownload.asp
[86] http://weather.lgfl.org.uk/qgraphs.aspx
[87] http://weather.lgfl.org.uk/qtables.aspx
[88] http://badc.nerc.ac.uk/home/index.html
[89] http://www.wunderground.com/history/

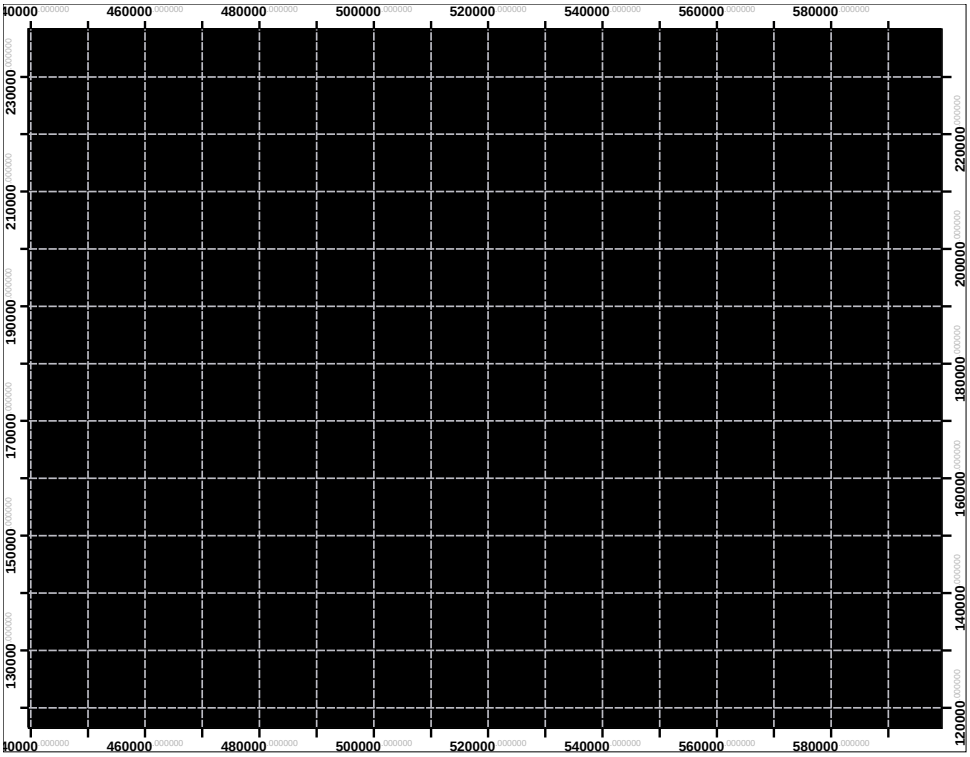

Figure 28: Location of stations incorporated within the London Meteorological Monitoring Network (LAQN (Red), LGfL (Orange), UKMO (Blue) and WU (Green), projection British National Grid). Shaded area is Greater London with the Boroughs shown.

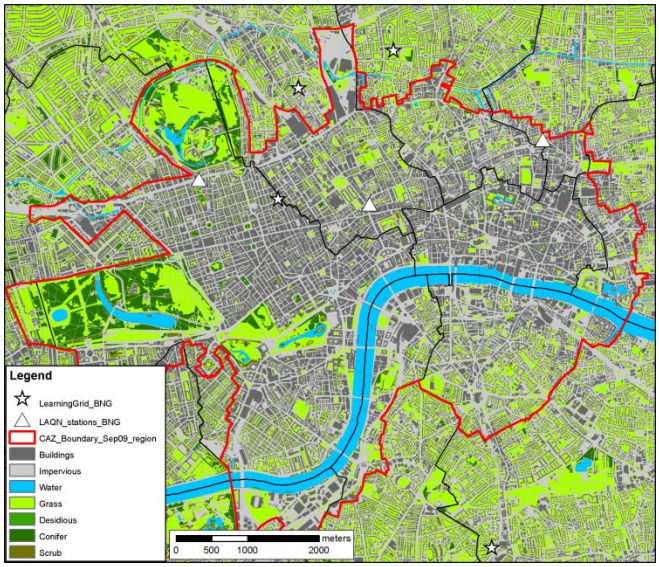

Figure 29: Location of climate stations within the Central Activity Zone.

Urban Climate Zone, UCZ[1]	Image	Rough-ness class[2]	Aspect ratio[3]	% Built (imperm-eable)[4]
1. Intensely developed urban with detached close-set high-rise buildings with cladding, e.g. downtown towers		8	> 2	> 90
2. Intensely developed high density urban with 2 – 5 storey, attached or very close-set buildings often of brick or stone, e.g. old city core		7	1.0 – 2.5	> 85
3. Highly developed, medium density urban with row or detached but close-set houses, stores & apartments e.g. urban housing		7	0.5 – 1.5	70 - 85
4. Highly developed, low or medium density urban with large low buildings & paved parking, e.g. shopping mall, warehouses		5	0.05 – 0.2	70 - 95
5. Medium development, low density suburban with 1 or 2 storey houses, e.g. suburban housing		6	0.2 – 0.6, up to >1 with trees	35 - 65
6. Mixed use with large buildings in open landscape, e.g. institutions such as hospital, university, airport		5	0.1 – 0.5, depends on trees	< 40
7. Semi-rural development, scattered houses in natural or agricultural area, e.g. farms, estates		4	> 0.05, depends on trees	< 10

Key to image symbols: buildings; vegetation; impervious ground; pervious ground

[1] A simplified set of classes that includes aspects of the schemes of Auer (1978) and Ellefsen (1990/91) plus physical measures relating to wind, thermal and moisture controls (columns at right). Approximate correspondence between UCZ and Ellefsen's urban terrain zones is: 1(Dc1, Dc8), 2 (A1-A4, Dc2), 3 (A5, Dc3-5, Do2), 4 (Do1, Do4, Do5), 5 (Do3), 6 (Do6), 7 (none).

[2] Effective terrain roughness according to the Davenport classification (Davenport *et al.*, 2000); see Table 2.

[3] Aspect ratio = z_H/W is average height of the main roughness elements (buildings, trees) divided by their average spacing, in the city centre this is the street canyon height/width. This measure is known to be related to flow regime types (Oke 1987) and thermal controls (solar shading and longwave screening) (Oke, 1981). Tall trees increase this measure significantly.

[4] Average proportion of ground plan covered by built features (buildings, roads, paved and other impervious areas) the rest of the area is occupied by pervious cover (green space, water and other natural surfaces). Permeability affects the moisture status of the ground and hence humidification and evaporative cooling potential.

Figure 30: Definition of Urban Climate Zones (Oke 2004).

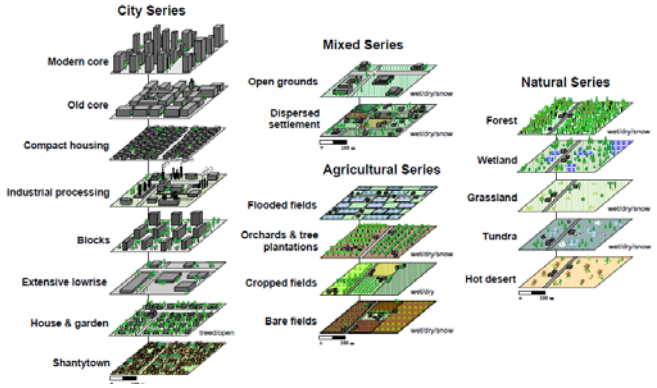

Figure 31 Schematic of Local Climate Zones in the City, Mixed and Natural series (Stewart and Oke 2009)

3.6.1 **LAQN** [Author: Robinson & Grimmond, Contributors: Lindberg, Pauscher, Thomas, Kotthaus]

The LAQN classify their measurement sites across Greater London into four main categories (LAQN 2010):

(1) urban background

(2) industrial locations
(3) roadside/ kerbside
(4) suburban

For the purposes of this work, these have been reclassified as the LAQN categories are too broad and encompass too much diversity within a single group (Table 14). For example, both the Stanford- le – hope (TK3) site in Thurrock Essex and Marylebone Road, Baker Street (MY1) site in Central London are categorised in the LAQN as roadside. Both are located near to the side of roads, but the MY1 site is on a major arterial road through Central London surrounded by a densely built up urban environment, while the TK3 site is located at the end of a cul-de-sac of low rise residential buildings which neighbours extensive undeveloped rural wetlands. In order to standardise descriptions of all the networks to enable comparisons of results, Oke's (2004) Urban Climate Zones have been employed. The LAQN 37 Automated Measuring Systems are located across most urban climate zones with 17 Boroughs. Of the 20 sites visited, eight UCZ were represented with only UCZ 7 (semi rural) not found.

The LAQN deploys instruments in a relatively consistent manner with the measurements of air temperature, barometric pressure, relative humidity and precipitation taken 0.2 m above the 2.4 m high AMS cabin roofs. Wind speed and direction are either sampled alongside the other variables at approximately 2.6 m agl, or mounted on a mast approximately 2 - 3 m above the cabin roof.

Based on site visits in summer 2010 (Robinson 2010), issues with the siting of wind speed - direction instruments were identified. At sites BT5 and WL1, for example, they were in close proximity to overhanging vegetation. At CD4 and HK6, they were situated in close proximity to high rise buildings. As noted by Oke (2004) in densely built-up urban environments in order to sample a more general flow which is not impeded by distortion from surrounding buildings and is representative of local conditions, wind speed - direction needs to be measured at a height of either 10 m or 1.5 times the mean height of the surrounding obstacles. Thus the LAQN wind measurements are not representative at the local scale. Another issue evident at several sites is the position of the rain gauge. At BX7 and BT5 this was particularly acute, with overgrown vegetation protruding above and around the gauges. In order to minimise the potential impact from interception and in-splash from dripping leaves, these gauges need either to be relocated or the vegetation removed. Until then, the data should be used with caution.

The LAQN is one of the main sources of air pollution data in London. The data are accessible from the LAQN website[90]. The website also provides links to various reports about air quality related to analysis of the data collected within the network.

[90] http://www.londonair.org.uk/london/asp/default.asp

Table 14 LAQN network stations. Where the site has been visited additional information is provided. Note these stations also observe various air quality variables. UCZ – Urban Climate Zone (Figure 27); LCZ – Local Climate Zone (Figure 28)

KUMA ID	Station name	UCZ 500 m	LCZ 500 m	Observations	Height (m)							Surface Cover (%)						
					Tair	RH	Press	ws	dir	preciptitation		Buildings	Impervious	Water	Grass	Deciduous	Coniferous	Shrub
0	BG1	5	City: House & garden	Tair; RH; press; ws; dir; rain	4.50	4.50	4.50	5.30	5.30	2.60		18	23	0	58	0	0	0
1	BN2	5	City: House & garden	Tair; RH; ws; dir	2.40	2.40	n/a	2.40	2.40	n/a		15	25	1	54	0	5	0
2	BT1	5	City: House & garden	Tair; RH; press; ws; dir	1.60	1.60	1.60	11.80	11.80	n/a		15	24	0	57	0	2	2
3	BT4	4	City: Extensive	Tair; RH; press; ws; dir	2.56	2.56	2.56	5.40	5.40	n/a		20	48	1	30	0	1	0
4	BT5	4	City: Extensive low rise & blocks	Tair; RH; press; ws; dir; rain	2.36	2.36	2.36	4.39	4.39	2.26		21	48	0	30	0	1	0
5	BT7	3	City: Extensive low rise & blocks	Tair; RH; press; ws; dir	2.50	2.50	2.50	n/a	n/a	2.30		23	43	0	33	0	1	0
6	BX1																	
7	BX2	4 & 5	City: 6 & 7	Tair; RH; press; ws; dir; rain	2.26	2.26	2.26	6.20	6.20	n/a		15	43	1	23	0	12	6
8	BX3																	
9	BX4	4	6	Tair; RH; press; ws; dir	2.60	2.60	2.60	6.60	6.60	n/a		14	35	20	31	0	0	0
10	BX7	4 & 5	City: 6 & 7	Tair; RH; press; ws; dir; rain	3.20	3.20	4.20	6.60	6.60	3.20		23	43	0	33	0	1	0
11	CD4	2	2	Tair; RH; press; ws; dir; rain	1.30	1.30	1.30	2.50	2.50	1.50		46	40	0	12	0	0	1
12	CY1																	
13	EA7	4	6	Tair; RH; press	2.95	2.95	2.95	n/a	n/a	n/a		20	44	3	31	0	0	2
14	GB6	5	7	ws; dir; rain	n/a	n/a	n/a	7.90	7.90	3.00		13	25	0	58	2	1	1
15	GN0	4	6	Tair; RH; press; ws; dir	2.26	2.26	2.26	6.20	6.20	n/a		27	48	0	23	0	2	0
16	GN2																	
17	GN3	3	7		2.50	2.50	2.50	6.60	6.60	n/a		22	31	0	44	0	0	2
18	GR7	3	5		2.60	2.60	2.60	6.60	6.60	n/a		21	31	0	44	6	4	1
19	GR8	4	6		2.65	2.65	2.65	6.60	6.60	n/a		22	50	0	28	0	0	0
20	GR9																	
21	HI1	5 & 6	City: 7 Mixed :1		2.95	2.95	2.95	9.80	9.80	n/a		3	3	3	10	10	n/a	n/a
22	HI2	5 & 6	City: 6 & 7		2.80	2.80	2.80	7.30	7.30	n/a		16	37	0	53	0	1	3
23	HK6	1 & 2	City: 2 & 5		2.36	2.36	2.36	n/a	n/a	n/a		42	43	0	11	0	0	0
24	HS4	3	City: 7		2.80	2.80	2.80	3.50	3.50	n/a		29	34	0	37	0	0	0
25	HS5	5 & 6	City: 5 & 7		2.40	2.40	2.40	2.80	2.80	n/a		23	40	1	36	0	0	0
26	IS6				2.36	2.36	2.36	5.00	5.00	n/a								
27	LH2																	
28	MY1	1 & 2	City: 1 & 2		3.40	3.40	3.40	4.80	4.80	n/a		35	40	2	13	0	9	1
29	RG1																	
30	RG3																	
31	RG4																	
32	TK1	5	City: 7		3.50	3.50	3.50	5.50	5.50	n/a								
33	TK3				2.50	2.50	2.50	4.80	4.80	n/a								
34	TH4	2 & 6	City: 5		2.50	2.50	2.50	4.70	4.70	n/a		19	47	5	29	0	0	0
35	WL1	5 & 7	City: C7 & M1		2.40	2.40	2.40	4.50	4.50	n/a		29	30	0	41	0	0	0
36	ZV1											18	23	0	58	0	0	0

3.6.2 **LGfL** [Author: Robinson & Grimmond]

The London Grid for London automatic meteorological stations have at least one site in every borough of London. From site visits and examination of the surroundings using GoogleEarth, the LGfL stations are located in a diverse range of residential areas. The AMS situated within school grounds with extensive open landscapes and a mix of buildings and vegetation fit the UCZ 6 classification. In contrast, the more centrally located stations within or on the peripheries of the CAZ, were more in keeping with UCZ 2 - 3 old city core or urban residential respectively. Overall the LGfL stations are located in each type of UCZs except for 1 and 7 but with high levels of inter-site variations.

Unlike the LAQN, the LGfL uses common instrumentation (Davis Vantage Pro2 Plus™) across the entire network (Figure 29). As the instruments are in a single unit at any site the variables are sampled at approximately the same height. This has the advantage that the corrections could be made for example for the influence of wind speed on precipitation, though this is not done routinely.

The key criterion of LGfL siting guidelines (LGfL Guidelines 2010) is the placement on "a wall, roof or pole with the solar panel pointing south". The four sites visited adhered to this but differences in building dimensions at each site means the sample height and immediate surroundings varied significantly. For example, the measurements heights for C42, C35 and C17 are 21, 5.8 and 9 m, respectively. The implications of the variability of sampling heights may be less of an issue for some meteorological variables such as temperature, which has a small vertical gradient within the urban canopy layer (Nakamura and Oke 1988). However, for wind the micro scale wind flow deformations may be significant (Oke 2006). The cup anemometers and vanes at each of the LGfL sites visited were in the lee of buildings, within close proximity to roofs and other surrounding obstacles, all of which presented unique micro- scale environments.

Another siting problem noted during the surveys was the relative exposure of the instruments. At several sites the temperature sensors were in close proximity to built surfaces. For example, at C35 and C42 there was bitumen roofing and aluminium sheeting within 5 m of the sensors. Although temperature shows little vertical change within the UCL, roofs present significant vertical and horizontal temperature gradients due in part to the surface characteristics and their thermal properties (Oke 2006). However, as the temperature and relative humidity sensors were enclosed within solar powered fan- aspirated radiation shields (Davis 2010) the relative impact of these surfaces may be reduced.

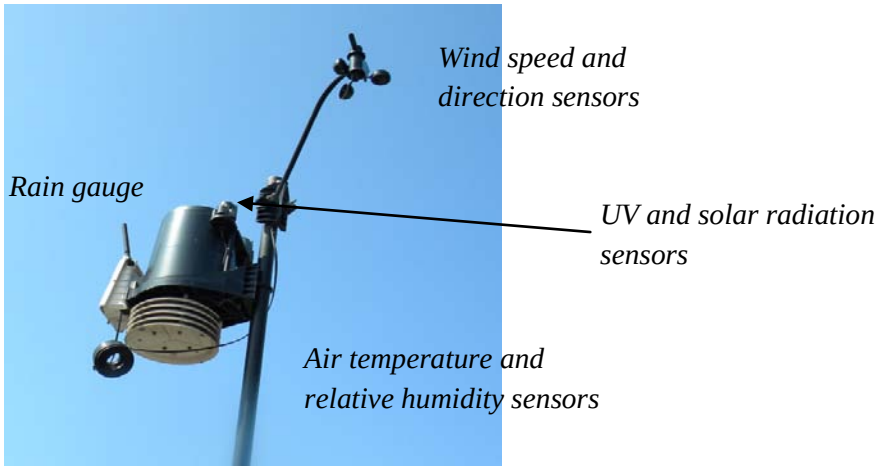

Figure 32 The Davis Vantage Pro 2 Plus as used by each LGfL Automated Meteorological Station

3.6.3 **WU** [Author: Robinson & Grimmond]

The Weather Underground (WU) network is the most heterogeneous of the networks, with a diverse array of instruments used and various approaches taken towards their siting. This is expected as are taken by individuals with an interest in weather. All the WU stations within the LMMN are located in private residences, but are situated in a broad variety of urban settings with the sites representative of all seven UCZs. In contrast to the LAQN and LGfL, WU employs no standardized approach towards instrumentation, with the choice of instruments and models at the discretion of the AMS owners. For example, at B9 temperature and relative humidity were sampled using a Davis Vantage Pro, whereas at B65 an Oregon Scientific WMR 918 AMS was employed to measure the same variables.

The siting guidelines on the Weather Underground website are based on Davis Instruments and Citizen Weather Observer Program (CWOP) (CWOP 2010). This guide emphasises the need for correct siting of meteorological sensors in order for them to represent the local scale. However, due to the nature of WU's operations, the guidelines are not used across the network. The two field surveys revealed that both owners had endeavoured to locate the wind sensors above roof level, with different masts used to mount the sensors. Although predominantly removed from surrounding obstacles, they were still within an area that would be exposed to wind influences from the buildings below. Other sensor siting issues included the proximity of the B9 Davis Pro to vegetation and its height above the ground approximately ~0.5 m. Due to the siting concerns evidence of their impact in the variables sampled, specifically temperature was examined in detail.

3.6.4 **UK Met Office** [Author: Robinson & Grimmond]

There are a number of official climate stations in the vicinity of London (Table 15). These include sites at airports which meet standard WMO criteria but not the Urban siting criteria of WMO.

Table 15 UKMO stations LWC is no longer operational

ID	Name	latitude	longitude	eastBNG	northBNG	original station name
0	A3	51.50950000	0.06162310	543053	181020	City airport
1	A5	51.32950000	0.25164600	556852	161392	Northolt airport
2	A6	51.87950000	0.23166900	553592	222510	Stanstead airport
3	A0	51.31950000	-0.02838540	537376	159719	Biggin Hill airport
4	A1	51.14650000	-0.18841700	526701	140195	Gatwick airport
5	A2	51.47950000	-0.44842900	507734	176811	Heathrow airport
6	A4	51.86950000	-0.36841200	512320	220302	Luton airport
						Kew Gardens
						St James Park
						London Weather Centre

3.6.5 **Spatial variability: Results** [Author: Pauscher & Grimmond, Contributors: Kotthaus, Thomas, Young]

Using the data collected from the four networks the variability of meteorological variables across London can be assessed. Here we present the raw temperature data for 2010. This provides clear insight into the continuity and availability of the data; and discrepancy/consistency in the data series across sites.

First we consider the UKMO stations (Figure 30) which we expect to be of the highest quality but the number of stations is small (Table 15). All the plots have the same convention with the time (day of year) on has time on the X axis and space/station on the Y axis. Given that the sampling and reporting resolution is different between stations this is evident in the plots. Stations A0 and A5 have a lower temporal resolution (60 mins rather than 30 mins). White indicates gaps in the data. Generally the data availability is good and consistent across the network. Though as evident for the WU network (Figure 31) there are some stations that are intermittent ord have incorrect values. These problems, not unexpectedly, are the most common in the WU data (compare also Figure 32, Figure 33).
Across all the networks one can see consistency when the temperatures clearly warmed and cooled. The warmest temperatures are generally recorded by the LAQN. This is not unexpected as these measurements are typically made closest to the surface (typically a roof of a metal cabin).

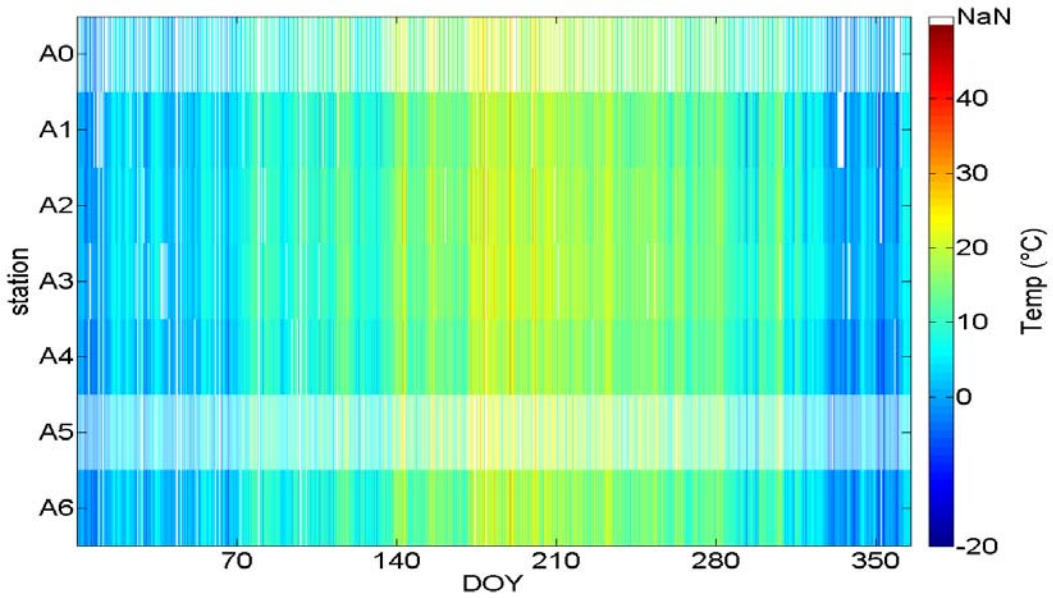

Figure 33 Temporal variability of air temperature for 2010 for the UKMO stations (see Table 15). DOY – day of year. NaN – Not a number.

KUMA ID	Station name	Latitude (°N)	Longitude (°E,°W)	eastBNG	northBNG	Name	KUMA ID	Station name	Latitude (°N)	Longitude (°E,°W)	eastBNG	northBNG	Name
0	B14	51.41150000	0.18363900	551843	170368	IHEXTABL1	31	B15	51.28150000	-0.96449200	472213	154159	IHAMPSHI22
1	B42	51.52050000	0.58469200	579299	183394	IESSEXCA1	32	B16	51.46350000	-0.36842200	513328	175152	IMIDDLES25
2	B44	51.43050000	0.41166100	567628	172977	IKENTGRA2	33	B17	51.50450000	-0.50743700	503580	179506	IBUCKSIV1
3	B46	51.37150000	0.51767200	575220	166665	IENGLAND88	34	B18	51.31950000	-0.09139340	532986	159603	IENGLAND67
4	B47	51.71950000	0.47768200	571127	205265	IESSEXCH3	35	B19	51.31450000	-0.61245700	496692	158232	IENGLAND142
5	B50	51.04440000	0.16862400	552004	129528	IEASTSUS4	36	B20	51.29250000	-0.32043000	517097	156211	IENGLAND104
6	B51	51.03240000	0.16861400	552043	128194	IEASTSUS7	37	B21	51.66950000	-0.55543400	499887	197789	IENGLAND127
7	B52	51.48750000	0.33565800	562143	179144	IESSEXGR2	38	B22	51.67150000	-0.56643600	499122	197996	IBUCKSAM1
8	B54	51.88950000	0.01763700	538832	223192	IHERTFOR2	39	B23	51.31850000	-0.53845300	501840	158778	ISURREYW4
9	B55	51.41350000	0.53267200	576103	171371	IKENTROC1	40	B24	51.26750000	-0.32243100	517021	153428	IENGLAND166
10	B56	51.36750000	0.62468400	582683	166481	IENGLAND10	41	B25	51.52250000	-0.46142400	506731	181574	IUXBRIDG2
11	B57	51.54950000	0.58168400	578977	186611	I90579233	42	B26	51.28450000	-0.95149400	473115	154505	IHOOK1
12	B58	51.56950000	0.67169600	585135	189059	IESSEXSO1	43	B27	51.55050000	-0.36341600	513460	184834	IMIDDLES8
13	B59	51.50050000	0.09863770	545649	180092	IENGLAND164	44	B28	51.48950000	-0.33842400	515346	178090	IMIDDLES12
14	B60	51.37150000	0.52666800	575846	166686	IKENTCHA1	45	B29	51.36150000	-0.14640800	529035	164175	ISURREYW1
15	B61	51.23190000	0.14642400	549840	150323	IESSEXEP1	46	B30	51.35150000	-0.77247500	485473	162149	IBERKSHI4
16	B62	51.54950000	0.58168400	578977	186611	I90579233	47	B31	51.41650000	-0.43243500	508994	169828	I90581027
17	B63	51.56650000	0.26866000	557220	187783	IESSEXUP1	48	B32	51.27950000	-0.09540020	532823	155148	ISURREYC2
18	B0	51.24550000	-0.76747200	486019	150367	IHAMPSHI2	49	B33	51.55950000	-0.32440800	516141	185897	IMIDDLES1
19	B1	51.41550000	-0.67546300	492099	169384	IBERKSWI1	50	B34	51.39650000	-0.57845100	498885	167398	ISURREYV1
20	B2	51.24450000	-0.72447000	489022	150307	IENGLAND90	51	B35	51.26650000	-0.44843800	508234	153124	ISURREYG1
21	B3	51.30350000	-0.27841700	519998	157503	IASHTEAD1	52	B36	51.23950000	-0.76847900	485960	149699	ISURREYF3

22	B4	51.40550000	-0.75946800	486277	168170	MD0125	53	B37	51.05740000	-0.08440360	534233	130482	IWESTSUS22
23	B5	51.52750000	-0.66244900	492776	181856	IENGLAND174	54	B38	51.38950000	-0.28143700	519563	167060	ISURREYS1
24	B6	51.60250000	-0.25940700	520532	190784	I90580969	55	B39	51.40750000	-1.27553000	450384	167912	ITHATCHA1
25	B7	51.36450000	-0.16240100	527914	164482	IENGLAND183	56	B40	51.09840000	-0.21142000	525222	134818	I90581052
26	B8	51.28450000	-0.09839790	532599	155699	ISURREYC5	57	B41	51.91050000	-0.63943100	493579	224480	IBEDSLEI1
27	B9	51.61050000	-0.54843700	500501	191237	IBUCKING4	58	B43	51.67250000	-1.05950000	465029	197554	IOXONCHA1
28	B10	51.57750000	-0.11538900	530576	188251	ILONDON7	59	B45	51.13440000	-0.12140200	531422	138978	I90580988
29	B11	51.29950000	-0.35443100	514710	156936	IENGLAND154	60	B48	51.10040000	-0.14940600	529558	135148	IWESTSUS10
30	B12	51.44450000	-0.05838910	534918	173564	ILONDONL3	61	B49	51.19950000	-0.89848900	476952	145107	KUKCROND1
							62	B53	51.43050000	-0.91948500	475107	170774	IENGLAND38

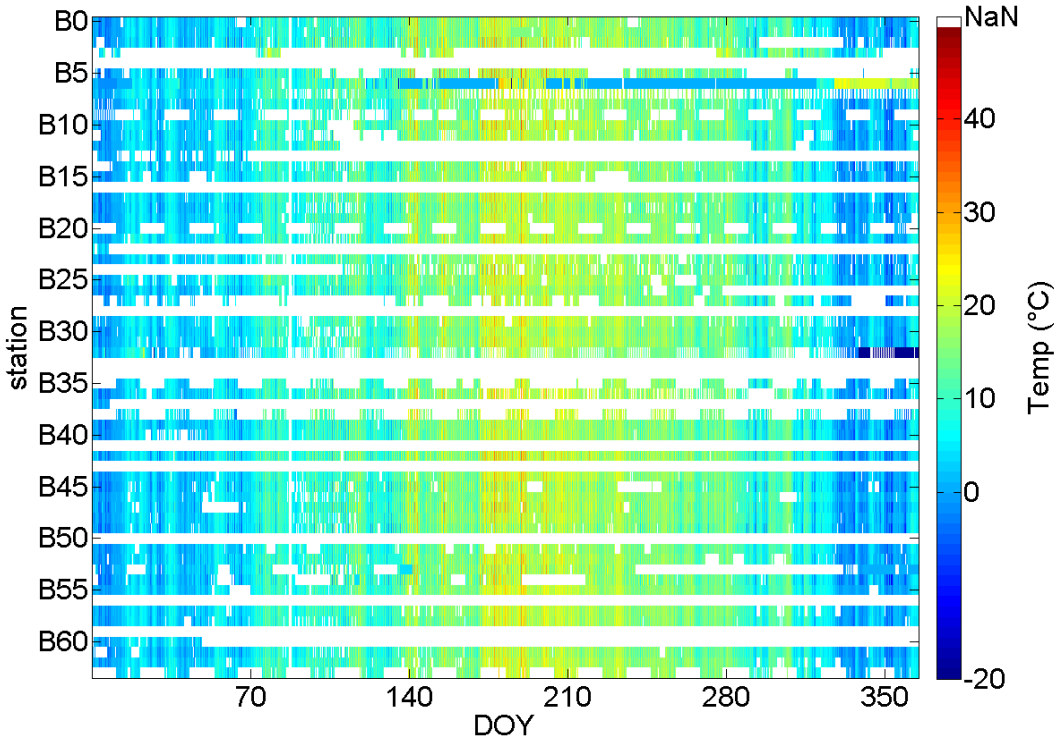

Figure 34 Air temperature variability for 2010 measured by stations in the WU network

KUMA ID	Station name	Latitude (°N)	Longitude (°E,°W)	eastBNG	northBNG	
0	C9	51.44450000	0.20664000	553332	174085	Dartford
1	C10	51.45050000	0.04062380	541778	174418	Eltham
2	C11	51.48750000	0.04363040	541873	178538	Greenwich
3	C14	51.37950000	0.00160995	539284	166448	Hayes
4	C19	51.53150000	0.03562940	541181	183416	Newham
5	C20	51.38850000	0.11207100	546941	167669	Orpington
6	C21	51.23370000	0.22368400	555226	150690	Rainham
7	C23	51.05360000	-0.44253200	509148	129467	Tunbridge Wells
8	C25	51.56150000	0.14763300	548850	186973	Dagenham
9	C26	51.58450000	0.22165000	553902	189684	Hornchurch (N)

10	C27	51.56450000	0.19764200	552306	187409	Hornchurch (W)
11	C30	51.47350000	0.12063400	547263	177133	Welling
12	C0	51.39650000	-0.67146600	492415	167276	Ascot
13	C1	51.79850000	-0.81545900	481675	211812	Aylesbury
14	C2	51.34550000	-0.20141000	525250	162301	Belmont
15	C3	51.81950000	-1.04449000	465853	213916	Brill
16	C4	51.36550000	-0.16540000	527702	164588	Carshalton
17	C5	51.44350000	-0.02638140	537144	173512	Catford
18	C6	51.71450000	-0.59543200	497025	202739	Chesham
19	C7	51.56250000	-0.06338770	534223	186676	Clapton
20	C8	51.59950000	-0.24540400	521510	190473	Colindale
21	C12	51.58550000	-0.10438500	531315	189159	Harringay
22	C13	51.08240000	-0.73347600	488704	132281	Haslemere
23	C15	51.67650000	-0.78845500	483762	198275	High Wycombe
24	C16	51.55750000	-0.38742600	511778	185576	Hillingdon
25	C17	51.51750000	-0.20639900	524435	181420	Kensington
26	C18	51.38450000	-0.26441100	520761	166532	New Malden
27	C22	51.47450000	-0.09539320	532260	176832	Southwark
28	C24	51.59850000	-0.02238270	536956	190756	Walthamstow
29	C28	51.44450000	-0.19640800	525328	173319	Wandsworth (S)
30	C29	51.44450000	-0.12038800	530610	173452	Streatham
31	C31	51.52750000	-0.02638690	536892	182853	Bow
32	C32	51.45450000	-1.01250000	468606	173352	Tilehurst
33	C33	51.41650000	-0.82147300	481945	169322	Wokingham
34	C34	51.45750000	-0.42942800	509106	174392	Bedfont
35	C35	51.53760000	-0.11262400	530882	183821	Islington
36	C36	51.41250000	-0.21140000	524373	169734	Merton
37	C37	51.62950000	-0.21306100	523668	193863	Mill Hill
38	C38	51.49850000	-0.38542900	512061	179017	Southall
39	C39	51.45350000	-0.34341400	515091	174078	Twickenham
40	C40	51.51950000	-0.13740000	529216	181761	Westminster

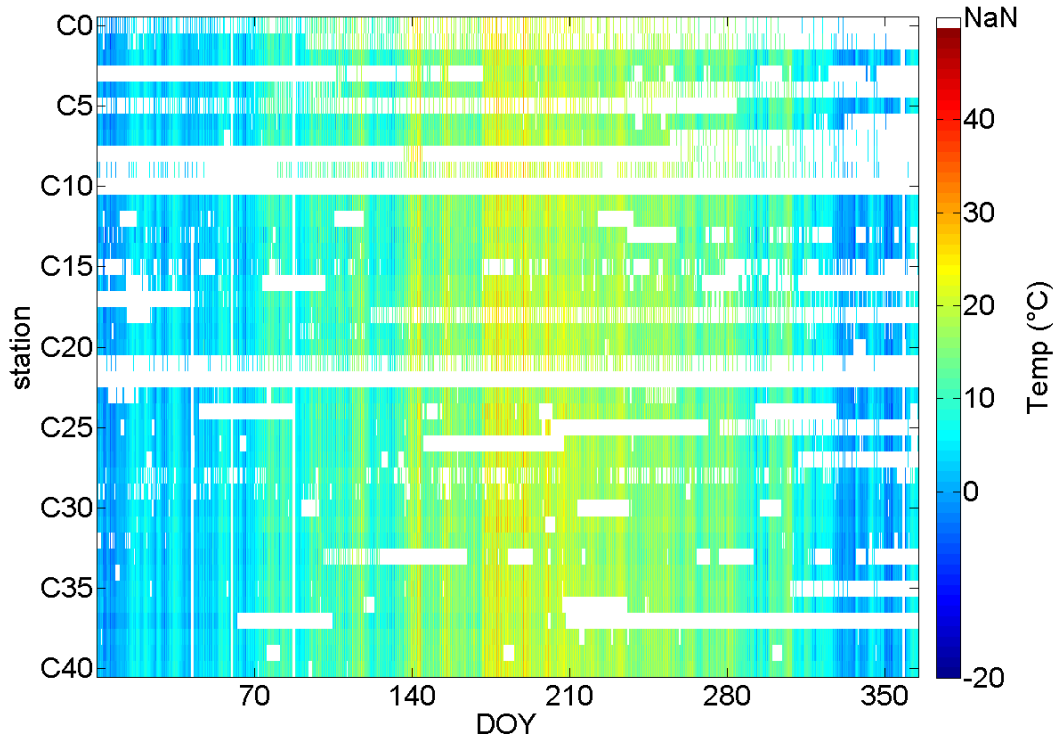

Figure 35 Air Temperature measured at stations in the LGfL network (**Error! Reference source not found.**) during 2010.

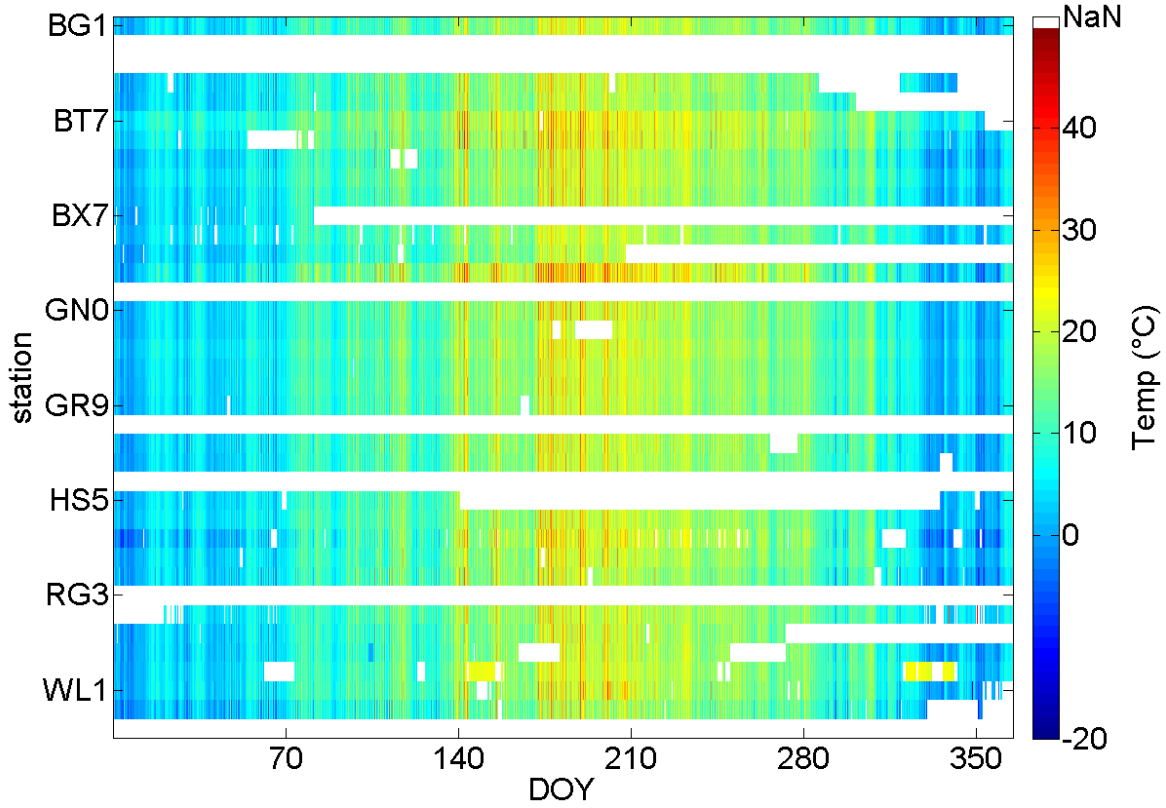

Figure 36 Air temperature observed at stations in the LAQN network (Table 14) for 2010.

3.7 **Air Quality** [Author: Grimmond]

As part of this study, two types of analyses have been conducted that are concerned with air quality:

a) The LAQN data were used to model the impact of vegetation cover on air quality using the UFORE model
b) Measurements were taken at one LAQN site to evaluate the fourier transform infra red spectroscopy (FTIR) for conducting air quality measurements.

3.7.1 **Air Quality Methods: UFORE** [Author: Tallis]

Using the adapted UFORE approach described in Tallis et al. (2011[91]) the potential of current street tree cover and a future maximum density of street tree cover is investigated to remove dust pollution (particulate matter of a diameter less than 10 x 10^{-6}m (PM_{10}) within the London case study site (the CAZ). The aim of this work is to provide estimates of total annual removal of PM_{10} resulting from dry deposition, from the mixing layer above the CAZ. Furthermore the removal of PM_{10} (g m^{-2} of canopy) was estimated for the whole range of PM_{10} concentrations [PM_{10}] experienced by street trees within the CAZ. This allowed for a comparison of modelled estimates with measured PM_{10} deposition to trees within the CAZ and also provides estimates of removal potential dependent on local [PM_{10}]. This approach was expanded to the whole Greater London Authority (GLA) area to examine the annual PM_{10} removal of the urban canopy for the whole of London and to allow comparisons with data from other cities and assess the applicability for a city wide approach (Tallis et al. 2011).

The input data required for the adapted UFORE model described in Tallis et al. (2011) to estimate dry deposition of PM_{10} to tree canopies are (i) [PM_{10}] (µg m^{-3}), (ii) tree canopy cover, deciduous or coniferous (m^2) and (iii) meteorology required to calculate Pasquill-Turner stability class (season, wind speed (m s^{-1}), cloud cover (Oktas). The model was applied to three different scenarios within the CAZ; these were (i) current street tree cover with current [PM_{10}] and meteorology (ii) a maximum possible street tree planting density with current [PM_{10}] and meteorology and (iii) a maximum possible street tree planting density with [PM_{10}] and meteorology estimated for 2050. Current and future [PM_{10}] were obtained from the LAEI pollution dispersal maps for London (LAEI 2009[92]) and Williams (2007[93]) respectively, the [PM_{10}] data used for model inputs are given in Table 16. Current and future street tree canopy covers within the CAZ were obtained from Lindberg and Grimmond (2011[94]) and the data used for model inputs are given in

Table 17. Mapped meteorological data for the GLA were extracted from the UKCP09 gridded data sets of monthly values[95] (Perry and Hollis 2005) for 2006 (cloud cover was for 2004 due to absent

[91] Tallis M, Freer-Smith P, Sinnett D & Taylor G 2011. *Estimating the removal of atmospheric particulate pollution by the urban tree canopy of London under current and future developments.* Landscape and Urban Planning – Under review.
[92] LAEI 2006. London Atmospheric Emissions Inventory 2006. Compiled by AEA, March 2009. (http://static.london.gov.uk/mayor/environment/air_quality/research/emissions-inventory.jsp)
[93] Williams ML 2007. UK air quality in 2050—synergies with climate change policies. *Environ. Sci. Policy*, 10: 169-175.
[94] Lindberg F and Grimmond CSB (2011). The influence of vegetation and building morphology on shadow patterns and mean radiant temperatures in urban areas: London case study – Under review
[95] www.metoffice.gov.uk

data) at a 5 km resolution for the whole GLA area. Input data to describe the future climate in the GLA were extracted from UKCP09[96] . The absolute values (for a 50% probability) were extracted from the 'UK probabilistic projections of climate change over land' based on the medium emissions scenario (SRES A1B) for London in the 2050s. Wind speed for the London area was estimated from the UKCP02 maps for the mean of the medium emissions scenarios for 2080 (the only data available at the time of analysis).

Table 16: The values of [PM_{10}] used as input data for the modified UFORE model. * extracted from a 20 m area either side of the street using ArcMap®, ** taken from the upper values of the range predicted by Williams (2007).

	Whole CAZ area (15.68 ha) [PM_{10}]			CAZ Street buffer* [PM_{10}]		
	Mean	Min	Max	Mean	Min	Max
Current (2006)	23.8	21.5	79.8	30	21.8	79.8
Future (2050)	19**	-	-	22**	-	-

Table 17 The values of street tree canopy cover used as input data for the modified UFORE model. *Estimated using the placement rules of Lindberg and Grimmond (2011).

Scenario	Canopy cover (m^2)	
	Deciduous	Coniferous
Current	21437 (14%)	9 (0.01%)
Maximum planting density*	36699 (23%)	9 (0.01%)

3.7.2 **Air Quality Modelling Results** [Author: Tallis]

Two adaptations to the UFORE model (described in detail in Tallis et al. 2011) allow deposition to be estimated assuming 50% re-suspension of particles (referred to as UFORE) and zero re-suspension (referred to as adapted UFORE). The results of both model outputs are given in Table **18**. The inputs from future climates had little influence in parameterising the values for resistance terms in the model and little change was estimated for the mixing layer height which reduced from an annual mean of 435 m (2006) to 430 m (2050) according to model calculations. The [PM_{10}] experienced by street trees within the CAZ ranged from 21 – 79 µg m^{-3} the estimated uptake to the tree canopy (g m^{-2}) across this range is given in Figure 34.

The estimated annual uptake of PM_{10} deposited to street trees (g m^{-2}) through dry deposition (Figure 34) were compared with measured data from a site within the CAZ (Portman Square 51° 30`55.32``N and 00° 09`21.90``W species *Platanus* x *hybrida*, (London plane) a common London street tree). Mean deposition to trees at the Portman square site was 1735 g $tree^{-1}$ (Beckett et al. 2000[97]) taking the diameter range (measured from Google Earth) of 15 – 25 m for trees at this site this allows a measured approximation of between 4 – 10 g m^{-2} of PM_{10} deposited to these canopies. This measured value is

[96] http://ukclimateprojections-ui.defra.gov.uk

[97] Beckett, K.P. Freer-Smith, P.H. Taylor, G. 2000. *The capture of particulate pollution by trees at five contrasting urban sites.* Arboricultural Journal. 24: 209–230

within the modelled estimates which range from 2 – 16 g m^{-2} for broadleaved trees depending on local [PM_{10}] and model type with outputs from the adapted UFORE model (no re-suspension) being closer to this range (Figure 37).

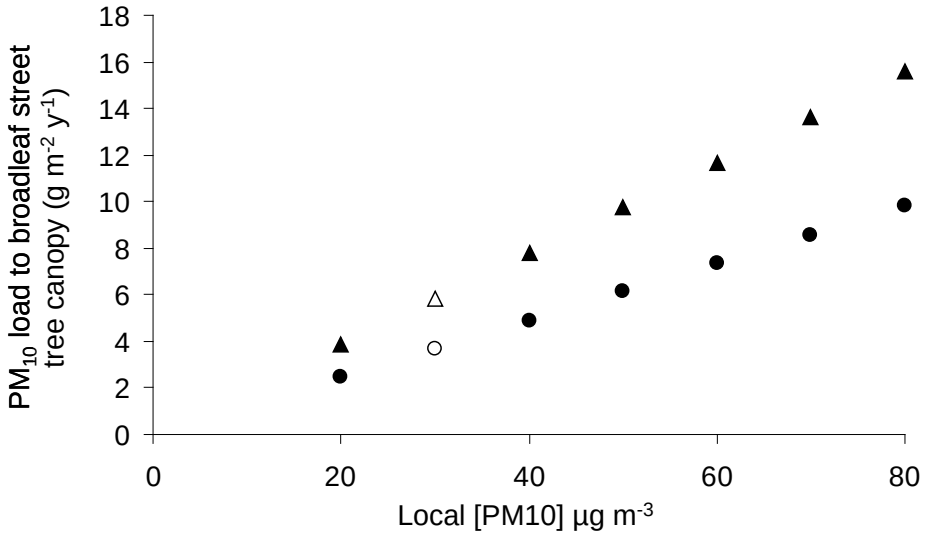

Figure 37 : Estimates of the annual dry deposition to street trees across the 20 m street buffer exposure range of [PM_{10}]. Estimates are given for UFORE (●) and adapted UFORE (▲) and clear symbols give the estimated PM_{10} load deposited to the street tree canopy for the mean street buffer exposure.

Table 18: Estimates of PM_{10} removal by the street tree canopy from within the CAZ using the mean exposure concentrations reported in Table 16.

	Scenario					
	Current canopy [PM_{10}] and climate		Maximum canopy, current [PM_{10}] and climate		Maximum canopy, current [PM_{10}] and climate	
	UFORE	Adapted	UFORE	Adapted	UFORE	Adapted
Total Uptake (kg y^{-1})	79	126	135	215	99	158
Reduction in CAZ boundary layer (%)	0.6	0.9	1.1	1.8	0.9	1.4
Uptake to Broadleaf (g m^{-2})	3.7	5.8	3.7	5.8	2.7	4.3
Uptake to Coniferous (g m^{-2})	6.1	62.0	6.1	62.0	4.4	45.5

3.7.3 **FTIR test: Remote sensing of Air Quality** [Authors: DeJong & Grimmond, Contributors: Smith & Wooster]

The open path (OP) fourier transform infra-red spectroscopy (FTIR) OP-FTIR technique was evaluated at the Blackwall Tunnel Northern Approach (BTNA), London (51° 30' 53.51" N, 0° 00' 29.79" W) (Figure 35). BTNA is a 6-lane road that experiences a high volume of traffic, and high concentrations of pollutants, ideal for testing the technique. The London Air Quality Network (LAQN) has a monitoring site located here (TH4), allowing for a comparison between LAQN and spectrometer measurements. The majority of the spectrometer path was located in an area with low pedestrian use, reducing path obstructions.

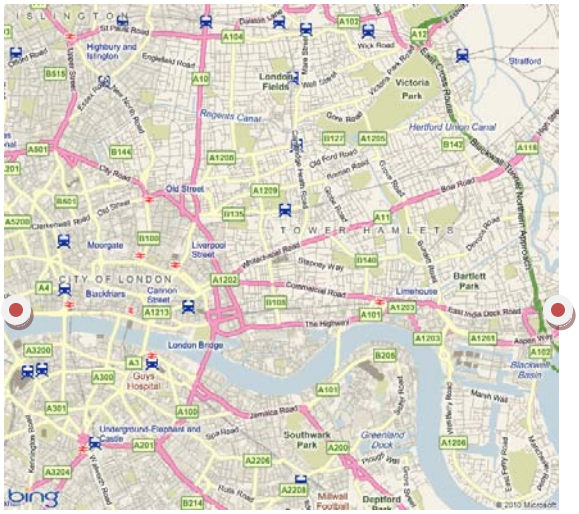

Figure 38 (left) [98] Location of BTNA site (right hand side dot) relative to KCL site (LHS dot) (right) FTIR sample site location (black square) (Google 2009)

[98] Source overview map: http://www.bing.com/maps/print.aspx?mkt=en-gb&z=13&s=c&cp=51.518190,-0.060062&poi=Blackwall%20Tunnel%2C%20London%20SE10%200&pp=skhf41gzzvm1&b=1&pt=pb

3.7.4 **FTIR Test: Methods** [Authors: DeJong & Grimmond, Contributors: Smith & Wooster]

Sampling was carried out on 04/11/09 between 15:15 and 20:30 in order to sample the afternoon traffic peak. A MIDAC M2000 spectrometer was aligned with a MIDAC 20 cm IR field source (bistatic configuration – Figure 36) adjacent to BTNA, providing a path length of 49.3 m. The path bisected Abbott Rd at the junction with BTNA, so the spectrometer and the IR source were raised on tripods (~ 1.5 m above street level), avoiding vehicle obstructions. 12 volt batteries were used as power sources for both the spectrometer and IR source.

A Vaisala WXT510 weather station was setup (aligned north) near the spectrometer, measuring relative humidity (RH), temperature, pressure, rainfall, wind speed and wind direction. Meteorological factors affect pollutant dispersal (and therefore concentration), so measurements are used to help interpret pollutant data. Temperature and pressure data was required to calculate pollutant concentration, and RH was used to validate spectroscopic water concentration data.

Spectrometer data were collected and transformed using MIDAC AutoQuant software (8 scans were averaged, producing a recorded spectrum every 7 - 9 s). WXT510 data was recorded every 5 s. A video camera setup on top of the spectrometer recorded traffic flow on BTNA. Figure 40 shows the sample site and instrument set up. A flow diagram showing the data collection process is provided in Figure 41. To identify specific chemical species, 21 spectra were averaged using Essential FTIR (Operant LLC 2009[99]) from around 17:30 (i.e. high traffic flow period) to increase the signal-to-noise (SN) ratio. Absorption spectra were then obtained (GATS Inc 2009[100]) for species expected to be present during sampling, and from these, strong species absorbance regions were identified. Absorbance features related to specific species could then be identified in the urban air spectrum. Despite the sample site being selected for having high levels of combustion related species, ambient concentrations were lower than concentrations of many species OP-FTIR is usually used to measure. Overlaying the urban spectrum with a biomass fire spectrum where much greater concentrations of combustion species are present, enabled easier identification of spectral features.

The forward modelling software MALT 5 was used to calculate species concentrations from the spectra. Using environmental data from the sampling site (mean temperature and pressure, path length), and species specific molecular data (for factors affecting molar absorptivity) from the HITRAN database (Rothman *et al.* 2005[101]) and approximate atmospheric concentrations for the species, MALT simulates absorption spectra at a specified wavenumber range. The synthetic spectrum is fit to the observed spectrum iteratively, with MALT adjusting species concentrations each iteration until the mean-squared

[99] Operant LLC (2009) Essential FTIR – FTIR Software. [Online]. Available from: http://www.essentialftir.com/ [Accessed 10th November 2009].

[100] GATS Inc. (2009) Spectral calculator, atmospheric gas spectra, infrared molecular absorption spectrum [Online]. Available from: http://www.spectralcalc.com/spectral_browser/db_intensity.php. [Accessed 15 Dec. 2009]

[101] Rothman, L. S. et al. (2005) The HITRAN 2004 molecular spectroscopic database. Journal of Quantitative Spectroscopy and Radiative Transfer. 96. 139 – 204.

residual between the spectra is minimised (Griffith 2006[102]). Background spectra are not required using this modelling method; MALT simulates the background by fitting polynomials to the sample spectra.

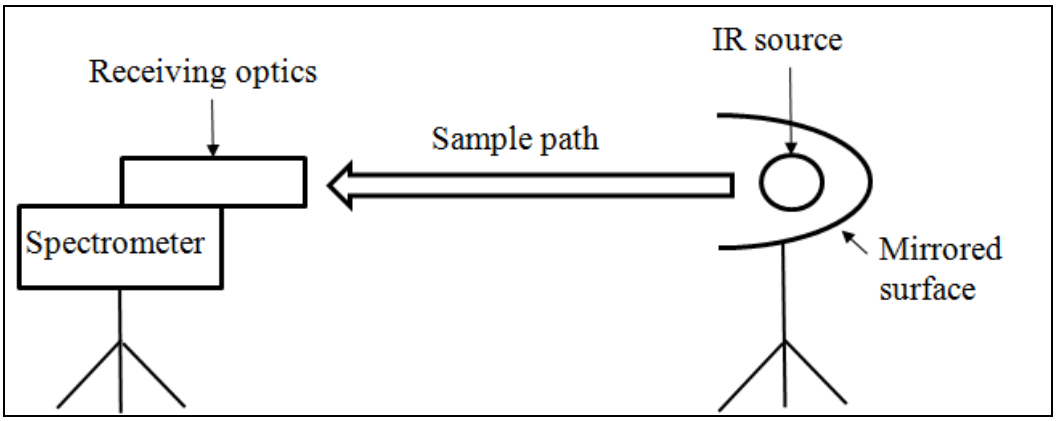

Figure 39 Bistatic spectrometer configuration (After Backsik *et al.* 2004[103]).

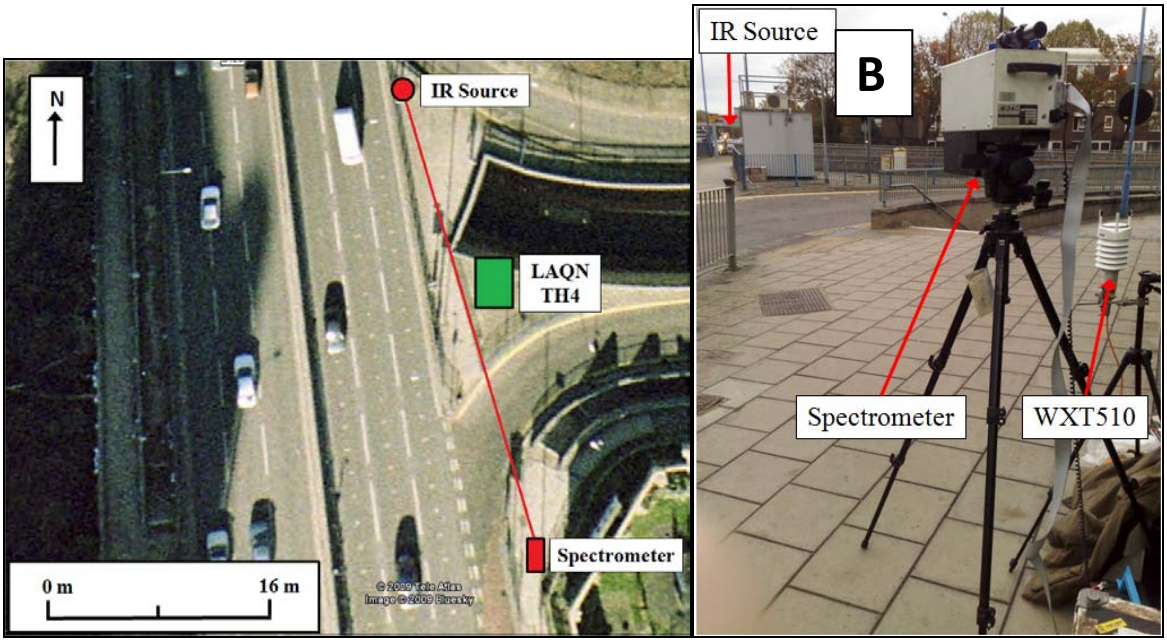

Figure 40 (A) Site setup and approximate spectrometer path (Google 2009) and (B) Looking north along the spectrometer path. LAQN TH4 station visible in top left.

[102] Griffith DWT (2006) MALT 5 User's Guide, Version 5.2. [Electronic document] Available with MALT 5 software.

[103] Backsik Z, Mink J & Keresztury G (2004) FTIR spectroscopy of the atmosphere. I. Principles and methods. *Applied Spectroscopy Reviews*. 39. 295 – 363.

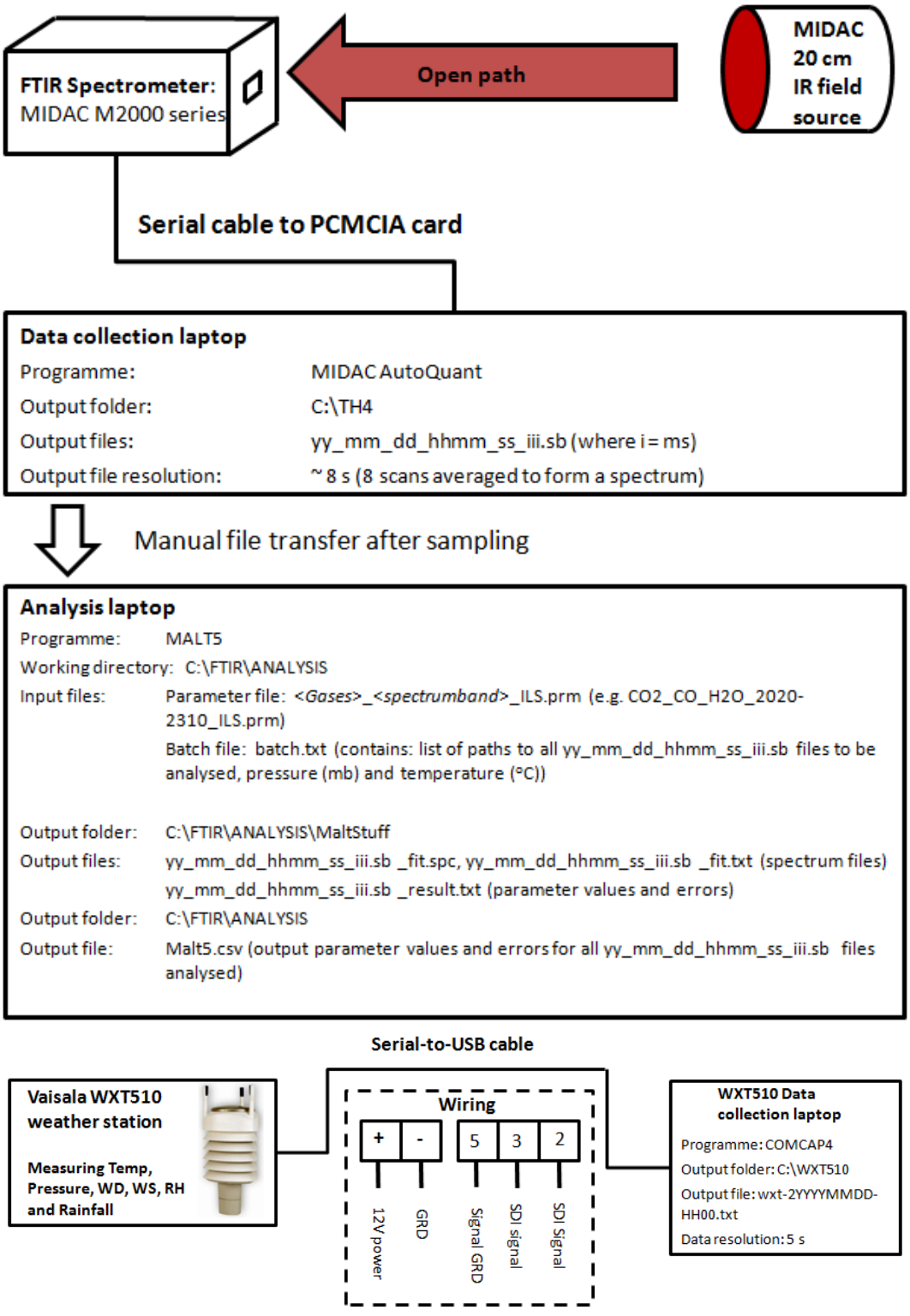

Figure 41 Flow diagram of FTIR data collection

Table 19 Species identified or quantified using FTIR spectroscopy.

Species	*Successful MALT quantification? (Yes/No)*	*Visual identification in spectra if not quantified? (Yes/No)*
Carbon dioxide (CO_2)	Yes	N/A
Carbon monoxide (CO)	Yes	N/A
Water (H_2O)	Yes	N/A
Methane (CH_4)	Yes	N/A
Nitrous oxide (N_2O)	Yes	N/A
Ozone (O_3)	No	Yes
Sulphur dioxide (SO_2)	No	Yes
Nitrogen monoxide (NO)	No	No
Nitrogen dioxide (NO_2)	No	No

Table 20 Mean species experimental and background concentrations. [a] Blasing (2009), [b] WHO (2000).

Species	***Mean FTIR Concentration***	***Average global background concentration***
	Concentrations in ppm	
CO_2	477.7	384.8 [a]
	Concentrations in ppb	
CH_4	1985.5	1865/1741 [a]
CO	785.6	50 – 120 [b]
N_2O	328.5	322/321 [a]

3.7.5 **FTIR test: Results** [Authors: De Jong & Grimmond, Contributors: Smith & Wooster]

Table 19 provides a summary of the species could and could not be quantified in this study. Unfortunately no gaseous pollutant species monitored at the LAQN site (Nitrogen monoxide (NO), nitrogen dioxide (NO_2) and ozone (O_3)) were able to be quantified using spectroscopy, so no direct comparison of measurements could be made. Plotting carbon dioxide (CO_2) and carbon monoxide (CO) against LAQN TH4 NO data (from Dr B. Barrett, personal communication, KCL, 12/11/09) however allows for a comparison of trends over the sampling period (Figure 39) as they are primary pollutants mainly sourced from vehicular combustion. No clear increase in pollutant concentrations is observed to indicate the start of the traffic peak, but a clear decrease in NO is mirrored in CO and very clearly in CO_2 between 18:45 and 19:45, when traffic flow at the site was observed from video data to have significantly decreased (Figure 40). Short term variation in NO concentration also agrees well with variation in CO and CO_2 data.

The evolution of methane (CH_4), water (H_2O) and nitrous oxide (N_2O) concentration is shown in Figure 41 and Figure 42. Methane is not a combustion product so does not correlate with traffic patterns, and is likely to be influenced by regional concentrations (Grutter 2003b). Temperature inversion development at the end of the day may partially account for the general increase in CH_4 concentration over time (Oke 1987[104]).

[104] Oke, T. (1987) *Boundary Layer Climates.* London: Methuen and Co. Ltd.

WXT510 RH data and FTIR water concentration show good agreement in the overall trend and in short term variation. The general concentration increase is likely to be a result of increased combustion from an increase in traffic and possibly the formation of a temperature inversion. Contrasting with other pollutant trends, N_2O concentration generally decreases over time, suggesting that concentrations are dominated by regional sources (Grutter 2003b[105]).

From a comparison with global background values (Table 20), FTIR concentration values appear reasonably accurate. Mean values for CO_2 and CO greatly exceed global background values, as expected in urban areas with large combustion sources. CH_4 and N_2O levels show relatively good agreement, evidence for concentrations being regionally dominated.

O_3 and sulphur dioxide (SO_2) concentrations were not successfully modelled with MALT (either unrealistic concentrations or very high % error values were calculated) but small spectral features associated with the species were observed in the urban air spectrum (Figure 44, Figure 45). The biomass fire spectrum is also shown to aid feature recognition.

A more objective identification analysis based on fit residuals was carried out. The mean of the squared residuals is smaller for a MALT run with O_3 defined as a component (1.33×10^{-5}) than a run without O_3 defined (1.40×10^{-5}). It was also smaller for a MALT run with SO_2 (1.47×10^{-5}) than without (1.57×10^{-5}), implying that both O_3 and SO_2 must be present as they can account for some absorption. Residuals for the model runs are shown graphically in Figure 45. Neither identification nor quantification was possible for NO_2 and NO, as they have large spectral features in regions where high absorbance occurs from interfering species.

Wind speed and direction can have a significant impact on pollutant dispersal and therefore concentrations (Harrison 2001[106]). Over the course of the sampling period, relatively little variation in wind speed or wind direction was observed (Figure 46). Average wind speed was 1-2 m s^{-1}, and the dominant direction was SSE, parallel to the road. As a result, variations in pollutant concentrations are more likely to have been caused by other factors.

Concentrations of pollutant species typically measured at urban monitoring sites (e.g. SO_2, NO_x, O_3) were below the detection limits (DL) of this FTIR setup. For this to prove a viable method for meso-scale monitoring of these species, method alterations are needed. Spectral features are very small in the urban spectra, resulting in poor MALT fits. According to the Beer-Lambert law (2) absorption increases (and therefore DL decreases) linearly as sample path length increases. Long path lengths are commonly used/recommended in literature to obtain low ppb concentration measurements (Griffith & Jamie

[105] Grutter M (2003b) Multi-gas analysis of ambient air using FTIR spectroscopy over Mexico City. Atmosfera. 16. 1-13.
[106] Harrison, R.M. (2001) Pollution: causes, effects and control. Cambridge: RSOC.

2000[107]; Grutter *et al.* 2003a[108]), though unobstructed paths of >100 m are difficult to find in urban areas. Raising equipment above street level may make this possible. Reducing DL by increasing SN would require much longer measurement averaging times, resulting in lower time resolution data than most continuous analysers. Using a modulated radiation beam like Grutter *et al.* (2003a) would also improve DL by reducing the detection of stray radiation.

Despite not having a direct comparison between FTIR and LAQN data, comparing primary pollutant levels and water vapour with RH showed that general trends and small scale variation is measured accurately using the FTIR. This suggests that if the DL are reduced, reliable FTIR measurements are likely to be obtained.

The OP-FTIR method used successfully measured species with concentrations in the high ppb – ppm range (H_2O, CO_2, CO, N_2O, CH_4) and data trends reflected those found in species monitored by other methods. Concentration values for these compounds are considered relatively accurate. The inability of the method to measure lower concentration pollutants (NO, NO_2, SO_2, O_3) that are widely monitored in urban areas mean that the technique, without alteration, is unsuitable for urban air quality monitoring. Reducing detection limits by increasing the sample path length and using a modulated IR beam should make this a more viable option.

[107] Griffith DWT & Jamie IM (2000) Fourier transform infrared spectrometry in atmospheric and trace gas analysis. *Encyclopaedia of Analytical Chemistry*. Meyers, R. A, Ed. Chichester: John Wiley & Sons Ltd

[108] Grutter M, Flores E, Basaldud R & Ruiz-Suarez LG (2003a) Open-path FTIR spectroscopic studies of the trace gases over Mexico City. *Atmospheric Ocean Optics*. 16. 232-236.

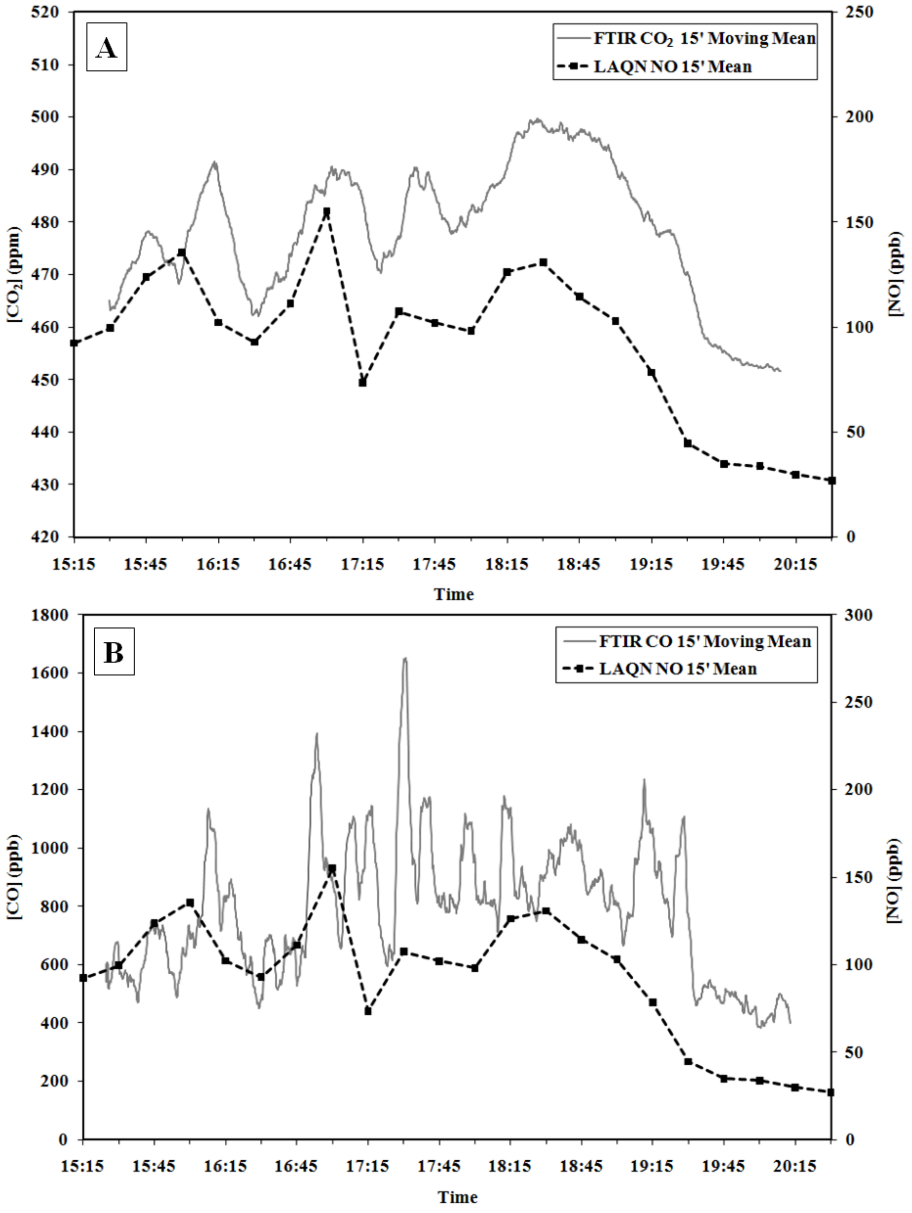

Figure 42 Time series of (**A**) CO_2 and (**B**) CO concentrations plotted against LAQN NO data, BTNA, London.

Figure 43: Video stills from (A) before (~18:30) and (B) after (~19:30) the decrease in afternoon peak traffic, Blackwall Tunnel Northern Approach. London

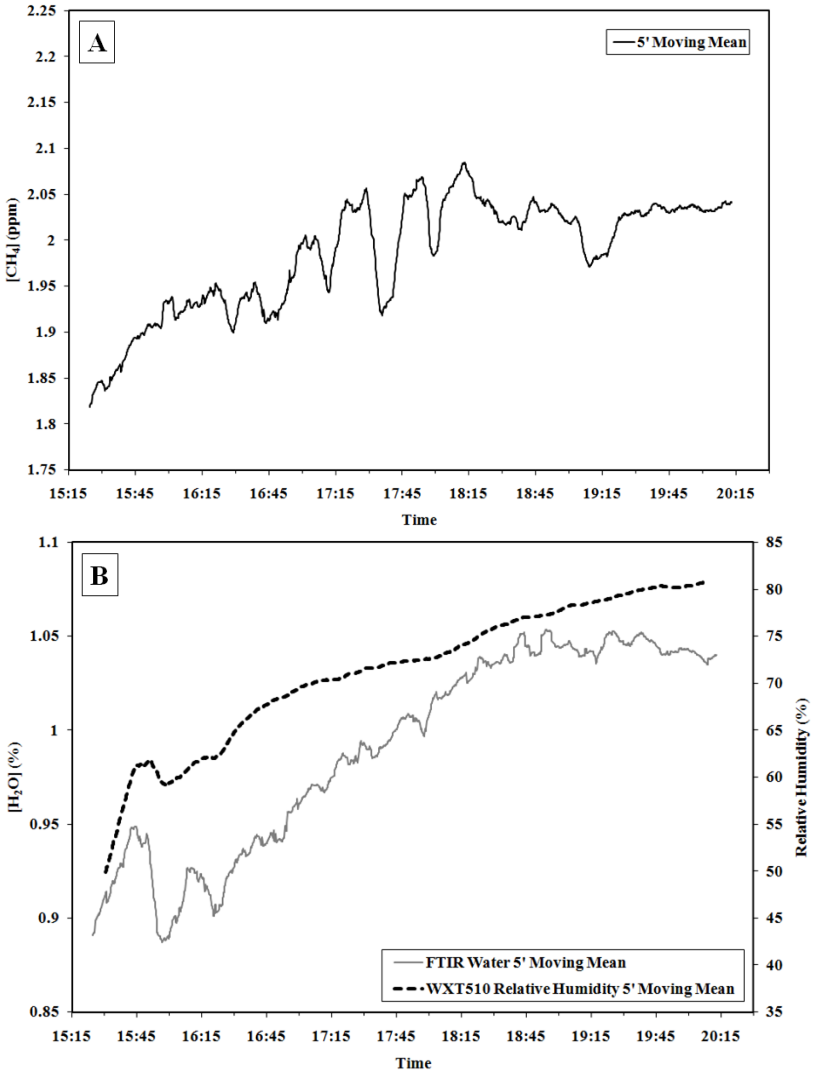

Figure 44: Time series of (**A**) CH_4 concentration and (**B**) H_2O concentration alongside WXT510 relative humidity data, BTNA, London.

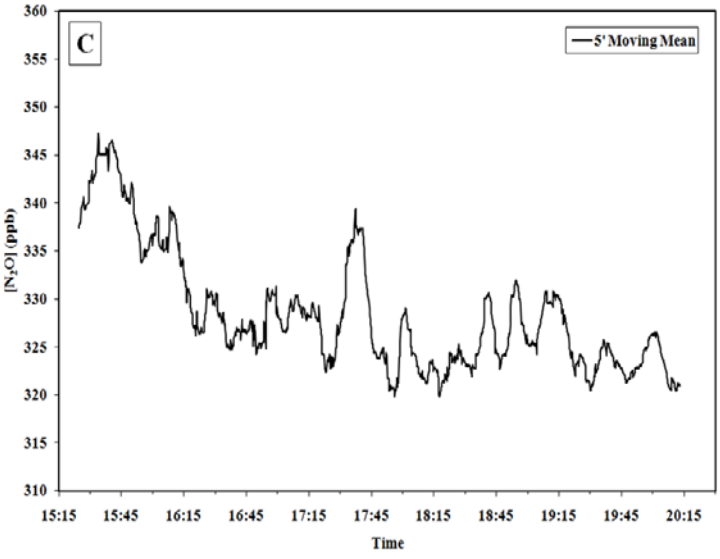

Figure 45 Time series of N_2O concentration, BTNA, London.

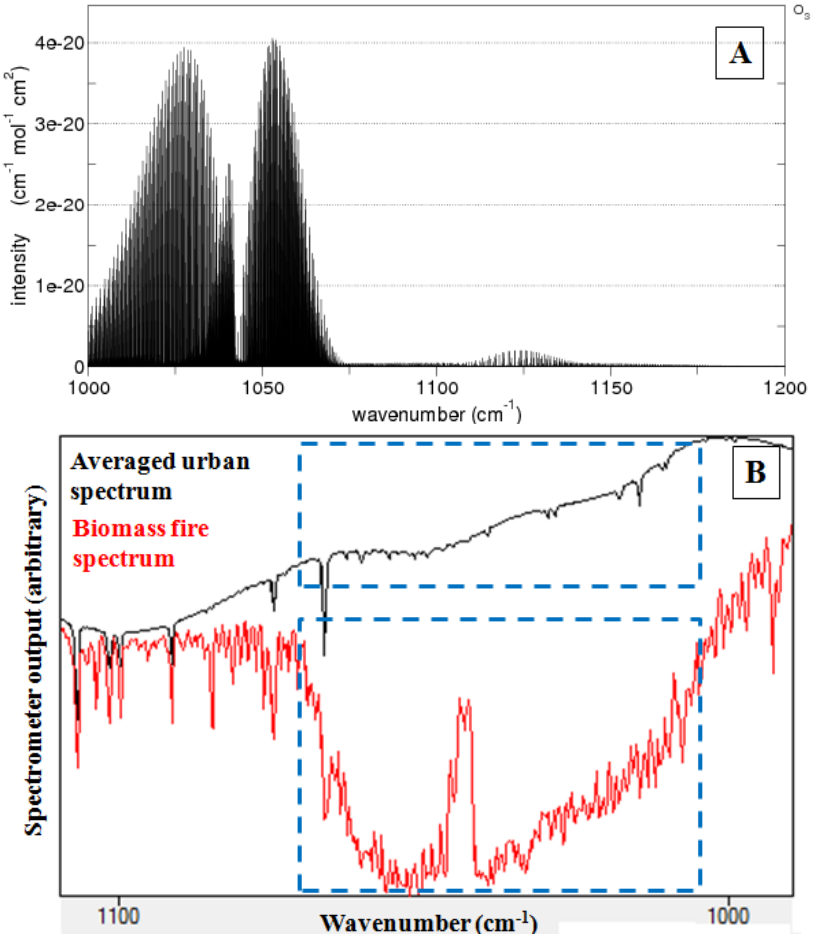

Figure 46 (**A**) ozone double peaked absorbance feature (1000 – 1070 cm^{-1}) (GATS Inc 2009) (**B**) identified in the biomass fire and urban air spectra (dashed boxes). Note that the absorbance double peak feature in (**A**) becomes a double trough in (**B**), as the y-axis is detector output of the spectrometer, not absorbance.

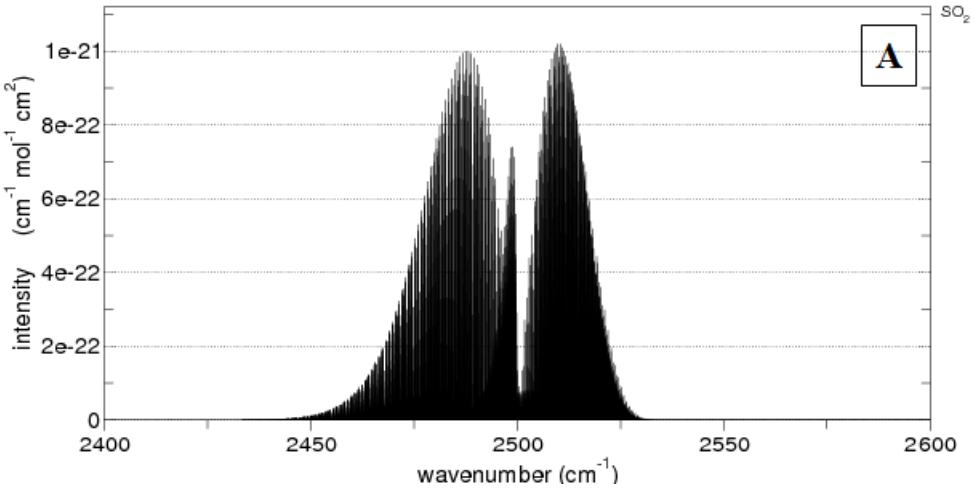

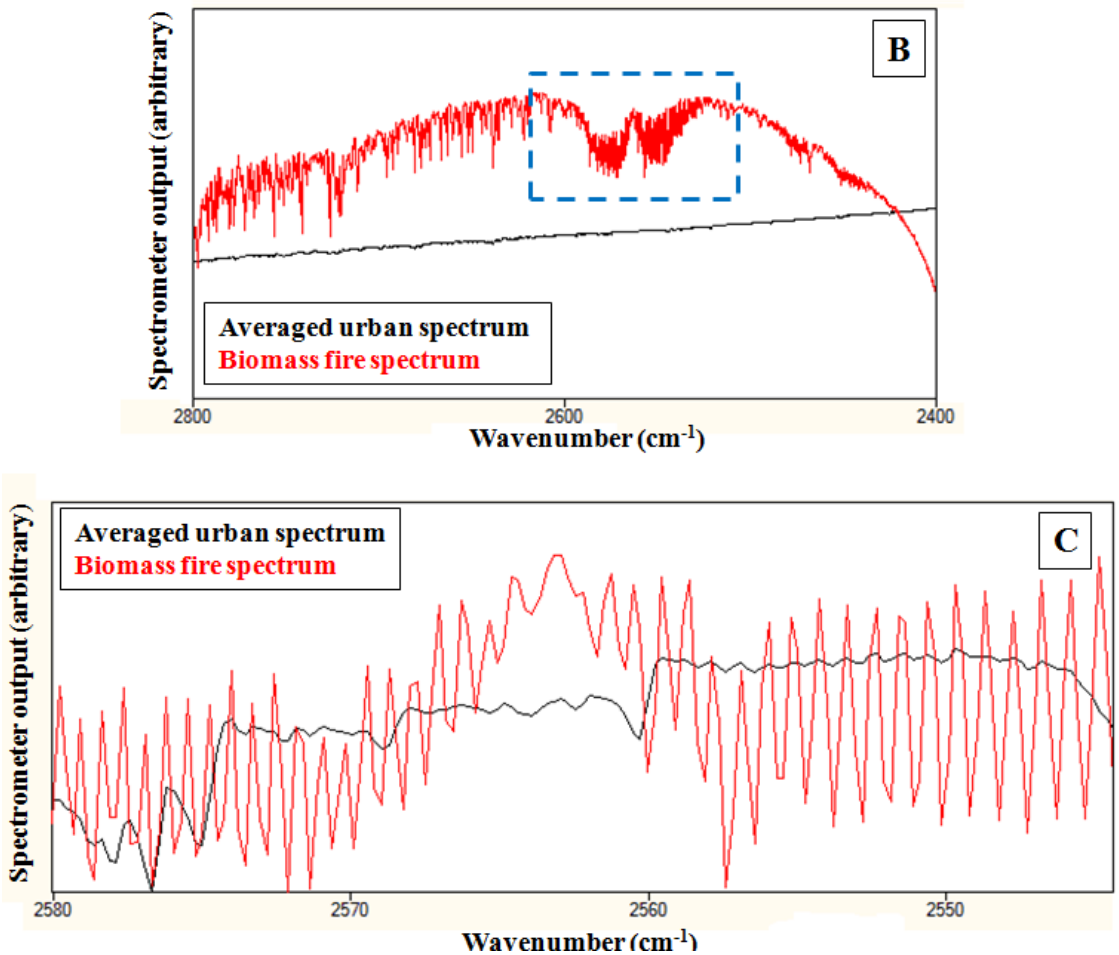

Figure 47 (**A**) SO_2 double peaked absorbance feature (2400 – 2600 cm^{-1}) (GATS Inc 2009) (**B**) SO2 large scale absorbance feature (only clear in biomass fire spectrum, (dashed box)) (**C**) Small scale SO2 absorbance features in both spectra.

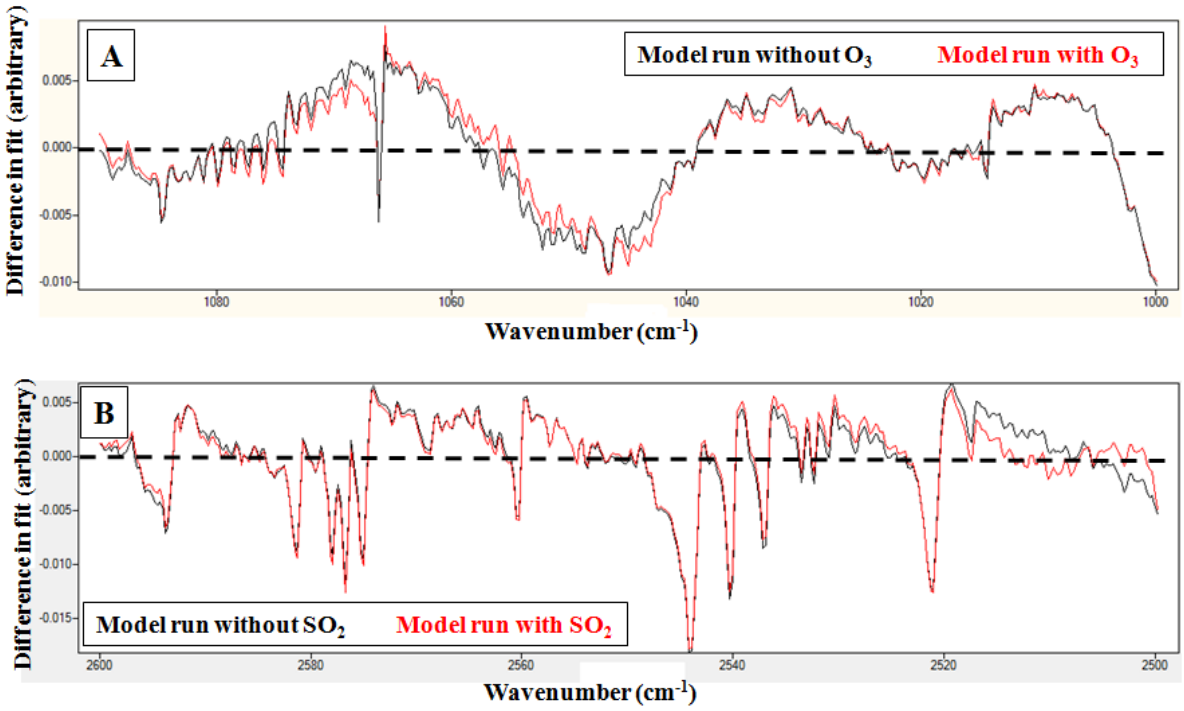

Figure 48 Comparison of fit residuals for (**A**) O_3 and (**B**) SO_2.

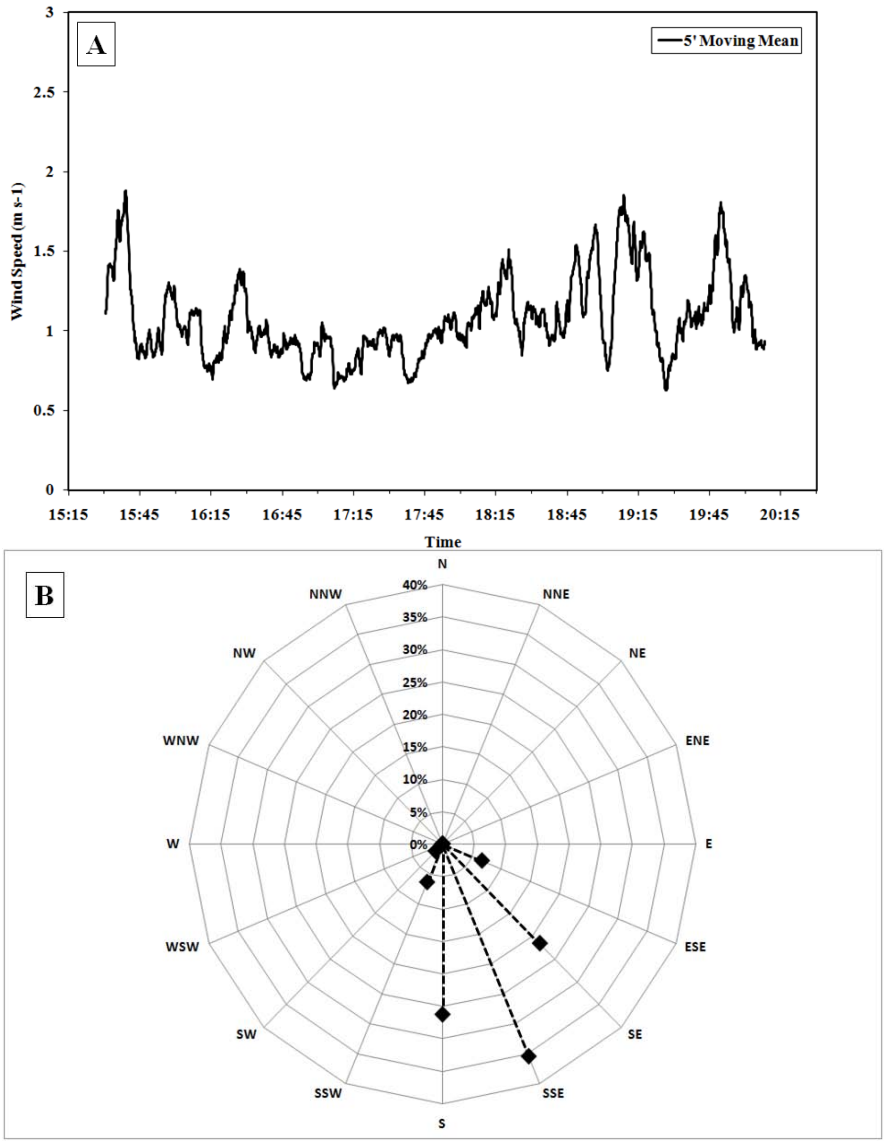

Figure 49 Plots of (**A**) mean wind speed and (**B**) wind direction, BTNA, London.

3.8 **Auxillary Sites** [Author: Grimmond]

This section describes sites that have been established to collect data for the BRIDGE project. They are located within the Central Activity Zone and typically involve sampling either intermittently or single variables. The data collected include:

a) Soil moisture and temperature
b) Phenology
c) External Water Use
d) River Thames water temperature
e) Surface temperature during remote sensing field campaigns

3.8.1 **Soil moisture and temperature: Observations sites** [Authors: Young & Grimmond; Contributors: Castillo, Lindberg, Sae-Jung, Smith]

Four central London parks/gardens were chosen for the measurement of soil moisture (Figure 47, Figure 48). Temple Gardens (TEM, 51.5112 °N; -0.113 °W) and Embankment Gardens (EMB, 51.5081 °N; -0.1217 °W) are on the Victoria Embankment (constructed 1874). These gardens are mainly grassed areas with planting beds and shrubberies (containing shrubs and trees). The other two sites are Jubilee Gardens (JUB, 51.5039 °N; -0.1183 °W), a large grassed area with limited flower beds on its periphery, and Hanover Square (HAN, 51.5139 °N; -0.1438 °W) which has a mixture of grass lawns, flower beds and shrubberies.

Sites were selected to enable analysis of spatial patterns within the gardens. These included locations under canopy and limited canopy cover to assess the impact of shading on evaporation and interception/drip flow from the canopy and the structure of the soil (i.e. loose or compact). Grass locations were also chosen as this is typically the largest fraction of vegetated surfaces found in urban parks, recreational fields and gardens from analysis of the GIS dataset for the CAZ. Areas with and without irrigation have been monitored (in EMB, no irrigation in TEM). At JUB irrigation of the grass areas occurs at night but the spatial extent of watering and the amount of water distributed remains unclear.

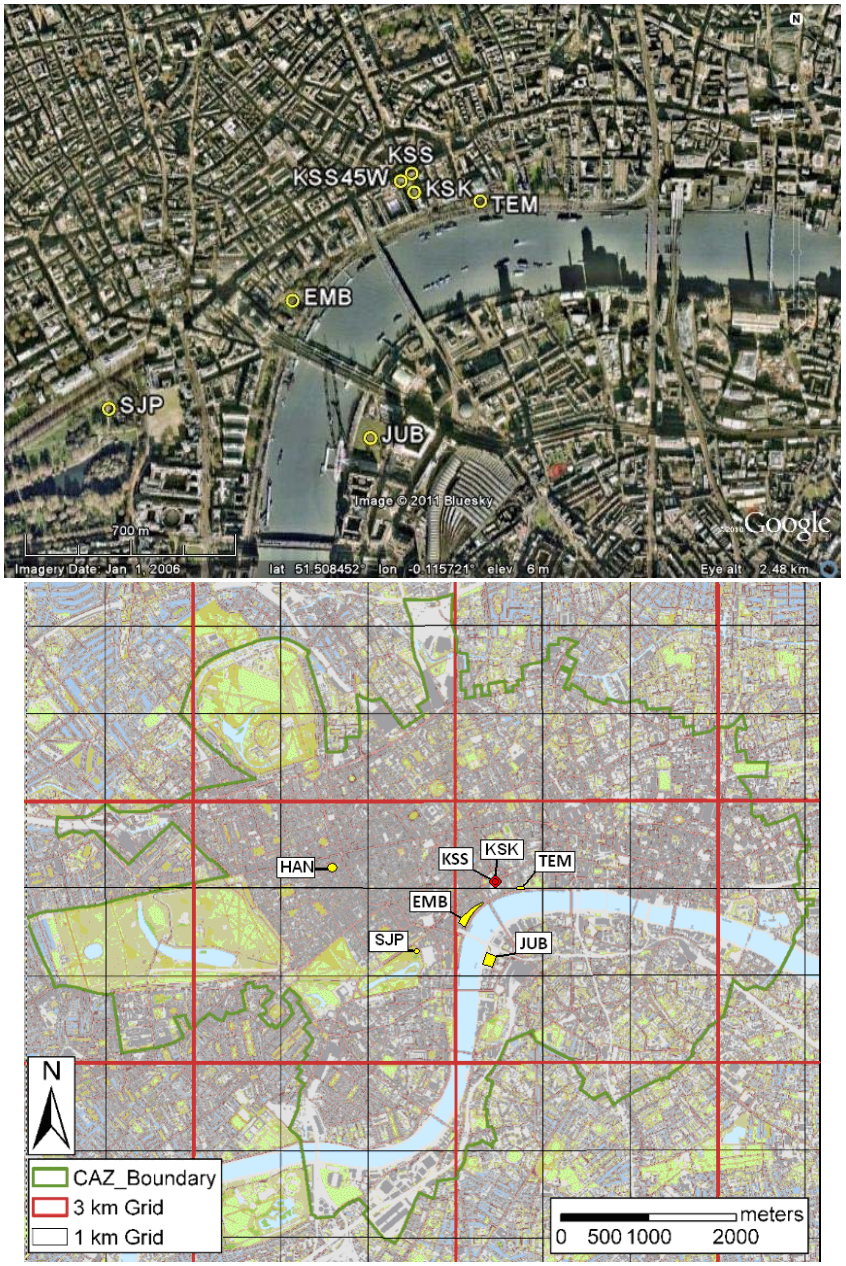

Figure 50. Location of precipitation sites and soil moisture sites (a) on Google Earth imagery (2011) relative to the Central Activity Zone with a 1 km and 3 km grid shown. Location of towers (KSS and KSK), soil moisture measurement sites (TEM, EMB, JUB and HAN) and St. James's Park meteorological enclosure are indicated.

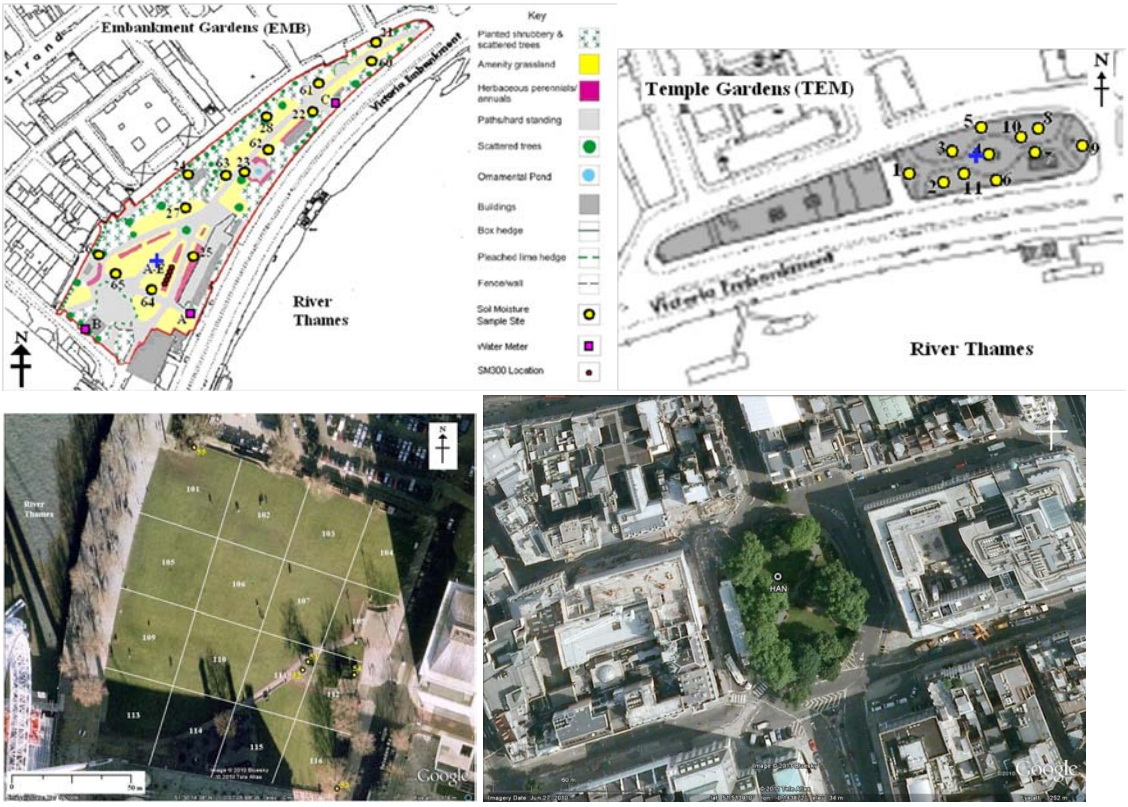

Figure 51 Location of soil moisture measurement and phenology photographs (blue plus). Maps not to scale. (top) EMB (middle Left) TEM (middle right) JUB (bottom) HAN. Adapted from Westminster City Council (2008), and Google Earth (2010) image (Picture taken December 2006).

3.8.2 Soil Moisture Measurement Methods [Authors: Young & Grimmond; Contributors: Castillo, Lindberg, Sae-Jung, Smith]

Soil moisture is measured using time domain reflectometry (TDR) and gravimetric methods.

Two types of TDR sensors (Delta-T 1998; 1999 & 2010)[109] have been used:

a) ML2x (and an earlier version ML2 prior to ML2x breaking)
b) SM300 which also measures soil temperature using the body temperature of the sensor.

TDR sensors observe the volumetric soil moisture using an electric field applied across an array of metallic prongs (4 - ML2x/ML2, 2 - SM300). The dielectric of water is much larger than that of air and soil the dielectric constant of the array is highly dependent on water content (Delta-T 1999).

Initially measurements were weekly with the ML2x probe at 45 locations across the three sites. This was reduced to 33 locations when the ML2x probe broke (2010/245). This sensor was replaced with a Theta Probe ML2 (Delta T 1998), an earlier version of the ML2x that has very similar response

[109] Delta-T 1998 *Theta probe soil moisture sensor: type ML2 user manual ML2-UM-1.* Delta-T Devices Ltd.
Delta-T 1999 *Theta probe soil moisture sensor: type ML2x user manual ML2x-UM-1.2.1.* Delta-T Devices Ltd.
Delta-T 2010 *User manual for SM300 soil moisture sensor – SM300-UM-1.1.* Delta-T Devices Ltd, Cambridge, UK.

characteristics with a smaller sample volume and lower overall accuracy (Table 21).

From 2010/211 soil moisture and temperature were sampled every 30 min from buried SM300 probes in EMB (Figure 48 red dots). Initially the sensors were deployed in pairs with 0.3 m between each probe at 0.14 - 0.17 m below the surface in pits ~ 1.5 m apart. A number of sensors replaced/removed at various times due to apparent sensor trouble.

Gravimetric samples were taken from bare soil sites after ML2x theta probe measurements and in the SM300 pits for soil specific calibration purposes and comparison of observed volumetric soil moisture. Samples were collected in 2010 on DOYs 211, 265, 286, 300, 307, 314, 316 and 327 at TEM, EMB and JUB using a metal sample ring (volume = 2.82 x 10^{-5} m^3) pushed into the ground by hand (when possible) or rubber mallet.

While taking gravimetric samples and installing the SM300 sensors, the soil contained a large amount of building material including pieces of chalk and red brick. The presence of such material can impact on the magnitude of error in estimates of gravimetric soil moisture, bulk density, organic content and SM300 soil moisture measurements especially if located directly in the sampling volume, this needs to be taken into account when analysing results.

The **bulk density** was calculated when core samples were taken. In theory the bulk density of a particular soil sampling location should be the same irrespective of the sample moisture, however due to differences in the exact location of where the sample was taken (i.e. unable to extract the same soil), measurement errors in the lab (e.g. weighing, transferring samples between containers) and compaction while taking the sample due to forcing the sample core using a mallet, leads to variation in observed densities (Christen et al. 2010[110]).

Organic content, f_{ORG}, (expressed as a % of total soil dry mass) of the original was determined for locations where soil samples were taken to look at its impact on observed soil moisture using the loss on ignition method (Rowell 1994[111]). Organic content was calculated from the material collected for gravimetric samples taken on DOYs 265, 286, 300 and 315 at both the ML2x and SM300 locations.

[110] Christen A, Crawford B, Liss K, Siemens C. 2010 Soil properties at the Vancouver EPiCC experimental sites. *Environmental Protection in Canadian Cities Technical Report No. 2*
http://www.geog.ubc.ca/~epicc/reports/Vancouver-EPiCC-Tech-Report-2.pdf
[111] Rowell DL 1994 *Soil science methods & applications.* Longman, Harlow, UK. 350pp

Table 21 Technical specifications of the TDR sensors (Delta-T 1999, Delta-T 1998 & Delta-T 2010) for measuring volumetric soil moisture (θ_V)

	ML2x	ML2	SM300
Measured variables	θ_V	θ_V	θ_V, Temperature, *T* (°C)
θ_V accuracy range	0.05 - 0.6 m^3 m^{-3}	0.05 - 0.6 m^3 m^{-3}	0.0 - 0.5 m^3 m^{-3}
θ_V accuracy	± 0.01 m^3 m^{-3} (0 - 40°C)[1] ± 0.02 m^3 m^{-3} (40 - 70°C)[1] ± 0.05 m^3 m^{-3} (0 - 70°C)[2]	± 0.02 m^3 m^{-3} (0 - 40°C)[1] ± 0.05 m^3 m^{-3} (0 - 70°C)[2]	± 0.025 m^3 m^{-3} (0 - 60°C)
T range	-	-	5.8 kΩ to 28 kΩ (0 - 40°C)
T accuracy	-	-	± 0.5°C (0 - 40°C)
T cable error	-	-	Negligible for GP1 & DL6
Soil Salinity Errors	0.0 - 250 mS m^{-1}, < -1x10^{-4} m^3 m^{-3} change per mS m^{-1}; 250 - 2000 mS m^{-1}, no significant change	0.0 - 100 mS m^{-1}	50 -1000 mS m^{-1} & 0 - 0.4 m^3 m^{-3}, ≤ 0.035 m^3 m^{-3}
Sampling Volume	7.54 x 10^{-5} m^3 (4 cm D, 6 cm L, >95% influence)	3.0 x 10^{-5} m3 (2.5 cm D, 6 cm L, 90% influence)	2.12x10^{-4} m^3 (7 cm D, 5.5 cm D)[3]
D-diamter, L length			
Stabilisation time	1 - 5 s from power up	1 - 5 s from power up	0.5 -1 s (optimal)

[1] After soil specific calibration. [2] Using supplied soil calibration, in all 'normal' soils. [3] % influence not stated in manual θ_V units: (m^3 m^{-3} or %vol)

3.8.3 **Soil Characteristics: Results** [Author: Young & Grimmond]

From the soil organic content (SOC) sampling (by loss of ignition) the mean (± 1 standard deviation) organic content (% of total oven dried soil) are 13.3 ± 4.5 % (N=53) for TEM; 20.0±7.6 % (N=21) % for EMB; EMB SM300 (pits A to C) 14.9 ± 0.6 % (N = 60) (JUB, HAN not determined) (Table 22). Within TEM the maximum average SOC observed was at location 2 (22.6 ± 1.7 %) and minimum at location 5 (9.5 ± 0.9 %). In EMB the mean range was between 11.1 ± 0.4 % (location 28) and 33.3± 0.3 % (location 26).

Given the mean conditions EMB is classed as organic (f_{org} > 15%) and the TEM and EMB SM300 soils are classed between mineral and organic (as averages 3% > f_{org} > 15 %) (Rowell 1994[112]). Christen *et al.* (2010[113]) observations froms 8 properties lawns in two suburban areas obtained: surface SOC of 5 % and 12.5 %. The latter is comparable to observed in TEM and EMB SM300 locations. The London values may be related to the use of mulch on the beds applied seasonally.

Comparison of in situ volumetric soil moisture (gravimetric and theta probe) with the SOC has a positive correlation (Figure 49) (R^2 = 0.447): $\theta_{Vg} = 0.664 f_{org} + 23.6$

Removal of the possible outlier point resulted in minimal change in the gradient and intercept so it was concluded this point was not an outlier. Comparison of organic matter content and ML2x/ML2 soil moisture, taken at the time of sampling, shows no clear pattern ($R^{2=}$ 0.016).

[112] Rowell DL 1994 *Soil science methods & applications.* Longman, Harlow, UK. 350pp

[113] Christen A, Crawford B, Liss K, Siemens C. 2010 Soil properties at the Vancouver EPiCC experimental sites. *Environmental Protection in Canadian Cities Technical Report No. 2*

Bulk densities (ρ_b) (Table 22) at TEM from 2 samples at each location (N = 18) is 1.057± 0.195 Mg m^{-3} and at EMB (N = 14, excluding location 25) had a lower mean of 0.771±0.216 Mg m^{-3}. This may relate to the higher average SOC observed in EMB. The mean ρ_b at the five SM300 EMB pits (1.124± 0.176 Mg m^{-3}) is larger than at TEM and the other EMB sites because of the depths the samples were taken (SM300 pits: surface to 0.2 m; rest: surface to 0.05 m). There is greater variability in ρ_b (see pit specific standard deviations), as expected, due to variation of SOC with height (as highlighted in Table 3 of Christen et al. 2010). Bulk density values at all sites are similar in magnitude to those observed by Christen et al. (2010). The typical range for a cultivated soil of medium to heavy texture is 0.8 to 1.4 Mg m^{-3} (Rowell 1994). The negative relation between ρ_b and SOC observations (Figure 50) is strongly correlated (R^2 = 0.806, $f_{org} = -18.60\rho_B + 32.64$). This explains the mean ρ_b observed in EMB are lower than the other sites (Table 22).

At all site soil moisture (θ_V) responded to precipitation and irrigation (Figure 51a,b,c,d). For TEM the θ_V range observed (3.0 %, location 8, 2010/193 to 54.3 % location 2, 2010/300) is similar in timing to the ensemble daily median range (9.0 % 2010/193 to 42.0 % 2010/302). The mean inter-quartile range (IQR) was 5.9% (range 10.7 to 2.4 %). At EMB (Figure 54b) the θ_V had a slight decrease in the first 30 days because irrigation was stopped. There is no clear trend in θ_V at JUB (Figure 54c, d) throughout the period with large variability at all locations, making it difficult to identify a clear response to precipitation events. This large variability is shown by an average IQR of 15.3 % (range: 22.8 to 6.1 %). For the non-grass locations (51-55, not included in the grid measurements) there are two trends apparent despite large variability (average IQR = 12.0 %): locations 54 and 55 have an increasing θ_V, while 51, 52 and 53 have θ_V reasonably constant if not slightly declining with time (Figure 54c).The compacted nature of some parts of the grass at JUB making it impossible to insert the sensor to take a reading.

The overall trends at TEM and EMB are very similar but slightly more pronounced in TEM due to lack of irrigation. The impact of irrigation at EMB is seen in the higher θ_V, but this is limited to the start of the monitoring period. The trend is as expected in London with the increased precipitation in the transition from summer to autumn and reduced evaporation from the surface due to a shortening day length.

Field testing of the SM300 sensors in an EMB flower bed (Figure 55) show an increasing θ_V with a large degree of variability related to periods of dry and wet weather. Surprisingly there is no response to precipitation during the first 11 days. On removal of the sensors different soil conditions were observed with some showing a higher rate of clay and others stones and debris within the sampling volume. A second period of low/no response to precipitation occurred 2010/266-273. On a number of days (e.g. 231, 245 and 246) where no rainfall is apparent in the St. James's Park time series there is an increase in observed soil moisture which is either a result of manual irrigation or missing rain data.

As the sensors were 0.3 m apart the large differences (up to 18 %) are not fully explained by measurement and accuracy error (10%). Despite constant contact with the manufacturer and return of

sensors (A01363/A01364 and A01358/A01359) no satisfactory reason for the difference has been identified. Therefore the sensors are performing poorly or there are very large differences despite the small distances. Therefore the observed magnitudes should be potentially used with caution, whereas the trends may be used with more confidence.

The observed soil temperature within the flower bed (Figure 53) has an overall gradual decrease in temperature (19 to 11 °C) with the expected diurnal pattern evident. Additional variation at longer time intervals most likely are related to synoptic conditions. The temperature difference between sensors is small (< 1 °C). At the end of the period on two nights the soil temperature reached a low of 7 °C which corresponds with the first two air frosts of the year.

A greater number (N = 33) of gravimetric samples were taken at the SM300 locations in EMB (Figure 53). The range of $\theta_{V,grav}$ are from 26.3± 5.0 % (Pit D) to 36.4± 10.4 % (Pit C) which highlights the degree of heterogeneity in soil moisture within a small area. The mean value for all pits was 30.2 ± 3.9 % which is within one standard deviation of the EMB ML2x/ML2 location average. Due to the relatively low amount of samples taken at the other locations further samples need to be taken to test the significance of the relatively close values.

Comparison of $\theta_{V,grav}$ and θ_V (ML2x/ML2) within TEM, EMB and JUB (Figure 54) show a strong positive correlation (R = 0.808). The θ_V is generally higher than $\theta_{V,grav}$. Slight differences in observed values may be explained by sampling errors. The strength of the correlation provides justification for using the soil moisture derived using gravimetric samples to aid calculation of soil specific calibration constants with care taken to consider the errors in both methods.

The soil moisture and temperature data are available in KUMA (section 3.5). The winter time data are from 2011 for two levels at EMB and HAN (Figure 55) show the slow warming occurring. There is the expected greater variation at the shallower than the deeper sensor.

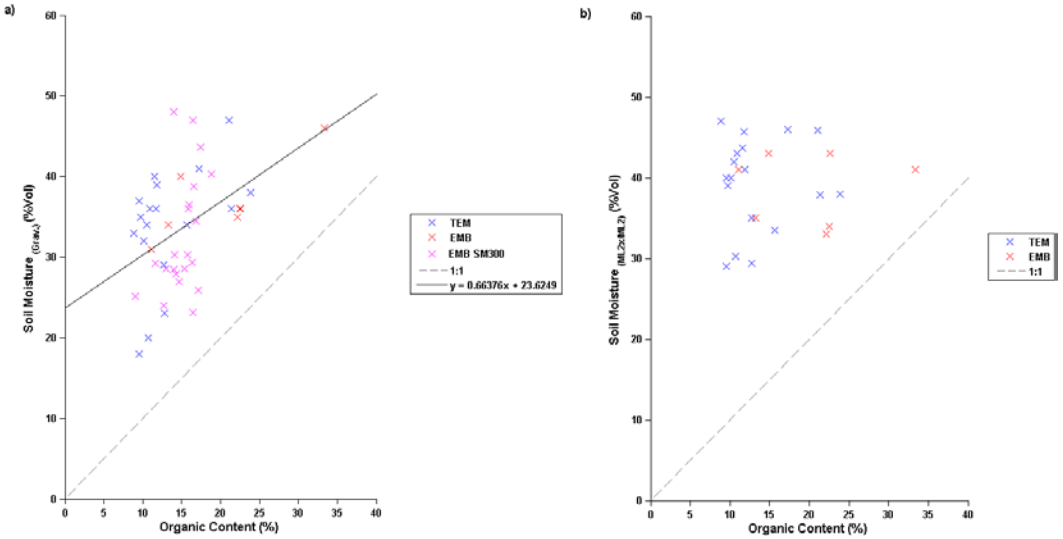

Figure 52: Organic content determined by loss on ignition versus volumetric soil moisture determined from a) gravimetric samples b) theta probe ML2x/ML2.

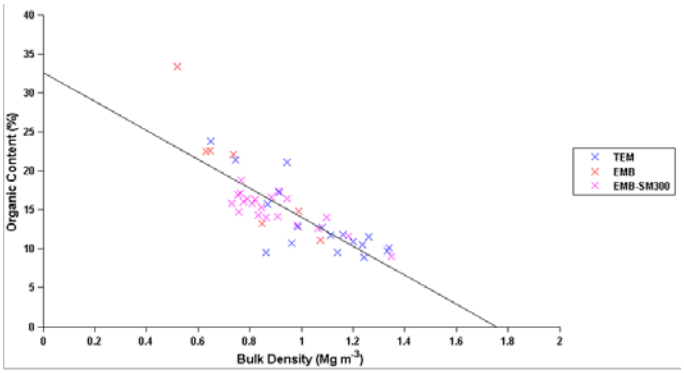

Figure 53 Bulk density and organic content determined from gravimetric samples at TEM, EMB and EMB-SM300 pits.

Table 22: Soil sampling results from TEM, EMB, JUB and EMB SM300 locations.

	Bulk Density ($Mg\ m^{-3}$)			Organic Content (% dry soil)			Soil Moisture (%vol)		
Location	Samples	Mean	Std Dev	Samples	Mean	Std Dev	Samples	Mean	Std Dev
TEM									
1	2	1.020	0.083	6	11.7	1.4	2	24.5	6.4
2	2	0.696	0.068	6	22.6	1.7	2	37.0	1.4
3	2	1.285	0.067	6	10.1	0.6	2	34.5	0.7
4	2	0.929	0.019	6	19.2	2.7	2	44.0	4.2
5	2	1.292	0.068	6	9.5	0.9	2	32.5	0.7
6	2	0.924	0.089	6	11.2	2.3	2	20.5	3.5
7	2	1.200	0.085	5	10.5	1.4	2	38.5	2.1
8	2	1.015	0.206	6	13.8	2.7	2	36.5	3.5
9	2	1.156	0.063	6	11.3	0.6	2	36.0	0
EMB									
21	2	0.622	0.161	3	22.1	0.5	2	30.0	7.1
22	2	1.028	0.052	3	14.9	0.1	2	35.0	7.1
23	2	0.657	0.017	3	22.6	1.4	2	33.0	4.2
24	2	0.842	0.010	3	13.2	0.5	2	33.0	1.4
25	1	0.680	-	0	-	-	1	22.0	-
26	2	0.514	0.008	3	33.3	0.3	2	37.0	12.7
27	2	0.657	0.036	3	22.5	0.3	2	35.0	1.4
28	2	1.079	0.008	3	11.1	0.4	2	29.0	2.8
JUB									
51	1	0.884	-	0	-	-	1	21.0	-
52	1	0.780	-	0	-	-	1	18.0	-
53	1	0.960	-	0	-	-	1	17.0	-
54	1	0.993	-	0	-	-	1	26.0	-
55	1	1.02	-	0	-	-	1	29.0	-
SM300: EMB									
A	7	0.914	0.146	17	14.2	0.8	7	27.9	1.8
B	15	0.960	0.251	37	15.4	2.7	15	31.0	6.8
C	5	1.246	0.221	6	15.2	1.7	5	36.4	10.4
D	3	1.193	0.210	0	-	-	3	26.3	5.0
E	3	1.306	0.263	0	-	-	3	29.2	4.5

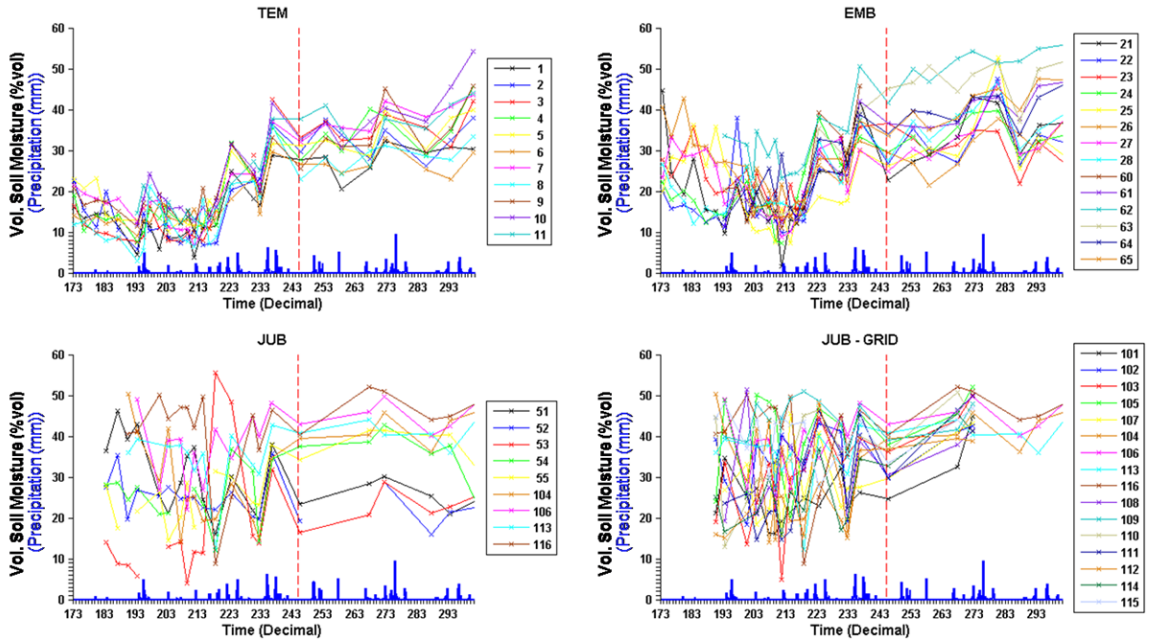

Figure 54: Soil moisture in 2010 (ML2x and ML2) a) TEM, b) EMB, c) JUB (continuous locations) and d) JUB grid. Vertical dashed red line represents the change over from ML2x to ML2

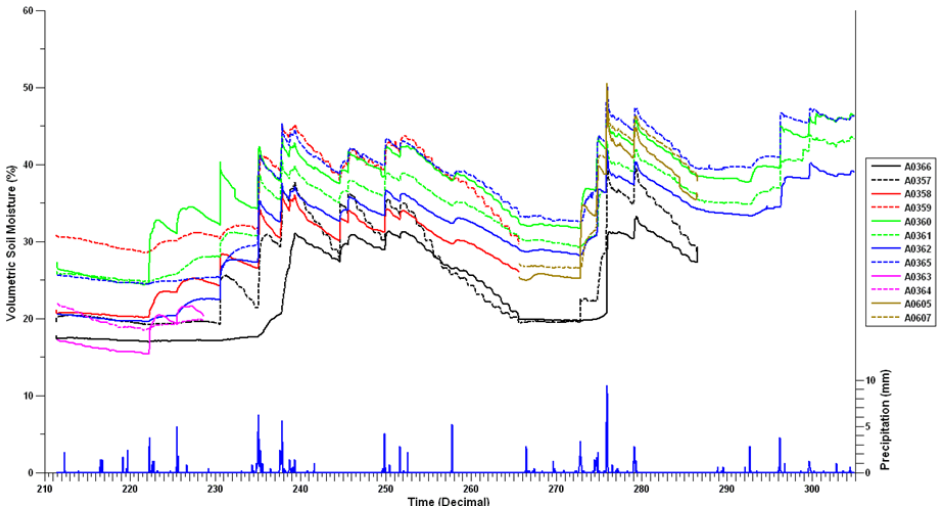

Figure 55: Volumetric soil moisture in 2010 at EMB (SM300 sensors).

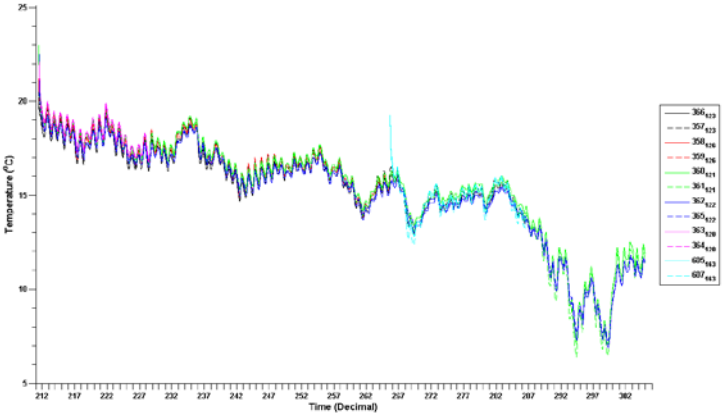

Figure 56: Soil temperature in 2010 in EMB (SM300 sensors).

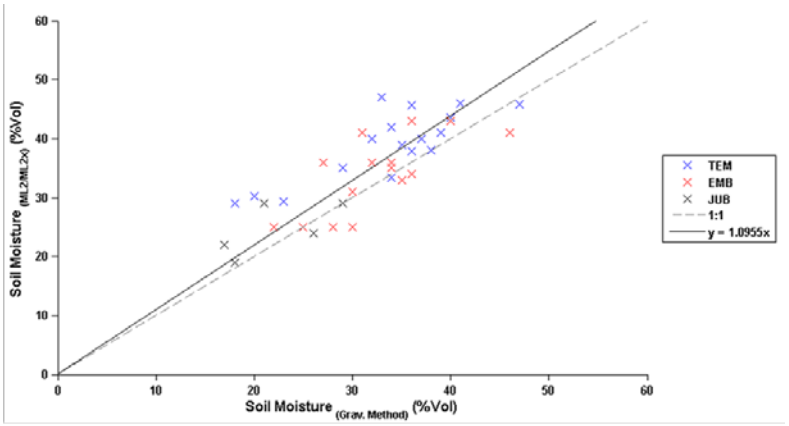

Figure 57 Comparison of soil moisture determined by gravimetric and theta probe sampling at TEM, EMB and JUB.

Conventions=CF-1.0
Institution=KCL
City=London
Site=EMB
Title=Soil.Moisture.& Temperature
Data.level=L0
QAQC=none
temporal.resolution=30 min
base.resolution=30 min
spatial.info=KUMA
serial.number=AA0011335676
datalogger=GP1-11.123
Comment=NA
Source=observations
CDO=Climate Data Operators version 1.5.0 (http://code.zmaw.de/projects/cdo)

lon=-0.1217
lat=51.5081
heights=-0.05;-0.05;-0.11

units=Celsius
_FillValue=-999
longname=Soil.Temperature
linked.variables=NA
category=Soil.Moisture

Capture Rate 100.0 %

Start Plot Date 09-Feb-2011 16:30:00
End Plot Date 08-Apr-2011 14:00:00
NO REPEATED DATA POINTS

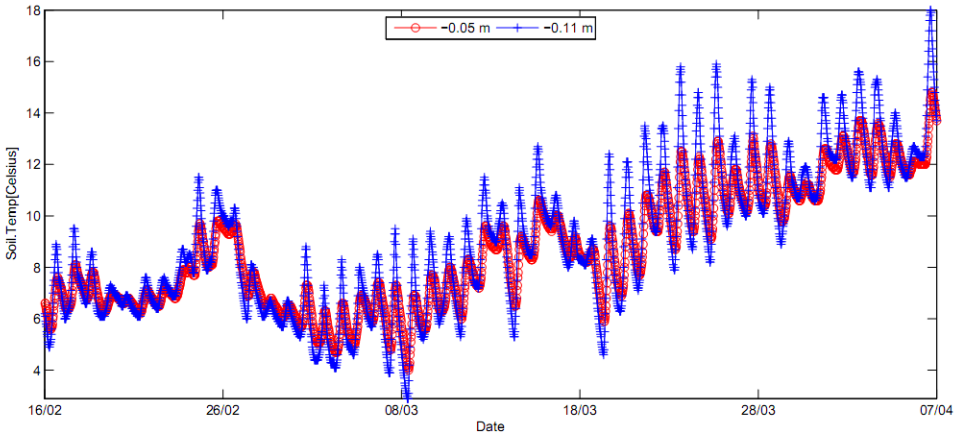

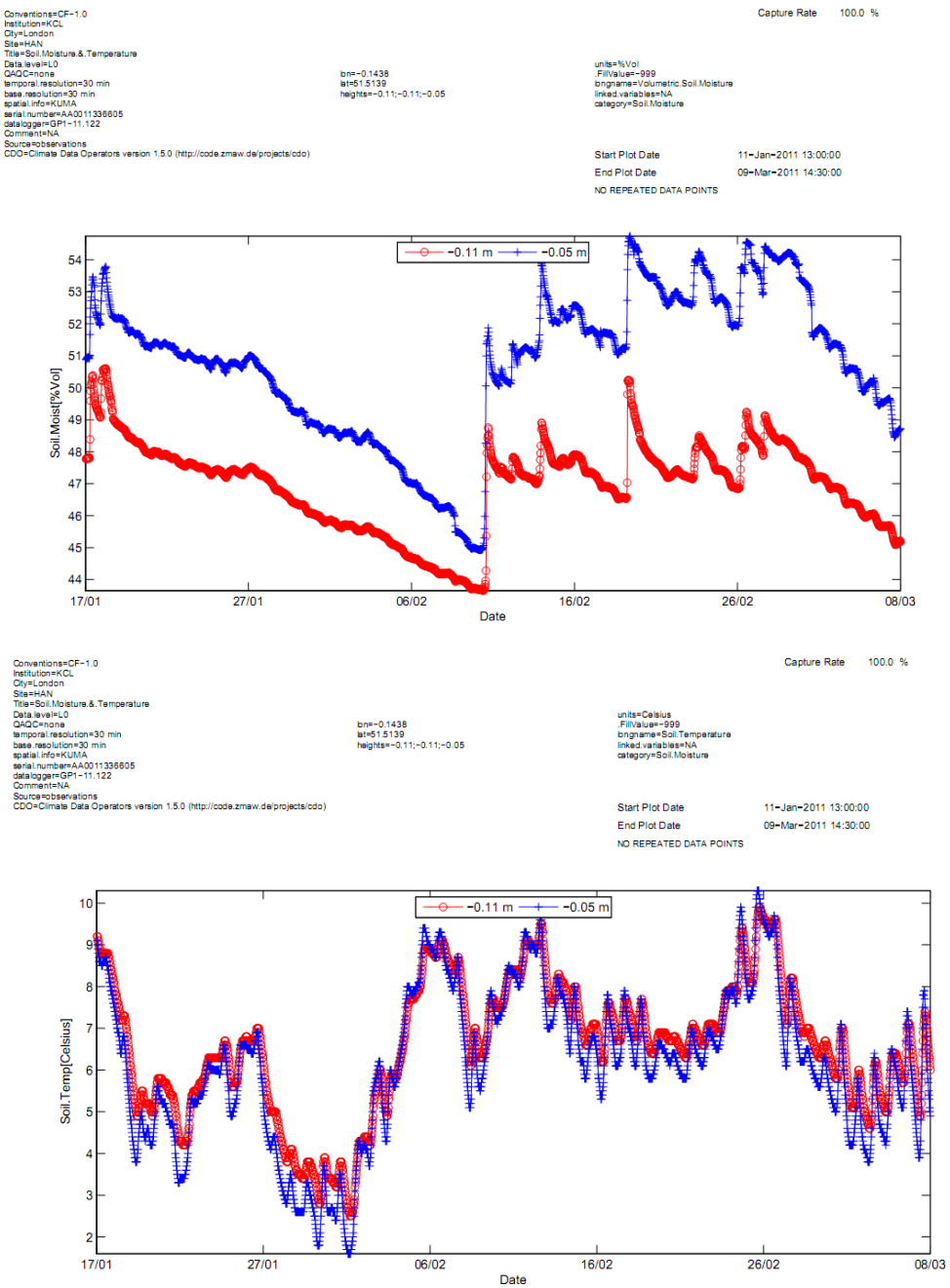

Figure 58: Soil moisture (b) and temperature (a, c) data observations at HAN (b,c) and EMB (a) for the early part of 2011 at two levels.

3.8.4 **Phenology observations: Methods and Result** [Contributors: Young, Sae-Young, Grimmond]

Digital photographs were taken regularly (approximately weekly) at the sites indicated in Figure 48 (TEM and EMB) to record phenological changes in leaf cover. The first photographs were taken 2010/201. In addition webcam data are being regularly captured to allow additional assessment of the state of vegetation. Clear changes in phenology can be observed (Figure 56) from the photographs taken.

Figure 59: Examples of photographs taken on a regular basis

3.8.5 **External Water Use** [Authors: Young, Grimmond]

Three water meters were monitored weekly in EMB (Figure 48) between 2010/218 and 2010/309 to investigate external water use in the gardens. The total water use for two meters (A and C) indicate significant water use throughout the period however is not all externally used (Personal communication members of garden staff). The two step changes in use (meter A) are likely due to watering activities throughout the gardens (not specifically the bed location of the SM300 sensors). Water meter C showed a constant increase throughout the period suggesting there may be a problem. Water meter B (located behind the bandstand) shows little change throughout the period and was not used for watering activities.

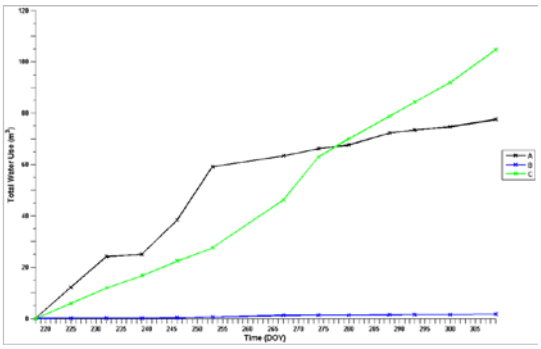

Figure 60: Total water use (with time) in 2010 from weekly observations of three water meters in EMB.

3.9 **Intensive Micrometeorology observations sites** [Authors: Kotthaus, Grimmond]

Intensive meteorological observations are being carried out at the Strand Campus of King's College London (KCL, 51°30' N, 0°7' W). The site is located in a central business district at the northern bank of river Thames (Figure 47). The site is a zone 5 Urban Climate Zone (Figure 27) classification or Old Core/Modern Core (Figure 28) Local Climate Zone. The area surrounding KCL is dominated by office buildings and commercial use, with a daytime population density (88000 people km^{-2}) that significantly exceeds the number of residents (1991 people km^{-2} in a 500 m radius, ONS 2001[114]). Within 500 m radius of the site the dominate land cover are buildings (36.6 %) and other impervious surfaces (35.8 %). Only 6.6 % of the area is covered by vegetation and the remaining area is open water (River Thames).

Two meteorological towers within close vicinity of each other have been installed, termed KSK and KSS (Table 23). KSK is located approximately 60 m south of KSS (Figure 58). Table 24 provides an overview of the measurements taken and the instruments used.

Table 23 Towers at KCL.

Site:	KSK	KSS
Site Name	King's College London/ **S**trand Campus/King's Building	King's College London/ Strand Campus/Strand Building

[114] Office of National Statistics 2001

Tower type	Clark Mast CSQT9/HP Telescoping tube	Aluma tower T-35H Telescoping triangular lattice
Height of eddy covariance system (m agl)	48.1	59.6

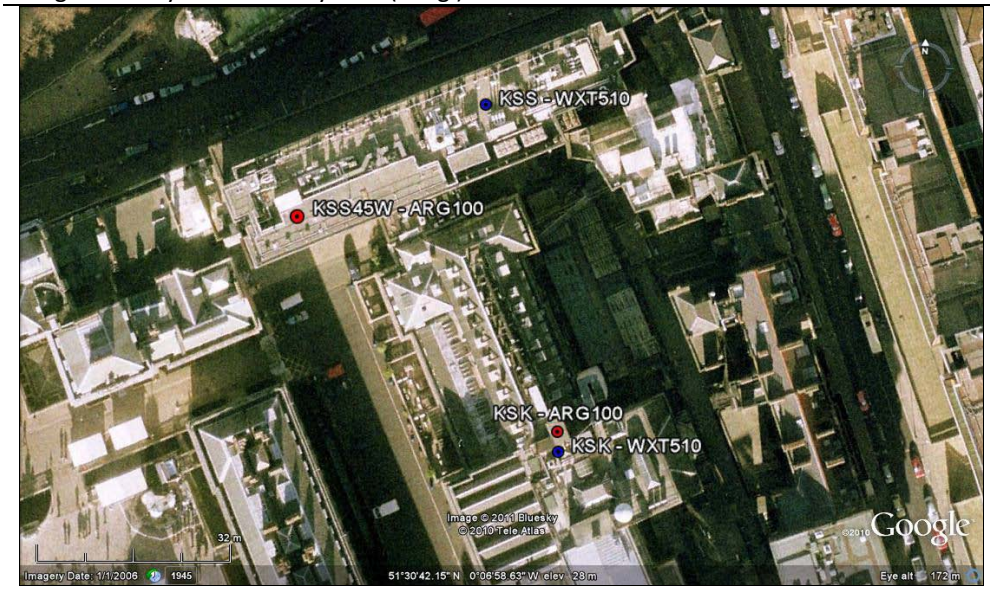

Figure 61 Location of instruments are at the KCL Strand site (KS). KSS45W is 45 m southwest of the KSS tower. Image: Google (2011).

Table 24 Instruments installed at the KCL sites and the time of operation.

Category	**Instrument**	**Model**	**Manufacturer**	**Site**	**years of operation**
Weather	Automatic Weather Station	WXT510	Vaisala	KSK	2008 - 2011
				KSS	2009 - present
		WXT520	Vaisala	KSK	2011 - present
Precipitation	Rain Gauge	ARG100	Campbell Sci.	KSK	2008 - present
				KSS45W	2009 - present
Radiation	Net Radiometer	CNR1	Kipp & Zonen	KSK	2008 - 2009
				KSS	2009 - present
		CNR4	Kipp & Zonen	KSK	2010 - present
	UVA sensor	SKU420	Skye	KSK	2008 - 2009
				KSS	2009 – present
				KSS45W	2009 - present
	UVB sensor	SKU430	Skye	KSK	2008 – 2009
				KSS	2009 – present
				KSS45W	2009 - present
	PAR sensor	SKP215	Skye	KSK	2008 - 2009
				KSS	2009 – present
				KSS45W	2009 - present
	Sunshine Pyranometer	SPN1	Delta-T	KSS45W	2010 - present
	Infrared radiometer	PIR	Eppley	KSS45W	2009 - present
	Spectral pyranometer	PSP	Eppley	KSS45W	2009 - present
Turbulence	Sonic Anemometer	CSAT3	Campbell Sci.	KSK	2008 - present
				KSS	2009 - present

	Boundary Layer Scintillometer	BLS900	Scintec	KSS45W	2010 - present
Turbulence	Large Aperture Scintillometer	LAS	Kipp & Zonen	KSS45W	2008 – 2010
				BTT	2010 - present
Gas concentration	Open Path Gas Analyser	Li-7500	Li-Cor Biosciences	KSK	2008 - 2009
				KSS	2009 - present
	Closed Path Gas Analyser	Li-840	Li-Cor Biosciences	KSK	2008 - 2009
				KSS	2009 - present
Surface Temperature	Infrared thermometer	IRT, K-Type and J-Type	Reytek	KSS	2009 - present
				KSK	2008 - present
		IRT, K-Type	Apogee	KSK15S	2010 - present
				KSK	2008 – present
Boundary Layer	Ceilometer	CL31	Vaisala	KSS45W,	2006/335 - present
				RGS	2009/085 - present
Temperature	Water temperature sensor	TG-4100	Tinytag	TLI	2010 - present
Soil Moisture	Soil moisture and temperature probe	SM300	Delta-T	HAN	2010 – present
				EMB	2010 - present
	Soil moisture probe	ML2, ML2x	Delta-T	TEM	2010 – present
				EMB	2010 - present

3.9.1 **Overview of Meteorological Conditions** [Author: Grimmond, Contributors: Castillo, de Jong, Kotthaus]

The data collected at these sites and reported here are still being subjected to final QAQC (quality assessment and quality control). Thus the analyses presented here are preliminary. Please consult authors before citing specific values. The KUMA website provides plots at each level for the data so that user can see what the conditions were, data availability and identify any issues of concern.

For most variables the means are provided by KUMA (e.g. Figure 59 for station pressure and Figure 60 for relative humidity) and standard deviations (e.g. Figure 61 for relative humidity). The later may help identify when additional QA/QC is needed. For example the standard deviation of relative humidity is generally less than 3% on a 15 min basis (Figure 61). There are a few instances when the relative humidity standard deviation is greater than 6% but none when it is greater than 10% (Table 25). This suggests that periods when standard deviation are greater than 6% should possibly be investigated to determine if the data have QC issues that need to be resolved. As this is an iterative process, if issues are identified then a lower threshold (e.g. standard deviation of 5 %) may need to be evaluated or if there is evidence that these are associated with real conditions then information about future outliers can be flagged up automatically. For example, if in the real time processing a value of greater than 10 % is observed an error email should be sent to ensure better real time data collection.

Table 25: Extreme and typical characteristics of the standard deviation of some variables observed in 2010.

Variable	15 min std.dev (max)	Typical	Data to investigate

Atmospheric Pressure	0.35 hPa	< 0.15 hPa	≥ 0.3 hPa
Relative Humidity	10 %	< 2 %	≥ 3%
Air temperature (WXT510,KSK)	2 °C	< 0.5 °C	≥ 0.6 °C
U, V component wind (WXT510,KSK)	10 m s^{-1}	<3 m s^{-1}	≥ 3.5 m s^{-1}
WS (WXT510,KSK)	8 m s^{-1}	<3 m s^{-1}	≥ 3.5 m s^{-1}
Kdn (CNR1)	450 W m^{-2}	seasonally varing	seasonally varying
Kup (CNR1)	160 W m^{-2}	< 40 W m^{-2}	≥ 45 W m^{-2}
Ldn (CNR1)	40 W m^{-2}	< 20 W m^{-2}	
Lup (CNR1)	6 W m^{-2}	< 5 W m^{-2}	
T (CNR1)	43 °C	< 1 °C	

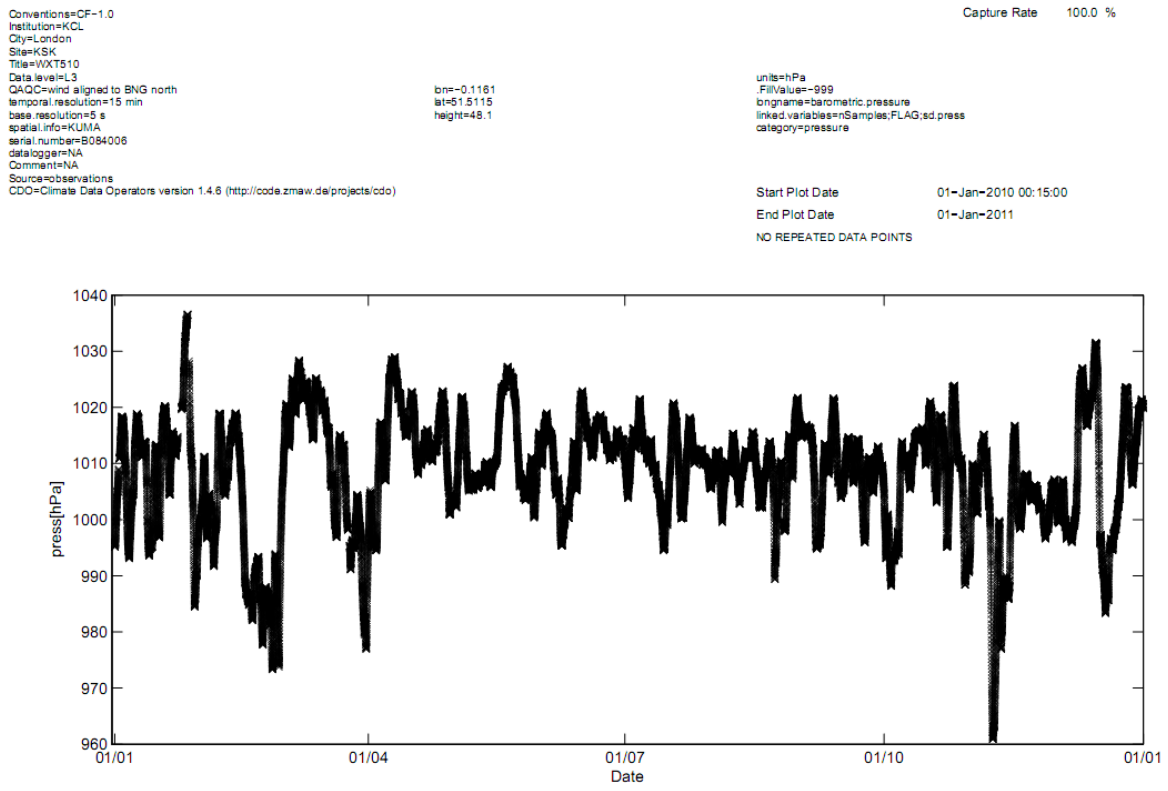

Figure 62 Station pressure (15 minute averages) collected at the KSK site measured using a WX510 (Level 3 data)

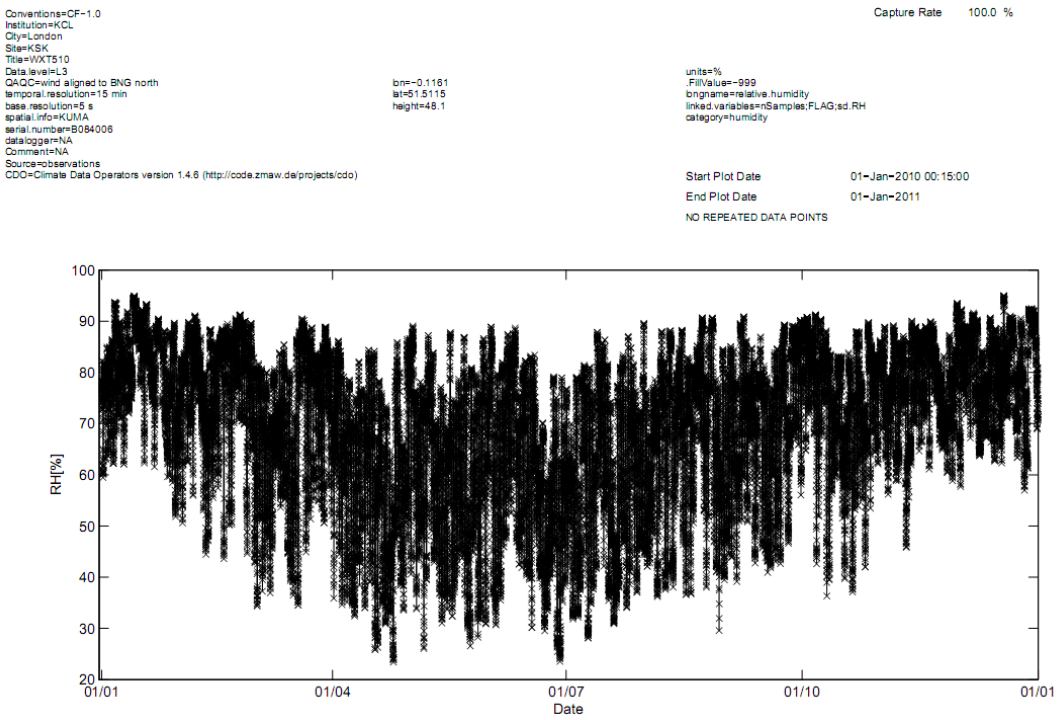

Figure 63: Relative humidity (15 minute means) measured with a WXT510 (Level 3) on KSK

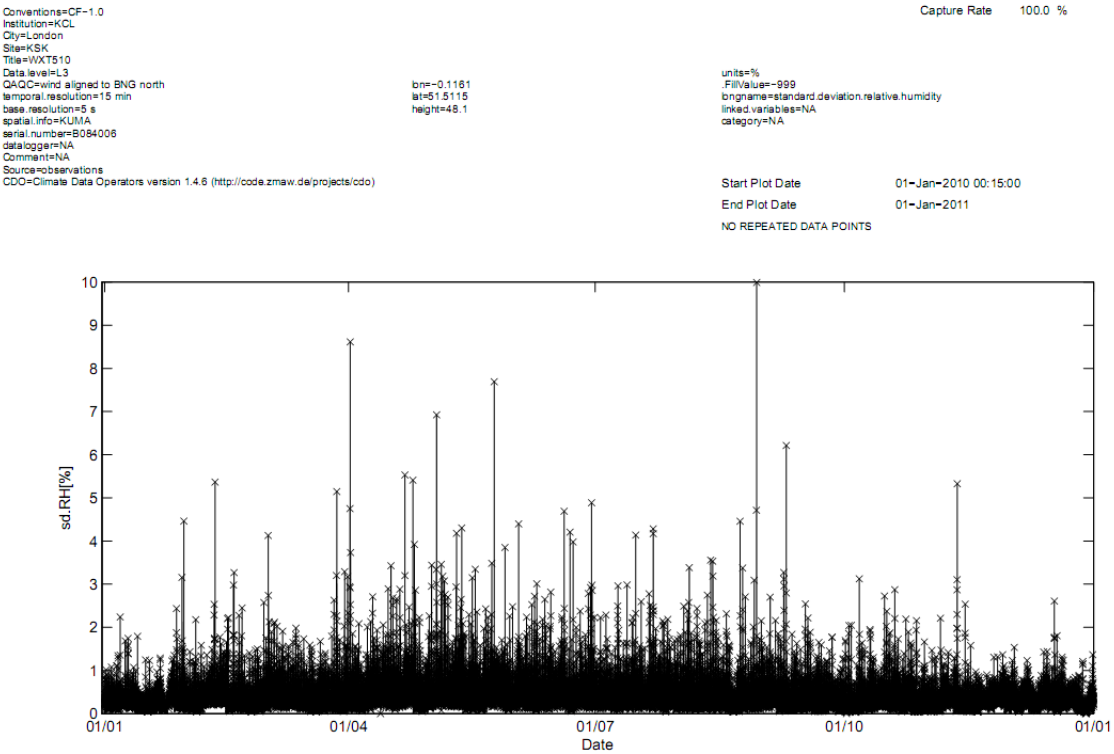

Figure 64: Standard deviation of relative humidity (15 min) for KSK WXT510.

3.9.2 **Precipitation: Methods** [Authors: Cabrita Andrade Dos Santos, Franks, Grimmond Contributors: Young, Smith]

To determine the rainfall at the KCL site rainfall and backscatter data observed at four locations are analysed. Three KCL rooftop sites (Figure 58) are complemented with the Met Office St James's Park (SJP, 51.5048 °N, 0.1311 °W) station 1.29 km WSW of KSS. The SJP data are from the MIDAS Land Surface Data (Met Office 2010) of the British Atmospheric Data Centre. The remaining data are from the KUMA (see section 3.5).

At SJP[115] the rainfall accumulation (mm) is measured with an Mk5 tipping bucket gauge with a temporal resolution of 60 min. At KCL there are four instruments that directly measure rainfall (Figure 58, Figure 62). At KSK and KSS45W, ARG100 tipping bucket gauges (Campbell Scientific Inc, Shepshed, UK) measure the amount of rainfall with a 0.2 mm resolution and an accuracy of 4 – 8 % (dependant on rainfall intensity) (Campbell Scientific 2010). The data are totalled for 15 min periods. Ideally the instrument would be placed into the ground so that the top of it is level with the ground surface, thus minimising any turbulence created around the object, with no obstruction from buildings or vegetation. This is difficult in urban environments with many tall buildings. Here they are located on the roof of KCL buildings which makes them vulnerable to the wind. The device is inspected regularly to remove any debris in the funnel or bucket.

Rainfall accumulation is also recorded with Vaisala WXT510 Weather Transmitters (Figure 63) at a temporal resolution of 10 s (resolution = 0.1 mm, accuracy 5 %) from which 15 min totals are calculated. The piezoelectric sensor acoustically detects the impact of each raindrop (RAINCAP® sensor[116]) on the smooth stainless steel surface at the top of the sensor. The signals from sources other than raindrops are eliminated through noise filtering (Vaisala 2007).

Although not directly measuring precipitation the Vaisala CL31 ceilometer (Helsinki, Finland) provides the mean aerosol backscatter. Information on the aerosol properties are retrieved from the magnitude of the return signal received from the time needed for a short pulse of light to traverse the atmosphere from the ceilometer transmitter (Vaisala 2006). The instrument (Figure 64) was located at the KSK site until 10 am 22/04/2009 it was moved to KSS45W. The ceilometer backscatter data were analysed to determine a threshold for the occurrence of precipitation. First the raw backscatter profiles were analysed to determine the mean backscatter in the lowest 500, 1000 and 1500 m. These were then compared with precipitation occurrence for the individual instruments. The rounded threshold was then used to determine the number of hours above the threshold during when none of the instruments detected rainfall.

To evaluate the performance of the WXT510 rainfall data from these instruments were compared for periods indicated in (Table 27). To maintain temporal consistency 15 minutes (minimum resolution for the ARG100) are analysed.
The analysis includes:

[115] Met Office, 2010
[116] http://www.vaisala.com/Vaisala%20Documents/Technology%20Descriptions/RAINCAP_Technology.pdf

- Comparison of precipitation accumulation based on 15 minute totals for each instrument for 2010.
- Comparison of measurements from each instrument during one rainfall event.
- Correlation by instrument for average precipitation per event. An event is defined as > 0.2 mm rainfall recorded at more than one site simultaneously, with a minimum of 60 minutes before the next event.

The difference in measurements is correlated with wind speed and wind direction and frequency distributions are presented for each instrument. All data sets contain missing values with KSS ARG100 having the lowest capture rate (95.2 %).

Table 26 Location of Precipitation stations

Site	Name	Latitude (°)	Longitude (°)
KSS	King's College London – Strand Campus – Strand Building	51.512 N	-0.11635 W
KSS45W	45 m to West of KSS	51.51133 N	-0.11608 W
KSK	King's College London – Strand Campus – King's Building	51.5114 N	-0.1161 W
SJP	St James's Park	51.5042 N	-0.12948 W

Table 27 Rainfall accumulation and mean backscatter data analysed. The start and end day and time are given for partial years. C – Indicates compete year . Int- interval in minutes available.

	Site	Int.	2007	2008	2009	2010
WTX510	KSK	15	-	275 00:15 – 366 00:00	C	C
ARG100	KSK	15	-	243 00:15– 366 00:00	C	C
WTX510	KSS	15	-	-	286 00:15–365 00:00	C
ARG100	KSS45W	15	-	-	351 00:15– 365 00:00	C
Mk5	SJP	60	C	C	C	C
Ceilometer	KSK-KSS	15	33 00:15 – 365 00:00	C	C	C
Ceilometer	KSK-KSS	60	33 01:00 – 365 00:00	C	C	C

Figure 65. ARG100 tipping bucket gauge at KSS45W site

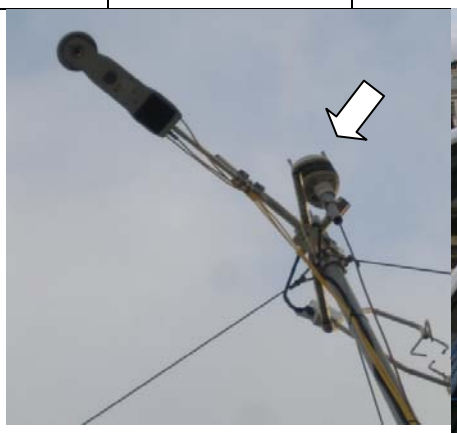

Figure 66. WXT510 Weather Transmitter located at KSK site

Figure 67. **CL31 Ceilometer A at KSS45W site**

3.9.3 **Precipitation Results** [Authors: Cabrita Andrade Dos Santos, Franks, Grimmond]

Precipitation measured by both ARG100 instruments is fairly similar throughout 2010 (Figure 65); total annual rainfall accumulation is 581.4 mm and 590.8 mm at KSK and KSS, respectively. Measurements taken with the WXT510 differ from each other and in comparison to the ARG100. Total annual accumulation from the WXT510 at KSK is 490.4 mm, and 620.6 mm at KSS (difference of 130.2 mm). Although the measurements follow the same pattern over the year the WXT510 at KSS records more rainfall than the ARG100 and the WXT510 at KSK records less.

The maximum accumulation rainfall event for both ARG100s was on 1 May 2010. During the first hour of the event the WXT510s register higher amounts of rainfall than the ARG100s (Figure 66). Subsequently the ARG100s record slightly higher values than the WXT510s for the most of the remainder of most of the event. This may be because the WXT510 is more responsive and has a higher resolution, therefore measuring rainfall exactly as it occurs and more accurately than the ARG100.

In 2010 there were 241 rainfall events. When the precipitation accumulation for each event is compared between all instruments (Figure 67, Figure 68) significant correlations are documented ($p < 0.01$). Measurements from the ARG100 instruments exhibit the highest correlation with each other (Figure 67). The lowest correlation (although still significant) is between the ARG100 and WXT510 at KSS.

Differences between ARG100 and WXT510 measurements for each event were compared to the mean wind speed and wind direction (Figure 69). No significant correlations were detected with mean wind speed and direction during each event, suggesting another factor responsible for the difference in measurements. If measurements were influenced by wind then greater differences between the ARG100 instruments would also be expected, however, this is not the case. The total accumulation measured by the ARG100s at KSK and KSS are remarkably similar and these instruments display the strongest correlation when rainfall events are compared. Thus suggesting that at this location wind induced error is either minimal, or has the same influence on both ARG100 instruments.

Frequency analysis of the 15 minute accumulation with values of zero excluded shows the datasets exhibit a leptokurtic peak and are positively skewed (Figure 70). For all instruments the mode is the same as its resolution, 0.2 mm for the ARG100 and 0.1 mm for the WXT510. The range is similar for the two ARG100 instruments, 4.6 mm and 4.7 mm (Table 28). The high values recorded by the KSS WXT510 appear to be technical errors as they appear to be recorded when there was no rainfall.

The WXT510 instruments exhibit larger variation in total accumulation for 2010 in comparison to each other and the ARG100s. Basara *et al.* (2009[117]) and Lanza *et al.* (2010[118]) have found WXT510s to overestimate precipitation. Basara *et al.* (2009) found the WXT510 to measure 26 % more precipitation than tipping buckets and weighing gauges. Whereas when compared to the RD-69 disdrometer ,

[117] Basara JB, Illston BG, Winning TE and Fiebrich CA (2009) Evaluation of Rainfall Measurements from the WXT510 Sensor for Use in the Oklahoma City Micronet. The Open Atmospheric Science Journal, 3, 39–47.

[118] Lanza LG and Vuerich E (2009) The WMO Field Intercomparison of Rain Intensity Gauges. Atmospheric Research, 94, 534–543.

Pohjola *et al. (*2008[119]) found the WXT510 to underestimate precipitation due to the instrument's inability to measure small droplets (diameter < 0.8 mm). However they found an overestimate of precipitation when droplet size is larger. The over- and underestimation suggested by previous research could explain the variation in precipitation measurements in this study; however, this would imply that the WXT510 is overestimating measurements at KSS and underestimating at KSK. Given the relatively small distance between the two sites this is unlikely.

The ARG100 is larger than the WXT510 but its shape has been developed with minimal resistance to airflow (compared with previous models) (Campbell Scientific, 2010[120]). The shape of the WXT510 may lead to increased turbulence around the object in comparison to the ARG100.

Now including the more distant SJP rain guage (to make 5 instruments), the different instruments at the different sites mostly observe the same behaviour: either all instruments or no instrument detects rainfall (Figure 71). However, there are times when a number of instruments detect rainfall while others do not. For example, when five instruments are working, 9 % of the time one instrument records rainfall while the other four do not. It appears that over 50 % of the time, the instrument that was not recording rainfall was the rain gauge from St James's Park (Figure 47) which is furthest from KCL. The non-parametric Spearman rank correlation coefficient between rainfall accumulation at the five sites (Table 29) supports that the type of instrument is more important than location. The KSK WXT510 data has a higher correlation with the KSS data from the same instrument type than with the tipping bucket gauge data at the same site. SJP often has the lowest correlation.

The backscatter data from the ceilometer is investigated to discriminate rainfall events. The distribution of ceilometer backscatter values are strongly positively skewed as high backscatter values correspond, amongst other things, to the presence of rainfall and there are comparatively fewer rainy hours. These results are consistent with those of Van der Kamp and McKendry (2010) who found relatively few high values corresponding to high concentrations of water droplets present in rain, fog and clouds and many low values corresponding to the particulate matter signals.

The backscatter threshold when precipitation occurred is given in Table 30a. The rounded threshold values (Table 30b) were used to determine the percentage of time when no instrument detected rainfall (Table 30c). The smallest percentage is found when three instruments are operating and for a mean backscatter in lowest 500 m of 124 x 10^{-6} sr^{-1} m^{-1}. Using this threshold when five instrument are operating 44.6 % had no rain (four operating instruments 23.2 %). When four instruments are operating, 6 h occur when all detect rainfall but the ceilometers backscatter is under the threshold. This represents only 0.5 % of all hours during which all the instruments detect rainfall. As the period when

[119] Pohjola H, Konkola L, Hoikkanen M and Schultz DM (2008) Adjusting radar-derived QPE with measured drop-size distributions at the surface. *In: The fifth European conference on radar meteorology and hydrology.* ERAD.

[120] Campbell Scientific Ltd. (2010) ARG100 Tipping Bucket Raingauge: User Guide. [Online] Available from: ftp://ftp.campbellsci.com/pub/csl/outgoing/uk/manuals/arg100.pdf [Accessed 21 December 2010].

there are five working instruments is relatively short (from 17/12/2009 to 01/01/2010) this has less statistical value.

Based on these results, the proposed strategy for precipitation data set is to use AR100 dataset. The ceilometer data should then be used to determine if there was rainfall when no data were recorded.

The rainfall for 2010 is shown in Figure 65 and Figure 72. Currently gaps have not been filled.

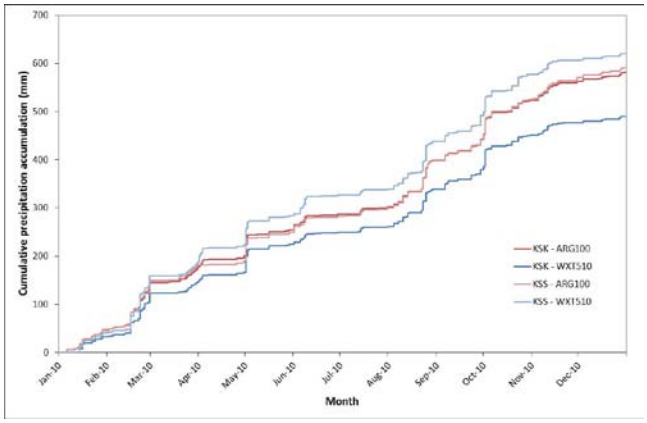

Figure 68 Cumulative precipitation accumulation measured with each instrument during 2010, based on 15 minute total accumulation data.

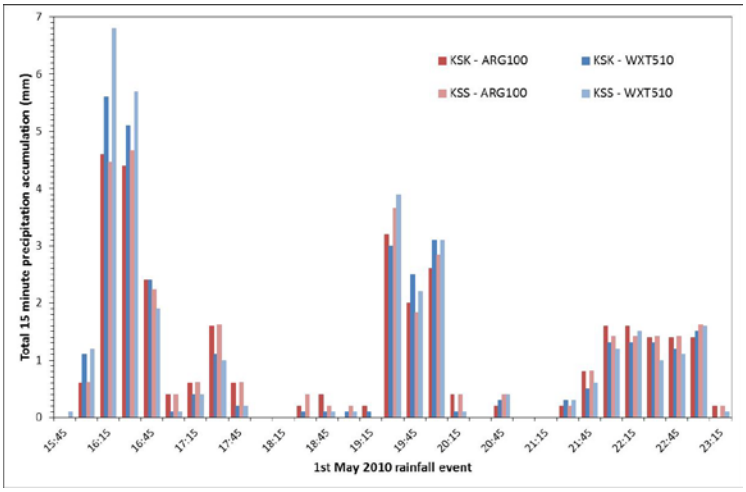

Figure 69 15 minute accumulation measured by each instrument during a rainfall event on 1st May 2010.

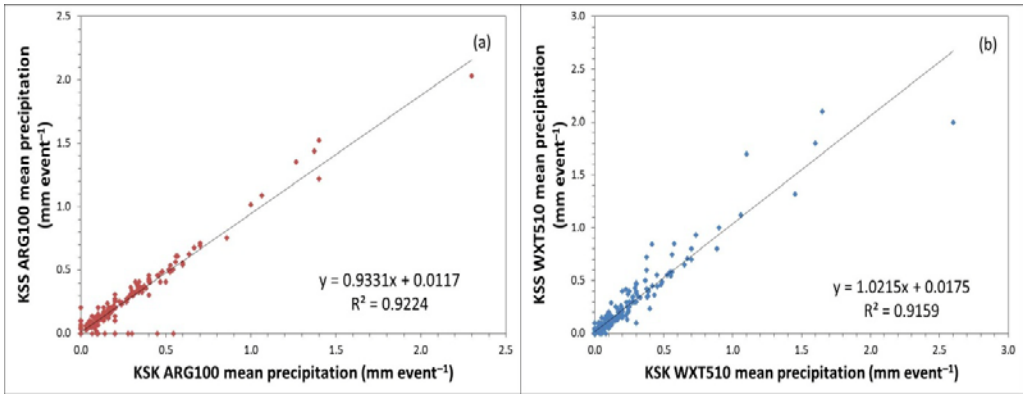

Figure 70 Correlation of instrument type, based on mean precipitation during each rainfall event in 2010 (a) KSK and KSS ARG100, (b) KSK and KSS WXT510.

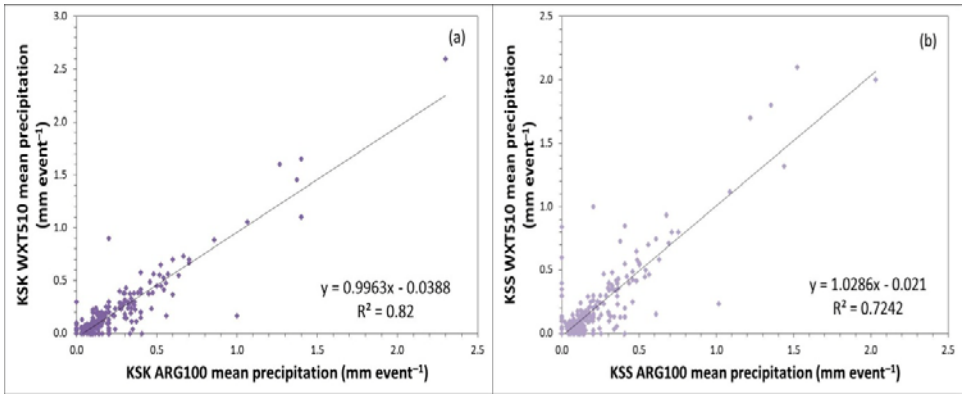

Figure 71 Correlation of instruments at each site, based on mean precipitation during each rainfall event in 2010: (a) at KSK, (b) at KSS.

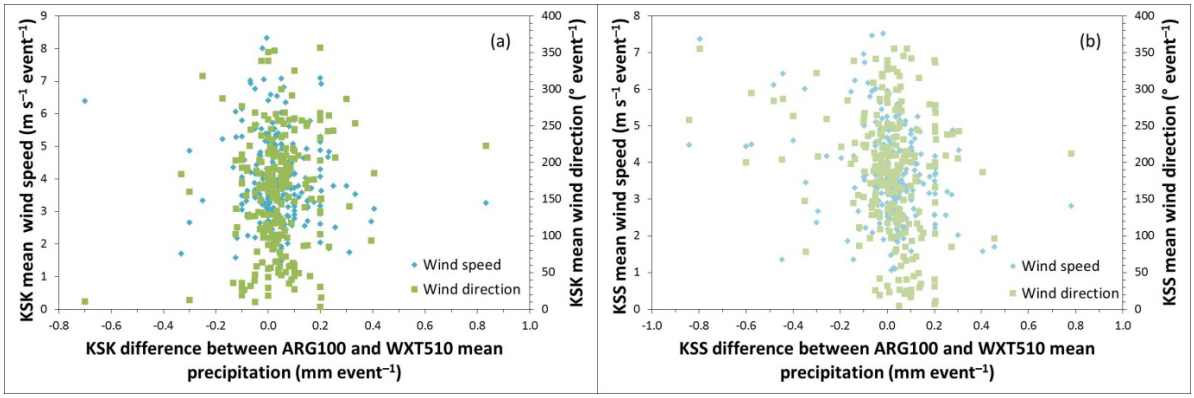

Figure 72 Correlation between the difference in instrument measurements at each site and wind speed and wind direction: (a) at KSK, (b) at KSS.

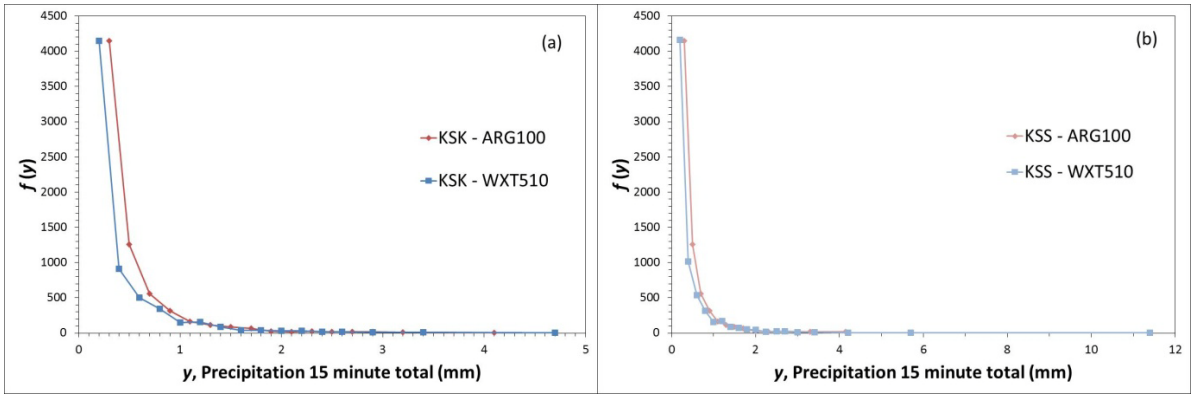

Figure 73 Noncumulative frequency size distribution of 15 minute precipitation accumulation: (a) KSK (b) KSS.

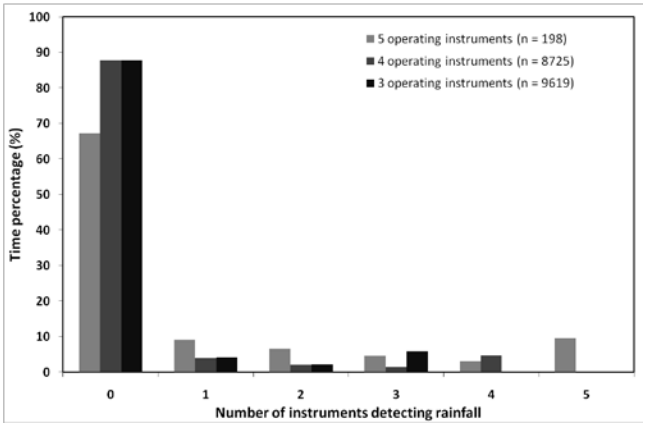

Figure 74. Percentage of time when rainfall is detected as a function of the number of instruments operational.

Table 28 Descriptive statistics based on 15 minute totals, excluding zero values for 2010.

	KSK		KSS	
	ARG100	WXT510	ARG100	WXT510
Total precipitation accumulation	581.4	490.4	590.8	620.6
Min	0.2	0.1	0.2	0.1
Max	4.6	5.6	4.7	16.1
Range	4.4	5.5	4.5	16.0
Quartile 1	0.2	0.1	0.2	0.1
Quartile 2/Median	0.2	0.2	0.2	0.2
Quartile 3	0.4	0.4	0.4	0.4
Interquartile range	0.2	0.3	0.2	0.3
Mean	0.4	0.4	0.4	0.5
Mode	0.2	0.1	0.2	0.1
Standard deviation	0.5	0.5	0.5	1.0

Table 29. Correlation matrix of rainfall accumulation data at five different study sites

	WXT510 KSK	**ARG 100 KSK**	**WXT510 KSS**	**ARG100 KSS**
ARG 100 KSK	0.70			
WXT510 KSS	0.74	0.63		
ARG100 KSS	0.61	0.83	0.61	
Mk5 SJP	0.54	0.69	0.50	0.72

Table 30: Backscatter threshold values for precipitation by depth of atmosphere analyzed relative to the surface and number of operating instruments (a) actual thresholds (b) rounded values chosen (c) the percentage of time the instruments are recording no precipitation using the thresholds given in (b)

No. Instruments operating	**Mean backscatter (x 10^{-9} sr^{-1} m^{-1}) in lowest** 500 m	1000 m	1500 m
(a) 5	146,632	383,065	837,839
4	85,473	222,374	353,437
3	124,771	246,188	446,515
(b) 5	146,000	383,000	837,000
4	85,000	222,000	353,000
3	124,000	246,000	446,000
(c) 5	42 %	43 %	36 %
4	26 %	34 %	40 %
3	23 %	36 %	42 %

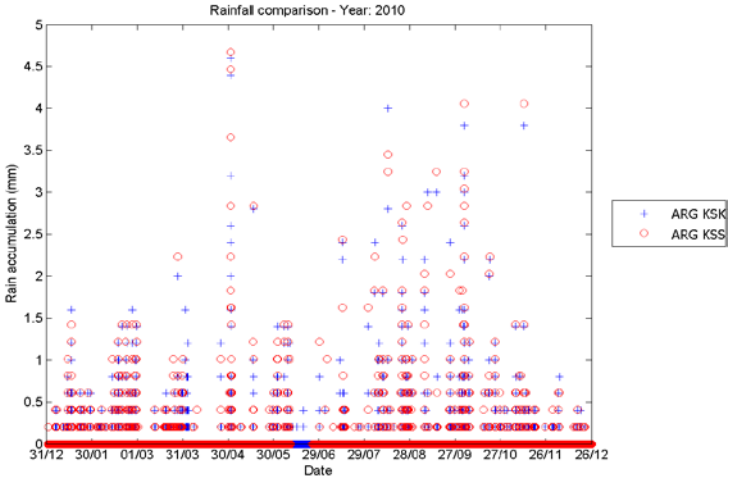

Figure 75:Rainfall recorded in 2010 at the KCL sites using ARG100 data.

3.9.4 Ceilometer data [Author: Young, Smith, Castillo & Grimmond]

The Vaisala CL31 Ceilometer (Vaisala Oyj 2004) (Figure 64) outputs high resolution (5, 10 or 20 m) vertical profiles of height normalised optical backscatter intensity of the atmosphere directly above up to a height of 7.7 km (in 10 m mode). It uses a low powered and eye safe Indium Gallium Arsenide (InGaAs) diode laser with wavelength 910 (± 10) nm which is pulsed at 10 kHz to negate the effect of Gaussian noise (Eresmaa et al. 2006). Table 31 gives the full technical specifications.

Ceilometer measurement on KSK began 2006/335 (year/day of year) with Ceilometer A (CLA) deployed at 51.5114 °N, 0.1161 °W, 39.49 m above sea level (asl). CLA remained on KSK until 2008/113 when it

was moved to KSS45W (46.63 m asl). CLA has run almost continuously. This provides a > 4 year data set of backscatter profiles and cloud height information.

Between December 2007/338 and 2008/232 a second CL31 ceilometer (CLB) was deployed on KSK close to CLA to undertake a period of inter-comparison before being located 4.2 km WSW of KSS at the Royal Geographical Society (with the Institute of British Geographers) (RGS-IBG) at Kensington Gore, London (51.502 °N, 0.175°W) on 2009/085.

The backscatter intensity data are generated every 15 s at 10 m vertical resolution from samples taken every 67 ms from 0 to 50 μs (the theoretical time taken for a reflection from 7.7 km to reach the receiver. Hourly files are transferred. Automatic emails are sent if a problem is identified allowing units to be rectified quickly (e.g. files to small, not been able to contact computer, instrument needs cleaning). The raw data files are processed using MatLab programs. At this stage no height or temporal averaging is applied.

Nightly, these data are added to KUMA (section 3.5) and plots sent to the web. Example plots from the four ceilometers are shown in Figure 73. In these the large backscatter values are associated with cloud at approximately 2000 m. The boundary layer development to the order of 500 m can be seen in the middle of the day. Close inspection between plots shows the temporal variability between sites but the similar conditions across the sites is clearly evident.

Qualitative analysis of ceilometer plots generated from data collected by CLA located on KSK and KSS45W, was undertaken to investigate the mixing layer height (MLH) climate over central London during 2008. This provides a data set for evaluating MLH determined from automatic algorithms which so far, despite showing promise, have required visual quality assurance due to the amount of false detections observed (Münkel et al. 2007[121]).Gradient and density plots were generated for 12 h periods for all available backscatter data (generated every 15 s and with 10 m resolution), with the raw data smoothed using a temporal window of 600 s and vertical averaging (and gradient calculation) window of 140 m with a moving average window in the lowest 7 profiles to account for noise. Only periods where there was no cloud or precipitation were analysed.

The qualitative analysis involved the interpretation of the MLH and multiple layers (to the nearest 10 m) by looking for a discontinuity in the backscatter density plot for each hour (where a threshold of 250 x 10^{-9} m^{-1} sr^{-1} was utilised) and then cross comparing this with the maximum gradient observed on the gradient plot. Additional information was collected on cloud cover, mean backscatter density values (using 5 points), hourly trend in the MLH/residual layer and its duration. The final observation made was to mark when near surface backscatter density values exceeded 800 x 10^{-9} m^{-1} sr^{-1} to identify periods of high air pollution. To ensure consistency and in an effort to reduce the effect of human interpretation a key was created (Figure 74) and a test period undertaken to check interpretation.

[121] Münkel et al. 2007

Table 31 Technical properties of the Vaisala CL31 Ceilometer (after Vaisala Oyj 2008).

Measurement Range	0-7700 m
Vertical Resolution	5 or 10 m
Laser	InGaAs diode
Emitted Wavelength	910 $\pm$ 10 nm
Laser Pulse Energy	1.2 μWs $\pm$ 20%
Pulse Repetition Frequency	10 kHz
Pulse Count	16384 (Single measurement cycle)
Lens Focal Length	300 mm
Effective Lens Diameter	96 mm
Field of View Divergence	0.83 mrad

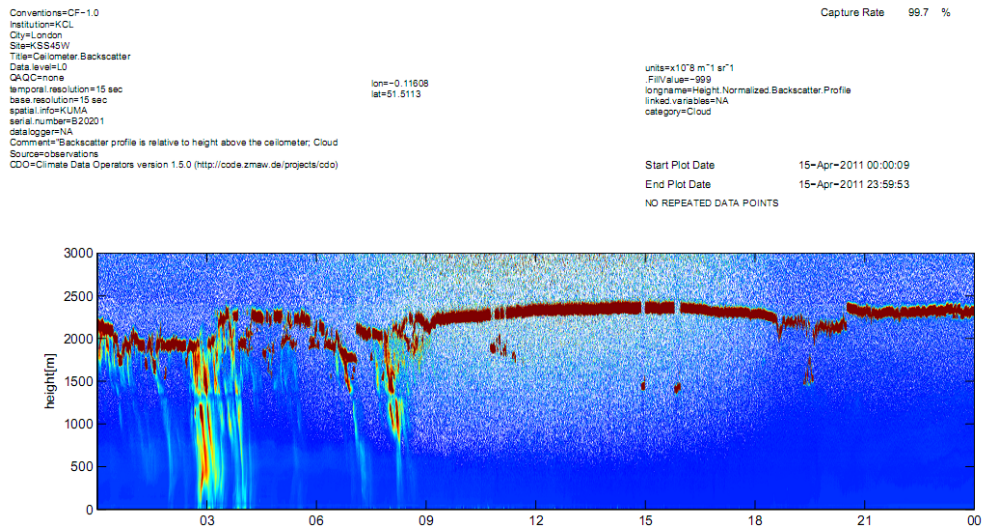

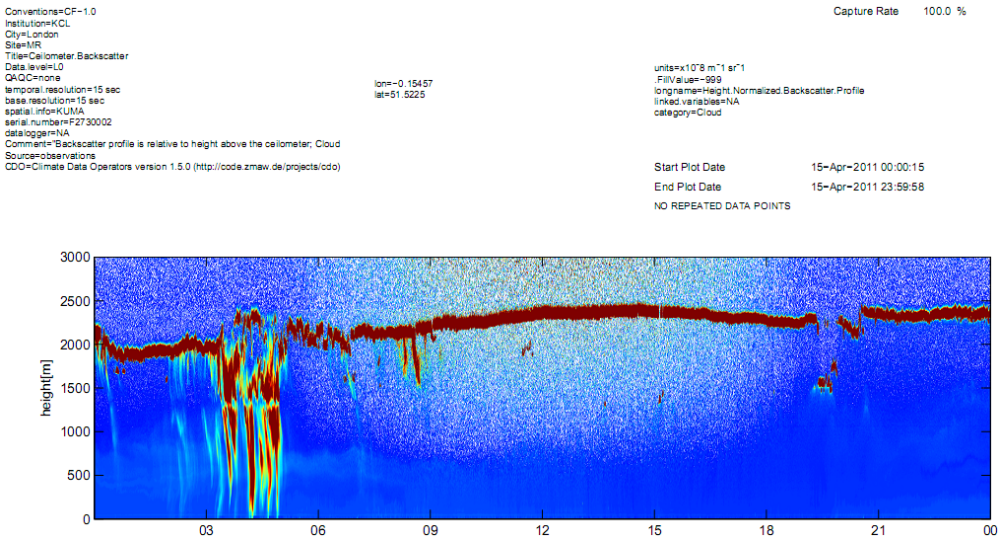

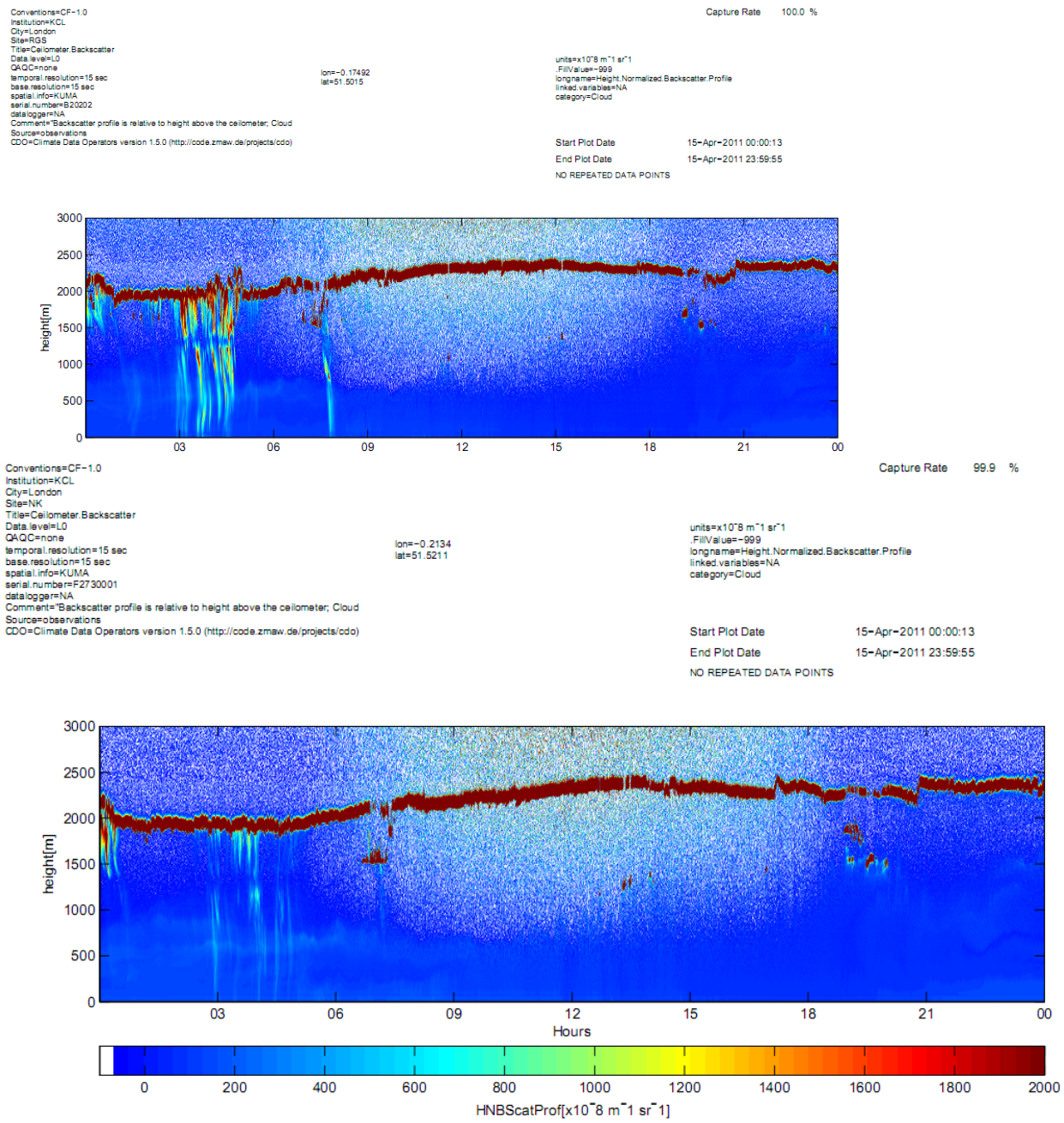

Figure 76: KUMA plots of ceilometer backscatter for the 15 April 2011 (a) KSK45W (b) MR (c) RGS (d) NK

New MLH Comment Key

Situation Comment

Data present	1	Data missing	-99

Precipitation Comment

Observation	Format/Code Value
No Precipitation	1
Precipitation observed	2

Cloud Comment

No cloud during hour	1
Cloud observed (t<30 mins)	2
Cloud observed (30<t<60)	3
Precipitation (t=60, whole hour)	4

Layer Comment

1 Layer Observed	1
2 Layers Observed	2
3 Layers Observed	3
1 Layer observed below cloud	4
2 layers observed below cloud	5
3 layers observed below cloud	6
No clear pattern observed (additional comment)	9

Individual Layer Comments

Observed MLH	100 (nearest 10m)
No Observed MLH	0
Missing data	-99

Gradient/Density Observations

Mean gradient value at each (at least 5 points)	375 (to the nearest whole number)
Mean density value (at least 5 points)	450 (to the nearest 10)

Trend Comment

Constant Height (within ± 50 m around mean)	1
Slowly rising	2
Rapidly rising	3
Slowly falling	4
Rapidly falling	5
Trend unclear (make comment)	9

Duration Comment

Layer duration (t<30)	1
Layer duration (30<t>60)	2
Layer duration (t=60, whole hour)	3
Duration unclear (make comment)	9

Pollution Comment

High backscatter values >800 (lowest 200m)	1

Figure 77: Key used for manual interpretation of the ceilometers data. Used for evaluation of automated processing techniques.

3.9.5 **Ceilometer Results** [Authors: Young and Grimmond]

Visual analysis of 8242 h ceilometer density and gradient data (CLA 2008) (542 h missing May not complete) classified: 2371 (29%) containing precipitation (so not considered), 40 % had total (60 minute) cloud cover and only 13 % had no observed cloud for any part of the hour. In the layer analysis 2938 hours (35.6 % of analysed hours) had one or more visible pollution layers of which 1076 were during clear sky periods and 1862 under cloudy skies. The rest of the hours (2932) were deemed to have no identifiable pollution layers. These values suggest a particularly wet and cloudy year which is likely to impact on the results of the MLH analysis.

The 2938 hours when at least one pollution layer was apparent, hourly mean MLH was determined with results plotted by month and then season (Figure 75). Results show clear diurnal variation for all months with peak MLH observed at mid- late afternoon. Unfortunately due to the way the MLH is defined in this analysis there is a lot of missing data during the summer (JUN-JUL-AUG, Figure 75) where there was few or no layers below cloud observed between 11 and 18 UTC due to the onset of fair weather cumulus on most days. Further work needs to be done to determine how to treat cloud when constructing MLH climatologies both visually and using automatic MLH algorithms. This missing data coupled with that from May makes any analysis of the full inter-seasonal pattern in MLH difficult. This is particularly the case with March which is higher than the observed MLH in August, this maybe correct as this is before vegetation is present but clearly needs verification. Summer had above average precipitation and cloud cover on most days which is may be responsible for the suppressed summer time MLH. From the available data it is possible to see that the peak observed MLH is in the late afternoon for all months. This is linked to the turbulent sensible heat fluxes (section 3.9.8). Despite the missing data the late autumn (SEP-OCT-NOV) and winter (DEC-JAN-FEB) show the expected lower maximum MLH between 600 – 900 m.

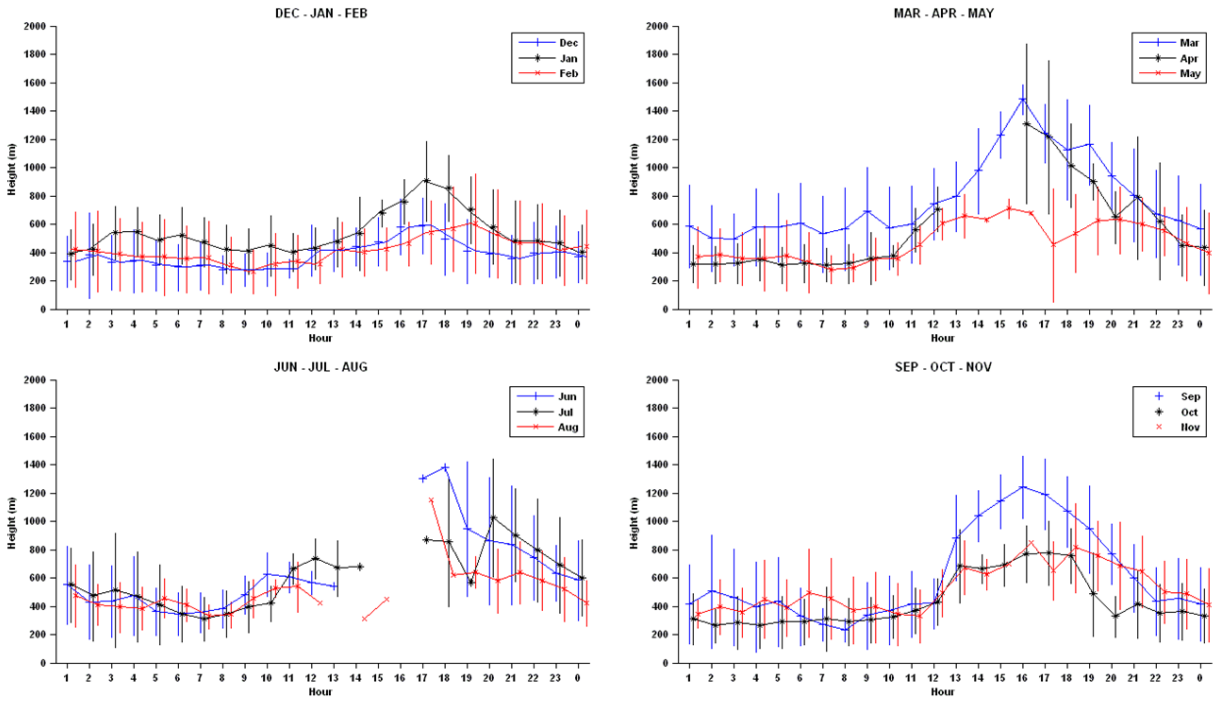

Figure 78: Mean hourly MLH determined by visual analysis from all observed lower layers (i.e. cloud not taken into account) plotted by month and season. The error bars represent ± 1 standard deviation Data is slightly offset on the x-axis for clarity.

3.9.6 **Surface Temperature** [Authors: Kotthaus & Grimmond Contributors: Finnemore, Wooster, Ward]

For the BRIDGE project, surface temperatures have been measured continuously using individual infrared thermometers pointing at different wall facets and roof types (Figure 76). These are complemented with an air temperature profile (Figure 77) which consists of fine wire unshielded thermocouples located on the KSS tower. The KSS_{roof} surface temperature is directly below the air temperature profile.

In addition, on occasion thermal cameras are used to collect wider spatial data (Figure 78). During the NERC flights over the city a number of thermal cameras were borrowed (EPSEC, NERC, other KCL researchers) to provide supplementary information. The NERC flights occurred in 14-15 August 2008 and 3-4 June 2010 during the day and night. The processing of that data is ongoing. The airborne observations are performed by ARSF (Airborne Research & Survey Facility) of NERC (Natural Environment Research Council, UK) were accompanied by extensive ground truth observations.

One TIR single channel and two hyperspectral instruments (VIS-SWIR) were operated on the plane 'Dornier 228: D-CALM' (Table 32), which had an average altitude of about 666 m during the day and 708 m at night. Data from TABI-320 (Thermal Airborne Broadband Imager) are deployed in the calculation of surface brightness temperature. It was set to Mode 3: Urban, with a temperature range of -20 to 110 °C and a thermal resolution of 0.1 °C. Observations from the AisaEAGLE sensor will be used for land cover classification. At maximum spectral binning this hyperspectral sensor still offers 60 spectral bands which contain sufficient information for the present study. Hence this setting is chosen in order to allow for maxiumum image rate (160 images s^{-1}). Currently, it is assumed that data gathered by AisaHAWK do not benefit the intended data processing since it's narrow FOV results in a rather small swath width. Additional information on heights of surface objects was collected with a ALS50-II LiDAR (Leica).

In 2010, four flight lines were acquired close to solar noon (12-13 UTC) and six close to maximum heat island intensity (23:50-01:00 UTC). All lines were flown in a north-south (or south-north) direction. An additional east-west orientated cross line completed the nighttime observations (around 01:20 UTC 04/06/2010). The acquired data cover a good fraction (at night >40%) of the CAZ area of interest (Figure 79). During day and night, the first line is centred over the flux towers and followed by three lines to the east, the prevailing surface wind direction on the study day.

Anticyclonic weather with clear sky conditions observed during the whole measurement period (Figure 80). The airborne measurements were accompanied by extensive ground truth observations. Fixed Infrared thermometers (IRT) from Raytek and Apogee are part of the permanent observations at the KCL sites (Figure 76). These sensors measure the brightness temperature of brick walls of four orientations (S, W, N and E) as well as roofs of different materials (concrete, gravel, roofing paper and black tiles). In addition, hand held IRTs (Omega and Maplin) were used to monitor surface temperature of large homogeneous areas including green spaces (Jubilee Gardens, Park at Imperial War Museum), roof materials (Macadam Roof), impervious surface materials (Southbank, Temple Tube Station, Paternoster Square, Waterloo Bridge) and water (River Thames). Water temperature is also monitored in River Thames using a TG-4100 data logger from Tinytag, which is installed at about 20 cm below water level. Temporal evolution of roof and wall temperatures was monitored with a FLIR SC640 thermal imager

which was installed on the Strand building (9UTC on 03/07/2010 to 2UTC on 04/07/2010). Additional mobile thermal cameras were used to observe wall and road temperatures during the flight time (Thermoteknix MIRICLE 307K and TESTO TESTO 875-2). All IRTs and thermal imagers - including the TABI -are calibrated against a black body system, allowing for a detailed comparison between the sensors.

Remote sensing in the VNIR range requires detailed information on the state of the atmosphere in order to allow for reliable atmospheric correction. Atmospheric transmissivity, water vapour content and aerosol optical depth is retrieved from sunphotometer observations which were collected by UCL (University College London). In addition, solar irradiance at the surface was measured with two field spectrometers (GER 1500, Spectra Vista Corporation and ASD Fieldspec3, Analytical Spectral Devices), collecting samples of spectralon reflectance panels in a frequency of 10 s. Also, downwelling longwave radiation is derived from FTIR spectrometer (Fourier Transform InfraRed) measurements during day- and nighttime observations. Atmospheric correction further requires knowledge on atmospheric temperature and humidity profiles. Radiosonde data from the nearest operational station at Herstmonceaux (WMO 03882) can provide this information.

The interpretation of spectral reflectance observations in the process of land cover identification can be improved if spectra of some locations of differing brightness are known. This information was collected before and after the daytime flight. Reflectance of three large ground targets (3 m x3 m, black, white and grey) that were located close to the centre of the first flight line, was measured using the ASD Fieldspec3. On the day after the flight observations (2010/155), weather conditions were very similar to the preceding day. No clouds were observed (Figure 80).

On the second day, further ground truth spectra were collected from impervious surfaces (Temple Tube Station and Waterloo Bridge) and grass (Jubilee Gardens). All field spectroscopy equipment is calibrated and quality controlled before and after the measurements by NERC FSF (Field Spectroscopy Facility).

All data collected during the SOP are incorporated into the retrieval of LST Ts (Figure 81). The radiometric calibration of TABI-320 Raw digital numbers (DN) is performed by the Laboratory of Remote Sensing, National Technical University of Athens, which is the owner of the airborne sensor. Hence, the TABI-320 output is provided in brightness temperature T_b [°C]. For the Eagle readings, the first processing step is undertaken by ARSF-DAN (Data Analysis Node). At-sensor radiance is compared to irradiance, allowing the calculation of at-sensor spectral reflectance (α).

Incorporating a DEM (digital elevation model) for the study area, the AZGCORR software is used to perform geometric correction of both remotely sensed datasets, resulting in maps of T_b and α. A combination of observations from radiosondes, field spectrometers (GER1500 and ASD Fieldspec3) and the sun photometer are used as input for the atmospheric transfer model MODTRAN5 (MODerate resolution atmospheric TRANsmission) in order to calculate atmospheric transmissivity t_a and downwelling longwave radiation $L\downarrow$. The latter is also measured by the FTIR spectrometer. Finally, effective mean atmospheric temperature T_a is required as a third input variable for atmospheric corrections.

The Eagle spectral information, supported by ground truth spectra and urban spectral libraries (e.g. Herold et al. 2004), is used to identify land cover types. Based on the derived land cover map, spatial variation of surface emissivity is incorporated. In order to gather a database which allows the assignment of spectral emissivity to land cover classes, samples of various urban surfaces are taken with a FTIR spectrometer. This instrument allows for the direct measurement of spectral emissivity ε_λ (Del Campo et al. 2006[122]).

The relation between at-sensor radiation, which is a function of T_b, and the desired LST, is not trivial. It can be solved using for example the mono window algorithm (MWA) developed by Pu et al. (2006[123]). Based on the land cover map, spectral emissivity is incorporated in the process in order to convert brightness temperature in actual Ts. Finally, ground truth observations of surface, wall and roof temperatures are combined to assess the reliability of the performed LST retrieval.

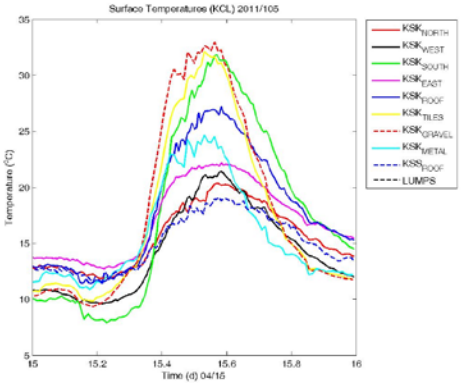

Figure 79: Infrared temperatures for one day from different facets.

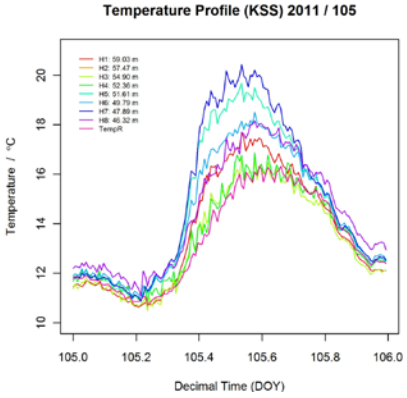

Figure 80: Air temperature profile on KSS.

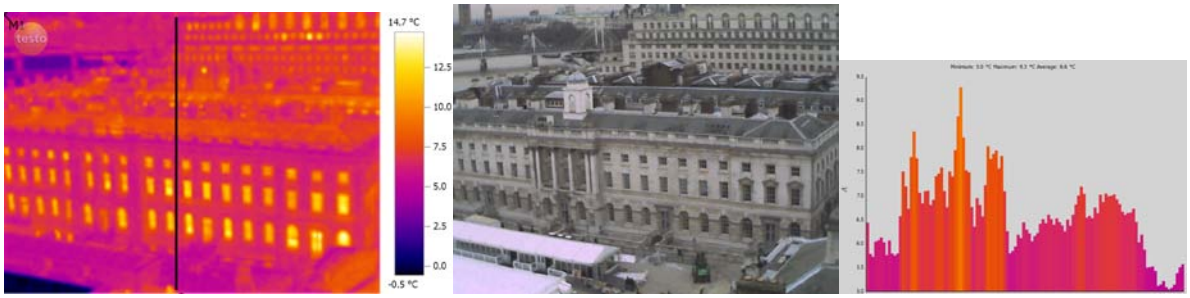

Figure 81: Example of imagery taken near KSS (a) Thermal (b) Visible (c) temperature profile along the line indicated in (a). These do not have emissivity corrections. Image taken 16:07 24 January 2011. Ice rink can be seen in the lower left hand corner.

Table 32: Remote sensing instrumentation and settings as operated by NERC Flight during 2010. The FOV (field of view) of Eagle applies for the chosen lens ($OLE_{18.5}$). Eagle is set to maximum spectral binning. All three instruments

[122] Del Campo L, R Pérez-Sáez, X Esquisabel, I Fernández, MTello, 2006: New experimental device for infrared spectral directional emissivity measurements in a controlled environment. Review of Scientific Instruments, 77,113 111.

[123] Pu, R, P. Gong, R. Michishita, and T. Sasagawa, 2006: Assessment of multiresolution and multi-sensor data for urban surface temperature retrieval. Remote Sens. Environ, 104, 211-225.

work on a push broom technique, pixels/swaths denotes the number of across track pixels. Swath width and pixel size are calculated for an altitude of 700m. AisaHAWK channels are mainly located in the short wave infrared (SWIR) region.

Sensor	TABI-320	AisaEAGLE	AisaHAWK
Manufacturer	*ITRES*	*Specim*	*Specim*
Spectral range	TIR, $8-12\,\mu$m	VNIR, $0.4-0.97\,\mu$m	SWIR, $0.97-2.45\,\mu$m
Spectral bands	single band	60	254
FOV	48°	37.7°	24°
Pixels/swath	320	1024	320
swath width [m]	623	482	298
pixel size [m]	1.9	0.5	0.9

Figure 82: Day and night time flight lines (03/06/2010). Centre of the lines (white), Outer boundary of area covered by TABI (Eagle) (red (green)). Pink scale indicates a) 5 km, b) 1 km, c) 500 m and d) 100 m. GoogleEarth 2010.

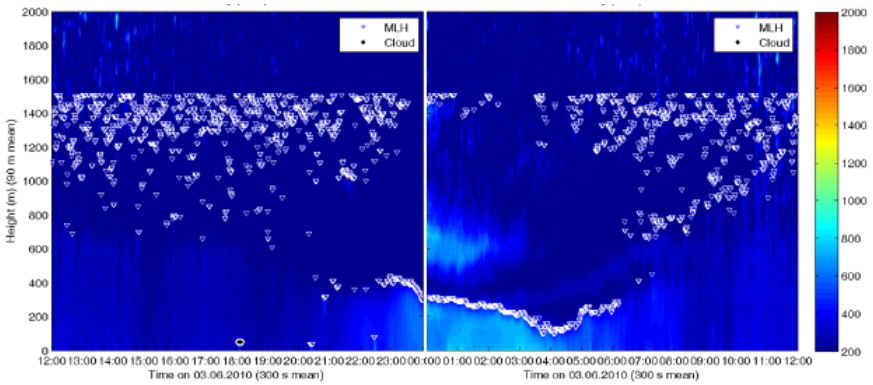

Figure 83: Ceilometer (KSK45W) observations of backscatter for 2010/154.

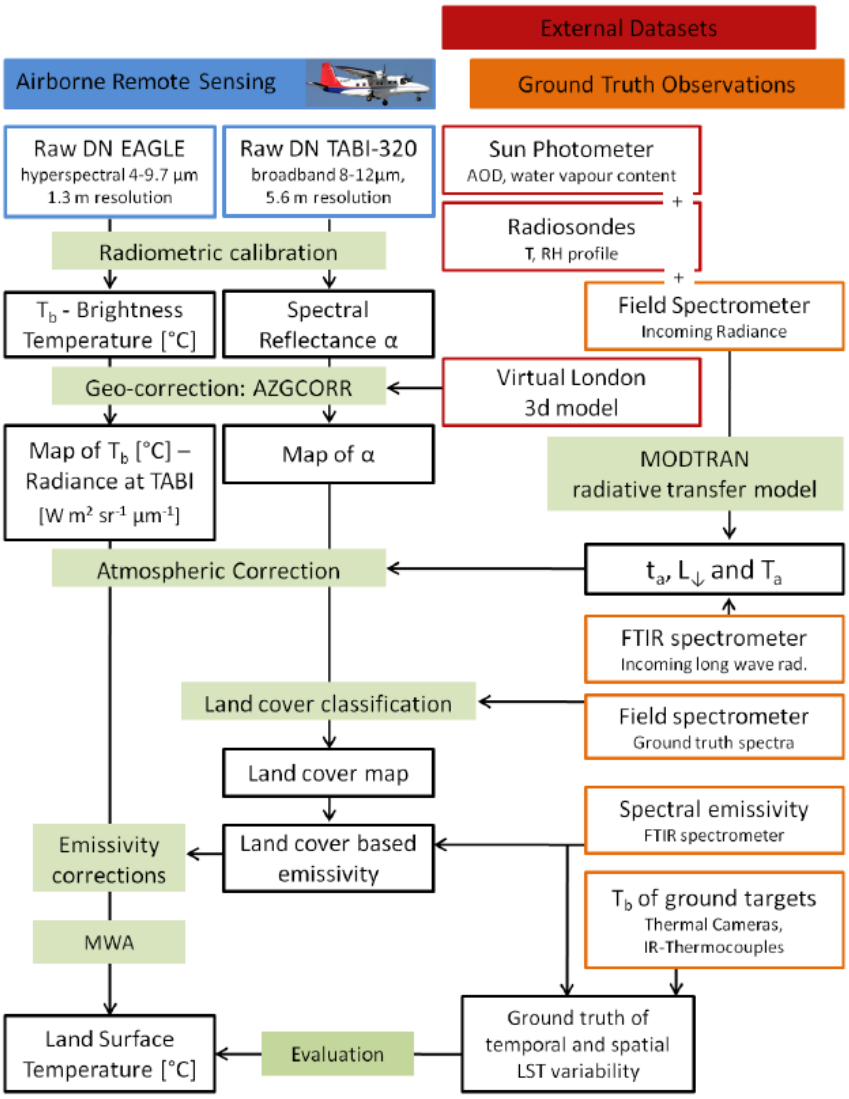

Figure 84: Overview of processing procedure for TABI and Eagle data to retrieve LST distribution. Airborne data (blue), ground truth measurements (orange), other input data (red), intermediate results (framed black), methods/ processing steps (light green).

3.9.7 **Fluxes at KCL** [Authors: Kotthaus and Grimmond]

On tall towers at KCL intensive observation site micrometeorological fluxes have been observed. Long wave and shortwave incoming and outgoing radiation ($L_{\downarrow}, L_{\uparrow}, K_{\downarrow}, K_{\uparrow}$) are measured by a net radiometer (CNR1 and CNR4, Kipp&Zonen) which allows for the calculation of net all-wave radiation. Sensible and latent heat flux are measured with Eddy Covariance (EC) systems consisting of a CSAT3 sonic anemometer (Campbell Scientific) and a Li7500 open path infrared gas analyzer (LiCOR Biosciences), both sampling at a frequency of 10 Hz. Sonic anemometers are installed oriented for the sectors of the predominant wind direction (SW) relative to the mast in order to minimize flow distortion.

Basic meteorological observations, namely air temperature, barometric pressure, horizontal wind speed and direction as well as relative humidity are obtained by a WXT510 automatic weather station (Campbell Scientific). This instrument is also used to monitor precipitation, simultaneously to a common tipping bucket rain rauge (ARG100). All instruments except from the weather station are connected to a datalogger (Campbell Scientific, CR3000 or CR5000). The flux tower at KSK was installed in 2008 and the one at KSS in 2009 (Table 33).

Meteorological observations and radiation balance components are recorded in 15 min intervals. Flux calculations are performed based on 30 min block averages. An Ogive test was used to determine the appropriate averaging interval for the sites to ensure no significant of energy is lost at the low frequency end of the spectrum. All recording and data analysis is done in UTC (Coordinated Universal Time) This is local time in the winter and an hour earlier during the period when daylight savings is observed.

ECpack (van Dijk et al. 2004[124]) is used for EC processing with several pre- and post processing steps performed using scripts written in R (R Development Core Team 2005[125]). Commonly used corrections are applied to the data in order to optimize reliability of the resulting fluxes. Firstly, the pre-processing addresses the possible time lag between the time series of IRGA and sonic readings. Not accounting for this can result in flux errors of the order of 10 % (Mauder et al. 2007[126]). Time series are shifted to meet maximal cross correlation between H_2O concentration and sonic temperature.

Subsequently, quality control identifies any raw data that are questionable. Gas concentration readings are excluded from all processing if the Li7500 gas analyzer reports path obstruction of at least 75%, indicated by the diagnostics value. Similarly observations from all variables are classified as erroneous if the CSAT3 diagnostic parameter indicates problems. The range of observed values is further restricted to physically reasonable values, which are defined by the measurement range of the instruments. In addition to these general restrictions, single values and short term periods which differ distinctly from the pattern observed during the respective 30 min period are detected. Those ‘spikes’ are commonly

[124] van Dijk A, A Moene and H de Bruin, 2004: The Principles of Surface Flux Physics: Theory, Practice and Description of the ECPACK library.
125 R Development Core Team, 2005: R: A language and environment for statistical computing. Vienna, Austria, R Foundation for Statistical Computing, URL http://www.R-project.org, ISBN 3-900051-07-0.
126 Mauder M, et al, 2007: The energy balance experiment EBEX-2000. part ii: Intercomparison of eddy-covariance sensors and post-field data processing methods. Bound. Lay. Met, 123, 29_54.

found in EC raw data (e.g. due to irregularities in power supply) but need to be removed because of their high impact on (co-) variance calculations. The despiking procedure used in this study is developed following the one described by Schmid et al. (2003). [127]It is adapted to site specific requirements .

The ECpack software package does the main flux processing. Planar fit coordinate transformation (Wilczak et al. 2001[128], Lee et al. 2004[129]) is performed based on a 24 h window and is followed by an additional yaw rotation (Kaimal and Finnigan 1994[130]). This supplementary rotation does not affect the calculation of turbulent fluxes but presents wind speed results aligned to the mean wind field. The sonic temperature is corrected for humidity effects (Schotanus et al. 1983[131]) and gas concentrations are corrected for density fluctuations (Webb et al. 1980[132]). Spectral corrections are based on Moore (1986).

In the post-processing, a combination of daily statistics and Li7500 diagnostics is used to exclude erroneous results of turbulent fluxes and friction velocity u*. Gaseous fluxes of CO_2 or H_2O are regarded as unrealistic if the discrepancy between the value and the daily average is larger than three times the daily standard deviation and at path obstruction is reported by the gas analyzer for at least 1% of the 30 min period. Less rigorous criteria are chosen for values calculated solely from sonic observation. Sensible heat flux and friction velocity with large deviation from the daily average are only discarded for times with a path obstruction for at least 90% of the period. Further all periods affected by precipitation events are detected because measurement paths of gas analyzer and sonic anemometer are obstructed. In a last stage of quality control the resulting fluxes are restricted to a fixed range. Adapted from seasonal statistics (calculated for one year of observations at KSK) thresholds are defined as a function of the inner quartile range (IQR). Reviving the concept of fences to detect extreme values in a set of data, modifications of the limits are calculated as $q_{99} + 3 \times IQR_{year}$ and $q_{95} + 3 \times IQR_{season}$ as well as $q_{50} - \frac{3}{2} \times IQR_{year}$ and $q_{25} - \frac{3}{2} \times IQR_{season}$ for upper and lower limits respectively. Final thresholds for fluxes and friction velocity are chosen manually by comparing the dataset to the explained boundaries. While the physically reasonable range of u_* and F_{CO_2} appears to be constant throughout the year, upper thresholds of both sensible and latent heat flux are chosen to be 100 W m^{-2} higher for warm seasons.

Well-founded data analysis and interpretation requires knowledge about data quality and quantity. For the current study the percentage of reliable observations in each month' number of time periods is generally quite high. The capture rate specifies the rate of successful raw data collection. From these

[127] Schmid et al. (2003).
[128] Wilczak J, S Oncley, and S. Stage, 2001: Sonic anemometer tilt correction algorithms. Bound. Lay. Met, 99, 127-150.
129 Lee X, J Finnigan, and K Paw U, 2004: Handbook of Micrometeorology : A guide for Surface Flux Measurement and Analysis, chap. Coordinate Systems and Flux Bias Error, Chapter 3. Kluwer Academic Publishers, Dordrecht.
130 Kaimal J. and J. Finnigan, 1994: Atmospheric Boundary Layer Flows: Their Structure and Measurement. Oxford University Press, New York, 289 pp.
131 Schotanus P, F Nieuwstadt, and H. de Bruin, 1983: Temperature measurements with a sonic anemometer and its application to heat and moisture fluxes. Bound. Lay. Met, 26, 81-93.
132 Webb E, G Pearman and R Leuning, 1980: Correction of the flux measurements for density effects due to heat and water vapour transfer. Quart. J. R. Met. Soc,106, 85-100.

potentially useful datasets, observations are classified as untrustworthy if they fail one or more of the steps describing the QAQC procedure. In general, criteria based on precipitation and instrument diagnostics values define the highest percentages of excluded data points. But even if the other considerations mask out only a small fraction of the dataset, the detection of unreasonable observations is important in order to improve the quality of the dataset and the reliability of it's interpretation.

Table 33: Overview on instruments with serial number operating at sites KSK and KSS used for this study. Time periods specified as day of year. See also Table 23 and Table 24.

	Instrument	Model [serial number]	2008	2009	2010	2011
KSK	Sonic anemometer	CSAT3 [0192-2]	274-366	001-280		
		CSAT3 [1188-1]			022-365	001-059
	Infrared gas analyser	Li7500 [75H-0995]	274-366	001-280		
	Weather station	WXT510 [084006]	274-366	001-365	001-365	001-059
	Radiometer	CNR4 [100312]	274-366	001-280		
		CNR1 [000220]			264-365	001-059
KSS	Sonic anemometer	CSAT3 [0192-2]		305-365	001-365	001-059
	Infrared gas analyser	Li7500 [75H-0995]		305-365	001-365	001-059
	WXT510 [B084005]	WXT510 [B084005]		286-356	001-365	001-059
	CNR1 [000220]	CNR1 [000220]		289-356	001-365	001-059

3.9.8 **Fluxes: Provisional Results** [Author: Kotthaus and Grimmond]

The flux processing methodology is undergoing further refinements so the following are preminary results not absolute final data. As such the authors should be consulted before data or conclusions are cited.

For the annual period October 2008 – September 2009, the radiative input to the surface energy balance shows a clear seasonal pattern (Figure 82). While day to day variations are relatively small during autumn and winter, they tend to be larger during months when average net all-wave radiation is higher. This is linked to the stronger absolute impact of cloudy conditions on incoming solar radiation when days are longer and incoming radiation is more intense.

The incident flow is characterised by an average horizontal wind speed of 2.8 m s^{-1} and prevailing wind directions from S and SW. The daily friction velocity is relatively constant throughout the year, it varies around a mean value of 0.5 m s^{-1}. The daily air temperature ranges from 0 to 22 °C and relative humidity indicates quite moist conditions with diurnal averages between 45% and 97%. Precipitation is observed throughout the year (with a periodicity typical for the synoptic time scale of European low pressure systems). Total precipitation in the studied year was 504.2 mm which is slightly less than the Normal of 583.6 mm (1971-2000)[133].

[133] http://www.meto_ce.gov.uk/climate/uk/averages/19712000/sites/greenwich.html

Sensible heat is transported away from the surface all year round with slightly higher fluxes during spring and summer (April - September). No distinct annual cycle, as in net all-wave radiation, is evident in the sensible heat flux. This suggests a strong anthropogenic heat flux source in the study area which sustains the high values.

Due to restricted moisture availability in urban areas, a rather small amount of energy is transported via the turbulent latent heat flux. Usually the presence of transpiring vegetation shapes the evolution of Q_E through the year (e.g. Christen and Vogt 2004[134]; Offerle et al. 2006[135]). In this study, no such seasonal differences is identified. This might relate to the vicinity of the river Thames providing a constant moisture source independent of the growth stage of vegetation. The distribution of fluxes by wind direction sectors (Figure 83) show that the main footprint of the sites is located in the S or SW but no evidence for wind direction dependant energy partitioning can be identified.

Typically, urban areas represent a source for CO_2 on a seasonal and daily timescale (Moriwaki and Kanda 2004[136]; Coutts et al. 2007a[137]). The annual overview of average daily carbon fluxes confirms this for the site in Central London. As observed in other long term studies (e.g. Järvi et al. 2009[138]), the flux of carbon dioxide is higher during the colder times of the year. With a mean daily average of 29.1 µmol m^{-2} s^{-1}, F_{CO2} between October and February, this is about 10 µmol m^{-2} s^{-1} larger than during the rest of the year. In these months distinct day to day variations are apparent, while in July and August extremely small variations are evident. The annual pattern could be explained by enhanced sources from heating (and transport) during the colder time of the year. This evidence is in agreement with the anthropogenic heat sources noted that impacts the sensible heat flux observations.

The frequency distribution of friction velocity and turbulent fluxes (Figure 84) gives insight into the seasonal changes in magnitude. Apart from the observations in June, the frequency of higher u* values is larger during the summer. Especially May and July are characterized by a broader distribution. This tendency is even clearer for the sensible heat flux. In the winter months (dark colours in Figure 84) a sharp maximum is reached at about 30 W m^{-2}. As expected, the times that sensible flux is greater than 100 W m^{-2} are detected more frequently in the summer months. The distribution of Q_E is reasonably symmetrical around a maximum of about 5 W m^{-2}. Especially during warmer months, the frequency of higher fluxes is increased leading to a widening of the curve towards greater magnitudes. Frequency distribution of carbon dioxide clearly divides the F_{CO2} results into two groups. From May to September, the range of magnitudes is about 50 µmol m^{-2} s^{-1} with maximum frequencies of about 200 -250 h. A

[134] Christen, A, and R. Vogt, 2004: Energy and radiation balance of a central European city. *International Journal of Climatology*, **24,** 1395-1421

[135] Offerle B, CSB Grimmond, K Fortuniak, K Klysik, and TR Oke, 2006: Temporal variations in heat fluxes over a central European city centre. Theor. Appl. Climatol, 84, 103-115.

[136] Moriwaki, R. and M. Kanda, 2004: Seasonal and diurnal fluxes of radiation, heat, water vapor, and carbon dioxide over a suburban area. J. Appl. Meteor, 43, 1700-1710.

[137] Coutts, A, J. Beringer, and N. Tapper, 2007b: Impact of increasing urban density on local climate: Spatial and temporal variations in the surface energy balance in Melbourne, Australia. J. Appl. Meteor. Clim, 46, 477-493.

[138] Järvi, J, et al, 2009: The urban measurement station SMEAR III: Continuous monitoring of air pollution and surface-atmosphere interactions in Helsinki, Finland. Boreal Env. Res, 14 (suppli. A), 86-109.

broader spectrum is observed in the rest of the year. The shift between colder and warmer months fluxes is more abrupt that for the energy fluxes. Since the flux of carbon dioxide in urban areas is mostly shaped by the amount of anthropogenic emissions, it is influenced by climate conditions only indirectly. Sensible heat flux responds to anthropogenic heat as well as heat storage and net radiation. Therefore it's magnitude changes are smoothed by the gradual change in incoming solar radiation. Unlike for Q_H, enhanced anthropogenic emissions in the colder time of the year are represented more obviously in the distribution of F_{CO2}.

The results from ECpack and TK2 are in really good agreement for sensible heat flux (Figure 85). Q_H as well as net radiation show a clear diurnal cycle throughout the year. This feature is more pronounced in the summer for both energy fluxes. Maximum sensible heat flux is observed in the afternoon. This asymmetrical diurnal cycle (Coutts et al. 2007a[139]) can be linked to the hysteresis pattern (Grimmond et al., 1991[140]) of the storage heat flux. The latter is greater in the morning reflecting the morning uptake of heat by the urban fabric. Usually the maximum of ΔQ_S is followed by Q* which in turn precedes when Q_H is largest.

In the warmer part of the year, the radiation budget is the main energy input into the system of the near surface atmosphere. When solar elevation is higher, the daily maximum of Q* exceeds that of Q_H, which is the case from March to October. The difference in peak energy flux reaches its maximum in June, when incoming solar radiation is highest. Summertime anthropogenic heat sources from air conditioning units that play an important role in other urban settings (e.g. in North America, Japan) are not yet very common in London. From November till February, net radiative input is notably lower. During these months, the main input to the surface energy balance is most likely given by the anthropogenic heat flux (Allen et al. 2010[141]). Due to winter-time heating, energy consumption is much higher than during spring, summer and autumn. During these months the average turbulent sensible heat flux exceeds the net radiation even during midday. The comparison between sensible heat flux exchanges during weekdays and weekends shows no clear differences. Hence, anthropogenic heat sources does not seem to be directly related to weekday activities. This interpretation should be handled with care since many buildings in the business study area are run (heated) even during weekends even though less people are using them. A more detailed inspection is currently being undertaken.

There are positive nighttime sensible heat fluxes throughout the whole year with storage heat flux ΔQ_S acting as a nighttime source for turbulent heat transfer. In addition, anthropogenic heat can be expected to be an important supply of energy at night. The nocturnal sensible heat loss found in this study, is more persistent (and may be of higher magnitude) than observations from other cities. For the central London site, positive Q_H is monitored consistently in each month (Figure 85) with average

[139] Coutts, A, J. Beringer, and N. Tapper, 2007a: Characteristics influencing the variability of urban CO_2 fluxes in Melbourne, Australia. Atmos. Environ, 41, 51-62.
[140] Grimmond CSB, HA Cleugh, and TR Oke, 1991: An objective urban heat storage model and its comparison with other schemes. Atmos. Environ, 25B, 311-326.
[141] Allen L, F Lindberg, CSB Grimmond (2010) Global to city scale model for anthropogenic heat flux, International Journal of Climatology doi: 10.1002/joc.2210 http://onlinelibrary.wiley.com/doi/10.1002/joc.2210/pdf

nighttime values reaching their maximum in April 2009 (61 W m^{-2}). Several studies observed nighttime sensible heat flux transporting energy away from the surface on a temporary basis (e.g. Nemitz et al. 2002[142], Moriwaki and Kanda 2004). While Offerle et al. (2006), Coutts et al. (2007a) and Järvi et al. (2009) identify positive nighttime Q_H on monthly averages during winter months, only Christen and Vogt (2004) found nighttime sensible heat loss during summer, at their highly urbanized site. In addition, they observe the unstable layer resulting from the buoyant flux to be quite shallow.

Turbulent latent heat flux is highly dependent on moisture availability. In contrast to sensible heat, whose sources like roads and buildings are widely distributed in urban areas, sources for latent heat are mainly located in parks and green spaces which supply moisture after rain or irrigation. When there has been rain or irrigation, street trees can play an important role. In the present case, the river Thames might act as the predominant moisture source. As a consequence, location of the source area or the footprint function as well as the vegetated fraction is of particular importance for the turbulent flux of latent heat. Since the source area is a function of wind direction and stability, which can change drastically throughout a day, the fluctuations of Q_E could be linked to these atmospheric conditions. Latent heat flux responses are less pronounced to changes in available energy than the sensible heat flux (Figure 86). Results from ECpack as well as TK2 show rather small fluxes with a large day to day variability. The hourly variations appear to be rather constant during the year, but a slight daily cycle can be identified in the months March to August.

As with the turbulent flux of sensible heat, the carbon flux calculated by ECpack and TK2 agree well on the monthly average diurnal basis (Figure 87). As a response to enhanced CO_2 emissions during the day, the flux of carbon dioxide shows a clear diurnal pattern. Extremely sharp increase in F_{CO2} related to morning rush hour times, as seen in studies from Tokyo (Moriwaki and Kanda 2004), Mexico City (Velasco et al. 2005[143]), Melbourne (Coutts et al. 2007a) and Helsinki (Vesala et al. 2008[144]) during winter months, are less apparent in the central London data. No twin-peak pattern as observed in Melbourne, occurs. Coutts et al. (2007a) relate the second peak in the afternoon to an increase in traffic and to emissions from domestic activities. In contrast to these other studies which were undertaken in domestic urban or suburban environments, the present analysis investigates carbon exchange in a business district. Most buildings are used as offices or for commercial purposes and tourist activities. Traffic flow is lower during nighttime but many night bus routes maintain CO_2 emissions between midnight and 6 am. These activities explain the smoother diurnal pattern of F_{CO2}. Traffic flow increases less abruptly in the morning hours and remains quite high throughout the working day while the absence of residential areas in the footprint eliminates a potential flux increase in the late afternoon. In the late afternoon there will typically a higher mixing layer height which results in reduced CO_2 concentrations.

[142] Nemitz E, K Hargreaves, A McDonald, J Dorsey, and D Fowler, 2002: Micrometeorological measurements of urban heat budget and CO_2 emissions on a city scale. Environ. Sci. Technol, 36, 3139-3146.
[143] Velasco E, S Pressley, E Allwine, H Westberg, and B Lamb, 2005: Measurements of CO_2 fluxes from the Mexico City urban landscape. Atmos. Environ, 39, 7433-7446.
[144] Vesala T, et al, 2008: Surface-atmosphere interactions over complex urban terrain in Helsinki, Finland. Tellus, 60B, 188-199.

Both, the hourly variation of the flux as well as the difference between daily minimum and maximum are larger in the colder months from November till March. The enhanced anthropogenic combustion in these months is linked to higher CO_2 emissions. As expected, the observations show decreased fluxes of carbon dioxide during the weekends, when less traffic occurs in the study area.

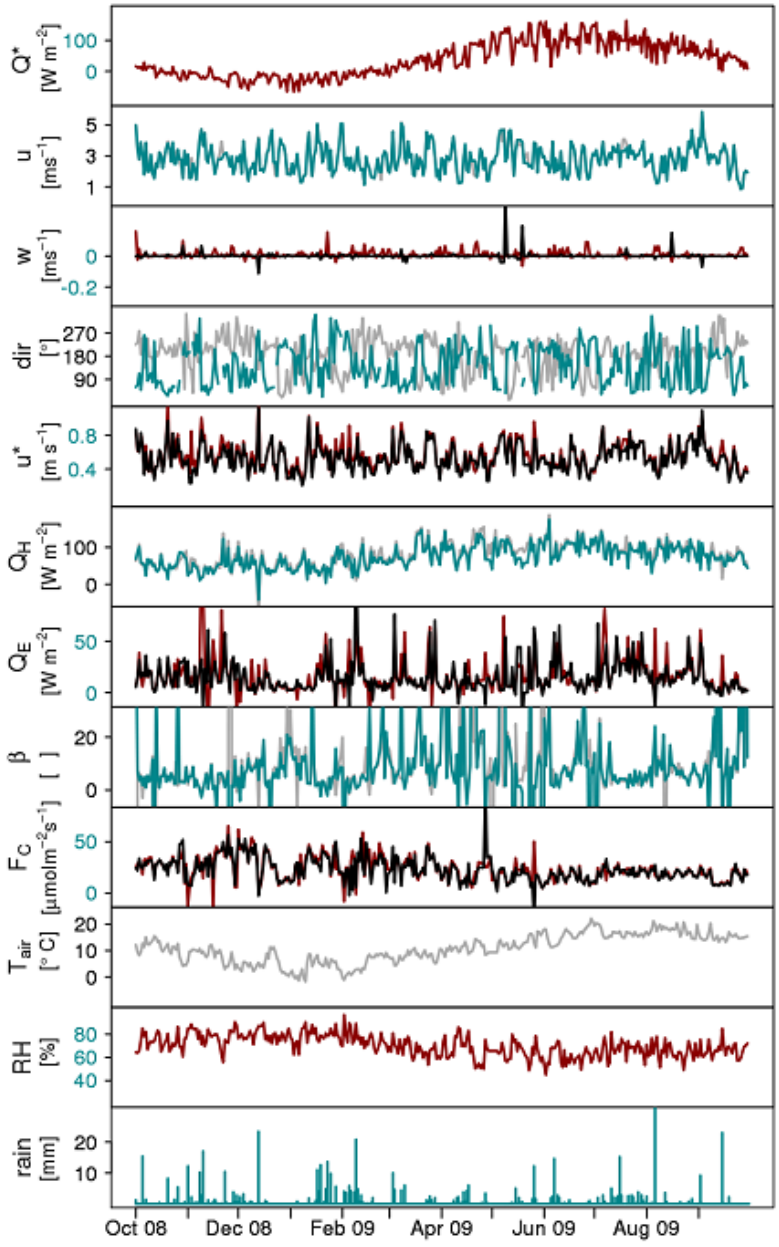

Figure 85: Daily mean (total) observations Oct 2008 - Sep 2009. Data gaps interpolated if ≤ 1h and replaced by the proceeding day's values otherwise in order to obtain complete 24h periods. If more than one time series is shown, black and turquoise lines is from TK2 and red and grey lines from ECpack. Variables from top to bottom: Net all-wave radiation Q∗, horizontal wind speed u, vertical wind speed w, wind direction dir, friction velocity u∗ , turbulent sensible heat flux Q_H, turbulent latent heat flux Q_E, Bowen ratio β calculated as $\Sigma Q_H/\Sigma Q_E$ when Q∗ > 0,

turbulent flux of carbon dioxide CO_2, air temperature T_{air}, relative humidity RH and precipitation from the rain gauge rain. Here TK2 wind direction is offset by 180°.

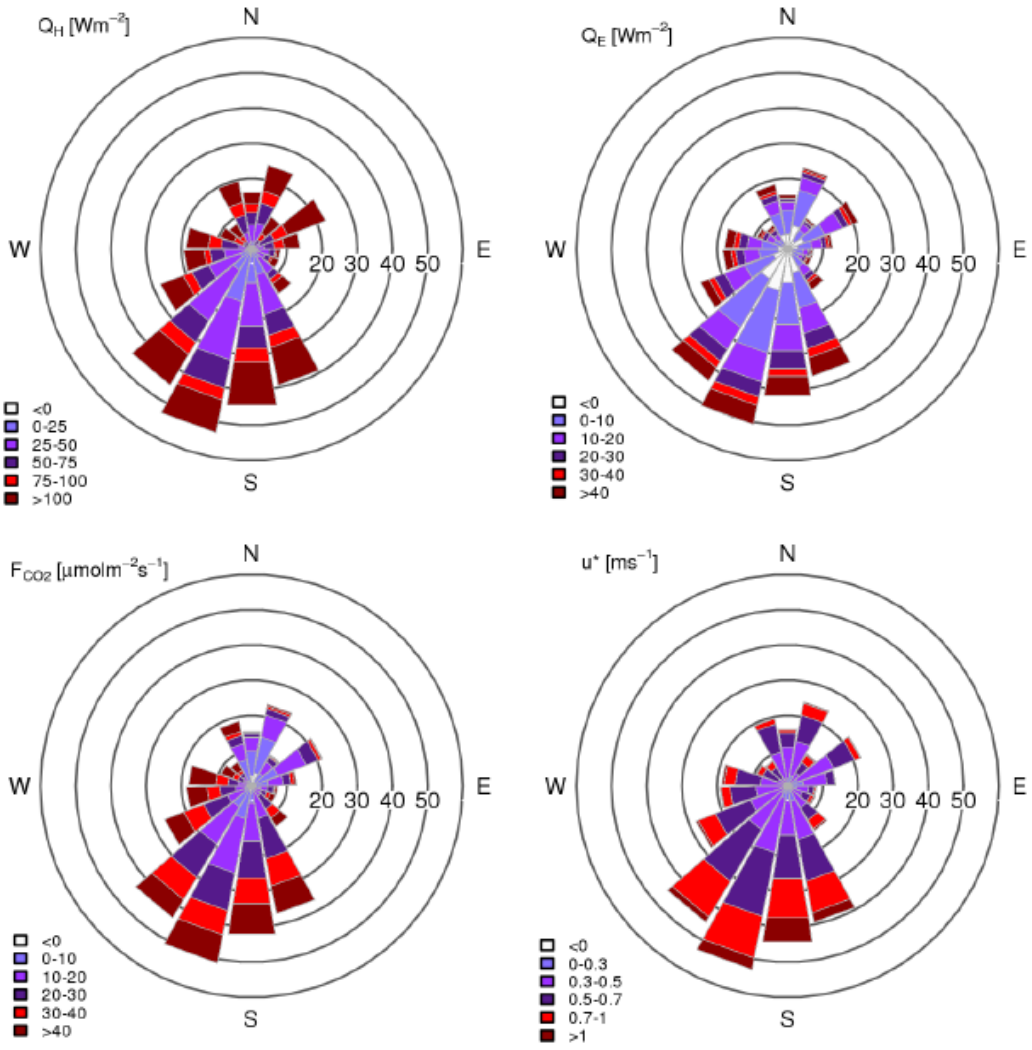

Figure 86: Flux results from KSK October 2008 to September 2009 by wind direction (20 ° wind sectors).

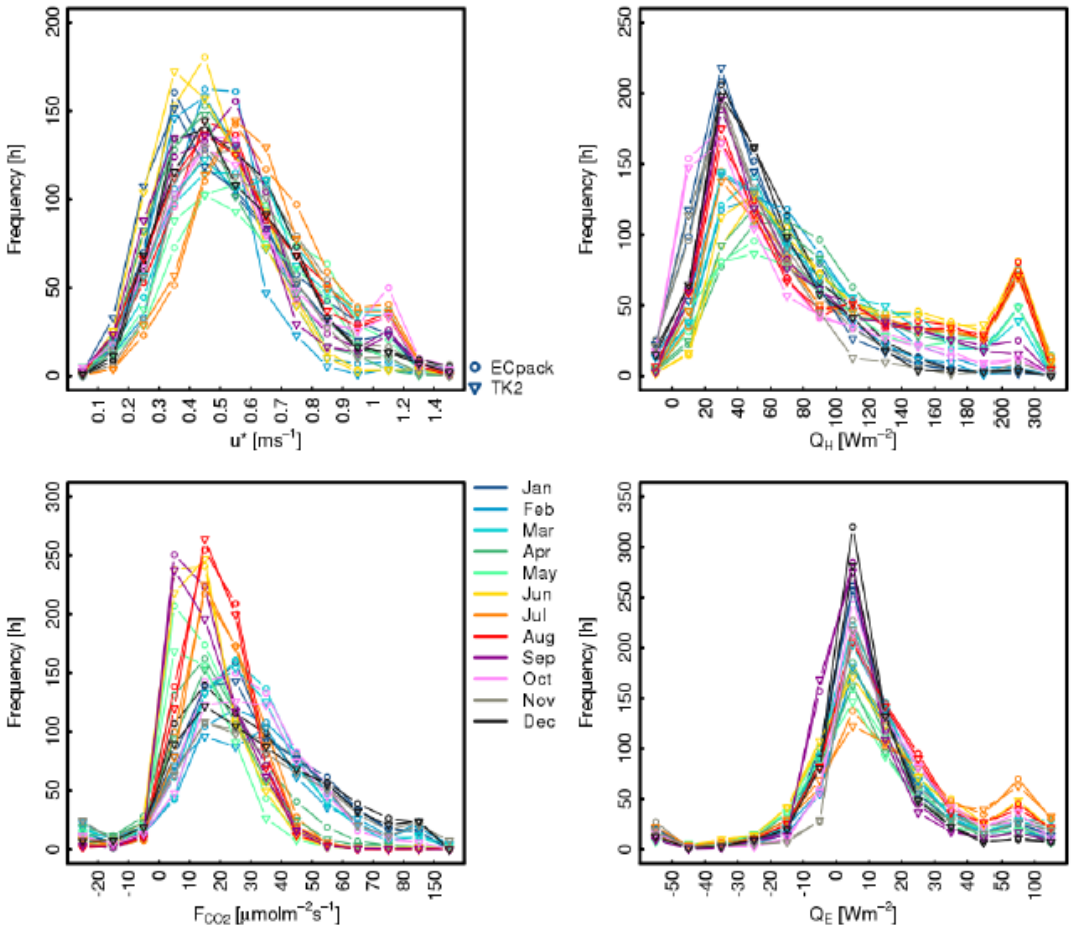

Figure 87: Frequency distribution of fluxes by month for KSK October 2008 to September 2009.

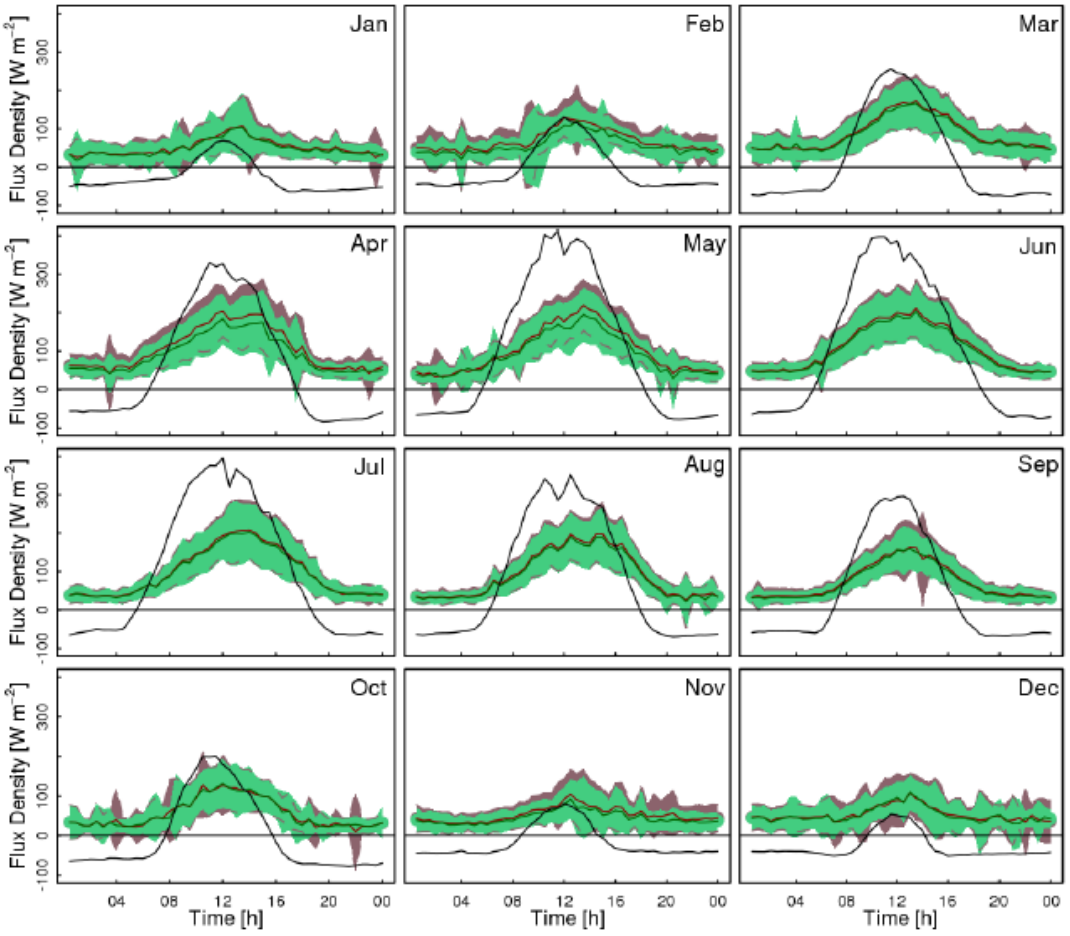

Figure 88 Monthly averaged diurnal cycle of net all-wave radiation (black) and turbulent sensible heat flux calculated with ECpack (dark red) and TK2 (green), standard deviation of Q_H is shaded. Turbulent flux calculations based on 30 min time periods.

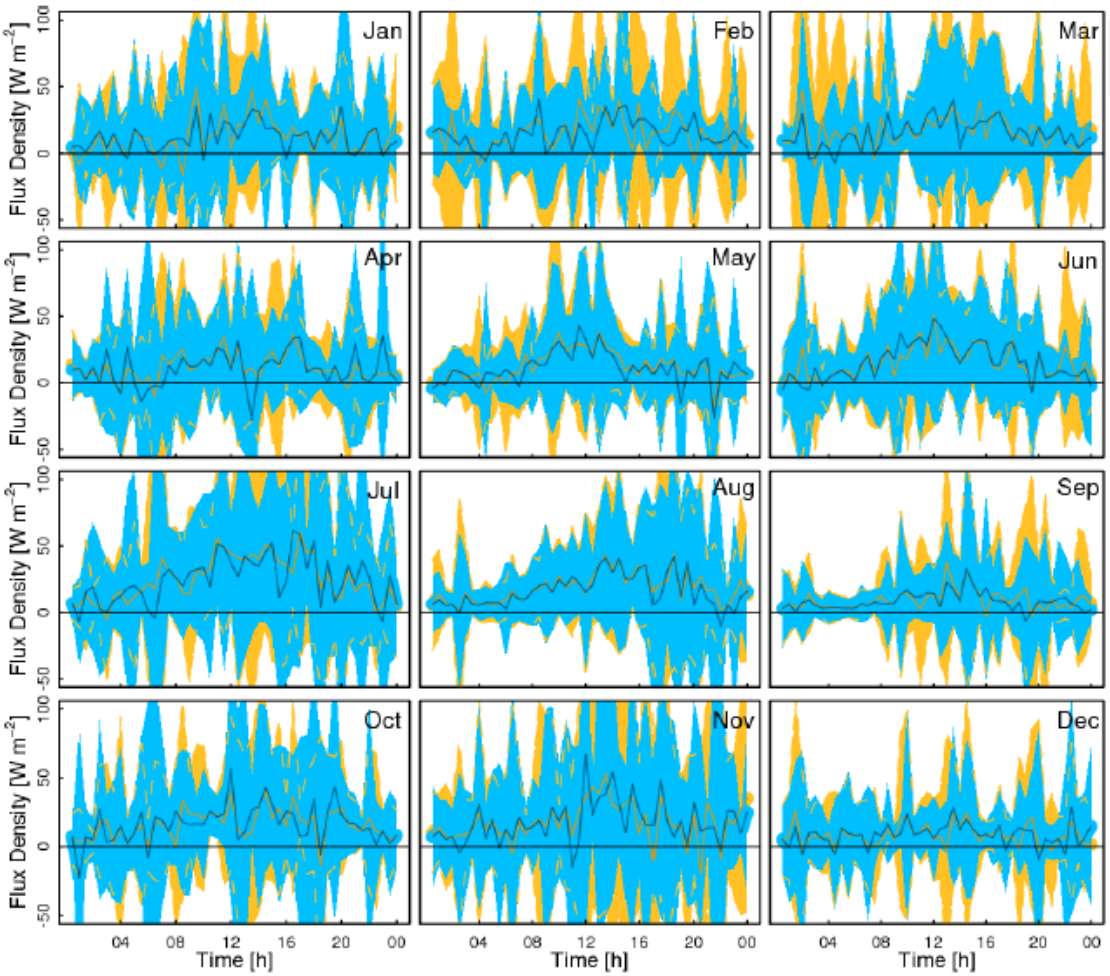

Figure 89 Monthly averaged diurnal cycle of turbulent latent heat flux calculated by ECpack (yellow) and TK2 (blue), standard deviations shaded. Turbulent flux calculations based on 30 min time periods.

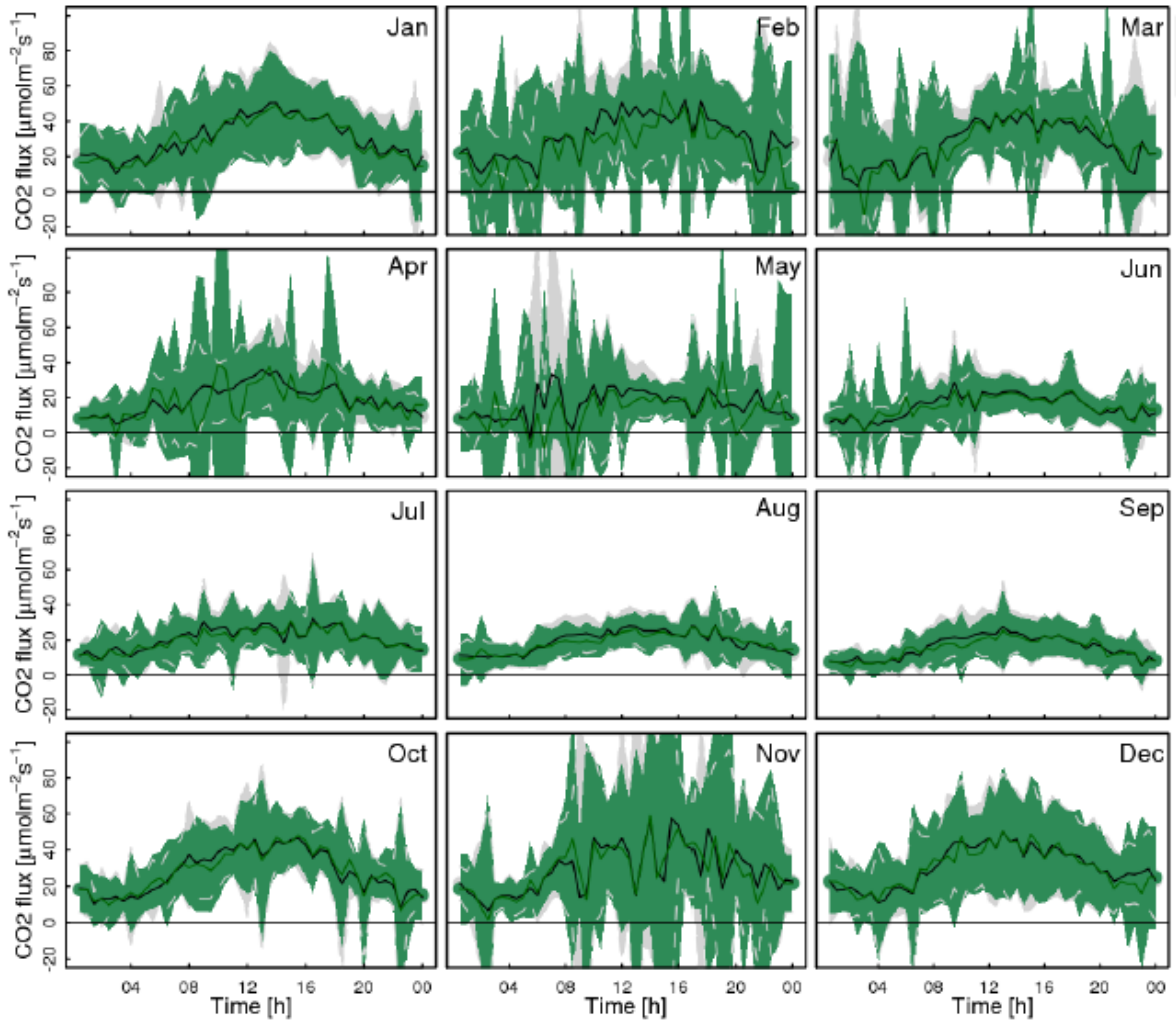

Figure 90 Monthly averaged diurnal cycle of carbon dioxide flux calculated by ECpack (grey) and TK2 (green), standard deviation shaded. Calculations based on 30 min time periods.

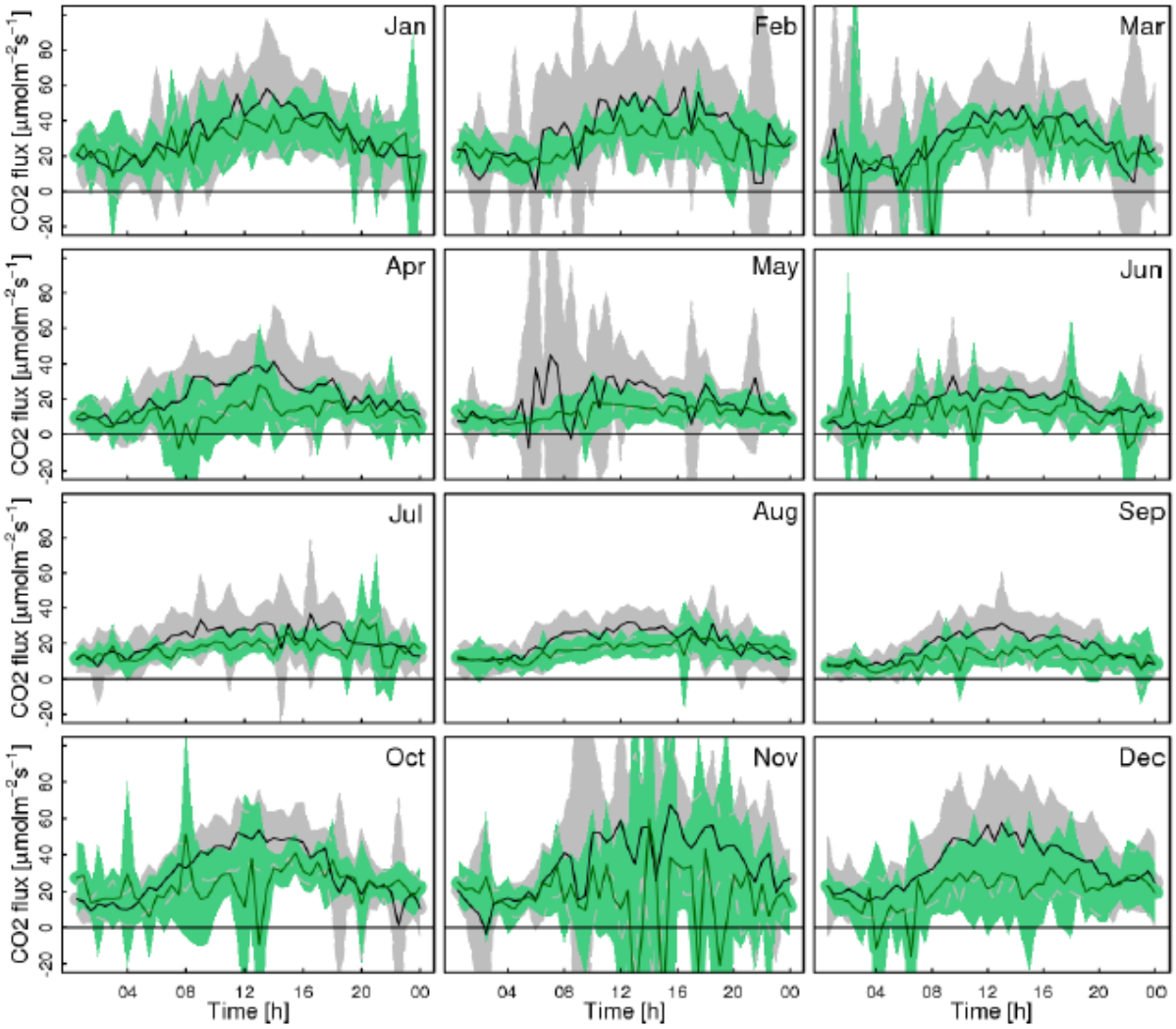

Figure 91 Monthly averaged diurnal cycle of carbon dioxide flux calculated by ECpack on weekdays WD (black) and weekends WE (green), standard deviation shaded (WD: grey, WE: green). Calculations based on 30 min time periods

3.10 Conclusions

In this section a few of the lessons learnt from the BRIDGE project are identified. These are subdivided into the main components of the report.

From the site characterization

- The locations of street trees in London are a very political issue (GLA 2007[145], 2011) which has meant that obtaining data about the current location of trees was very time consuming.
- The Street Tree Inventory which was obtained was incomplete so could not very reliably used as a basis for identifying where new trees could be located.
- LiDAR data provided complete data coverage. Analysis of these data using methods developed here have allowed for consistent analysis across the CAZ.
- Green roofs have been built in locations beyond those identified as potential locations.
- The total roof area that could potentially be retrofitted with green roofs in the CAZ is 4,987,104 m^2 (~15 % of the total CAZ area) or ~ 92 % of the total roofed area. The target increase green roofs in of 100,000 m^2 by 2012 would require the development in 2011-12 to be over five times that of the past two years.
- Currently about 0.6% of the CAZ roofs are green.
- From comparison of field and LiDAR data, tree characteristics are well correlated with the LiDAR yielding greater diameters and very similar heights.
- Public trees are generally taller and have wider crown diameter than trees on private land.

From observations:

- Automated data archive and delivery system (KUMA) has been developed. This has facilitated the use of data and identification of potential data issues in a more rapid manner.
- Redundancy in instrumentation is extremely useful for evaluating and verifying data.
- There is the potential to use a wide range of different sources of climate data in London. However, care needs to be taken as the network have different siting, instrumentation and aims which mean that modifications to the data may be necessary to make one consistent data set.
- WXT510 rain gauges do not appear to be usable for precipitation measurements within the central city in somewhere as acoustically noisy as London.
- It may be possible to use ceilometer backscatter to identify rainfall occurrence. This will provide additional redundancy for rainfall observations.
- Data once ratified will provide new insight into a range of processes occurring in the central part of a European mega-city.
- The data collected will be used to evaluate models which are used within the Decision Support System.

[145] http://legacy.london.gov.uk/assembly/reports/environment/chainsaw-massacre.pdf

3.11 References

Akbari H, Pomerantz, M, Taha, H. (2001) Cool surfaces and shade trees to reduce energy use and improve air quality in urban areas. Solar Energy. 70(3), 295-310.

Allen L, F Lindberg, CSB Grimmond (2010) Global to city scale model for anthropogenic heat flux, International Journal of Climatology doi: 10.1002/joc.2210 http://onlinelibrary.wiley.com/doi/10.1002/joc.2210/pdf

Backsik, Z, Mink, J. & Keresztury, G. (2004) FTIR spectroscopy of the atmosphere. I. Principles and methods. *Applied Spectroscopy Reviews*. 39. 295 – 363.

Baldwin, V.C. Jr, Peterson, K.D, Burkhart. H.E, Amateis, R.L, and Dougherty, P.M. (1997) Equations for estimating loblolly pine branch and foliage weight and surface area distributions, Canadian Journal of Forest Research. 27, 918–927

Basara, J.B, Illston, B.G, Winning, T.E. and Fiebrich, C.A (2009) Evaluation of Rainfall Measurements from the WXT510 Sensor for Use in the Oklahoma City Micronet. The Open Atmospheric Science Journal, 3, 39–47.

Beckett, K.P. Freer-Smith, P.H. Taylor, G. 2000. *The capture of particulate pollution by trees at five contrasting urban sites.* Arboricultural Journal. 24: 209–230

Bhaskaran, S, Paramananda, S. and Ramnaryan, M. (2010) Per-pixel and object-oriented classification methods for mapping urban features using Ikonos satellite data. Applied Geography, 30, 650-665

Brandtberg T, Warner T, Landenberger RE, and McGraw JB (2003) Detection and analysis of individual leaf-off tree crowns in small footprint, high sampling density LiDAR data from the eastern deciduous forest in North America. *Remote Sensing of Environment*, 85, 290−303.

Bulletin of the American Meteorological Society, 90: 922–923.

Campbell Scientific Ltd. (2010) ARG100 Tipping Bucket Raingauge: User Guide. [Online] Available from: ftp://ftp.campbellsci.com/pub/csl/outgoing/uk/manuals/arg100.pdf [Accessed 21 December 2010].

Chen Y, Su W, Li J, Sun Z. (2009) Hierarchical object oriented classification using very high resolution imagery and LIDAR data over urban areas. Advances in Space Research, 43, 1101-1110.

Christen A, Crawford B, Liss K, Siemens C. 2010 Soil properties at the Vancouver EPiCC experimental sites. *Environmental Protection in Canadian Cities Technical Report No. 2*

Christen A, Crawford B, Liss K, Siemens C. 2010 Soil properties at the Vancouver EPiCC experimental sites. *Environmental Protection in Canadian Cities Technical Report No. 2*

Christen, A, and R. Vogt, 2004: Energy and radiation balance of a central European city. *International Journal of Climatology*, **24,** 1395-1421

Clark, M.L, Clark, D.B. and Roberts, D.A. (2004) Small-footprint LiDAR estimation of sub-canopy elevation and tree height in a tropical rain forest landscape, Remote Sensing of Environment, 9 (1), 68–89.

Coutts, A, J. Beringer, and N. Tapper, 2007a: Characteristics influencing the variability of urban CO_2 fluxes in Melbourne, Australia. Atmos. Environ, 41, 51-62.

Coutts, A, J. Beringer, and N. Tapper, 2007b: Impact of increasing urban density on local climate: Spatial and temporal variations in the surface energy balance in Melbourne, Australia. J. Appl. Meteor. Clim, 46, 477-493.

Del Campo L, R Pérez-Sáez, X Esquisabel, I Fernández, MTello, 2006: New experimental device for infrared spectral directional emissivity measurements in a controlled environment. Review of Scientific Instruments, 77,113 111.

Delta-T 1998 *Theta probe soil moisture sensor: type ML2 user manual ML2-UM-1.* Delta-T Devices Ltd.

Delta-T 1999 *Theta probe soil moisture sensor: type ML2x user manual ML2x-UM-1.2.1.* Delta-T Devices Ltd.

Delta-T 2010 *User manual for SM300 soil moisture sensor – SM300-UM-1.1.* Delta-T Devices Ltd, Cambridge, UK.

ERG – KCL: Environmental Research Group – King's College London

GATS Inc. (2009) Spectral calculator, atmospheric gas spectra, infrared molecular absorption spectrum [Online]. Available from: http://www.spectralcalc.com/spectral_browser/db_intensity.php. [Accessed 15th December 2009].

Getter K & Rowe D (2006) The role of green roofs in sustainable development. HortScience. 41, 1276–1286

Goodwin, N.R, Coops, N.C, Tooke, T.R, Christen, A, and Voogt, J.A. (2009) Characterizing urban surface cover and structure with airborne LiDAR Technology. *Canadian Journal of Remote Sensing*. 35, 297-309.

Grant G (2006) Extensive Green Roofs in London. Urban Habitats, 4 (1), 51-65

Griffith, DWT & Jamie IM (2000) Fourier transform infrared spectrometry in atmospheric and trace gas analysis. *Encyclopaedia of Analytical Chemistry*. Meyers, R. A, Ed. Chichester: John Wiley & Sons Ltd

Griffith, DWT (2006) MALT 5 User's Guide, Version 5.2. [Electronic document] Available with MALT 5 software.

Grimmond CSB, HA Cleugh, and TR Oke, 1991: An objective urban heat storage model and its comparison with other schemes. Atmos. Environ, 25B, 311-326.

Grimmond CSB, Oke TR (1999) Aerodynamic properties of urban areas derived, from analysis of surface form. Journal of Applied Meteorology 38:1262-1292

Grutter M (2003b) Multi-gas analysis of ambient air using FTIR spectroscopy over Mexico City. Atmosfera. 16. 1-13.

Grutter, M, Flores, E, Basaldud, R. & Ruiz-Suarez, L. G. (2003a) Open-path FTIR spectroscopic studies of the trace gases over Mexico City. *Atmospheric Ocean Optics*. 16. 232-236.

Harrison, R.M. (2001) Pollution: causes, effects and control. Cambridge: RSOC.

Hinsley SA, Hill, RA, Gaveau DLA & Bellamy PE (2002) Quantifying woodland structure and habitat quality for birds using airborne laser scanning. *Functional Ecology*, 16, 851– 857.

Holmgren J, Persson Å (2004) Identifying species of individual trees using airborne laser scanner. Remote Sensing of Environment 90:415-423

Honjo T and Takakura T (1990-91) Simulation of thermal effects of urban green areas on their surrounding areas. Journal of Energy and Buildings, 15–16, 443–446.

http://aurn.defra.gov.uk/

http://badc.nerc.ac.uk/home/index.html
http://cf-pcmdi.llnl.gov/
http://geography.kcl.ac.uk/micromet/index.htm
http://geography.kcl.ac.uk/micromet/wordpress/?page_id=425,
http://livingroofs.org/2010022858/green-roof-types/greenrooftypes.html (17 April 2011)
http://livingroofs.org/2010030161/green-roof-types/intens.html
http://ukclimateprojections-ui.defra.gov.uk
http://weather.lgfl.org.uk/
http://weather.lgfl.org.uk/qgraphs.aspx
http://weather.lgfl.org.uk/qtables.aspx
http://www.bauder.co.uk/media-centre/
http://www.bauder.co.uk/media-centre/project-gallery
http://www.geog.ubc.ca/~epicc/reports/Vancouver-EPiCC-Tech-Report-2.pdf
http://www.greenbuildingpress.co.uk/article.php?article_id=700
http://www.greenbuildingpress.co.uk/article.php?article_id=700
http://www.greenroofs.com/projects/pview.php?id=1066
http://www.greenroofs.com/projects/pview.php?id=393
http://www.greenroofs.com/projects/pview.php?id=510
http://www.greenroofs.com/projects/pview.php?id=549
http://www.greenroofs.com/projects/pview.php?id=550
http://www.greenroofs.com/projects/pview.php?id=648
http://www.greenroofs.com/projects/pview.php?id=660
http://www.greenroofs.com/projects/pview.php?id=77
http://www.greenroofs.com/projects/pview.php?id=85
http://www.greenroofs.com/projects/pview.php?id=894
http://www.greenroofs.com/projects/pview.php?id=91
http://www.greenroofs.com/projects/pview.php?id=95
http://www.langley.co.uk/asx/six_acres_case_study_-_newsletter.pdf
http://www.langley.co.uk/asx/stonegrove_case_study.pdf
http://www.langley.co.uk/asx/william_gunn_case_study.pdf
http://www.lda.gov.uk/Documents/Economic_Development_Strategy_%282010%29_6543.pdf
http://www.lgfl.net/learningresources/curriculum/geography/weatherstations/pages/weatherstations.aspx
http://www.london.gov.uk/shaping-london/
http://www.london.gov.uk/shaping-london/london-plan/
http://www.london.gov.uk/shaping-london/london-plan/docs/london-plan.pdf
http://www.london.gov.uk/shaping-london/london-plan/docs/london-plan.pdf
http://www.london.gov.uk/thelondonplan/about.jsp [accessed 12 March 2011]
http://www.london.gov.uk/thelondonplan/caz/central_activities.jsp
http://www.london.gov.uk/thelondonplan/caz/central_activities.jsp
http://www.london.gov.uk/thelondonplan/docs/londonplan08.pdf
http://www.londonair.org.uk/london/asp/datadownload.asp

http://www.londonair.org.uk/london/asp/default.asp
http://www.londonair.org.uk/london/asp/default.asp
http://www.meto_ce.gov.uk/climate/uk/averages/19712000/sites/greenwich.html
http://www.metoffice.gov.uk/
http://www.tfl.gov.uk/corporate/13980.aspx
http://www.unidata.ucar.edu/software/netcdf/Unidata
http://www.urbanhabitats.org/v04n01/london_pdf.pdf
http://www.vaisala.com/Vaisala%20Documents/Technology%20Descriptions/RAINCAP_Technology.pdf
http://www.wunderground.com/
http://www.wunderground.com/history/
https://code.zmaw.de/projects/cdo/

Järvi, J, et al, 2009: The urban measurement station SMEAR III: Continuous monitoring of air pollution and surface-atmosphere interactions in Helsinki, Finland. Boreal Env. Res, 14 (suppli. A), 86-109.

Kaimal J. and J. Finnigan, 1994: Atmospheric Boundary Layer Flows: Their Structure and Measurement. Oxford University Press, New York, 289 pp.

[1]Kim, S,. McGaughey, R.J, Andersen, H.E, Schreuder, G. (2009) Tree species differentiation using intensity data derivedfrom leaf-on and leaf-off airborne laser scanner data. *Remote Sensing of Environment,* 113, 1575-1586.

Knott W (2011) LiDAR: An Application for Measuring Urban Vegetation Parameters? A London Case Study. Independent Geographical Study, King's College London, 64 pp.

LAEI 2006. London Atmospheric Emissions Inventory 2006. Compiled by AEA, March 2009. (http://static.london.gov.uk/mayor/environment/air_quality/research/emissions-inventory.jsp)

Lanza, L.G. and Vuerich, E. (2009) The WMO Field Intercomparison of Rain Intensity Gauges. Atmospheric Research, 94, 534–543.

Lee X, J Finnigan, and K Paw U, 2004: Handbook of Micrometeorology : A guide for Surface Flux Measurement and Analysis, chap. Coordinate Systems and Flux Bias Error, Chapter 3. Kluwer Academic Publishers, Dordrecht.

Lee, A.C. and Lucas, R.M. (2007) A LiDAR derived canopy density model for tree stem and crown mapping in Australian forests Original Research Article. Remote Sensing of Environment, 111(4), 493-518.

Lefsky, MA (1997) Application of LiDAR remote sensing to the estimation of forest canopy and stand structure, Ph.D. thesis, Department of Environmental Science, University of Virginia, Charlottesville, VA

Lindberg F and Grimmond CSB (2011). The influence of vegetation and building morphology on shadow patterns and mean radiant temperatures in urban areas: London case study – Under review

Lindberg F, CSB Grimmond (2011) The influence of vegetation and building morphology on shadow patterns and mean radiant temperatures in urban areas: London case study, *Urban Ecosystems* (in review)

Lindberg F, Grimmond CSB (2011) The influence of vegetation and building morphology on shadow patterns and mean radiant temperatures in urban areas: Model development and evaluation. Theoretical and Applied Climatology DOI10.1007/s00704-010-0382-8

Living Roofs and Walls Report GLA 2008a

Livingroofs.org
London Councils (2004) [online]. Available from: www.londoncouncils.gov.uk.
London Natural History Society (2011) Londons Wildlife Habitats. [online]. Available from: http://www.lnhs.org.uk/habitats.htm last accessed 10/12/10.
Mauder, M, et al, 2007: The energy balance experiment EBEX-2000. part ii: Intercomparison of eddy-covariance sensors and post-field data processing methods. Bound. Lay. Met, 123, 29_54.
Mayor of London (2011) [online]. Available from: http://www.london.gov.uk/streettrees/ last accessed 7th February 2011.
McGaughey, R.J. (2009) FUSION/LDV: Software for LiDAR Data Analysis and Visualization. United States Departmentof Agriculture, Seattle.
Met Office, 2010
Moriwaki, R. and M. Kanda, 2004: Seasonal and diurnal fluxes of radiation, heat, water vapor, and carbon dioxide over a suburban area. J. Appl. Meteor, 43, 1700-1710.
Münkel et al. 2007
Næsset E (2004) Accuracy of forest inventory using airborne laser scanning: evaluating the first Nordic full scale operational project. Scandinavian journal of forest research.19, 554-557.
Nemitz E, K Hargreaves, A McDonald, J Dorsey, and D Fowler, 2002: Micrometeorological measurements of urban heat budget and CO_2 emissions on a city scale. Environ. Sci. Technol, 36, 3139-3146.
Offerle B, CSB Grimmond, K Fortuniak, K Klysik, and TR Oke, 2006: Temporal variations in heat fluxes over a central European city centre. Theor. Appl. Climatol, 84, 103-115.
Office of National Statistics 2001
Oke TR (2004) Initial Guidance to Obtain Representative Meteorological Observations at Urban Sites. IOM Report 81, World Meteorological Organization, Geneva.
Oke, T. (1987) *Boundary Layer Climates*. London: Methuen and Co. Ltd.
Operant LLC (2009) Essential FTIR – FTIR Software. [Online]. Available from: http://www.essentialftir.com/ [Accessed 10th November 2009].
Ordinance Survey (2010) © Crown database right 2010. An Ordnance Survey/EDINA supplied service. Assessed 2009-10-13
Pohjola, H, Konkola, L, Hoikkanen, M. and Schultz, D.M. (2008) Adjusting radar-derived QPE with measured drop-size distributions at the surface. *In: The fifth European conference on radar meteorology and hydrology.* ERAD.
Popescu SC, Wynne RH, and Nelson RF (2003) Measuring individual tree crown diameter with lidar and assessing its influence on estimating forest volume and biomass. *Canadian Journal of Remote Sensing*, 29, 564–577.
Pu, R, P. Gong, R. Michishita, and T. Sasagawa, 2006: Assessment of multiresolution and multi-sensor data for urban surface temperature retrieval. Remote Sens. Environ, 104, 211-225.
R Development Core Team, 2005: R: A language and environment for statistical computing. Vienna, Austria, R Foundation for Statistical Computing, URL http://www.R-project.org, ISBN 3-900051-07-0.
Reitberger, C, Schnörr, P, Krzystek and Stilla, U. (2009) 3D segmentation of single trees exploiting full waveform LIDAR data. ISPRS Journal of Photogrammetry and Remote Sensing, 64 (6), 561–574.

Roberts, S.D, Dean, T.J, Evans, D.L, McCombs, J.W. and Harrington R.L. (2005) Estimating individual tree leaf area in loblolly pine plantations using LiDAR-derived measurements of height and crown dimensions, Forest Ecology and Management, 213, 54–70.

Robinson P (2010) The London Meteorological Monitoring Network. MSc Environmental Monitoring, Modelling and Management Thesis, King's College London, London, UK

Rothman, L. S. et al. (2005) The HITRAN 2004 molecular spectroscopic database. Journal of Quantitative Spectroscopy and Radiative Transfer. 96. 139 – 204.

Rowell DL 1994 *Soil science methods & applications.* Longman, Harlow, UK. 350pp

Rowell DL 1994 *Soil science methods & applications.* Longman, Harlow, UK. 350pp

Schmid et al. (2003).

Schotanus P, F Nieuwstadt, and H. de Bruin, 1983: Temperature measurements with a sonic anemometer and its application to heat and moisture fluxes. Bound. Lay. Met, 26, 81-93.

Source overview map: http://www.bing.com/maps/print.aspx?mkt=en-gb&z=13&s=c&cp=51.518190,-0.060062&poi=Blackwall%20Tunnel%2C%20London%20SE10%200&pp=skhf41gzzvm1&b=1&pt=pb

Stewart ID, and TR Oke (2009). Conference notebook– A new classification system for urban climate sites.

Streutker, D.R. and Glenn, N.F. (2006) LiDAR measurement of sagebrush steppe vegetation heights. *Remote Sensing of Environment*, 10, 135-145.

Tallis, M, Freer-Smith, P, Sinnett, D. & Taylor, G, 2011. *Estimating the removal of atmospheric particulate pollution by the urban tree canopy of London under current and future developments.* Landscape and Urban Planning – Under review.

Tharpa, R. B. and Murayama, Y. (2009) Urban mapping, accuracy, & image classification: A comparison of multiple approaches in Tsukuba City, Japan. Applied Geography, 29, 135-144.

Upmanis H, Eliasson I, Lindqvist S (1998) The influence of green areas on nocturnal temperatures in a high latitude city (Goteborg, Sweden). International Journal of Climatology, 18, 681-700.

van Dijk, A, A. Moene, and H. de Bruin, 2004: The Proinciples of Surface Flux Physics: Theory, Practice and Description of the ECPACK library.

Velasco E, S Pressley, E Allwine, H Westberg, and B Lamb, 2005: Measurements of CO_2 fluxes from the Mexico City urban landscape. Atmos. Environ, 39, 7433-7446.

Vesala T, et al, 2008: Surface-atmosphere interactions over complex urban terrain in Helsinki, Finland. Tellus, 60B, 188-199.

Webb E, G Pearman and R Leuning, 1980: Correction of the flux measurements for density effects due to heat and water vapour transfer. Quart. J. R. Met. Soc,106, 85-100.

Wilczak J, S Oncley, and S. Stage, 2001: Sonic anemometer tilt correction algorithms. Bound. Lay. Met, 99, 127-150.

Williams, M.L. 2007. UK air quality in 2050—synergies with climate change policies. *Environ. Sci. Policy*, 10: 169-175.

www.metoffice.gov.uk

Annex 4 - Gliwice case study in situ measurements

Turbulent fluxes

authors: Christian Feigenwinter, Roland Vogt

Material and methods

Site and instrumentation

The site is located on a building of the Silesian University of Technology on a balcony at the side of a gable roof (50°17'38.01"N, 18°40'53.21"E). The building up to the gable is approx. 25 m high. The mast was installed in the balcony and was 8 m high, i.e. the top of the mast is ≈3 m above the gable. The distance to the gable is ≈6 m. The line gable-to-mast points towards SW. In the direction WNW in approximately 70 m there is a higher roof which is a disturbing obstacle.

In Table 1 the instruments are listed. Fig. 1 shows the close environment of the site while Fig. 2 the station is displayed with 1 km circle.

Table 1. Overview on instrumentation at the flux tower in Gliwice

Variable	Frequency	Equipment
Meteorological mast 8 m		
Eddy-Covaraince system		CS Data-Logger CR1000
Wind vector (u,v,w)	10 Hz	Young 81000V
Temperature fluctuations	10 Hz	Young 81000V
Conc. of H_2O and CO_2	10 Hz	LiCor LI-7500
Air Temp. and humidity	1 min	Vaisala HMP45
Components of net radiation SW up/down, LW up/down	1 min	Kipp & Zonen CNR1

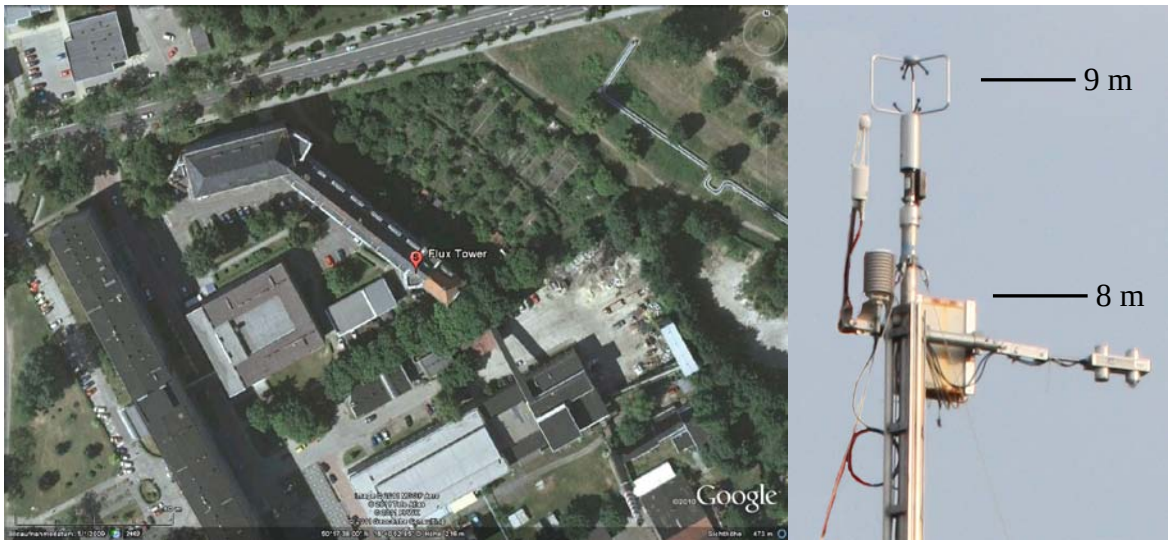

Fig. 1. Left: Close surrounding of the flux tower in Gliwice. Scale in lower left of the picture. Right: Instruments at top of the mast

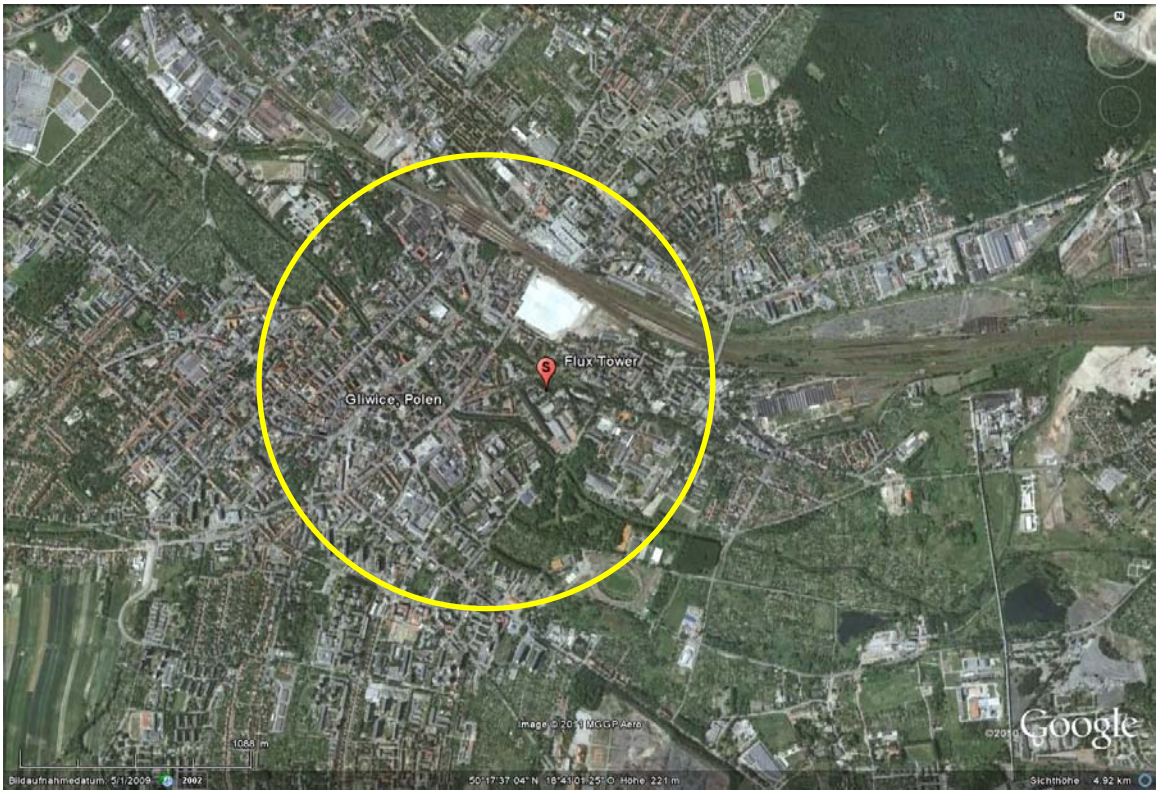

Fig. 2. City of Gliwice with the flux tower. 1 km circle around station

Methods

The raw covariances (half hourly means) were rotated into a streamline coordinate system according to McMillen (1988). Sensible heat flux was calculated using the sonic temperature corrected for buoyancy effects of humidity fluctuation on the speed of sound (Schotanus et al., 1983). Latent heat flux and CO_2 flux were adjusted after Webb et al. (1980) to compensate for the fluctuations of temperature and water vapor that affect the measured fluctuations in the density of CO_2 and H_2O.

Measurements of sonic anemometers (i.e. the Young 81000V) and open path gas analyzers (Li-7500) are subject to errors during rainfall. Rainy periods were therefore excluded from the analysis. Further on there were some longer periods of power failure. Fig. 3 gives an overview on data availability. Monthly totals were calculated from monthly daily means to account for missing data.

Maintenance of the station was performed every 2 weeks. Windows of the Li-7500 were cleaned with ethanol and the domes of the CNR1 were cleaned with distilled water. Storage card was exchanged and data was backed up. Raw data (the 10 Hz time series) are kept for further analysis.

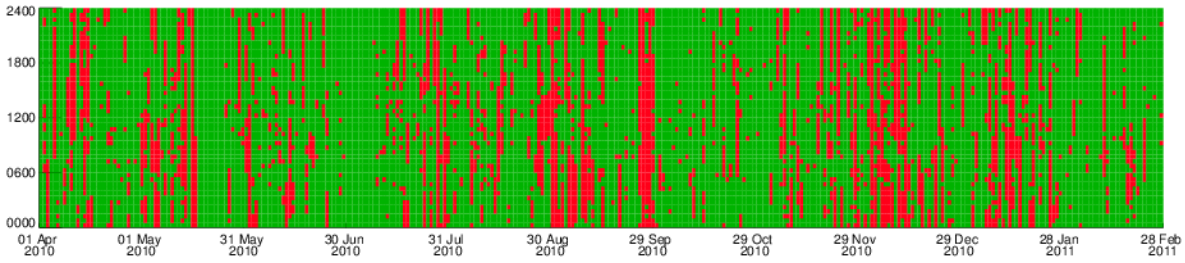

Fig. 3. Overview on data availability. Red color marks missing or bad data (≈23 %).

Results

Meteorological conditions

Fig. 4 shows the mean monthly temperature and the mean specific humidity for the time period under consideration. Fig. 5 and Fig. 6 show the wind statistics for the whole period and for every month of the time period under consideration. Main wind directions were the SSW-NNW sector and the eastern sector. Wind regimes are very variable from month to month and probably depend heavily on the dominating synoptic situation, e.g. June is dominated by winds from the North-West, while August is dominated by south-westerly winds. Some months show frequent easterly winds during nighttime (e.g. APR, MAY, JUL, SEP, OCT, FEB). However, in general, the patterns during daytime and nighttime are very similar due to the flat terrain and the absence of large water bodies. Note that the sector from NW to NE may be influenced by the roof of the nearby building.

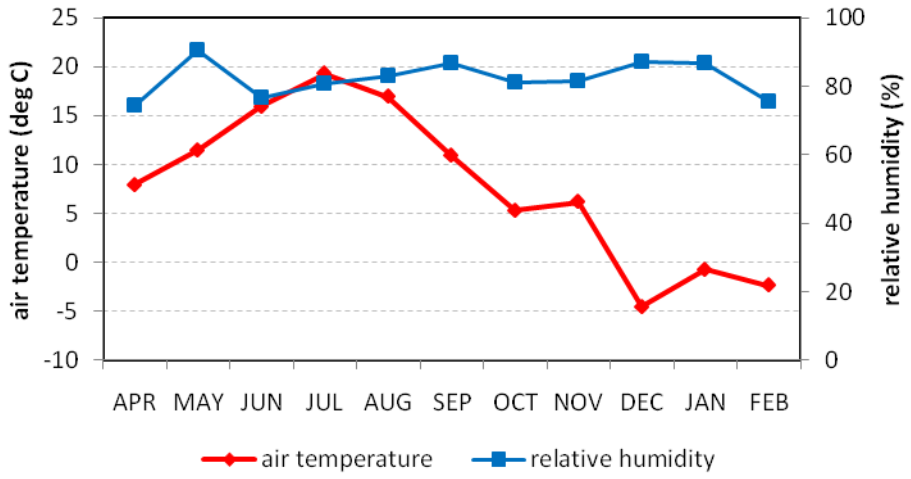

Fig. 4. Mean monthly air temperature and relative humidity from APR 2010 to FEB 2011

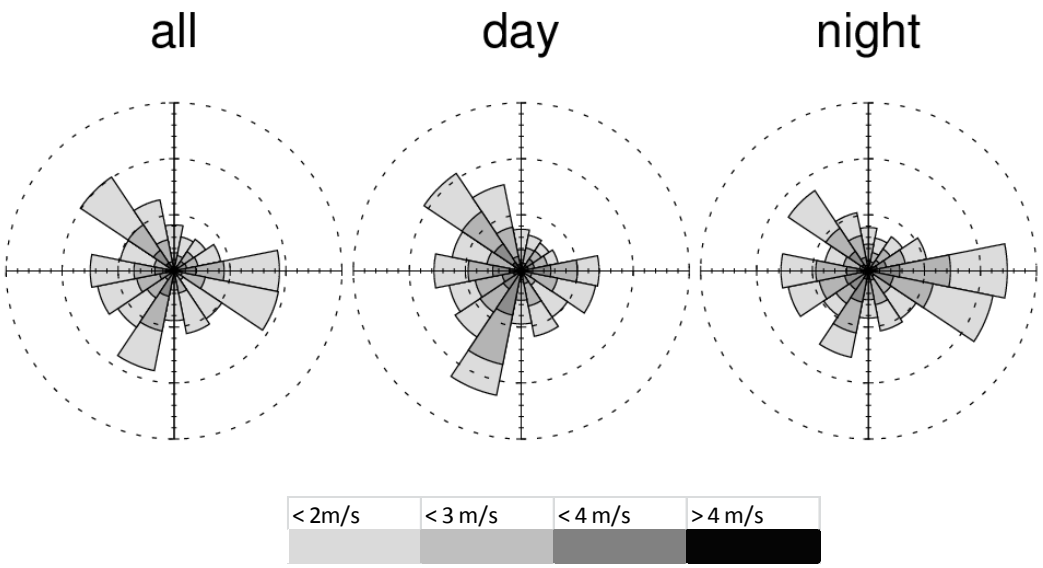

Fig. 5. Wind statistics for the period from APR 2010 to FEB 2011. Left: all data, center: daytime data (8 am to 4 pm). Right: nighttime data (8 pm to 4 am). Circles refer to a frequency of 5, 10 and 15 %

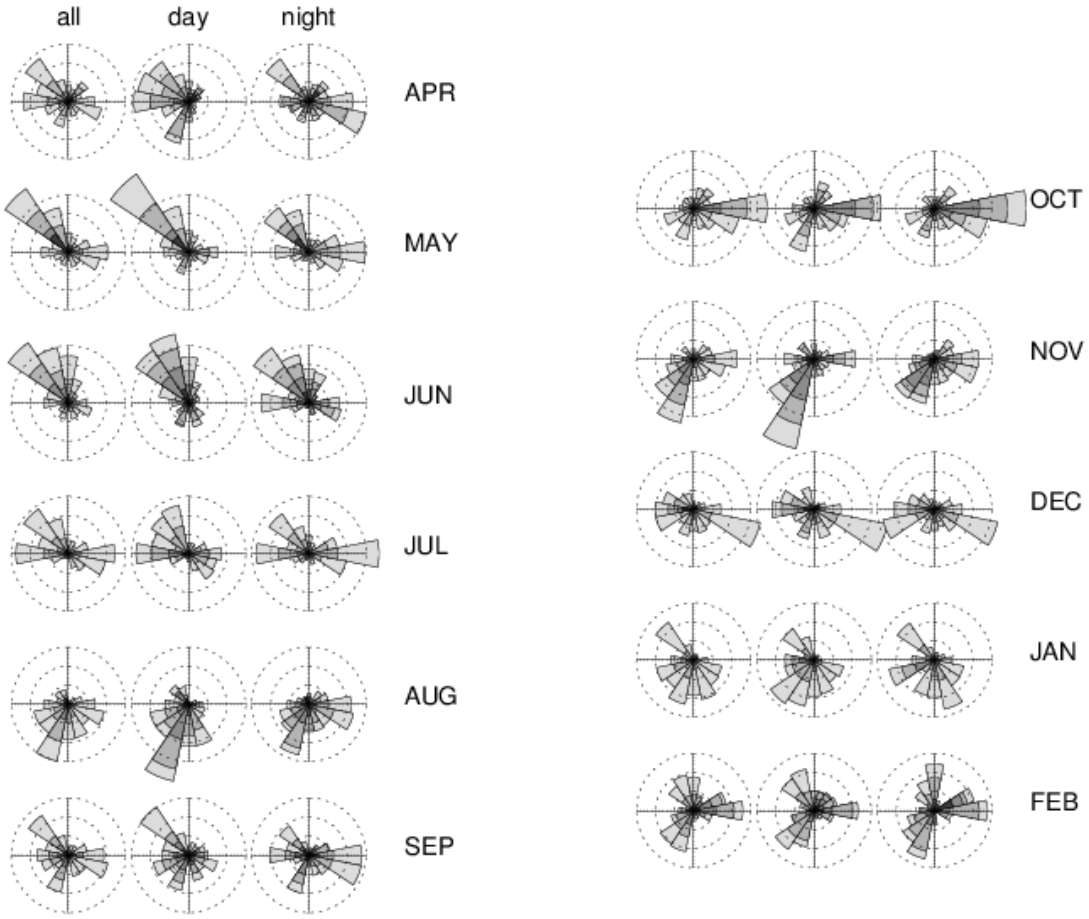

Fig. 6. As fig. 5 but for monthly wind statistics for the period from APR 2010 to FEB 2011

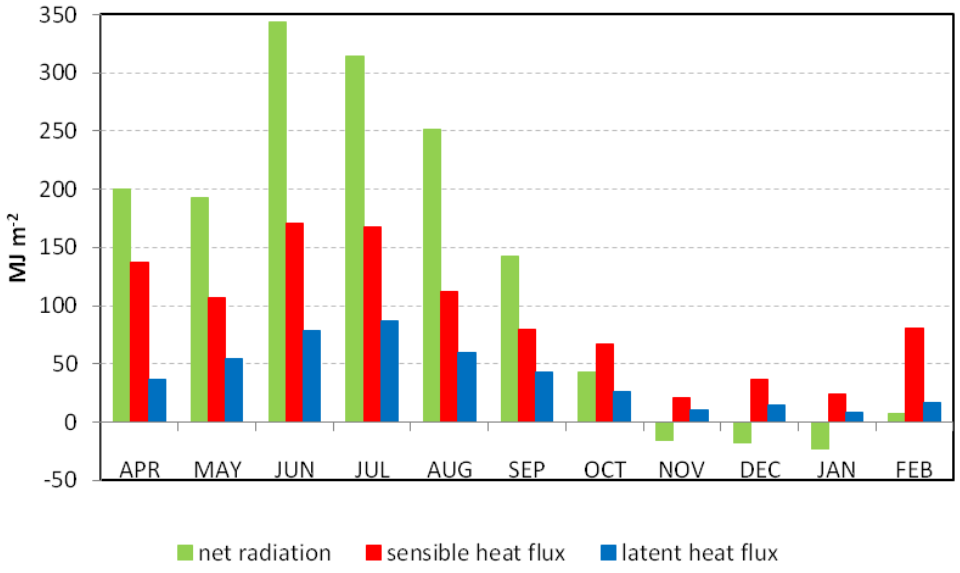

Fig. 7. Monthly sums of net radiation, sensible and latent heat flux

Fluxes (Latent heat, sensible heat, net radiation, CO_2 flux, CO_2 concentration)

Fig. 7 shows the monthly sums of net radiation and sensible and latent heat flux. As expected, summer months show the highest energy input and accordingly the largest heat fluxes. Net radiation becomes negative in winter. During May 2010 unusually wet conditions prevailed and resulted in below average net radiation. Low net radiation in Nov/Dec/Jan may also be associated with snow and/or ice covered radiation instruments. February 2011 was dominated by fine weather and many clear days.

Fig. 8 shows a detailed view on the monthly mean diurnal course of net radiation and its components short/long wave downward/upward radiation. Low monthly sums in Fig. 7 correspond to low peak values around midday in Fig. 8. Note that during wintertime snow covered radiation sensors may give erroneous measurements of the radiation terms. This was obviously the case in DEC and resulted in a long-wave balance that was close to zero. A more detailed analysis of such events would require reliable precipitation data.

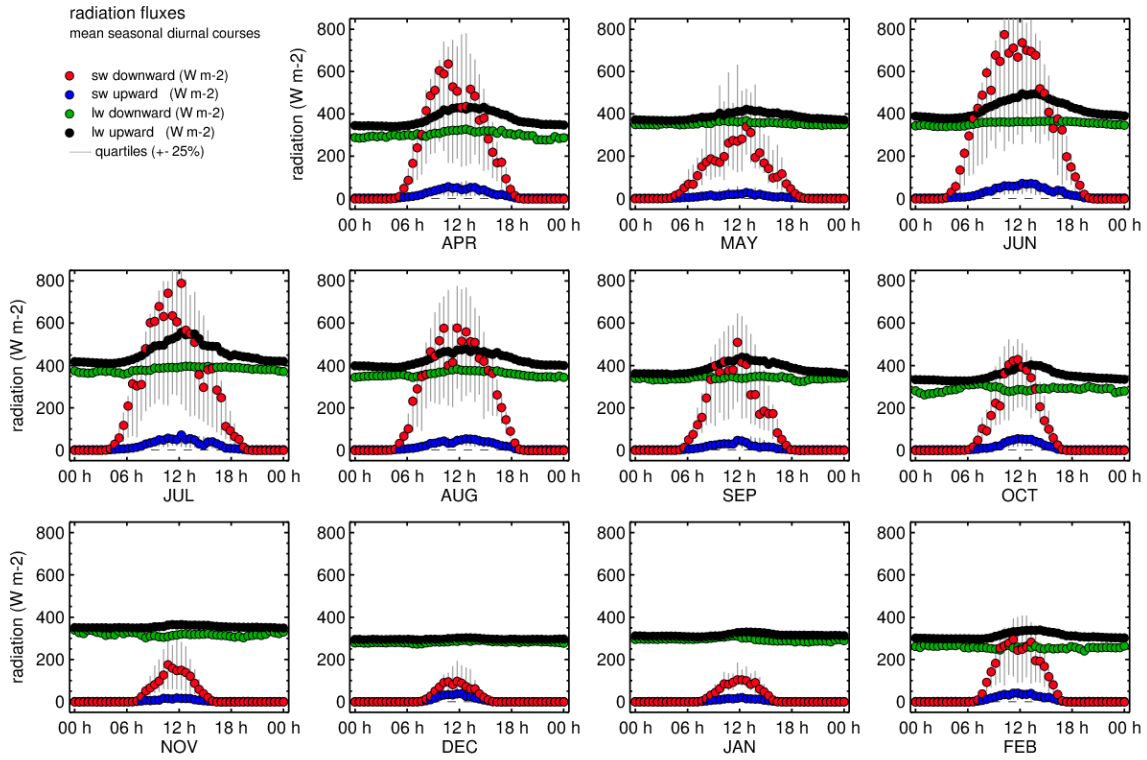

Fig. 8. Average diurnal courses of radiation balance terms

The mean diurnal courses of sensible and latent heat flux are shown in Fig. 9. As expected the sensible heat flux dominates evapotranspiration during the whole year, which is typical for cities because the different land use compared to rural environments (large impervious areas and reduced vegetation). Table 2 shows that sensible heat flux accounted for 53% and latent heat flux for 15% of net radiation during peak hours (11h to 13h), respectively, when averaged for the whole measurement period. Monthly percentages are also presented in Table 2.

Table 2. Percentage of sensible and latent heat flux during peak hours of net radiation (11 pm to 1 am)

	APR	MAY	JUN	JUL	AUG	SEP	OCT	NOV	DEC	JAN	FEB	AVG
H/Rn	53%	43%	41%	42%	36%	42%	51%	58%	91%	54%	74%	**53%**
LE/Rn	11%	18%	14%	19%	15%	17%	12%	11%	23%	13%	10%	**15%**

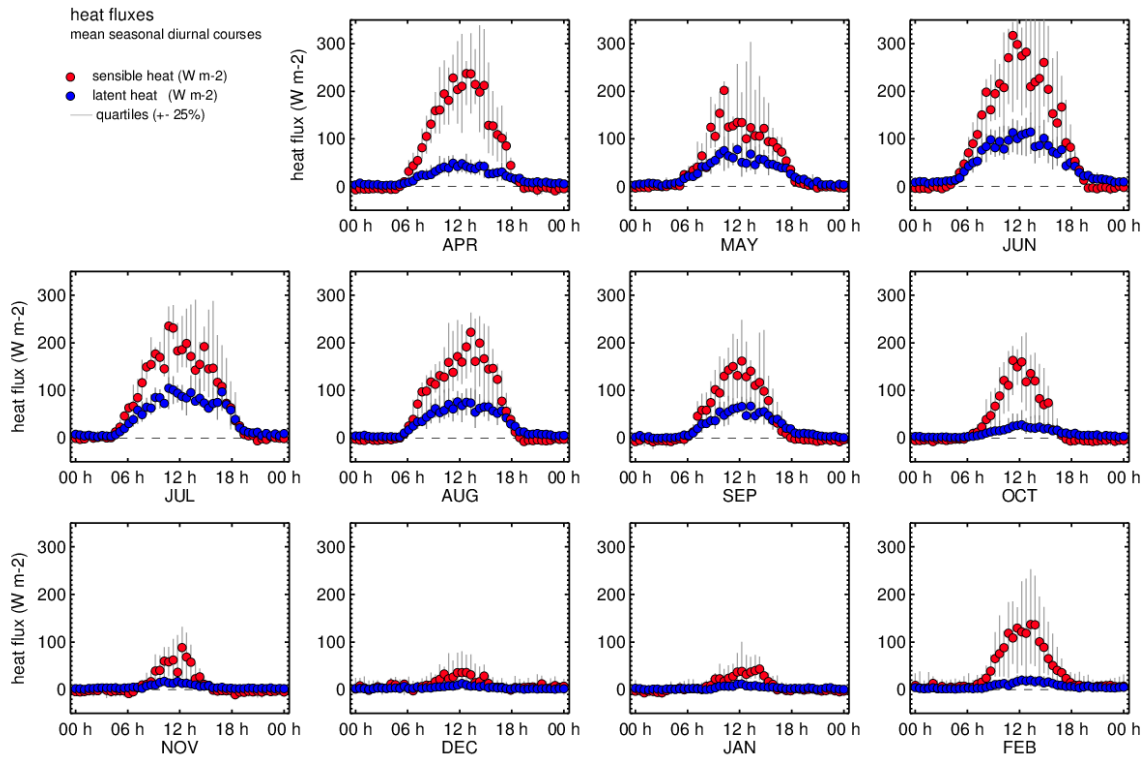

Fig. 9. Average diurnal courses of sensible and latent heat flux

Fig. 10 gives an overview on monthly mean diurnal courses or CO_2 flux. Lowest CO_2 flux values were measured during the vegetation period in JUN/JUL/AUG/SEP (partly). During these months the mean diurnal courses of CO_2 flux and CO_2 concentration in Fig. 10 and Fig. 11 show a minimum around midday, which is related to photosynthesis of the vegetation in the footprint of the flux tower. On the other hand, during fall/winter months OCT/NOV/DEC/JAN/FEB CO_2 flux peaks around midday, while CO_2 concentration is more or less uniform.

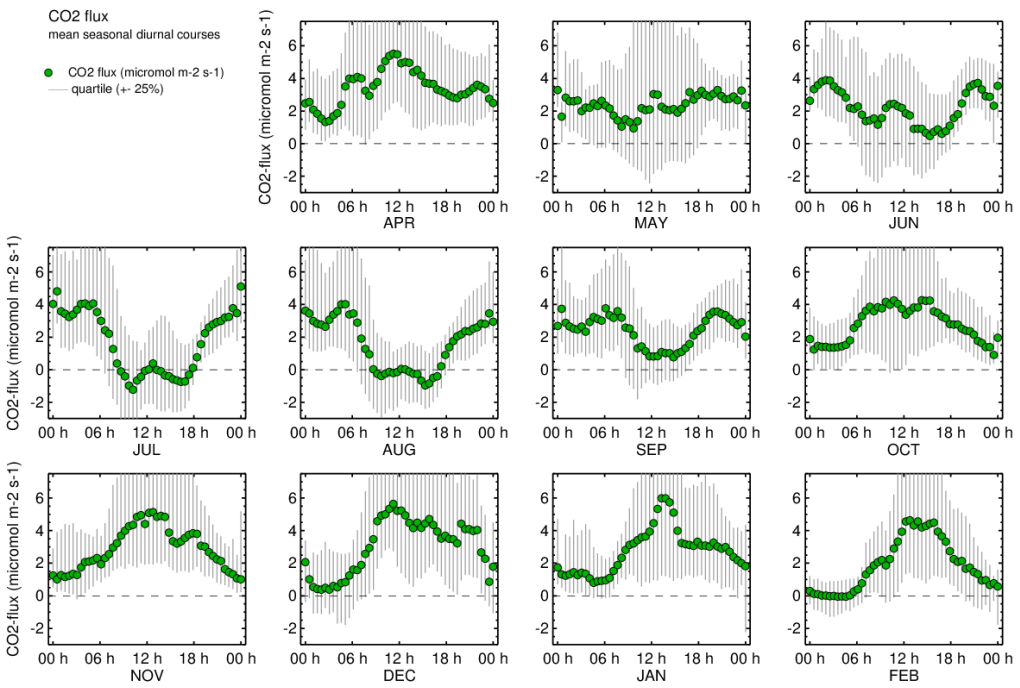

Fig. 10. Average diurnal courses of CO_2 flux

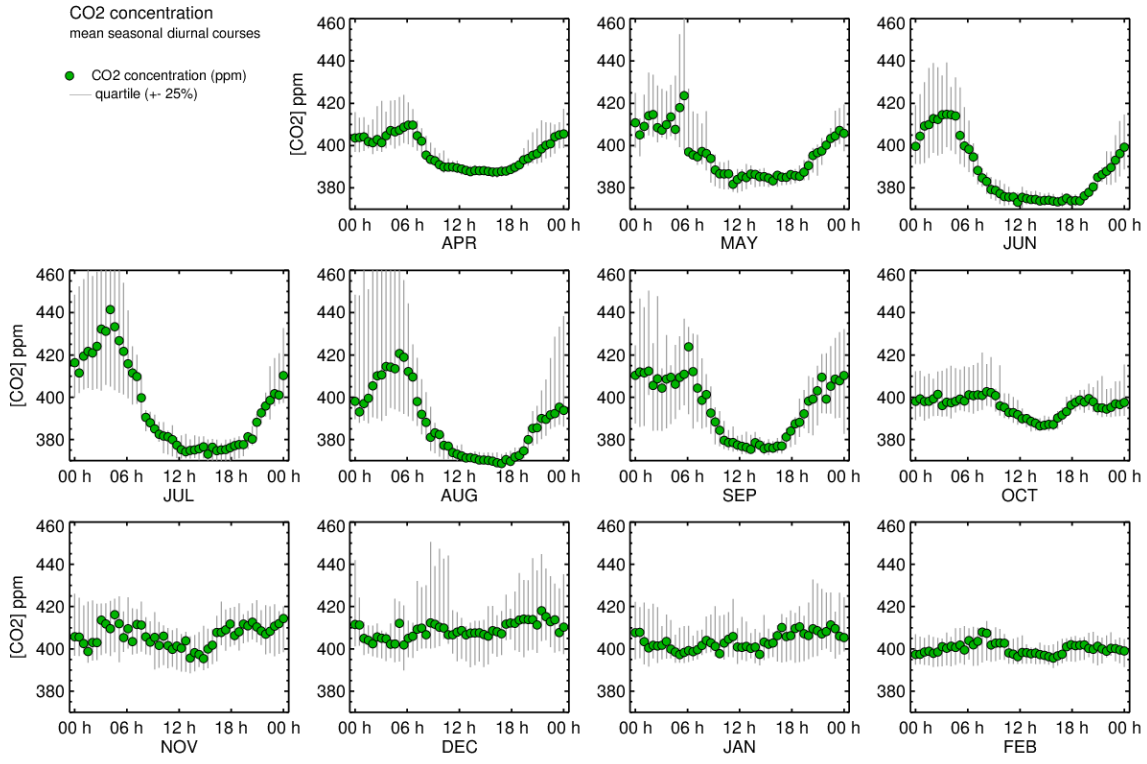

Fig. 11. Average diurnal courses of CO_2 concentration

If analyzed for weekdays, the mean diurnal courses of CO_2 flux for weekends (SAT/SUN) in Fig. 11 show minimum values during the day, while for working days MON-FRI a prominent peak around midday and partly a secondary maximum in the evening can be observed. MON-FRI daytime values are related to increased traffic volume.

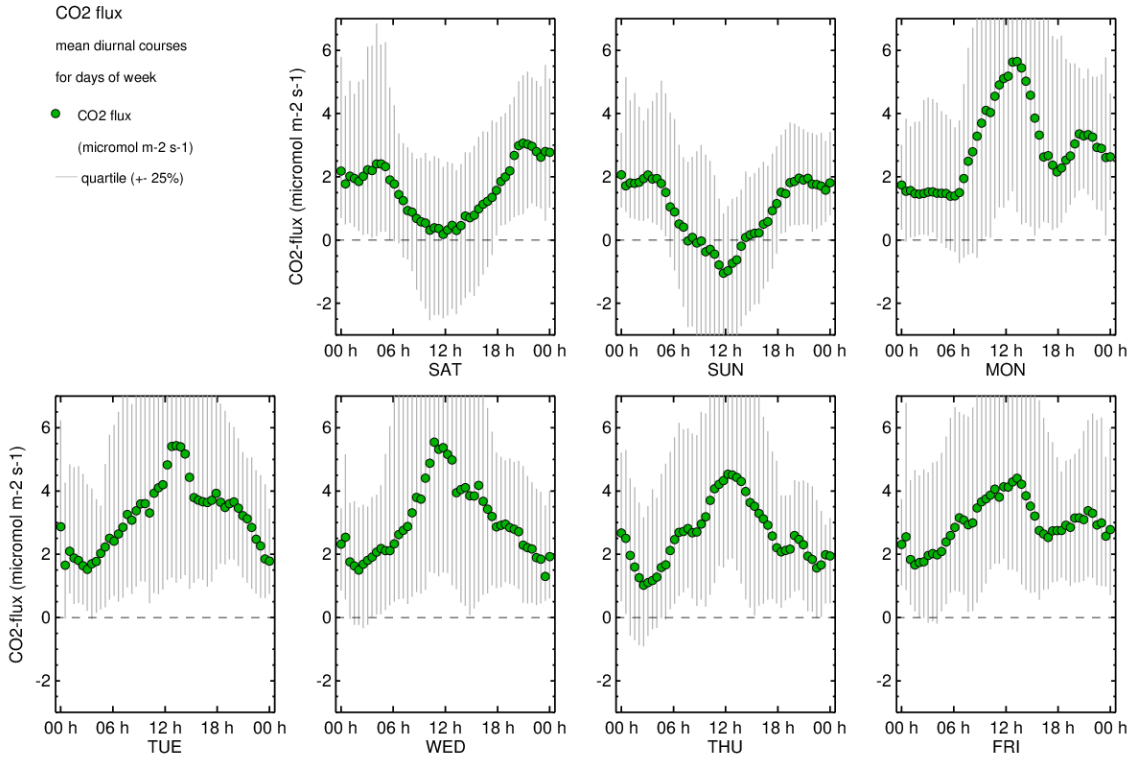

Fig. 12. Average diurnal courses (weekdays) of CO_2 flux

Monthly CO_2 exchange was always positive (Fig. 12), i.e. the flux is directed upward and the source area of the measurement station is a source of CO_2 throughout the year. This means that the emission of CO_2 prevails over the uptake. Based on mean monthly net fluxes shown in Fig. 13 the estimated total annual flux is 2.8 kg CO_2 m^{-2} $year^{-1}$. This is probably a too low value when compared with other studies. Local influences are dominating at the measurement site. The relation between mean monthly air temperature and total monthly CO_2 exchange shown in Fig. 14 is surprisingly good if data from JAN/FEB are excluded from the calculation of the regression line. CO_2 exchange and air temperature are negatively correlated, low temperatures relate to high CO_2 exchange and vice versa. Though the shape and the direction of this ratio are typical for cities, absolute values are highly site specific and may not be regarded as representative for the city of Gliwice.

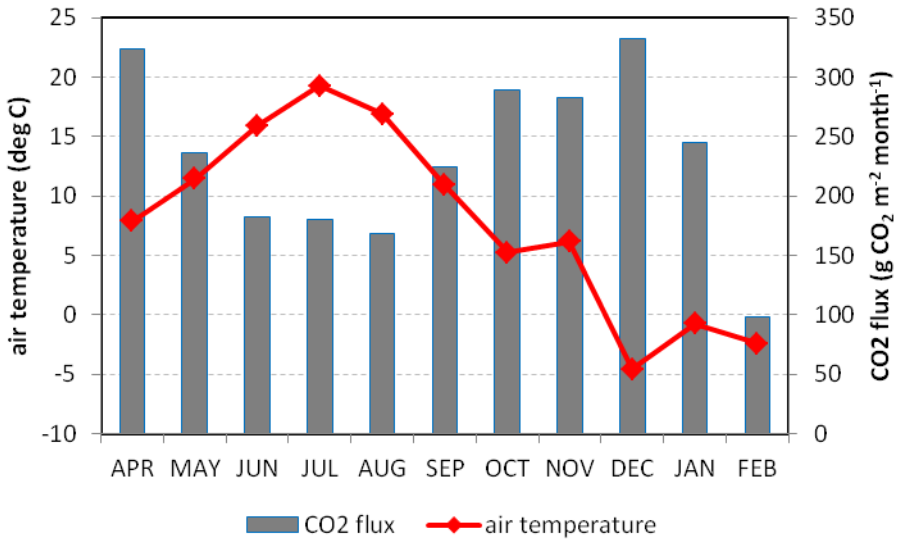

Fig. 13. Monthly sums of CO_2 exchange and mean monthly air temperature

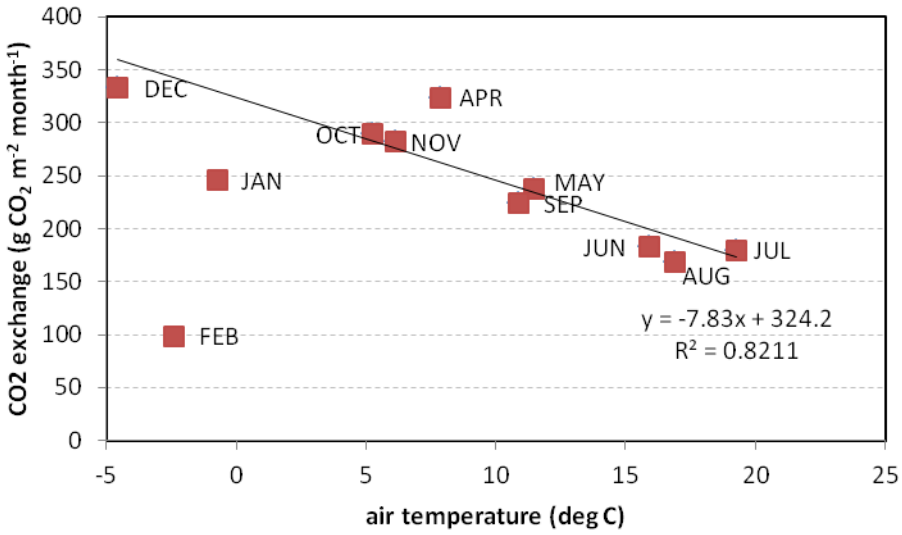

Fig. 14. Relation between mean monthly air temperature and total monthly CO_2 exchange. Regression line calculated with exclusion of JAN and FEB data points

Summary

Measurements of the Gliwice flux tower are presented for the period from APR 2010 to FEB 2011. Average and total values of the whole measurement period are shown as well as monthly averages/sums and mean monthly diurnal courses of radiation, energy and CO_2 fluxes. Main features are:

- Positive CO_2 flux dominates over the whole period which means that the source area of the flux tower is a net source of CO_2 regardless of the season. However, the source is reduced during the vegetation period in summer.
- CO_2 flux shows a strong linear dependence on air temperature, i.e. high CO_2 fluxes are related to low air temperatures.
- Significant differences in mean diurnal courses calculated for weekdays suggest a specific weekly variability with lower emissions of CO_2 during weekends due to reduced car traffic and industrial activities.

Air Quality

authors: Tomasz Staszewski

Characteristic of air quality was elaborated based on continuous measurements carried out at Voivodeship Inspectorate of Environmental Protection monitoring station in Gliwice, and reported online (http://stacje.katowice.pios.gov.pl/monitoring/).

Table 3. Characteristics of air pollution in Gliwice in 2008

Compound	Averaging period	Permissible level of compound in the air [μg/m^3]	Permissible incidence of exceedance in year	Data for Gliwice
Nitrogen dioxide	1 hour	200 a)	18 times	Maximum value 130 μg/m^3 Lack of exceedances
	Year	40 a)	-	26 μg/m^3
Nitrogen oxides	Year	30 b)	-	43 μg/m^3
Sulfur dioxide	1 hour	350a)	24 times	Maximum value = 145 μg/m^3 Lack of exceedances
	24 hours	125 a)	3 times	Maximum value = 75 μg/m^3 Lack of exceedances
	Year	20 b)	-	11 μg/m^3
	8 hours	120a)	20 days	Maximum value = 130 μg/m^3 8 days with exceedance
Ozone*	Growing period (1 V - 31 VII)	24000b) [(μg/m^3)×h]	-	3276 (μg/m^3)×h
Particulate matter	24 hours	50a)	35 times	**68 times**
PM10	Year	40a)	-	**45 μg/m^3**
Benzene	Year	5 a)		1.8 μg/m^3
Benzo(a)pyrene	Year	5 a)		3.3 μg/m^3

a) Admissible value considering human health protection,
b) Admissible value considering plants protection,
* Data for ozone were taken from the Monitoring Station in Zabrze 10 km far from Gliwice

In Gliwice in the measurement period of 2008 the Polish standards for concentrations of NO_x and PM10 were exceeded (Official Journal of Laws No. 87 item 796 of 2002) (Table 3).

Maximal concentrations of SO_2 NO_2, NO_x, and PM10 were found in the winter-time, (Fig. 15, Fig. 16, Fig. 17 and Fig. 18).

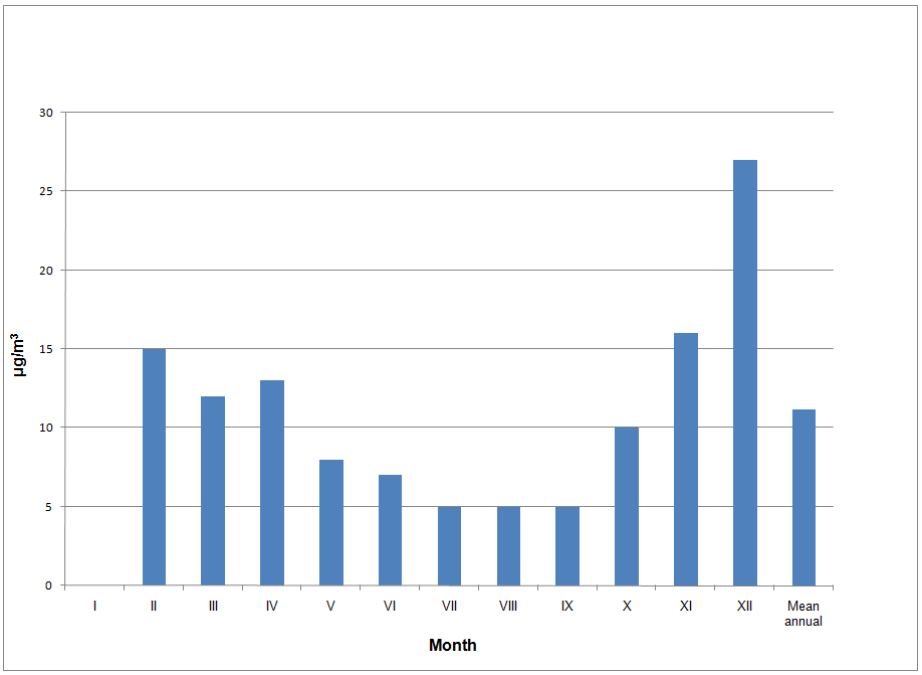

Fig. 15. Mean monthly and annual SO_2 concentrations in Gliwice in 2008

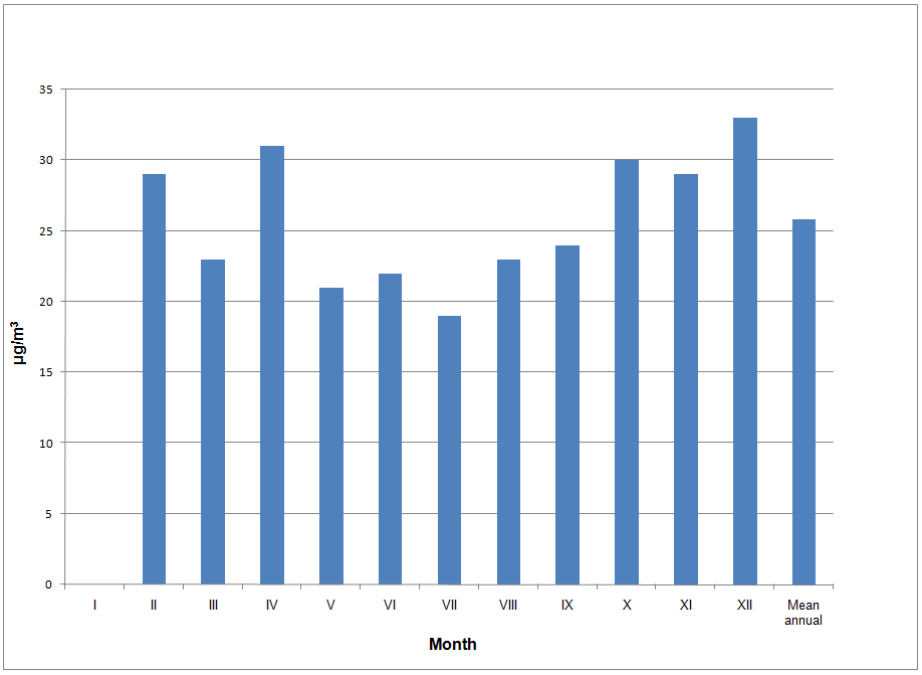

Fig. 16. Mean monthly and annual NO2 concentrations in Gliwice in 2008

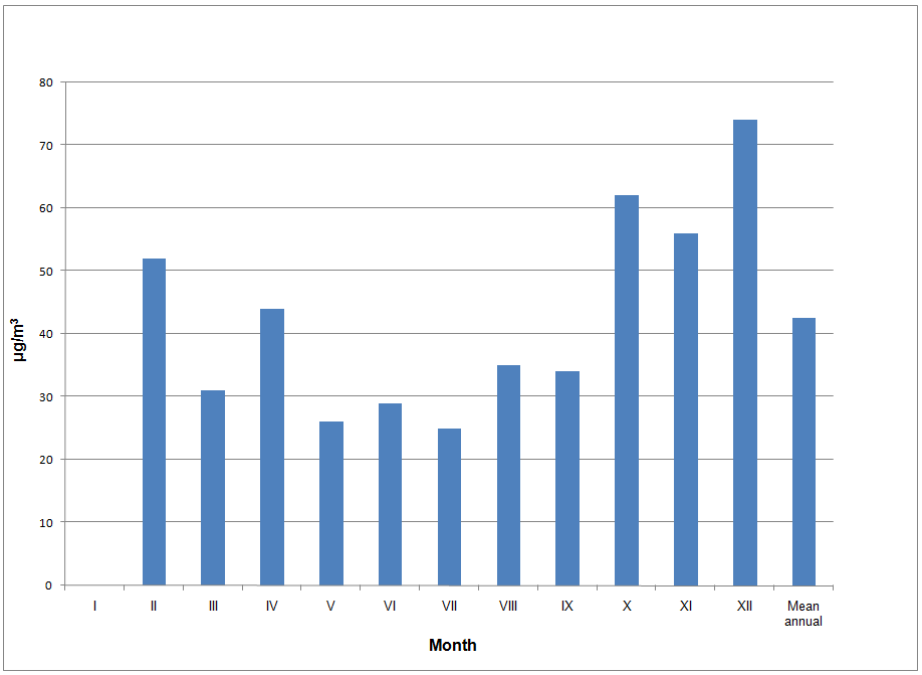

Fig. 17. Mean monthly and annual NOx concentrations in Gliwice in 2008

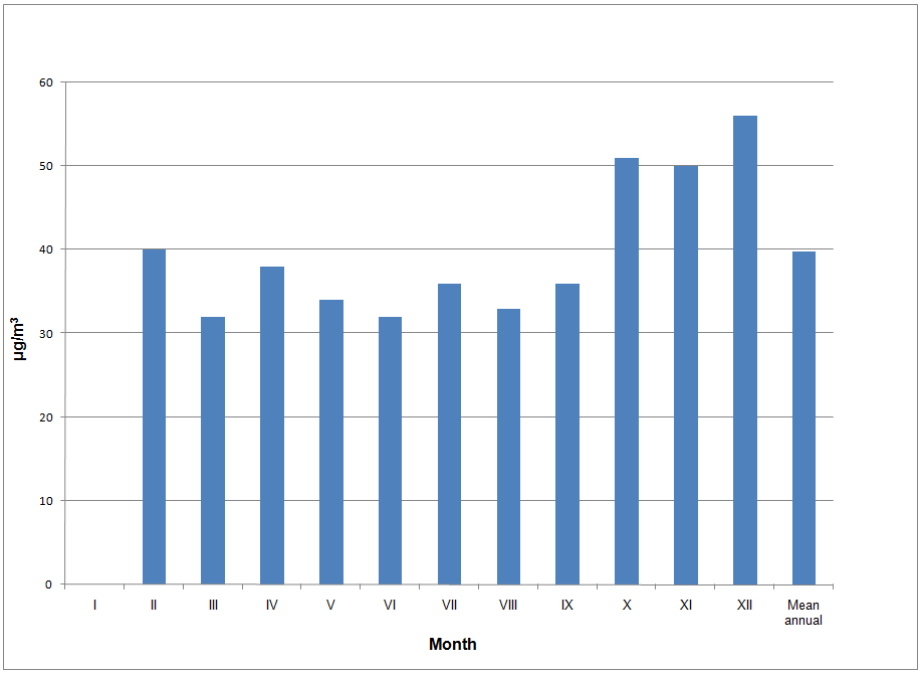

Fig. 18. Mean monthly and annual PM10 concentrations in Gliwice in 2008

Adversely to primary air pollutants, for ozone – secondary air pollutant the highest concentrations in spring–summer time were observed (Fig. 19).

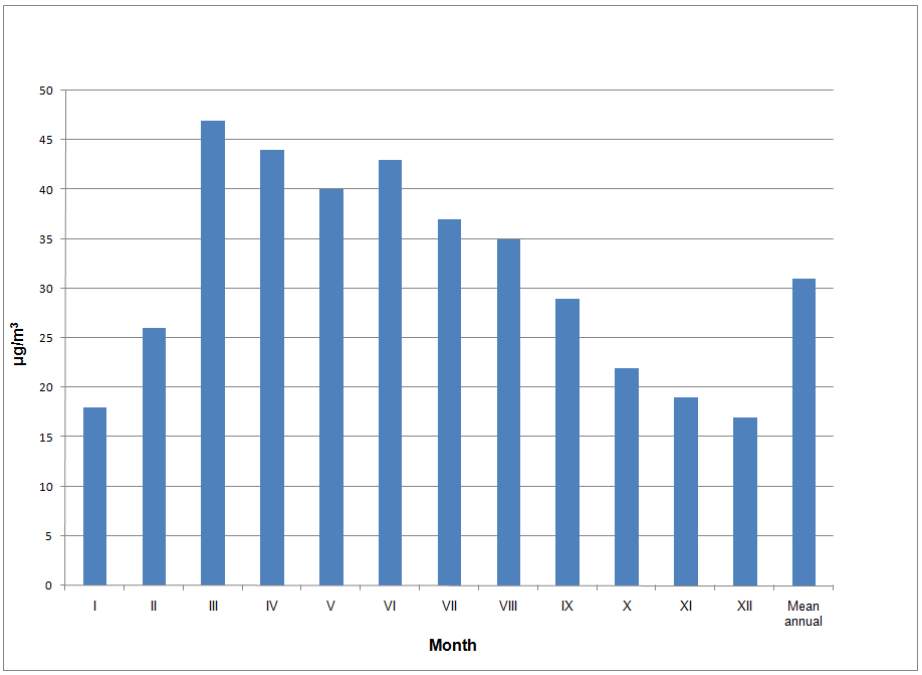

Fig. 19. Mean monthly and annual O3 concentrations in Gliwice in 2008

Generally, monthly pattern of air pollutants levels testifies to effect of low emissions on the air quality in Gliwice.

On the basis of the measurements and mathematical modeling was shown that the permissible mean annual concentrations of BaP and PM10 were exceeded in a whole Upper Silesian Agglomeration area (Fig. 20 and Fig. 21). In Gliwice the exceedance of 24 hour permissible level of BaP has occurred practically in the entire town area. The highest concentrations were found in Sobieszowice and Żerniki Districts along the road No 78 (Tarnogórska Str.) and in Bojków District (Fig. 20). The exceedance of 24 hour permissible level of PM10 was found on the area of 115 km^2 inhabited by 168 400 persons (density amounting to 1465 persons/km^2) (Fig. 22).

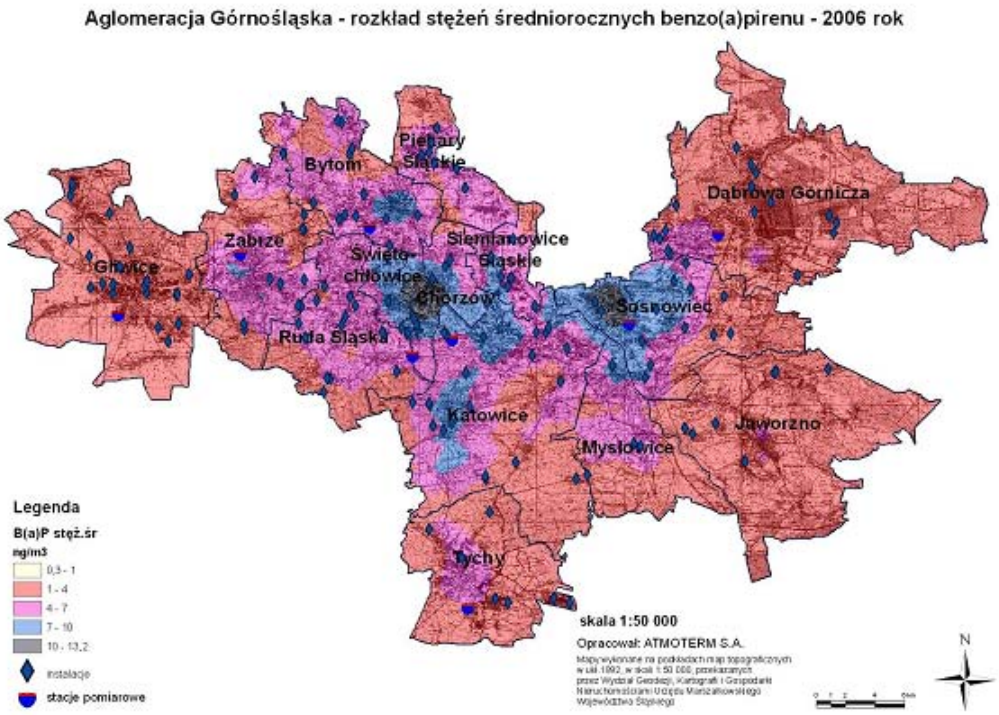

Fig. 20. Upper Silesian Agglomeration – Distribution of mean annual BaP concentrations in 2006

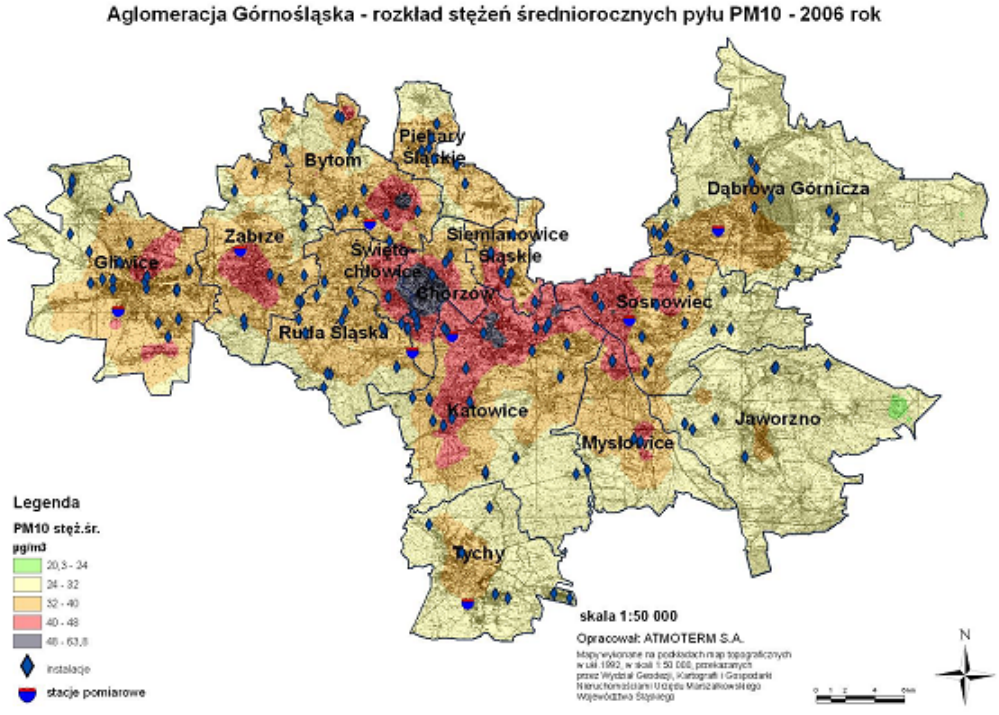

Fig. 21. Upper Silesian Agglomeration – Distribution of mean annual PM10 concentrations in 2006

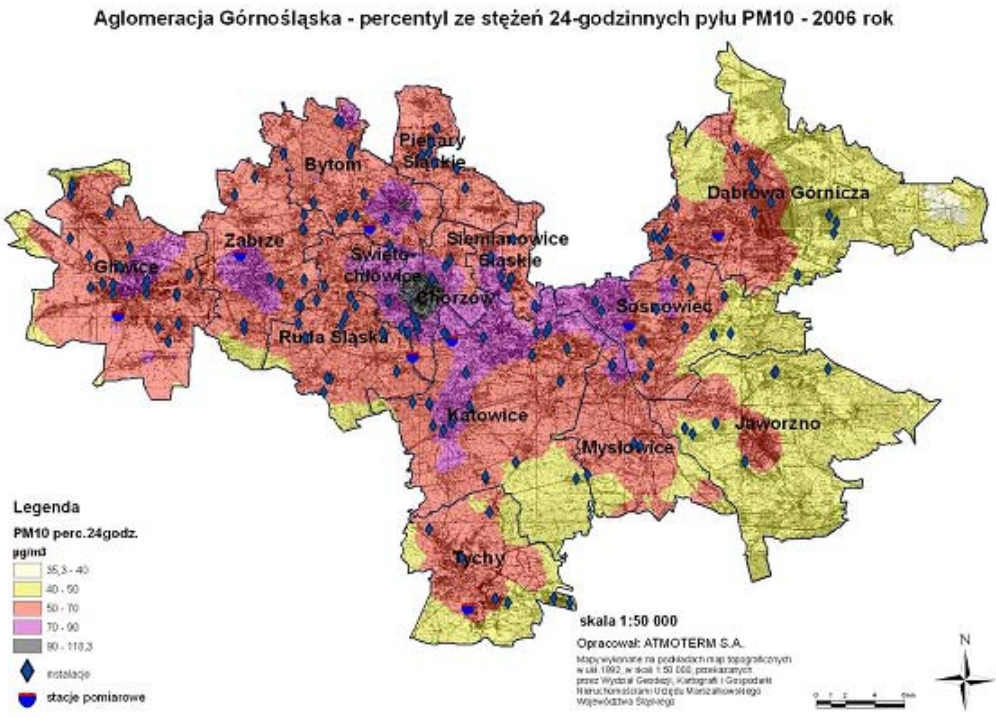

Fig. 22. Upper Silesian Agglomeration – 90.4 percentile of 24-hour average PM10 concentrations in 2006

Exceedance of BaP and PM10 permissible levels is caused be three types of emitters – surface, point and linear.

Emission values for these emitters are presented in Table 4.

Table 4. Emissions of PM10 and BaP from different sources in Gliwice [Mg/year]

Source	**PM10**	**BaP**
Surface	356.5	0.221
Point	314.0	0.069
Linear	127.22	0.0032

In Upper Silesian Agglomeration 35% of the heating needs is covered by a stable fuel combustion in individual combustion sources - 13.1 mln GJ. Modernization and/or liquidation such sources (surface) responsible for the highest emission of air pollutants to the air is a crucial to achieve air quality standards (among others for BaP and PM10). In the "Program Ochrony Powietrza" (http://www.slaskie.pl/zalaczniki/2010/07/01/1277972301/1277974183.pdf, Programme for Air Protection, 2010) established in 2010 two scenarios are proposed which together with the modernization of point and linear emitters should led to the fulfillment of these requirements up to 2020 year. The scenarios for Gliwice are presented in Table 5.

Table 5. Amount of premises subjected to remedial action in Gliwice

	Scenario 1	Scenario 2
	Number of investments in Gliwice	
Replacement of coal boilers with retort boilers	2500	500
Thermo-modernization	400	700
Connection to heat distribution network	1000	2000
Replacement of coal boilers with ecological boilers (e.g. briquette-fired)	50	0
Replacement of coal boilers with gas boilers	1900	2700
Alternative sources (e.g. collectors)	300	150
Total	**6 150**	**6 050**
Cost	**16.4 mln Euro**	**15.9 mln Euro**
Ecological effect [Mg/year] (reduction in emission of PM10)	106.18	106.32
Ecological effect [Mg/ year] (reduction in emission of BaP)	0.067	0.066

Modernization in two other types of emitters comprises:

- *Point emission*s
    - Modernization of heat distribution network belonging to main heat distributors for citizens.
    - Development and integration of heat distribution.
- *Linear emission*
    - Construction of the highway No 1 through Gliwice.
    - Construction of the Intercity Road in Gliwice area.
    - Construction of the western part of Gliwice town Ring Road.

6.5 Stormwater quality and urban hydrology

authors:Tomasz Staszewski, Anicenta Bubak

Data for monthly precipitation in Gliwice in 2008 was elaborated based on continuous daily measurements carried out at Voivodeship Inspectorate of Environmental Protection monitoring station in Gliwice (http://stacje.katowice.pios.gov.pl). Tendency for storming rains was observed during summer months (Fig. 23). Sum of precipitation during two summer months shared in 40% of total annual volume.

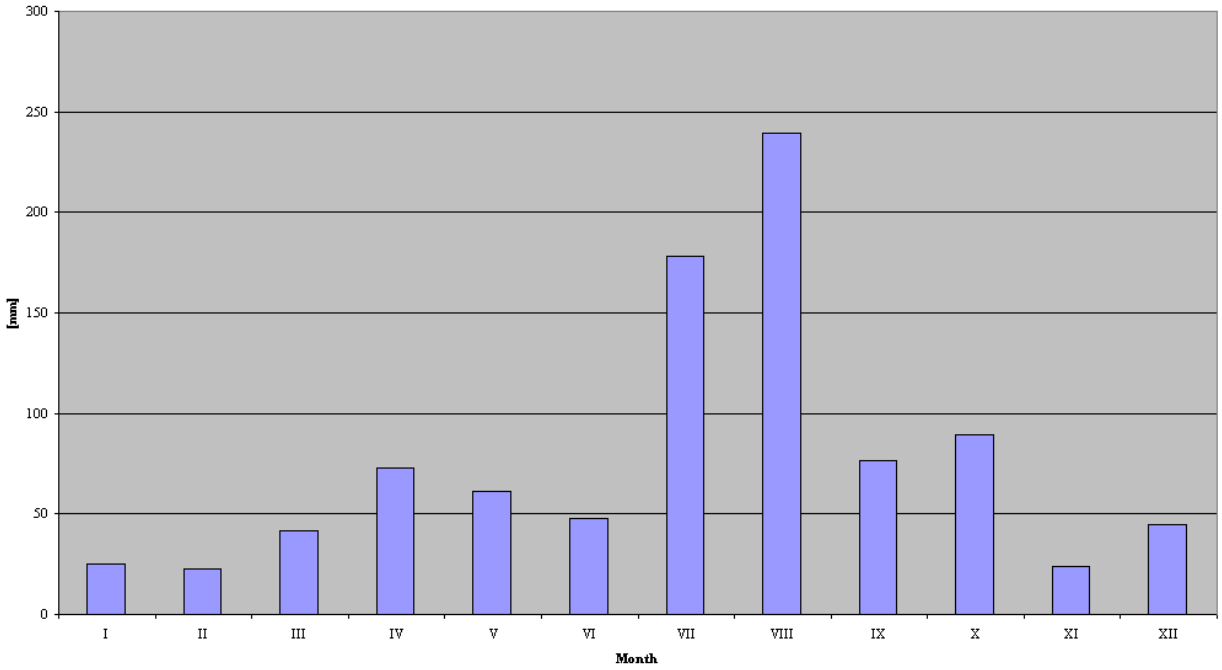

Fig. 23. Monthly precipitation in Gliwice - 2008

Table 6. Indicators of water quality and quantity and water infrastructure in Gliwice

No	Indicator	2008	2009	2010 (months I-X)
1	Water quality and quantity			
2	Urban water use	9 183 336 m^3	8 946 781 m^3	7 457 959 m^3
3	Urban water supply	11 342 394 m^3	11 321 230 m^3	9 447 671 m^3
4	% of waste water treated	55,87%	42,23%	50,21%
5	Infrastructure			
6	Sewage capacity (volume)	7 678 282 m^3	7 456 597 m^3	6 263 653 m^3
7	% of houses connected to the WWT	no data		
8	Volume of discharge	12 000 898 m^3	12 493 719 m^3	12 352 233m^3
9	Water use by sector: households industry others	 6 593 707 m^3 1 818 305 m^3 771 324 m^3	 6 564 776 m^3 1 696 584 m^3 685 421 m^3	 5 376 098 m^3 1 526 380 m^3 555 481 m^3
10	% of population connected to waste water treatment	95%	95%	95%

In Table 6 some indicators related to water quality and quantity and water infrastructure in Gliwice for 2008, 2009 and 2010 received directly from Water Supply and Sanitation Company in Gliwice, as a member of CoP. Year by year, continuous decreasing water consumption was noted, due to rising charges. It was found in all sectors, households, industrial and other activities.

The networks of water-supply and sewerage in Politechnika District are presented in Fig. 24.

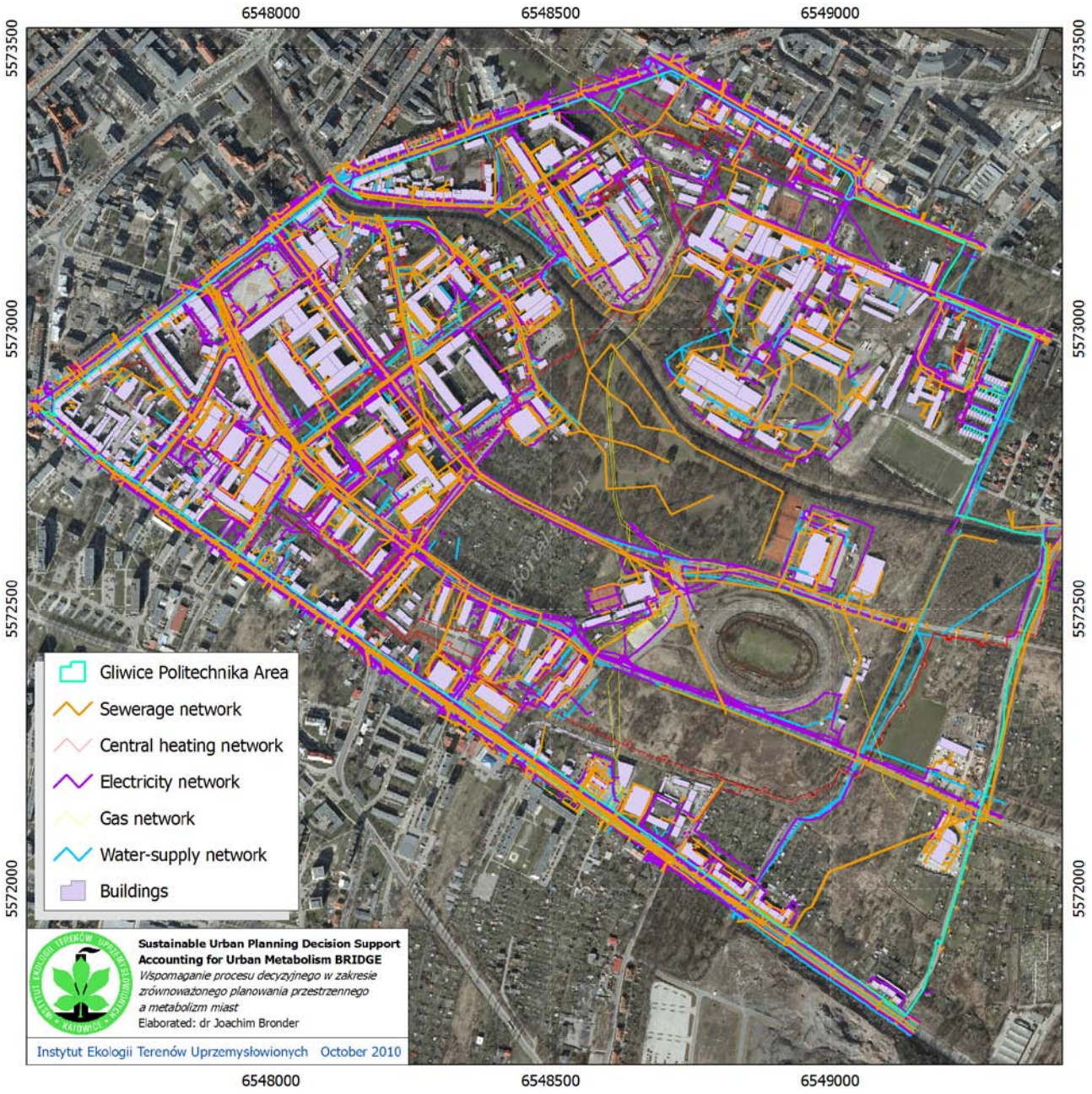

Fig. 24. Water-supply and sewerage networks in Politechnika District

Urban soils & vegetation

authors: Joachim Bronder,Tomasz Staszewski, Włodzimierz Łukasik

The material presented here was elaborated on the data prepared beyond the frameworks of BRIDGE project. The main source of information is digital soil map of Gliwice elaborated on the basis of soil-agriculture map sheets in scale 1:5000. On this map classification of Polish Soil Association from year 1978 is applied.

Soil type

Percentage distribution of soil types within boundaries of Gliwice town is presented in the table (Table 7). According digital soil map of Gliwice, natural and semi-natural soils constitutes about 57% of town area. Among them podzolic and brown soils of different types constitute about 89%.

Table 7. Percentage distribution of soil types in Gliwice

Number	Symbol	English name of Polish classification	Percentage
1	A	podzolic and pseudopodzolic soils	33.73
2	Ad	podzolic and pseudopodzolic soils - deluvial	0.20
3	B	typical brown soils	2.16
4	Bd	typical brown soils - deluvial	0.02
5	Bw	leached brown soils and acid brown soils	14.49
6	Bwd	leached brown soils and acid brown soils - deluvial	0.02
7	D	typical meadow black earth	0.04
8	Dz	degraded meadow black earth and grey soils	1.91
9	Dzd	degraded meadow black earth and grey soils - deluvial	0.07
10	Emt	alluvial muck soils on peat subsoil	0.08
11	Tn	peat soils and half bog soils - fen	0.04
12	F	alluvial soils	4.27
13	RN	agricultural barren land	0.15
14	Ls	woods	0.03
15	PGL, ALP	State Forests National Forest Holding	11.23
16	Tz	built-up areas	25.22
17	dr	roads	0.05
18	W	water bodies	0.04
19	WN	running waters	0.47
20	Wp	unused waters	0.31
21	N	waste land	5.47
	Total	%	100.00
	Total area	ha	13 514.47

Source: Calculation of IETU

In the structure of the Gliwice area, crucial roles play also built-up areas (about 25%) and area belonging to State Forests National Forest Holding (about 11%). As the areas are not occupied by agriculture - soil type is not determined for them.

Spatial distribution of soil types is presented on the map bellow (Fig. 25).

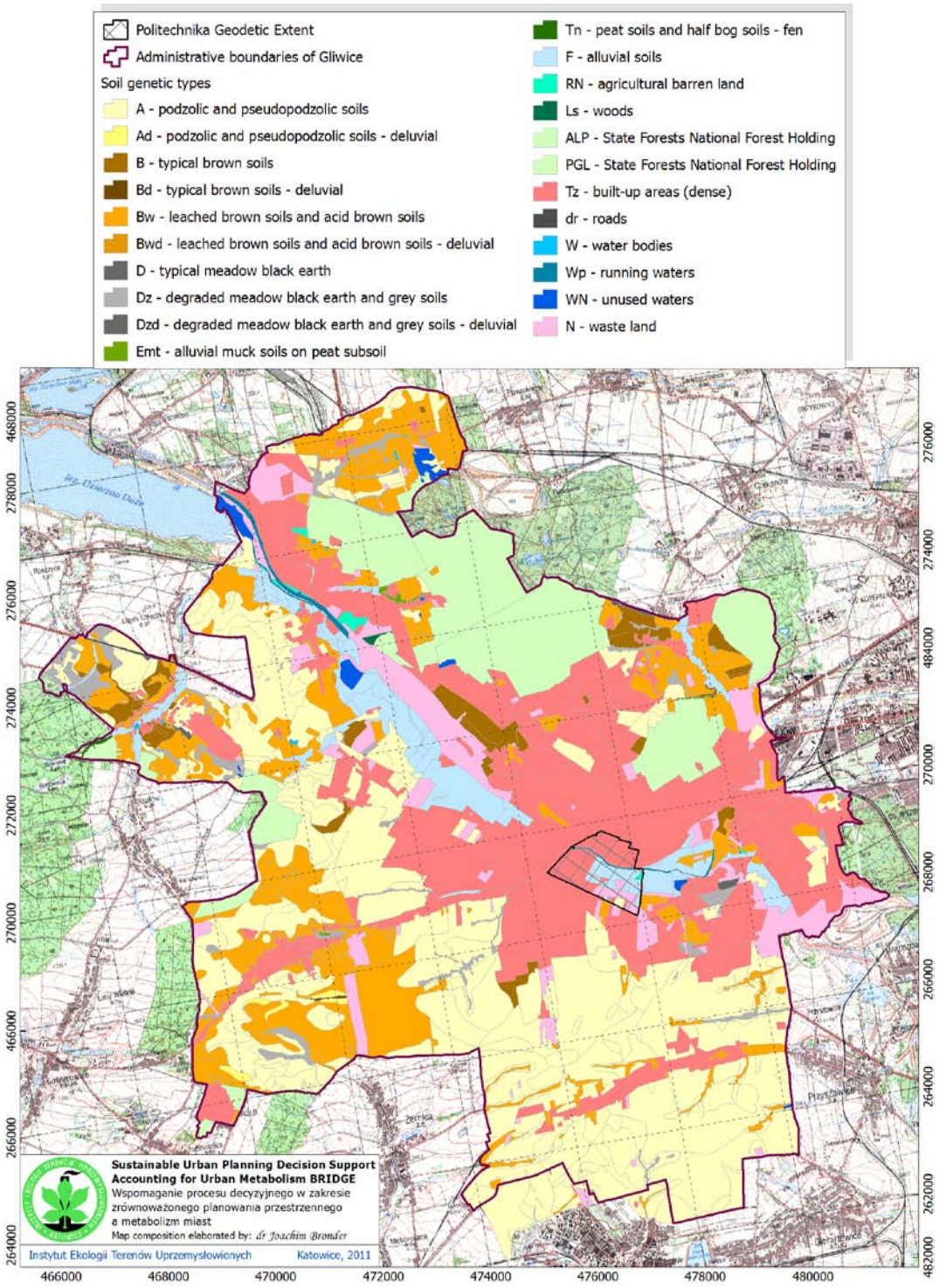

Fig. 25. Soil genetic types

One may see that besides this two above mentioned soil type groups and two types of land use one may see considerable area of alluvial soils crossing through the city. Generally the alluvial soils occupy area of Kłodnica river valley.

Alluvial soils are the only natural soils existing within the boundaries of Politechnika Geodetic Extent.

Soil textural groups

Percentage contribution of given textural group is presented in the Table 8. Detailed spatial distribution of soil textural groups within Gliwice area is presented on the map below (Fig. 26). Within the Gliwice area one may distinguish soils belonging to 13 soil textural classes and 4 textural groups (Table 8, Fig. 26).

Table 8. Percentage distribution of soil textural groups in Gliwice

Number	Symbol	English name of Polish classification	USDA classification	Soil group	Percentage
1	pl	Loose sand	sand	Very light soils	0.17
2	ps	Weakly loamy sand	sand	Very light soils	5.45
3	pgl	Light loamy sand	loamy sand	Light soils	11.09
4	pglp	Silty light loamy sand	loamy sand	Light soils	0.23
5	pgm	Heavy loamy sand	loamy sand	Light soils	3.96
6	pgmp	Silty heavy loamy sand	sandy loam	Medium soils	0.62
7	gl	Light loam	sandy loam	Medium soils	2.06
8	glp	Silty light loam	sandy loam	Medium soils	28.82
9	gs	Medium loam	sandy clay loam	Heavy soils	0.32
10	gsp	Silty medium loam	loam	Heavy soils	1.16
11	gc	Heavy loam	clay loam	Heavy soils	0.06
12	płz	Silt	silt	Heavy soils	0.74
13	płi	Silt loam	silt loam	Heavy soils	18.83
14	sz	Skeleton soils	skeleton soils		0.14
15	-	Shallow soils	shallow soils		0.96
16	no	Soil class uncertain	Class not determined		25.39
	Total	%			100.00
	Total	ha			13514.47

Source: Calculation of IETU

As one may see the dominant soil textural group are sandy loam soils belonging to the group medium soils group. They constitute about 31,5% of the area of Gliwice soils. About 26,5% constitute soils of not determined class, shallow and skeleton soils.

Among soils of determined class medium soils (sandy loam soils) occupy the largest area.

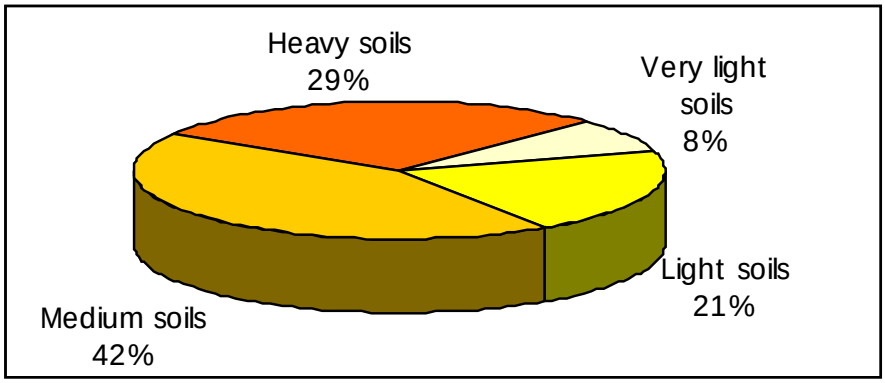

Fig. 26. Contribution of soil groups within agricultural soils of Gliwice town

In spatial distribution one may distinguish three main regions within Gliwice administrative boundaries. The first region - represented by heavy soils (silt and silt loam soils) is situated on the south of the Gliwice municipality. The second – represented by medium soils (sandy loam soils) is located south-west of the Kłodnica river valley. The third - represented by light and very light soils (loamy sand and sand soils) occupies the area north-east of Kłodnica river valley.

Within Politechnika Geodetic Extent one may distinguish soils belonging to the classes of sandy loams and loamy sands. The first class dominates here (Fig. 27).

6.6.3. Soil contamination in Gliwice

Polish Geological Institute caries out the monitoring of the soil contamination in Poland.

Results of this monitoring are published in the form of the Geochemical Atlases. Below, results from the "Atlas of urban soils contamination in Poland" are presented. They are limited only to trace elements, specially those ones which have elevated levels in this area (Table 9).

Table 9. Trace element content in Gliwice soils (top soil 0-0,2 m, sub soil 0,4-0,6 m below terrain level)

Element	Top soil median	Sub soil median	Top soil lower content from map	Top soil upper content from map	Sub soil lower content from map	Sub soil upper content from map
As			<5	16	<5	18
Cd			<0.5	3.3	<0.5	7.1
Cr		7.0				
Cu	9.0		<1	43	<1	72
Hg			<0.05	0.24	0.05	0.4
Ni	6.0	6.0				
Pb	50.7		<3	**244**	<3	**107**
Zn	118.5		2	300	6	**1125**

Source: Pasieczna, A., 2003, Atlas of urban soils contamination in Poland, Ministry of the Environment, Polish Geological Institute, Warsaw

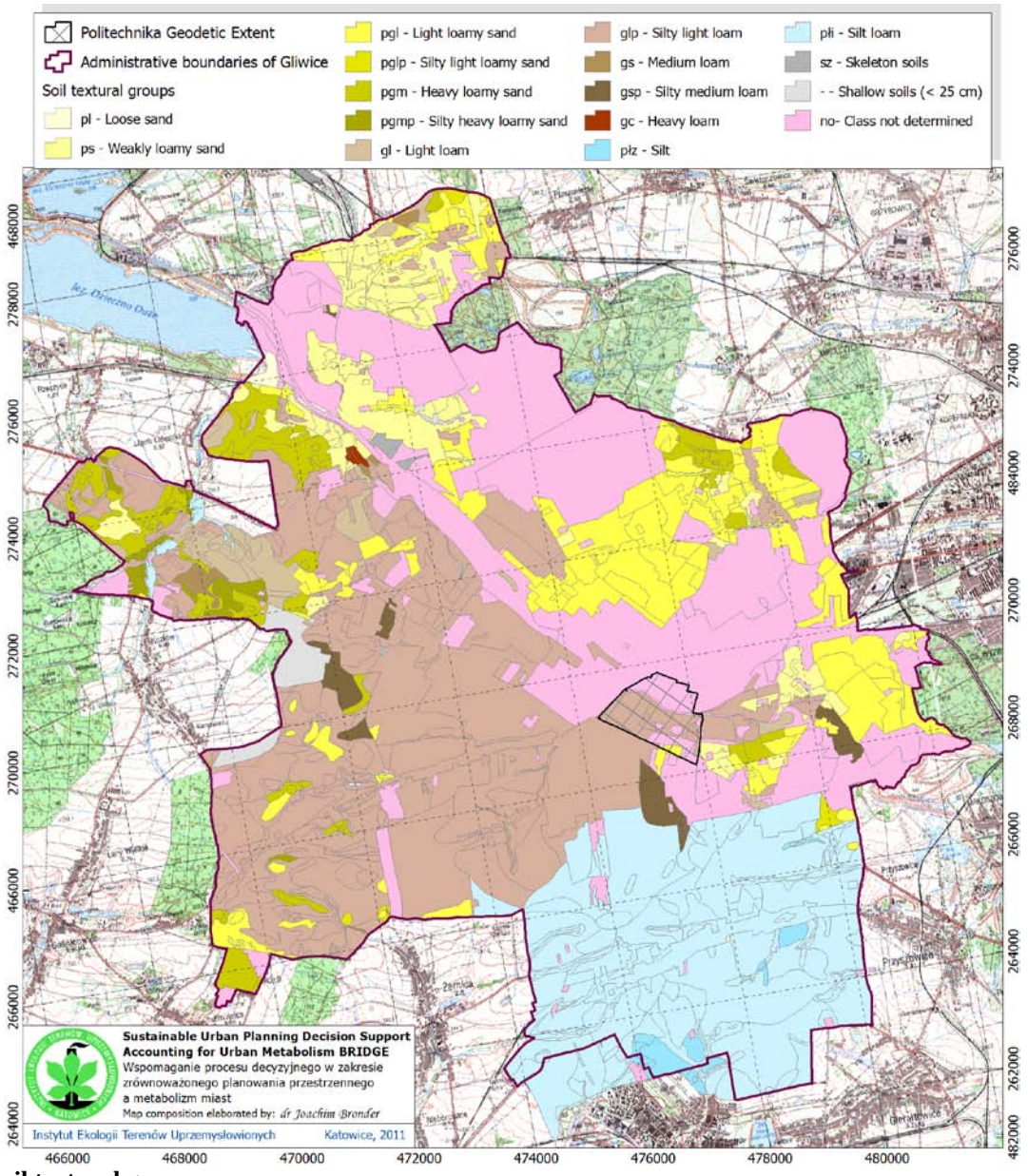

Fig. 27. Soil textural groups

Comparison with maximum admissible levels of contaminant concentrations in soils in Poland point out that average concentrations of analysed trace elements do not exceed MAL for agricultural and residential areas. Only locally occur exceedances of MAL by lead and zinc (bolded numbers in Table 10).

Table 10. Maximum admissible levels (MAL) of heavy metal concentrations in soils in Poland

Element	Layer 0.0-0.3 m - agricultural and residential [mg/kg]	Layer 0.3-15.0 m - agricultural and residential [mg/kg]	Layer 0.0-2.0 m – industrial and transportation [mg/kg]
As	20	20[1]	60
Cd	4	5	15
Cr	150	150	500
Cu	150	100	600
Hg	2	3	30
Ni	100	50	300
Pb	100	100	600
Zn	300	350	1000

Source: Ordinance of the Ministry of Environment dated 9 September 2002 on soil and land quality standards; Official Journal of Laws No. 165, Clause 1358 and 1359

Local soil contamination within Politechnika Geodetic Extent in Gliwice

The industrial areas constitute quite important part of the Politechnika area. The category of Urban Atlas number 12100: industrial, commercial, public, military and private units constitute about one third of the whole district. Huge complex of this category one may distinguish north of Kłodnica river (see Fig. 28).

[1] Water permeability of soils above 10^{-7} m/s

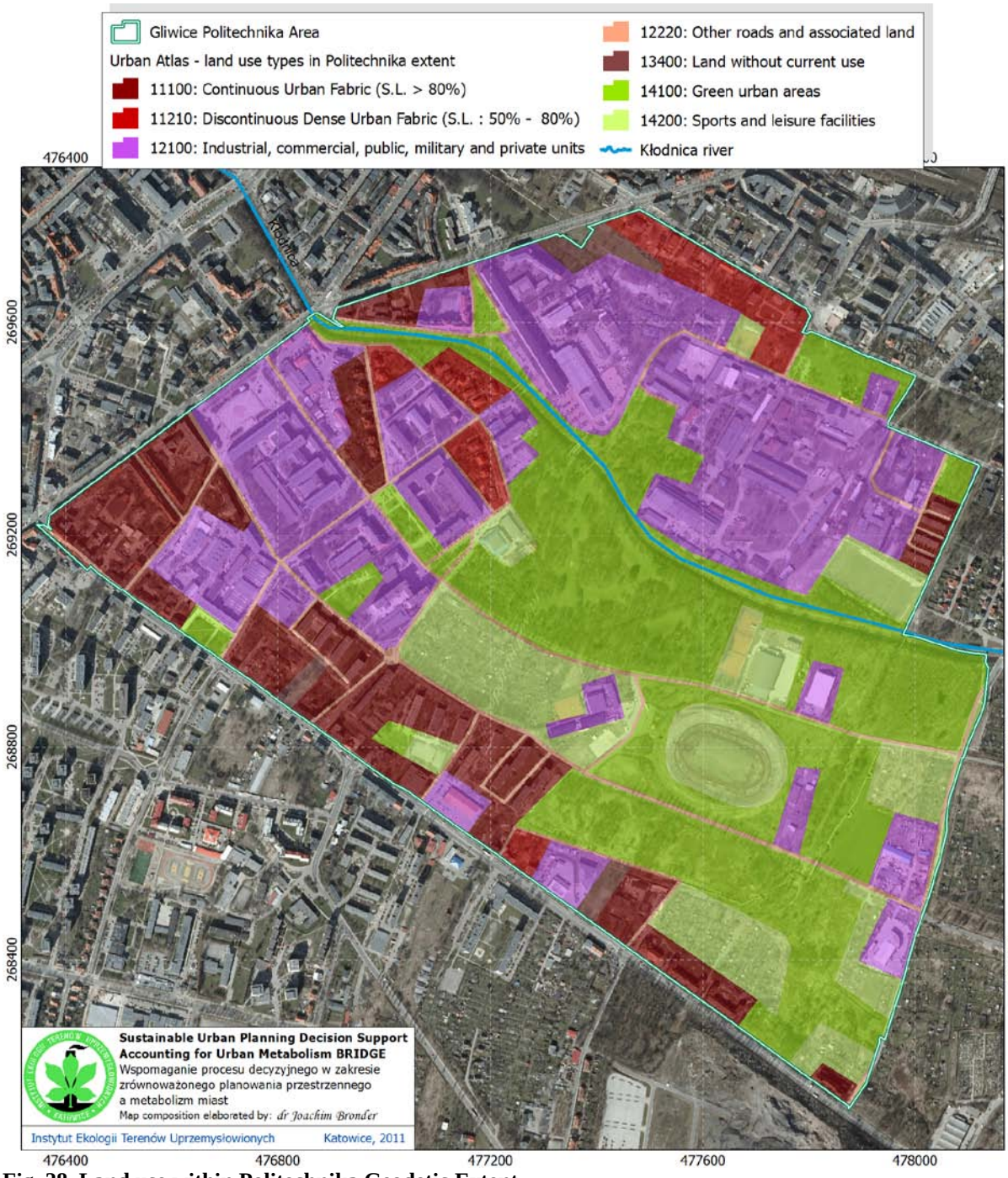

Fig. 28. Land use within Politechnika Geodetic Extent

One industrial object belonging to the mentioned above land use category has been investigated from the point of view of soil contamination. The result of that measurements concerning top layer soils from that object are presented below (Table 11). The result concern soil up to 2 meters depth. Analysis of Table 11 point out on the fact that average contaminants content do not exceed the threshold for industrial areas.

Table 11. Statistical characteristics of metal content in soils of the investigated industrial area

Trace element	Arsenic [mg/kg]	Barium [mg/kg]	Tin [mg/kg]	Zinc [mg/kg]	Cadmium [mg/kg]	Cobalt [mg/kg]	Copper [mg/kg]	Nickel [mg/kg]	Lead [mg/kg]

Trace element	Arsenic [mg/kg]	Barium [mg/kg]	Tin [mg/kg]	Zinc [mg/kg]	Cadmium [mg/kg]	Cobalt [mg/kg]	Copper [mg/kg]	Nickel [mg/kg]	Lead [mg/kg]
Number	22	22	22	22	22	22	22	22	22
Minimum	2.50	20.86	2.64	37.3	1.05	1.74	11.94	13.52	20.70
Maximum	76.50	1414.34	90.66	8160.3	29.91	30.05	742.10	119.40	5537.04
Arithmetic Mean	21.82	353.47	17.29	1452.2	6.76	11.34	184.07	28.63	628.74
Standard deviation	18.41	317.80	20.06	1845.1	9.13	6.90	170.45	25.11	1138.40
Variability coefficient	84.35	89.91	116.04	127.1	135.10	60.86	92.60	87.72	181.06
Shapiro-Wilk statistics W	0.96	0.93	0.96	1.0	0.82	0.88	0.97		0.96
Central value	15.78	257.14	11.27	806.0	2.83	8.93	123.56	13.52	315.93
Parameter	Geometric mean	Geometric mean	Geometric mean	Geometric mean	Median	Median	Geometric mean	Median	Geometric mean
Threshold value[1]	60	1000	350	1000	15	200	600	300	600

Source: Calculation of IETU

Vegetation

Flora of Gliwice as well as Politechnika district is characterized by a diverse composition (Fig. 29). There is a mixture of native, synathropic and invasive species. Two types of ecosystems are dominant*: natural green areas* and *secondary green areas* - cultivated green areas, isolating green space, post-industrial areas and reclaimed heaps.

Urban green areas in Politechnika District play double role as a recreational areas (e.g. Chrobry Park) and flooding areas near the Kłodnica River. Three types/categories of greenery areas have been identified in Politechnika District (Fig. 30):

- with trees exceeding 10 m in height – 51.15 ha;
- allotment and house gardens – 30.28 ha;
- lawns, meadows and shrubs – 12.46 ha.

[1] Maximum permissible level of soil contamination for layer between 0-2.0 m depth

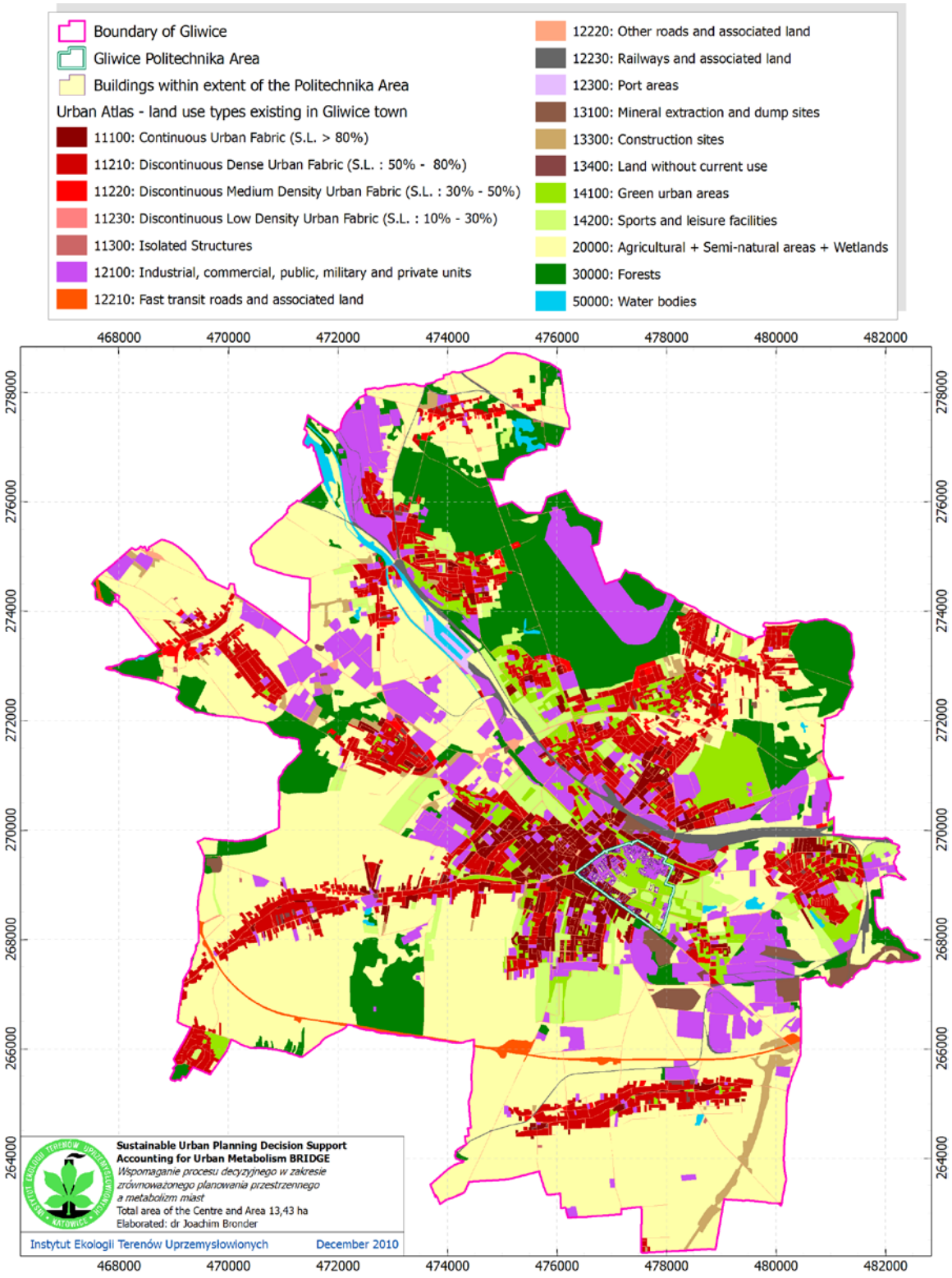

Fig. 29. Natural and anthropogenic urban green areas in Gliwice and Politechnika District

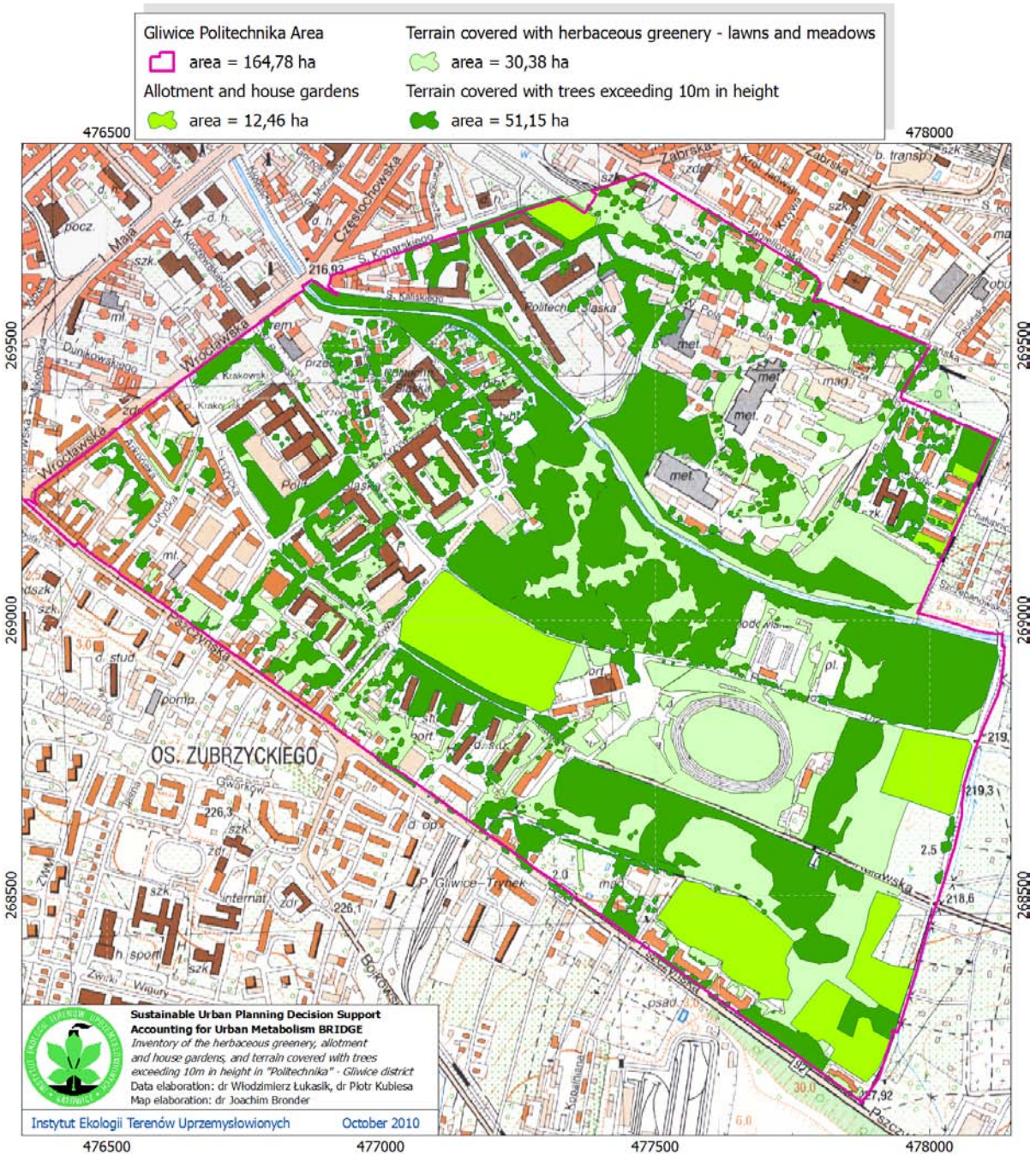

Fig. 30. Detailed characteristic of Vegetation in Politechnika District

Forest in Gliwice belong to 2 forest grounds - Table 12.

Table 12. Percentage share of forest habitat types in two forest grounds located in Gliwice

Forest habitat	Rachowice forest ground		Wieszowa forest ground	
	Area [ha]	%	Area [ha]	%
Fresh coniferous forest			2.60	0.1
Fresh mixed coniferous forest	1089.98	14.9	110.97	2.7
Moist mixed coniferous forest	249.31	-3.4	158.54	3.8
Boggy mixed coniferous forest	-	-	3.82	0.1
Fresh mixed broadleaved forest	1854.13	25.4	1151.41	27.5
Moist mixed broadleaved forest	220.87	3.0	1718.82	41.0
Fresh broadleaved forest	3029.94	41.5	872.61	20.8
Moist broadleaved forest	634.56	8.6	118.31	2.8
Boggy mixed forest	5.34	0.1	-	-
Floodplain forest	188.71	2.6	-	-
Alder forest	4.76	0.1	43.28	1.0
Alder-ash forest	31.12	0.4	9.45	0.2
Total	7308.72	100	4189.81	100

Dominant tree species are as follows:

- Pine - 69.66%
- Oak – 11.70%
- Birch – 11.08%
- Spruce – 3.1%

Annex 5 - Helsinki case study in situ measurements

1. Meteorological measurements

Measurements of the meteorological variables are mainly carried out in Kumpula while some of the most important ones to support the urban ecology are made in Viikki.

1.1 Kumpula

The basic weather station is situated on the roof of the University of Helsinki buildings at the height of 51 meters. The measurements cover air pressure and relative humidity measured with a barometer and platinum resistance thermometer and thin film polymer sensor (Vaisala DPA500 and Vaisala HMP243, respectively, Vaisala Oyj, Vantaa, Finland), respectively. A rain gauge was used for precipitation measurements. The time resolution for these is four minutes.

In addition, the vertical profiles of wind speed and direction and air temperature are measured at levels 4, 8, 16 and 31 meters at the measurement tower. At all levels, the horizontal wind speed components are measured with a 2-dimensional ultrasonic anemometer (Thies CLIMA v2.1x, Goettingen, Germany) with a time resolution of 10 seconds, and air temperature with a platinum resistant thermometer Pt–100 ("home-made", ventilated and shielded from rain and solar radiation) with a time resolution of one minute. On the top level the components of the net all-wave radiation (incoming and outgoing short- and long wave radiations) and PAR (photosynthetically active radiation) are measured with a net radiometer and photodiode sensor (CNR1+PAR lite, Kipp&Zonen, Delft, the Netherlands), respectively. The time resolution for these is one minute.

In 2009-2010, air temperature showed a strong annual cycle with temperatures ranging from -23°C in winter to 30°C in summer. Year 2010 was untypical for Helsinki with colder winter and warmer summer than typically observed in Helsinki. The 30-year average monthly air temperatures vary from 4.9°C in February to in 17.2°C in July (Drebs *et al.* 2002) while an average temperature of -10.7°C in Jan 2010 and 22.1°C in August were observed. Wind speed and air pressure did not have a distinct annual behaviour while relative humidity inversely followed the air temperature with lower values in summer than in winter. In both years the annual behaviour of precipitation was typical for Helsinki with maximum precipitation in winter/late summer and minimum in spring. The most typical wind direction at the measurement site is south-west corresponding to flow downwind from the area of high vegetation.

In 2009-2010, the downward short-wave radiation has a strong annual behaviour with winter time values typically below 100 W m^{-2} and reaching 1000 W m^{-2} in summer. The periods of snow cover can clearly be distinguished from the reflected short-wave radiation with increased values in winter due to increases surface albedo. From a median summer value of 0.14 the surface albedo increases to 0.49 in 2009 and to 0.63 in 2010 in winter. Both downward and upward long-wave radiations have maxima in summer and minima in winter. The upward long-wave radiation is generally higher than the downward component reflecting the effect of higher surface temperatures of impervious surfaces.

1.2 Viikki

In addition to the meteorological measurements carried out in Kumpula, local PAR, air and soil D are measured at both streets in Viikki. PAR is measured with QS2 sensors (Delta-T Devices Ltd)

and air temperature with radiation shielded Pt100 at 7 meters height. The time resolution of the measurements is 2 minutes in spring, summer and autumn, and 10 minutes in winter.

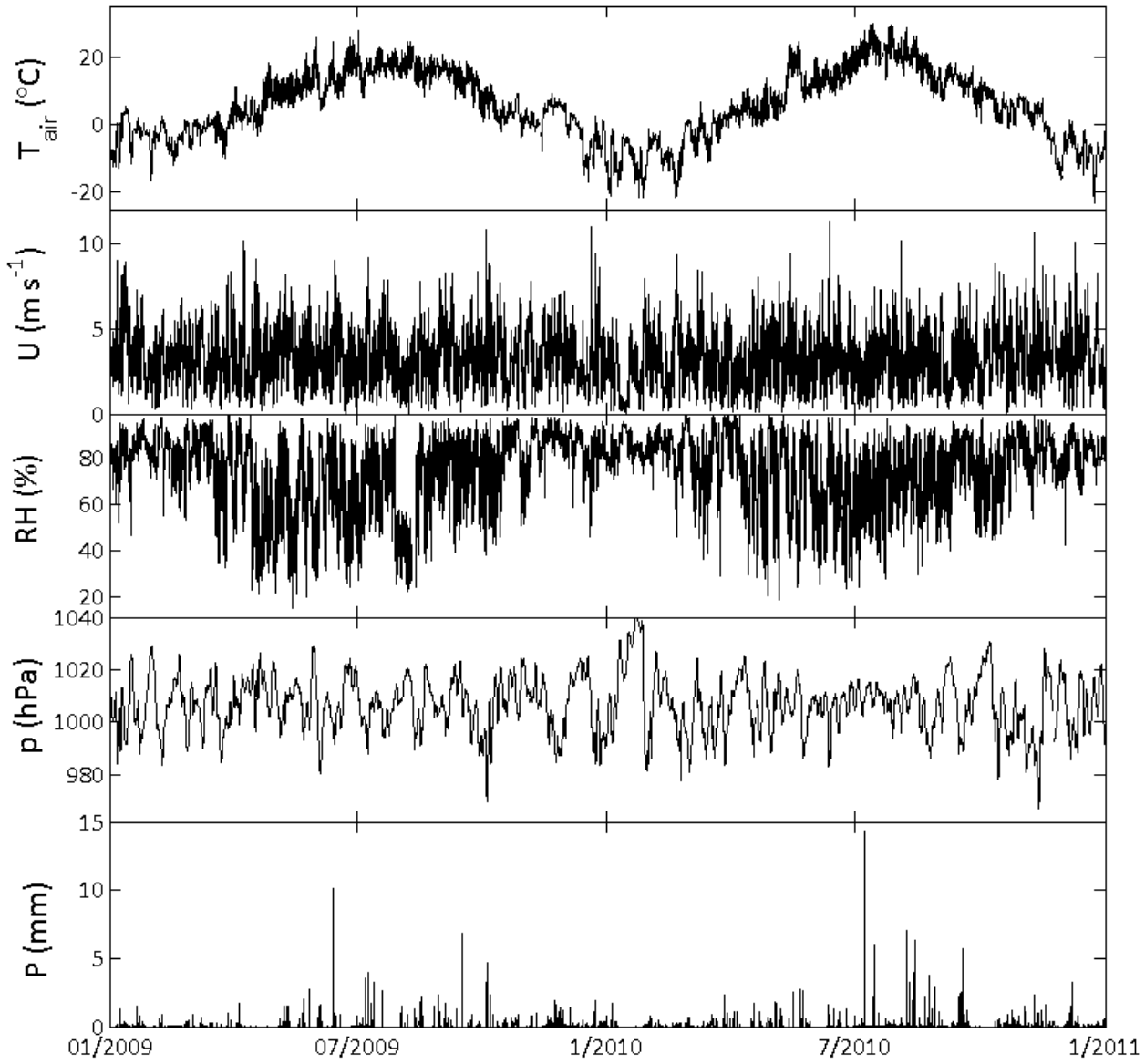

Figure 3. Time series of air temperature (*T*), wind speed (*U*), relative humidity (RH), air pressure (*p*) and precipitation per 30-min (*P*) measured at the Kumpula site in 2009--2010.

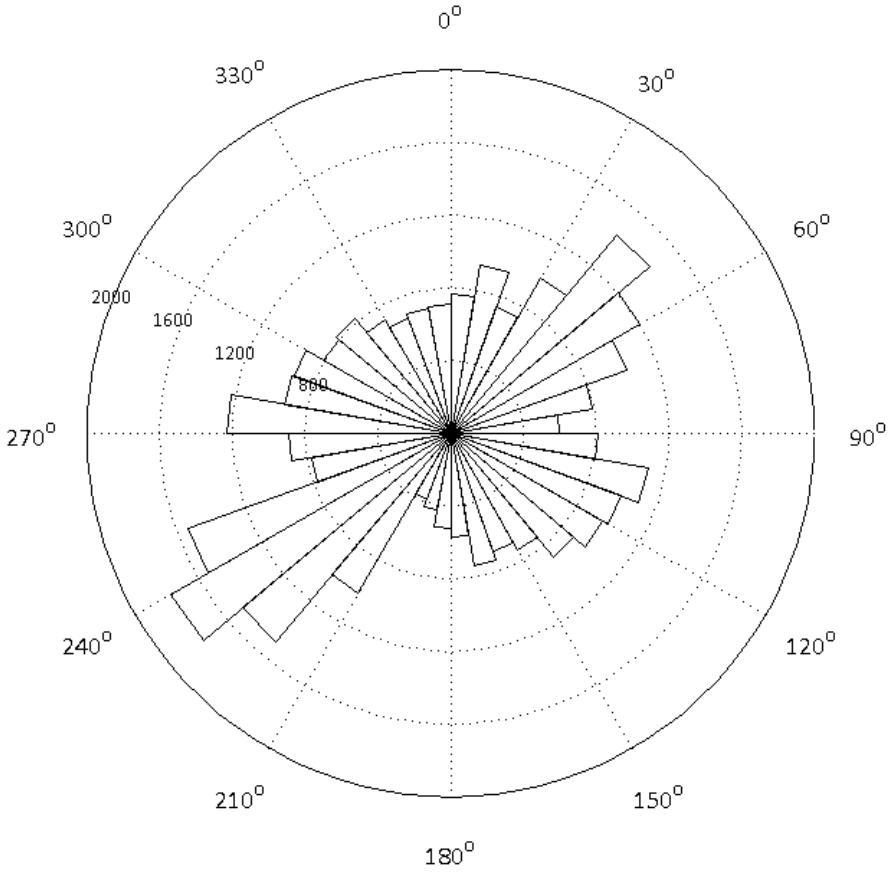

Figure 4. Wind rose for 2009--2010.

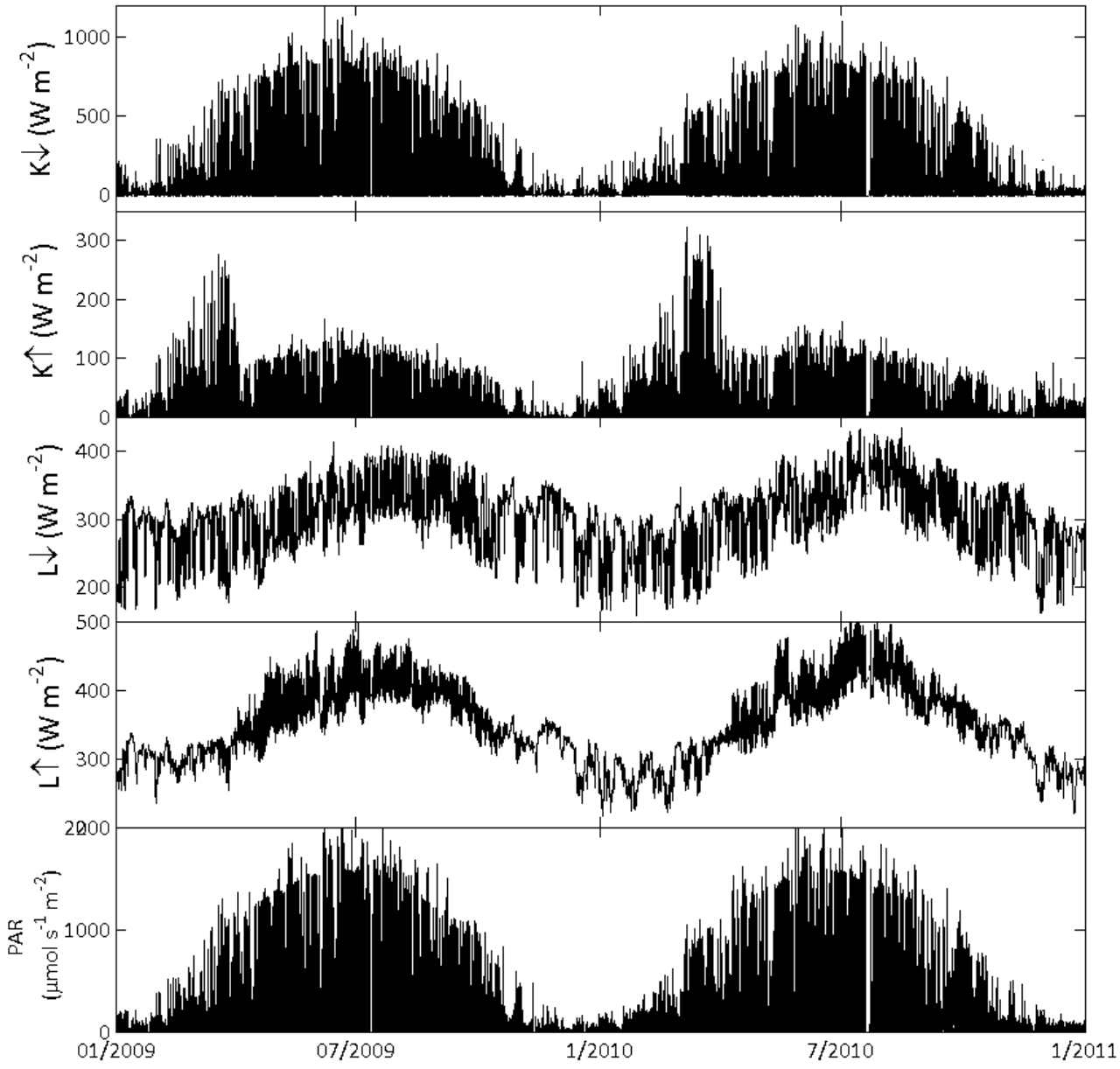

Figure 5. Time series of downward and up-ward short-wave radiation (K↓ and K↑, respectively), similarly for long-wave radiation (L↓ and L↑, respectively) and PAR at the Kumpula site in 2009--2010.

3. Air quality measurements

The aerosol particle and gas concentration instrumentation is situated in an air conditioned container next to the measurement tower. Sample air for the instrumentation is drawn through inlets located at four meters from ground.

The measurements of aerosol particle size range from 3 to 950 nm are made with a twin differential mobility particle sizer (DMPS, e.g. Aalto *et al.* 2001). In the set-up, the first DMPS measures particles in the size range of 3--50 nm and it consists of a Hauke-type DMA (10.9 cm in length) and a TSI Model 3025 CPC. The sample and sheath flows are 3 and 171 l min^{-1}, respectively. The second DMPS measures particles in the size range of 10--950 nm with a Hauke-type DMA (28 cm

in length) and a TSI Model 3010 CPC. For this, the sample and sheath flows are 1 and 5 l min^{-1}, respectively. Each sheath flow is arranged as a closed loop with air filter and aerosol dryer. The sampling line is a 2 m long stainless steel tube with an inner diameter of 4 mm and an aerosol flow rate of 4 l min^{-1}. The time resolution of the combined system is 10 minutes.

The concentration of nitrogen oxides (NO_x) is measured with a chemiluminescence analyser (TEI42S, Thermo Environmental Instruments Inc., MA, USA), the concentration of ozone (O_3) with an IR-absorption photometer (TEI49, Thermo Environmental Instruments Inc., MA, USA) and the concentration of sulphur dioxide (SO_2) with a UV fluorescence analyser (APSA 360, Horiba, Kyoto, Japan). For all gas measurements, a time resolution of one minute is used (See details from Järvi *et al.* 2009a).

As different sized of particles have different sources and physical properties, the measured aerosol particle size range has been divided to 3-30 nm, 30-100 nm and 100-950 nm sized particles corresponding to nucleation mode, Aitken mode and accumulation mode particles, respectively. All aerosol particle concentrations have their maxima in winter due to increased emissions from various combustion processes. These concentrations are strongly also affected by the mixing conditions of the boundary layer and in winter this is limited due to the lack of solar radiation. O_3 gets its maximum 35 ppb in spring/early summer and minimum 10 ppb in winter. This annual behaviour is determined by the intensity of solar radiation and photo-oxidation of the precursor gases (Järvi *et al.* 2009a). NO_x and SO_2 get their maxima 20.7 and 1.6 ppb, respectively in winter when there is limited mixing and increased emissions from traffic and stationary emission sources.

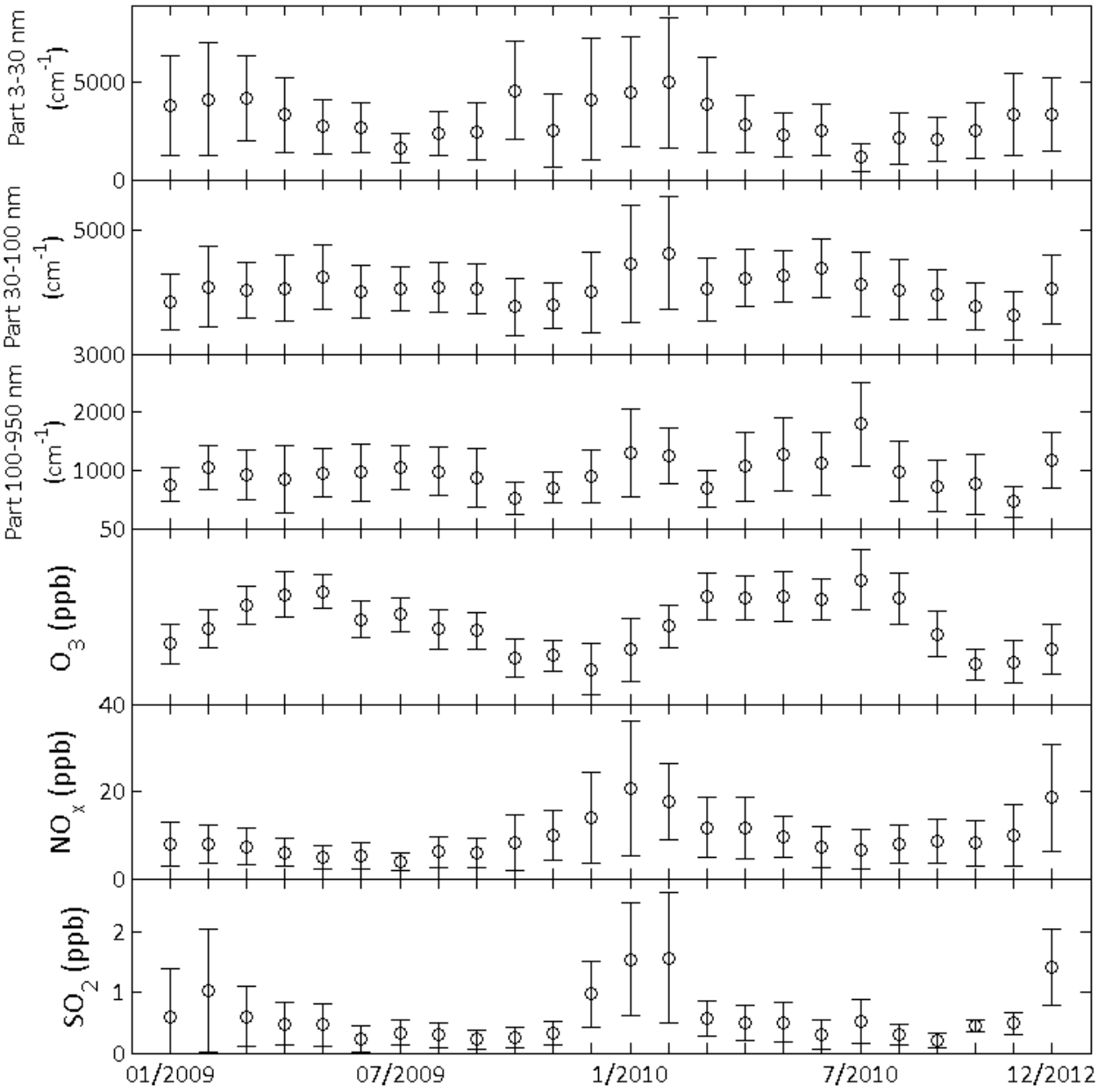

Figure 6. Monthly medians of aerosol particle number concentration of 3 – 30 nm, 30 – 100 nm and 100 – 950 nm particles, ozone (O_3), nitrogen oxides (NO_x) and sulphur dioxide (SO_2) in 2009-2010.

4. Turbulent fluxes

The turbulent fluxes of momentum, sensible and latent heat, carbon dioxide (CO_2) and aerosol particle number are measured with the eddy covariance (EC) technique. These measurements are made on the top boom of the measurement tower at a height of 31 meters. The measurement setup consists of a Metek ultrasonic anemometer (USA-1, Metek GmbH, Germany) to measure all three wind components and sonic temperature, open- and closed-path infrared gas analyzers (LI-7500 and LI-7000, respectively, LI-COR, Lincoln, Nebraska, USA) to measure CO_2 and H_2O densities and mixing ratios, respectively, and a water-based condensation particle counter (WCPC, TSI-3781, TSI Incorporated, USA) to measure aerosol particle number concentration starting from a size of 6 nm (Järvi *et al.* 2009b). The EC setup is located on a boom 1.3 meters to south-west from the tower. The open-path analyzer is mounted 0.2 meters away from the anemometer and it is tilted 30 ° in order to allow rain water to drip off. In addition the surface temperature of the open-path gas analyzer was measured with a thermocouple in order to correct latent and CO_2 fluxes due to surface heating. Both the closed-path analyzer and WCPC use the same inlet situated 13 cm below the anemometer. The inlet is covered with a rain cover and a 6 mm diameter filter with a mesh size of 0.1 mm. A 40 meters long steel tube with an inner diameter of 8 mm is connected to the closed-path analyzer located in the container next to the measurement tower- WCPC is situated in the tower and a side flow to WCPC is drawn through a 0.1 meters long tube from the main tube at a distance of 3.6 meters from the inlet. The inlet is heated with a power of 16 W m^{-1} to avoid water condensation on the walls. The open-path gas analyzer and WCPC are connected to the analogue input channels of the anemometer, whereas the closed-path gas analyzer data is recorded separately using the RS-232 output. Measurement resolution for EC measurements is 10 Hz and raw data is stored for later post-processing described in deliverable 3.5.

In 2009-2010 latent heat and CO_2 flux measured with closed-path gas analyzer were used in the plot. Friction velocity (momentum flux) did not have any distinct annual cycle and on average it remained below 1.8 m s^{-1}. Sensible and latent heat fluxes (Q_H and Q_E, respectively) followed measured solar radiation well with maxima in summer and minima in winter. Q_H was higher than Q_E and daytime averages of Q_H reached 300 W m^{-2} in summer while Q_E stayed below 225 W m^{-2}. In winter, both fluxes were close to zero. The source area around the tower acted as a source of CO_2 (F_c) in winter with an average strength of 15.4 μmol m^{-2} s^{-1}. In summer, carbon uptake exceeded the emissions and a minimum average downward flux of 11 μmol m^{-2} s^{-1} was measured. The strong carbon sink visible from data in summer is caused by the prevailing wind direction downwind from the area of high vegetation cover. Highest particle emissions were measured in winter and the average daytime fluxes reached $1.2 \cdot 10^9$ m^{-2} s^{-1}.

F_c and particle flux (F_p) had strong dependence on wind direction as it is clear from the diurnal plots for each surface type area in summer. The highest emissions for both were measured from the road sector due to emissions from road traffic with F_c reaching 16 μmol m^{-2} s^{-1} and F_p $0.4 \cdot 10^9$ m^{-2} s^{-1}. Urban and vegetation sectors acted as a carbon sink in daytime reaching values of -8 and -11 μmol m^{-2} s^{-1}, respectively. For F_p, the fluxes in these directions stayed below $0.2 \cdot 10^9$ m^{-2} s^{-1}. Heat fluxes did not have such a strong dependence on wind direction but a slightly lower Q_H was observed in the area with high vegetation fraction in daytime than in other areas. Similarly highest Q_E was observed in the same direction as heat is consumed in evapotranspiration instead of direct heat flux. Nocturnal Q_H and Q_E were about the same for all directions.

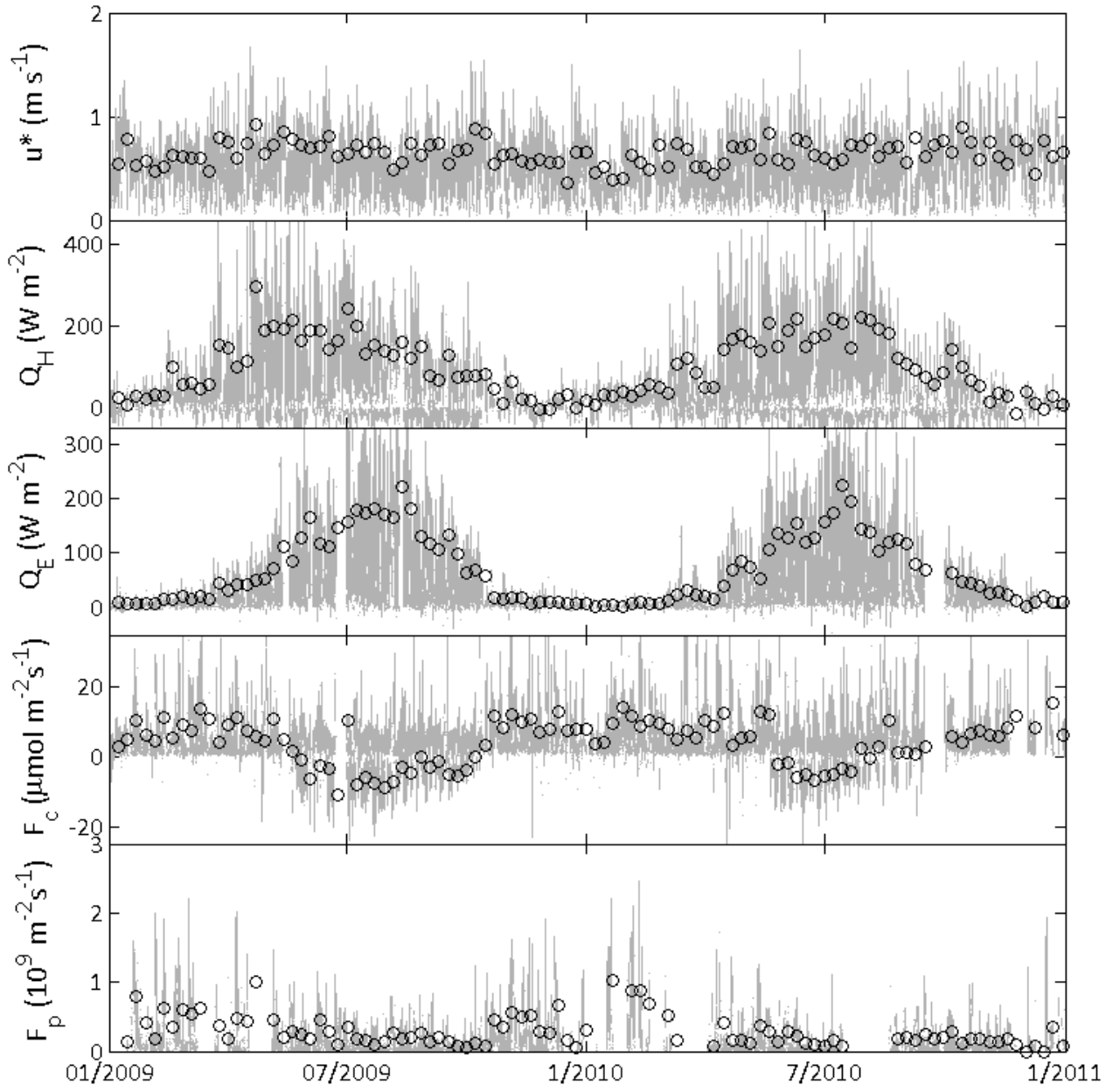

Figure 7. Time series of turbulent fluxes of momentum, sensible heat (Q_H), latent heat (Q_E), CO_2 (F_c) and aerosol particle number (F_p) measured at the SMEAR III station in 2009-2010. Momentum flux is expressed as friction velocity (u*). Grey lines are the 30-min flux values and circles show the daytime (10:00 – 14:00) 7-day mean values.

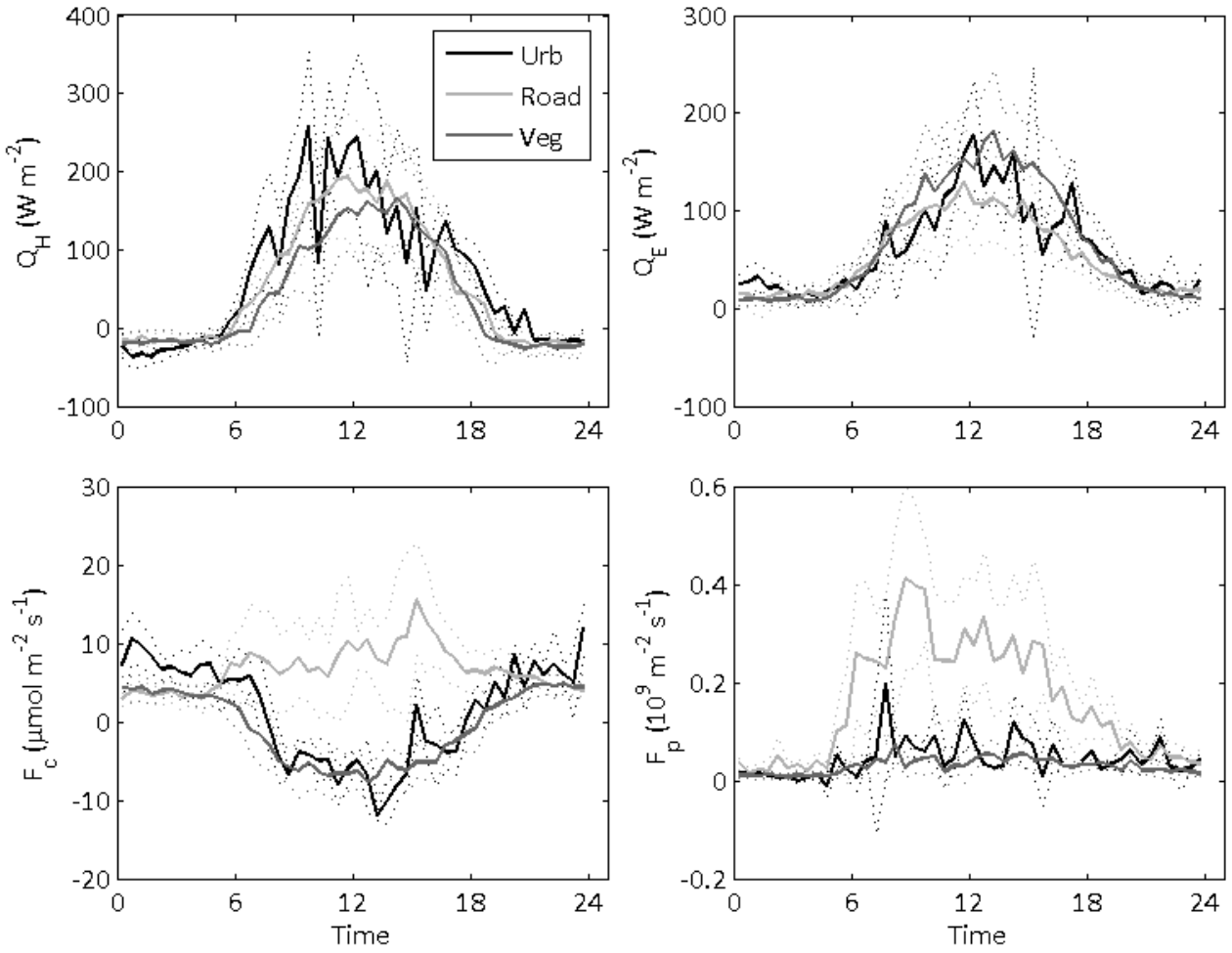

Figure 8. Diurnal behavior of sensible heat (Q_H), latent heat (Q_E), CO_2 (F_c) and aerosol particle number (F_p) fluxes during summer in 2009-2010.

5. Tree and soil measurements

Viikki measurement site, where tree and soil measurements were performed, consists of two streets with street trees planted in late 2002 and set up with automated monitoring. Site 1 is planted with

Tilia × vulgaris Hayne (dbh 8.2-10.8 cm at planting time) and site 2 with Alnus glutinosa (L.) Gaertn.'Sakari' (dbh at plainting time 6.7-11.0 cm). Trees were planted in three different structural soil mixes on both sites. Structural soils were installed as 1-m-deep, 3-m-wide paved planting pockets (site 2) or as continuous 1-m-deep, 3-m-wide tree trench under a paved parking strip between the road and sidewalk (site 1). The site is described in detail in Riikonen *et al.* (2011).

5.1 Tree trunk diameter changes

Three trees of each species (referred to as intensive monitoring trees) were fitted with automated trunk diameter monitoring (half bridge gauging probes, model AX/5/S, Solartron Metrology Inc., West Sussex, UK). Two probes were mounted on the trunk of each monitored tree at height of 30-60 cm from ground, on a rigid frame. One sensor was set to measure the trunk diameter change and increment on top of the tree bark and another was placed against a stainless steel screw sunk into the xylem of the tree to measure daily variation of wood brought about by daily transpiration changes. A rigid black plastic sheet was fitted inside tree trunk guard to protect the probes from direct solar radiation. Data was stored into a datalogger (Envic Ltd., Turku, Finland) at intervals of 2 minutes during the growing season and at 10 minute intervals outside the growing season. Data was sent to central data storage via gsm modem connection and processed to half-hourly average trunk diameter (xylem and xylem+bark) data.

5.2 Tree sap flow and crown gas exchange

Tree sap flow was measured at Viikki sites 1 and 2 from 3 Tilia and 3 Alnus street trees (intensive monitoring trees) with Granier type thermal dissipation probes. Thermocouples placed inside stainless steel needles were installed on tree trunk (30-60 cm from the ground) one above the other, the distance between needles was about 10 cm. The upper needle was heated with constant power and temperature difference between the needles was read to datalogger. Data was stored and processes similarly to trunk diameter change data.

The photosynthetic capacity of tree crowns was measured once or twice a summer (in early June and/or late August). Six representative Alnus and Tilia trees were selected and gas exchange was measured for three leaves in each tree in the upper 1/5 of the crown with Ciras-2 portable photosynthesis system (PP Systems International Inc, Amesbury, USA) set up with a Parkinson leaf cuvette. The leaves were subjected to a regime of changing CO2 (4 concentrations ranging from 100 to 1500 ppm) and light (6 PAR levels from 0 to 1500 umol/m2/s) levels. Gas exchange was recorded for each measured leaf and response curves to PAR radiation and CO2 was estimated.

5.3 Tree growth and crown allometry

The intensive monitoring trees as well as 1–3 additional, randomly sampled trees per species were measured for annual shoot extension and crown allometry in late August, resulting in 6-12 measured trees per species per year. Electric boom skylifts were used to gain access to tree crowns. The crowns of sampled trees were divided horizontally into three sections of equal length to gain an even sampling profile for both shoot growth and allometry measurements.

10 randomly chosen shoots in each section were measured annually for shoot extension in August. From each crown section, the basal diameter of each branch right above branch collar was measured with a digital caliper. A median diameter branch was selected from each crown section for leaf area measurement. Leaves were collected and leaf area was measured (Li-Cor LI-3000A, Li-Cor Biosciences, Lincoln, NE, USA). The leaf area for branches with more than 50 leaves was estimated by measuring the area of every 10th leaf on the sample branch, and by multiplying the mean area of the leaves measured with the total number of leaves on that branch; for smaller branches, all leaves in the branch were collected and measured.

5.4 Soil gas content and soil CO_2 flux measurements

Soil air CO_2 content

Soil gas samples were collected from aluminium soil air samplers installed permanently in tree soils. Samplers were located 10, 30 and 60 cm below the pavement installation layer in eight locations in site 1 and in 11 locations in site 2. Samplers were built from 300 mm aluminium tube with diameter 1 mm holes drilled on first 50 mm from tip, tube inside diameter 6 mm. The drilled tip of the tube had GoreTex coating against water entry to the sampler. Gas samplers were connected to aboveground sampling head (butyl rubber and neoprene septa) with 700 mm of diam. 3 mm nylon tubing. Gas samples (volume approx. 5-10 ml) were taken every 3-4 weeks and analyzed in laboratory with gas chromatography system described in Jaakkola and Simojoki (1998). The O_2, CO_2, ethylene, methane and dinitrous oxide content of the soil air samples was determined (water vapour content not included).

In late July 2009, continuous measurement of soil air CO_2 content was started with Vaisala CARBOCAP GMM221 sensors (Vaisala Ltd, Vantaa, Finland). These were installed into tree soils 10 cm below the pavement installation layer approx. 1 m southwards from each intensive monitoring tree on both sites (6 sensors altogether). The sensors were protected from water with porous PTFE tube and placed inside a 32 mm diam., 15 cm long, open ended rigid plastic pipe, with holes along its length, for mechanical protection. Soil temperature sensor (thermistor) was attached to the side of each CO_2 sensor. Both sensors were connected to dataloggers and data produced was stored and processes similarly to trunk diameter change data.

Soil CO_2 flux measurements at Viikki site

Since September 2006, simultaneous CO_2 flux measurement was conducted several times per year from above the pavement on top of the soil air samplers with portable closed chamber CO_2 exchange measuring system (Kolari *et al.* 2005) with the chamber protected from light with aluminium foil. The CO_2 sensor in the system was GMP343 (Vaisala Ltd, Vantaa, Finland). One measurement lasted 5 minutes and CO_2 concentration was measured every 5 seconds. The CO_2 flux from the soil was calculated from the average concentration increase corrected for air pressure and temperature effects. Separate plastic collar was sealed against the pavement with wetted quartz sand.

Soil CO_2 flux at Kumpula site

Soil CO_2 flux measurements at Kumpula were performed using the same system described for Viikki measurements, but plastic collars for the measurements were permanently placed in the 36 measuring plots in the area. Measuring plots were chosen at roughly equal intervals along 6 lines radiating in different directions from the measurement tower. Plots were selected to represent different vegetation types in the area in proportion to which they are present in the footprint areas of the measuring tower. However, a minimum of three plots were sampled for all vegetation types. Some deviation from ideal sampling was necessary to avoid damage to or loss of research equipment (eg. to attain enough distance from footpaths so that equipment was not clearly visible from the path). The plots in figure 11 represent grassland (3 plots), low vegetation and moss covered rock outcrop (3 plots), mainly deciduous forest (11 plots), botanical garden (5 plots) and cultivated allotment gardens (9 plots), and heavily constructed office area (7 plots). The plots were measured for CO_2 flux approximately every 2 weeks in spring, summer and autumn until snowfall in random order; measuring all 36 plots was done in 2 or 3 consecutive days.

5.5 Soil water content measurements

Soil volumetric water content was continuously monitored in Viikki with Theta-probes (ML2x, DeltaT Devices Ltd., Cambridge, UK). At Viikki site 1, a polystyrene insulated plastic well with a manhole cover was installed through the structural soil layer. Theta probes with built-in calibration were installed 10 and 30 cm below the tree soil surface through holes drilled the well wall. At the site 2 in Viikki, soil moisture sensors were installed at a depth of 10 cm in tree soil, under manhole covers resting on a concrete base. The soil moisture sensors at a depth of 30 cm were placed directly into the soil without a manhole cover, approximately 100 cm away from the intensive monitoring tree. Data was stored and processes similarly to trunk diameter change data (see 5.1).

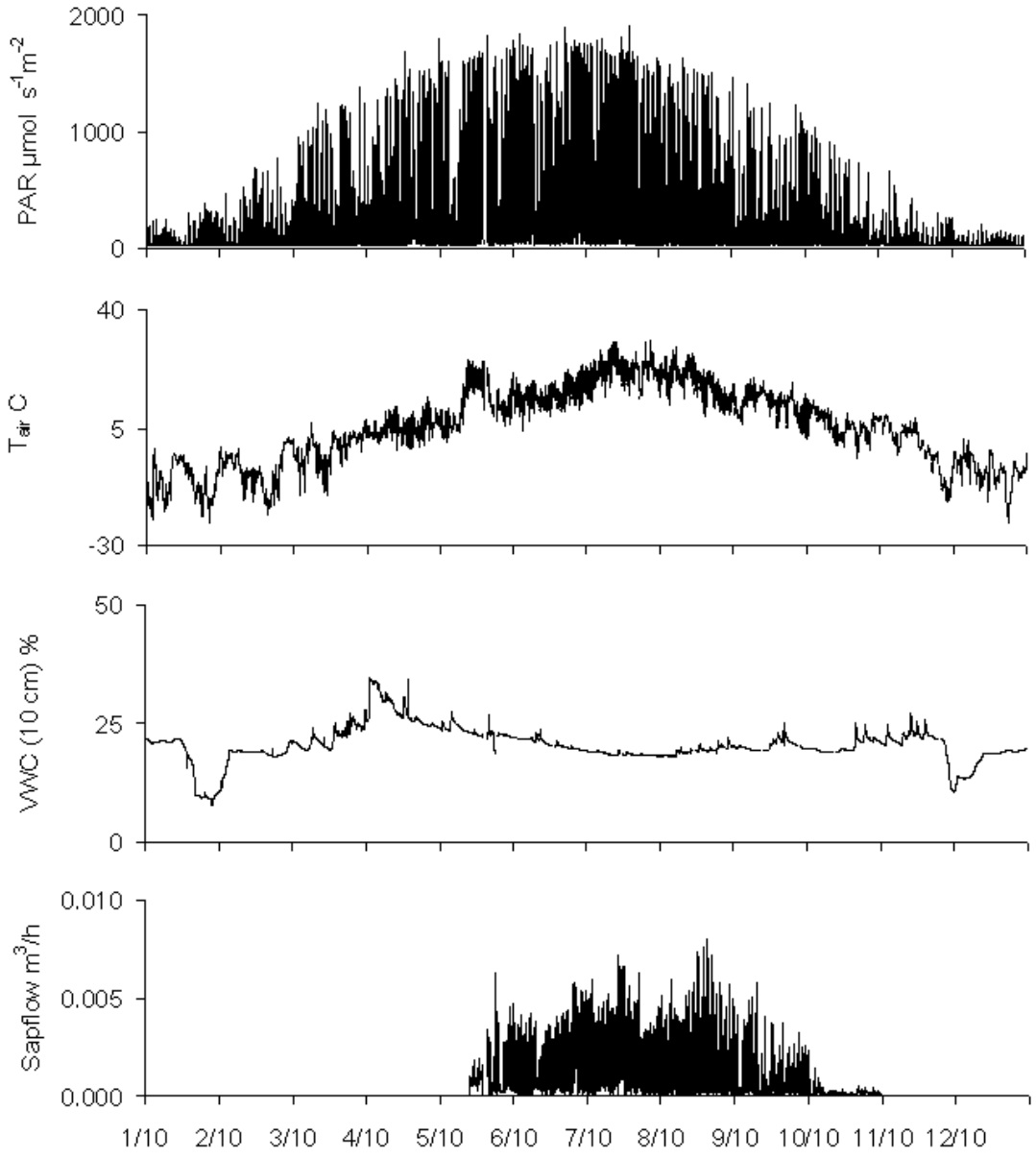

Figure 9. PAR radiation, air temperature, soil water content (% of volume), and tree sap flow measured at Viikki site 1 in 2010 (averages of 3 observation points, 30 min. averages).

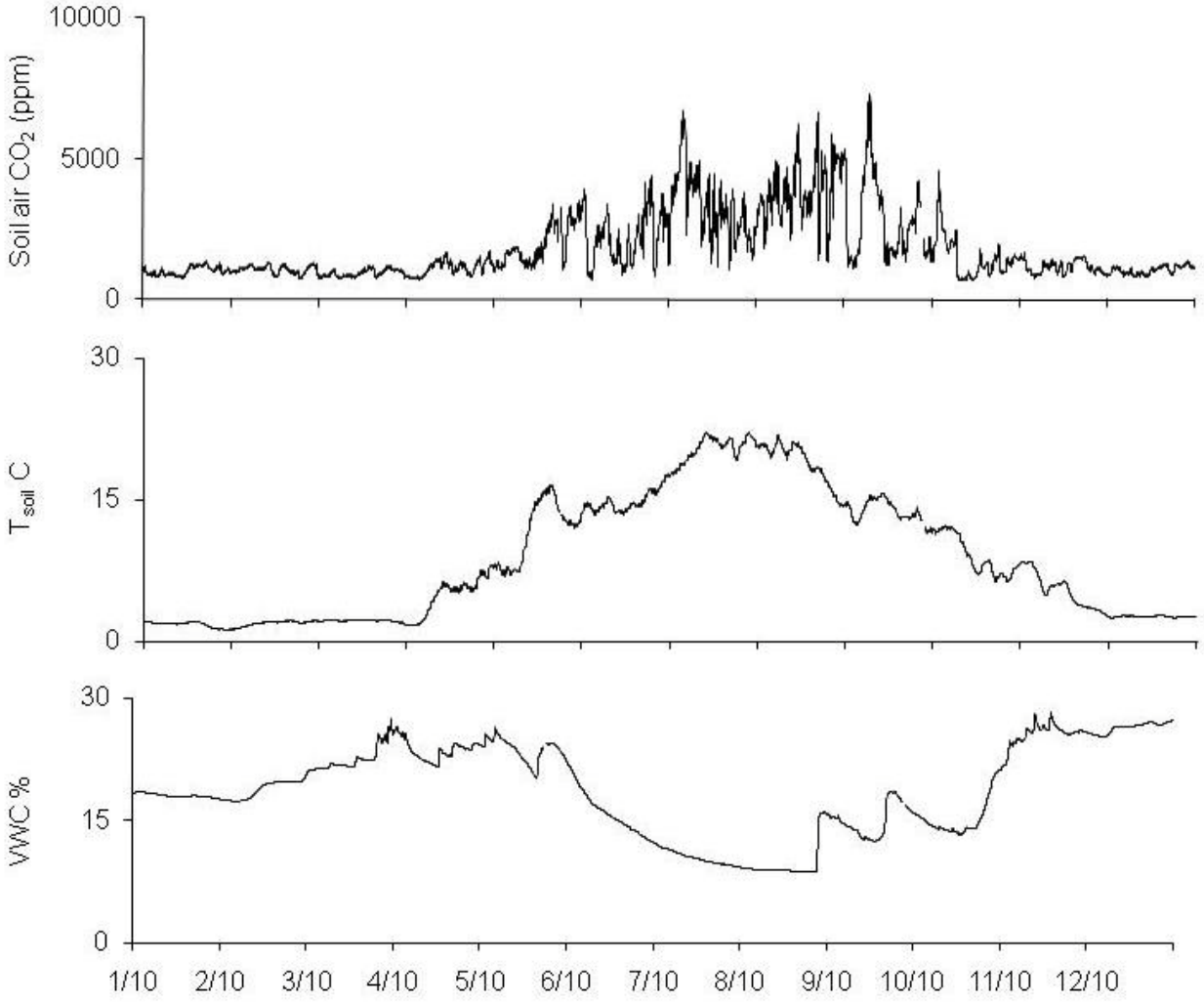

Figure 10. Soil air CO_2 content, temperature and water content (30 min. averages) measured simultaneously at observation point 2, Viikki site 2, 2010.

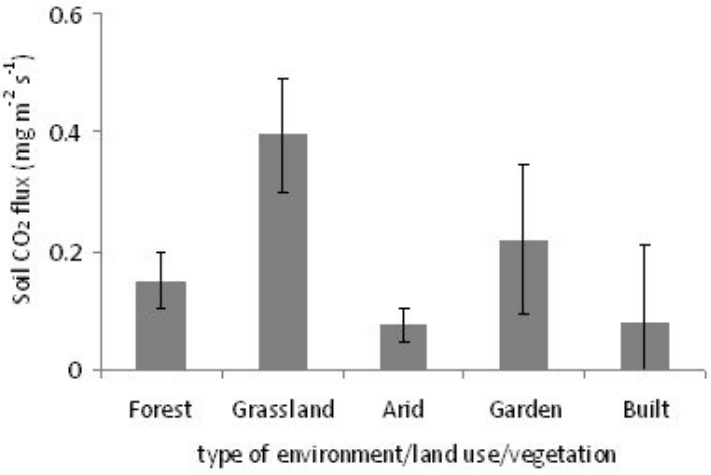

Figure 11. Measured soil CO_2 flux (average ± standard deviation of all representative points) at Kumpula from soils with different surface cover and vegetation, May 2009.

6. Stormwater measurements

Data collection took place at three sub-catchment areas in Helsinki. The studied catchment areas differ in their population density and the amount of pervious and impervious surfaces, and are thus called low-density, medium-density and high-density catchment areas accordingly. The sites can also be referred to as low-, medium – and high-intensity areas as land use intensity determines the proportion of permeable and impermeable soil in the area.

MapInfo software was used to define the amount and distribution of pervious and impervious surfaces in the three different catchment areas (Figure 12). Data was proved by field observations.

6.1 Low-density catchment area (Veräjämäki)

Veräjämäki is situated in a suburban area, where the population density is ca. 2 400 inhabitants km^{-2}. This residential area is an example of suburban planning and construction from the 1980's, where buildings were made lower and the layout of residential blocks allowed more room for garden-like green areas in around the blocks. Green areas cover 70% of the catchment area.

6.2 Medium-density catchment area (Pihlajamäki)

Pihlajamäki is situated in an urban/suburban area in the City of Helsinki, where the population density is ca. 5 500 inhabitants km^{-2}. This residential area represents an early idea of suburbs from the 1960's. The fraction of green areas is slightly lower (around 53%) than in the low-density catchment area.

6.3 High-density catchment area (Itä-Pasila)

Itä-Pasila is situated in the core urban area in the City of Helsinki, where the population density is high (4 200 inhabitants km^{-2}) and pervious surfaces are rare and highly fragmented. Itä-Pasila area represents thinking typical in the 1970's: compact steel-concrete structures, massive decks etc.

6.3 Urban runoff quantity and quality

Due to difficulties getting electricity at the stormwater-stations, the automatic measurements started in September/October 2010. Therefore only data from September onward has so far been analyzed and can be presented. In figure 13, urban runoff data for November 2010 is presented. During each rain event the amount of nutrients (N and P) and heavy metals (Cd, Cu, Al etc.) was analyzed. However, so far data on conductivity and turbidity of the run-off water according to Table 2 is available. The runoff flow was measured once per minute using an ultrasonic flow meter installed in a manhole of a sewer pipe at the catchment outlet. The amount of runoff differed clearly between the three catchment areas (Figure 13). Especially the high-density site showed extensive stormwater flows – even at times when the precipitation was low. The monthly total (cumulative) runoff was about seven times larger in the high-density area as compared to the low-density area. At the low-density site 7% of the precipitation in November escaped the system via runoff, while in the medium-density and high-density areas the numbers were 38% and 46 %, respectively.

At this stage of our project only a limited set of runoff quality data is available. However, the conductivity data described below can be applied as an indicator for the concentrations of soluble nutrients (e.g. nitrate and phosphate), metals, and chlorides in the water. Water samples were collected during each rain event using an automatic water sampler, but these data are under analysis at the time of writing this report. The conductivity of the runoff water is measured at 10 second intervals during the entire study period (September 2010 to September 2012) using a conductivity sensor. Conductivity, an indicator of e.g. dissolved salts and metals in stormwater, was lowest in the low-density Veräjänmäki catchment and clearly highest in the medium-density area. The stormwater was clearly most turbid in the high-intensity area, followed by medium-intensity area and clearly cleanest in the low-intensity catchment.

Table 2: Precipitation and the amount and quality (conductivity, mS cm^{-1} and turbidity, NTU) of stormwater in the Helsinki catchment sites in November 2010.

November 2010	**SITE**		
	Itä-Pasila (high-intensity)	**Pihlajamäki** (medium-intensity)	**Veräjänmäki** (low-intensity)
Precipitation (mm)	89*	89*	89*
Stormwater runoff (mm)	35,1	30,2	5,1
Median runoff conductivity	0,5	1,9	0,2
Median runoff turbidity	195,7	9,4	1,4

*) Precipitation value taken from the Kaisaniemi weather station (Finnish Meteorological Institute) ca. 5 km south of the Itä-Pasila catchment.

Figure 12. The proportion of impervious (Asphalt, Buildings, Paved (such as tiled surfaces) area and Rock cover) and pervious (Trees, Other green and Sand) surfaces in the sub-catchment areas in Helsinki. Itä-Pasila = high-density, Pihlajamäki = medium-density, Veräjämäki = low-density areas.

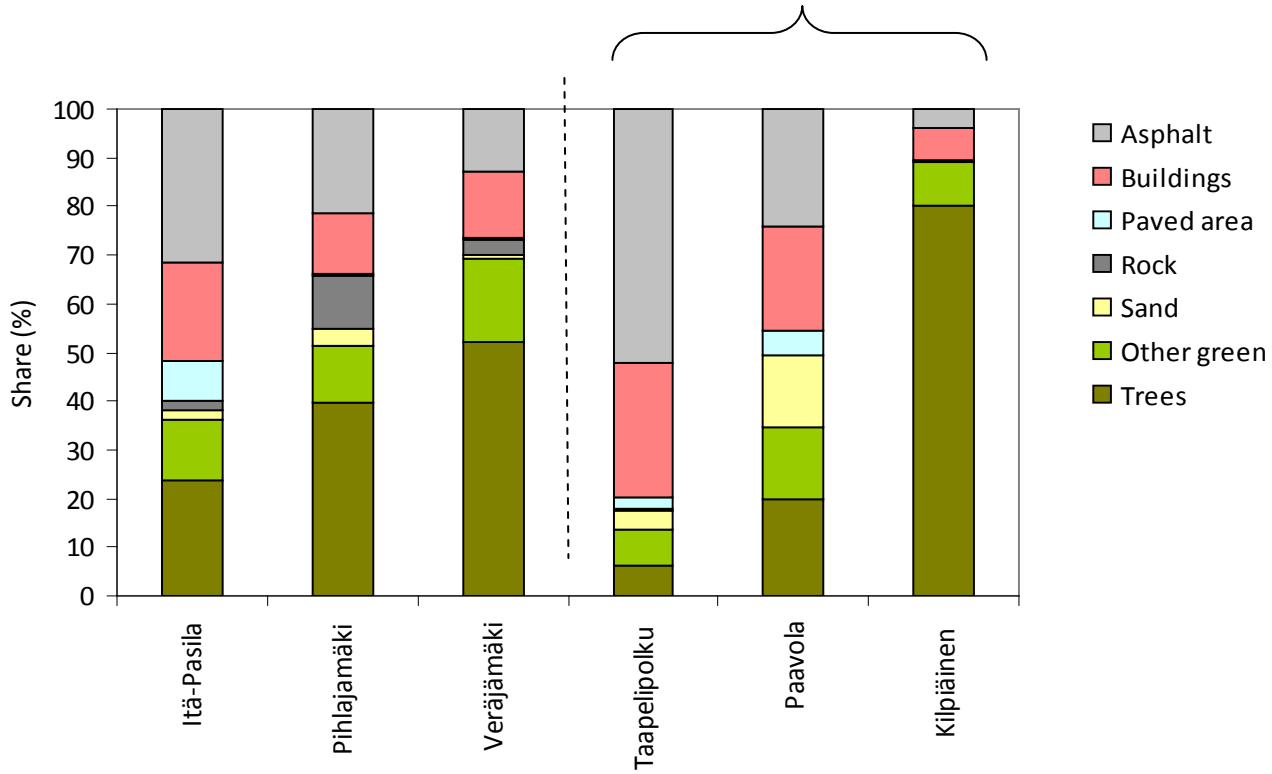

I

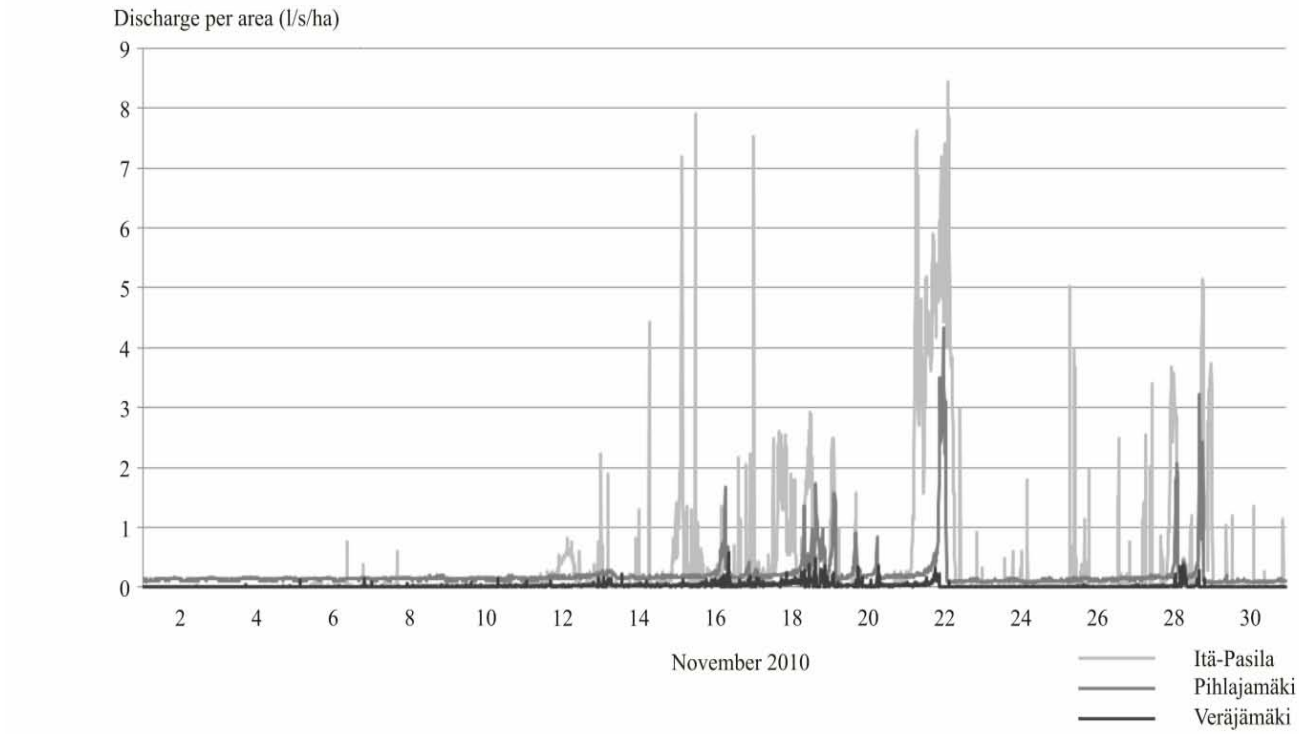

Figure 13. Stormwater flow (l s^{-1} ha^{-1}) at the three catchement sites in Helsinki in November 2010. Itä-Pasila = high-density area (light grey line), Pihlajamäki = medium-density area (medium-grey line) and Veräjämäki = low density area (dark line).

7. ACASA modeling_Helsinki

The Advanced-Canopy-Atmosphere-Soil Algorithm (ACASA) model is a SVAT (Soil-Vegetation-Atmosphere- Transport) model developed by the University of California, Davis (Pyles et al., 2000; 2003). It has been applied by the Euro-Mediterranean Centre for Climate Change (CMCC) over Helsinki case study and used to simulate energy and mass fluxes at the Kumpula measurement site. Turbulent fluxes have been simulated for the year 2008 from January to December, at 30 minute time steps.

In Helsinki, Eddy Covariance (EC) data were collected at the Kumpula measurement site (5 Km from the city center) by the University of Helsinki. A deciduous forest is present in the area. Meteorological data used to drive the model consisted of air temperature, air pressure, relative humidity, precipitation, and wind speed. Also, short wave and long wave downward radiation data were used to drive the model simulation, and measured CO_2 concentration values were input to initialize the model.

Simulated fluxes were compared with Eddy Covariance flux measurements collected at the Kumpula site in the period January-December 2008. The main results of the analyses are presented here.

Simulated net radiation (Rn) flux perfectly matched the observed flux during the entire year. Examples for three months are given in Fig. 14. The model perfectly reproduced the trend and the magnitude of the observed Rn values. Comparing half-hourly data at annual scale, we observed that simulated and measured values were similar. For example, measured values ranged from -107 Wm^{-2}

to 101 Wm^{-2} in January to -102 Wm^{-2} to 889 Wm^{-2} in June, while simulated values ranged from -92 Wm^{-2} to 126 Wm^{-2} in January and from -77 to 876 Wm^{-2} in June. Figure 15 shows the comparison between simulated and observed half-hourly data during 10 days in June 2008.

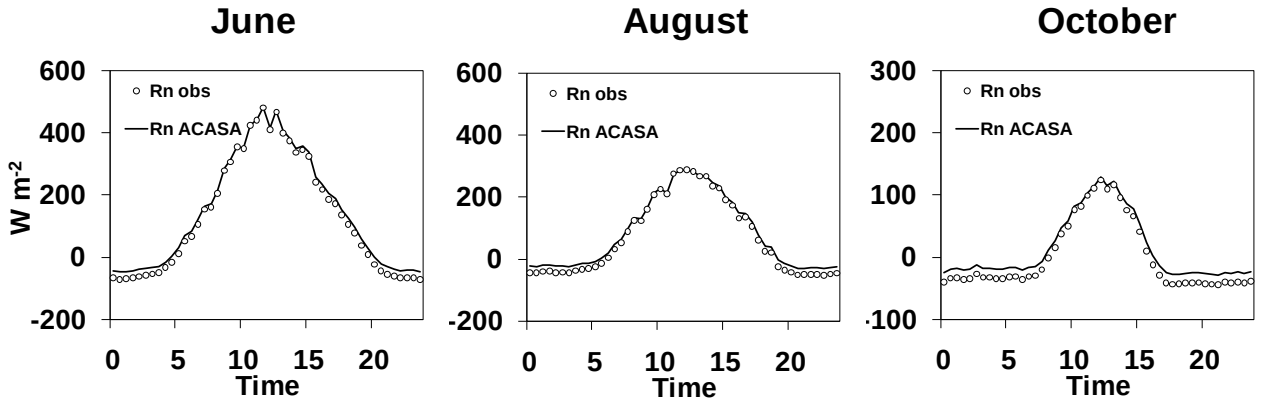

Figure 14. Comparison between simulated (solid line) and observed (dots) net radiation flux (Rn). Data are sorted by time and averaged.

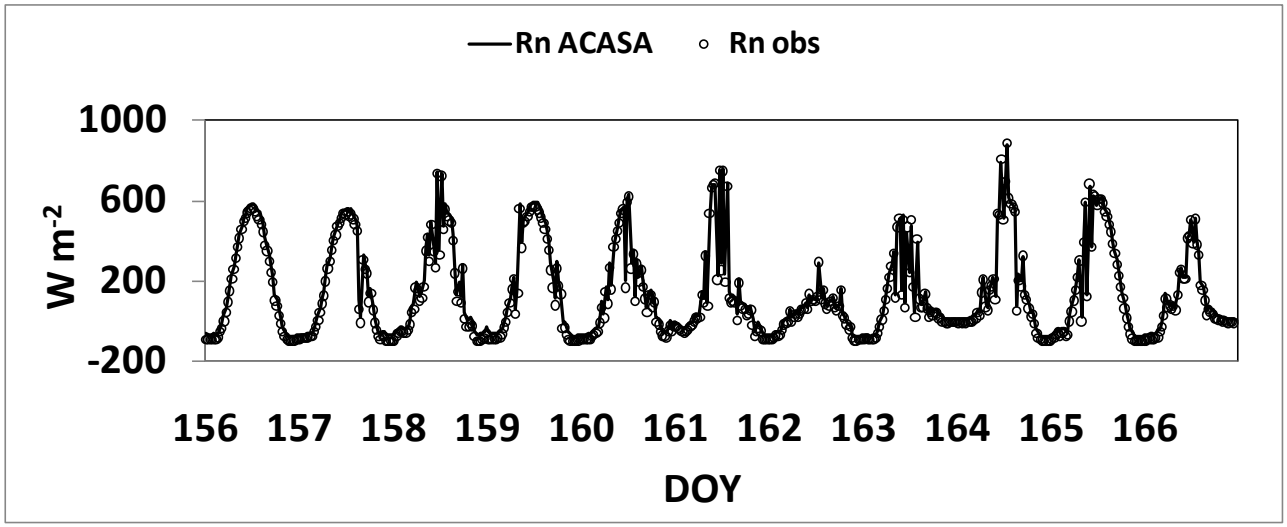

Figure 15. Comparison between half-hourly simulated (solid line) and observed (dots) net radiation flux (Rn) during 10 days in June.

Sensible heat flux (H) was well simulated by the model during the entire period with only small differences (Fig. 16). Similar trend between simulated and observed fluxes was observed confirming the model ability to reproduce the diurnal variation in H flux all over the months.

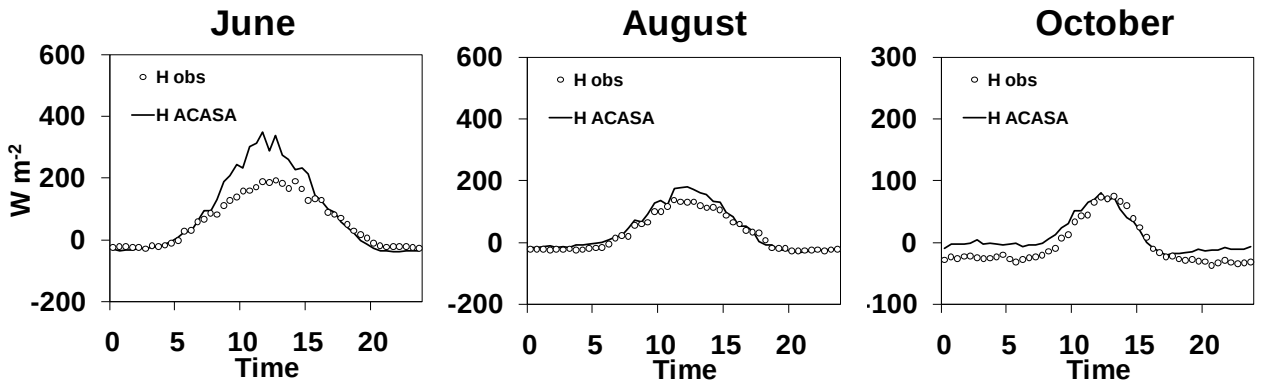

Figure 16. Comparison between simulated (solid line) and observed (dots) sensible heat flux (H). Data are sorted by time and averaged.

A slightly overestimation of H during the central part of the day was observed in March, June, and September. The observed maximum values (at half-hourly time step) in March was 398 Wm^{-2} while the model simulated a value of 580 Wm^{-2}. In June the difference between observed and modeled maximum values was grater with a model overestimation of 267 Wm^{-2}. A week at the end of September is shown in Fig. 17 and the model overestimation is evident in some days. Further investigation are needed in order to better understand the causes of the model overestimation.

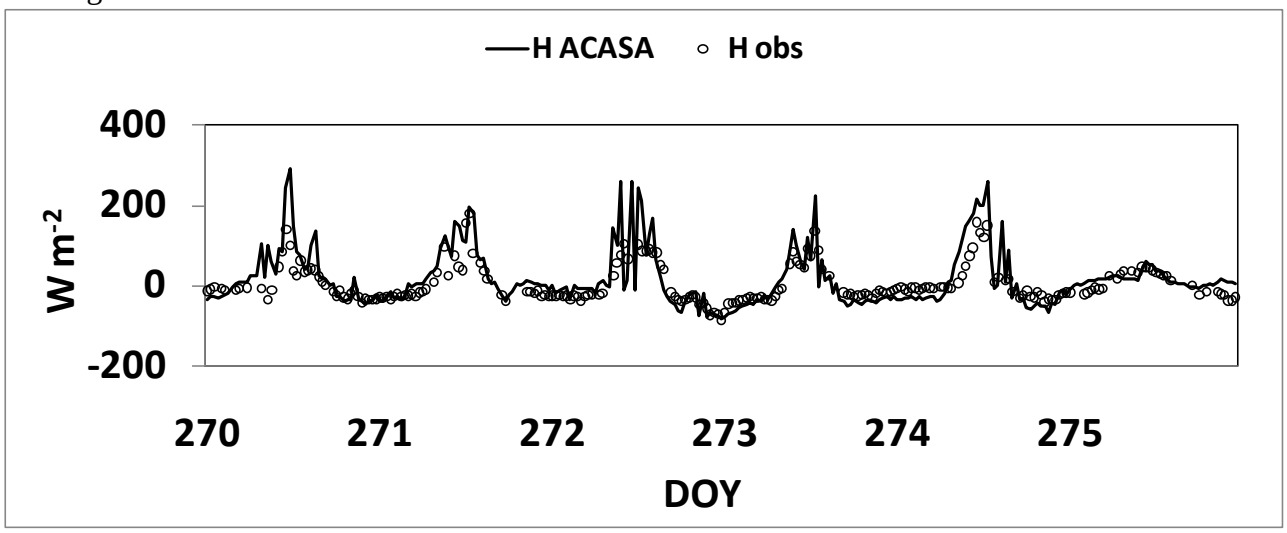

Figure 17. Comparison between half-hourly simulated (solid line) and observed (dots) sensible heat flux (H) during a week at the end of September.

Latent heat flux (LE) simulations matched well the observed flux during the year. In Helsinki, vegetation is present in the investigated area and the model takes it into account in reproducing the trend and magnitude of LE flux all over the year (Fig. 18).

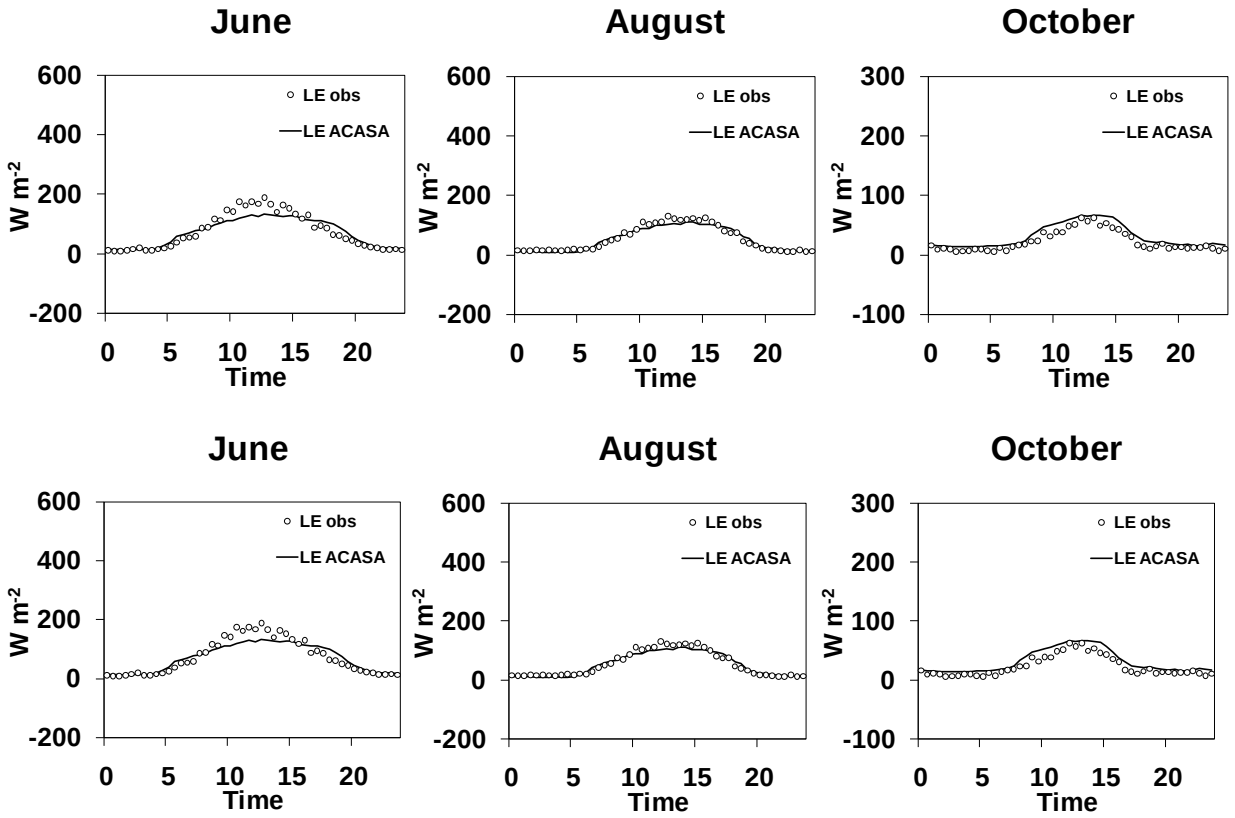

Figure 18. Comparison between simulated (solid line) and observed (dots) latent heat flux (LE). Data are sorted by time and averaged.

Half-hourly values of modeled LE are shown in Fig. 19 for a 10 days period in October. From November to March (when the global radiation forcing is lower), the model slightly overestimated LE both during the day and the night. An average, the overestimation was of about 23.8 Wm^{-2} in maximum half-hourly values and 38 Wm^{-2} in the minimum half-hourly values. In general, we can say that ACASA was able to reproduce the measured LE values with only small differences.

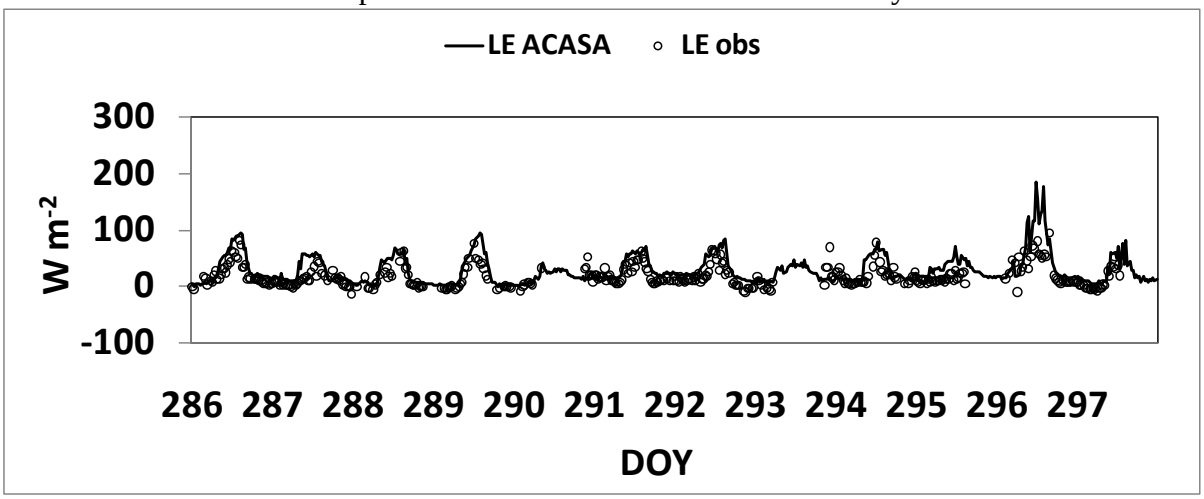

Figure 19. Comparison between half-hourly simulated (solid line) and observed (dots) latent heat flux (LE) during 10 days in October.

In order to simulate the diurnal cycle of carbon flux, the emission curve of CO in Helsinki was used to parameterize the model, and the comparison between simulated and observed net ecosystem exchange is shown in Fig. 20. Also for CO_2 flux, a short period of half hourly data is shown in Fig.

21. In general, the model was able to capture the diurnal trend of CO_2 flux. In addition to the two typical peaks in CO_2 flux in the early morning and late afternoon in correspondence of the rush traffic hour, CO_2 flux produced by vegetation is included. Major differences between observations and model results were observed during the fall, when foliage in the trees fall down. A constant LAI value is set in the model, so adjustment are needed to take into account for LAI seasonality and improve NEE estimation during fall.

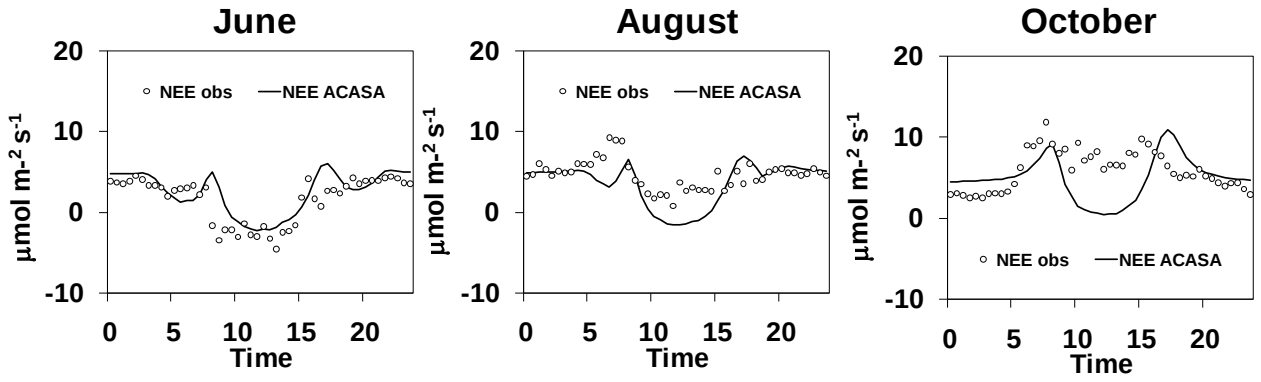

Figure 20. Comparison between simulated (solid line) and observed (dots) net ecosystem exchange (NEE). Data are sorted by time and averaged.

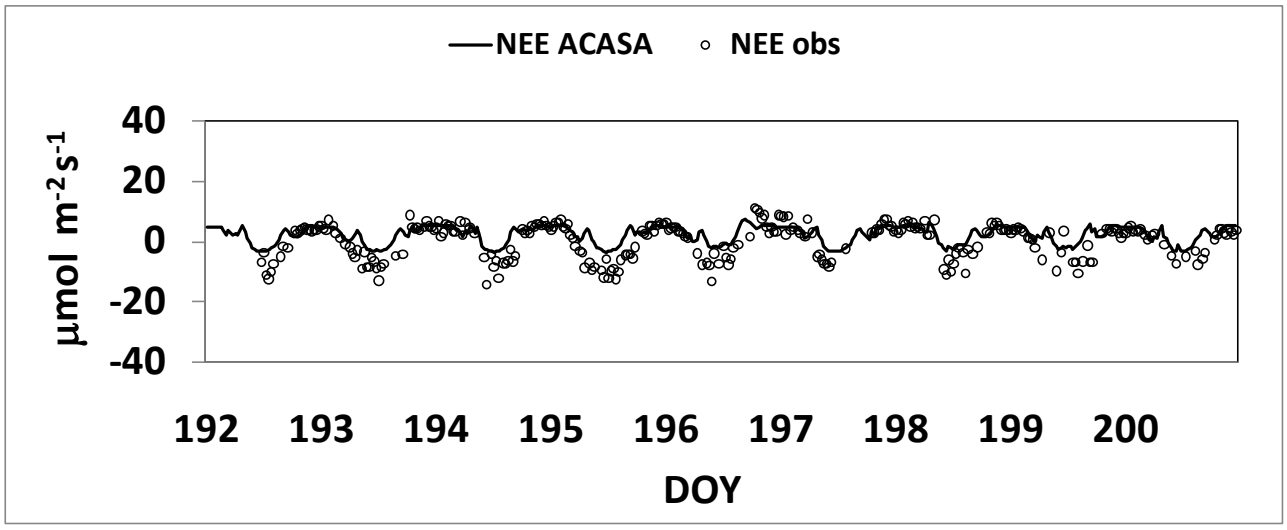

Figure 21. Comparison between half-hourly simulated (solid line) and observed (dots) net ecosystem exchange (NEE) during a week in July.

Table 3. Root mean squared error (RMSE) and relative error (%) per net radiation, sensible, latent and CO_2 flux during the period January-December 2008.

Flux	Range	RMSE	Relative Error (%)	N
Rn (Wm^{-2})	1004	16	1	17284
H (Wm^{-2})	806	72	9	10688
LE (Wm^{-2})	558	37	6	10002
NEE ($\mu molm^{-2}s^{-1}$)	87	6	7	12691

In order to evaluate the model performance, the root mean squared error (RMSE) and the relative error (%) of half-hourly data were calculated both for net radiation, sensible, latent, and CO_2 flux during the period January- December 2008. Values are reported in Table 3. Errors are generally low and the differences in simulated and observed data are not statistically significant at 95 % confidence level. Best results were obtained in simulating the net radiation (Rn), while the error was similar for other fluxes. Further analyses is necessary to better investigate on the small differences between modeled and measured data. Anyway, from these results we can say that the ACASA model could be accurately used to simulate urban fluxes.